

SAFIR2022 – The Finnish Research Programme on Nuclear Power Plant Safety 2019-2022

Final Report

Jari Hämäläinen | Vesa Suolanen (eds.)

**SAFIR2022 –
The Finnish Research
Programme on Nuclear
Power Plant Safety
2019–2022**

Final Report

Jari Hämäläinen & Vesa Suolanen (eds.)



ISBN 978-951-38-8776-6

VTT Technology 414

ISSN-L 2242-1211

ISSN 2242-122X (Online)

DOI: 10.32040/2242-122X.2023.T414

Copyright © VTT 2023

JULKAISETA – PUBLISHER

VTT

PL 1000

02044 VTT

Puh. 020 722 111

<https://www.vtt.fi>

VTT

P.O. Box 1000

FI-02044 VTT, Finland

Tel. +358 20 722 111

<https://www.vtresearch.com>

Preface

The Finnish Research Programme on Nuclear Power Plant Safety 2019–2022, SAFIR2022, continues a series of Finnish national research programmes in nuclear energy that started in 1989. The programmes were initially carried out separately in the fields of operational aspects of safety (YKÄ 1990–1994, RETU 1995–1998) and structural safety (RATU 1990–1994, RATU2 1995–1998, OHA 1995–1998), and then in combined programmes (FINNUS 1999–2002, SAFIR2003–2006, SAFIR2010 2007–2010, SAFIR2014 2011–2014, SAFIR2018 2015–2018). Simultaneously research has been carried out in the national nuclear waste management programmes (KYT2022 in parallel with SAFIR2022).

SAFIR2022 consisted of four main research areas: (1) Overall safety and systemic approach to safety; (2) Reactor safety; (3) Structural safety and materials; and (4) Research infrastructure. Research was carried out annually in around 35 projects that were guided by eight reference groups. The research results of the projects have been published in scientific journals, conference papers and research reports.

The programme management structure consisted of the Management Board, four steering groups managing the research areas, eight reference groups, and programme administration. SAFIR2022 Management Board had representatives of the Radiation and Nuclear Safety Authority (STUK), the Ministry of Economic Affairs and Employment (MEAE), Fennovoima Oy, Fortum, Teollisuuden Voima Oyj (TVO), Technical Research Centre of Finland Ltd (VTT), Lappeenranta-Lahti University of Technology (LUT University), Aalto University (Aalto), and the Swedish Radiation Safety Authority (SSM).

The research in the programme was carried out by VTT, LUT, Aalto, Tampere University of Technology (TAU), Finnish Meteorological Institute (FMI), Finnish Institute of Occupational Health (FIOH), University of Helsinki (Institute of Seismology, ISUH), RISE Research Institute of Sweden, and AFRY Finland Oy. A few subcontractors also contributed to the work in the projects.

This report has been prepared by the programme management in cooperation with the project leaders and project staff. More information about SAFIR2022 can be found on the programme website <http://safir2022.vtt.fi/>. Finnish national research on nuclear power plant safety continues in SAFER2028 programme for the years 2023–2028, see <https://safer2028.fi/>.

Contents

Preface.....	3
1 Introduction.....	6
1.1 SAFIR2022 and Finnish nuclear safety research	6
1.2 Research areas and projects.....	8
1.3 Financial and statistical information.....	13
2 Overall Safety and Organisation	20
2.1 Building operational readiness of control room crews (BORS).....	20
2.2 Development of framework for justification of overall safety (OSAFE)	32
2.3 Participative development for supporting human factors in safety (PARSA).	43
2.4 Effective improvement of leadership and safety culture (EPIC).....	54
3 Plant Level Analysis.....	62
3.1 Co-simulation model for safety and reliability of electric systems in a flexible environment of NPP (COSI)	62
3.2 New developments and applications of PRA (NAPRA)	82
3.3 Predicting extreme weather and sea level for nuclear power plant safety (PREDICT)	100
3.4 Safety and security assessment of overall I&C architectures (SEARCH).....	117
3.5 Uncertainty management in fire risk analyses (URAN).....	147
4 Reactor and fuel	173
4.1 Coupled analysis of transient scenarios (CATS)	173
4.2 Interdisciplinary fuels and materials (INFLAME).....	187
4.3 Developing the working arms of Kraken, the next generation computational framework for reactor design and licensing analyses (LONKERO)	207
4.4 Radiation shielding and criticality safety analyses (RACSA)	227
4.5 Enhanced multi-physics calculation capabilities for fuel behaviour and reactor analyses (EMBER)	245
5 Thermal Hydraulics	252
5.1 CFD methods for reactor safety assessment (CFD4RSA).....	252

5.2	Passive heat exchanger experiments (PAHE).....	274
5.3	PWR PACTEL tests (PATE).....	280
5.4	Sparger separate effect tests (SPASET)	297
5.5	Safety through thermal-hydraulic analyses and cooperation (THACO) ...	309
5.6	Containment safety research (CONTSA)	322
5.7	Critical flow separate effect test facility (CRITFLOW).....	333
6	Mechanical Integrity	348
6.1	Advanced materials characterisation for structural integrity assessment (AMOS).....	348
6.2	Effect of long-term operation on aging and environmentally assisted cracking of nuclear power plant component materials (ELIAS)	361
6.3	Extended lifetime of structural materials through improved water chemistry (ELMO).....	370
6.4	Fatigue and evolving assessment of integrity (FEVAS).....	384
6.5	Reactor pressure vessel repair welding collaboration (FENIX).....	392
6.6	Non-destructive examination of NPP primary circuit components and reliability of inspection (RACOON)	401
6.7	Fatigue Management for LTO (FATIMA)	414
7	Structures and materials	432
7.1	Additive manufacturing in nuclear power plants (AM-NPP).....	432
7.2	Critical studies in support of the ageing management of NPP concrete infrastructure (CONAGE).....	450
7.3	Modelling of aged reinforced concrete structures for design extension conditions (CONFIT).....	479
7.4	Safety criteria and improved ageing management research for polymer components exposed to thermal-radiative environments (SAMPO)	492
7.5	Valorisation of probabilistic seismic hazard results in Finland (VALERI) .	506
8	Severe Accidents.....	517
8.1	Analytical severe accident research (ANSA)	517
8.2	Mitigation and analysis of fission products transport (MANTRA)	534
9	Research Infrastructure	547
9.1	Barsebäck reactor pressure vessel material used for true evaluation of embrittlement (BRUTE)	547
9.2	Infrastructure development at LUT safety research laboratory (IDEAL) ..	573
9.3	Participation in the Jules Horowitz Reactor Project (JHR2022)	603
9.4	Radiological laboratory facility costs of the Centre for Nuclear Safety (RADCNS)	608

1 Introduction

1.1 SAFIR2022 and Finnish nuclear safety research

The Finnish Nuclear Power Plant Safety Research Programme 2019–2022, SAFIR2022, was a 4-year national technical and scientific research programme on the safety of nuclear power plants. The programme was funded by the Finnish State Nuclear Waste Management Fund (VYR), as well as other key organisations operating in the area of nuclear energy. The programme provided conditions for maintaining expertise needed for ensuring the continuance of safe use of nuclear power, for developing new expertise, and for participation in international co-operation. Major part of Finnish public research on nuclear power plant safety during the years 2019–2022 was carried out in the SAFIR2022 programme.

In accordance with the Finnish Nuclear Energy Act, the objective of SAFIR2022 was to ensure that should new matters related to the safe use of nuclear power plants arise, the authorities possess sufficient technical expertise and other competence required for rapidly determining the significance of the matters. High scientific quality was required of the research projects in the programme and the results were published.

The SAFIR2022 programme's planning group, nominated by the Ministry of Economic Affairs and Employment in November 2017, defined the following mission for national nuclear safety programmes:

National nuclear safety research aims at high national nuclear safety assessment capability. It develops and creates expertise, experimental facilities as well as computational and assessment methods for solving future safety issues in close cooperation with competent international partners.

The vision of SAFIR2022 was defined as follows:

The SAFIR2022 research community is a vigilant, internationally recognised and strongly networked competence pool that carries out research on topics relevant to the safety of Finnish nuclear power plants on a high scientific level and with modern methods and experimental facilities.

The Framework Plan [1] describes the research to be carried out in SAFIR2022. The new programme essentially covers the themes of the preceding SAFIR2018 programme [2].

The total volume of the research and administration projects in the SAFIR2022 programme in 2019–2023 was 25,0 M€ and 168 person years. The main funding organisations were the Finnish State Waste Management Fund (VYR) with 16,4 M€ and VTT Technical Research Centre of Finland Ltd (VTT) with 4,9 M€. Research projects of SAFIR2022 were chosen on the basis of annual call for proposals and in 2022, research was carried out in 35 projects. The results are utilised by the Radiation and Nuclear Safety Authority (STUK), Teollisuuden Voima Oyj (TVO) and Fortum, in addition to the research organisations carrying out the projects. However, international co-operation is involved in most of the projects and thus the results are more widely utilised also by the international partners.

In addition to the funding of the research projects, SAFIR2022 programme involved special funding for the VTT Centre for Nuclear Safety (CNS). In 2019–2022, the research equipment investments were funded by 5,7 M€ (RADINFRA project) and laboratory facility by 8,0 M€ (RADCNS project). KYT2022 programme also funded the two projects with 4,3 M€. Thus, the total volume of the SAFIR2022 programme in 2019–2022, including the research projects and infrastructure development, was 38,6 M€.

VYR funding is collected from the Finnish utilities Fennovoima Oy (until 31.12.2022), Fortum and Teollisuuden Voima Oy based on their MWth shares in Finnish nuclear power plants (units in operation, under construction, and in planning phase according to the decisions-in-principle). In addition to VYR, other key organisations operating in the area of nuclear safety also funded the programme.

International co-operation was an essential part of the SAFIR2022 programme. Participation in several OECD Nuclear Energy Agency (NEA) projects was one of the key international activities. Further, international contacts included co-operation with Swedish organisations within Energiforsk and the Nordic Nuclear Safety Research (NKS), and participation in other international experimental research programmes and activities (NUGENIA, US NRC, IAEA, EPRI, DEBORA, SILENCE, COST). Several projects in Euratom Fission Programme complementing Horizon 2020 also had connections to research carried out in SAFIR2022.

National research programmes on nuclear safety have had a significant role in the maintenance of expertise and the training of new experts. Since 1990 the programmes (YKÄ & RATU 1990–1994, RETU&RATU2 1995–1998, OHA 1995–1998, FINNUS 1999–2002, SAFIR 2003–2006, SAFIR2010 2007–2010, SAFIR2014 2011–2014, SAFIR2018 2015–2018 and SAFIR2022 2019–2022) have had a total volume of 197 M€ and 1 542 person years (Figure1, Table 1).

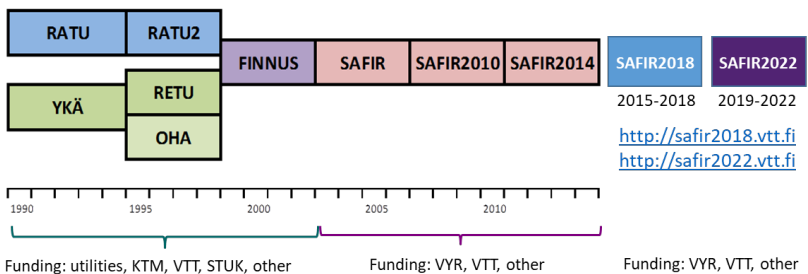


Figure 1. Finnish research programmes on nuclear power plant (NPP) safety. The numbers of SAFIR2018 and SAFIR2022 do not include infrastructure funding.

Table 1. Finnish national research programmes on NPP safety in 1990–2022.

Programme	Volume, M€	Volume, person years	Total number of publications	Academic degrees		
				Dr.	Lic.	M.Sc.
YKÄ 1990–1994	15,4	168	318	6	5	10
RATU 1990–1994	8,2	76	322	1	3	3
RETU 1995–1998	9,8	107	405	3	2	2
RATU2 1995–1998	7,5	60	280	3	4	11
FINNUS 1999–2002	14,4	130	564	6	2	18
SAFIR 2003–2006	19,7	148	545	6	1	17
SAFIR2010 2007–2010	27,5	197	866	8	1	31
SAFIR2014 2011–2014	40,1	279	1244	12	2	27
SAFIR2018 2015–2018	29,6	209	1095	18	0	26
SAFIR2022 2019–2022	25,0	168	838	16	0	25
Total	197,2	1542	6477	79	20	170

The programmes have produced 6477 publications and reports in various categories as well as 79 Doctor, 20 Licentiate and 170 Master level academic degrees. Nuclear safety research continues in the SAFER2028 programme during the years 2023–2028.

1.2 Research areas and projects

Research in SAFIR2018 was carried out according to the research needs described in the Framework Plan [1], the Annual Plans [6] and decisions of the Management Board. Guidance on programme practices was given in the Operational management handbook [3]. The research in many topics was based on results of SAFIR2018 programme [2].

SAFIR2022 had four main research areas that were managed by the steering groups (SG1-SG4): SG1 Overall safety and systemic approach to safety, SG2 reactor safety, SG3 Structural safety and materials, and SG4 Research infrastructure (see <http://safir2022.vtt.fi/>). The research areas were defined in the SAFIR2022 Framework plan [1] as follows.

The *Overall safety and systemic approach to safety (SG1)* includes a wide range of nuclear safety research areas that overarch between several topics, as well as topics affecting the nuclear power plant as a whole. Such topics include the concept of overall safety itself, organisational issues, automation architecture, control room design and operations, human factors, external hazards, safety and security interfaces, electrical systems, setting the safety requirements, and controlling the plant design throughout its lifetime.

Reactor safety (SG2) research focuses on the development of experimental and computational methods aimed at ensuring that a nuclear facility and its systems are able to implement the safety requirements set for them. The research questions focus on the fundamental safety aspects and on an understanding of the behaviour of nuclear fuel, plant processes and plant systems in both normal and abnormal situations, including phenomena relevant to accident progression and the resulting consequences. In addition to general method development for complex physical phenomena, the tools need to be validated and the uncertainties managed. Important topics are also severe accident analysis and management, internal and external hazards, including the fire risks analysis and phenomena related to the climate change and fuel research. (In the beginning of the programme, the topics related to fire risks and climate phenomena were included in the SG1 area.)

The aim of research on *Structural safety and materials (SG3)* is to increase knowledge that supports the long-term and reliable use of the nuclear power plants, particularly with respect to matters involving the integrity of barriers or material issues that affect the reliability of the safety functions. The research targets the ageing phenomena of the existing devices and structures and the correctly timed management of their progress. Attention is also paid to the utilisation of structure- and device-specific ageing information and the operative capability of the devices and structures in exceptional conditions. The research topics include ageing (metallic, concrete, polymer, water chemistry, automation systems), non-destructive testing (NDT, metallic and concrete), structural safety analysis, preparation for new technologies and new material solutions.

Research infrastructure (SG4) related research is funded in order to ensure modern research facilities and equipment. Domestic infrastructure is vital for the maintenance and enhancement of national competences. It is also useful for leveraging international experimental capabilities for national needs. The safety assessment of nuclear power plants requires deep knowledge about physical processes taking place inside the plant systems, structures, and components. Such knowledge ultimately rests on representative experimentation and physical modelling. A similar understanding is also needed for the assessment of operational safety and plant ageing. Up-to-date research capabilities should satisfy the needs of both existing and future power plants and other nuclear facilities. The strong

infrastructure development phase in the SAFIR programmes started with the development of VTT research capabilities realising the VTT Centre for Nuclear Safety. The next phase will be to continue the development of thermal hydraulic facilities at LUT University.

Research in SAFIR2022 was carried out under the guidance of eight reference groups:

1. Overall safety and organisation
2. Plant level analysis
3. Reactor and fuel
4. Thermal hydraulics
5. Mechanical integrity
6. Structures and materials
7. Severe accidents
8. Research infrastructure.

The results achieved by all SAFIR2022 projects in each year and the summaries of the research plans for the next year are reported in the annual reports and plans (e.g., [5] and [6]). The Interim report [4] summarises the results of 2019–2020.

Table 2 shows the actualised costs and volumes of SAFIR2022 projects in 2019–2023.

Table 2. SAFIR2022 projects 2019–2022.

Project	Acronym Years	Participating organisations	Funding k€	Person years
1. Overall safety and systemic approach to safety				
Building operational readiness of control room crews: preparing for the unexpected	BORS 2019–2022	VTT, FIOH	528	4,4
Co-simulation model for safety and reliability of electric systems in flexible environment of NPP	COSI 2019–2022	VTT, Aalto	618	4,7
New developments and applications of PRA	NAPRA 2019–2022	VTT	690	4,5
Development of framework for justification of overall safety	OSAFE 2019–2022	VTT, LUT	346	3,2
Participative development for supporting human factors in safety	PARSA 2019–2022	FIOH, VTT	353	2,6
Predicting extreme weather, sea level and atmospheric dispersion for nuclear power plant safety	PREDICT 2019–2022	FMI	851	7,4
Safety and security assessment of overall I&C architectures	SEARCH 2019–2022	VTT, Aalto	1402	11,2
Uncertainty management in fire risk analyses	URAN 2019–2022	VTT, Aalto	875	7,6
Effective improvement of leadership and safety culture	EPIC 2020–2022	VTT	156	1,1
Small Modular Nuclear Reactors (SMRs), Siting and Waste Management	SMRSIMA 2022	VTT, GTK	83	0,6

Project	Acronym Years	Participating organisations	Funding k€	Person years
2. Reactor safety				
Analytical severe accident research	ANSA 2019–2022	VTT	920	5,5
Coupled analysis of transient scenarios	CATS 2019–2022	VTT	622	4,8
CFD methods for reactor safety assessment	CFD4RSA 2019–2022	VTT	797	4,8
Interdisciplinary fuels and materials	INFLAME 2019–2022	VTT	781	5,4
Developing the working arms of Kraken, the next generation computational framework for reactor design and licensing analyses	LONKERO 2019–2022	VTT	1018	8,8
Mitigation and analysis of fission products transport	MANTRA 2019–2022	VTT	559	2,8
Passive heat exchanger experiments	PAHE 2019–2020	LUT	252	2,2
PWR PACTEL tests	PATE 2019–2022	LUT	833	6,0
Radiation shielding and criticality safety analyses	RACSA 2019–2022	VTT	641	4,9
Sparger separate effect tests	SPASET 2019–2020	LUT	293	2,5
Safety through thermal-hydraulic analyses and co-operation	THACO 2019–2022	VTT	838	5,5
Enhanced multi-physics calculation capabilities for fuel behaviour and reactor analyses	EMBER 2019–2022	LUT	139	1,4
Fuel microstructure and radium solubility	PORA 2020–2021	VTT	198	1,4
Containment safety research	CONTSA 2021–2022	VTT	214	1,3
Sub-Channel Analysis of Reflooding Phenomena	SCARP 2021	VTT	57	0,4
Critical flow separate effect test facility	CRITFLO 2022	LUT	45	0,4
3. Structural safety and materials				
Additive manufacturing in nuclear power plants	AM-NPP 2019–2022	VTT, Aalto, LUT	280	1,9
Advanced materials characterisation for structural integrity assessment	AMOS 2019–2022	VTT	641	3,9
Critical studies in support of the ageing management of NPP concrete infrastructure	CONAGE 2019–2022	VTT, Aalto	573	4,0
Modelling of aged reinforced concrete structures for design extension conditions	CONFIT 2019–2022	VTT, TAU	359	2,0
Effect of long-term operation on aging and environmentally assisted	ELIAS 2020–2021	VTT, Aalto, TAU	395	2,6

Project	Acronym Years	Participating organisations	Funding k€	Person years
cracking of nuclear power plant component materials				
Extended lifetime of structural materials through improved water chemistry	ELMO 2019–2022	VTT	573	3,4
Fatigue and evolving assessment of integrity	FEVAS 2020–2021	VTT, Aalto	331	2,1
Non-destructive examination of NPP primary circuit components, machine learning and reliability of inspection	RACOON 2019–2022	VTT, Aalto	623	4,6
Safety criteria and improved ageing management research for polymer components exposed to thermal-radiative environments	SAMPO 2019–2022	VTT, RISE	765	4,2
Fatigue management for LTO	FATIMA 2020–2022	VTT	622	3,4
Cobalt-free hardfacings	NOCO+ 2021	Aalto, VTT	39	0,3
Reactor Pressure Vessel Repair Welding Collaboration	FENIX 2021–2022	VTT, Aalto, TAU	164	1,4
Valorisation of the recent probabilistic seismic hazard projects and results	VALERI 2022	VTT, AFRY, Univ Helsinki	28	0,4
4. Research infrastructure				
Barsebäck RPV material used for true evaluation of embrittlement	BRUTE 2019–2022	VTT	1481	9,6
Infrastructure development at LUT safety research laboratory	IDEAL 2019–2022	LUT	1641	9,6
Participation in Jules Horowitz Reactor project – towards first criticality in 2022	JHR2022 2019–2022	VTT	484	2,6
Pre-emptive reduction of radiological laboratory legacy waste	LABWAST 2019	VTT	309	1,9
Programme administration				
SAFIR2022 Administration	ADMIRE	VTT	1587	4,3
			Total	25004
				167,7

The costs of ADMIRE are actualised until 31.3.2022 and estimated until 31.3.2023.

The costs include subcontracted small study projects (max 100 k€ per year) and value-added tax 24%.

PORA and SMRSIMA projects reported to the KYT2022 programme (see <http://kyt2022.vtt.fi/>).

1.3 Financial and statistical information

The total volume of the SAFIR2022 programme in 2019–2022 was 25,0 M€ and 168 person years. The funding partners were VYR with 16,443 M€, VTT with 4,944 M€, LUT University with 0,869 M€, Aalto University with 0,511 M€, NKS with 0,449 M€, SSM with 0,181 M€ and Halden Reactor Project in-kind with 0,106 M€. In addition to their shares of the collected VYR funding, TVO, Fortum and Fennovoima directly funded specified projects with 0,277 M€, 0,166 M€ and 0,037 M€, respectively. Several other partners funded different projects by 1,021 M€ in total. The funding proportions of the major funding partners are illustrated in Figure 1. The costs structure of the projects is shown in Figure 2. The personnel costs make up the major share.

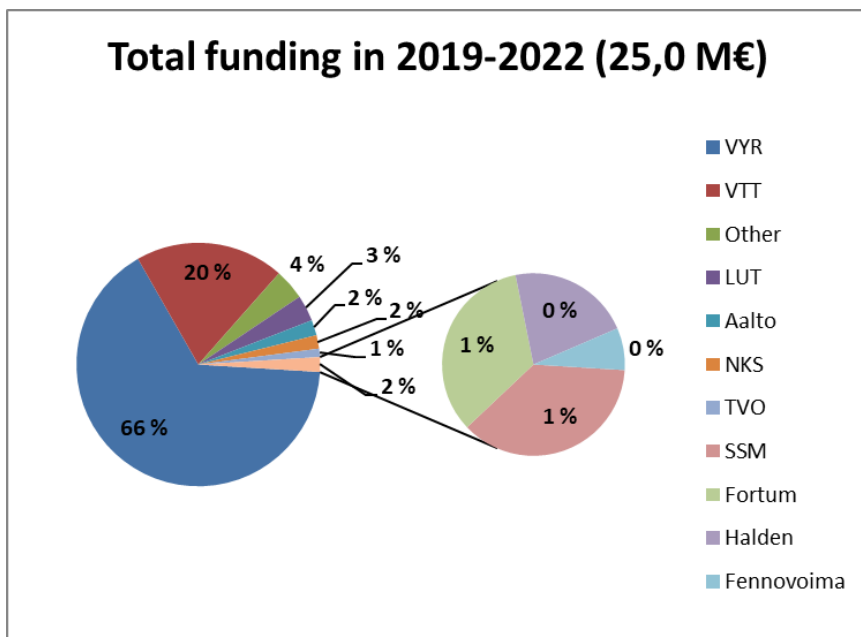


Figure 1. Funding of the SAFIR2022 programme in 2019–2022.

Figures 3–5 show the funding and volumes of SAFIR2022 research areas in 2019–2022. In the area Research infrastructure (SG4) and also in SG3 area the share of person-years was lower than the share of total funding because of infrastructure investments and other costs related to experimental work (Figures 3–4). In SG1 and SG2 the shares of the person-years were bigger than the shares of the total funding, respectively.

The total funding of the research projects decreased from 6,4 M€ in 2019 to 5,4 M€ in 2022 which can be seen in Figure 5. However, the total funding of SG3 area projects did not decrease.

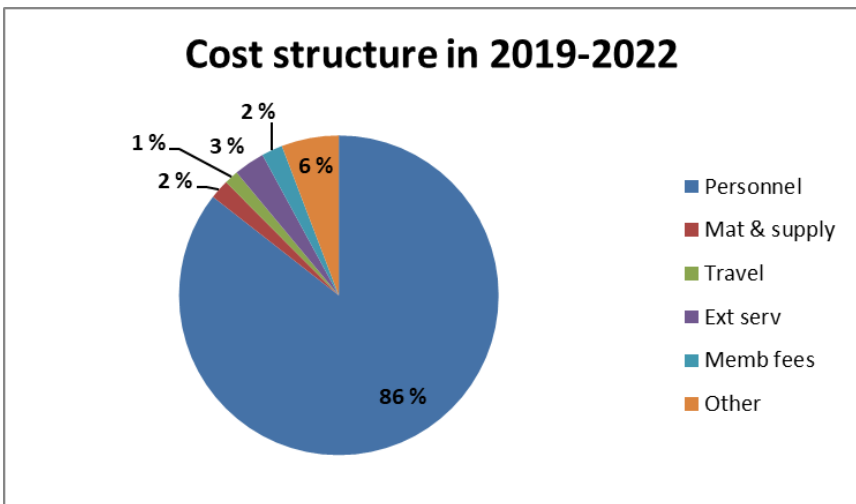


Figure 2. Cost structure of SAFIR2022 in 2019–2022.

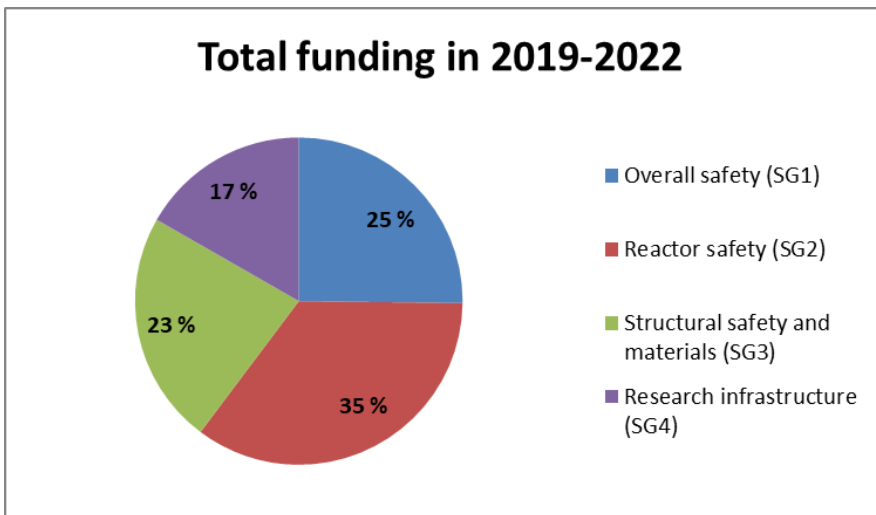


Figure 3. Division of funding to the research areas in 2019–2022.

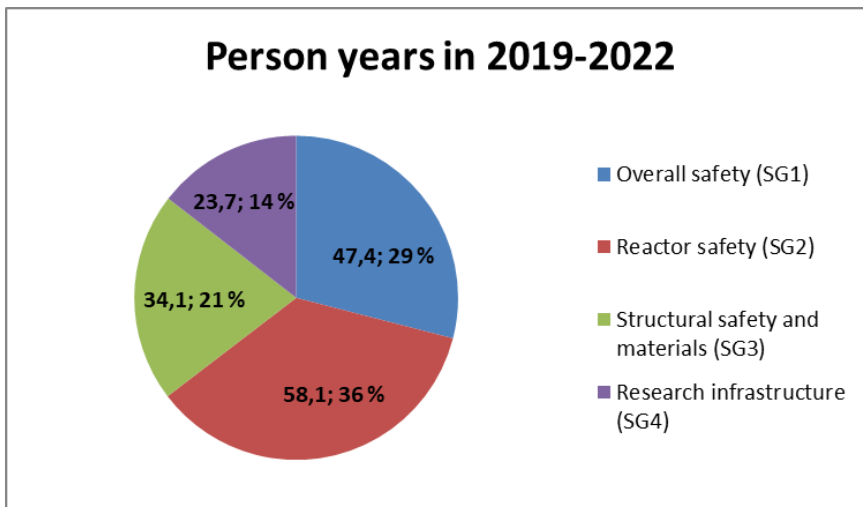


Figure 4. Volumes of the research areas in 2019–2022.

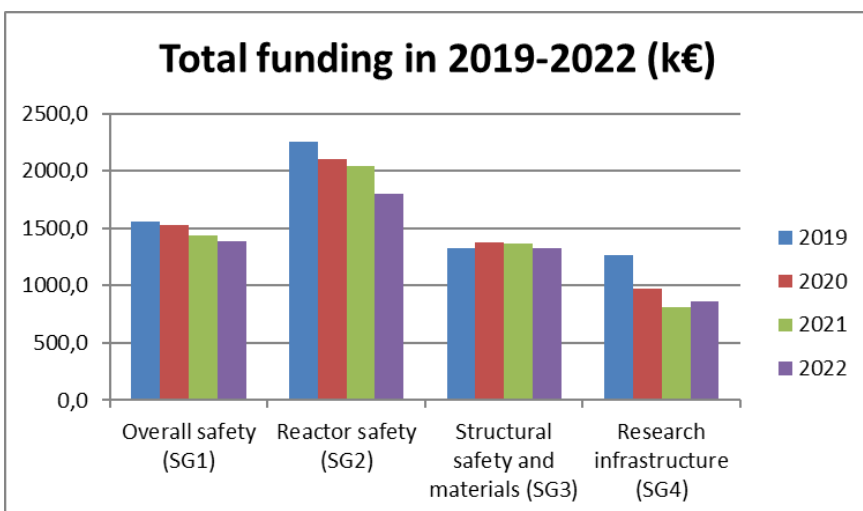


Figure 5. Total funding of the research areas in 2019–2022.

The research projects of the programme have produced 644 publications and 182 other deliverables (“Others”) in 2019–2022 (Table 3). Major part of the publications consisted of public research reports and conference articles. A total of 135 scientific journal articles and dissertations were made. The average number of publications in the research projects was 3,9 per person year (“Others” excluded), and the average number of scientific journal articles and dissertations was 0,83 per person year. The projects had different scopes and there were also clear differences in the

number of publications between the projects even when the project volumes are considered. Some projects also mainly published the results as research reports that allow more extensive reporting and are useful for the end-users of the results of certain research areas.

Table 3. Publications in the SAFIR2022 projects in 2019–2022.

Projects	Volume (person years)	Publications					Total
		Research reports	Scientific journal articles	Conference articles	Theses	Others	
Total	168	344	119	151	41	183	838
BORS	4,4	2	6	11	1	31	51
COSI	4,7	10	2	1	1	2	16
NAPRA	4,5	20	3	3	0	0	26
OSAFE	3,2	2	2	1	3	3	11
PARSA	2,6	0	2	5	0	20	27
PREDICT	7,4	1	13	17	8	23	61
SEARCH	11,2	4	6	16	2	3	31
URAN	7,6	10	10	1	1	2	24
EPIC	1,1	2	0	2	0	0	4
ANSA	5,5	11	4	1	1	21	38
CATS	4,8	11	0	2	1	6	20
CFD4RSA	4,8	22	4	3	0	1	30
INFLAME	5,4	17	3	5	2	9	36
LONKERO	8,8	5	10	15	3	5	38
MANTRA	2,8	14	5	4	0	4	27
PAHE	2,2	5	0	0	0	0	5
PATE	6,0	15	2	1	0	0	18
RACSA	4,9	11	8	6	1	8	34
SPASET	2,5	4	2	1	1	0	8
THACO	5,5	11	2	1	2	0	16
EMBER	1,4	3	1	1	1	0	6
PORA	1,4	2	0	0	0	1	3
CONTSA	1,3	3	0	0	1	0	4
SCARP	0,4	1	0	0	0	0	1
CRITFLOW	0,4	1	0	0	0	10	11
AM-NPP	1,9	7	2	0	0	0	9
AMOS	3,9	11	7	1	1	0	20
CONAGE	4,0	18	1	14	3	0	36
CONFIT	2,0	7	3	4	0	0	14
ELIAS	2,6	3	1	6	0	2	12
ELMO	3,4	15	3	0	2	0	20
FEVAS	2,1	3	2	6	2	0	13

Projects	Volume (person /years)	Publications					Total
		Research reports	Scientific journal articles	Conference articles	Theses	Others	
FENIX	1,4	2	0	1	1	2	5
RACOON	4,6	8	6	0	1	3	18
SAMPO	4,2	26	2	0	1	0	29
FATIMA	3,4	1	0	10	0	1	12
NOCO+	0,3	1	1	0	0	0	2
VALERI	0,4	1	0	1	0	0	2
BRUTE	9,6	21	5	4	1	7	38
IDEAL	9,6	10	0	3	1	1	18
JHR2022	2,6	5	1	3	0	15	24
LABWAST	1,9	7	0	1	0	2	10
ADMIRE	4,3	11	0	0	0	1	12

See Table 2 for the durations and budgets of the projects.

Altogether 41 higher academic degrees were obtained in the research projects in 2019–2022: 16 Doctoral degrees and 25 Master's degrees (Table 3).

Table 4. Academic degrees obtained in the projects in 2019–2022.

Project	Doctor	Master
BORS		1
COSI		1
OSAFE		3
PREDICT	7	1
SEARCH	1	1
URAN	1	
ANSA		1
AMOS	1	1
CATS		1
INFLAME		2*
LONKERO		2**
RACSA		1
EMBER	1	
THACO		1
CONTSA		2
SPASET	1	
CONAGE		3
ELMO		2
FEVAS	2	
RACOON		1

Project	Doctor	Master
SAMPO	1	
BRUTE		1
IDEAL	1	

*) One Master's thesis together with the LONKERO project.

**) One Master's thesis together with the RACSA project.

Structure of the report

This report describes on the main results of the projects during 2019–2022. Chapters 2–9 include summaries of the projects in the eight reference groups of SAFIR2022. More detailed statistical information of the programme and lists of project publications can be found in the annual reports on SAFIR2022 website.

Acknowledgements

The results of the SAFIR2022 programme during 2019–2022 have been produced by all who have been involved in the research projects. Their work is highly esteemed.

The contributions of project managers and researchers that form the essential contents of this report are acknowledged with gratitude.

The work of the persons in the Management Board, the steering groups and the reference groups that has been carried out with the expense of their own organisations is highly appreciated.

Jari Hämäläinen and Vesa Suolanen

References

- [1] National Nuclear Power Plant Safety Research 2019-2022. SAFIR2022 Framework Plan. Publications of the Ministry of Economic Affairs and Employment, Energy 22/2018. 101 p. ISBN: 978-952-327-314-6. <http://urn.fi/URN:ISBN:978-952-327-314-6> (available on <http://safir2022.vtt.fi/>).
- [2] Hämäläinen, J. & Suolanen, V. (eds.) SAFIR2018 – The Finnish Research Programme on Nuclear Power Plant Safety 2015-2018. Final Report. VTT, Espoo, 2019. VTT Technology 349. 498 p. ISBN 978-951-38-8682-0 (available on <http://safir2018.vtt.fi/>).
- [3] SAFIR2022 – The Finnish Research Programme for Nuclear Power Plant safety 2019-2022. Operational Management Handbook. 2019. 19 p + 26 app. <http://safir2022.vtt.fi/>.
- [4] Hämäläinen, J. & Suolanen, V. (eds.) SAFIR2022 – The Finnish Research Programme on Nuclear Power Plant Safety 2019-2022. Interim Report. VTT, Espoo, 2021. VTT Technology 383. 472 p. ISBN 978-951-38-8743-8, DOI: 10.32040/2242-122X.2021.T383. <https://www.vtresearch.com/sites/default/files/pdf/technology/2021/T383.pdf> (available on <http://safir2022.vtt.fi/>).
- [5] Hämäläinen, J. & Suolanen, V. (eds) SAFIR2022 Annual Report 2022. Research Report VTT-R-00192-23. 141 p + 41 app (available on <http://safir2022.vtt.fi/>).
- [6] Hämäläinen, J. & Suolanen, V. (eds) SAFIR2022 Annual Plan 2022. Research Report VTT-R-00216-22. 50 p (available on <http://safir2022.vtt.fi/>).

2 Overall Safety and Organisation

2.1 Building operational readiness of control room crews (BORS)

Jari Laarni¹, Hanna Koskinen¹, Marja Liinasuo¹, Tuisku-Tuuli Salonen¹, Satu Pakarinen², Kristian Lukander², Tomi Passi²

¹VTT Technical Research Centre of Finland Ltd
P.O. Box 1000, FI-02044 Espoo

²Finnish Institute of Occupational Health
P.O. Box 40, FI-00251 Helsinki, Finland

Abstract

We investigated the Joint Cognitive System between an operator and nuclear power plant process systems from the perspective of human-system interfaces, procedures, operators' resources for action and skills training.

Our goal was to advance and deepen our understanding of operator practices and cognitive processes in complex incidents and severe accidents and develop tools and methods for the analysis of simulator data and/or promotion of resilience skills assessment and skills training.

We found among others that skillful use of operating procedures is a key to successful performance, field operator training has to be better tailored to their needs, and virtual training environments are especially suitable for training of rarely performed operator tasks. New methods and tools were introduced for HSI and procedure design and simulator training.

Introduction

The BORS project investigated the Joint Cognitive System (JCS) between an operator and nuclear power plant (NPP) process systems from the perspective of human-system interfaces (HSIs), procedures, operators' resources for action and skills training. We advanced and deepened our understanding of resilience skills

and developed specific tools and methods for the analysis of simulator data and/or promotion of resilience skills assessment and skills training. We also promoted our understanding of operator practices and cognitive processes in complex incidents and severe accidents by conducting simulator tests that were unique in a sense that they were either performed in a new kind of environment (i.e., virtual control room or virtual plant settings) or that they addressed topics that had not been widely studied (e.g., stress management and procedure use in complex incidents). Furthermore, we aimed to better understand how the JCS is shaped and evolved, and how cognitive readiness and resilience skills are acquired. Therefore, we developed training material for the advancement of cognitive readiness and resilience skills in operator work.

Skilful use of procedures

In nuclear domain, it is not possible to predict all possible operative situations when designing HSIs and procedures, and therefore, arriving to the optimal solution in these situations requires adaptive problem solving and decision making. To put it another way, there is always a tension between work-as-imagined and work-as-done (Saurin & Wachs, 2018). HSIs and procedures are designed based on how the designers interpret the work of operating personnel – which is only partly based on the work-as-done (Laarni, Tomminen et al., 2020). We have investigated this tension from different vantage points: for example, by analysing the management of a complex incident together with process experts and procedure developers in focus group settings, and by conducting a simulator study in which main control room (MCR) operator crews had to detect, diagnose and correct malfunctions in a training simulator.

Fifty-three operators, comprising 14 operator crews, participated in the simulator study. Two scenarios were included, a minor incident (loss of one coolant pump) and a major incident (failed reactor shutdown), in which there is a risk for a serious accident. We found that stress and workload were lower in the more minor incident involving a loss of a reactor coolant pump, as compared to the more severe incident of a failed emergency shutdown (Pakarinen, Laarni et al., 2020). On the one hand, procedures were applied quite fluently, indicating that usage practices are quite stable in each crew. On the other hand, there was quite much variation in procedure usage practices between crews. The crews which were skilful in using procedures were faster at resolving the incident than those crews who received lower performance scores and thus had some difficulties in using the operating procedures (Pakarinen et al., submitted; Figure 1). According to our findings, an optimal mode of procedure use depends on operator skill level, their ability to manage stress, support provided by HSIs and various contextual factors.

According to operator interviews conducted in connection of the simulator study, the operators were quite satisfied with the present procedures irrespective of whether they are in prose or flowchart format (Laarni, Pakarinen et al., 2021). When one option has to be chosen among several alternatives, operators preferred the

prose format. All in all, it seems to be that the operators are familiar with the procedures available, and the procedures are good enough for the operating purposes.

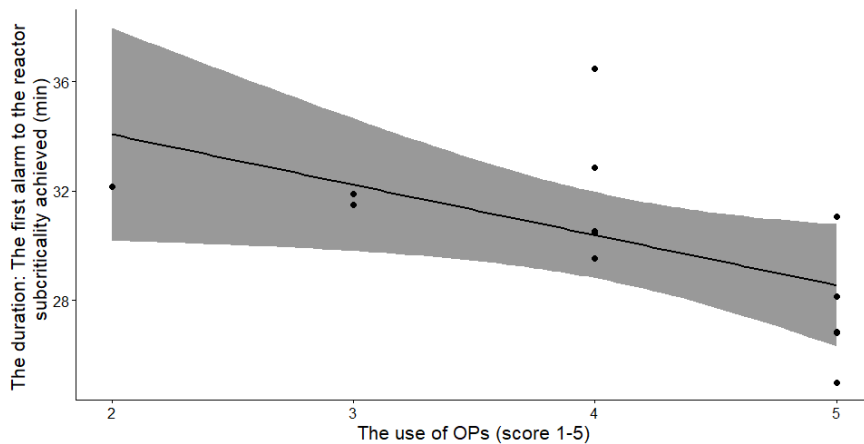


Figure 1. Significant negative association was observed between the use of procedures and performance time.

The analysis of the eye movements revealed that the reactor operators differed in how they devoted their attention to different user interfaces and other objects (Laarni, Pakarinen et. al., 2021). Proportionally, more attention was allocated to computer displays of their workstation, procedures and other operators than to other information sources (e.g., some sections of the operator desk). Higher glance rate to the operating procedures was associated with higher levels of situational awareness (SA), whereas longer glances to other operators and to a particular section of the reactor operator's desk including, e.g., interfaces for manual control rod operation and reactor status monitoring, was associated with lower levels of SA (Laarni, Pakarinen et al., 2021). We also analysed shift supervisors' (SSs) eye movement data by calculating the time between the alarm and the first glance to the procedure and correlating it with the completion time and with the expert evaluation scores. It was found that the sooner the SS looked at the procedure, the faster the situation was resolved. However, no significant correlation was found between the overall gaze duration to the procedure and performance ratings.

Our results suggest that since problem-solving and decision-making are challenged in stressful, demanding and time-critical situations, decision-making support, such as emergency/incident operating procedures, are needed. It is important that operators have needed skills to apply the procedures in practice. Skilful use of procedures includes among others the selection of a suitable procedure, finding the right location of the procedure, fluent reading the procedure and timely execution of actions, and communication among crew members and with other stakeholders.

Skilful use of procedures can support performance in many ways: it promotes retention, decision making and collaboration, and reduces stress and workload. As a precondition, it is important that the procedures are easily available and well-designed.

Procedure development

How do we design good procedures? We have studied this question from two vantage points. First, we developed an analysis framework for the identification of resilience skills that enable intelligent use of procedures (Laarni, Pakarinen et al., 2021). An analysis of critical functions and tasks and their interaction was conducted by using the Functional Resonance Analysis Method (FRAM; Hollnagel, 2012). The results showed that the FRAM methodology was suitable for the analysis of the selected proceduralized activity (Laarni, Tomminen et al., 2020). An iterative ‘zooming in’ approach is to first create an overview FRAM model describing the main functions of the task from the perspective of the nuclear process, and after that, create a more detailed model, looking at the activity from the CR operators’ perspective (Laarni, Tomminen et al., 2020). Some potential variability of the functions was identified – mainly related to the communication and collaboration between operators and between operators and personnel in the field. A summary of the variability associated with some key functions in the failed reactor shutdown scenario is shown in Figure 2.

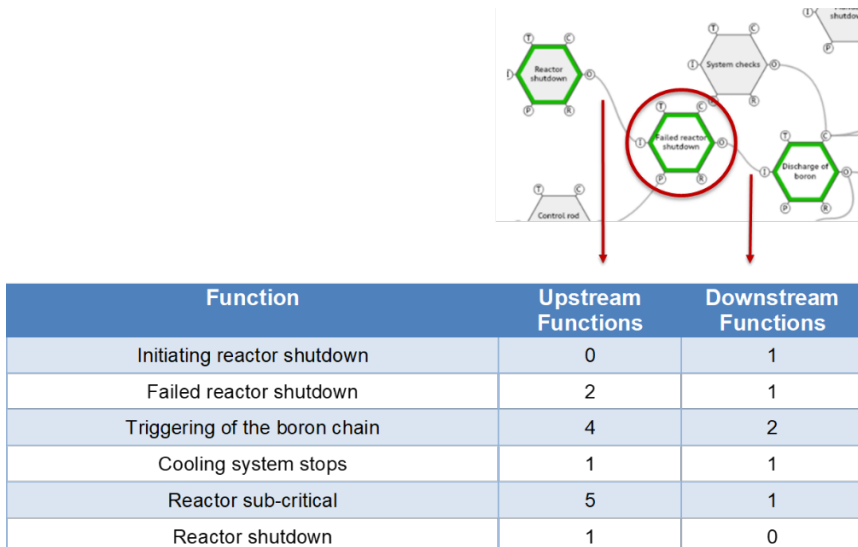


Figure 2. A summary of the variability associated with some key functions in the failed reactor shutdown scenario. A piece of the FRAM model is shown on the top right corner of the figure. Upstream functions have already been completed, and downstream functions follow a particular function (Laarni, Tomminen et al., 2020).

Second, we investigated procedure development practices in two Finnish NPPs. We interviewed procedure developers and other practitioners and analysed the findings using methodological tools of Practice Theory and Cultural-Historical Activity Theory. Based on the interview data, some potential tensions and contradictions in the procedure developers' work were identified, and they are discussed through the lens of Activity Theory (Laarni & Liinasuo, submitted). Procedure development activity can be considered as a social practice, which is in part supported by methodological guidance. The conceptualization of procedure design as a social practice is based on the idea that procedure developers have a freedom to do things differently if needed (Laarni & Liinasuo, submitted).

It was found that it is very difficult to describe in detail the early phases of the procedure development activity (Laarni & Liinasuo, submitted). At these early stages, the project is partly an individual endeavour, partly a collective enterprise of several teams; it is also partly a strictly proceduralised, analytical activity, partly an activity in which both individual and collective creativity is needed (Laarni & Liinasuo, submitted). Typically, the periods of individual versus collaborative and analytical versus creative activity follow each other cyclically.

Even though the procedure development is partly a collective endeavour, there is always the designer in charge, who has to overcome the fear of white paper and outline the first guess. After the first guess has been drafted, it is easier for others to contribute to the design work.

Operator training in virtual reality

Advanced technologies, such as virtual and augmented reality (VR/AR), are nowadays widely applied in a variety of industrial applications and settings (Koskinen et al., 2022). Also in the nuclear domain there has been an increasing interest to study how VR/AR technologies can be applied, e.g., in training, design and HSI evaluation (Pakarinen, Laarni et al., 2020; Pakarinen et al., under revision). We, for example, conducted experimental tests in virtual reality and explored, how VR could promote CR operator and field operator (FOP) training. We also conducted an interview study about the training of field operators in two Finnish NPPs to better understand how the field operators foresee the potential of virtual reality in operator training (Koskinen, Salonen et al., 2022). The interview results were analysed and reflected against the literature review to draw conclusions about the present state of field operator training and about the possible targets for improvement (Koskinen, Salonen et al., 2022).

In both NPPs, the FOPs thought that their training program had improved during the years (Koskinen, Salonen et al., 2022). For example, training has become more systematic, and specific contents had been developed for field operator training. It was thought that VR-based solutions will provide new possibilities for FOP training. In order to appropriately support learning the VR training contents should change and develop over the course of the program. Both Finnish NPPs have already used VR-based solutions, and the FOPs have some experiences on the benefits and

limitations of VR. In the future, the aim is to promote FOP's active participation in VR training, for example, by adding new functionalities to the VR models. In addition, our aim is to conduct experimental studies in which traditional training methods are compared to VR/AR-based training. Overall, since the FOPs had a positive attitude towards VR training, it is worthwhile to continue to develop VR training for field operators.

Some small-scale simulator studies have been conducted in VR. In one study, we conducted a study in a VR CR consisting of some brief incidents and one longer accident situation (Laarni, Liinasuo et al., 2021; Figure 3). Three operator crews participated in this study. In brief incidents operators detected faults that are quite difficult to detect and recognize, diagnosed the fault and started to repair it. The results showed that all the malfunctions were successfully detected and identified with one exception (Laarni, Liinasuo et al., 2020; Laarni, Liinasuo et. al, 2021). The participants were able to construct hypotheses about the cause of the malfunction and make plans on how to test each hypothesis and evaluate the evidence. On the negative side, the participants experienced some problems in problem monitoring and process control due to some technical problems (Laarni, Liinasuo et al., 2020; Laarni, Liinasuo et. al, 2021).



Figure 3. Example image from the virtual simulator environment.

In another study, we investigated the use of virtual reality applications for training of field operation skills and competencies (Pakarinen et al., in preparation). Eight

FOPs conducted rarely performed tasks in which they had to first close and then open a particular valve. Two conditions were compared: in one condition, they received guidance from a CR operator via radio; in another condition, they were able to use an operating procedure embedded in VR. We evaluated the effect of guidance on the task load and user experience and on the usability of the VR environment. It was found that the FOPs rated their task load as lower and their performance as better, when the task was performed under the guidance of the MCR operator than when they completed the task by using the written instruction. The VR learning environment received fairly positive ratings from the participants. In the beginning of the test, the participants had some problems in using the virtual tools, but since the problems were resolved, the tasks were performed fluently. The scores of mission awareness and sense of presence were quite high, indicating that the environment was immersive. The participants also thought that the VR system was easy and intuitive to use even with little or no previous experience in VR. All in all, the results suggest that this type of VR training provides a rather realistic method to learn FOP tasks.

According to our findings, VR has great potential for evaluation and training of operator skills in the nuclear domain (Laarni, Pakarinen et al., 2021). Positive effects depend on how plant facilities and functions have been implemented in VR: If VR experience is immersive and realistic, the user is able to build accurate mental models, transfer the learned skills to actual work, and has an overall positive learning experience (Pakarinen, Laarni et al., 2020; Pakarinen et al., under revision). Training results also depend on level of support and guidance from the trainer, and the trainee's familiarity with the task content.

Human factors issues in flexible operation

In flexible operation, the amount of electrical power output is adjusted to match the current power demand. More advanced control methods may be required to meet flexible operation capability which may, in turn, have implications to human performance (O'Hara et al., 2008). We conducted a couple of interviews to investigate the potential human factors issues that may rise from the more regular application of flexible operation (Koskinen et al., in preparation). Altogether 12 interviews were carried out with relevant stakeholders in the Finnish and Swedish nuclear power industry. Even though we could not find any specific human factors challenges, it was noted that even quite small power adjustments may affect the division of labour and responsibilities between different stakeholders. For example, if power decreases are more frequent, CR operators may have a larger role in reactivity calculations that are currently mainly performed by reactor engineers. It was also found that to better understand the impact of flexible operation on some operative functions (e.g., maintenance) more investigation is required.

In Finland, operating personnel's opinions for and against flexible operation varied quite much. For example, some practitioners seem to think that power manoeuvres are a pleasant change to daily routines, some were against of them.

One reason for these differences may be that operators have varied experience and skills on power manoeuvring. It is especially challenging that power manoeuvres are implemented during the night shift, when CR operators are less vigilant.

In Finland, power manoeuvring typically requires quick decision making at the plant level: a decision on whether to accept the request or to reject it has to be made in less than two hours. It is possible that in old NPPs frequent power manoeuvres lead to equipment failures, the treatment of which may bring about additional load and stress among maintenance personnel and field operators.

All in all, as long as power changes are quite small and infrequent, there is no need for considerable changes regarding, e.g., training, procedure and HSI development, but in case power manoeuvring becomes more frequent, the possible human factors implications of flexible operation have to be more carefully analysed (Koskinen et al., in preparation).

New insights and perspectives on HFE analysis, design and evaluation

Function requirements analysis/allocation and task analysis are some of the key activities in the planning and analysis phase of the HFE program model which have a major impact on all the later HFE activities. Their importance has sometimes undermined, even though the determination of respective roles of operators and automation is one of the most issues in the design of complex systems (Challenger et al., 2013). We conducted a literature review on recent advancements in function requirements analysis/function allocation and task analysis. It was found that as the role of process automation increases, there is a need for new methods and criteria for function allocation and analysis. More sophisticated forms of task analysis are also needed. There is an endeavour to adopt dynamic function allocation (i.e., flexibility in how functions are allocated between the operating team) instead of fixed allocation of functions to resiliently act and respond to a variety of operational situations. Overall, it would be essential to explore optional function allocations and their meaning for the operative whole both in the context of new builds and upgraded plant systems.

We have explored the involvement of operators in the design of HSIs for safety-critical operations of a nuclear power plant during a period of three decades. A careful look at historical turns of operator involvement in one CR design case provided insights promoting a construction of a general account of human-centred design in safety-critical domain (Koskinen; Laarni & Bergroth, 2022). It was found that tightened safety regulations and technological advances have been the main driving force behind the design changes. Simultaneously, operators' increased experiences on the CR systems have made them more capable of commenting the design products and better engaged in their implementation (Koskinen, Laarni & Bergroth, 2022). In this study, we presented examples of participatory design interventions from several phases of the CR life-cycle, discussed the prospects and challenges of user involvement in the design of CR systems and presented some

reflections on them. All in all, the interaction between the end-user and the designer is typically built around concrete mock-ups and prototypes, and it occurs at later phases of the design process (Koskinen, Laarni & Bergroth, 2022). We also found that end-user participation often lacks rigor and depth that would make easier to understand the contents of work activities, promote critical reflections on this understanding and help to construct the overall vision for future work (Koskinen, Laarni & Bergroth, 2022).

We applied the Systems Usability Case (SUC) approach to real data from an integrated system validation (ISV) of the modernized main control room of the Loviisa NPP (Koskinen, Laarni, Liinasuo et al., 2022). The results of the validation tests were discussed from the perspective of how the SUC approach enabled creating a statement about the acceptance of the CR HSIs. All in all, it has to be determined in advance under what conditions it can be said that the system is successfully validated (Koskinen, Laarni, Liinasuo et al., 2022). Often there is no single answer to the validation questions, but several possible answers, which have to be explored and summarized in a systematic way (Koskinen, Laarni, Liinasuo et al., 2022). The resolution of identified design deficiencies provides one answer to the questions, but it is not necessarily the only one. Validating a complex system is a temporarily extended process with no clear end point, and there is a need for further monitoring and follow-up since the system has been launched (see the next paragraph; Koskinen, Laarni, Liinasuo et al., 2022). Therefore, SUC is a living document that has to be updated after each new validation.

According to NUREG-0711 (O'Hara et al., 2012), human performance has to be monitored to ensure that conclusions made in ISV remain valid with time, and no significant safety degradation has occurred due to any change made in the plant. Our literature review showed that the program may, at least in part, be incorporated in other HFE program activities (ie., operating experience review, OER, and training program development). OER activity aims at collecting and revealing relevant operating experiences so that the past mistakes are not unnecessarily repeated, and the meaningful and good operating practices are nurtured and put forward. In the operating NPPs, operating experience is found as an effective mechanism to provide lessons learned from events and the related corrective actions, resulting in improved safety (Shokr & Rao, 2015).

Applications

Based on our research, methods, tools, guidance and training activities have been developed for promotion of operators' resilience skills that expand their resources for action in demanding operational situations. First, we have developed a concept for a retrospective video-based think- and reason-aloud process tracing method for operator training purposes (Laarni, Pakarinen et. al, 2021). In this method, video showing both gaze direction and psychophysiological recordings are presented to the operator. Video from the test will be presented twice, in the first presentation the operator is instructed to think and reason-aloud what he/she was thinking during the

session on the basis of the gaze-direction video; in the second presentation he/she is asked to describe his/her feelings (feel-aloud) during the session (Laarni, Pakarinen et. al, 2021). Second, in order to build a framework for resilience skills training for nuclear domain, we prepared training material on the application of virtual reality in operator training, promotion of cognitive readiness and operational resilience among operating personnel and development of operating procedure in the nuclear domain.

Summary

It was found that

- skilful use of procedures is a key to successful performance;
- hazard analysis methods such as FRAM help to identify the bottlenecks and pitfalls of a particular operator task;
- development of a new procedure is a learning process requiring both collective creativity and analytical and logical thinking;
- field operator training should be better tailored to operator needs;
- virtual environments are especially suitable for training new and rarely performed activities;
- development of virtual reality training should be based on explicit learning objectives and systematic methods; and
- if flexible operation becomes more common in the future, its human factors implications should be carefully considered.

Acknowledgements

The authors would like to thank all the designers, the simulator trainers and the operators involved in our studies.

References

- Challenger, R., Clegg, C.W., & Shepherd, C. 2013. Function Allocation in Complex Systems: Reframing an Old Problem. *Ergonomics* 56, 1051-1069.
- Hollnagel, E. 2012. FRAM: The Functional Resonance Analysis Method: Modelling Complex Socio-Technical Systems. Burlington: Ashgate.
- Koskinen, H., Laarni, J., & Bergholm, J. 2022. User Involvement in Design of a Safety-critical Operating Panel System. *International Journal of Industrial Ergonomics* 92, 103358.
- Koskinen, H., Laarni, J., Liinasuo, M., & Salo, L. 2022. Application of Systems Usability Case in an Integrated System Validation of Control Room. *Nuclear Technology*.
- Koskinen, H., Laarni, J., Liinasuo, M., Salonen, T.-T., Pakarinen, S., Lukander, K., & Passi, T. 2021. Augmenting Field Operator Training through Virtual Reality. In: *Proceedings of the 12th Nuclear Plant Instrumentation, Control*

- and Human-Machine Interface Technologies (NPIC&HMIT 2021), June 14-17, 2021, p. 79-88.
- Koskinen, H., Laarni, J., Simonsen, E., & Pakarinen, S. In preparation. Investigating Human Factors Issues in Flexible Operation of Nuclear Power Plant.
- Koskinen, H., Salonen, T.-T., Laarni, J., Liinasuo, M., & Pakarinen, S. 2022. Foreseeing the Potential of Virtual Reality in Nuclear Power Plant Field Operator Training. In: Boring, R., & McDonald, R. (eds.) Human Factors in Energy: Oil, Gas, Nuclear and Electric Power. AHFE (2022) International Conference. AHFE Open Access, vol 54. AHFE International, USA.
- Laarni, J., & Liinasuo, M. Submitted. Procedure Development Practices in Finnish Nuclear Power Plants. Conference article manuscript to be submitted to 17th Multi Conference on Computer Science and Information Systems (MCCSIS 2023).
- Laarni, J., Liinasuo, M., Pakarinen, S., Lukander, K., & Passi, T. 2021. Control Room Operators' Cognitive Strategies in Complex Troubleshooting. In: Ayaz H., Asgher U., & Paletta L. (eds.) Advances in Neuroergonomics and Cognitive Engineering. AHFE 2021. Lecture Notes in Networks and Systems, vol 259, p. 238-245. Springer, Cham.
- Laarni, J., Liinasuo, M., Pakarinen, S., Lukander, K., Passi, T., Pitkänen, V. & Salo, L. 2020. Building Cognitive Readiness and Resilience Skills for Situation Assessment and Diagnostic Reasoning in a VR CR. In: Stephanidis C., & Antona M. (eds.) HCI International 2020 - Posters. HCII 2020. Communications in Computer and Information Science, vol 1225. Cham: Springer.
- Laarni, J., Pakarinen, S., Koskinen, H., Liinasuo, M., Lukander, K., Passi, T., & Salonen, T.-T. 2021. Building Operational Readiness of Control Room Crews (BORS). In: Hämäläinen, J., & Suolanen, V. (eds.) SAFIR2022 – The Finnish Research Programme on Nuclear Power Plant Safety 2019–2022. Interim Report. VTT TECHNOLOGY 383.
- Laarni, J., Tomminen, J., Liinasuo, M., Pakarinen, S. & Lukander, K. 2020. Promoting Operational Readiness Through Procedures in Nuclear Domain. In: Harris D., & Li WC. (eds.) Engineering Psychology and Cognitive Ergonomics. Cognition and Design. HCII 2020. Lecture Notes in Computer Science, vol 12187. Cham: Springer.
- O'Hara, J.M., Higgins, J.C., Brown, W.S., Fink, R., Persensky, J., Lewis, P., Kramer, J., & Szabo, A. 2008. Human Factors Considerations with Respect to Emerging Technology in Nuclear Power Plants. NUREG/CR-6947. Washington, D.C.: U.S. Nuclear Regulatory Commission.
- O'Hara, J.M., Higgins, J.C., Fleger, S.A., & Pieringer, P.A. 2012. Human Factors Engineering Program Review Model, NUREG-0711. Washington, D.C.: U.S. Nuclear Regulatory Commission.

- Pakarinen, S., Laarni, J., Koskinen, H., Passi, T., Liinasuo, M., & Salonen, T.-T. 2020. Virtual-Reality Based NPP Field Operator Training. Research Report. Finnish Institute of Occupational Health.
- Pakarinen, S., Laarni, J., Koskinen, H., Passi, T., Liinasuo, M., & Salonen, T.-T. Under revision. Virtual-Reality Based Training Solutions for Nuclear Power Plant Field Operators: A Review. Journal article manuscript is under revision in Progress in Nuclear Energy.
- Pakarinen, S., Laarni, J., Lukander, K., Inkilä, V.-P., Passi, T., Liinasuo, M., & Salonen, T.-T. 2020. Promoting Operational Readiness of Control Room Crews Through Biosignal Measurements. In: Ahram T. (ed.) Advances in Artificial Intelligence, Software and Systems Engineering. AHFE 2020. Advances in Intelligent Systems and Computing, vol 1213. Springer, Cham.
- Pakarinen, S., Passi, T., Lukander, K., Laarni, J., Liinasuo, M., Koskinen, H., & Salonen, T.-T. Submitted. Skillful Use of Procedures Decreases Stress and Workload, and Supports Crew Performance in Demanding Simulated Fault Situations. Journal article manuscript submitted to Journal of Safety Research.
- Pakarinen, S., Passi, T., Lukander, K., Laarni, J., Koskinen, H., & Salonen, T.-T. In preparation. Developing Expertise and Collaboration of Nuclear Power Plant Field Operators in Virtual Reality.
- Saurin, T. A. & Wachs, P. 2018. Modelling Interactions between Procedures and Resilience Skills. Applied Ergonomics 68, 328-337.
- Shokr, A. M., Rao, D. 2015. Operating Experience Feedback from Safety Significant Events. Kerntechnik 80, 133-137.

2.2 Development of framework for justification of overall safety (OSAFE)

Juhani Hyvärinen¹, Juhani Vihavainen¹, Kim Björkman², Essi Immonen²,

¹LUT University

P.O. Box 20, 53850 Lappeenranta

²VTT Technical Research Centre of Finland Ltd

P.O. Box 1000, FI-02044 Espoo

Abstract

The general objective of the OSAFE project was to advance the understanding of nuclear power plant safety and security, i.e., overall safety by applying a set of methods and improving of these methods for the purposes of safety assessment and safety justifications.

We have worked to reach the objective by improving methodologies for creating a framework for evaluating overall safety and by developing of overall safety framework, security and safeguards and implementing them into Overall Safety Conceptual framework (ORSAC). Three Master's thesis have been performed related, e.g., to small modular reactors and evaluating risks in non-nuclear areas of society. Annual Overall Safety seminars have been organized during 2015–2022.

Introduction

The general objective of the OSAFE project (2019-2022) is to advance (the understanding of) nuclear power plant safety and security, i.e., overall safety by applying a set of methods (risk-informed, graded approach, safety justification, safety culture, institutional strength-in-depth, system modelling) and improving of these methods for the purposes of safety assessment and safety justifications in the context of operating plant's electric systems and the new technologies, such as small modular reactors (SMR). Thus, the project focused on both the current challenges in the operating plans and the projections to the futures in terms of SMRs and non-baselload operation of nuclear power plant and integrated management of safety, security and safeguard. The general objective is divided into the following specific objectives:

- Improving methodologies for overall safety and safety justifications. Looking at the core safety principles and approaches to safety and risks.
- Developing methods for dealing with overall safety as a sociotechnical issue. Sociotechnical perspective and required complementing approaches, such as holistic approach, resilience and new risk perspective, and system modelling. Improving sociotechnical perspective
- Tailoring safety justification and safety culture to specific targets, such as to electric systems in operating plants and to non-baselload operation of

nuclear power plant, or to new technologies, such as SMRs. Adopting sociotechnical perspective.

- Integrated management of safety and security as part of the improved overall safety.
- Improved methods, tools and guidelines for taking better into account the overall safety. The goal was to examine the SMRs and related requirements and challenges for nuclear safety justification. Emphasis was on assessment of design features. Impact of SMR safety features to the demonstration of compliance of plant safety requirements. SMRs are considered as an interesting option for electricity and heat production. They are expected to be easier to build and to operate under certain site conditions. The smaller size of the reactor offers interesting safety features, notably in terms of residual heat removal and size of containment structure. In addition, passive systems for heat removal are introduced to most of the SMR designs right from the beginning.

Master's thesis in 2020

The master's thesis by Mikko Turunen during 2020 was prepared to study the safety systems of U.S. EPR and NuScale SMR design and compared with each other by researching their Design Control Documents. The objective was to create a comprehensive framework for the overall safety of SMRs from a functional Defence-in-Depth (DiD) point of view.

The starting point of this assessment was the proposal of overall safety concept based on the functional Defence-in-Depth principle developed by International Atomic Energy Agency (IAEA). This concept contains Normal Operation (NO) and Anticipated Operational Occurrences (AOOs) are defined as Operational States, while Design Basis Accidents (DBAs) and Design Extension Conditions (DECs) without significant fuel degradation and with core melting are defined as Accident Conditions (Figure 1).

Operational states		Accident conditions		
Normal operation	Anticipated operational occurrences	Design basis accidents	Design extension conditions	
			Without significant fuel degradation	With core melting

Figure 1. Functional Defence-in-Depth concept developed by IAEA.

The overall safety concept was developed further by combining the main safety functions and the functional DiD concept developed by IAEA (Figure 2). The front-line safety systems were attached to the DiD frame by adding the three main safety functions: 1) subcriticality, 2) heat removal and 3) containment functions. The subcriticality refers to control of reactor power containing the capability to shut down the reactor. The heat removal refers to fuel heat removal and cooling that is

proportionate to the reactor power. The containment refers to confinement of radioactive materials inside closed systems, or capability to isolate the containment, maintain it leak-tight, and also prevent leakages from process systems carrying radioactive materials. To the new presentation of the overall safety concept two main support functions were attached: power supply and HVAC. Power supply refers to emergency power supply, to power safety features of the plant including control room. The HVAC refers to heating, ventilation and cooling to maintain operating conditions in safety equipment rooms.

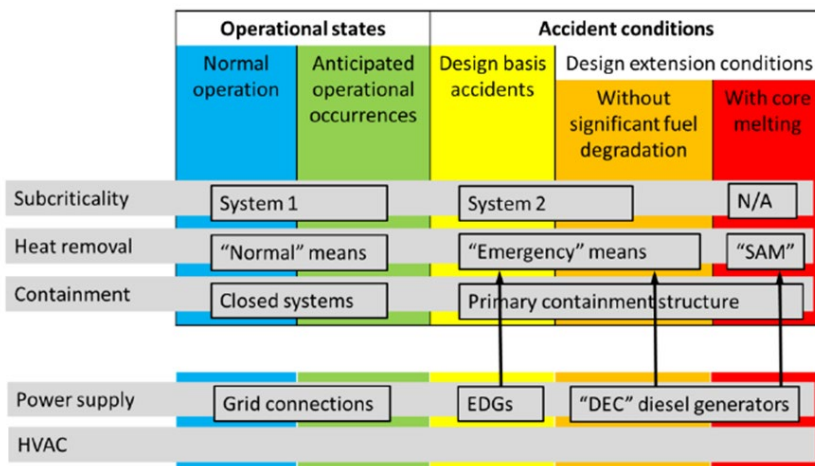


Figure 2. Main safety and support functions and functional Defence-in-Depth concept by IAEA combined.

The developed concept was then used by analysing the front-line safety systems of two different nuclear power plants and comparing them to get a better understanding of the overall safety for Small Modular Reactors. The first facility representing large power reactor was an Evolutionary Pressurized Reactor (EPR) originally designed by Areva NP. The actual EPR concept had been modified and implemented to a U.S. EPR design. The second facility representing SMR concept was NuScale, which is a Pressurized Water Reactor (PWR) with an integrated primary circuit designed by NuScale Power. The main reason to end up to the comparison of these designs was because U.S. NRC is the governing authority for both NuScale and U.S. EPR. They are designed through the same set of regulatory requirements. In addition, the majority of the technical details are public and available online from Agencywide Documents Access and Management System (ADAMS).

	Operational States		Accident Conditions		
	Normal Operation	Anticipated Operational Occurrences	Design Basis Accidents	Design Extension Conditions	
				Without significant fuel damage	With core melting
Subcriticality	CVCS	CVCS			"N/A"
	CRA	CRA	CRA		
	Soluble boron				
	Gadolinia				
Heat removal	SG → Condenser → CWS → Atmosphere	SG → Condenser → CWS → Atmosphere			
	RCCWS → SCWS → Atmosphere	RCCWS → SCWS → Atmosphere			
		ECCS → CNV → UHS	ECCS → CNV → UHS	ECCS → CNV → UHS	
		SG → DHRS → UHS	SG → DHRS → UHS	SG → DHRS → UHS	
			RPV → CNV → UHS	RPV → CNV → UHS → Atmosphere	
				CFDS	
Containment	Closed piping (RCPB)	Closed piping (RCPB)	RPV	RPV	
	RSVs → CNV	RSVs → CNV			
	CIVs	CIVs	CIVs	CIVs	
Power supply	TG				
		EDSS	EDSS		
			BPSS	BPSS	
HVAC	CRVS	CRVS	CRHS	CRHS	
	RBVS	RBVS			

Figure 3. The major operating systems as well as front-line safety systems implemented in NuScale placed on the functional Defence-in-Depth template.

The systematic analysis and going through the documentation material concluded first the creation of large template of 5 x 5 matrix, where front-line safety systems and support systems were placed to their respective positions for both studied designs separately. The observations were made that there were certain interdependencies between safety systems, which were credited in more than one DiD levels. Example of resulting NuScale template is presented in Figure 3. In NuScale design, some systems are shared between modules and these systems are indicated by a blue font in Figure 3. Decay Heat Removal System (DHRS) is designed to remove decay and residual heat from the reactor core and to retain RCS inventory in the RPV. DHRS provides residual heat removal and decay heat removal during AOOs, DBAs and DECs, and especially during non-LOCAs when the normal secondary side cooling is unavailable or otherwise not used. DHRS has safety-related functions during both Operational States and Accident Conditions.

The results of this assessment show that U.S. EPR implements more safety systems as compared to a simple and compact NuScale design. NuScale Power Module design implements an integrated primary circuit, which utilizes natural circulation to cool the reactor core. U.S. EPR design requires forced circulation with Main Coolant Pumps to create sufficient coolant flow to remove heat from the

reactor core. Additionally, emergency heat removal systems are passive in NuScale design as opposed to more complex active heat removal systems in U.S. EPR design. Table 1 shows the gathered information of how many safety systems combinations and support systems have safety-related functions between different levels of defence in both facilities.

Table 1. The number of safety system combinations and support systems that have safety-related functions between different levels of defence.

Number of safety system combinations and support systems	AOOs	DBAs	DECs
U.S. EPR	17	21	15
NuScale	12	9	8

Master's thesis and other topics in 2021

Master's thesis on SMRs from the perspective of safety, security and safeguards (3S) was prepared and finalized during 2021. The thesis contributes to research on Overall Safety in two different ways. The already existing tool (ORSAC) is developed further (Figure 4). Such development is done in the theory part by looking for similarities between 'the 3S'. In addition, 3Ss are being surveyed in the context of small modular reactors. The work has been done as a case study for four different SMR designs (NuScale, BWRX-300, RUTA-70, and KLT-40S). The main emphasis has been on assessing the implementation of current technical requirements and safeguard aspects of the designs.

The safety design was found to fulfil current requirements well. Regarding Security, the SMR designs under review were found to be following current requirements. With respect to Safeguards, conventional nuclear material accountancy and verification practices were largely identified as applicable. The simultaneous presence of several modules (NuScale), the design capability for misuse (RUTA-70), and the mobility of the floating power unit (KLT-40S) were identified as major challenges for Safeguards. Organizational requirements and design considerations were identified as important for Security and Safeguards.

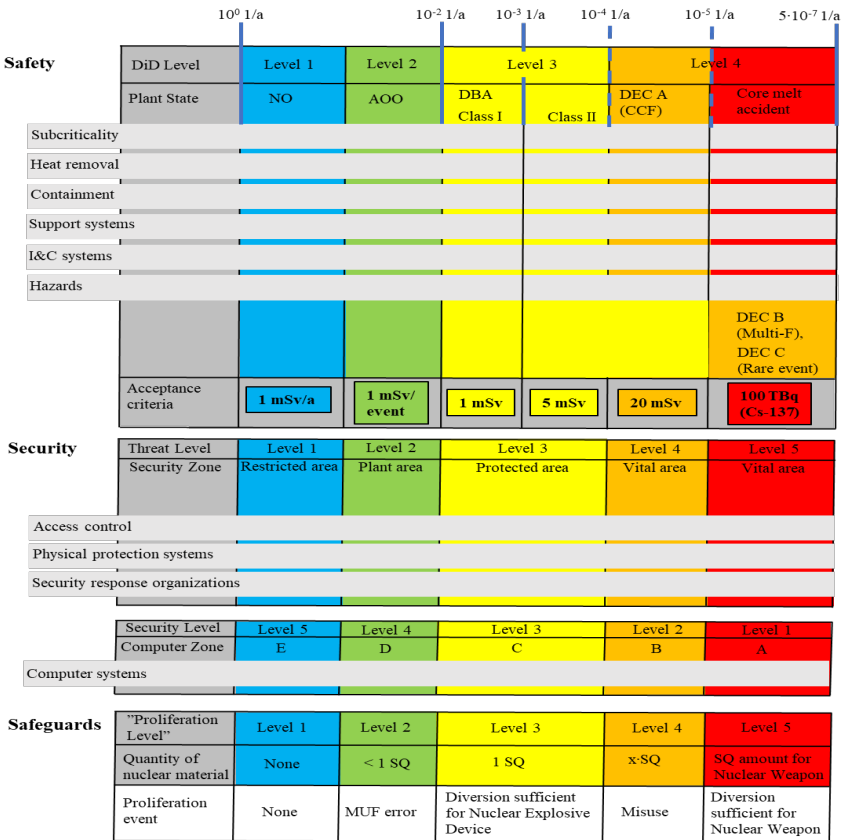


Figure 4. Safety-Security-Safeguards (3S) in ORSAC Framework.

Other topics

WP3 of OSAFE aimed to contribute to the creation of improved overall safety framework. In 2021, WP3 focused on studying the integrated management of safety, security (and safeguards) in the nuclear industry in Finland. The study was motivated by the changing risk landscape that refers to the convergence of process-safety, physical security and cybersecurity risks, which may lead to major accidents.

The data used in the study consisted of articles on digitalisation in the high risk industry, integrated management of safety and security in high-risk industry, and six interviews with the safety and security experts from two power companies and the regulatory body. The method of analysis was qualitative content analysis. The analytical framework used in the study is illustrated in Figure 5.

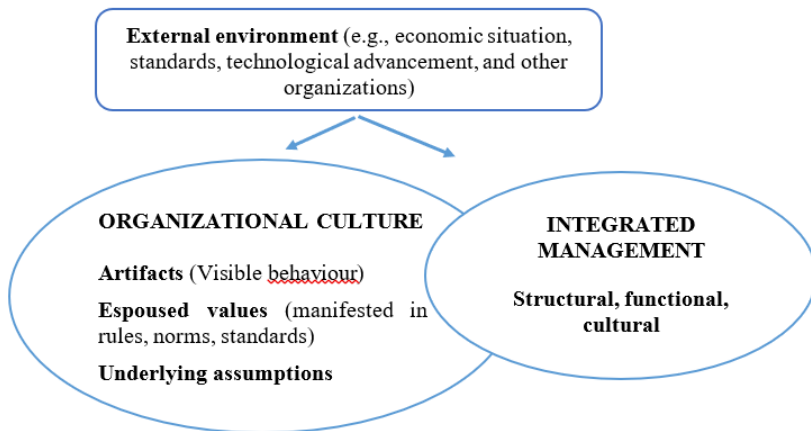


Figure 5. Analytical framework consisting of 3 levels of organizational culture and 3 levels of integration of management, affecting each other, and to which also organization's external environment affects.

The conclusions of the study included that the reasons for safety and security domains being apart relate also to different logics between these domains, when safety management adheres openness and transparency as well as questioning attitude, the security management resorts to secrecy. The integrated management of safety and security (IMSS) would require efficient information exchange and communication between safety and security experts, across different organizational units.

The development of IMSS may be hindered by the current organizational culture with espoused values related to the denial of the need of a separate security culture and subordinating it to the broader organizational culture framework. The underlying assumption of organizational culture being a combining mechanism between safety and security, is not adequate to make the content of security and safety domains either visible and clear, or contribute to their better coordination.

Objectives in 2022

WP2 of OSafe aims at improving methodologies for creating a framework for evaluating overall safety. In 2022, WP2 focused on studying the graded approach to nuclear safety from literature perspective. The study aimed to obtain an overall understanding on graded approach and its main issues in relation to overall safety and to identify future development needs for a risk-informed graded approach.

The definitions of graded approach were collected from different regulatory sources, and they were found quite consistent. Graded approach is generally seen as a process of ensuring, that actions or controls (such as level of analysis) are commensurate to the risks. The methodology used in the process of grading was

presented from the perspectives of some regulators and the International Atomic Energy Agency (IAEA). For example, the IAEA method for applying graded approach in regulating nuclear installations has similarities to the risk-informed decision-making approach. Examples of the use of graded approach in different applications were presented from the literature. Also, management systems and risk-informed decision-making were studied in relation to graded approach.

Achieving an effective and formulated graded approach to safety would require the use of multiple assessment approaches in an integrated way. An outline for a risk-informed approach to grading is presented in Figure 6. When graded approach is applied to the classification of items such as systems, structures and components (SSCs), a risk-based graded approach would include qualitative and quantitative analysis for each item, followed by an overall assessment.

Based on the literature review it is concluded that graded approach is so far still a concept in nuclear safety, that could be developed in more detail to achieve an integrated framework applicable to most situations and users. Utilising an integrated collection of methods and tools in a risk-informed graded approach would require firstly integrating technical aspects with the other areas of overall safety, such as organisational factors.

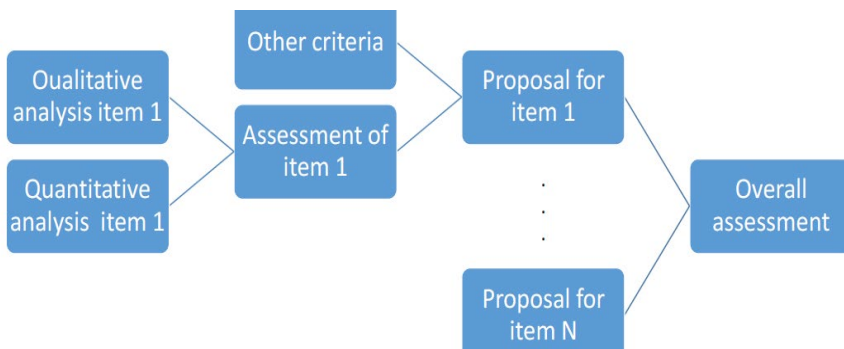


Figure 6. Risk-informed approach to grading.

WP4 of OSAFE in 2022 concentrated on evaluating risks in the other areas of society. The goal of this task was to investigate the risk assessment and valuation on areas of different areas of society and to compare their risk assessment formulations to the practices in the nuclear area. Risk assessment has been successfully practiced in e.g., aviation, maritime, industry, road and railroad design and construction sectors. Their risk assessment practices address both components of risk – the frequency and the value lost. In particular, traffic (aviation, marine, road and rail) industry has very long experience and well-established practices to assign the (lost) value associated with undesirable events. Moreover, in such areas, the risks assumed by designers have been subject to a market mechanism that has produced levels of risk acceptable to the public using such services.

The research of this task is concentrated to the comparison how these risk characterisations (frequencies and values lost) at the other areas are related to the nuclear field risk evaluation and gives perspective to the design, operation, and management of nuclear power plants, large and small. This task is realized as master's thesis.

Thesis results showed that the criteria to define a maximum amount for the radioactive material and a maximum frequency for a release that is larger than the set limit. Somewhat similarly to the case with individual risk criteria, the fact that the criteria in nuclear industry are not defined in terms of fatalities makes comparing them with the criteria in other industries rather difficult. Example of the criteria used in process industry and nuclear industry criteria are shown in Figure 7.

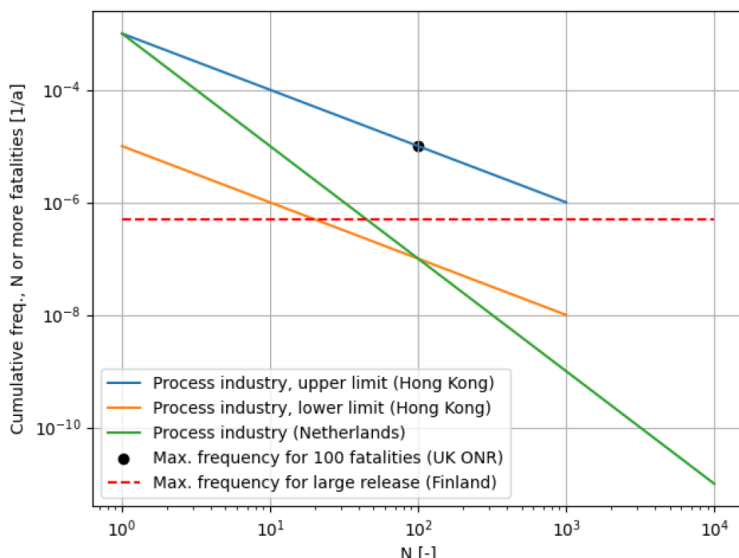


Figure 7. The societal risk acceptance criteria in nuclear industry compared with some criteria from other industries.

WP5 focused on project coordination and dissemination of the results. Project coordination was crucial in the multi-disciplinary project where development of framework for evaluation of overall safety requires real collaboration and dialogue. WP 5 consisted of two tasks:

T5.1 included project cooperation and T5.2 dissemination of results. The goal of Task 5.1 was to ensure that the knowledge of the different disciplines is effectively integrated and that the high practical and scientific targets will be achieved. The task continued throughout the project.

The goal of Task 5.2 was to disseminate the findings of the project through end user-oriented seminars and workshops. Overall safety seminar was be arranged in the year 2022, the seminar took place on September 2nd at LUT premises also in

hybrid mode. The participants consisted of main all stakeholders in nuclear area in Finland from MEAE, power companies, STUK and VTT. The seminar was successful with interesting discussions of topical issues.

The journal article on overall safety concept was also finalized and published during 2022. This article concluded most of the work that has been done in OSafe during the SAFIR2022 programme. This journal paper sought to clarify the concept of defence-in-depth using the Overall Safety Concept (ORSAC) developed at LUT, and the sociotechnical systems view in the nuclear power industry context, extending defence-in-depth thinking to the organizational context in one transparent framework. Also, organizational, and technical aspects have affected each other in the operation of nuclear power plants. Example of the visual presentation of overall safety is presented in Figure 8. This figure illustrates the levels of overall safety, but it does not examine the sociotechnical interactions between them, or between different organizations, which have different roles, responsibilities, expectations, and strategies. These aspects create complex interactions between them. In addition, as the sociotechnical aspect is defined as the interconnectedness and complexity of social and technical systems, the overall safety framework needs to be improved so that it can deal with the interconnectedness of technical and organizational factors simultaneously. This paper paves the way for systematic modelling of how technical and organizational aspects affect each other.



Figure 8. Visualization of overall safety. The overall safety of nuclear power plants is affected by macro-, meso- (organizational-level) and micro-level factors.

References

- Hyvärinen, J., Vihavainen, J., Ylönen, M., Valkonen, J., An overall safety concept for nuclear power plants, Annals of Nuclear Energy, 178 (2022).
- Immonen, E., Graded approach to nuclear safety – State of the practice, VTT Research Report VTT-R-00996-22.

Turunen, M., Overall safety of small modular reactors, Master's thesis, LUT University publication, 12/2020. <http://urn.fi/URN:NBN:fi-fe2020120499439>

Valkeapää, A., Overall safety and the '3S' of small modular reactors, Master's thesis, LUT University, 2021. <https://urn.fi/URN:NBN:fi-fe2021120859615>.

Rapeli, H., Comparison of societal risk acceptance criteria in different areas of society, MSc thesis, LUT University, Jan 2023.

2.3 Participative development for supporting human factors in safety (PARSA)

Anna-Maria Teperi¹, Timo Kuula², Arja Ala-Laurinaho¹, Kaupo Viitanen²; Ilkka Asikainen¹, Vuokko Puro¹, Mikael Wahlström²

¹ Finnish Institute of Occupational Health (FIOH) P.O. Box 40, FI-00032 Helsinki

² VTT Technical Research Centre of Finland Ltd
P.O. Box 1000, FI-02044 Espoo

Abstract

The PARSA project developed and examined measures and tools to foster participative development (PD) of safety in the nuclear industry. We developed and applied collaborative, cross-organisational work process analysis (CWPA), video-based method for collaborative learning, and analysis of documentation practices related to specific human performance tools in case studies conducted in the nuclear maintenance.

Results showed that applying PD methods has benefits and their application may respond to current needs in the nuclear industry such as skills renewal, organisational learning or cross-organisational collaboration at critical work processes.

However, challenges to implement to current safety practices, cultural features or resources may hinder PD applications.

Introduction

New technologies, new ways of organizing and structuring work at nuclear power plants (NPP), aging personnel and technology, and recruiting new generation to positions of operators and other experts challenge the resilience and capabilities of nuclear personnel and organisations (MEE, 2018; Wahlström, 2021). Also, regulative changes and recent threats, such as pandemics, geopolitical tensions and energy crisis affect management and operations at NPPs. Especially, the nuclear industry has attracted increased interest in climate change and green transition debate, due to its benefits of producing climate-friendly electricity, and its share of reducing CO₂ emissions in the world (Wahlström, 2021).

Dynamicity in the functional environment has effects on various work processes and procedures, collaboration and ways of learning. The skills and tacit knowledge of the personnel working at the various levels of the organisation are essential to identify potential risks and to implement the necessary corrective actions. Thus, ways to commit and motivate personnel, and to develop competence, work practices and new learning become valuable adaptive capabilities, to maintain and improve safety in changing times, too.

The operative personnel and experts themselves are essential in enabling transition and development of organising work and knowledge (Boreham, 2002). Supporting good safety climate and participative decision making are critical in NPPs, to provide energy in a sustainable manner. In high-reliability organizations, front-line employees' suggestions and concerns enable the early identification of potential problems that might have catastrophic consequences (Dekker, 2015). Despite this, previous research has mostly focused on person-centered antecedents of participation and, to a lesser extent, the importance of contextual factors at work and organisations (Silla et al., 2020).

Researchers, too, can be of assistance in knowledge sharing, in providing a context for mutual learning and development, by modelling work assignments, sharing ideas, understanding demands and needs of operative work and finding solutions, as focused on design thinking and co-creation, for example (Buchanan, 2019; Teperi et al., 2021). Theoretical and methodological groundings of learning studies, work, organizational and social psychology, combined with the emphasis on safety, provides a fascinating setting for this kind of developmental research.

The PARSA project aimed to develop and examine measures and tools to foster participative development (PD) of safety in the nuclear industry. We developed and applied collaborative, cross-organisational work process analysis (CWPA), video-based method for collaborative learning with reflection, and analysis of documentation practices related to specific human performance tools in case studies conducted in the nuclear maintenance. International Round Table for improving collaboration between industry and academy was organized.

The case studies were scoped and implemented in maintenance operations of NPPs. Safety experts and managers of the NPPs and researchers participated in the collaborative part of the research.

The entity of PARSA project is depicted in Figure 1.

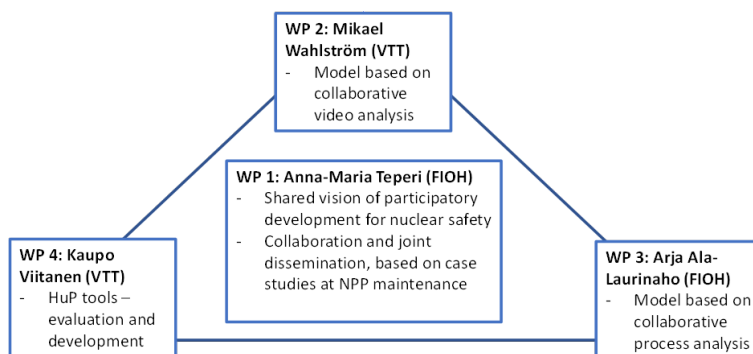


Figure 1. Four workpackages and their basic aims at the PARSA-project.

Synergy and coordination – bridge building between academy and industry

Building bridge between scientific work and industry has high relevance in the nuclear industry, which has ultimate goal for safety. Human Factors (HF)- focused frameworks and models may facilitate this kind of ‘bridge-building’ by means of PD, which is embedded in HF thinking. The core intention is to be aware of operative voice, for example weak signals, which could inhibit learning or be potential risks at maintaining or improving safety in NPPs.

A well-known finding is that issues connected to human and organisational factors (HOF) have had a large influence on nuclear safety over decades (Schöbel et al., 2021). The operational environment at the nuclear power plants (NPPs) has changed considerably over the last two decades. This has led to a felt need for a better understanding of how HF/HOF issues contribute in reality to nuclear safety at the NPPs.

A small international Round Table to further reflect this issue and the current state of the HF/HOF implementation in the European nuclear industry was held in Helsinki in September 2022. Participants were from NPPs and research institutions from Finland, Sweden and Switzerland and in hybrid mode also from Spain.

The safety area has been the target of intensified research since the three major nuclear accidents (TMI, Chernobyl, Fukushima). All three accidents were characterised with HF/HOF deficiencies in the safety precautions both during design and operations (Schöbel et al., 2022). The evaluation of the impact of HF/HOF interventions at the NPPs has anyway been scarce.

Although academic research in safety science has increased considerably in the last two decades, they don't automatically serve safety experts at the NPPs while their needs are mainly pragmatic and their activities are bind to the given roles, and also internationally guided procedures. Also competencies vary among the safety experts, to apply valid HF methods and tools in every-day-operations or to market benefits of HF approach to the organisation and management. One conclusion was, that responsible persons sometimes feel at loss, whether they are strictly responsible for safety assessments or should they also participate in the design and education of groups that organise HF activites. The main basic task of the HOF/HF/safety culture/safety experts at the NPPs is however to support capability of the NPPs to operate safely and economically. Conducting this task, requires knowledge on dynamic relations between conditions at the plant, several systemic and multi-level human factors and the safety management system.

To conclude, there seemed to be a need for better contacts between experts at the NPPs and the researchers, who are involved in safety activities concerned with HF/HOF issues. Proposal for organizing regular, informal annual meetings was launched.

Video-based method for collaborative learning and development

We have introduced the video-based method for collaborative learning for maintenance personnel. The idea is that learning takes place as the workers observe their own work practices from the video recording. This allows that the workers can discuss what could be done differently and what was done right by watching the events that took place during the activities. The idea on using video in the development of expertise at the nuclear domain draws from a strong line of research made at Électricité de France (EDF) by Lahoulou (2010) and others (Le Bellu & Lahoulou, 2010; Fauquet-Alekhine et al. 2018). We aim at transferring this line of research into Finland and developing it by using prominent Finnish research traditions. In particular, this relates to the way in which the researchers could facilitate the video-observation sessions with the workers. Overall, in addressing the requirement of high-quality research in SAFIR2022, we synthesize established lines of study: work on interpretive-practice (Norros, 2004; Savioja, et al., 2014; Norros, 2018; Wahlström et al., 2018), use of first-person camera for uncovering tacit knowledge line work developed at EDF (Lahoulou, 2010) as well as workplace learning developed especially in the change laboratory tradition in Finland (Engeström, 2001). Figure 2 provides a visual illustration of the developmental method.

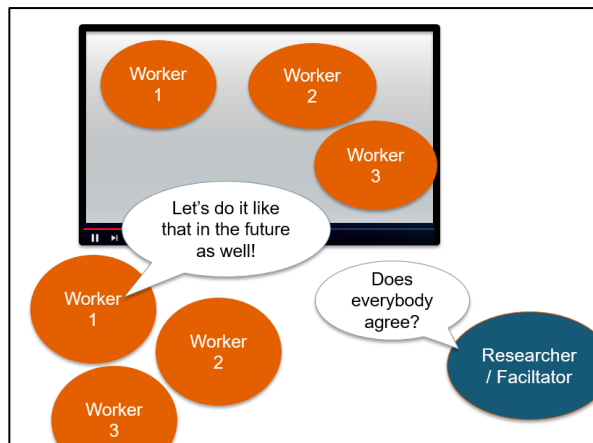


Figure 2. Basic idea of the self-confrontation method.

In 2019–20, it was agreed that maintenance workers' heavy lifting activities during yearly maintenance (outage) could be video-taped for training and learning purposes. The selected case was the lifting of reactor shield unit, as it is one of the critical tasks during the yearly outage, and lifting accidents could lead to serious consequences. The operating organization collected the video data on this heavy-lifting task and first version of guidelines for video-based session was created in

collaboration with the researchers and NPP personnel. A test session based on the video data and guidelines was organized at the end of 2020.

After the first session, it was agreed with the NPP personnel that the next session would be held before the lifting tasks began. The second test session was thus held for the maintenance workers directly before the outage and its heavy lifting activities. The second session took place in 2021.

Finally in 2022, a new lifting simulator was provided for the personnel in the NPP. A workshop was organised with lifting crews and NPP's video development team to discuss about the possibilities of combining the video method and simulator training. Furthermore, the possibility to support pre-job briefings and post-job reviews (HU tools) with the method was examined.

The video-based method can have a number of useful purposes in maintenance activities. The method supports various pre-job and post-job learning activities, and it can be utilised both in real situations and in simulator training as well. The video-viewing session should be designed according to its main purpose and goal. For the successful implementation of the method, it is important to select suitable task to be video-recorded. The task should be complex, communicative, involve physical activities, and have safety-critical relevance. Furthermore, careful selection of video material is essential. There are also several technical and organisational requirements that should be taken into consideration for the successful implementation. The video method has the potential to support pre-job briefings and post job-reviews (HU tools) as well, when appropriately designed for this purpose.

The video-based method provides an effective way to prepare for work and to learn from previous activities. The method provides viewpoints that possibly cannot be acquired anywhere else. The most significant challenges are related to the responsibilities and usefulness of the method, and to the selection and editing of the actual video material. To be recognized as an official method in the nuclear power plant it needs to be included in the power plant's existing guidelines and procedures. The ultimate goal would be that the power plant personnel would utilize the video-based method by themselves as practical tool for improving organisational learning.

Organizational learning through collaborative work process analysis

Collaborative Work Process Analysis (CWPA) (Leppänen, 2001; Leppänen, Hopsu, Klemola & Kuosma, 2008) aims to facilitate building of work process knowledge and shared understanding of work. It aims to increase the participants' ability to see the work process as an entity and to encourage them to take an active role in improving and developing the process. In this case study, we introduced CWPA in NPP maintenance to model work processes, their critical phases, interfaces and collaboration needs, to support organizational learning, knowledge sharing as well as safety and improvement of work.

The method is based on steered discussions, and the participants work in different kinds of groups to analyze their work processes, ways of action, materials, products and co-operation as well as problems and development needs related to these.

We used a modified version of the method that was developed in the safety-critical air traffic management (Teperi & Leppänen, 2011), and in the aviation maintenance (Teperi et al., 2019), to help define and create a mutual understanding of the safety-critical characteristics of work among the organizational actors, which could be further supported by improving work processes in practice.

In choosing CWPA for this study, we aimed to 1) make tacit expertise in maintenance work more visible and concrete, 2) analyze and learn directly from everyday work (not only from operative events, audits, or other current practices), 3) develop work by modeling it collaboratively, with the personnel from operative to expert and management levels, and 4) collaboratively find appropriate corrective measures.

At first, we interviewed nine experts and operative personnel to obtain preliminary information to select accurate work processes for further analysis. In the second phase, CWPA was conducted at a nuclear power company (NPC), including three work process samples: a) five fault repairs b) a planning process, and c) component and system health reporting. The CWPA was conducted at one-day-workshops, which were conducted as steered sessions in cooperation with the operative personnel and experts themselves.

At the first set of CWPA, development plans regarded, for example, needs to digitalize guidelines and pictures of on-sight damage, improve lighting in dark spaces, improve work order forms, and improve spare part ordering procedures.

The experiences highlighted the importance of the modeling being done by people who work in the process in question, while they have the every-day-work view. Focusing on processes that continuously require reworking and maintenance and often have flaws, defects, and disturbances, were seen as good targets for CWPA.

At the second set of CWPA, development plans paid attention to the need of improving collaboration and keeping up a shared situational awareness and understanding of operations between organizational units in the planning phase of major component modifications. The group sketched a plan for regular annual series of meetings, to handle how the scheduling and planning of component modification will be conducted, following up the process, taking corrective measures if needed, preliminary review and quality check of the plant modification documentation and pre-job briefing of work planning and control.

The experiences highlighted the potential of the CWPA method to facilitate constructive face-to-face communication between people who work in different units and have shared projects. Facilitation from outside the NPC and creating a constructive atmosphere by also focusing on the positive aspects arose as important features of CWPA for promoting collaboration between units.

At the third set of CWPA, development plans regarded data collection for reporting and aimed to clarify the purposes of the reporting procedures related to

the life-span control of machinery. A plan was made to clarify the goals and justifications for component and system health reporting, as well as the relatedness of these two documents. Several other development plans were made, too.

The experiences gained from workshops highlighted the potential of the CWPA method to clarify the overall picture of work processes in a participative manner. Reporting forms a complex system constructed of different procedures and distributed across the NPC, and it was considered that the modeling helped pool the experiences of those who do the reporting and revise and streamline procedures.

Knowledge and understanding of the overall picture of the NPC was vital for properly conducting the CWPA workshops. The interviews helped gain a relevant understanding of the changes in the NPC. In choosing the targets for the CWPA, the expertise of the health, safety and environment officials of the NPC and the shop floor level of maintenance was important to find relevant targets for modeling.

The NPC had no similar method in use prior to the project. The work and production processes had been analyzed, but not with the aim of facilitating collaboration among the organizational units and levels. The findings revealed benefits of CWPA. It helped them verbalize tacit work process knowledge, concretely identify the aspects of work that needed development, and define corrective actions. The method also helped them openly discuss the needs for information sharing and mutual feedback between the units.

The lessons learnt were that it is essential that the case for collective analysis and learning is selected carefully in order to ensure practical relevance and to motivate participants to join the discussions. It was also important to first observe and discuss strengths and best practices, as this made the joint handling of potential conflicts, disturbances, or other failures easier.

CWPA requires skillful facilitators, as group dynamics may affect the group's work. The participation of the upper management level is recommended. Although middle management actively participated in the workshops, questions on how to proceed with the development plans may have remained. Long-term follow-up of how the development plans are realized is important, to finalize the evaluation of the efficiency of the CWPA process.

The disadvantage of the CWPA method is that it may be experienced as an additional work task to daily work processes, which increases workload. However, developing work should be regarded as an important part of normal daily work.

HU tools development: Organizational learning and documentation practices in pre-job briefings and post-job reviews

HU tools are a diverse set of good working practices originated from various industrial contexts. They are usually applied in operational context by shop-floor workers (especially maintenance and control room). The most commonly used HU tools include Pre-job Briefing, Post-job Review, STAR Principle (Self-Checking),

Peer Checking, Independent Verification and Clear Communication (Oedewald, Skjerve, Axelsson, Viitanen, & Bisio, 2015). Detailed descriptions of HU tools, instructions regarding when to use them and what kind of behaviors to avoid are provided for nuclear industry practitioners in U.S. Department of Energy Human Performance Improvement Handbook, Volume 2 (DoE, 2009).

In 2021-2022, our focus was on studying the documentation practices in pre-job briefings and post-job reviews. Pre-job briefings are held before a task is performed. According to the DoE Human Performance Improvement Handbook, their function is to review tasks, roles and responsibilities, critical steps, hazards, safety precautions, and operating experience (DoE, 2009, p. 34). Post-job reviews, on the other hand, are held after the task has been completed, and their primary function is to serve as a self-assessment to collect feedback and lessons learned (DoE, 2009, p. 54). One important mechanism of organizational learning is that lessons learned by individuals or teams are disseminated and utilized by the whole organization. In the context of pre-job briefings and post-job reviews, the documentation produced could be considered “organizational memory” which facilitates the organizational learning process. We conducted a case study and discussed the following research questions:

- What is naturally documented and what is not?
- What should be documented?
- How to facilitate the generation and use of documented information?

The case study was conducted in a Finnish nuclear power company. Data collection methods were document analysis and interviews. We reviewed all the Level 3 and 4 (two most extensive levels) pre-job briefings and post-job review feedback fields in the work permit system for 2020 (n=1372) and used a selection of minutes of meetings as an additional data source (n=12). Three remote interviews were conducted with power company employees that perform pre-job briefings and post-job reviews and one remote group interview (4 participants) was arranged with the managers and experts that do not primarily work in the field and arrange pre-job briefings and post-job reviews but are responsible for monitoring and facilitating the implementation of pre-job briefings and post-job reviews.

We found that open feedback fields have varying and often low information value and focus on occupational hazards. Minutes of meetings help ensure that all expected topics were covered, but their preparation required significant effort. The motivation to document and the effectiveness of documentation for organizational learning was observed to be linked to how the IT solutions are implemented: e.g., motivation and usability decreases if data entries or minutes of meetings are not easily retrievable or if the user experience is bad.

The main purpose of pre-job briefing and post-job review documentation for performing group is to help perform the same task again. In addition, we observed that pre-job briefing and post-job review documentation may serve multiple purposes that are useful for different stakeholders in the organization: demonstrating that the meetings were held as expected (oversight function),

encouraging employees to systematically conduct the meetings (leadership function), and enabling organizational learning (continuous improvement function).

Finally, we formulated the following generic success factors to facilitate the generation and use of documentation from pre-job briefing and post-job review:

- Management support
- The purpose of the documentation is defined and communicated
- Coordinating supervisors' ownership and awareness is ensured
- Other stakeholders and their interests are identified
- Expectations and instructions for using open feedback fields are clear
- Tools used for documentation are effective and easy to use
- Storage medium choice facilitates organizational learning

Summary and conclusions

The PARSA project aimed to apply, test and improve participative development (PD) at work by conducting case studies at the nuclear maintenance units. PD approach is deeply embedded in Human Factors (HF) science and practice, to realize human-centered thinking and practices for better system performance, safety and well-being. Our specific focus was on self-reflection skills and evaluation of working practices, and on facilitation of organizational learning and mutual co-operation among and across organizational levels and units.

PARSA has used video-based reflection and collaborative work process analysis as methods and conducted an analysis on nuclear specific human performance tools' documentation practices, with applicative targets.

The practical implications of PARSA are producing a training concept, guidelines and a booklet to be used by NPPs, to reframe workplace learning, good working practices, as well as mutual communication and organizational learning procedures. The scientific contribution is made by offering new information and conceptualizations regarding needs, measures and prerequisites of PD to improve safety in the highly proceduralized nuclear industry, as well as other safety critical fields and industries. PARSA results can be utilized by NPPs, regulatory bodies and design organizations. New tools and practices are immediately exploitable by NPPs and the Finnish regulator.

References

- Boreham, N., 2002. Work process knowledge in technological and organizational development. In: Boreham, N., Samurcay, R., Fisher, M. (eds). *Work process knowledge*. Routledge, London, pp. 1-14.
- DoE. 2009b. *Human Performance Improvement Handbook Volume 2, Human Performance Tools for Individuals, Work Teams, and Management*. Department of Energy Washington, DC: Government Printing Office.
- Engeström, Y. 2001. Expansive learning at work: Toward an activity theoretical reconceptualization. *Journal of education and work*, 14(1), 133-156.

- Fauquet-Alekhine, Philippe and Le Bellu, Sophie and Buchet, Marion and Bertoni, Jérôme and Bouhours, Guillaume and Daviet, Frédéric and Granry, Jean-Claude and Lahlou, Saadi. 2018. Risk assessment for subjective evidence-based ethnography applied in high risk environment: improved protocol. *Advances in Research*, 16 (3). pp. 1-15
- Hollnagel E. 2014. Safety-I and Safety-II: The Past and Future of Safety Management. Farnham, UK: Ashgate.
- Huttunen, R., Aurela, J., Melkas, E., Avolahti, J. 2012. Kansallisen ydinenergia-alan osaamistyöryhmän raportti. Työ- ja elinkeinoministeriön julkaisuja. Energia ja ilmasto 2/2012.
- Kruse, W. 1986. On the necessity of labour process knowledge. In: Schweitzer, J. (ed.) (1986). Training for a Hu-man Future, Weinheim, 188-193.
- Lahlou, S. 2010. Digitization and transmission of human experience. *Social science information*, 49(3), 291-327.
- Le Bellu, S., & Lahlou, S. 2010. Comment capter le savoir incorporé dans un geste métier du point de vue de l'opérateur?. *ISDM: Informations, Savoirs, Décisions, Médiations*, (36).
- Leppänen, A. 2001. Improving the mastery of work and the development of the work process in paper production. *Industrial Relations*, 56:3, 579-605.
- Leppänen A., Hopsu L., Klemola S. & Kuosma E. 2008. Does multi-level intervention enhance work process knowledge? *Journal of Workplace Learning*, 20, 416–430.
- MEE. 2018. National Nuclear Power Plant Safety Research 2019-2022. SAFIR2022 Framework Plan. Publications of the Ministry of Economic Affairs and Employment of Finland. 22/2018. Helsinki.
- Norros, L. 2004. Acting under uncertainty: The core-task analysis in ecological study of work. Espoo: VTT.
- Norros, L. 2018. Understanding acting in complex environments: Building a synergy of cultural-historical activity theory, Peirce, and ecofunctionalism. *Mind, Culture, and Activity*, 25(1), 68-85.
- Oedewald, P., Skjerve, A. B., Axelsson, C., Viitanen, K., & Bisio, R. 2015. Human performance tools in nuclear power plant maintenance activities - Final report of HUMAX project (No. NKS-328). NKS.
- Oedewald, P., Skjerve, A. B., Axelsson, C., Viitanen, K., Pietikäinen, E., & Reiman, T. 2014. The expected and experienced benefits of Human performance tools in nuclear power plant maintenance activities - Intermediate report of HUMAX project (No. NKS-300). NKS. Retrieved from <http://www.nks.org/scripts/getdocument.php?file=111010112048626>
- SAFIR2022 Supplement. 2020. SAFIR2022 – Supplement to the Framework Plan for 2021 Call.

- Sandberg, J. 2000. Understanding human competence at work: an interpretative approach. *Academy of Management Journal* 43:1, 9-25.
- Savioja, P., Norros, L., Salo, L., & Aaltonen, I. 2014. Identifying resilience in proceduralised accident management activity of NPP operating crews. *Safety Science*, 68, 258-274.
- Schöbel, M., Silla, I., Teperi, A. M., Gustafsson, R., Piirto, A., Rollenhagen, C., & Wahlström, B. (2022). Human and organizational factors in European nuclear safety: A fifty-year perspective on insights, implementations, and ways forward. *Energy Research & Social Science*, 85, 102378.
- Silla, I., Gracia, F. J., & Peiró, J. M. 2020. Upward Voice: Participative Decision Making, Trust in Leadership and Safety Climate Matter. *Sustainability*, 12(9), 3672.
- Skjerve, A. B., & Axelsson, C. 2014. Human-Performance Tools in Maintenance Work - A Case Study in a Nordic Nuclear Power Plant (No. NKS-321). NKS. Retrieved from <http://www.nks.org/scripts/getdocument.php?file=111010212620555>
- Teperi, A-M., Asikainen, I., Ala-Laurinaho, A., Valtonen, T., Paajanen, T. 2019. Modeling Safety Criticality in Aviation Maintenance Operations to Support Mastery of Human Factors. Springer International Publishing AG, part of Springer Nature 2019. P. M. F. M. Arezes (Ed.): AHFE 2018, AISC 791, pp. 1–11, 2019. https://doi.org/10.1007/978-3-319-94589-7_32
- Teperi, A-M. & Gotcheva, N. 2021. Human Factors in the Nuclear Industry. A Systemic Approach to Safety. 1st Edition. Elsevier, Woodhead Publishing. Elsevier, 2021. <https://doi.org/10.1016/B978-0-08-102845-2.00006-5>
- Teperi, A-M., Gotcheva, N., Aaltonen, K. 2021. Utilizing design thinking for renewal of safety management practices in the nuclear industry. 2021. In: Teperi, A-M., Gotcheva, N. Human Factors in the Nuclear Industry. A Systemic Approach to Safety. 1st Edition. Elsevier, Woodhead Publishing. Elsevier, 2021. <https://doi.org/10.1016/B978-0-08-102845-2.00006-5>
- Viitanen, K. Human Performance Tools as a Part of Programmatic Human Performance Improvement. In: Teperi, A-M. & Gotcheva, N. 2021: Human Factors in the Nuclear Industry. A Systemic Approach to Safety. 1st Edition. Elsevier, Woodhead Publishing. Elsevier, 2021. <https://doi.org/10.1016/B978-0-08-102845-2.00006-5>
- Wahlström, M., Seppänen, L., Norros, L., Aaltonen, I., & Riikonen, J. 2018. Resilience through interpretive practice – A study of robotic surgery. *Safety Science*, 108, 113-128.
- Wahlström, B. 2021. Human factors in nuclear power: Reflections from 50 years in Finland. In: Teperi, A-M., Gotcheva, N. Human Factors in the Nuclear Industry. A Systemic Approach to Safety. 1st Edition. ISBN: 9780081028452. Elsevier, Woodhead Publishing. <https://doi.org/10.1016/B978-0-08-102845-2.00006-5>

2.4 Effective improvement of leadership and safety culture (EPIC)

Kaupo Viitanen¹, Merja Airola¹, Nadezhda Gotcheva¹

¹VTT Technical Research Centre of Finland Ltd
P.O. Box 1000, FI-02044 Espoo

Abstract

The general objective of the project was to develop knowledge and approaches that support effective improvement of leadership and safety culture. First, the project examined how methodical safety culture improvement has been implemented in Finnish nuclear power companies, and what the experts' experiences were. Good practices for implementing effective safety culture improvement were summarized according to the framework based on collected empirical data. Second, the project examined safety leadership in three different contexts: the operational decision-making process, activities of middle managers, and safety walks. Third, the project examined effectiveness assessment of safety culture improvement from a systemic, multilevel perspective. Two complementary approaches were identified: phenomenon-based approach and process-based approach. Four practical tools were developed to illustrate the practical application of these two approaches.

Introduction

Safety culture draws from the concept of organizational culture, which refers to the pattern of shared basic assumptions learned through adaptation, and the espoused values and artefacts that reflect and influence the basic assumptions (Guldenmund, 2000; Schein, 1985). In the nuclear industry, safety culture is defined as “*the assembly of characteristics and attitudes in organizations and individuals that establishes that, as an overriding priority, nuclear plant safety issues receive the attention warranted by their significance*” (IAEA, 1991, p. 1). Good safety culture is expected in nuclear industry and licensees are required to implement *systematic safety culture improvement* activities to assure good safety culture (e.g., IAEA, 2016; STUK, 2019).

Leadership is a fundamental characteristic of a strong safety culture (IAEA, 2016, 2006, 1991; WANO, 2013). GSR Part 2 defines leadership for safety as “*the use of an individual's capabilities and competences to give direction to individuals and groups and to influence their commitment to achieving the fundamental safety objective and to applying the fundamental safety principles, by means of shared goals, values and behaviour*” (IAEA, 2016, p. 2). Leadership activities influence culture and are critical for directing the organizational attention and resources to continuous improvement of safety (e.g. Barling et al., 2002; Clarke, 2013; Donovan et al., 2016; Flin and Yule, 2004; Krause, 2005). After the Fukushima Daiichi

accident in 2011, leadership for safety has received increased international attention and has been more explicitly included in the requirements for licensees (e.g., IAEA, 2016; STUK, 2019).

The general objective of EPIC was to develop knowledge and approaches that support effective improvement of leadership and safety culture. The effectiveness of leadership and safety culture improvement activities was viewed from a multi-level perspective (sociotechnically, Rasmussen, 1997; and culturally, Schein, 1985). Such an approach acknowledges that leadership activities and safety culture improvement initiatives can influence phenomena at different levels of culture (e.g., artefacts, behaviour, attitudes, norms, basic assumptions), and at different levels of the sociotechnical system (e.g., organizational, social, individual or technological level).

Specific project objectives included modelling the best practices of methodical safety culture improvement, safety leadership activities in Finnish power companies and examining effectiveness assessment of safety culture improvement. The research study resulted in a framework describing effective approaches to methodical safety culture improvement, characterizations of safety leadership best practices observed in selected contexts. In addition, the study produced descriptions of approaches to effectiveness assessment, and four practical tools to illustrate these approaches. The outcomes of the study are expected to support the design and evaluation of effective nuclear safety improvement through culture development and leadership activities.

Methodical safety culture improvement

Methodical safety culture improvement is done according to a systematic or established procedure, and with a planned and target-oriented approach (cf. YVL A.3 314). It requires applying a systemic approach. Nuclear power companies have implemented methodical safety culture improvement in their organizations, for example, by means hiring experts in social sciences and implementing safety culture programs. Safety culture improvement has therefore become an organizational function, to be ensured by the top management, and whose implementation is supported by safety culture experts.

We modelled the different approaches to implement safety culture improvement to identify what practices and methods experts consider to be effective for safety culture improvement. A framework was developed for modelling safety culture improvement function to provide a structure for data collection and analysis (Figure 1). Remote workshops were held with safety culture experts from all Finnish nuclear power companies (Fortum, TVO, Posiva and Fennovoima). Nine workshops (approximately two hours each) were conducted, 2–4 in each power company. Document analysis of relevant materials (e.g., safety culture programmes, implementation plans and other related procedures) was also conducted.

We found that safety culture experts' work is steered by the conceptualization of safety culture in the company and its formal organization. Safety culture experts can

implement a wide variety of activities and are extensively connected to other organizational functions. Fifteen generalized good practices which describe the characteristics or preconditions for effective safety culture improvement were formulated based on the findings (reported in Viitanen et al., 2022). These good practices can be used as guidance by those nuclear industry organizations aiming to launch a systematic safety culture improvement initiative, or by those aiming to continuously improve their existing practices.

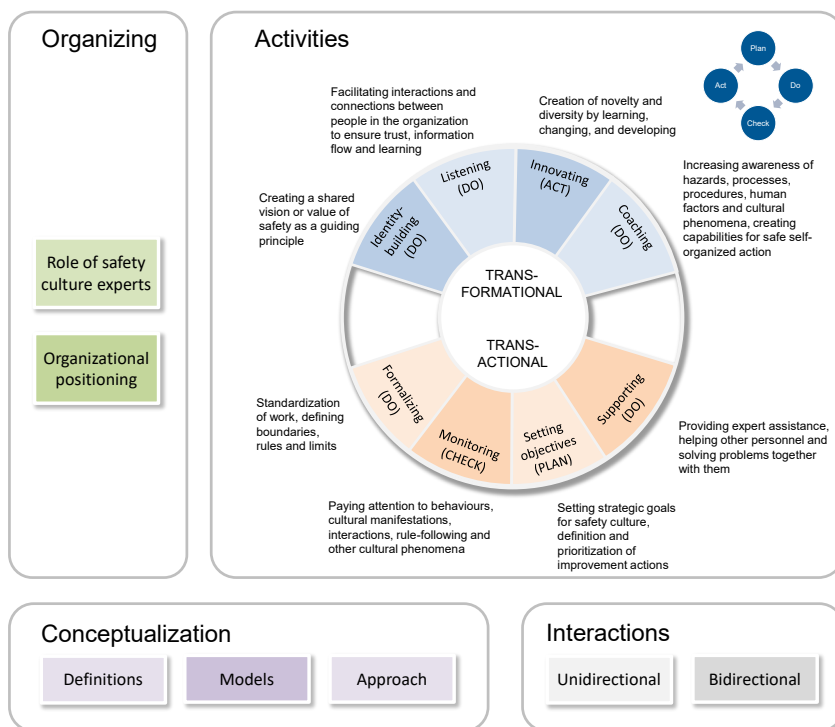


Figure 1. High-level illustration of the framework used for safety culture improvement function modelling (Viitanen et al., 2022).

Good safety leadership practices in Finnish nuclear industry

International requirements have recognized effective leadership as critically important for ensuring long-term safety performance of nuclear power organizations (e.g., IAEA, 2016). However, despite the global nature of the nuclear industry, what is considered good leadership may vary from one country to another. Moreover, the actual intended impacts and unintended consequences of leadership activities in the organizations may remain elusive. Sometimes leaders perform activities, which are seen as good but may have negative effects in the long-term.

We identified how safety leadership activities in selected contexts enhance safety culture, and what are the preconditions for good safety leadership, best practices and observed challenges. We carried out focused case studies on leadership activities in all Finnish nuclear power companies (Fortum, TVO and Fennovoima). Leadership contexts were selected together with the power companies, and they included operational decision-making process and the related meeting practices, safety leadership best practices of middle managers, and safety walks.

Our approach involved reflecting the data from multiple theoretical perspectives. First, nuclear industry expectations for leadership and its outcomes (e.g., behavioural or cultural change) serve as the baseline (e.g., GSR Part 2, IAEA Harmonized Safety Culture Model). Due to the general nature of how leadership is described in the nuclear industry documents, we complemented them with additional models or approaches to leadership. Leadership style maturity model (Watts and Paciga, 2011) was utilized to characterize the extent to which leadership activities cover all relevant aspects of the sociotechnical approach to safety, including technical leadership (focus on technology), systematic leadership (focus on processes and systems), systemic leadership (focus on people), and unitive leadership (focus on integration and alignment of human, technology and organization). Organizational tensions and contradicting goals approach (Reiman, 2015; Reiman et al., 2015) was utilized to identify the types of (contradicting) roles safety leaders may assume.

Main findings from the three case studies were:

- Operational decision-making process: The system is working well for its purpose and is a matured practice. Factors behind the successful ODM process included procedural and cultural preconditions, and leadership activities (e.g., promoting open atmosphere and ensuring that everyone gets heard)
- Leadership practices of middle managers: Well-performing managers emphasised both task-orientation and people-orientation, were highly motivated for leading (not just managing) and had developed their own ways of working with their subordinates, emphasizing trust and loyalty to their team
- Safety walks: Great variety of safety walks was observed, but they often focused on technology rather than people. Interacting with people was perceived easy, but discussing “people issues” (well-being, perception of work, etc.) was harder

In summary, safety leadership best practices included successful balancing between people and task orientation, people and technology orientation, and creation of procedural and cultural preconditions.

Effectiveness assessment of safety culture improvement

We examined the approaches to assess the effectiveness of safety culture improvement activities. This was motivated by the scarcity of guidelines for effectiveness assessment and follow-up in scientific and nuclear industry literature.

For example, IAEA document SRS-83 on performing safety culture self-assessments provides very little guidance on effectiveness follow-up part of the overall process of continuous safety culture improvement. This examination was conducted primarily as a desktop study (literature review and modelling), supplemented with two co-creation workshops with safety culture experts from Finnish nuclear power companies and the regulator where research findings were presented, further developed and their practical applicability reviewed. Two approaches to effectiveness assessment of safety culture improvement were identified. They were then illustrated with four practical tools that were developed during the project.

The *phenomenon-based approach* views safety culture improvement from the perspective of cultural dimensions or manifestations, and how they interrelate with each other and with other sociotechnical elements of the organization (e.g., technology, individual perceptions, values and attitudes, organizational functions, etc.). From this perspective, safety culture improvement is seen as a complex, systemic activity. Explicating the system elements and their interrelations can help identify indicators that can be used for effectiveness assessment, as well as for finding leverage points for improvement. Phenomenon-based approach can answer questions such as: What sociotechnical phenomena influence procedure adherence and how can change in it be measured?

To further examine the phenomenon-based approach, we designed a model development process that aimed to identify the interconnections between a selected safety culture attribute and various related phenomena. The expected outcome was to reveal the systemic nature of the attribute, and to identify potential effectiveness assessment indicators and intervention strategies. Two safety culture attributes were selected for piloting the modelling process. Raising concern behaviour was selected as the first attribute by the research team. It has been widely scientifically studied, which provided a good starting point for analysis. Procedure compliance attribute was suggested by industry practitioners during a joint workshop.

After selection of the safety culture attribute to be modelled, the model development process involved the identification of a network of factors that contribute to the attribute, identification of outcomes of the attribute, creating a visual representation of the model, identification of existing and potential assessment and improvement methods in co-creation workshop with practitioners and researchers, and further development of the model based on feedback.

Based on the workshop and feedback, the researchers made two practical tools for assessing reporting behaviour and procedure compliance in nuclear power plants. The tools can be used by managers and supervisors, as well as experts responsible for organizational development, safety culture, and leadership in case there are signs of challenges in reporting behaviour or procedure following, or if they want to assess their status. The tools aim to make the cultural phenomena and their dynamics more visible, and they can be used to facilitate constructive and comprehensive discussion to identify strengths and weaknesses, and effective ways to improve reporting behaviour and procedure following.

The *process-based approach* views safety culture improvement as an organizational function. This organizational consists of a process dedicated for safety culture improvement, as well as specific activities that aim to improve safety culture. Effectiveness assessment is seen both as verifying that the process and the related activities are implemented, that the implementation is sufficiently comprehensive, and validating that the process and the related activities have positive impact on safety culture. Process-based approach can answer questions such as: What constitutes an effective safety culture self-assessment process, and how to measure it?

To illustrate the process-based approach, two most commonly applied and required subprocesses of safety culture improvement were chosen: safety culture assessment and safety culture trainings. We identified the best practices concerning these two activities based on nuclear industry standards, previous research of safety culture expert work done within SAFIR2022 EPIC, a cursory selection of other literature, and expert judgement. Two tools were developed that can be used to evaluate the effectiveness of these two activities.

First, a maturity evaluation tool for safety culture assessment process was developed. This tool can be applied by managers or experts in licensee organizations, and it can also be useful for regulatory or supply chain oversight. The tool can be used as part of continuous improvement of safety culture assessment process, or when evaluating the maturity of safety culture assessment processes of third parties. It describes fourteen safety culture assessment process evaluation criteria and how they manifest at four levels of maturity. The maturity levels include lack of achieving the evaluation criteria (i.e., non-conformance), as well as basic, advanced, and best practice levels.

Secondly, a tool for assessing the effectiveness of safety culture trainings was developed. It details how four levels of Kirkpatrick's (Kirkpatrick, 1994) training effectiveness assessment model (reaction, learning, behaviour, results) may manifest in the context of safety culture training and what questions could be reviewed as part of effectiveness assessment of safety culture trainings. This tool elaborates what types of effects safety culture trainings may have and what assessment measures can be utilized for following them up. The tool can also be used to further develop the content of safety culture trainings. In addition, the tool can provide insights for safety culture assessment and thus facilitate organizational learning and development.

In summary, effectiveness assessment of safety culture improvement can be viewed from phenomenon and process-based approaches, which lead to complementary insights and tools.

Summary

SAFIR2022 EPIC research study aimed to identify effective leadership and safety culture improvement practices in Finnish nuclear industry. We conducted empirical case studies in all three Finnish nuclear power companies, and developed

frameworks, data analysis approaches and practical tools. The findings and resulting tools can be utilized by Finnish power companies (and other nuclear organizations such as regulators, technical support organizations and suppliers) in their activities to improve nuclear safety by means of leadership and safety culture development. Figure 2 summarizes the approaches, case studies and outcomes of the study.

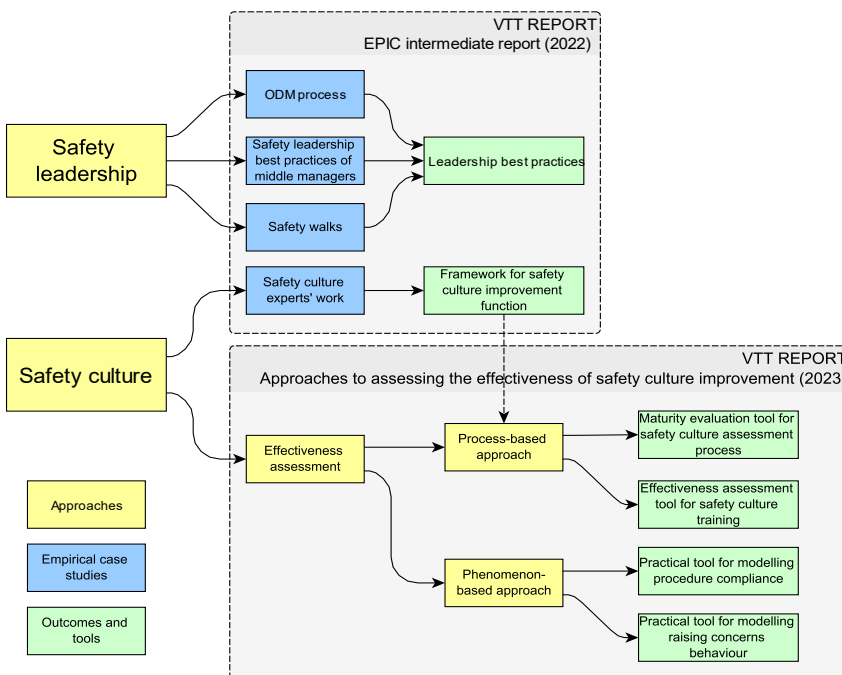


Figure 2. Diagram summarizing the approaches (yellow), empirical case studies (blue) and outcomes and tools (green) applied or created during the implementation of SAFIR2022 EPIC. Dashed boxes indicate the deliverables where the results were reported

References

- Barling, J., Loughlin, C., Kelloway, E.K., 2002. Development and test of a model linking safety-specific transformational leadership and occupational safety. *Journal of Applied Psychology* 87, 488–496. <https://doi.org/10.1037//0021-9010.87.3.488>
- Clarke, S., 2013. Safety leadership: A meta-analytic review of transformational and transactional leadership styles as antecedents of safety behaviours. *J Occup Organ Psychol* 86, 22–49. <https://doi.org/10.1111/j.2044-8325.2012.02064.x>

- Donovan, S.-L., Salmon, P.M., Lenné, M.G., 2016. Leading with style: a literature review of the influence of safety leadership on performance and outcomes. *Theoretical Issues in Ergonomics Science* 17, 423–442. <https://doi.org/10.1080/1463922X.2016.1143986>
- Flin, R., Yule, S., 2004. Leadership for Safety: Industrial Experience. *Quality and Safety in Health Care* 13, 45–51. <https://doi.org/10.1136/qshc.2003.009555>
- Guldenmund, F.W., 2000. The nature of safety culture: a review of theory and research. *Safety Science* 34, 215–257. [https://doi.org/10.1016/S0925-7535\(00\)00014-X](https://doi.org/10.1016/S0925-7535(00)00014-X)
- IAEA, 2016. Leadership and Management for Safety (No. GSR Part 2). International Atomic Energy Agency, Vienna, Austria.
- IAEA, 2006. Application of the Management System for Facilities and Activities (Safety Guide No. GS-G-3.1). International Atomic Energy Agency, Vienna, Austria.
- IAEA, 1991. INSAG-4. Safety Culture (No. 75- INSAG-4), Safety Series. International Atomic Energy Agency, Vienna, Austria.
- Kirkpatrick, D.L., 1994. Evaluating Training Programs: The Four Levels. McGraw-Hill Ryerson, San Francisco : Emeryville, CA.
- Krause, T.R., 2005. Leading with safety. John Wiley & Sons, Hoboken, New Jersey.
- Rasmussen, J., 1997. Risk management in a dynamic society: a modelling problem. *Safety Science* 27, 183–213. [https://doi.org/10.1016/S0925-7535\(97\)00052-0](https://doi.org/10.1016/S0925-7535(97)00052-0)
- Reiman, T., 2015. Turvallisuusasiantuntijoiden roolit, toimintatavat ja tarvittavat kyvyt ja taidot, VTT Technology. VTT Technical Research Centre of Finland, Espoo.
- Reiman, T., Rollenhagen, C., Pietikäinen, E., Heikkilä, J., 2015. Principles of adaptive management in complex safety-critical organizations. *Safety Science*, WOS2012 71, Part B, 80–92. <https://doi.org/10.1016/j.ssci.2014.07.021>
- Schein, E.H., 1985. Organizational culture and leadership. Jossey-Bass Publishers, San Francisco.
- STUK, 2019. Guide YVL A.3 Leadership and management for safety. Säteilyturvakeskus, Helsinki, Finland.
- Viitanen, K., Airola, M., Gotcheva, N., 2022. Effective Improvement of Leadership and Safety Culture – Intermediate Report. VTT Technical Research Centre of Finland.
- WANO, 2013. Traits of a Healthy Safety Culture (No. PL 2013-01). World Association of Nuclear Operators.
- Watts, G., Paciga, J.J., 2011. Conscious Adaptation: Building Resilient Organizations, in: 2011 AAAI Fall Symposium Series.

3 Plant Level Analysis

3.1 Co-simulation model for safety and reliability of electric systems in a flexible environment of NPP (COSI)

Sergio Motta¹, Marius Baranauskas¹, John Millar², Pasi Laakso¹, Mikael Opas¹,
Matti Lehtonen²

¹VTT Technical Research Centre of Finland Ltd
P.O. Box 1000, FI-02044 Espoo

²Aalto University
P.O. Box 15500, FI-00076 Espoo

Abstract

The general objective of the COSI project (2019–2022) is to develop a co-simulation platform for the analysis of thermomechanical and electrical behaviour of a nuclear power plant (NPP) and its supporting electrical grid infrastructure, both on- and off-site. The platform was developed in MATLAB, and connects detailed simulations of the NPP behaviour in Apros Nuclear with grid models developed in Simulink and DIgSILENT PowerFactory.

This platform was tested with the evaluation of impacts on NPP operations and safety caused by disturbances in the on-site and in the off-site electric grids, as well as with the evaluation of NPP operations during future grid scenarios of large-scale renewable energy integration. A detailed model of the Finnish transmission system was developed in Simulink to support these studies, and is another important output of the project.

Introduction

The COSI project main goal is to develop and implement a platform for the co-simulation of the interaction between electrical systems (on- and off-site) and thermomechanical and reactor-physical systems in nuclear power plants (NPP).

This is motivated by the need to fully consider the impacts of disturbances in electric systems, both off-site and on-site, and how the robustness of the grids to which the NPP is connected influence on the plant's safety assessment and internal behaviour. Traditionally, the loss of off-site power is a critical case that drives the design of NPPs and back-up generation, but other grid disturbances are also extremely relevant to be addressed when considering safety enhancements in NPPs. The plurality of relevant disturbances in electric systems is much larger and recent changes in electric grid circumstances in terms of the increased role of renewable power producers, possible increased frequency of extreme weather events, and implementation of digital control systems for electric systems, mean that the previously thought design basis philosophy for electric systems is not fully valid anymore.

Typically there are detailed models available for NPP thermal, reactor physical, and automation systems, but the electrical systems are usually modelled in small detail in such cases. Similarly, power system models typically represent NPPs in simplified ways. This "black-box" approach is detrimental when trying to analyse interconnected phenomena such as grid disturbances and their impacts on NPP operations. Existing electrical simulation studies have not considered thermomechanical system feedback effects and other transient dynamics in much detail. Most of the NPPs in Finland use Apros as the main simulation tool for the thermomechanical and automation process. However, since Apros cannot simulate the detailed electrical system events, e.g., unsymmetrical faults such as single-phase faults in the electric system, detailed electrical power system models are simulated using other simulation tools. In these circumstances, the interaction of the electrical system and the thermomechanical system tends to be neglected.

The project "co-simulation model for safety and reliability of electric systems in a flexible environment of NPP – COSI" was thus conceived to try and address these challenges and mitigate the loss of information yielded by the "black-box" approach. The project was accepted to the SAFIR2022 programme as one-year projects from 2019–2022, each year focusing on the development and improvement of the co-simulation platform (Work Package 1), on testing it for different conditions and scenarios (Work Package 2), and in establishing national and international collaborations to further understand the challenges and applicability of the developed platform (Project Management Work Package).

The co-simulation platform ("COSI platform") was developed in MATLAB, connecting a thermomechanical simulation software (Apros Nuclear) with an electrical simulation software (Simulink, and later DlgSILENT PowerFactory). At the end of the project cycle in 2022, the COSI Platform was at a state where it can be used by external partners, with a published User Manual to instruct on the installation and usage of the platform.

The platform architecture was designed in 2019, and its initial implementation was performed in 2020, with its first results from co-simulations using basic motor-pump sets (thermomechanical) and a small grid (electrical). The description of these preliminary results and the description of the COSI platform during these initial co-simulations are described in the project's Interim Report [1].

Following the requests of the COSI Steering Group, the project implemented the specific co-simulation model for the Loviisa NPP during 2021–2022, with the thermomechanical, reactor physical, and automation models of the NPP in Apros Nuclear and the on-site grid model in Simulink being supplied by the COSI steering group.

A model for the Finnish transmission system was developed as a by-product of the COSI project, to support the implementation and testing of the platform with various disturbance scenarios in the off-site grid. Initially, the off-site grid was considered as a Thevenin equivalent; subsequently it was modelled as an 8-node system, and finally during 2021 and 2022 a robust and detailed 50-node model was developed in Simulink.

During 2021, the COSI Platform was tested with co-simulations of grid fault scenarios in the on-site and in the off-site electric grid, and the thermomechanical behaviour of a generator unit in the NPP was evaluated, as well as the behaviour of specific motor-pump sets within the nuclear power plant. A comparison with a purely electrical simulation was also performed to assess the benefits yielded from a co-simulation approach.

For 2022, the focus was on assessing the NPP behaviour and integration in future transmission system scenarios, specifically with a high penetration of wind power generation at the transmission level. The NPP behaviour in a system with a high proportion of renewable energy generation and in the case of a slow voltage collapse was analysed. Moreover, in 2022, the platform functionalities were expanded to support a second electrical simulation software, DiGILENT PowerFactory.

COSI Platform concept, architecture, and early results

The COSI platform architecture was designed in 2019, and described in details in [1, 2, 3]. The concept behind the co-simulation approach is to combine data generated by two different simulation software – one focusing on the thermomechanical, reactor physical, and automation components of the NPP, and one focusing on the detailed behaviour of the on- and off-site grids connected to the NPP. The coupling between the two simulations happens in a component that is present and has a detailed model implemented in both simulation models. In the case of a NPP, the coupling happens in the generator and its mechanical shaft.

A significant challenge when implementing a co-simulation is to establish a reliable and fast communication channel to enable the data exchange between simulators. The COSI platform utilises the Open Platform Communications (OPC), a protocol supported by all simulation software considered in this project. With this standard, one server and one client need to be established to enable the data communication between different sources.

The master program, which coordinates the data exchange between simulators, was implemented in MATLAB, with plans for future implementation in an open-source language (e.g. Python). The master program is set as the OPC client,

whereas the thermomechanical simulation software – Apros Nuclear – is set as the OPC server. In the initial version of the COSI platform, where the electrical simulation software supported was Simulink, the data communication was performed within the same MATLAB environment. That is, there was only one communication channel implemented in the initial version of the COSI platform, between Apros Nuclear and MATLAB/Simulink, with the latter consisting both of the master program coordinating the co-simulation, and the environment in which the electrical simulation was performed.

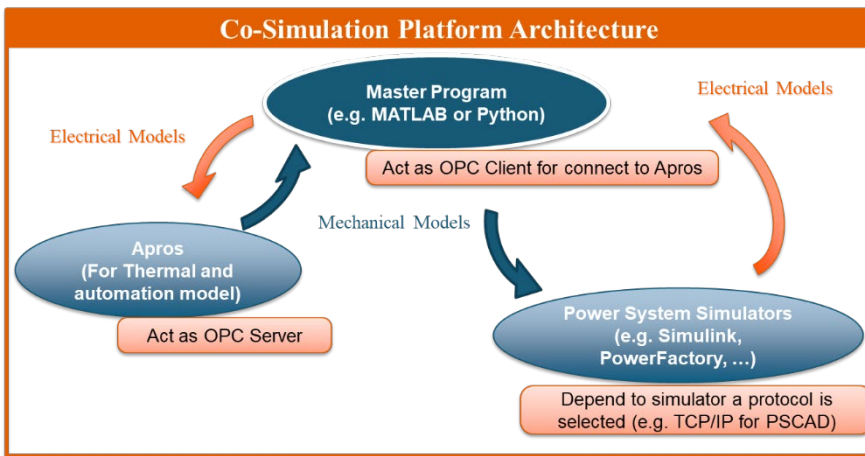


Figure 1. The overall architecture designed for co-simulation between a thermomechanical and an electrical simulation software coordinated by the COSI Platform.

The platform architecture was developed with the intention of expanding its support to other power system simulation software, such as PSCAD or DiGILENT PowerFactory. The integration of PowerFactory was implemented in 2022, and will be described in more detail further in this report.

Following the architecture design in 2019 [2], the first version of the co-simulation platform was developed and made available in 2020. To verify the co-simulation platform, simplified thermomechanical and electrical models have been used in Apros Nuclear and Simulink, respectively. The initial results of the COSI platform can be explored in more details in [4].

In 2021, the platform was further developed to enable the integration of large-scale models that are more representative of nuclear power plants and transmission systems (off-site grids). During this year, the platform has evolved to enable detailed simulations using robust and realistic models. Following the decision from the COSI Steering Group, a detailed model for the Loviisa 1 NPP supplied by Fortum was used. A user manual [5] was also developed to support the installation and utilisation of the platform by external partners.

Implementation of PowerFactory as an additional Power System Simulation Software

The co-simulation platform was already in a usable state at the end of 2021, but the ambition of the COSI project was to further develop the platform to expand its usability and suitability to different contexts. Thus, for 2022, the main goal in WP1 was to expand the platform's compatibility to a new electrical simulation software, to provide an alternative to Simulink. The software selected to be integrated to the COSI platform was DIgSILENT PowerFactory, due to its wide use in the Power Systems industry. The decision to expand the COSI platform to support PowerFactory was taken based in discussions with the project's Steering Group.

There were several challenges with the integration of a new electrical simulation software. The communication architecture in PowerFactory was different than in Simulink, requiring the co-simulation to be coordinated by a flag set in PowerFactory, not in the COSI platform (as it was previously implemented). Moreover, PowerFactory acts as the OPC Client, and the implemented MATLAB script for the COSI platform set-up, save, and show results from the co-simulation.



Figure 2. The cover of D1.1, 2022, the updated version of the COSI Platform user manual that describes the installation process, tips to use the platform, and the integration of PowerFactory as an additional option for electrical simulation software.

The challenges faced in the implementation and the instructions to use the co-simulation platform with PowerFactory were described in [6], an updated version of

the COSI User Manual. The manual was delivered as a research project report in conjunction with a `.zip` file that contains the implemented co-simulation platform in MATLAB and example files for the Apros, Simulink, and PowerFactory integration.

Modelling the Finnish Transmission System

There are a multitude of reasons justifying the development of an open-source model of the Finnish transmission system that is close enough to reality to serve several purposes, both for research and industry. The co-simulation platform initially used an equivalent Thevenin circuit (in the form of a voltage source in series with an inductor and resistor). This has proved very useful, both in itself and as a benchmark for the transmission model under development in the project. However, the project is intended to investigate the impact of events in the NPP on the transmission grid, and vice versa, and so it is clear that there is a need for a spatially relevant model of the grid.

Therefore, the COSI project has the development of a transmission system model as one of its main outputs. This enabled the extent of the impact of grid faults in NPP operations to be ascertained, both in terms of magnitude and distance of the fault from the NPP. In addition, having a working model of the Finnish transmission grid (with sufficient but less-detailed representation of the rest of the Nordic grid) is important for assessing future grid scenarios regarding the rapidly changing generation and demand mix in the power system. In such a context, it is not sufficient to assume the grid is a copper plate, and the consideration of the grid in many energy-based studies will increase the real-world relevance of research in Finland and beyond.

Over the four years of the COSI project (2019–2022), the Finnish transmission system model has significantly developed from initially a Thevenin equivalent to a robust and spatially detailed 50-node model, considering the 400kV part of the Finnish transmission system having around 50 nodes, the reasoning behind using this number as the scale of the developed model in COSI.

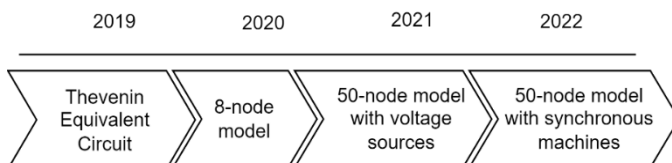


Figure 3. The progress on the Finnish transmission system model development throughout the COSI project.

More details about the 8-node model and the initial version of the 50-node model with generation modelled as voltage sources is available in [7]. Although it was pragmatic to initially model generation as voltage sources to avoid stability issues, it is clear that in order to capture dynamic behaviour we need to represent the generation more accurately, although obviously not as accurately as Loviisa, the

NPP under investigation. This report focuses only in the latest version of this open-source 50-node transmission system model with generation modelled as synchronous machines.

While all hydro, nuclear and CHP generation units are modelled as synchronous machines, the parametrisation follows Matlab default parameters as much as the actual values used, e.g., in Fingrid's PSS/E modelling. Generic multi-band voltage stabilizers have been added to the synchronous machines, and require further refinement specific to each generation unit. More details on the transmission system model and its specific modelling strategies for different components is available in [8].

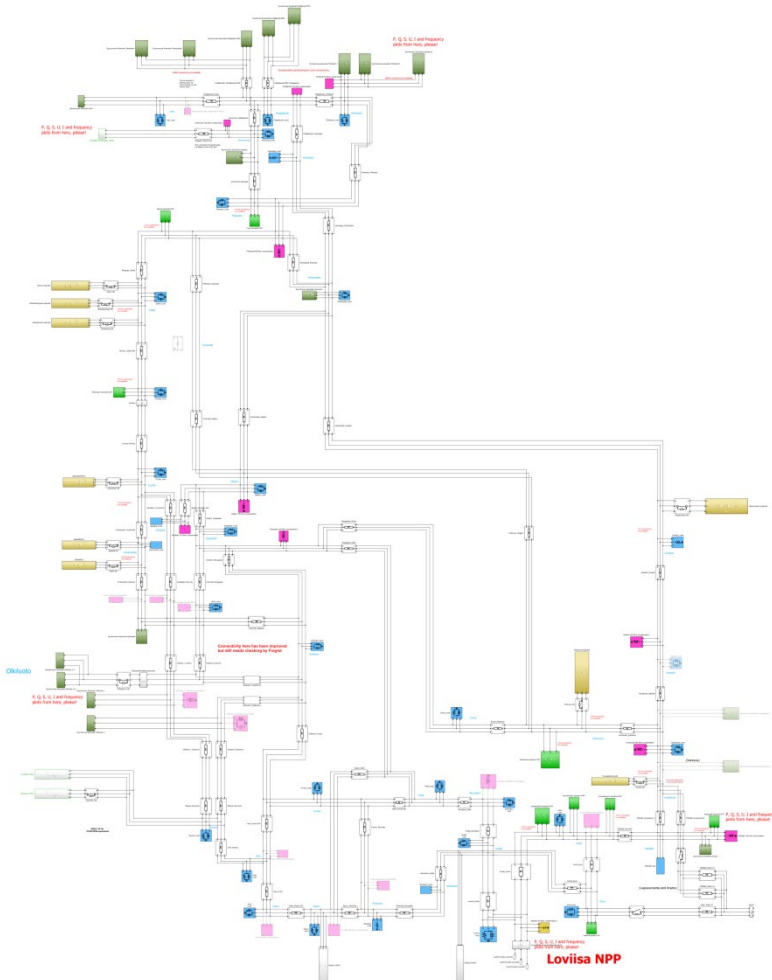


Figure 4. Latest version of the Finnish transmission system model developed in Simulink to support the implementation of grid fault and future grid scenarios, and to assess their impacts on NPP operations through a co-simulation approach.

Short-term grid faults and their impacts on NPP operations

The COSI project aimed to verify the performance of the co-simulation platform with multiple different applications and scenarios. During 2021, the focus was to evaluate the benefits brought by the platform to assess the impacts on NPP operations and safety caused by short-term grid faults in the on- and off-site grids.

An important part of the work performed was to identify relevant scenarios that are interesting and relevant in the context of Loviisa 1's operations for faults occurring both in the on-site electrical grid and the off-site grid, or the transmission system. Selecting the most relevant fault scenarios is a challenging task, given the complexity and variability of grid fault behaviour. There is an infinite combination of potential fault scenarios that could be simulated for the NPP model; different NPPs may also indicate that different scenarios are more relevant, depending on the power system layout both on- and off-site.

Several indicators were considered, such as the severity of fault events, likelihood of fault detection, the profile of the faults and their duration, as well as the total rate of fault occurrence (including all types of faults) estimated for each location based on ENTSO-E and Fingrid historical data [9]. More details on the fault profiles and the considerations behind each fault scenario are available in [7, 10].

With this analysis, the following table was compiled with the fault locations, their types, and their profiles. The checked boxes describe which scenarios were considered.

Table 1. Short-term fault scenarios co-simulated to verify the performance of the COSI platform to assess the NPP behaviour under grid disturbance scenarios.

	Fault location	LG	LLLG	OPC (1 phase)	Fault profile	Total rate of occurrence
Faults in Internal Grid (on-site)	Location 4		✓		SC2	low
	Location 5			✓	OPC3	medium
	Location 6		✓	✓	SC4, OPC5	very low
Fault scenarios in external grid (off-site)	Location 2	✓	✓	✓	SC1, OPC1	high
	Location 3	✓	✓	✓	SC2, SC3, OPC2	medium

The results for some cases in the on-site and off-site are summarised below. Only a few selected cases are exhibited in this report for the sake of space, considering that an in-depth analysis and description for all 10 co-simulations are available in [7, 10].

On-site grid faults

The fault locations considered in the on-site grid of the NPP are described in the Figure below. The naming convention for the fault locations were agreed with the COSI Steering Group, and were maintained for clarity and consistency throughout the project communications.

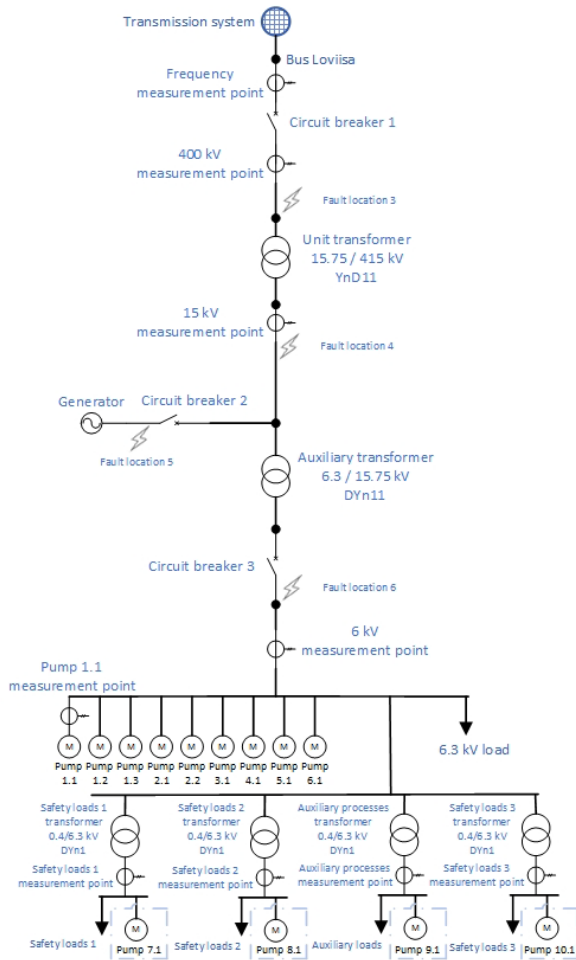


Figure 3. Simplified representation of the on-site grid and the fault locations considered during the COSI project.

A three-phase (LLLG) short circuit fault simulated in Location 4 lasting 250ms, in a situation that on-site protection fails to operate properly, represents well the benefits and the added information gained by performing a co-simulation (COSIM) when comparing to a purely electrical simulation (SIM).

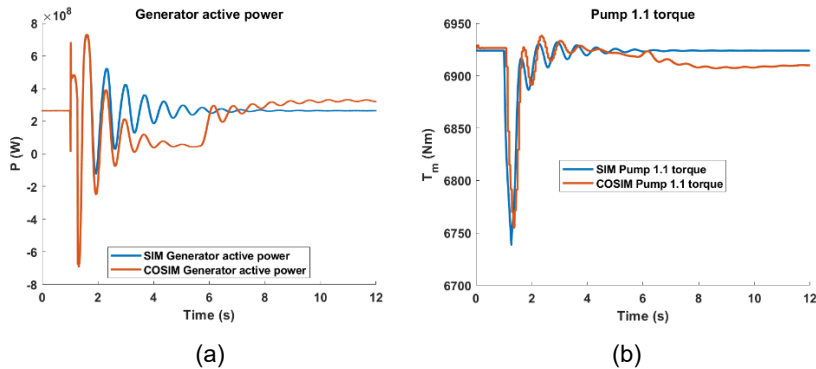


Figure 4. (a) Active power behaviour of the generator unit in Loviisa NPP after a three-phase short circuit fault lasting 250ms (b) Torque behaviour of Pump 1.1 inside the NPP.

The co-simulation shows that after the fault event, the generator active power (Figure 4.a) settles on a new level (lower) after the fault and recovers close to initial value after about 8 seconds. This new active power level is a consequence of valve shutting down completely on a turbine steam line. After about 5.6 seconds the valve opens completely and generator active power starts to increase rapidly. After about 6 seconds there is a small overshoot in generator active power. Such a behaviour is not detected in the purely electrical simulation. Similarly, the co-simulation shows a different behaviour for one of the internal pumps in the NPP after such a fault event. The co-simulated pump 1.1 torque experiences a slightly lower drop. A smaller decrease in torque is beneficial from process viewpoint, as stresses in the system are smaller.

An open-phase condition fault (OPC) lasting 200ms in Location 5 shows also a significant difference in behaviour between COSIM and SIM. These differences between SIM and COSIM yield from the electrical simulation utilising only static values to model the thermomechanical behaviour and the automation processes in the NPP, whereas the co-simulation considers the constant updates in control variables at the NPP based on the automation responses.

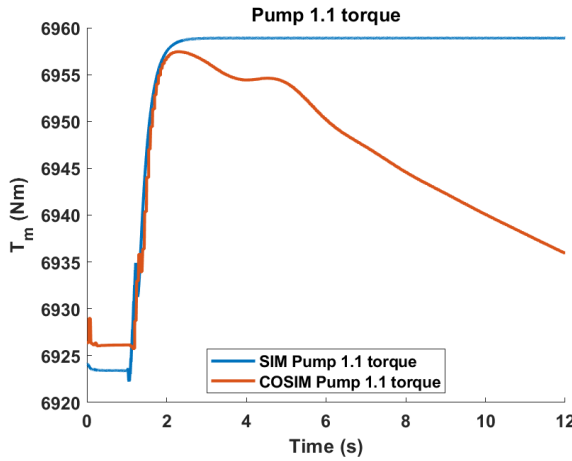


Figure 5. Pump 1.1 torque showing significantly different behaviour between the co-simulation and the simulation cases for an open-phase condition implemented in Location 5.

Finally, a three-phase short circuit (LLLG) fault in Location 6 with duration of 200ms also shows different behaviours between COSIM and SIM cases, with the results from the co-simulation showing higher active power oscillations with the SC4 fault profile. This indicates higher stresses from related systems, which is not desirable.

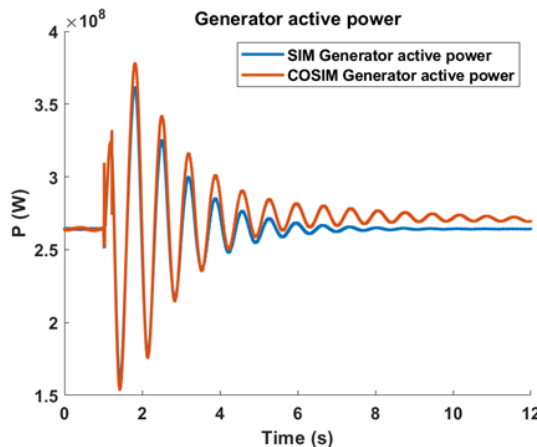


Figure 6. Active power of the generation unit presents higher oscillations in the co-simulation when compared to the purely electrical simulations.

Off-site grid faults

Similarly as with the on-site grid faults represented before, the off-site grid fault scenarios were implemented in different locations following the same naming convention as agreed.

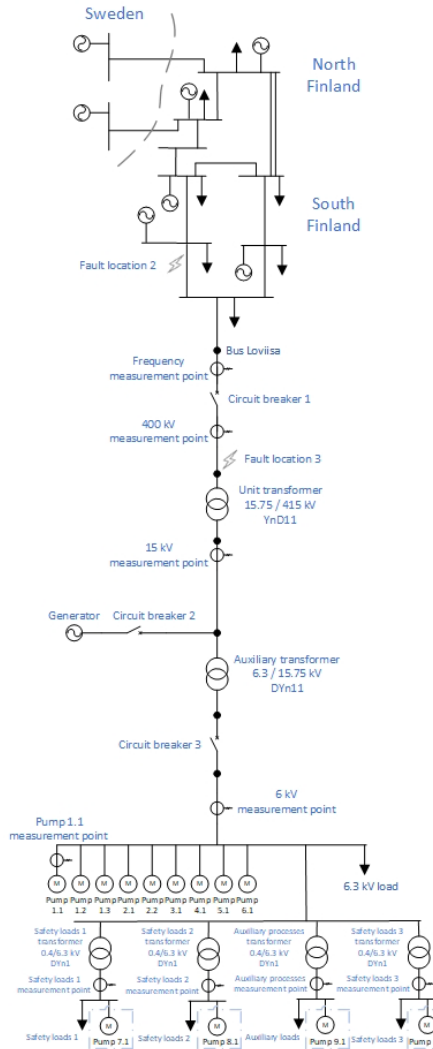


Figure 7. Simplified representation of the off-site grid (transmission system model) and the locations of the implemented faults.

A single line to ground short circuit fault (LG) was implemented in Location 2 with a duration of 500ms. In this fault scenario, the main protection fails and backup protection operates. Backup fault clearance of busbar and line faults, with fault duration of 500 ms. Before the fault one bus is out of operation. The bus protection is supposed to fail to operate and the fault is cleared by remote zone 2 distance protection.

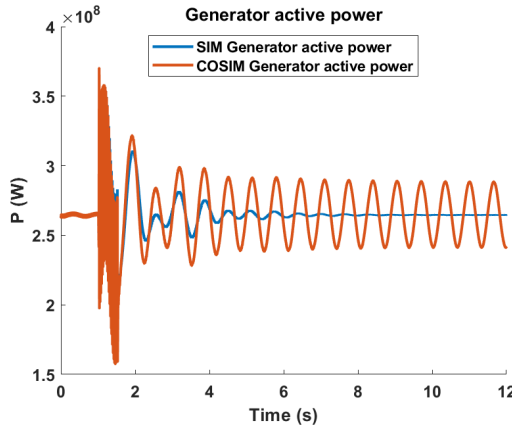


Figure 8. Generator active power behaviour after a line-to-ground fault in Location 2 in the off-site grid.

In this scenario, the co-simulation does not differ greatly from the electrical simulation except for the oscillation after the fault is cleared. The generator experiences an overvoltage but it is within limits established. Evaluating the behaviour of Pump 1.1 torque, we also detect a difference between the COSIM and SIM, as shown in Figure 9.

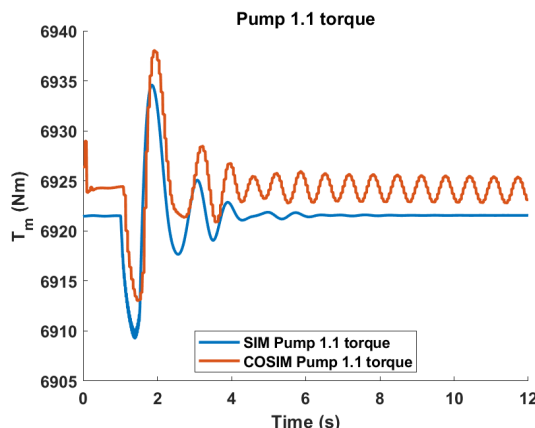


Figure 9. Torque of pump 1.1 shows higher oscillations in a co-simulation, information which is not captured in the purely electrical simulation.

An open phase condition lasting 200ms was simulated in the high-voltage side of the unit transformer (Location 3). The behaviour of the Pump 1.1 torque is also shown in such a scenario, in Figure 10. the pump 1.1 response with and without co-simulation are similar during the fault. For few seconds after the fault the results settle to almost the same level. Then, however, the torque (and speed) results start to differ since the Simulink simulation uses static input values as setpoints instead of updating them according to process needs.

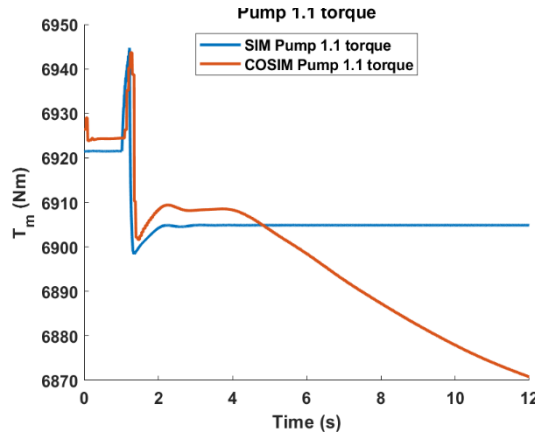


Figure 10. Torque of pump 1.1 in the event of an open phase condition in Location 3 that is cleared after 200ms.

The simulations and results covered two backup and three normal protection cases in off-site grid fault locations 2 and 3. The cases included scenarios where a line section is disconnected in the transmission grid (location 2), NPP fault-ride-through, NPP transfer to house load operation, and NPP generator disconnection (location 3). The cases represent extreme situations in the system, include necessary simplifications and hopefully also underline the current state of the models.

The results from the on- and off-site fault scenario co-simulations show that in many cases, the differences between co-simulation and purely electrical simulation are quite small. However, results show that co-simulation produces differing results to pure electrical simulation and could therefore be beneficial to use in certain cases. In 2021, fault profiles included relatively fast fault scenarios, where the benefit of co-simulation may be questionable, as the results doesn't differ much between COSIM and SIM. However, in situations when the fault durations were longer and the fault clearance slightly delayed, the importance of the co-simulation was verified. This indicates that scenarios with slightly longer duration fault profiles benefit the most from the added complexity of a co-simulation including the thermomechanical models of an NPP. Furthermore, the results showed the importance of counting with more detailed electrical models, especially including more information about protection systems, as the co-simulations were limited to test only scenarios where protection systems would fail to act in some manner. These results motivated the

continuation of the project and the exploration of longer fault scenarios, as well as the integration of NPPs in future transmission systems with high penetration of renewable energy generation.

NPP integration in future grid scenarios

In 2022, the objective of the COSI project was to expand the co-simulation platform to enable the assessment of longer-duration events in the transmission system and their impacts on NPP operations. Following the developments in the transmission system model described in this report, three scenarios were implemented:

- Scenario I: Transmission system with Spring-time demand and generation – to assess the behaviour of the NPP connected to a system with lower general inertia;
- Scenario II: Transmission system with Spring-time demand and generation, plus the addition of wind power generation – to evaluate the behaviour of the NPP in a system with higher inertia (more generation) but lower average inertia per generation source;
- Scenario III: slow voltage collapse caused by the loss of wind power generation, the tripping of a HVDC link, and the tripping of a large NPP.

Scenarios I and II provided a good baseline for the disturbance results, and also explored the impacts of inertia in the behaviour observed at the NPP. It becomes clear that the transmission system model still requires further development in terms of modelling its generation sources, work which is proposed as future developments. Figure 11 shows that the main generator in Loviisa has lower oscillations when connected to a higher inertia grid, a behaviour that follows the expectations. Furthermore, the co-simulation shows a slightly different behaviour when compared to the purely electrical simulation.

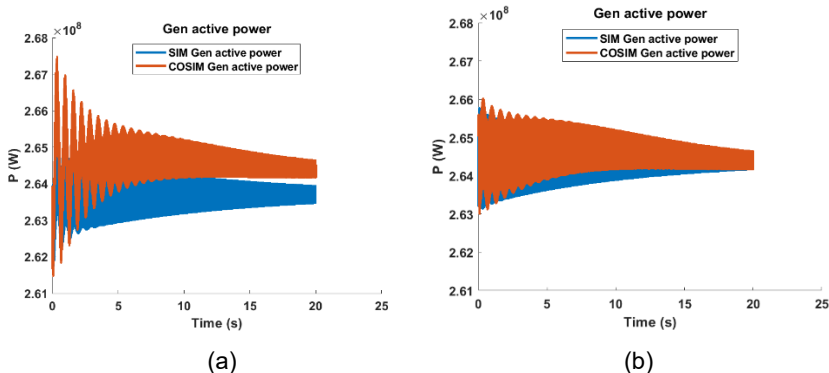


Figure 11. Active power behaviour of the generator unit in Loviisa NPP for Scenario I a) lower inertia system in Scenario I (b) higher inertia off-site grid in Scenario II .

The co-simulation also presented different behaviour for the thermomechanical components within the NPP, namely the primary circulation pumps and the feedwater pumps. Figure 12 shows the differences in speed and torque for Pump 1.1 between the co-simulation and the purely electrical simulation, for Scenario II.

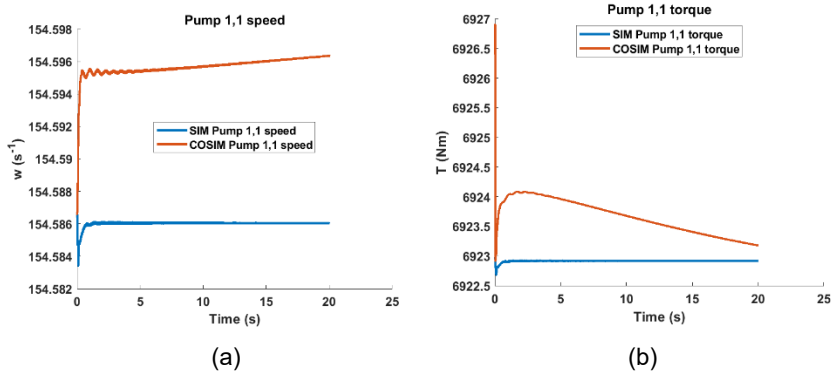


Figure 12. Different behaviour between co-simulation (COSIM, in orange) and purely electrical simulation (SIM, in blue) for Pump 1.1 (a) speed and (b) torque.

The differences were observed COSIM torque and speed – speed increasing, torque decreasing. This difference in water pump behaviour is one of the COSI platform benefits. This extra detail in the thermomechanical behaviour of the NPP is worth investigating, and is observable only in the case of a co-simulation. Given the time limitations, and the fact that the co-simulations were taking an extremely long time to be performed, further analysis of this behaviour with a longer time horizon were not possible to be carried out in this project. If COSI platform were to be developed further, even longer simulations could be carried out to see where these values settle.

Scenario III implemented an event with a slow frequency variation and voltage drop in the transmission system. However, similarly to Scenarios I and II, this implementation clarified the need for further developments in the transmission system model, given that the current version is unable to produce similar results as the ones measured by Fingrid in characterising a significant frequency deviation. Figure 13 shows the frequency oscillations measured at the Loviisa bus in the transmission system. It is shown that the frequency oscillation does not reach the levels to be characterised as a frequency deviation, and their duration is not long enough – which indicates a need for further development of the transmission system model to properly model such frequency events.

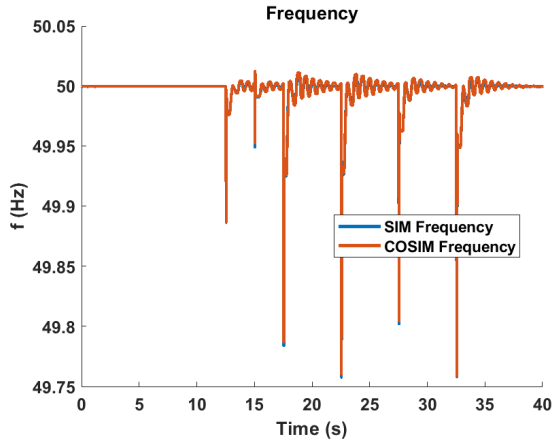


Figure 13. Frequency variations caused by the slow voltage collapse.

Generator oscillations can be a source of concern in this Scenario. Each disturbance caused oscillations in generator measurements as seen in Figure 14. The largest active power and speed deviations were 600 kW and 10 rpms. The stator current increased during the voltage collapse but the active power of the generator remained somewhat stable. Referring to the reactive power measurement at Loviisa bus (Figure 15b), we see that it increased significantly. The extra current generates more reactive power to balance the grid while increasing the power factor ($\cos\phi$) of the generator.

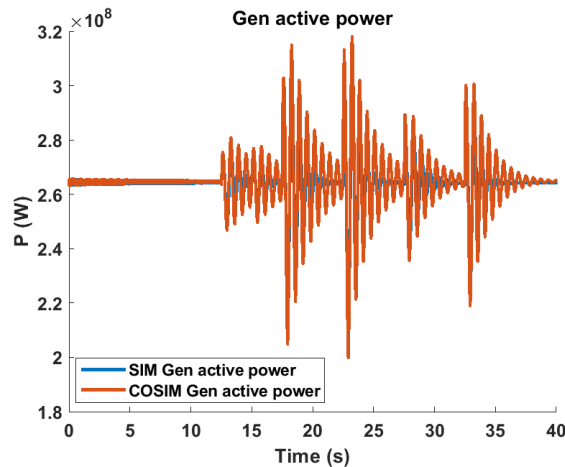


Figure 14. Loviisa NPP generator active power remains at a stable level during the voltage collapse in the system, albeit with high oscillations in each step of the events in Scenario III.

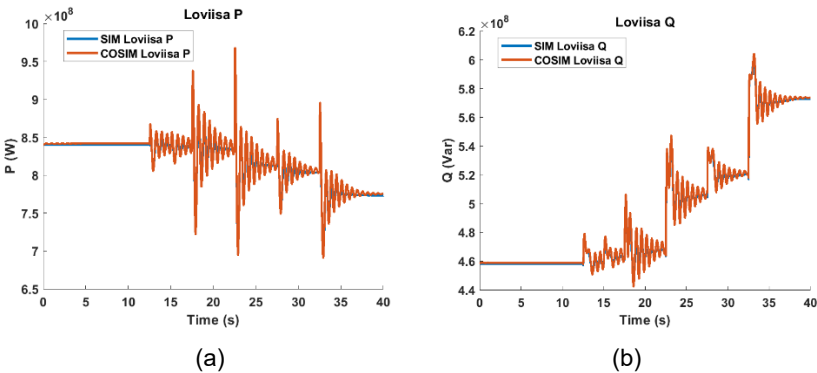


Figure 15. Active (a) and reactive (b) power measurements at the Loviisa bus in the transmission system model shows a decrease in power factor in the NPP bus.

The COSI platform presented its expected behaviour, with the most relevant differences towards a purely electrical simulation being shown in analysing the internal components of the NPP, namely the primary circulation and feedwater pump sets, which had significantly different behaviours in SIM and COSIM. The main generator in Loviisa also presented more pronounced oscillations caused by the voltage drops in the transmission system during the co-simulation when compared to the simulation, a result of having mechanical inertia and internal automation systems modelled in detail from the thermomechanical simulations.

The time for the co-simulations to be performed were significantly increased when compared to the ones performed for short fault durations in 2021 [7, 10]. Implementing longer-lasting events clearly has an impact and is expected to produce longer co-simulation runs, but the increase in length has reached a state that greatly limited the possibility for running longer and slower events. This is in great part caused by the more detailed implementation of components in the transmission system model, increasing the computational load for the co-simulations to be performed.

At its current state, the transmission system model shows great promise, but further work is needed in implementing more detailed components. On the other hand, such efforts will also yield greatly increased co-simulation times. This trade-off between having a robust and detailed model while also keeping in mind the co-simulation times is a significant question proposed as a continuation for the COSI project. The development of a simplified transmission system model that reflects the geographical behaviour and is able to provide the same level of detail while still being less computationally expensive is one of the goals of the follow-up SINARP project.

Moreover, there is a need to evaluate alternatives to optimise the implementation of the COSI platform in terms of its run-time, be it through an implementation in computationally lighter programming languages or with the use of distributed computing. Moreover, the COSI platform would benefit from further development in

establishing a more secure and stable communication between the thermomechanical simulation and the electrical simulation. Identifying these alternatives is proposed as a natural continuation of the COSI project.

Summary and conclusions

The COSI project has developed a co-simulation platform to connect thermomechanical simulations (performed in Apros Nuclear) with electrical simulations (performed in Simulink, and later also in DlgSILENT PowerFactory). The COSI platform was implemented in MATLAB and made publicly available as one of the project's final deliverables [6], accompanied by a user manual that guides the utilisation of the platform with basic example models.

The platform was tested with several configurations throughout the project. Initial testing with basic motor-pump sets implemented in Apros Nuclear and Simulink had shown great promise, and the platform was expanded to enable the integration of large-scale NPP thermomechanical models and on- and off-site grid electrical models. Even with a significant increase in the number of components being considered in the co-simulation, the platform has maintained its stability and consistency.

In addition to the development of the platform, the COSI project has also produced an open-source model of the Finnish transmission system, a significant undertaking that has the potential to be exploited by several future research. This model, developed in Simulink, accurately represents the Finnish transmission system in 50-nodes. However, it was noted in the final year of the COSI project that, despite being already a robust and detailed model, there is still plenty of space for further improvements and increasing the accuracy of the model when compared to the real-world system. This development is proposed as future work.

The platform and the transmission system model were used to support the research on the impacts on NPP operations and safety caused by disturbance scenarios in the on- and off-site grids. During 2021, short-term disturbances and grid faults were tested; in 2022, the focus shifted to longer-duration scenarios.

The benefit of the co-simulation, when compared to a purely electrical simulation, was evident when considering the detailed behaviour of components in the thermomechanical models of the NPP. In some cases the difference in detail level were not significant, whereas other scenarios presented very relevant differences in behaviour for Loviisa's main generator and primary circulation and feed water pumps.

Acknowledgement

The COSI project gratefully acknowledges the support and guidance from its Steering Group, with participants from TVO, Fortum, Fingrid, STUK, Vattenfall, and Energiforsk.

References

- [1] Hämäläinen, J., Suolanen, V. (eds). 2020. SAFIR2022 – The Finnish Research Programme on Nuclear Power Plant Safety 2019-2022: Interim Report. Espoo: VTT. VTT Technology 383. Plant Level Analysis, p.51-63.
- [2] Divshali, P, Hänninen, S, Laakso, P & Korvola, T. 2020. Architecture Design for NPP Co-Simulation Platform. VTT Technology, no. 371, VTT Technical Research Centre of Finland. <https://doi.org/10.32040/2242-122X.2020.T371>
- [3] Hasanpor Divshali, P.; Laakso, P.; Hänninen, S.; Millar, R.J.; Lehtonen, M. Electrical and Thermomechanical Co-Simulation Platform for NPP Energies 2021, 14, 939. <https://doi.org/10.3390/en14040939>
- [4] Lehtonen, M, Rosenström, M, Hänninen, S & Divshali, P. 2020. Description of baseline simulation. VTT Technology, no. 372, VTT Technical Research Centre of Finland. <https://doi.org/10.32040/2242-122X.2020.T372>
- [5] Baranauskas, M., Keski-Koukkari, A., Laakso, P., Motta, S., Millar, R.J. 2021. COSI: Co-simulation tool user manual. VTT Research Report VTT-R-00775-21.
- [6] Baranauskas, M., Keski-Koukkari, A., Laakso, P., Motta, S., Millar, R.J. 2022. COSI: Co-simulation Platform User Manual – PowerFactory Integration. VTT Research Report VTT-R-00809-22.
- [7] Keski-Koukkari, A., Baranauskas, M., Millar, R.J., Motta, S. 2022. COSI – Critical fault-based events in the off-site electrical system and co-simulation results. VTT Research Report, VTT-R-01061-21.
- [8] Baranauskas, M., Laakso, P., Motta, S., Millar, R.J. 2022. COSI – Future grid scenario simulation. VTT Research Report VTT-R-00949-22.
- [9] ENTSOE, "Nordic and Baltic Grid Disturbance Statistics 2019," 2020. [Online]. Available: https://www.fingrid.fi/globalassets/dokumentit/en/electricity-market/cross-border-transmission/nordic_and_baltic_grid_disturbance_statistics_2019_22.10.2020.pdf
- [10] Keski-Koukkari, A., Baranauskas, M., Motta, S., Millar, R.J. 2022. COSI – Critical fault-based events in on-site electrical system and co-simulation results. VTT Research Report, VTT-R-00781-21.

3.2 New developments and applications of PRA (NAPRA)

Ilikka Karanta¹, Terhi Kling¹, Tero Tyrväinen¹

¹VTT Technical Research Centre of Finland Ltd
P.O. Box 1000, FI-02044 Espoo

Abstract

Groundwork for PRA with long time windows has been laid in the Nordic PROSAFE project; NAPRA pilot model of a spent fuel pool integrates deterministic behavior and probabilistic analysis, and takes into account repairs and recoveries. Dynamic features of human reliability, and human error possibilities and circumstances conducive to it have been identified for nuclear power plant planned outages in general, and for a heavy lifting case in particular. Modelling issues of digital I&C PRA have been clarified in the international DIGMAP and DIGMORE benchmark projects. The DIGMAP study showed that the same results can be produced with very different modelling approaches. A fire PRA model has been created that integrates results of deterministic fire analyses, fire brigade behavior and probabilistic aspects; it is robust and straightforward to apply on the PRA part.

Introduction

NAPRA project has aimed at generating new knowledge about various topical issues in probabilistic risk assessment (PRA). The subfields of PRA dealt with include seismic and fire hazards, PRA with long time windows, PRA of spent fuel pools, dynamic human reliability analysis (HRA), HRA of maintenance breaks, digital I&C reliability and risk analysis, multi-unit and site-level PRA, and PRA of small modular reactors.

Hazards

Typically, a significant portion of core damage risk comes from external and internal hazards (OECD 2014; OECD 2015). Therefore, it is important that hazard analyses, estimated frequencies and modelling of the consequences of hazards are sufficiently realistic. To achieve this, proper integration of deterministic and probabilistic hazard analyses is needed. In addition, it is important to analyse human behaviour in hazard scenarios.

Seismic PRA

The Finnish seismic PRA procedure has been outlined and compared with international practices (Helminen 2020). The outline is shown in Fig. 1. The international reference considered was a draft technical opinion paper (OECD 2019)

that represents the technical opinion consensus of risk analysts and experts in OECD NEA member countries concerning seismic PRA for nuclear facilities. Based on the comparison, and discussions with the PRA experts of Fennovoima, differences and potential topics for more detailed research were identified. The following two were identified as central: connecting risk significance and fragility analysis of systems, structures and components (SSC); and developing general seismic PRA modelling principles. The following three were also identified as interesting: more detailed study of seismic HRA; failure correlation and seismic grouping of SSCs; assumptions applied to the seismically induced LOCA, fires and floods.

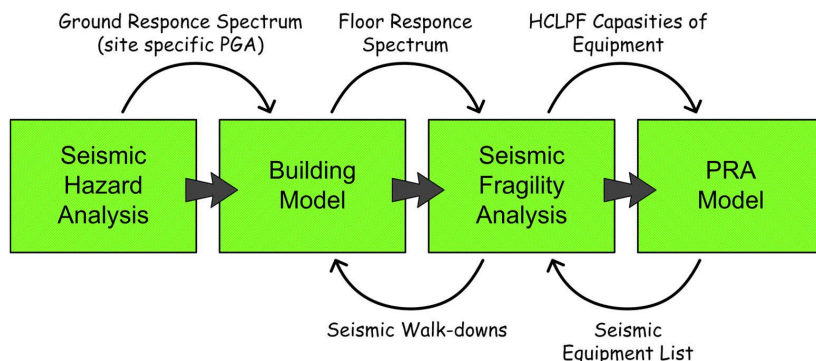


Figure 1. An outline of the Finnish seismic PRA procedure.

Fire PRA

We have implemented an old nuclear power plant cable room fire scenario (Hostikka et al. 2012) in a new tool, simulation-based event tree of FinPSA, to explore possible benefits of the tool in modelling time-dependencies related to the scenario (Tyrväinen et al. 2020b, Tyrväinen et al. 2021b). Simulation-based event trees are event trees with user-written computation scripts that calculate probabilities of event tree branches and possibly other variable values; a module in the FinPSA code implements this functionality (VTT 2014). The scenario concerns a fire occurring in a cable room that contains both power and instrumentation and control (I&C) cables of two redundant subsystems. The cables of the subsystems are physically separated in a multi-level metallic cable tray system. In the places where the cables of different subsystems are near each other, mechanical shield plates have been installed between the cable trays. The cables are the primary fire load in the room, and the power cables are the most probable source of ignition. In the study, the ignition was assumed to occur in one subsystem, and the analysis aimed at estimating cable damage probability in the other subsystem.

The main components of the model are the event tree, Monte Carlo fire simulations, and a stochastic operation time model for firefighting. Fire simulations from the old case study (Hostikka et al. 2012) were utilised. In that study, 200 fire

simulations were performed separately using deterministic Fire Dynamics Simulator (FDS) (McGrattan et al. 2013), 100 for the case with sprinklers operating and 100 for the case with sprinklers failed. To get a representative sample, the Excel-based Probabilistic Fire Simulator (PFS) (Hostikka & Keski-Rahkonen 2003) was used for generating the inputs to FDS with Latin hypercube sampling. The random variables included the location and size of the initial fire, properties of power cables and concrete, and the response time of the sprinkler system (if working). For each simulation, the time when the temperature of the insulation material of the cables reaches the critical temperature at which the cable is assumed to fail was determined. The uncertainty related to the critical temperature of the cable was taken into account by using two alternative critical temperatures, 180 °C and 215 °C. Results of the fire simulations were imported to FinPSA as vectors (Tyrväinen et al. 2020b). The relevant variables imported were the detection time, cable damage time and time when firefighting conditions become intolerable.

The stochastic operation time model is implemented in FinPSA scripts in eight parts corresponding to different operational phases, including fire detection, guard centre actions, control room actions and fire brigade actions. The event tree is presented in Figure 2. The FinPSA model was simulated 10000 times. For each individual fire simulation and operation time simulation, it was checked whether the fire brigade was able to suppress the fire before cable damage. Furthermore, it was checked whether the firefighting conditions (temperature, visibility, heat radiation) were tolerable when the fire brigade arrived in the room. The results calculated using FinPSA are approximately same as the results calculated by the old tool, PFS, but FinPSA offers better model structure, better readability and better maintainability than PFS.

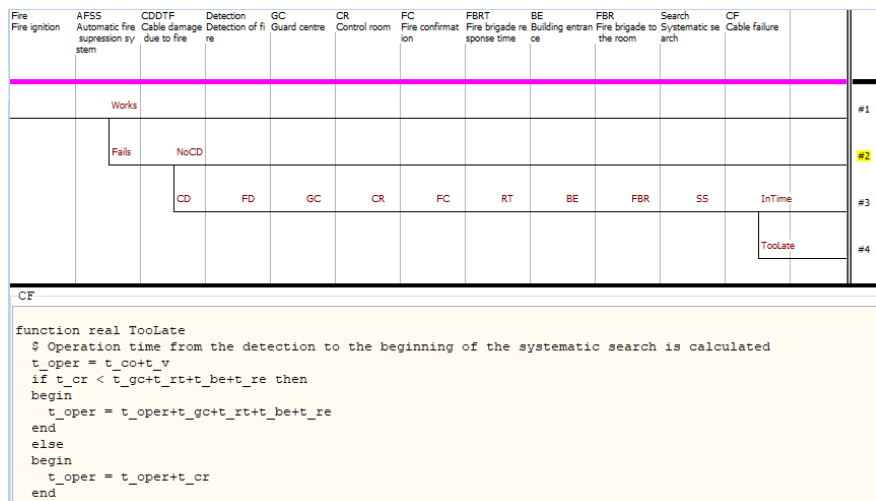


Figure 2. Simulation-based event tree model for cable room fire scenario including stochastic operation time model for firefighting.

A large number of uncertainties have been identified for the cable room fire PRA study. The uncertainties are related to fire simulation parameters, interpretation of fire simulation results, fire simulation model itself, computation methods, time delays of firefighting actions and reliability of the automatic suppression system. The significances of different uncertainties have been assessed according to possibilities. Most of the uncertainties were assessed to have a minor impact on the results. The most significant uncertainties are related to some fire simulation parameters (particularly time of maximum heat release rate), reliability of the automatic suppression system and some central firefighting actions.

We have studied reliability analysis of sprinkler systems by reviewing previous analyses found in the literature and conducting a simplified fault tree analysis for a generic wet pipe system (Tyrväinen et al. 2021b). Such reliability analyses have been quite rare or at least not published. Collection of sufficient amount of failure data for sprinkler system components is necessary for credible reliability analysis.

Probabilistic risk assessment with long time windows

PRA models are mostly very simplified with regard to mission times of safety functions, timings of events and repairs of components (Tyrväinen et al. 2020a). Typically, a mission time of 24 hours is assumed for most safety functions in level 1 PRA. The Fukushima nuclear power plant accident however pointed out that it might be relevant to consider longer time windows in some accident scenarios. In addition, spent fuel pool accidents typically last at least several days. In such long accident scenarios, it is important to model recoveries and component repairs, because there is plenty of time to perform the actions and without crediting the repairs and recoveries the results would be very conservative. Also, existing human reliability analysis methods have mainly been developed for shorter time windows, and the static PRA methodology has limited capability to represent long-lasting accident scenarios, which are dynamic in nature. There are also other issues related to long time windows, such as how to specify mission times and success criteria, that needed clarification. Due to these issues, a Nordic project called “Prolonged available time and safe states” (PROSAFE), funded partially by NKS and NPSAG, was implemented in 2019-2020 in cooperation with Swedish and Norwegian research partners.

Literature review and stakeholder survey on long time windows

Two surveys were carried out in PROSAFE, a literature survey and a stakeholder survey (Tyrväinen et al. 2020a). The topics encompassed by the surveys included safe state, acceptance criteria, success criteria, mission time, HRA methods (especially regarding long time window), and crediting recoveries and repairs. The literature related to long time windows appears to be very limited, because PRA is typically limited to the mission time of 24 hours. Scenarios with long mission times are generally recognized as a challenging area that needs to be studied more.

Ideally, successful PRA sequences should lead to a safe, stable end state. Therefore, the definition of the safe, stable state can affect success criteria and mission times. However, in practise, that does not seem to be usually the case. Success criteria analyses focus typically on avoiding core damage within a fixed time window rather than reaching safe, stable state. Different safe (stable) state definitions found from the literature and specified by the stakeholders of the PROSAFE project vary significantly, and there does not seem to be common way to define successful PRA end states. Some also apply the concept of a controlled state in PRA instead of safe state.

Mission time may be defined as “the time period that a system or component is required to operate in order to successfully perform its function” (ASME 2009). In level 1 PRA, mission time of 24 hours is usually applied for most safety functions and components. In level 2 PRA, the mission time is typically 24 hours or 48 hours, but in some cases, even 72 hours has been applied. In spent fuel pool analyses, longer mission times may also be used, e.g. 72 hours. It is usually not accurately analysed how long it takes to bring the plant to a safe, stable state. Extending the mission time is however generally recommended if plant conditions are not stable at the end of normal mission time. Modelling of different mission times is considered challenging because it increases the model complexity and the number of basic events.

Some recovery actions are usually modelled in PRA, e.g. for offsite power, emergency diesel generators and emergency core cooling. Repairs are usually not modelled in PRA, except when long mission times are modelled. Probabilities of recoveries and repairs are estimated based on HRA methods, plant data or expert judgments depending on the case. Dependencies between recoveries, repairs and other human actions are usually not taken into account. Modelling of recoveries and repairs is considered a challenge because it significantly increases the model complexity.

Answers to the questionnaire highlighted spent fuel pool accidents and human reliability analysis in long mission time scenarios as important topics to be studied. Longer time windows also bring in the need to model repairs that are usually neglected in normal scenarios with mission time of 24 hours. Modelling of different time windows and time-dependent success criteria could also make PRA models more realistic. In addition, there has been some concern over the applicability of normal failure data to long mission time scenarios. In addition, more consistent and realistic consideration of safe end states could improve PRA analyses, e.g. by making mission times and success criteria more realistic, but it was not considered the most important development area according to the questionnaire answers.

Modelling dynamic success criteria

A dynamic success criterion is a success criterion that changes during the mission time. For example, two cooling water pumps may be needed in the beginning of an accident for sufficient cooling, but later as the amount of residual heat decreases only one pump may be sufficient. Dynamic success criteria have been rarely

modelled in PRA. Typically, conservative static success criteria are used, e.g. that two pumps are required for the whole mission time regardless of the decrease in residual heat.

In fault trees, a dynamic success criterion can be modelled by creating separate fault trees for different success criteria, e.g. one for 2-out-of-4 criterion and one for 1-out-of-4 criterion. In addition, failure to run basic events need to be divided between the time intervals, i.e. for each component, there is one basic event for the first interval and one basic event for the second interval. It has to also be modelled that components that fail during the first time interval remain failed for the second interval unless they are repaired.

We have developed a simple example of dynamic success criteria modelling using fault trees (Tyrväinen et al. 2020a). The modelling is not logically difficult but may significantly increase the complexity of a large PRA model. If there is need to model dynamic success criteria for several safety functions, it would be convenient to have some of the modelling or analysis process automated, e.g. automatic generation of needed fault trees based on one master fault tree. Modelling of repairs and dynamic time windows are issues that can also potentially make dynamic success criteria modelling more complicated and should be studied more in this context. Modelling of dynamic success criteria may require more comprehensive success criteria analyses than normally used, e.g. more thermo-hydraulic simulations to determine the time windows.

Simulation-based PRA for spent fuel pool

We have developed a simulation-based PRA approach for spent fuel pool (Tyrväinen & Immonen 2022a; Tyrväinen & Immonen 2022b; Tyrväinen et al. 2021a). It integrates deterministic spent fuel pool behaviour and probabilistic analysis. The spent fuel pool water level and temperature are calculated in the simulations at every time point of interest, e.g., when a make-up water system is started or fails. The time windows for probabilistic analysis are dynamically calculated based on the current spent fuel pool conditions. For example, the mission time of a make-up system is calculated based on how long it takes to reach the safe state, i.e., the water level is normal, and the spent fuel pool cooling system is back in operation. Durations of manual actions, repair times and failure times are drawn from probability distributions to determine accident progression timings on each Monte Carlo simulation cycle. The modelling approach has been implemented in the simulation-based event trees of FinPSA (the same tool as used for fire PRA in the Hazards chapter).

The time-dependent behaviour of the spent fuel pool is calculated by a deterministic model implemented in the scripts of FinPSA. The modelling approach was chosen based on a survey of literature (Tyrväinen & Immonen 2022a). The zero-dimensional model of Ramadan et al. (2018) was selected, because it is sufficiently simple but realistic enough. The modelling approach is based on solving the spent fuel pool water mass and energy balances. The differential equations are solved numerically using Euler's method. For real application, the model should still

be validated against a more realistic computer code. This study anyway demonstrated how a deterministic physical model can be integrated in FinPSA scripts and used as a part of a dynamic PRA model.

We have analysed two spent fuel pool accident scenarios, transient and loss of offsite power (LOOP) (Tyrväinen & Immonen 2022b). The analysis has been performed based on a fictive and simplified static PRA model created for the PROSAFE project (Tyrväinen et al. 2020a; Tyrväinen et al. 2021a). The simulation-based event trees have been developed to quantify top minimal cut sets of the static PRA model more realistically. The upper part of the simulation-based event tree for LOOP is presented in Figure 3.

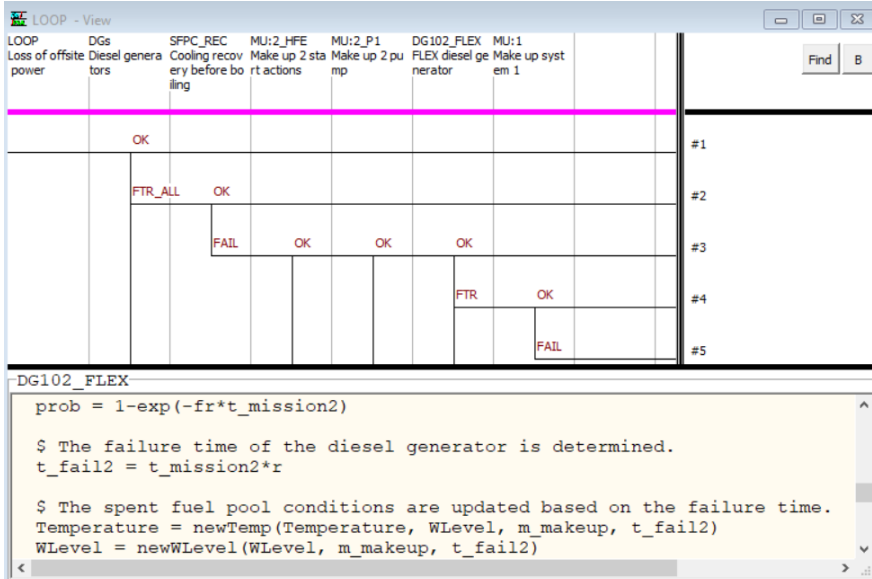


Figure 3. Simulation-based event tree model for loss of offsite power of a fictive spent fuel pool.

The results of dynamic (simulation-based) and static analyses have been compared in detail (Tyrväinen & Immonen 2022b). The dynamic analysis resulted in smaller fuel damage frequencies in both scenarios, but the results were of the same order of magnitude. Larger differences appeared at the minimal cut set level: the frequencies of minimal cut sets with failure to run events were significantly smaller in dynamic analysis, because the mission times were on average much shorter than the 24 hours used in static analysis. It was also observed that crediting the operation time of emergency diesel generators before failure decreased the frequencies of minimal cut sets significantly in the LOOP case. On the other hand, the common dependency of the mission times on the offsite power recovery time increased the frequencies of some minimal cut sets compared to the static PRA that did not model the dependency. In the LOOP case, the effects of dynamic analysis were larger than

in the transient case. In the transient case, static analysis gave a relatively good approximation of the risk, except for the minimal cut sets that included a failure to run basic event.

Modelling repairs decreased the fuel damage frequencies significantly in both cases. Addition of a make-up system repair to analysis decreased the fuel damage frequency around 90%. The impact was however smaller when a second make-up system repair was added to the transient model, because human failure events to diagnose the need to start make-up systems started to dominate results. Repairs were modelled also in the static analysis, and in some cases, it could be done well with small difference compared to dynamic analysis. On the other hand, in some cases, repair modelling could not be performed in static manner due to complex time-dependencies.

There are some challenges related to application of the approach for full-scope spent fuel pool PRA. The simulation-based event tree becomes easily very complex when there are many failure combinations to analyse, and there is no good tool support to integrate the minimal cut sets of static PRA and the simulation results. One possibility would be to develop simulation-based event trees as independent PRA model so that there would be no need for static PRA model. However, the minimal cut set information would be lost, and the identification of all relevant failure combinations could be a challenge. Another potential solution would be to develop a simulation module for automatic quantification of minimal cut sets. There is no particular need to tie the simulations to an event tree. The execution of the simulation scripts could be controlled by attributes related to the basic events in the minimal cut sets. This would provide more flexibility than a simulation-based event tree and would give wider possibilities to perform advanced minimal cut set quantifications. We have also investigated whether the simulation-based model could be solved more efficiently by discretizing the time distributions of the model (e.g. timings of manual actions), which is applied often in the context of dynamic event trees. One sequence from both LOOP and transient models has been analysed using the discretization (Tyrväinen & Immonen 2022b). In the transient case, the approach produced only slightly conservative result with a small number of simulation cycles. On the other hand, in the LOOP case, the result was very conservative even with a very dense discretization, because the tails of the offsite power recovery time and diesel generator repair time distributions dominated the result. The usefulness of the time discretization approach seems to be case-specific. It can be useful to perform Monte Carlo simulations for comparison so that the conservativeness of the analysis can be evaluated.

Human reliability analysis for long time windows

Long time windows affect also human reliability analysis. In short time window scenarios (with a time span of 24 hours), repairs of systems, structures or components, or even recoveries do not need to be taken into account because it can be assumed that there is too little time for them. However, when longer time is available, there is time for repairs and recoveries, and taking them into account

helps avoiding unnecessary conservatism in the results. Another factor influenced by the long available time windows is that there is ample time in each task for both diagnosis and all necessary actions. This affects human error probability (HEP) estimates in two ways. First, the stress level of workers conducting the activities are lower than they would be when available times are short. Second, there is enough time to recover from memory lapses and other factors that may have led to human errors. Both of these diminish the HEPs. However, HRA of repairs poses some issues of its own. First, the repairs are conducted by field operators (mechanics) and not by operators; it is uncertain to what extent the HEP estimates that usually describe operator performance are generalizable to this worker group. Second, task analyses of repair tasks may not be available, and they have to be constructed. Third, equipment failures are usually noticed by the operators, and they call a mechanic; thus, there are elements of crew effects in every repair task. Also human activities related to the deployment and use of mobile (FLEX) equipment – pumps, diesel generators, hoses - were considered, although only FLEX diesel generators were eventually taken into the HRA model.

We conducted human reliability analyses for the two scenarios (transient, LOOP) described above. Three tasks were modelled, all of them post-initiator tasks: deployment of the second redundancy of the main SFP cooling system, deployment of make-up system 1 before uncovered fuel, deployment of make-up system 2 before uncovered fuel. Also three repair tasks were considered: repair of the main SFP cooling system before boiling (repair items: pump stopping, heat exchanger failure), repair of make-up system 1 before uncovered fuel (repair item: pump failure), repair of make-up system 2 before uncovered fuel (repair items: FLEX diesel generator failure and pump failure). The method used was the human reliability analysis procedure (Swain 1987) of the Accident Sequence Evaluation Program (ASEP). It turned out that ASEP is easy to learn and follow. It is also easy to apply to repairs, once the required repair actions are known for each repair task. The results were reasonably well in line with those obtained by Swedish partners with different methods. We also constructed a recovery model in the form of an event tree for each task.

Dynamic human reliability analysis

The concept of dynamic HRA is somewhat unclear in the scientific debate. It may seem like a commonly known concept, but a closer look shows that dynamism is sometimes a property of the object and sometimes a property of the method. Typically, dynamic HRA tends to look at human errors closely from contextual aspects, which is in stark contrast to the current static approach where humans themselves are prone to make mistakes. Thus, dynamic HRA represents a more modern view of human performance, which also allows compensating for deficiencies in the technical environment. Even if HRA itself focuses on examining human errors, the possibility of seeing humans also as capable of improving safety is a perspective and an opportunity to increase the safety of the nuclear industry.

Long-lasting events and especially event periods increase the need for a dynamic approach. Reality is dynamic, whether it is inside a person (i.e. in mental states and cognitive processes) or beyond (such as group dynamics expressed as crew collaboration and changing state of the nuclear power plant). As a result, the dynamics make the HRA more realistic and give it a better chance of being more accurate and reliable. On the other hand, taking dynamic phenomena into account is more demanding than assuming statics.

Based on a stakeholder survey, the greatest potential benefit of dynamic HRA is increased realism. However, the methods should not lead to the complexity of the models and increasing workload of the analyses, because the resources available to HRA are limited and the models are already complex. According to them, the dynamism is mainly related to long time windows and scenarios of yearly maintenance outages.

Human reliability analysis of maintenance outages

The safety-critical nature of an outage is well recognized, and there is a wealth of literature on the specifics of outage and the challenges associated with the successful completion of work (Kling et al 2022). HRA methods have mostly been developed for full power conditions where the operator's actions are well trained and laid down in procedures, in time frames typically less than 60 minutes. In the planned shutdown the work concentrates outside the control room, is less in procedures and less trained and the time frames may be much longer. The environment is continuously changing, there are huge number of workers, large variety of work activities, tight schedule and the requirements are high concerning both safety and productivity. The key issues that should be considered in the HRA are errors of commission (EOCs), dependencies between human actions and the dynamism of the operating environment.

Heavy lifting is the most critical of the procedures during the maintenance outage, and the lifting of the protective tube unit (PTU) was chosen as the object of closer examination, because its lifting process is complicated and the possible damages associated with it are serious due to its weight (Liinasuo et al 2022). Based on interviews with crane drivers and assistant drivers, dynamic and error-causing factors were analyzed and a hierarchical task analysis was prepared to identify the main and sub-tasks of PTU lifting. Five dynamic and potentially error-inducing factors were identified: Shift extension, working for a long time without a pause, background noise, constant haste, and multitasking. Hierarchical task analysis produced 13 main tasks, and related sub-tasks, as well as possible sources of errors were identified. Various sources for errors were found: Human communication related issues, procedure related issues, human resource related issues, malfunction of machine or device, difficult lifting circumstances, and timing related issues. The main focus was in the proceeding of the lifting session, and the identified errors serve more like examples of possible errors. The identified errors are related to human injury, weakened situation awareness of crane operator and crane operator assistant, faulty operation of crane, outsiders in the reactor hall during

lifting, and insufficient of matters in finishing meeting. The reasons for human error can be a complex combination of factors, some affecting constantly and some occasionally, in a more unique manner.

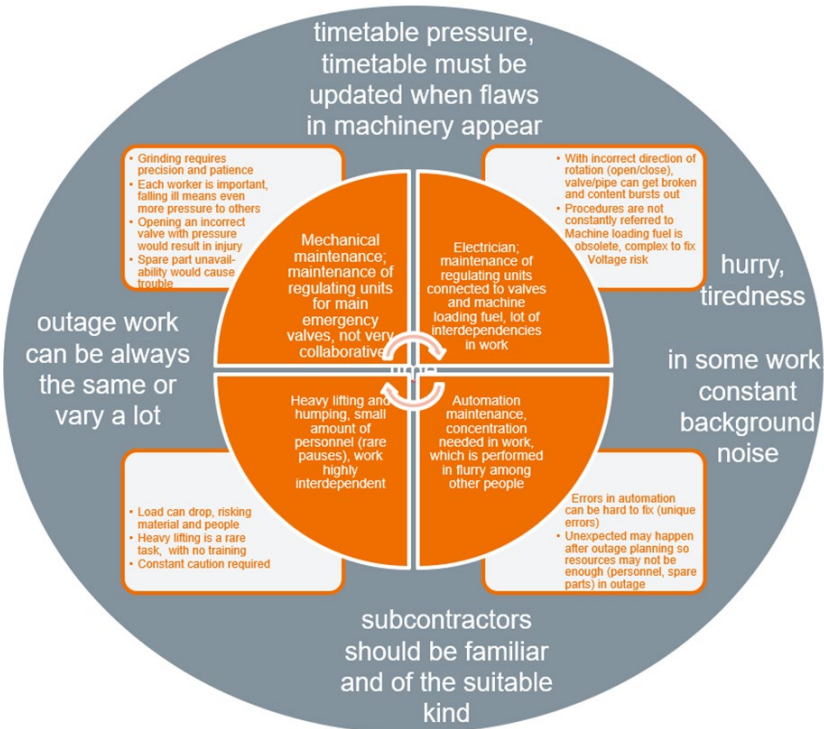


Figure 4. Outage related work qualities as revealed by interviews. Text on orange background shows some basic features in the role of outline workers, four roles as a whole; text with outline provides more details to the role in question. Text on the grey background describes general outage related features.

Digital I&C reliability and risk analysis

Despite of significant research efforts, there is still no international consensus on PRA modelling methods for digital I&C systems. Therefore, digital I&C has been modelled in overly simplified and conservative manner in most PRAs currently. Challenges include particularly modelling and quantification of software failures, modelling of fault-tolerant features, postulation of common cause failures and common cause failure parameter estimation. It should be noted that these issues are not only relevant for PRA but also in the deterministic safety demonstration, which includes e.g. fault tolerance analyses.

International benchmark study

We have participated in an OECD/NEA WGRISK task DIGMAP, which is an international benchmark study on PRA modelling of digital I&C (OECD 2022a; OECD 2022b). In DIGMAP, six participants have prepared PRA models for a fictive reactor protection system (RPS), and the modelling approaches and results have been compared. VTT's modelling approach was to use simple fault trees and to perform complex computations in background (OECD 2022b). The approach was selected because it did not seem practical to handle all common cause failure (CCF) combinations of large CCF groups explicitly in the PRA model. All RPS related basic events in the model are CCFs that cause one or multiple safety functions to fail. CCFs were modelled separately for different modules and for application software, system software and hardware. CCF combinatorics and probabilities were calculated using separate spreadsheets. The top fault tree for one signal is presented in Figure 5.

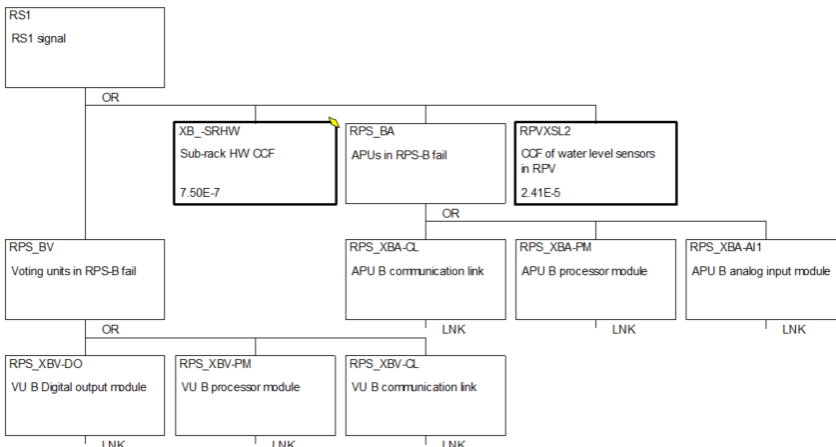


Figure 5. Fault tree for RS1 signal in VTT's model.

The DIGMAP project particularly has demonstrated the importance of understanding the diversity of the reactor protection systems (or lack of it) and the identification of CCF groups. Both high level and low level modelling approaches were used among DIGMAP participants, but the level of modelling detail did not really have impact on the overall results. Both approaches have their benefits and drawbacks, and the most suitable approach can also depend on the application. It has to be noticed that the development of a compact PRA model for digital I&C requires quite detailed background calculations and good modelling skills, i.e. there is no easy shortcut. Large CCF groups were technically the most challenging modelling issue of the project that caused some differences in the results. It was found that one has to be very careful when using simplifying workarounds.

Common cause failures in digital I&C systems

We have performed a state-of-the-art review on PRA modelling of CCFs in digital I&C systems (Tyrväinen 2021). There is relatively little literature addressing these CCFs. Concerning both software and hardware, lack of data is the main challenge, and there is need for data collection and method development activities.

There are some references on software CCF probabilities used in PRA studies. The estimates are usually based on either expert judgments or operating experience, but even the estimates based on operating experience seem quite uncertain. Many software reliability analysis methods can be found from literature, but they have mostly not been used in practise and do not specifically address CCFs, though software failures modelled in PRA are usually CCFs. The Nordic method (Bäckström et al. 2015; Authén et al. 2016) seems to be the only practical method that analyses software CCFs of a digital reactor protection system.

It is generally agreed that CCFs between identical redundant software modules can be modelled using beta-factor of 1. However, when there is some diversity present, the modelling is challenging. There is lack of methods to estimate CCF parameters between non-identical software modules. EPRI (2012) recommends a beta-factor of 0.001-0.1, when similar platforms are used to implement similar functions activated at different plant conditions. Functional diversity is often assumed to prevent application software CCFs between subsystems. On the other hand, operating system CCFs between functionally diverse subsystems are usually modelled.

Hardware CCFs can be analysed according to normal CCF analysis principles. However, lack of data on digital I&C components often makes it necessary to use generic parameters or engineering judgment -based methods, which can lead to quite conservative results. Large and asymmetric CCF groups are one particularly challenging area related to digital I&C hardware.

Detected failures causing spurious signals

Failures detected by automatic and periodic testing in digital I&C systems can cause spurious signals, e.g. spurious start or stop of a safety function, depending on the fail-safe behaviour of the system. Even a behaviour that has been defined as fail-safe can be harmful, because e.g. the fail-safe behaviour may have to be defined to shut down a safety system for protective reasons. Detected failures causing stop signals for safety functions were quite important in the previous DIGREL study (Authén et al. 2015), whereas they were omitted in the DIGMAP project. Therefore, we have extended the DIGMAP model and evaluated the significance of detected hardware failures in that case (Tyrväinen 2022). Two different cases were analysed: spurious signals to prevent safety functions and spurious signals causing initiating event by stopping the pumps of the main feedwater system. In this case, only spurious signals causing initiating event were important for the results. The importance of detected failures with regard to digital I&C related risk is sensitive to

detection coverage parameters and fail-safe behaviour. Also, the diversity (or lack of diversity) between subsystems has significance for this matter.

Modelling of a priority unit

A fault tree model has been developed for a fictive priority unit that is responsible of the actuation of an emergency feedwater system (Tyrväinen 2022). The model was developed based on an FMEA that was constructed for the modules of the priority unit. The fault tree is presented in Fig. 6. The priority unit gets its input signals from an RPS, back-up I&C system and operating I&C system. The RPS model from DIGMAP was used for the RPS signal failures, whereas the other systems were modelled in a very simplified manner. The most important contributors to the safety function failure were specific failures in the priority units, but also spurious off-signals caused by detected hardware and software failures in the RPS were important. Other contributors were almost negligible. Detected RPS failures dominated over undetected failures in this case, because the detected failures can alone cause the safety function failure through the spurious off-signals, whereas undetected RPS failures only “pass the control” to the back-up I&C. However, the contribution of detected failures depends on the definition of the fail-safe behaviour and the priorities of signals.

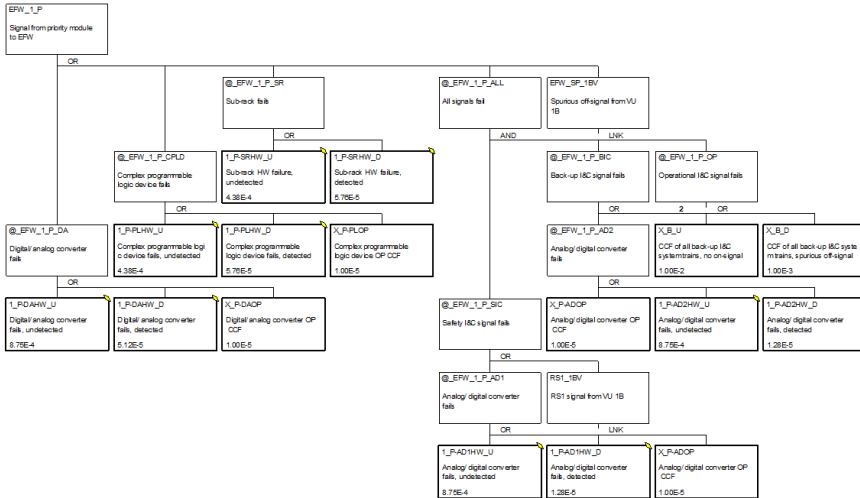


Figure 6. Fault tree for a priority unit.

PRA of small modular reactors

SMRs are a novel approach to nuclear reactor design, and practical experience about them is as of yet scarce. This poses challenges to PRA of SMRs. PRA tool, method and risk metric development is needed to account for the SMR reliability

and the uncertainties related to SMR risk. Especially methods to handle passive features and multi-module issues in PRAs should be investigated or enhanced. We have reviewed the literature related to SMR PRA (Björkman & Tyrväinen 2019). Several approaches have been suggested for passive system reliability modelling. Either traditional methods are used or dynamic methods (mainly dynamic event trees) are suggested for accounting for unique features of SMR risk. SMR risks have also been considered from level 2 and 3 perspective.

We have considered the applicability of multi-unit PRA methods to multi-module PRA of SMRs (Björkman & Tyrväinen 2021). Even though SMR modules are not equivalent to units of large reactors, the challenges considering modelling of multi-module accidents in PRA are similar to those of modelling of multi-unit accidents. Therefore, multi-unit PRA approaches could provide a good starting point for multi-module accident modelling. Most multi-unit PRA methods are based on a single-unit model (for each unit) developed conventionally using event trees and fault trees. If SMR PRA is developed using the conventional PRA approach for a single module, the multi-unit PRA methods seem in general quite well applicable to multi-module PRA. However, there are aspects in multi-module PRA of SMRs that can differ from multi-unit PRA of large reactors. These include risk metrics, plant operating states, initiating events, human dependencies and CCF groups. In summary, many analysis details may need to be reconsidered for SMRs compared to large reactors.

Even though dynamic multi-module PRA methodology has been proposed e.g. in (Dennis et al. 2016), there is no evident reason why PRA of SMRs would require such dynamic approach and the conventional PRA approach would not be sufficient. For NuScale SMR design, the conventional approach has been applied (NuScale 2020). However, the most suitable PRA approach can depend on the SMR design in question, as there are quite many types of SMR designs.

Applications

The PRA research conducted in NAPRA is related to applications on three levels. Some of the results may be directly applied, some others support the PRA efforts of Finnish nuclear stakeholders, and yet others provide groundwork for improving and enhancing application-oriented PRA research.

The fire PRA model developed may serve as an example on how to conduct integrated, dynamic, realistic and holistic fire PRA analyses.

When PRA is conducted on spent fuel pools, it is important to take into account the long time windows in order to get realistic results. Long time windows may also come about in some scenarios that concern NPP units. When the need or will to consider long time windows in plant PRA arise, the results of the PROSAFE project offer both information on several relevant issues, and methodological support to carry out the analyses in practice.

Dynamic HRA literature review results will be useful when dynamic HRA efforts are started. Needs or strong motivation for this may emerge if conducting risk or accident analyses in a dynamic manner – for example, integrating human actions,

plant response and risk considerations in a set of dynamic simulation models. The work on outage HRA has resulted in many identified error possibilities that can be utilized in plant HRA.

The studies of digital I&C PRA help PRA experts in modelling by giving examples of models that improve the realism of digital I&C PRA models while avoiding overly complex models.

Acknowledgement

The authors thank Jan-Erik Holmberg, Alessandro Mancuso, and Ahti Salo for contributions to the initial project plan.

References

- ASME. 2009. PRA standard: ASME/ANS RA-Sa-2009 Standard for Level 1/Large Early Release Frequency Probabilistic Risk Assessment for Nuclear Power Plant Applications. American Society of Mechanical Engineers 2009.
- Authén, S., Bäckström, O., Holmberg, J.-E., Porthin, M. & Tyrväinen, T. 2016. Modelling of digital I&C, MODIG - Interim report 2015, NKS-361. Nordic nuclear safety research, Roskilde, Denmark. 59 p. + app. 22 p.
- Authén, S., Holmberg, J.-E., Tyrväinen, T., Zamani, L. 2015. Guidelines for reliability analysis of digital systems in PSA context – Final Report. Roskilde: Nordic nuclear safety research (NKS). NKS-330. 63 p. + app. 37 p.
- Björkman, K. & Karanta, I. 2021. A simple failure tolerance analysis case study for a fictive boiling water reactor. Espoo: VTT. VTT Research Report VTT-R-00038-21.
- Björkman, K. & Tyrväinen, T. 2019. Probabilistic risk assessment of small modular reactors - Literature review. Espoo: VTT. VTT Research Report VTT-R-01041-19. 12 p.
- Björkman, K. & Tyrväinen, T. 2021. Managing multi-module issues in SMR PRA. Espoo: VTT. VTT Research Report VTT-R-00444-21. 18 p.
- Bäckström, O., Holmberg, J.-E., Jockenhövel-Barttfeld, M., Porthin, M., Taurines, A. & Tyrväinen, T. 2015. Software reliability analysis for PSA: failure mode and data analysis, NKS-341. Nordic nuclear safety research, Roskilde, Denmark. 72 p. + app. 13 p.
- Dennis, M., Modarres, M. & Mosleh, A. 2016. Framework for Assessing Integrated Site Risk of Small Modular Reactors Using Dynamic Probabilistic Risk Assessment Simulation. 13th International Conference on Probabilistic Safety Assessment and Management (PSAM 13), Seoul, Korea, 2-7 October, 2016: 13 p.

- Electric Power Research Institute (EPRI). 2012. Modelling of digital instrumentation and control in nuclear power plant probabilistic risk assessment. Palo Alto, California. 84 p. + app. 8 p.
- Helminen, A. 2020. International and Finnish Practices on Seismic Probabilistic Risk Assessment. Espoo: VTT. VTT Research Report VTT-R-00023-20. 9 p.
- Hostikka, S. & Keski-Rahkonen, O. 2003. Probabilistic simulation of fire scenarios. Nuclear Engineering and Design 224, 301-311.
- Hostikka, S., Kling, T., Paajanen, A. 2012. Simulation of fire behaviour and human operations using a new stochastic operation time model. 11th International probabilistic safety assessment and management conference & the annual European safety and reliability conference (PSAM11 & ESREL 2012), Helsinki, 25-29 June, 2012. 10 p.
- Karanta, I. & Björkman, K. 2020. A survey on the use of PRA to support failure tolerance analysis. Espoo: VTT. VTT Research Report VTT-R-00192-20.
- Kling, T., Liinasuo, M., Karanta, I. 2020. Dynamic HRA in outage from literature and outage personnel interview perspectives. Espoo: VTT. VTT Research Report VTT-R-00015-22. 36 p.
- Liinasuo, M., Karanta, I. & Kling, T. 2020. Dynamic human reliability analysis (HRA) - a literature review. Espoo: VTT. VTT Research Report VTT-R-00193-20. 27 p.
- Liinasuo, M., Karanta, I. & Kling, T. 2021. Dynamic human reliability analysis – A stakeholder survey and an empirical study. Espoo: VTT. VTT Research Report VTT-R-00189-21. 33 p.
- Liinasuo, M., Karanta, I. & Kling, T. 2022. Heavy lifting – dynamic factors, hierarchical task analysis and human errors. Espoo: VTT, VTT Research Report VTT-R- 01014-22. 27 p.
- McGrattan, K., McDermott, R., Weinschenk, C., Overholt, K., Hostikka, S. & Floyd, J. 2013. Fire Dynamics Simulator User's Guide, Sixth edition. Gaithersburg: National Institute of Standards and Technology. NIST special publication 1019. 262 p.
- NuScale Power LLC. 2020. NuScale standard plant design certification application, Chapter nineteen: Probabilistic risk assessment, Part 2 - Tier 2, Revision 5. 424 p. <https://www.nrc.gov/docs/ML2022/ML20224A508.pdf>.
- OECD. 2014. Probabilistic safety assessment (PSA) of natural external hazards including earthquakes, NEA/CNRA/R(2014)9. Paris: OECD Nuclear Energy Agency. 47 p. + app. 357 p.
- OECD. 2015. International workshop on fire probabilistic risk assessment (PRA), NEA/CSNI/R(2015)12. Paris: OECD Nuclear Energy Agency. 51 p. + app. 400 p.
- OECD. 2019. Seismic Probabilistic Safety Assessment for Nuclear Facilities. CSNI Topical Opinion Paper, No. 2, Nuclear Energy Agency, OECD, 2019-05-27 Draft.

- OECD. 2022a. Digital I&C PSA – Comparative application of digital I&C modelling approaches for PSA, Volume 1: Main report and Appendix A, NEA/CSNI/R(2021)14. Paris: OECD Nuclear Energy Agency. 74 p. + app. 15 p. DRAFT.
- OECD. 2022b. Digital I&C PSA – Comparative application of digital I&C modelling approaches for PSA, Volume 2: Appendices B0-B6, NEA/CSNI/R(2021)14/ADD. Paris: OECD Nuclear Energy Agency. 226 p. DRAFT.
- Ramadan, A., Hasan, R. & Penlington, R. 2018. Zero-dimensional transient model of large-scale cooling ponds using well-mixed approach, Annals of nuclear energy 114, 342–353.
- Swain, A.D. 1987. Accident Sequence Evaluation Program human reliability analysis procedure. Washington, DC: Sandia National Laboratories for the U.S. Nuclear Regulatory Commission. NUREG/CR-4772.
- Tyrväinen, T. 2021. Probabilistic modelling of common cause failure in digital I&C systems – Literature review. Espoo: VTT. VTT Research Report VTT-R-00728-21. 14 p. + app. 1 p.
- Tyrväinen, T. 2022. Probabilistic risk assessment studies for digital I&C: detected failures and priority unit. Espoo: VTT. VTT Research Report VTT-R-00940-22. 21 p. + app. 4 p.
- Tyrväinen, T. & Immonen, E. 2022a. Simulation-based probabilistic risk assessment for spent fuel pool. Espoo: VTT. VTT Research Report VTT-R-00016-22. 27 p. + app. 20 p.
- Tyrväinen, T. & Immonen, E. 2022b. Simulation-based PRA for spent fuel pool: Final report. Espoo: VTT. VTT Research Report VTT-R-00990-22. 31 p. + app. 30 p.
- Tyrväinen, T., Karanta, I., Kling, T., He, X., Olofsson, F., Bäckström, O., Massaiu, S., Sparre, E., Eriksson, C., Cederhorn, E. & Authén, S. 2020a. Prolonged available time and safe state. Roskilde: Nordic nuclear safety research (NKS). NKS-432. 116 p.
- Tyrväinen, T., Karanta, I., Kling, T., He, X., Olofsson, F., O., Massaiu, S., Sparre, E., Eriksson, C., Cederhorn, E. & Authén, S. 2021a. Prolonged available time and safe state. Roskilde: Nordic nuclear safety research (NKS). NKS-444. 143 p. + app. 22 p.
- Tyrväinen, T., Kling, T. & Korhonen, T. 2020b. Analysis of cable fire scenario with simulation-based event tree. Espoo: VTT. VTT Research Report VTT-R-01302-19. 22 p.
- Tyrväinen, T., Korhonen, T. & Kling, T. 2021b. Extensions to cable room fire PRA study and method. Espoo: VTT. VTT Research Report VTT-R-01545-20. 38 p.
- VTT Technical Research Centre of Finland Ltd. 2014. FinPSA – Tool for promoting safety and reliability. <https://www.simulationstore.com/finspa> (link accessed 25.11.2022)

3.3 Predicting extreme weather and sea level for nuclear power plant safety (PREDICT)

Kirsti Jylhä, Ulpu Leijala, Milla M. Johansson, Marko Laine, Terhi K. Laurila,
Anna Luomaranta, Taru Olsson, Meri Virman, Mika Rantanen,
Jenni Rauhala, Olle Räty, Jani Särkkä

Finnish Meteorological Institute (FMI)
P.O. Box 503, FI-00101 Helsinki

Abstract

The safety management over the life cycle of a nuclear power plant requires probability estimates of single and compound weather and sea level events in the changing climate. Sea-effect snowfall typically results in larger accumulation of snow than non-convective winter precipitation. Severe convective wind storms due to derechos last longer and cause damage over wider areas than other major convective wind events. Characteristics of both historical and synthetic low-pressure systems causing extreme sea levels in Finland were studied. In most cases, coastal flooding events require more than one cyclone to pass by. Hierarchical extreme value models for calculating return levels of annual maximum sea level in Finland were found to have less uncertainty in the calculated estimates than tide gauge specific reference extreme value models.

Introduction

The Finnish regulatory guides require that the design of a nuclear facility shall take into consideration abnormally high and low sea water levels and a number of exceptional meteorological phenomena (Guide YVL B7, 2019). Furthermore, meteorological data affecting dispersion of radioactive releases in the atmosphere shall be known (Guide YVL C4, 2019). Accordingly, the main topics of the PREDICT project (<https://en.ilmatieteenlaitos.fi/predict>) in 2019–2022 were: 1) extreme weather events in a changing climate; 2) extreme sea level; and 3) forecasts of extreme weather and sea level events.

The research on the first two topics, extreme weather and sea level, aims to improve the reliability of estimates about the likelihood of exceptional single and co-occurring weather and sea level events in the surroundings of the Finnish nuclear power plant (NPP) sites (Jylhä et al. 2018). Impacts of climate change also need to be considered. Globally, 2011–2020 was the warmest decade on record (WMO, 2021). In Finland, the year 2020 was warmer than ever recorded (FMI, 2021). In 2021, an unprecedentedly long heat wave of 32 days, without interruptions, was experienced in Kouvolan (Lehtonen, 2021). Record-breaking many hot days also occurred in summers 2014 and 2018 (FMI, 2022). Unusually high sea water temperatures in summers 2010, 2018 and 2021 affected the normal operation of

the Loviisa NPP: the power was temporarily reduced to keep the reactors' cooling system's discharge water temperature below the limits of the local environmental water permit (Fortum, 2021). Furthermore, in January 2019, the Aapeli storm broke the record for highest average wind speed in Finnish sea areas, and storm-force gusts were measured even inland (FMI, 2019a). Also, a new wave height record in the Central Bothnian Sea was achieved (FMI, 2019b). In February 2020, a record-high sea level (135 cm over mean water) was observed at the Rauma tide gauge.

It is not possible to attribute a single event, such as an exceptionally warm summer, to anthropogenic increases in greenhouse gas emissions (Trenberth et al. 2015). However, it is evident that human induced long-term trends in the mean values affect the probabilities of occurrence of values near both ends of the frequency distributions, depending also on potential changes in the variance or shapes of the distributions.

In PREDICT, we i) clarified climatology of intense coastal snowfall in the past; ii) initiated studies about compound events, including joint occurrence of intense precipitation and high sea level; iii) explored derechos and other major convective wind events; iv) studied extratropical cyclones, their characteristics and cyclone clustering associated with extreme sea levels on the Finnish coast; v) evaluated extreme sea level estimates and associated uncertainties; and vii) focused on simulated low-pressure systems and sea level extremes.

Short-term forecasts of extreme weather and sea level events, i.e., the 3rd main topic of PREDICT, was addressed during the first two years of the project. High wind speeds were examined as an object of probabilistic weather forecasting (Hämäläinen et al., 2020) and a workshop on probabilistic forecasting was organized (Fortelius et al., 2019). A review of that topic is given by Jylhä et al. (2021) in the SAFIR2022 Interim report.

Climatology of intense coastal snowfall in the past

Intense snowfall together with strong winds can cause considerable danger to infrastructure. Large snow accumulations in Finland can result from both convective (local) and stratiform (large-scale) snowfall. Convective snowfall, i.e., sea-effect snowfall (SES, Figure 1), is typical in coastal regions during late autumn and early winter when the sea is still ice-free and relatively warm and the airmass above much colder. Stratiform snowfall, however, can occur regardless of the sea-ice, and also far inland.

So far, the snowfall season in 2022–2023 has been extremely varying in coastal Finland. In mid-November, after multiple SES events occurring on only three consecutive days, the snow depth in the southern coastline was larger than that in northern Finland. By mid-December, a snow depth of ca. 50 cm was measured in Loviisa. In January, however, melting of snow associated with warm temperatures and heavy rain resulted in exceptional winter flooding in southern Finland.

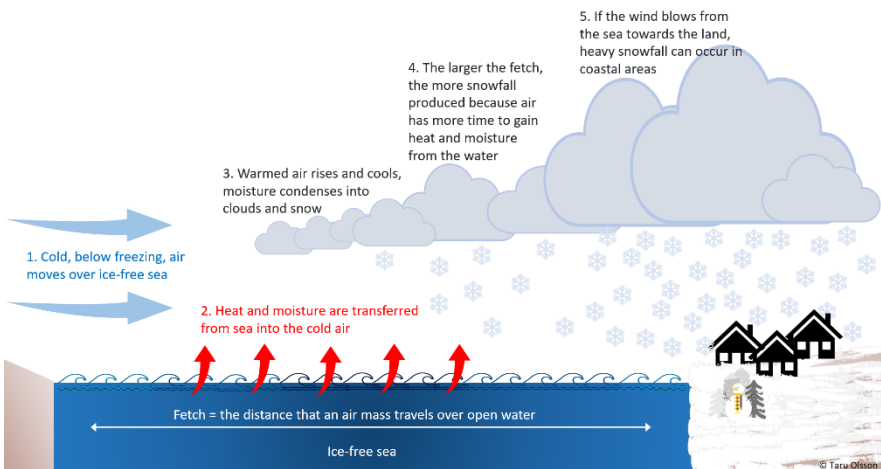


Figure 1. Schematic illustration of sea-effect snowfall formation (Modified from Olsson, 2022b).

In PREDICT, the SES climatology in Finland was investigated. First, in 2019–2020, a method for detecting SES events in Finland was tested. The detection method was based on finding days with atmospheric conditions favourable for the occurrence of SES and had previously been used by Jeworrek et al. (2017) in the east coast of Sweden. The criteria for atmospheric conditions used by Jeworrek et al. in the detection method were slightly modified based on four case studies of past SES events in Finland. The detection method was tested with data from the regional climate model RCA4 (Olsson et al., 2020a) for an 11 year long time period (2000–2010). The tests were then continued by Olsson et al. (2020b) who considered a 40-year long period (1979–2018) and used the ERA5 reanalysis data (Hersbach et al., 2020) together with FMIClimGrid gridded observations (Aalto et al., 2016). The results were assessed separately for five different study regions along Finland's coastline. On average, two to eight SES days were detected on the separate areas annually. The height of the SES season was found from November, December, and January. The detection method was concluded to be suitable for SES studies as it correctly detected the past known events.

In PREDICT in 2021–2022, the SES studies were continued by, first, extending the SES statistics based on ERA5 data to cover a longer time period (1973–2020, Figure 2a) and the whole Finnish coastline and, second, kickstarting testing the detection method with new regional climate model data. According to ERA5 and observations, an average of 16 SES days occurred annually in the Finnish coastal regions in 1973–2020, and most of the SES days occurred in December (Figure 2b, Olsson et al., 2022). It was also shown that the peak of the SES season has shifted forward in time, from late autumn towards mid-winter, since the 1970's (Figure 2b, Olsson et al., 2022). Similar monthly and annual distribution of the amount of SES days was obtained with a convection-permitting regional climate model

HARMONIE-Climate (HCLIM) for 1998–2018 (Figure 2c, Virman 2022). However, in HCLIM, the SES days occurred most frequently in the southern coast of Finland (not shown), whereas in ERA5 SES days were most prevalent in the western coast (Figure 2a). Interestingly, the spatial distribution of mean snowfall on SES days resembled that of observed snow depth increase (not shown) in Olsson et al. (2022). These results support the use of HCLIM in assessing the effects of climate change on SES in the future.

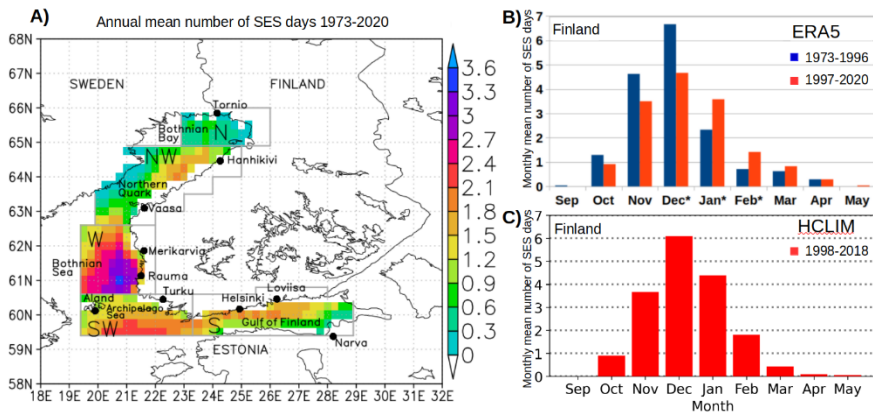


Figure 2. (a) Annual mean number of SES days based on ERA5 reanalysis and FMIClimGrid gridded observations in 1973–2020. Monthly mean number of SES days in Finland based on (b) ERA5 in 1973–1996 and 1997–2020 and (c) HCLIM in 1998–2018.

Lastly, daily and hourly snowfall (both convective and stratiform) in ERA5 was compared with observations to estimate the validity of the snowfall distribution in ERA5 (Olsson & Jylhä, 2022). Comparison with daily observations indicate that the ratio of monthly mean snowfall to total precipitation (snow+rain) might be too high in ERA5, but that the monthly mean and seasonal total precipitation were similar compared to observed precipitation in Finland. The largest hourly snowfall (up to 0.7 mm/h) were found between November and January, but the largest daily snowfall (9–11 mm/day) were found between October and March. Coastal areas and lake regions stood out as the most frequent places for heavy snowfall to occur (Figure 3). The proximity of water bodies and areas of extreme snowfall indicates convective origin of the snowfall, or that the snowfall is intensified in the vicinity of the water areas due to added moisture content. In addition, in SES studies the accumulated daily snow on ground was found to be larger during SES days than during “normal” stratiform snowfall days in the coastal areas (Olsson 2022a).

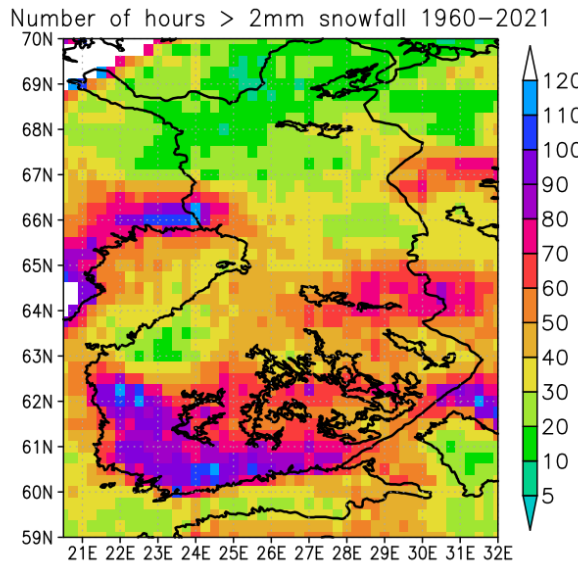


Figure 3. Number of hours exceeding snowfall rate of 2 mm/h during 1960–2021 in ERA5.

Compound weather and sea level events

Combinations of anomalous (but not necessarily extreme) weather conditions is a rather new research topic which has internationally gained attention during the recent years, less so in Finland (Seneviratne et al., 2012; Helander, 2017; Zscheischler et al., 2018). In PREDICT, we studied high sea levels jointly with heavy precipitation, potentially leading to external floods. First based on rain gauge measurements (Räihä et al., 2020) and then using gridded precipitation data together with tide gauge data since 1961 (Rantanen et al., 2020), single and joint frequency distributions of heavy precipitation and high sea level were calculated, considering two magnitude levels. It was found that along the Finnish coast these compound events typically occur a few times per year and tide gauge location, mainly in late autumn and early winter. Their occurrence is associated with strong extratropical cyclones which bring moisture and push the storm surge towards the coast (Rantanen et al., 2020).

In 2022, we started to expand the research of combinations of weather and/or sea level events that may have plant-level impacts and are meteorologically probable. Based on the feedback of NPP representatives, a compound event of relevance is jointly occurring high winds and intense snowfall, resulting in snow storms. As a first step, intense snowfall (both due to convective snow bands and wintertime cyclones) simulated in ERA5 atmospheric reanalysis were evaluated (Olsson & Jylhä, 2022). The results are reviewed in the end of the previous section (Figure 3).

Derechos and other major convective wind events

Derechos are long-lived convective wind events that cause damage in vast areas. Since little was known before about derecho occurrence in Finland, the purpose of this study was to search for previously unidentified derecho events and describe derecho occurrence and characteristics in Finland. In this study we use similar criteria to those used in derecho studies by Evans & Doswell (2001) for the United States and Gatzen et al. (2020) for Germany. To identify derecho events, we use following criteria:

- Measured wind gusts ≥ 25 m/s or F1 wind damage
- Damage area ≥ 400 km in length
- No more than 2 h break in damage reports along the damage path
- Damage caused by same convective system

To determine the climatology of derechos in Finland, two datasets were used. For the first dataset, a limited time period, years 2010–2018, potential derecho events in the summer season between 1 May and 30 September were systematically searched. The second dataset included other known possible and confirmed derecho cases that we were aware of. These were events where large-scale wind damage were known to have occurred with convective storms. Derechos were identified by comparing radar reflectivity development of a convective storm to the maximum wind gust measurements and reported wind damage.

The search for derechos in this study resulted in 27 convective wind events that were analyzed in detail (Figure 4). In Finland two derecho cases had been confirmed before this study. This preliminary study found eight new, previously unidentified derecho cases. Derechos have occurred in Finland from June to October (Figure 4); the maximum number of known cases was in August. The August maximum is influenced by a family of derechos on 7–8 August 2010, with three separate derecho cases that formed in a weather situation favourable for derechos. Based on a small dataset, like the one used in this study, a lasting favourable weather pattern or even a single weather event may have large impact of the frequency distributions. Thus, no definite conclusion on the monthly occurrence in general can be drawn.

The length of the observed derecho tracks in Finland vary between 400 km and 660 km. In two of the events, derecho started already in neighbouring countries, resulting in much longer tracks. The 8 August 2010 case had a 950 km-long track from Latvia to Finland. The 16-17 October 2022 case started from Denmark and impacted Sweden, Finland and Estonia, resulting in a total track length of 1300 km. The derecho tracks and direction of movement of all documented derechos in Finland is shown in Figure 5. Most of the observed derechos were moving towards the northeast and only a few were moving towards northwest. The most typical start location of a derecho track has been in southwestern Finland. This could be partly explained by the fact that if for the same event the starting point were a few hundred kilometers northwards, it would be less likely to meet the 400-km derecho length criteria. To full fill the derecho criteria in a relatively narrow and long country, like

Finland, the events seem to need a favourable start location and direction of movement to be classified as derechos. Each derecho case was classified based on its radar reflectivity evolution. Figure 6 shows an example radar image of an analyzed derecho case.

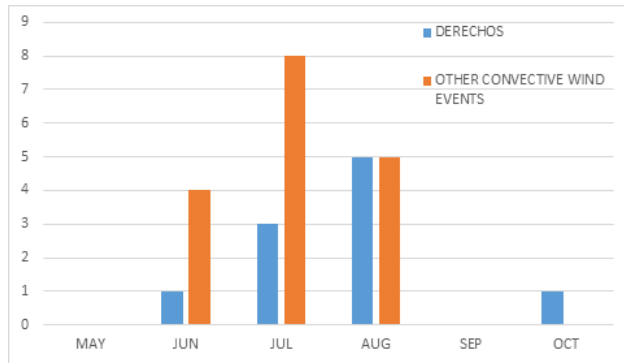


Figure 4. Monthly distribution derechos and other convective wind events in Finland analyzed in this study.

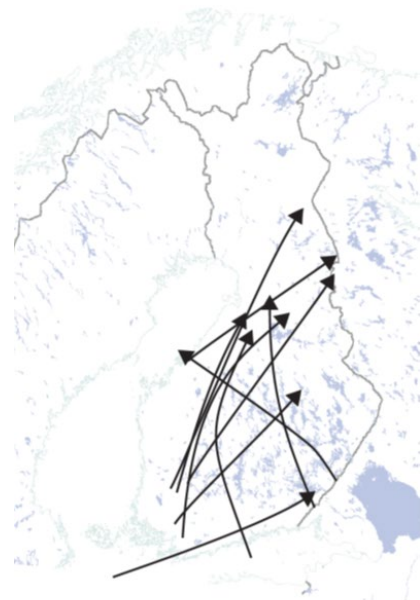


Figure 5. Major axis and direction of movement of 10 documented derechos in Finland.

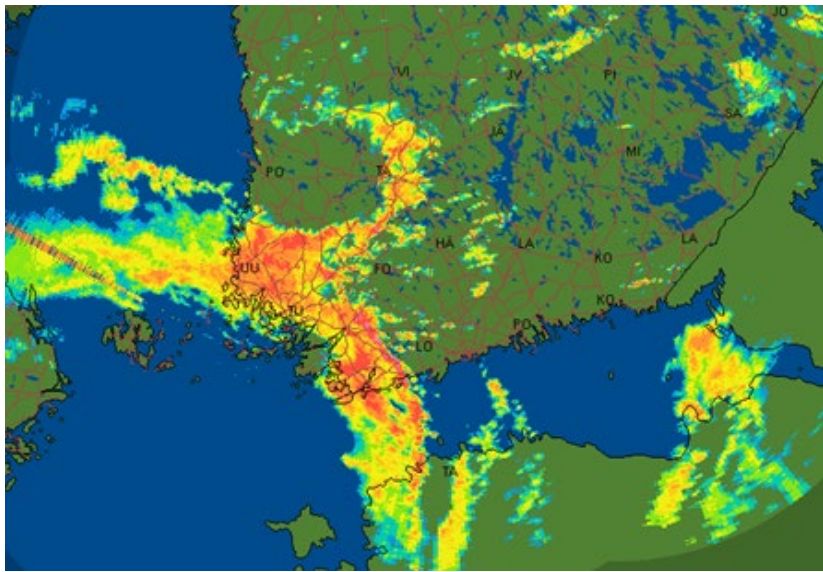


Figure 6. A squall line producing derecho moving east on 16 October 2022 at 20:00 UTC.

Extratropical cyclones, their characteristics and cyclone clustering associated with extreme sea levels on the Finnish coast

Extratropical cyclones (sometimes also referred to as mid-latitude cyclones or low-pressure systems) are very common weather systems across the mid- and high latitudes. In favourable atmospheric conditions they can strengthen to powerful windstorms and cause damage to society. On the coast, extremely high sea levels and the resulting coastal flooding events are often induced by the passage of intense extratropical cyclones which cause the sea level to rise due to their powerful winds and low air pressure. Although strong extratropical cyclones are one of the most damaging weather phenomena in northern Europe, their connection to the coastal flooding events on the Finnish coast and elsewhere in the Baltic Sea has been studied mostly in single case studies. Especially in Finland, a comprehensive analysis of the properties of extratropical cyclones and their relation to sea level extremes is still lacking.

In 2021–2022, we initiated a new study on extratropical cyclones and extreme sea levels on the Finnish coast. The study period spans the years from 1980 to 2019, and all extratropical cyclones from the 40-year time period were tracked and their characteristics were analysed. Compared to previous studies, this sample size is larger and gave us robust dataset from which different extreme situations and their variability could be analysed.

The aims of the study were twofold: in the first part (conducted in 2021) we investigated how the clustering of extratropical cyclones (clustering=the number of consecutive extratropical cyclones within a 7-day period) affects the sea level in various tide gauge locations on the Finnish coast. In the second part (in 2022), we focused more on the characteristics of single extratropical cyclones which have caused extreme sea levels on the tide gauge locations.

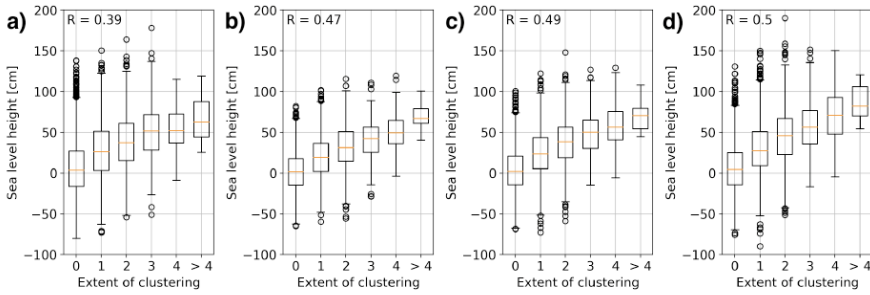


Figure 7. The relationship between the extent of cyclone clustering (x-axis) and the maximum sea level height (y-axis) in a) Kemi, b) Rauma, c) Helsinki and d) Hamina tide gauge. The extent of clustering in x-axis means the number of passing extratropical cyclones within a 7-day period. The cyclones have been counted from a circle with 700-km radius centred on each tide gauge.

The main result from the first part was that the clustering of extratropical cyclones and the maximum sea level on the Finnish coast were found to be positively correlated (Figure 7). The relationship between the extent of clustering and the sea level height was stronger in tide gauges located in southern Finland (Helsinki, Hamina) than those in northern Finland (Kemi). Our results suggest that the probability of coastal flooding event in Finland is considerably higher in those situations when several extratropical cyclones pass the tide gauge in a short time period compared to situations when only one single cyclone passes the tide gauge.

In the second part, it was found that on average, those extratropical cyclones that have caused extreme sea levels in Finland have been longer living, propagated faster, have lower minimum pressure and stronger wind gusts in comparison to all extratropical cyclones (i.e., also those that have not caused extreme sea levels). The cyclone characteristics were found to be mainly similar between Helsinki, Hamina and Rauma tide gauges, while the cyclones causing extreme sea levels in Kemi tide gauge were longer living and slower propagating than in the other three locations.

Extreme sea level estimates and associated uncertainties

Coastal flooding hazards go hand in hand with the way how warming of the climate proceeds in the future. The more the mean sea level rises, the higher the rarely

occurring coastal flooding events may reach. Climate change adaptation in a flexible and safe manner in the coastal areas seeks for up-to-date information on the sea level behaviour as well as understanding of the uncertainties related to the future estimates. The sparse amount of data on extreme events causes challenges both to the evaluation of the sea level extremes and uncertainties in the related estimates. Recent studies have provided important knowledge on coastal flooding risks in Finland (e.g., Johansson et al., 2022; Pellikka et al., 2020; Leijala et al., 2018; Pellikka et al., 2018), but more work is required to improve uncertainty quantification as well as statistical and physical modelling of sea level extremes on the Finnish coast.

During the first two years of PREDICT, we investigated different extrapolation functions on the uppermost sea level estimates and stationarity of sea level time series, demonstrating the outcomes at the three Finnish NPP sites (Leijala et al., 2020a, 2020b). Secondly, we initiated studies on utilizing Bayesian statistical modelling on sea level extremes, first taking part in an OECD/NEA benchmark exercise (Räty & Laine, 2019). The methods used in that exercise were then preliminarily applied to actual sea level data from the Finnish coast (Räty et al., 2020). Work on this task during 2021–2022 focused on employing Bayesian statistical modelling to reduce uncertainty in the extreme sea level estimates.

In year 2021, we continued studies initiated in the previous year, in which Bayesian hierarchical extreme value models based on the generalised extreme value distribution (GEV) were developed for estimating return levels of annual maximum sea level on the Finnish coast. A manuscript was written about the main results obtained with the hierarchical models and submitted for a peer-review (Räty et al., 2022a). The results demonstrated that the hierarchical models usually have a narrower uncertainty range in the estimated return levels especially when very rare events (e.g., 1000-year return levels) are considered. In addition, work on developing non-stationary model extensions for the extreme value models was initiated. The location parameter of the GEV distribution was modelled both as a function of time and different atmospheric circulation indices. Several circulation indices were first considered for this purpose, but after a pre-screening, two indices were eventually selected and used separately as predictors in the models: the North Atlantic Oscillation (NAO) index (Hurrell, 1995) and the zonal component of geostrophic wind over the southern Baltic Sea (e.g., Johansson & Kahma, 2016). The main results of the initial tests with the non-stationary models were reported by Räty et al. (2021). They showed that the non-stationary models have better fits to observations than their stationary counterparts. Furthermore, it was found out that high sea levels are positively associated both with the NAO index and zonal geostrophic wind. The results also indicated that there might be a small positive trend in some tide gauge locations, although with marked uncertainties in the trend estimates.

In year 2022, the development of the non-stationary models was further continued. The scale parameter of the GEV distribution was modelled as a linear function of time. This extension was made to allow the non-stationary models capture possible changes in the variability of annual sea level maxima. The main

results for this extension, reported by Räty et al. (2022b), however, did not give any strong evidence for the trend in the scale parameter. The non-stationary extreme value models were also used to calculate time dependent 50-year return levels, which showed variations throughout the observational period. Due to the strong dependence on circulation conditions, however, the interpretation of the time dependent return levels was difficult, and it was left for future research to address this issue using alternative modelling approaches.

Simulated low-pressure systems and sea level extremes

Because time series of sea level records are relatively short, return level estimates corresponding to return periods of 100 years or longer tend to exceed the observed sea level extremes. The physical factors leading to these extremes can be studied by simulating the effect of large-scale wind storms to the sea levels. In the Baltic Sea, short-term sea level variations are caused by atmospheric factors (wind and air pressure) and internal sea level oscillations. The highest extremes are related to large-scale wind storms created by low-pressure systems (cyclones). The local sea level extremes are sensitive to the properties of the low-pressure systems. By investigating how these properties affect the sea level at the coast, we seek for the parameters that give rise to the highest maxima.

The study was initiated in 2019 by developing a numerical method that generates low-pressure systems in which the spatial variation of air pressure at the sea level is described using a Gaussian distribution (Räihä et al., 2019). An ensemble of synthetic low pressure systems was then used to as input to a barotropic numerical sea level model to get the first preliminary estimates for the highest sea levels at the three Finnish NPP locations (Särkkä et al., 2020).

In 2021, the parameters of the low-pressure systems, or extratropical cyclones, were studied from ERA5 data, defining realistic ranges for these parameters in collaboration with research on cyclones described earlier. Based on this study, synthetic low-pressure systems were generated and the effects of the tracks of the low-pressure systems on the sea level on the Finnish coast were analyzed.

The internal Baltic Sea water level variations were simulated using the numerical sea level model, having as atmospheric input data an ensemble of time-dependent wind and air-pressure fields taken from the synthetic cyclones. The long-term water level component in the Baltic Sea is controlled by the water exchange from the North Sea at the Danish Straits, and a fixed upper estimate of this component was used. We studied highest sea levels at three locations on the Finnish coast: Kemi, Hamina and Pori. The highest extremes were found at Kemi and at Hamina, where the peak value of the internal fluctuation was 2.5 meters, whereas at Pori the peak value was only 1.5 meters (Figure 8, Särkkä et al., 2021).

In 2022, the studies were widened to cover the entire Baltic Sea coast (Särkkä et al., 2022), and a manuscript draft on the results of the extreme sea level simulations was prepared. The highest extremes were found in the ends of bays, caused by large and slowly moving low-pressure systems. Estimates for the maximum sea

levels were calculated at four locations on the eastern Baltic coast (Oulu, St. Petersburg, Riga and Gdansk). In the northern Bothnian Bay and in the eastern Gulf of Finland the maximum sea level due to the internal fluctuation can be from 3.0 to 3.5 meters. In the case when long-term water level has a maximal value (1 meter) during the fluctuation, highest extremes of 4.5 meters could be reached on the Baltic Sea coast.

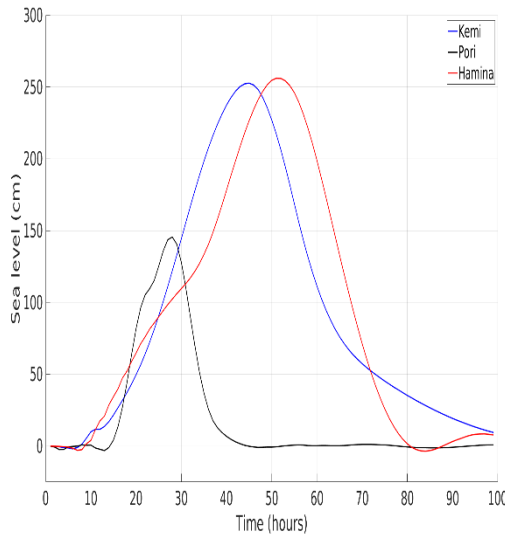


Figure 8. The highest simulated sea levels at Kemi, Pori and Hamina. Simulations were performed using synthetic low-pressure systems as an input to a numerical sea level model (Modified from Särkkä et al., 2021).

Summary and conclusions

The general objective of PREDICT was to develop and maintain research expertise and methods needed for assessing probabilities of occurrence of safety-relevant single and compound extreme weather and marine events. The project aimed to provide information that can be applied for the determination of the design basis for new NPP units, for probabilistic risk assessments of new and existing NPPs, and for periodic safety reviews of existing NPPs. The study topics of the project included climatology of intense coastal snowfall in the past; compound events, including joint occurrence of intense precipitation and high sea level; derechos and other major convective wind events extratropical cyclones, their characteristics and cyclone clustering associated with extreme sea levels on the Finnish coast; uncertainty in the exceptional sea level estimates; influences of properties of low-pressure systems (cyclones) on sea levels; and probabilistic weather forecasts.

The main findings of PREDICT in 2019–2022 are given below:

- Conditions favouring sea-effect snowfall were analysed to occur most often in December, in coherence with actual observations. Daily accumulated snow depth was found to be larger during days associated with sea-effect snowfall compared to “normal” stratiform snowfall.
- A recently developed high-resolution regional climate model HCLIM represented the past climatology of sea-effect snowfall in Finland promisingly well, which supports the use of HCLIM in assessing climate change impacts on sea-effect snowfall in the future.
- Joint heavy rain and high sea level events are typically caused by passing extratropical cyclones. Most of these compound events occur during a positive North Atlantic Oscillation period.
- Derechos seem not to be as rare events in Finland as we have thought. Altogether 10 convective-wind events in Finland were classified as derechos. The observed derechos occurred from May to October and caused damage tracks up to 660 km long in Finland.
- The number of passing extratropical cyclones was found to be positively correlated with the maximum sea level on the Finnish coast. The cyclones that caused extreme sea level heights were found to be generally stronger than the average cyclones in northern Europe.
- Stationary and non-stationary Bayesian hierarchical models were developed for modelling sea level extremes on the Finnish coast and were shown to reduce the range of uncertainty in the estimated distribution parameters and the corresponding return levels in comparison to the tide gauge specific fits.
- A sea level model, with input data from synthetically generated low-pressure systems, was used to study extreme sea levels on the Baltic coast. The highest extremes, caused by large and slowly moving low pressure systems, were found in the ends of bays like the northern Bothnian Bay and eastern Gulf of Finland.
- A probabilistic approach and increasing spatial resolution in weather forecasting bring more confidence on decision making in case of nuclear emergency.

Acknowledgement

In addition to the funding granted by the State Nuclear Waste Management Fund in Finland (VYR), the studies of sea-effect snowfall have been partly financed by the Finnish Cultural Foundation, Satakunta Regional Fund, and by the Finnish Meteorological Institute (FMI). ERA5 reanalysis data were downloaded online through the web interface of the Climate Data Storage (CDS) of the Copernicus Climate Change Service (C3S). Finally, we thank CSC – IT Center for Science for computing resources.

References

- Aalto, J., Pirinen, P. & Jylhä, K. 2016. New gridded daily climatology of Finland: permutation-based uncertainty estimates and temporal trends in climate. *Journal of Geophysical Research – Atmospheres*, 121, 3807–3823.

- Evans, J. S. & Doswell, C. A. 2001. Examination of derecho environments using proximity soundings. *Wea. Forecasting*, 16, 329–342.
- FMI, 2018. The summer from May to August was warmer than ever in recorded history. Finnish Meteorological Institute Press release archive, 6.9.2018; <https://en.ilmatieteenlaitos.fi/press-release/656561883>
- FMI, 2019a. Aapeli storm marked the beginning of a cold January. FMI Press release 7.2.2019; <https://en.ilmatieteenlaitos.fi/press-release/872470162>
- FMI, 2019b. Wave height records in the Baltic Sea. FMI Scientific themes; 1.3.2019; <https://en.ilmatieteenlaitos.fi/wave-height-records-in-the-baltic-sea>
- FMI, 2021. 2020 – warmest year since Finland started keeping records. FMI Press release 12.1.2021. <https://en.ilmatieteenlaitos.fi/press-release/3j2EOkB0jThiRSUOo7Gj37>
- Fortelius C., Hämäläinen K., Jylhä K., Kangas A. & Rantamäki M. 2019. PREDICT workshop on probabilistic forecasts. PREDICT/SAFIR2022 deliverable D3.1.1 in 2019, Finnish Meteorological Institute.
- Gatzen, C., Fink, A. H., Schulz, D. M. & Pinto, J. G. 2020. An 18-year climatology of derechos in Germany. *Nat. Hazards Earth Syst. Sci.*, 20, 1335—1351.
- Guide YVL B7, 2019. Provisions for internal and external hazards at a nuclear facility. Radiation and Nuclear Safety Authority (STUK).
- Guide YVL C4, 2019. Assessment of radiation doses to the public in the vicinity of a nuclear facility. Radiation and Nuclear Safety Authority (STUK).
- Helander, J. 2017. Identification and Analysis of External Event Combinations for Hanhikivi 1 PRA, Nuclear Engineering and Technology, Volume 49, Issue 2, Pages 380-386, <https://doi.org/10.1016/j.net.2017.01.007>
- Hersbach, H., Bell, B., Berrisford, P., Hirahara, S., Horányi, A. et al. 2020. The ERA5 global reanalysis. *Quarterly Journal of the Royal Meteorological Society*, 146, 1999–2049.
- Hurrell, J. W. 1995. Decadal trends in the North Atlantic Oscillation: Regional temperatures and precipitation, *Science*, 269, 676–679.
- Jeworrek, J., Wu, L., Dieterich, C., & Rutgersson, A. 2017: Characteristics of convective snow bands along the Swedish east coast. *Earth System Dynamics*, 8, 163–175.
- Johansson, M., Boman, H., Kahma, K.K. & Launiainen, J. 2001. Trends in sea level variability in the Baltic Sea. *Boreal Environment Research*, 6, 159-180.
- Johansson, M. & Kahma, K. 2016. On the statistical relationship between the geostrophic wind and sea level variations in the Baltic Sea, *Boreal Environment Research*, 1–2, 25–43.
- Jylhä, K., Kämäräinen, M., Fortelius, C., Gregow, H., Helander, J., Hyvärinen, O., Johansson, M., Karppinen, A., Korpinen, A., Kouznetsov, R., Kurzeneva, E., Leijala, U., Mäkelä, A., Pellikka, H., Saku, S., Sandberg, J., Sofiev, M., Vajda, A., Venäläinen, A. & Vira, J. 2018. Recent meteorological and

- marine studies to support nuclear power plant safety in Finland. *Energy*, 165 (A), 1102-1118.
- Jylhä, K., Leijala, U., Fortelius, C., Olsson, T., Rantanen, M., Räty, O., Särkkä, J., Hämäläinen, K., Laine, M., Luomaranta, A., Räihä, J., Johansson, M. & Rantamäki, M. 2021. Predicting extreme weather and sea level for nuclear power plant safety (PREDICT). In: Hämäläinen J, Suolanen V. (eds): SAFIR2022 – The Finnish Research Programme on Nuclear Power Plant Safety 2019–2022. Interim Report. VTT Technology 383. Pages 85-96. DOI: 10.32040/2242-122X.2021.T383
- Leijala, U., Björkqvist, J.-V., Johansson, M. M., Pellikka, H., Laakso, L. & Kahma, K.K. 2018. Combining probability distributions of sea level variations and wave run-up to evaluate coastal flooding risks. *Natural Hazards and Earth System Sciences*, 18, 2785-2799.
- Leijala, U., Johansson, M. M. & Pellikka, H. 2020a. Analyzing the extrapolation techniques and uncertainty related to the coastal flood risk estimates in Finland. PREDICT/SAFIR2022 deliverable D2.3.1 in 2019, Finnish Meteorological Institute.
- Leijala, U., Johansson, M. M. & Pellikka, H. 2020b. Analysing the extrapolation techniques and uncertainty related to the coastal flood risk estimates in Finland - Implications to Finnish Nuclear Power Plant (NPP) sites. PREDICT/SAFIR2022 deliverable D2.3.2 in 2019, Finnish Meteorological Institute.
- Olsson, T. 2022a. Sea-effect snowfall events in the Finnish NPP regions in the recent past climate. PREDICT/SAFIR2022 deliverable D1.1.1 in 2022, Finnish Meteorological Institute.
- Olsson, T. 2022b. Sula meri nostattaa sakeita lumikuuroja talvella, Ilmastokatsaus, 11/2022, Ilmatieteen laitos, DOI: 10.35614/ISSN-2341-6408-IK-2022-11-00, <https://www.ilmastokatsaus.fi/2022/12/21/sula-meri-nostattaa-sakeita-lumikuuroja-talvella/>
- Olsson, T. & Jylhä, K. 2022. Appraisal of intense snowfall in atmospheric reanalysis. PREDICT/SAFIR2022 deliverable D1.2.1 in 2022, Finnish Meteorological Institute.
- Olsson, T., Luomaranta, A., Jylhä, K., Jeworrek, J., Perttula, T. et al. 2020a. Statistics of sea-effect snowfall along the Finnish coastline based on regional climate model data, *Adv. Sci. Res.*, 17, 87–104.
- Olsson, T., Luomaranta, A., & Jylhä, K. 2020b. Statistics of sea-effect snowfall in Finland based on ERA5 reanalysis. PREDICT/SAFIR2022 deliverable D1.1.1 in 2020. Finnish Meteorological Institute. Olsson, T., Luomaranta, A., Nyman, H., & Jylhä, K. 2022. Climatology of sea-effect snow in Finland. *International Journal of Climatology*, 1–18. <https://doi.org/10.1002/joc.7801>

- Pellikka, H., Leijala, U., Johansson, M. M., Leinonen, K. & Kahma, K. K. 2018. Future probabilities of coastal floods in Finland. *Continental Shelf Research*, 157, 32–42.
- Rantanen, M., Jylhä, K., Särkkä, J., Leijala, U. & Räihä, J. 2020. Characteristics of joint heavy rain and high sea level events. PREDICT/SAFIR2022 deliverable D1.2.1 in 2020, Finnish Meteorological Institute.
- Räihä, J., Kämäräinen, M., Jylhä, K. & Särkkä, J. 2019. A method for generating synthetic low-pressure systems to support studies of sea level extremes. PREDICT/SAFIR2022 deliverable D2.4.1 in 2019, Finnish Meteorological Institute.
- Räihä, J., Leijala, U. & Jylhä, K. 2020. Co-occurrence of heavy precipitation and high sea level. PREDICT/SAFIR2022 deliverable D1.2.1 in 2019, Finnish Meteorological Institute.
- Räty, O. & Laine, M. 2019. OECD/NEA Benchmark on External Events Hazard Frequency and Magnitude Statistical Modelling. PREDICT/SAFIR2022 deliverable D1.3.1 in 2019, Finnish Meteorological Institute.
- Räty, O., Laine, M., Leijala, U., Särkkä, J. & Johansson, M. M. 2020. Bayesian hierarchical modeling of sea level extremes in the Finnish coastal region. PREDICT/SAFIR2022 deliverable D2.1.1 in 2020, Finnish Meteorological Institute.
- Räty, O., Laine, M., Leijala, U., Särkkä, J. & Johansson, M. M. 2021. Non-stationary Bayesian hierarchical models for sea level extremes in the Finnish coastal region. PREDICT/SAFIR2022 deliverable D2.1.2 in 2021, Finnish Meteorological Institute.
- Räty, O., Laine, M., Leijala, U., Särkkä, J. & Johansson, M. M. 2022a. Bayesian hierarchical modeling of sea level extremes in the Finnish coastal region, *Nat. Hazards Earth Syst. Sci. Discuss.* [preprint], <https://doi.org/10.5194/nhess-2021-410>, in review.
- Räty, O., Laine, M., Leijala, U., Särkkä, J. & Johansson, M. M. 2022b. Non-stationary Bayesian hierarchical modeling of sea level extremes on the Finnish coast. PREDICT/SAFIR2022 deliverable D2.1.1 in 2022, Finnish Meteorological Institute.
- Seneviratne, S., Nicholls, N., Easterling, D., Goodess, C., Kanae, S., Kossin, J., Luo, Y., Marengo, J., McInnes, K., Rahimi, M., Reichstein, M., Sorteberg, A., Vera, C., Zhang, X. 2012. Changes in climate extremes and their impacts on the natural physical environment. *Managing the Risk of Extreme Events and Disasters to Advance Climate Change Adaptation*, 109-230.
- Särkkä, J. & Räihä, J. 2020. Sea level simulations using synthetic low-pressure systems. PREDICT/SAFIR2022 deliverable D2.2.2 in 2020, Finnish Meteorological Institute.
- Särkkä, J., Räihä, J., Rantanen, M. & Kämäräinen, M. 2021. Sea level extremes simulated from synthetic low-pressure systems in the Baltic Sea,

- PREDICT/SAFIR2022 deliverable D2.2.2 in 2021, Finnish Meteorological Institute.
- Särkkä, J., Räihä, J., Rantanen, M. & Kämäräinen, M. 2022. Sea level extremes simulated from synthetic low-pressure systems in the Baltic Sea, PREDICT/SAFIR2022 deliverable D2.2.2 in 2022, Finnish Meteorological Institute.
- Trenberth, K. E., Fasullo, J. T., Shepherd, T. G. 2015. Attribution of climate extreme events. *Nature Climate Change*, 5, 725–730.
- Virman, M., 2022. Tests of the sea-effect snowfall detection method to high-resolution climate model data. PREDICT/SAFIR2022 deliverable D1.1.2 in 2022, Finnish Meteorological Institute.
- WMO, 2021. 2020 was one of three warmest years on record. Press Release Number: 14012021, published 15 January 2021.
<https://public.wmo.int/en/media/press-release/2020-was-one-of-three-warmest-years-record>
- Zscheischler, J., Westra, S., van den Hurk, B.J.J.M. et al. 2018. Future climate risk from compound events. *Nature Clim Change* 8, 469-477,
<https://doi.org/10.1038/s41558-018-0156-3>

3.4 Safety and security assessment of overall I&C architectures (SEARCH)

Antti Pakonen¹, Jarmo Alanen¹, Kim Björkman¹, Atte Helminen¹, Joonas Linnosmaa¹, Timo Malm¹, Teemu Mätäsniemi¹, Nikolaos Papakonstantinou¹, Juha Pärssinen¹; Polina Ovsiannikova², Valeriy Vyatkin²

¹VTT Technical Research Centre of Finland Ltd
P.O. Box 1000, FI-02044 Espoo

²Aalto University, Department of Electrical Engineering and Automation
P.O. Box 15500, FI-00076 Aalto

Abstract

The objective of SEARCH (2019–2022) was to develop methods and tools for assessing technical design solutions related to overall instrumentation and control (I&C) system architectures, based on Model-Based Systems Engineering (MBSE) practices. We developed (1) tools for analysing Defence-in-Depth properties, (2) methods for the hybrid assessment of safety and security, as well as (3) data models to support conformity assessment and design iteration.

A particular focus was on broadening the scope in which a formal verification method called model checking could be used. We developed methods for software verification, where we also account for failures and communication delay in the underlying hardware architecture. We also developed tools for finding the root cause of counterexamples, and our capabilities to verify infinite-domain models.

Introduction

The overall I&C system architecture of a nuclear power plant must fulfil the Defence-in-Depth (DiD) principle – there have to be successive levels of protection independent of each other. In theory, the architecture could be designed in a way where I&C systems on each level would have their own instrumentation and human-system interfaces, and no system would communicate across the DiD layers. Such a design, however, is not only prohibitively costly, but potentially less safe in terms of complexity, operability or maintainability. As a result, the overall I&C architecture needs to be optimised, meaning that the requirements on separation are deliberately relaxed (see Figure 1).

To ensure that key requirements for safety are still achieved by the optimised design, we need a suitable combination of deterministic and probabilistic safety analyses. The architecture needs to be constantly re-assessed during the design life-cycle, as new details about the plant and the I&C systems become available (IAEA 2018). Cybersecurity also needs to be addressed from the start. We also need to ensure that the computer security measures do not overtly compromise other vital aspects (IAEA 2018), in particular safety, but also availability.

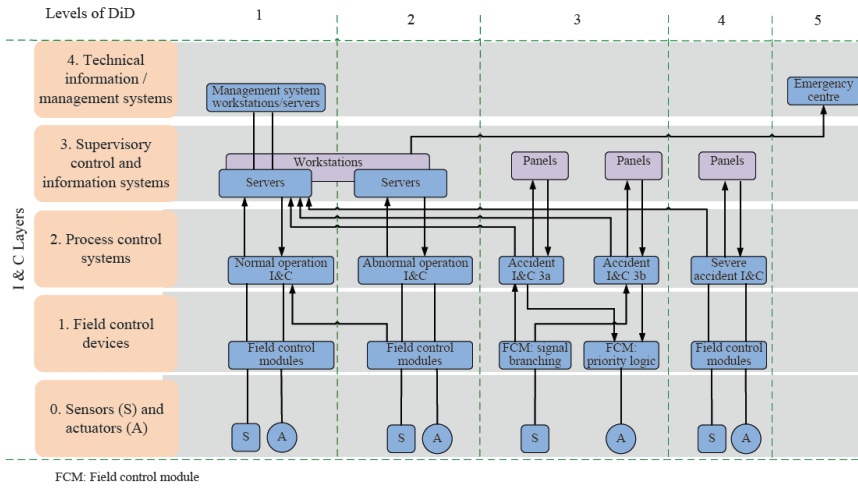


Figure 1. The separation of DiD layers can be compromised when the overall I&C architecture is optimised (IAEA 2018).

Throughout the four project years, SEARCH developed models, methods, and tools for analysing the safety and security of overall I&C architectures.

We demonstrated the use of formal semantics in analysing non-functional requirements about DiD, such as separation, safety classification, failure tolerance, and diversity. Knowledge bases built on Semantic Web languages combine information from different sources to flexibly answer complex queries.

We built models for assessing Reliability, Availability, Maintainability, Safety and Security (RAMSS) risks in tandem. A method we developed for hybrid safety and security assessment has already been successfully applied in a practical project – although not in the nuclear domain. The semi-formal data models we created support conformity assessment and design iteration.

We also broadened the way formal verification method called model checking can be applied, by developing methods to verify both software and hardware specific aspects against both functional and non-functional requirements. These methods allow us to account for hardware failures, communication delay, and asynchrony. We also proved the practical capability of infinite-domain algorithms in verifying logics with real number math. Furthermore, we developed new, user-friendly tools for better understanding the analysis results that model checking tools produce. In practice, VTT has already detected a real-world design issue in a Finnish NPP, which was only possible to find based on the new model-checking capabilities developed in SEARCH.

DiD assessment of I&C architectures

Ontology-based assessment of DiD properties

In the design and implementation of an overall I&C architecture the following issues related to defence-in-depth need to be considered; the degree of independence between the DiD levels, the manner in which non-safety systems are separated from safety systems, the number of independent channels in safety systems, and the degree of separation between the safety channels (IAEA 2018). Approaches with extensive tool support for ensuring that the design solutions of nuclear overall I&C architectures realize relevant DiD properties are scarce.

In SEARCH, we developed an ontology-based approach for assessing that an NPP I&C architecture fulfils different DiD properties (Pakonen & Mätäsniemi 2021). In our approach, we aimed at checking requirements related to physical separation, electrical isolation, communication independence, diversity, safety classification, and failure tolerance. For each of these categories, we listed competency questions (CQ), questions stated in natural language defining the scope of knowledge represented by an ontology (Wiśniewski et al. 2019).

The ontology needs to support querying the knowledge base for answers to the specified competency questions. Therefore, knowledge we wish to collect from the base affects the structure the ontology. The ontology class structure and the related object relationships we developed in SEARCH consist of three main classes PhysicalEntity, FunctionalEntity, and Classification (see Figure 2). The PhysicalEntity class covers I&C systems (and the interfaces between them), I&C devices (e.g., sensors, processors, actuators, HMI panels), support systems (e.g., power supply, HVAC), and their locations. The FunctionalEntity class covers initiating events, DiD levels, I&C functions (and their parts and connections), signals (e.g., alarms, control actions, measurements) and variables (control and measured variables). Classification has subclasses such as SafetyClass, SeismicCategory, which can be applied to either the functional or the physical entities. In addition, Classification includes the subclass DiversityAttribute that covers, e.g., logic, manufacturer, product, and technology. Some object properties are also shown in Figure 2. We used an OWL ontology to facilitate machine reasoning.

Based on the ontology, we specified SPARQL queries that can be considered as formalizations of competency questions. With the SPARQL queries we can address the different dependencies between I&C systems in the architecture.

To enhance the assessment task, we developed a work process for the ontology-based analysis of nuclear overall I&C architectures (see Figure. 3). The work process consists of three main phases: (1) ontology and knowledge base specification, (2) I&C architecture assessment and (3) documentation.

During ontology and knowledge base specification, the first tasks are to specify the competency questions and to start the collection of the needed data. The competency questions guide what data should be collected. The modelling work starts with the specification of the ontology class structure and the object

relationships. The ontology serves as the schema for SPARQL query specification. In addition, during this phase the source data is written in (or mapped to) suitable format supported by the knowledge base.

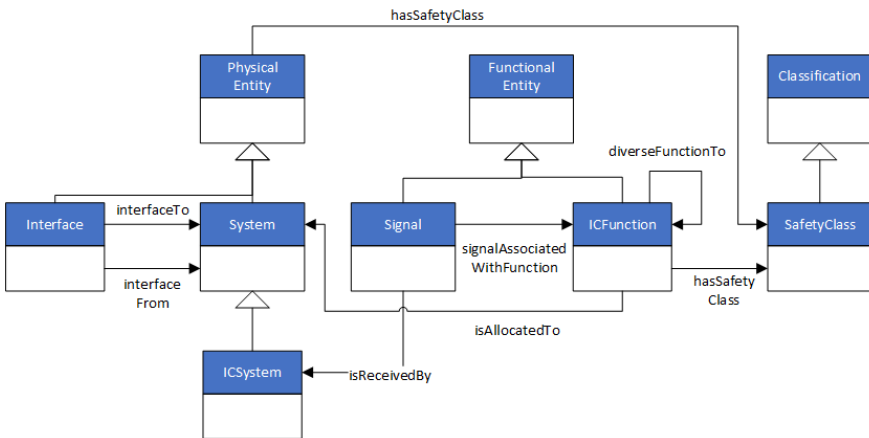


Figure 2. Key classes and properties from our ontology.

The I&C architecture assessment phase consists of two subtasks: running the queries in a knowledge base and interpreting the results from the queries. During this phase, SPARQL queries may be reformulated or new queries are created based on the analyst's needs. The results from the analysis may reveal errors or shortcomings in the queries, in the ontology or in the competency question, in which case the shortcomings are fixed. Finally, the results are documented.

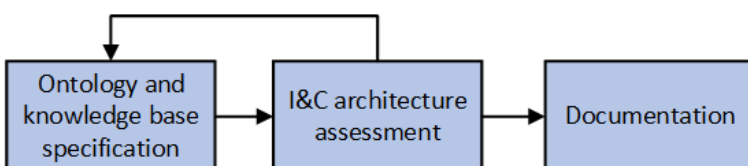


Figure 3. The high level work process for ontology based I&C architecture assessment.

We demonstrated the use of the ontology and the work process with on two case studies. The first example system was based on the proposed US variant of the European Pressurized Water Reactor (U.S.EPR) (Areva NP 2013). The second example system was the overall I&C architecture the NuScale small modular reactor (NuScale 2022). The objective of the case studies was to evaluate our approach and not to actually assess a real design. Thus, we did not expect neither of the architectures to necessarily fulfil the requirements we based our competency

questions and SPARQL queries on. In addition, aiming for total independence between DiD levels is not practical. However, they should be sufficiently independent, and the adequacy of the independence should be justified, e.g., by deterministic and probabilistic means. Our approach is a deterministic approach.

The case studies showed that OWL supports analysing requirements related to defence-in-depth. Based on queries, the semantic knowledge base enables the computer to deduce different classifications and connections that have may not have been explicitly stated in the source data.

In another research task, we focused on the subtask of suggesting fixes to the design issues revealed in the I&C architecture assessment phase. Assuming that the SPARQL queries response is not empty, and the queries are correct, the analyst processes a response and makes the required adjustments to the design (ontology). Next, the result ontology must be rechecked as, commonly, the I&C architectures are complex, and one change can make one property hold while failing another property. To save time and effort, we proposed a method for the automatic suggestion of fixes.

Our method is based on a graph representation of the design facts found with SPARQL queries, in other words, the facts that violate the specification. We can view a SPARQL query as a graph, where nodes are individuals from the ontology (or variables that substitute the individuals) and the edges correspond to the relations between them (or variables that substitute such relations). Our method does not aim at changing the structure of the ontology or TBox (e.g., its class and property hierarchies and definitions) but to change the relations between existing individuals or ABox statements. Therefore, in our graph, we do not consider the statements from the query that refer to the structure of the ontology itself.

When a SPARQL query is executed, the result we obtain is a set of sets of substitutions for the variables in the query, hence, for each such set of substitutions, we can get a graph, by cloning the SPARQL query graph and replacing the variables in nodes and edges with their found values. For each query, we get a set of such graphs. To infer fixes, we intersect all the graphs for all the SPARQL queries and get intersections subgraphs that belong to multiple graphs of the query results. The fix is then a set of modifications to this graph of type change/remove an individual (node) and change/remove a relation (edge) between individuals.

We evaluated our method using the model of the overall I&C architecture of the U.S.EPR created earlier. We chose the following two Competence Questions: (1) whether there exist interfaces between systems with different safety classes, where the information flows from the system of the lower safety class to the system with the higher safety class and (2) whether there exist systems whose support systems are of a lower safety class, and ran their corresponding SPARQL queries. In total, we discovered 13 issues for both of these queries and derived their graph representations, which intersected in 28 subgraphs. We sorted them by the count of the query results they belong to and ran the method over the first 10 as changes in these subgraphs can eliminate the biggest number of issues.

As a result, we noticed, that the subgraphs where the most queries results are intersected typically consist of just one node, so the only suggestion that can be

provided in this case is to remove such a node. This result is nevertheless helpful during the analysis as, for example, in case the node is an individual, representing a system, it points out that most problems with the architecture are connected with such a system. The intersections where more complex fixes can be applied (e.g., change or replace the relation) belong to fewer queries results, however, fixes found for them are meaningful straight away and can be implemented. One tactic of using this method during the I&C architecture design, for example, is to find several such intersections and choose the appropriate fixes for them so that all the results of the queries are covered.

In another research direction, we investigated how the complex non-functional requirements or design principles, such as diversity, can be formulated and evaluated, and devised rule systems, which define the complex requirements using CQs and logical operators in form of function block diagrams. To evaluate such rule systems, we translate them to Prolog. We found Prolog to be a more flexible language for formulating CQs and designing the rules systems than SPARQL and ontologies. We also compared time and resources spent on checking the CQs formulated as SPARQL queries over U.S.EPR ontology from the previously described case study with the CQs formulated in Prolog and ran over U.S.EPR ontology translated into Prolog and found out that Prolog overperforms for the most CQs for both the original ontology and an artificially enlarged one. The intermediate conclusion is that Prolog can be successfully used for modelling and checking the I&C designs. The major drawback of Prolog is the steep learning curve and lack of user-friendliness, as we speak here of supporting instruments for the analysts that can be applied without extensive training.

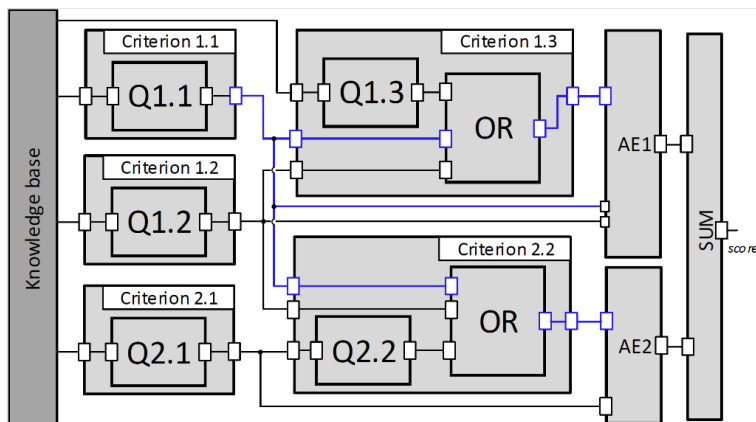


Figure 4. Part of a function block diagram of the rule system created for assessing the diversity principle.

Our rule systems, however, are a concept and can be implemented using various programming languages. They especially benefit the analyst when can be created using a tool with a graphical interface. The rule system itself is a function block

diagram which alongside common logical and arithmetic function blocks, is equipped with a special type of function block that queries the knowledge base where the information about the I&C architecture is stored. To test the concept, we manually created such a system for a diversity principle from NUREG CR-7007 (NRC 2009). According to CR-7007, the result of assessing the diversity principle is not a logical value but a score. The score depends on whether the architecture complies with the rules formulated based on the CQs, however, in addition, the rules have weights, sets of rules form attributes, that have weights as well and the result is calculated based on the values of the attributes. Figure 4 shows a part of such a rule system.

The additional advantage of rule systems formulated as FBD is that we can explain the end score by implementing and running the explanation technique from (Ovsianikova et al. 2020) This creates a powerful instrument for the assessment of design principles, where instead of dealing with a number obtained as a result, the analyst will see the reasoning behind the particular value.

Balancing safety and security

Safety and security of complex critical infrastructures are very important principles for economic, environmental, and social reasons. Although safety and security have different foci, in many areas they overlap with each other, and actions to advance one activity in complex system can have implications for the other. The complexity of these systems introduces difficulties in the identification of safety and security risks that emerge from interdisciplinary interactions and dependencies. Modern systems have become increasingly complex, leading to unintended vulnerabilities to both nominal mishaps and mishaps imposed by an attacker. The discovery of safety and security design weaknesses late in the design process can lead to increased costs, additional system complexity and delays to the deployment of the system. Safety and security system capabilities are currently often evaluated independently using separate assessments and specific methods that are performed by specialized experts at different system design phases. The methodologies we developed in SEARCH attempt to introduce hybrid models including both safety and security concepts that can support a concurrent safety and security assessment at an early design phase. These models and methods were developed with three principles in mind:

- Safety and security need to be assessed early and concurrently. Assessment methodologies are similar, and in many cases, the goal is the same (ensure the resilience and survivability of the system). Although the basic events are different in nature, there are scenarios where a safety scenario can start with a security attack. Additionally, there may be cases where there is a trade-off between safety and security (e.g. safety advocates for “openness” while security needs strict control).
- There is value in doing holistic system modelling, safety and security weaknesses often emerge from interactions between system disciplines.
- The methods need to be easy to be used by the practitioner, and should have the potential to become a tool.

In (Papakonstantinou et al. 2020), we developed an interdisciplinary model-driven method and a prototype tool for hybrid DiD assessment of early complex systems. Instead of focusing on removing vulnerabilities, we assumed that a determined attacker can always find a way to penetrate defence. The method can assess basic safety and security design principles (e.g., redundancy, separation, diversity, security zones) concurrently, and provide feedback in early system design. To support the security assessment of complex systems the UML profile proposed for safety assessment in (Papakonstantinou et al. 2017) was extended with security concepts of facility functions, security levels, authorization levels, computer and facility security zones, conduits and physical gates. Based on this modelled set of safety and security attributes, the developed prototype tool can assess aspects of the safety and security DiD capabilities of an early design. The four steps needed for the proposed combined early safety and security assessment are:

- Step 1: Develop the multidisciplinary dependency model of the system focusing on interdisciplinary connections.
- Step 2: Add the known safety and security aspects (safety/security system components and attributes).
- Step 3: A software tool automatically assesses the safety and security capabilities of the system based on a set of safety and security rules.
- Step 4: Safety/security engineers and system engineers evaluate the feedback of step 3. Use the results to improve the system design. If changes are done, return to step 3.

The results can be then used to identify errors, improve the design and cut costs before a formal human expert inspection. We demonstrated the tool on a case study of an early conceptual design of a NPP fuel cooling pool system.

Table 1. Harmonised basic concepts between safety, security and dependability.

Safety	Security	RAM	Harmonised term
Fault	Vulnerability	Fault	Imperfection
Hazard	Threat	Loss scenario	RAMSS hazard
Harm	Impact	Loss	Negative impact
Protective measure	Countermeasure	Improvement measure	Risk control

In another effort in SEARCH (Alanen et al. 2022a), in order to support and combine multidisciplinary modelling and assessment, we developed, together with the AUTOPORT (Business Finland) project team, a model-driven methodology for a hybrid Reliability, Availability, Maintainability, Safety and Security (RAMMS) risk assessment. This work enhances and extends our safety risk assessment ontology and data model, originally developed as a part of our System Engineering Artefact Model (SEAModel) (Tommila & Alanen 2015), to also support security and dependability engineering. To create such a hybrid risk assessment ontology, we first needed to harmonize some basic concepts between dependability, safety and security. The harmonisation results are shown in Table 1.

Using these harmonised terms, we created a hybrid risk assessment ontology, which supports creation of a structured work item (artefact) storage (such as a database), with traceability links, of the input and output work items related to the risk assessment activity. This RAMSS ontology is presented in Figure 5.

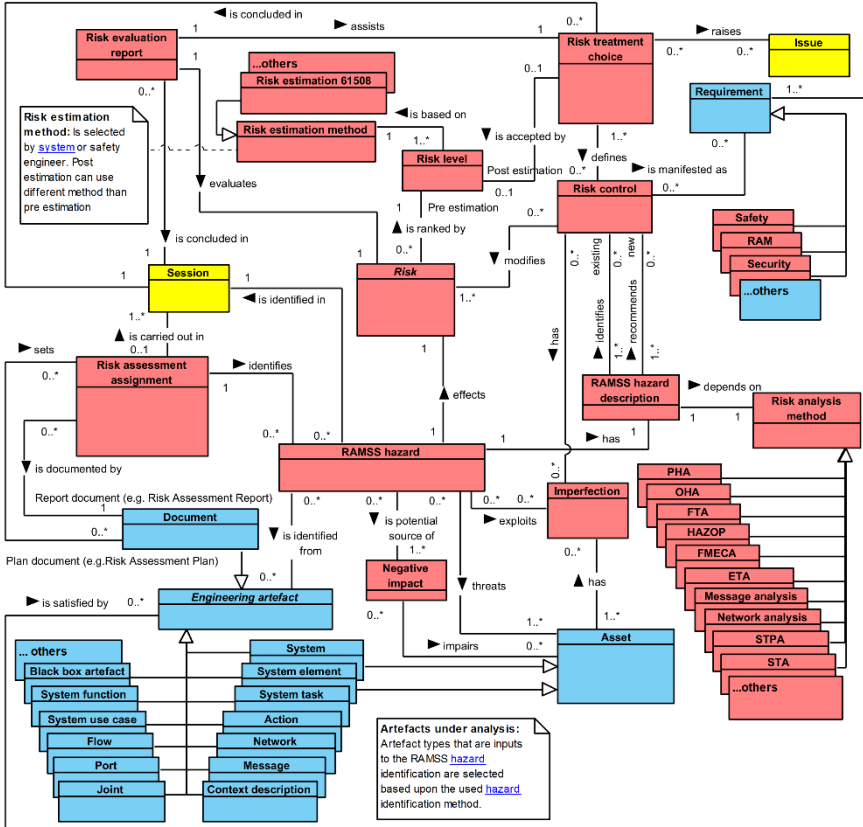


Figure 5. RAMSS risk assessment ontology. The risk assessment related artefact types are with red colour, the blue ones are general systems engineering artefact types, and the yellow artefact is a project management related artefact (Alanen et al 2022a).

The RAMSS risk assessment ontology should support any risk analysis method, but we wanted also to create a SEAModel compatible ontology for an early nuclear I&C cybersecurity risk assessment called Security Threat Assessment (STA). The idea was not to define a new cybersecurity risk assessment procedure, but an ontology and the derived data model, which can be used in the context of any typical security risk assessment procedures, such as the ones presented in ISO 31000 or IEC 62443-3-2. The STA data model is presented in Figure 6.

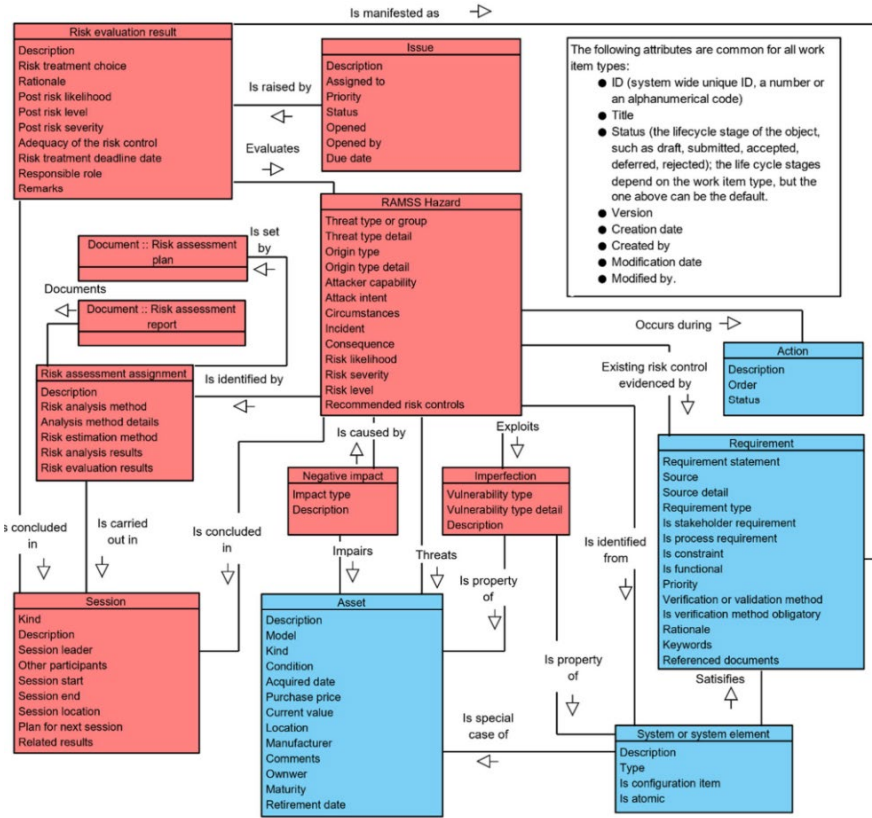


Figure 6. Data model for STA artefacts and their relations (Alanen et al 2022a).

We also implemented the STA data model onto the Polarion REQUIREMENTS requirements management tool and demonstrated the models with an I&C related security threat case (a threat to lose fuel pool cooling due to an attack by a malicious IT service person).

To further the knowledge on the cybersecurity discipline (which is probably not so well defined as safety), we first identified the main sources for cybersecurity related I&C requirements in the nuclear domain, this was based on discussions with STUK and the Finnish utilities (Linnosmaa et al. 2021b). Numerous international cybersecurity initiatives, groups and committees develop, publish, and maintain a wide range of standards, standard families, frameworks, and guidelines. While the ways of securing and managing the cyber environment differ, the concepts and topics are often similar or shared. The standards found most important are summarised in Figure 7.

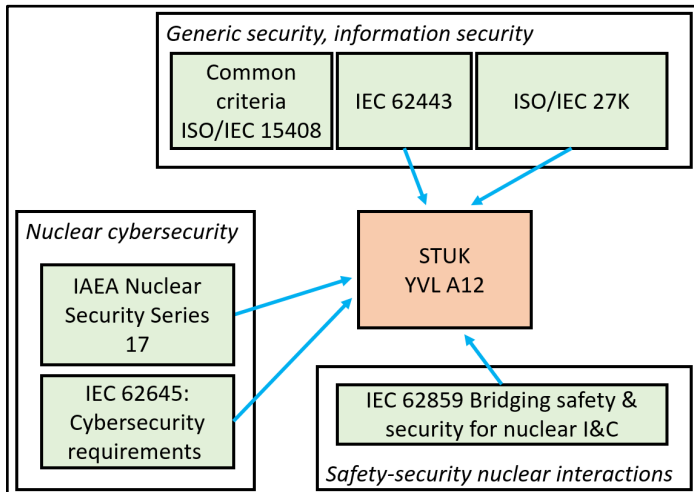


Figure 7. The most important cybersecurity standards from the Finnish perspective.

To continue the effort, we studied the literature on integration of security and safety for the I&C systems (Linnosmaa et al. 2022). We specifically focused on nuclear domain, where integration of the two disciplines is needed to ensure safety and secure operation. We briefly summarized the most important content of the major publications about the topic from this perspective. It was noted that both safety and security are disciplines which are strongly built on legal and regulatory frameworks, and such frameworks should be developed and maintained by the combined stakeholders at all levels of both disciplines, to make sure that synergies between the two are leveraged while the potential conflicts are avoided. Safety related requirements can easily turn into security requirements (and vice versa) when I&C or office software is considered. The goal has therefore been to survey and provide perspectives on how to integrate the two disciplines. It remains a complicated effort to find synergy, and the right balance, while avoiding unwanted interactions and side effects. For each discipline, the main principle for managing risks is nevertheless the successful application of the DiD principle.

I&C security engineering methods and tools

During the SEARCH project, we created an ontology and a consequent data model to model the data objects relevant to cybersecurity risk assessment. The ontology and data model are an extension to the risk assessment part of the SEAModelNPP that we have presented in (Tommila & Alanen 2015) and extended to cover a conformity assessment model in (Alanen et al. 2017), which is demonstrated in (Linnosmaa & Alanen 2019). In context of the security ontology, we also developed Security Threat Analysis (STA) (Alanen et al. 2022a) method, to identify, evaluate and estimate the cybersecurity risks of I&C systems. The information (input and

output) relevant in context of STA is captured and stored according to the security risk data model. During the years, we have tested and demonstrated engineering data models with different tools, such as MySQL (with MS Access user interface), Polarion ALM, IBM Rational Doors (both 9.x and Next Generation versions), MS SharePoint and ARAS PLM. Implementation of SEAModel data models is rather straightforward with such tools, but they lack discipline specific profiles and user interfaces. Thus, we searched and studied off-the-shelf tools that are specific to cybersecurity analysis, tools that could be utilised in cybersecurity threat analysis of nuclear I&C systems (Alanen et al. 2022b). We also tried to find established cybersecurity analysis methods to be used instead of or as a complement to our STA method (Alanen et al. 2022b).

The main finding of the review was that the array of cybersecurity risk analysis methods is vast, both dedicated cybersecurity analysis methods and methods that also concern safety, but that the practices are not that well established than with pure safety risk analyses, and more work is needed to determine the optimal security analysis methods in general or for each domain separately, such as nuclear power plant instrumentation and control systems. But there are good methods already, such as the ones presented. There are also some software tools suitable for security risk analysis of industrial control systems, but not too many to select upon. In both cases – methods and tools – the company implementing safety and security critical control systems must be prepared to select more than one method and more than one tool to comply with the regulator requirements and the company specific safety and security policy. A holistic platform to manage, with traceability, the diverse data from the different methods and tools is needed. (Tommila & Alanen 2015) present an ontology for such a holistic repository; with the conformity assessment model developed by (Alanen et al. 2017) and demonstrated by (Linnosmaa & Alanen 2019), the traceability between the risk assessment artefacts and other systems engineering artefacts, such as system elements and requirements, is achieved.

Integrated framework for I&C engineering

Model based systems engineering (MBSE) is the preferred approach for system development and knowledge representation in the nuclear industry. To move from document-centric engineering towards MBSE, it is necessary to construct a structured and well organised systems engineering (SE) data repository and to model the system-of-interest. Hence all the engineering artefact types and their relationships have to be identified. We have earlier created a semi-formal systems engineering ontology, called Systems Engineering Artefacts Model (SEAModel) (Tommila & Alanen 2015) to identify the artefact types and their relationships. Over the SEARCH project, we have used these semi-formal representations as a basis for a data model of an SE data repository. In addition, we have noticed that semi-formal models are relevant in conceptualization discussions with stakeholders. However, the semi-formal models and their integrity constraints do not fully support

artificial intelligence (AI) aided engineering of complex safety related systems. Therefore, we developed an integrated framework for I&C engineering in nuclear domain. The framework covers the SE artefacts which are relevant during conformity assessment of an I&C system.

On the way to formal systems engineering, we created some additional semi-formal models, one for the system analysis and one for model checking. Furthermore, we created models to map the model checking artefacts to the system analysis and conformity assessment semi-formal ontologies to support the cases that model checking can be used both in the conformity assessment phase and in the system analysis phase. Similarly to our earlier demonstrations, also the model checking conformity assessment ontology was tested as a basis for a data repository with an industrial tool (Polarion) (Linnosmaa et al. 2023). In addition, the tool's ability to (semi)automatically generate the required documentation, such as analysis report was studied. We also mapped the risk assessment artefacts depicted in Figure 8 to the system analysis semi-formal model.

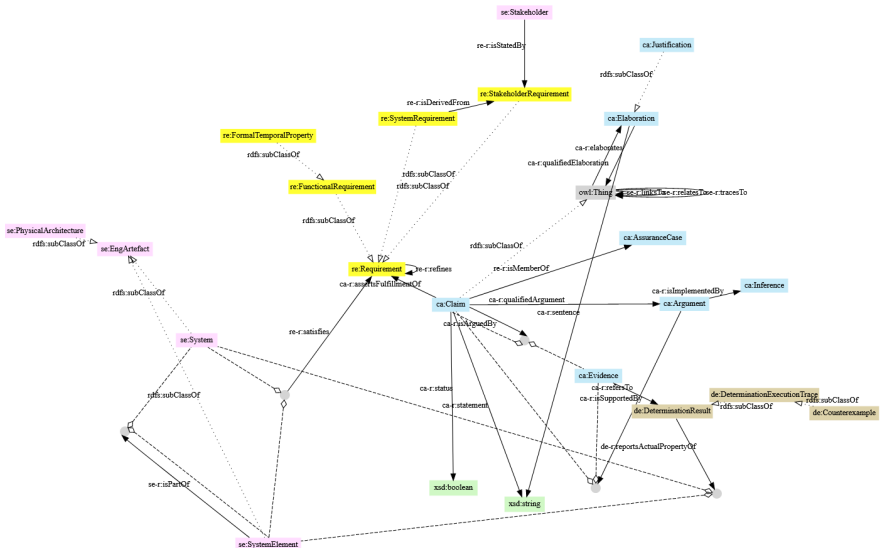


Figure 8. Formal conformity assessment ontology.

Finally, we developed, using formal ontology language OWL (Web Ontology Language), a conformity assessment ontology based on the semi-formal model of the conformity assessment artefacts. The scope and information needs of such a formal conformity assessment ontology were studied with the help of competency questions, and the designed ontology was validated by Description Logic (DL) class queries with an example. Also, the challenges and findings during the framework development were encountered. The ontology based conformity assessment data model and its precise semantics are suitable for definition of well-formed assurance cases. In addition, less updates are required at later stages because an external

evaluator interprets the structures in a similar way. However, the open world assumption (OWA) of ontology modeling requests modelling decisions for an unknown information.

Review of Architecture Description Languages

Supported by in-kind participation from OECD Halden Reactor Project (run by Institute for Energy Technology (IFE)), SEARCH reviewed and studied the use of Architecture Description Languages (ADL) in I&C architecture modelling and analysis to enable Model-Based System Engineering (MBSE) in design and assessment. ADLs can enable the modelling of both hardware and software aspects of systems and components, supporting the “plant-as-a-whole” approach.

We started in (Hauge et al. 2019) with a systematic survey of the literature identifying current model-based techniques, methods, and approaches that can support the assessment of safety and security in the early system stages like the concept stage, architecture, or early design stages, as well as support the building of confidence that both of those quality factors are satisfactorily addressed early. The selected search strings generated an initial set of 178 papers. The most mature and promising direction for further exploration of model-based approaches supporting safe and secure DI&C design was represented by papers that used the AADL (Architecture Analysis and Description Language) as its basis.

Other objective was to study the use of ADLs for standardized and structured ways to model the overall I&C architecture, a set of selected DiD related requirements of the dependencies formed with the connections between systems, and automatic assessment of the fulfilment of those requirements using the model. In (Linnosmaa et al. 2020) we studied the capabilities of AADL against this goal. We first specified an example case for a part of an overall I&C architecture (including safety functions, safety classes, DiD levels and I&C systems) loosely based on the APR-1400 design. In addition, we crafted some basic separation related DiD requirements based the Finnish YVL guides. We then studied the AADL version 2.2 and an open-source tool called OSATE2 to model and assess the system.

We demonstrated that even though AADL may not a standardized components or methods for modelling a system at the level of overall architecture, it still offers support for modelling the primary components. However, we did not find a way to express our wanted requirements using the standard AADL notation, at least not in a way we could have analysed their fulfilment. We did gather a set of promising analyses from literature based in various annexes to the language, which could be used to expand the model to offer more DiD related assessment capabilities. To conclude, the AADL components are more geared towards specifying the physical decomposition of a single system.

In (Sechi et al. 2020), the focus was shifted a little to focus studying early stage architecture modelling and safety assessment of a single system under modernization. Our case was the Halden Safety Fan (HSF), which was an initiative to research model-based design, assurance and digitalization of old analogy

emergency ventilation system based on the real system part of the Halden research reactor in Norway. Digitalization steps, in general, include establishing a concept description, the development and safety assessment plans, system requirements specification, risk analysis and safety assessment report. It is an interesting possibility for researchers to get hand-on experience working with real-life equipment and the related documentation. Our work included also defining some of the properties for HSF case, for example describing the overall functions of the system, the main sub-systems and components, and the inter-connections between these. We also started to outline the functional behaviour of the system. Based on our system descriptions we modelled the structural aspects (standard AADL) and non-nominal behaviour (AADL error modelling annex EMV2) of the system. AADL and the tool OSATE, offered constructs for effective composition and linking of specification parts. The information of a specific part can be focused on one place but can be accessed from many places. The navigation within a model is not constricted to linear navigation, from the textual representation, different kinds of graphical diagrams are generated and linked to allow navigation to any part of the specification quickly. A system defined with OSATE2 includes clear syntax and semantics allows for automatic or semi-automatic analysis such as FHA, FTA, FMEA. We used FTA to find minimum cut sets for redundant train failure state of the system. We also used this information to inject a failure in a dynamic process model modelled with APROS.

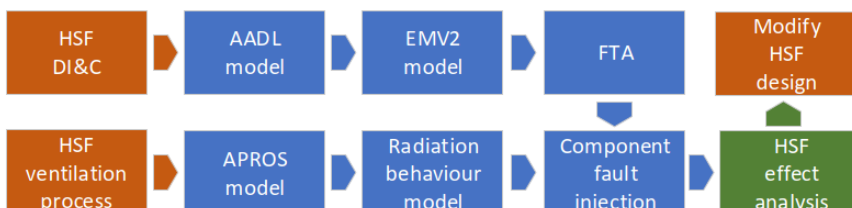


Figure 9. Our concept of combining AADL with APROS for fault effect analysis.

The idea of combining architecture modelling with dynamic process simulation was further studied in (Linnosmaa et al 2021a). Designing of complex process plants, such as a nuclear power plant, requires the development of the physical process and the automation system controlling it. When dynamics of the physical processes are included, it becomes challenging to identify all possible consequences arising from different component failures, including common cause failures or degraded modes of operation. We presented a concept for supporting fault and effect analysis using architecture description language capable of modelling software and hardware components and their faults of the system with a dynamic process modelling simulator (shown in Figure 9). We first used the error modelling and analysis of the architecture to find potential critical combinations of component faults within a complex system. Secondly, we simulated the effects of combined faults on the controlled process to analyse system effects. We tested the method on an early

design of HSF, while using AADL for architecture modelling and APROS for the dynamic simulation. Results indicate that proposed early-stage failure assessment can easily be performed using a model as input, gaining confidence on design choices.

Formal verification methods and tools

I&C hardware issues in model checking

Certain safety functions of I&C systems are designed to be fault tolerant. Checking fault tolerance formally requires hardware failures to be formally modelled in addition to the I&C logic. Due to the focus of SEARCH on overall I&C architectures, we decided to extend our previous results from the SAUNA/SAFIR2018 (Pakonen & Buzhinsky 2019) to support architecture level analyses.

In our recent works (Buzhinsky & Pakonen 2019; Buzhinsky & Pakonen 2020a), we allow safety functions to be allocated to one or more I&C systems and allow each I&C system to have several divisions. The typical assumption of failure tolerance is the single failure tolerance criterion: the safety functions must work correctly with arbitrary failures in any single division.

The structure of the most comprehensive case study that we considered is shown in Figure 10. It consists of one non-safety system, the process automation system (PAS), and three safety systems: the protection system (PS), the safety automation system (SAS), and the priority and actuator control system (PACS). These systems have been allocated different functions: normal operation, preventive protection and reactor protection. The relation between the systems and the safety functions is shown in Figure 11. We developed this case study based on the U.S. EPR NPP materials (Areva 2013) and our own invention and tried to make the implementations of units realistically detailed.

As before, we perform model checking in NuSMV (Cimatti et al. 2002), model the elements of the system in MODCHK (Pakonen et al. 2021), remove unit/division pairs that do not influence the temporal property to be verified, and examine only one division of the verified unit (Pakonen & Buzhinsky 2019). To support the structural assumptions mentioned above, other aspects of the approach were refined.

First, we made the processing of symmetries in the overall model automatic. Previously, when we dealt with only one redundant system, we used the facts that the implementations of the units in all the divisions of this system are identical and the connections between the units are symmetric (which is the case for the PS in Figure 10) to only consider one configuration during model checking as verification outcomes for other configurations would be necessarily identical. However, when the overall structure of the system becomes as complex as the one shown in Figure 10, it is no longer apparent which configurations are equivalent. To solve this problem, we developed an approach that computes the domination relation between configurations. Once this relation is computed, it is sufficient to model-check a

subset of configurations that dominates all possible configurations under the considered failure assumption (Buzhinsky & Pakonen 2020a).

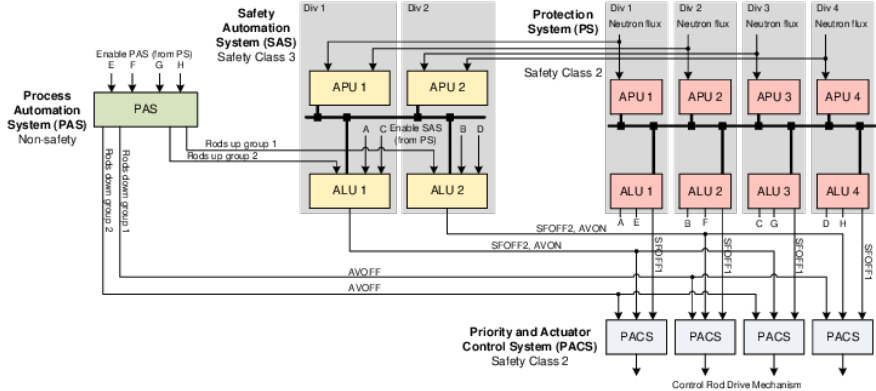


Figure 10. Case study for failure tolerance model checking (Buzhinsky & Pa-konen 2020a).

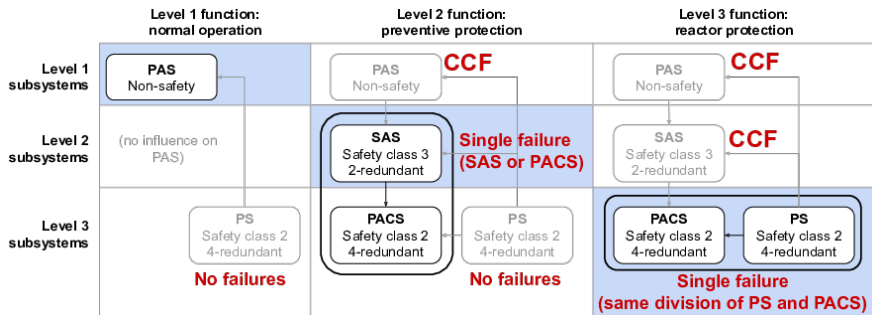


Figure 11. Connections between the systems and the safety functions, and the used failure criteria (Buzhinsky & Pakonen 2020a). “CCF” stands for a common cause failure (modelled as a failure in all the divisions).

Second, we agreed on several conventions regarding the temporal properties to be verified. Formulation of some temporal properties becomes non-trivial due to the following problems: (1) for each temporal property, verification may potentially be performed for several configurations, meaning that the divisions of the components to be verified become known only after symmetry analysis; (2) the divisions where failures are possible also become known only after symmetry analysis; (3) we only model failures on connections between the units. To solve the first problem, when referring to the concrete divisions of the components in a temporal property, we utilize a division placeholder, which will be replaced by the index of the actual division to be verified after symmetry analysis. To solve the second problem, when we need to express a property that refers to multiple divisions of the system, we use

only AND, OR and other counting operations over all the divisions. The results of these operations do not depend on the order of their arguments, and thus on the divisions selected for failure injection. To solve the third problem, we avoid temporal properties referring to the internal variables of the units. It is in principle possible to verify temporal properties that do refer to these variables, but then they need to be carefully checked to be meaningful.

Third, we have found that a mere optimization of the model of failure injection blocks, which are inserted on the connections of the model in the divisions that may be affected by failures, notably decreases the model checking time. Essentially, the optimized version of the failure block is a mere replacement of the failing signal with a nondeterministically generated value. However, we have also found that the use of such a simple model may lead to false positive results when model-checking computation tree logic (CTL) properties. For a subclass of such properties that expresses the possibility of a Boolean output to produce both values in the future (AG-EF properties), we have enhanced the failure model to restore the reliability of verification.

On the theme of failure modelling, we also experimented with the xSAP safety analysis platform, but found that it is not feasible for analysing the kinds of logics we work with, since it is more suitable for verifying “system is alive” type properties than detailed input-to-output behavior. We also had significant practical problems with installing and running xSAP, as well as debugging our models.

In parallel to the work on failure modelling: we also tried accounting for communication delays between the components and their asynchrony. We tried two techniques: the one developed previously (Pakonen & Buzhinsky 2019), where discrete-time delay blocks may non-deterministically delay the signals between the components of the system, and a new approach based on real-time modelling of delays (Buzhinsky & Pakonen 2020b) in the nuXmv model checker.

In the new approach, we modelled each unit of the system as a timed automaton that operates cyclically, making a step once per a fixed time duration. Executions of different units are not necessarily synchronous. In addition, we modelled the buffers between the units that store the data which has not yet been received. These buffers model the delays by being able to hold the old version of the received signal for a duration within a specified range. Figure 12 shown an example of a timeline in the real-time model of the PS.

In most of our experiments, we focused on the situation of modelling hardware failures, but not delays and asynchrony. In this failure-only setting, we succeeded in verifying the system shown in Figure 10 with model checking algorithms based on binary decision diagrams (BDDs). Our experiments encompassed three failure scenarios shown in Figure 11, and also an artificial scenario where the single failure criterion was applied to all the subsystems of our case study independently. Checking a single temporal property took up to several seconds.

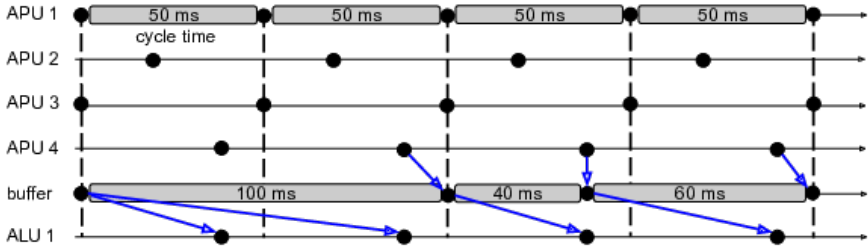


Figure 12. Example of a timeline of the PS in a timed nuXmv model (Buzhinsky & Pakonen, 2020b). Blue arrows show the information flow from APU 4 to ALU 1.

The situation of both failures and delays being modelled is more challenging. With the basic, cycle-based delay modelling, BDD-based algorithms usually no longer terminate within reasonable (i.e., several hours) time limits, but incomplete bounded model checking (BMC) handles such situations well. To evaluate the real-time communication modelling approach (Buzhinsky & Pakonen 2020b), we only included the PS into the overall model. On such a reduced case study, we found that BMC is again successful, and in addition a small fraction of properties can be verified by a complete model checking algorithm (IC3). Finally, the real-time communication modelling approach opens the opportunity of verifying temporal properties with explicitly specified time durations (e.g., required response time), but we found such properties more computationally complex to verify than regular ones.

Explanation of counterexamples

While model checking is an efficient instrument for detecting failures in I&C logics, finding a particular problem location in a model or its specification can still be a daunting task. Overall, model checking tools take the formal model of the system and its specification as input and produce a counterexample as output if the latter is violated. In our case, the system is represented as a function block diagram implemented using NuSMV and its properties are formulated using linear temporal logic (LTL). We define a state of the system as a list of all the system variables with their values at a particular discrete time step. Thus, a counterexample is a sequence of such states that starts from the initial system state and defines a behaviour that violates the specification. At the same time, a counterexample is a mere table of values that lacks information about the system structure, contains dozens of variables, and requires pen and paper to be analysed. Therefore, we developed Oeritte, a tool for visual counterexample analysis that combines a technique for counterexample explanation using the LTL property that was developed during SAFIR2018 (Pakonen et al 2018) with highlighting of possible failure paths in the diagram of the system.

We define an assignment as a value of a variable at a particular discrete time step. As an LTL formula failure can be explained through a set of assignments of

the variables included in it (Pakonen et al. 2018), we can decompose the process of explaining the false outcome of the formula to the one of explaining a number of individual assignments in the counterexample. We can then focus on explaining a single assignment, called an explanation target. Informally, a cause of a target is a set of assignments of system variables such that it is possible to infer the target by applying logical inference starting from these assignments and proceeding in the direction of information flow through function blocks. A cause is inclusion-minimal if it contains no subset of assignments that satisfy the statement above. Thus, to explain the target is to find the union of all its inclusion-minimal causes.

In order to find such causes, we, first, decomposed the system into a net of interconnected atomic blocks that represent atomic operators (e.g., $+$, $-$, $*$, \vee , \wedge) or simple functions (e.g., counting, conditional operators, delays) and have a finite number $n > 1$ of inputs and one output. Then, for each of these blocks, we defined a function that explains their outputs. We also defined an explanation function for a connection between blocks, which basically states that a cause of the end assignment of the connection is its start assignment at the same step. To explain the target in the function block diagram, we developed a recursive algorithm that searches for inclusion-minimal causes of the assignments included in every next found cause starting from the explanation target and terminating in the assignments of the variables that belong to system inputs or lack incoming connections. We implemented the algorithm in a graphical tool, Oeritte (Ovsianikova et al. 2020, Ovsianikova et al. 2021a).

In 2020, we formulated a theoretical base under our definitions and proved that the result of the algorithm corresponds to a union of all the inclusion-minimal causes. We also removed some of the restrictions on input files, allowing explanation in the diagrams with several levels of hierarchy (or, speaking in terms of NuSMV, that include nested modules). To enhance user experience, we implemented an automatic visual connection of the cause of the LTL formula with the variables in the diagram.

The graphical user interface of Oeritte (see Figure 13) includes three main areas: (a) FBD diagram where the explanation is depicted, (b) a diagram explanation graph and (c) LTL formula explanation view. In the diagram area, a tooltip with the variable name appears when the cursor hovers over any of the squares (called pins) on the sides of the blocks that correspond to their input and output variables. Blocks with the single input or output pin on the left and right sides of the diagram represent the interface of the current diagram. Lines connecting module inputs and outputs are connections between the variables. The LTL formula explanation view contains two tabs: parsing tree view, and the other from (Pakonen et al. 2018) shown in Figure 13. Oeritte incorporates two kinds of explanation techniques: the cause identification algorithm (Pakonen et al. 2018) for LTL formula failures and individual assignment explanation, described above. The result of the latter, which includes all the minimal causes for the target, is depicted in the diagram in the form of highlighted pins and connections in between. The causes are shown in the diagram explanation graph, which is read from right to left. Its nodes are assignments and edges represent the causal relation between them.

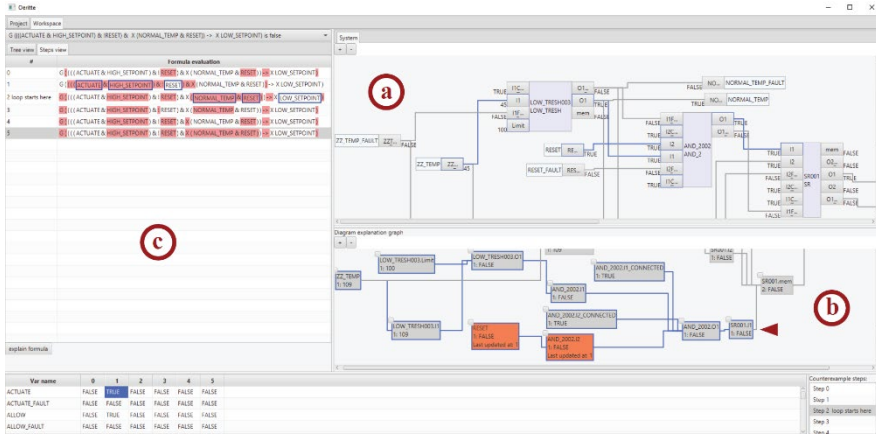


Figure 13. The graphical user interface of Oeritte.

As our most recent case study, we used a semi-fictitious I&C application logic (Buzhinsky & Pakonen 2020a) partly based on the U.S. EPR protection system (Areva 2012) encoded in NuSMV. We consider this system to be of an industrial size as it contains approximately 650 lines of code describing 20 different function block types and 32 function block instances. For this system, we verified the formula saying that the “rods down” command shall be deactivated when the safety criterion is satisfied, and the operator issues a manual reset. The property was violated and the counterexample for it had three steps, each of which contained values of all 375 system variables. The visual counterexample explanation revealed the situation where the value of the variable of the system was locked in its active state, therefore, preventing the “rods down” command to be deactivated. Figure 14 shows the example of a graphical explanation received by the analyst when searching for a cause of variable RODS_DOWN being active at counterexample step zero.

We continued our investigation on causality in FBDs in 2021, where we added a notion of a change-based cause and defined a new type of explanation – a hybrid influence graph (Ovsianikova et al. 2021b). Our motivation is to reduce the area where the fault most likely originates even more and sort out the assignments that despite influencing the explanation target, are not directly related to the issue.

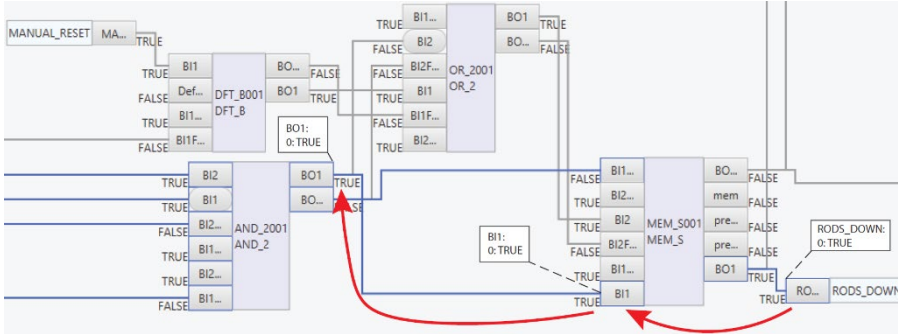


Figure 14. The FBD diagram opened in Oeritte with the explanation of RODS_DOWN at step 0 highlighted in blue. The *true* output of AND_2001 at the current step immediately moves the rods down.

Assume, some LTL property holds on a finite prefix of length m of a counterexample trace and fails at step $m + 1$. There can be two ways of explaining this, either something undesirable has happened or something desirable has not. In the second scenario, we output the analyst inclusion-minimal causes as they show what happened in the system that led to such a result. In the first scenario, meanwhile, we can be more precise and show not all the assignments that make the explanation target have its value at step $m + 1$, but those that are causes of the explanation target and have changed from the previous counterexample step m . Such causes we call change-based and they highlight to the analyst the dynamics of the system at the critical step of a failure trace.

At last, we discovered that combining the two explanation strategies – with inclusion-minimal and change-based causes gives the most useful explanation. This is due to the fact that the majority of the properties fail because something expected has not happened, while the values of system variables have changed. The valuable information here we can retrieve with the synthesis of the approaches is which changes influenced the system in a way its state has not changed in the desired way. Thus, changes that cancel each other will be highlighted, for instance, the output of a function block computing logical AND of two variables a and b was false when a was true and b was false, and it remained false, when a changed to false and b changed to true.

To display both change-based and inclusion-minimal causes, we created the hybrid explanation graph and equipped Oeritte with a new tab showing it (Figure 13). Here, grey and orange rectangles mark inclusion-minimal and change-based cause correspondingly.

Generation of fix suggestions for design issues

In 2022, we continued in the direction of improving the user experience during the design of control programs for I&C systems. Having a tool (Oeritte) that highlights

possible failure paths composed of changed-based and inclusion-minimal causes we thought of yet another way to focus the attention of the analyst on the problem parts of an FBD – automatic generation of repair suggestions. We concentrated on the behavioural offline repair, meaning that our suggestions aim to change an FBD itself before the execution.

An FBD can be viewed as a program, where FBs are functions and connections are assignments, therefore, in our review of the state-of-the-art, we addressed the software repair domain. There exists research on finding perfect fixes for any failure, for a specific failure (e.g., null pointer exceptions or integer overflows), and fixes that are generated using machine learning techniques based on Q&A websites or existing codebases. One common trait is that none of them guarantees that a fix is 100% applicable, even though some methods claim the rate of successful fixes is over 90%. The main idea of suggesting a repair is still to give an engineer a clue on the location of the issue. This conclusion was explicitly stated in (Campos et al. 2021), where the authors developed a plugin for an IDE that analyses the code and suggests repairs following the development process. To suggest fixes, they use not the most precise approaches but a combination of existing computationally light methods. This kind of approach matches our motivation and points to the future development branch of Oeritte.

The basis of our method is the result of the previous works on causality in FBDs and our starting point is the same, i.e., the I&C control logic implemented as a NuSMV formal model (that is translatable to an FBD) was verified against an LTL formula and the counterexample was obtained. Then, the explanation of the LTL formula produced the assignments that caused its failure, the analyst chose the assignment of interest (an explanation target) and Oeritte inferred its explanation (or causal) graph. The baseline of the method is to modify the FBD in a way that (1) such a causal graph ceases to exist in the execution scenario defined by the counterexample (i.e., the sequence of input values), (2) the explanation target changes its value and (3) the LTL property holds on the execution scenario.

After the requirement holds on a particular scenario, we perform model checking again to check whether new counterexample scenarios emerged or whether the other properties that were satisfied do not hold anymore. If we have a novel counterexample and the explanation graph for the problem assignments from the LTL formula contains our change, we cancel them and try to change other FBD areas, otherwise, we accept the applied changes and start looking for a repair for the next issue discovered. The final set of changes we call a fix.

We developed three approaches to finding the changes to be considered as fix candidates: connection replacement, block injection and combined strategies. The first one aims to replace connections in a way that the desired value is supplied to the explanation target. The second one tries to replace the FBs, whose assignments belong to the explanation graph, so that the new FB calculates the different output values from the same inputs, thus changing the value of the explanation target. Lastly, we combine the two previous strategies and insert “dummy” blocks that do not affect the causality relations. After such blocks are placed, we try to connect

them with existing FBs with the same goal – to change the value of an explanation target.

We applied our method to real-world design issues from (Pakonen 2021c), found the fixes for three issues and revealed the need not only for an FBD but also a requirement redesign for one of the issues. An example of the fix found by applying the combined strategy is shown in Figure 15. It calls the attention of the analyst to the unset priority between START and STOP signals.

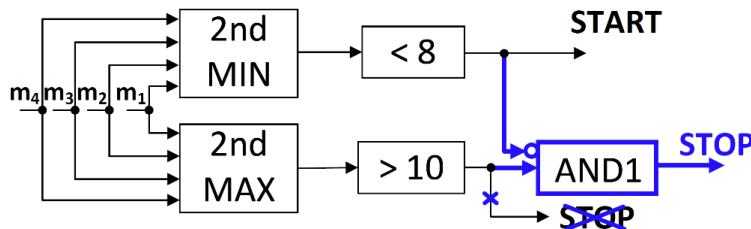


Figure 15. The fix found by a combined strategy that proposes adding a block AND and connecting its remaining input to output START.

The fixes generated by the method may be overfitting, meaning that they do eliminate the issue but cannot be implemented as they hinder some required functions or sometimes no fixes can be generated as the requirements contradict. In both cases, the result adds information on system behaviour and – combined with visual explanation techniques – assists the analyst in the localization of the fault.

Model-to-model translation

VTT's model checking work is supported by the graphical front-end MODCHK (Pakonen et al. 2021), but the analyst still must manually recreate the application logic (function block diagram), even if the diagram is already available in some electronic format. A lot of the research in model translation assumes that the logic is based on the IEC 61131-3 standard, but nuclear vendors rely on closed, non-standard languages (Pakonen et al. 2021). The source code is not usually available, and third parties only have access to diagrams as PDF or MS Office files. We therefore created a methodology (Pakonen et al. 2020) for transforming generic I&C diagrams into an intermediate UML model, which in turn supports transformations to target formats like IEC 61131-3 PLCOpen XML, or the input language of the NuSMV model checker.

MS Visio is used in basic design by companies like Framatome (Teleperm XS block diagrams) or Atomproekt (Hanhikivi-1 NPP functional diagrams) (Pakonen et al. 2020). We therefore demonstrated the methodology by importing exemplar diagrams from MS Visio, and then generating the inputs file for both NuSMV and a generic I&C development tool based on IEC 61131-3 (Codesys).

In developing the MS Visio importer, we ran into several issues, since Visio does not use the kinds of proper semantics or syntax checks that a proper I&C engineering tool would. In our exemplar diagrams, we noticed connections that only look as such (but actually float), connections wires drawn in the “wrong” direction, and groups of components that only look like a single component. In the transformations based on Visio’s XML file format, some connections had to therefore be deduced based on “proximity” on the diagram.

In the end, even if a transformation is not able to capture every aspect of the original logic, the analyst would benefit from having even a part of a complex logic automatically generated in the model checking tool. Errors or omissions made in the transformation would likely be revealed through the resulting counterexamples.

Extending the model checking tool portfolio

Since 2008, the open-source model checker NuSMV has been successfully used by VTT in practical industry projects to detect I&C software design issues (Pakonen et al. 2021). However, one of the limitations that NuSMV imposes is that models of I&C application logics containing analog signal processing logics have to be abstracted, as NuSMV only allows integer variables and simple math.

In the above, we discussed real-time modelling with the nuXmv model checker. Since nuXmv supports infinite-state models, we can also model real number variables. The research question we sought to answer was: does the improved capability come at a prohibitive computational cost?

To evaluate the scalability of nuXmv infinite-state algorithms, we first collected eleven real-world industrial NuSMV models of I&C applications with analog logic (Pakonen 2021a). We then remodelled the logics for nuXmv, by remodelling the basic function blocks containing math, and changing the integer model variables to real number variables. Then, we compared the time it took to verify the NuSMV model against the different algorithms that nuXmv provides.

In most of the cases, the IC3 algorithm performed very well, and was faster than NuSMV. The overall fastest method was IC3 invariant checking, but only a limited number of generally interesting properties can be expressed as invariants.

The verification results did not change, in the sense that the checks produced the same results for both the finite-domain and infinite-domain case. It can therefore be argued that the simplifications used by VTT in NuSMV analyses are a reasonable approach at practical verification. Still, it is clear that nuXmv out-performs NuSMV (Pakonen 2021a).

Co-use of model checking and probabilistic safety assessment

Probabilistic Safety Assessment (PSA) is a well-established convention in the nuclear industry. PSA complements deterministic methods like model checking by determining the probability of failure of systems that constitute the overall

architecture (IAEA 2018). However, digital I&C PSA remains a challenge, and it is generally agreed that there is a lack of a common basis for quantifying software reliability (IAEA 2015).

In SEARCH, we looked for ways in which model checking could benefit PSA. We collected the 57 design issues VTT had by then detected in practical model checking customer projects in the Finnish nuclear industry. We defined the failure mode and possible systems level end effect(s) of each issue. We then compared the results against the I&C software failure modes and end effects for PSA found in the literature (Helminen & Pakonen 2020).

Table 2. Examples of software design issues with non-trivial failure modes and end effects. See (Helminen & Pakonen 2020) for the complete list.

Suggested failure mode	Notes on possible system level end effect(s) and relevance to PSA
Indecisive / conflicting output state	Safety function may be limited.
Fluctuating output state	A failure mode that might endanger a component protection function. Not likely modelled in PSA.
Incorrect control parameter	Incorrect setpoint due to incorrect internal system state. More analysis would be needed to recognize the failure mode(s) and potential end effects(s) for PSA.
N/A	Control function related. Not modelled in PSA.
N/A	Periodic test fails, no effect on plant operation.
N/A	Redundant systems can be put to test mode simultaneously. More analysis would be needed to recognize the failure mode(s) and potential end effect(s) for PSA.

For most of the 57 real-world issues, it was possible to assign a failure mode based on a common taxonomy (OECD/NEA/CSNI 2015). For some issues, it was difficult to assign a specific failure mode, or see any direct relevance to PSA. Based on some issues, we suggested new software failure modes: (1) indecisive / conflicting output state, (2) fluctuating output state, or (3) incorrect control parameter (Helminen & Pakonen 2020). Table 2 lists examples of issues where the classification or the relevance to PSA was non-trivial.

In general, if some design inconsistency is found using model checking, the issue can be fixed (if the cost of redesign is justifiable). Once found and fixed, a fault might no longer be relevant in PSA. Still, information about the existence or non-existence of design faults increases the confidence on system reliability. Since software failures are hard to predict, model checking can provide valuable support for software reliability estimation (Helminen & Pakonen 2020).

References

- Alanen, J., Linnosmaa, J. & Tommila, T., 2017, Conformity assessment data model, VTT Technical Research Centre of Finland. 34 p. (VTT Research Report, Vol. VTT-R-06743-17).
- Alanen, J., Linnosmaa, J., Malm, T., Papakonstantinou, N., Ahonen, T., Heikkilä, E. & Tiusanen, R. 2022a. Hybrid ontology for safety, security, and dependability risk assessments and Security Threat Analysis (STA) method for industrial control systems. *Reliability Engineering and System Safety*, Vol. 220, 2022, 108270.
- Alanen, J., Linnosmaa, J., Pärssinen, J., Kotelba, A., Heikkilä, E., 2022b, Review of cybersecurity risk analysis methods and tools for safety critical industrial control systems, VTT Research Report VTT-R-00928-22, VTT Technical Research Centre of Finland. 46 p.
- Areva 2013. U.S. EPR Final Safety Analysis Report. [Online]. Available: <https://www.nrc.gov/reactors/new-reactors/design-cert/epr/reports.html>
- Buzhinsky, I. & Pakonen, A. 2019. Model-checking detailed fault-tolerant nuclear power plant safety functions. *IEEE Access*, vol. 7, 2019, pp. 162139–162156.
- Buzhinsky, I. & Pakonen, A. 2020a. Symmetry breaking in model checking of fault-tolerant nuclear instrumentation and control systems. *IEEE Access*, vol. 8, 2020, pp. 197684–197694.
- Buzhinsky, I. & Pakonen, A. 2020b. Timed model checking of fault-tolerant nu-clear I&C systems. 18th IEEE International Conference on Industrial Informatics (INDIN). July 20–23, 2020, Warwick, UK, pp. 159–164. IEEE.
- Campos, D., Restivo, A., Ferreira, H.S., Ramos, A. 2021, Automatic program repair as semantic suggestions: An empirical study. In: 2021 14th IEEE Conference on Software Testing, Verification and Validation (ICST). pp. 217–228. IEEE.
- Cimatti, A., Clarke, E., Giunchiglia, E., Giunchiglia, F., Pistore, M., Roveri, M., ... & Tacchella, A. 2002. NuSMV 2: An OpenSource tool for symbolic model checking. In *International Conference on Computer Aided Verification*, pp. 359–364. Springer, Berlin, Heidelberg.
- Hauge, A. A., Linnosmaa, J., Fredriksen, R. & Sechi, F. 2019. Safety and security in DI&C design – systematic literature study. HWR-1247. OECD Halden Reactor Project. Institutt For Energiteknikk (IFE). Halden, Norway. 40 p.
- Helminen, A. & Pakonen, A. 2020. Potential applications of model checking in probabilistic risk assessments. VTT Research Report VTT-R-00017-20, VTT Technical Research Centre of Finland. 13 p.
- IAEA 2015. Technical Challenges in the Application and Licensing of Digital Instrumentation and Control Systems in Nuclear Power Plants. IAEA Nuclear Energy Series, No. NP-T.13.

- IAEA 2018. Approaches for Overall Instrumentation and Control Architectures of Nuclear Power Plants. IAEA Nuclear Energy Series, No. NP-T-2.11.
- Linnosmaa, J. & Alanen, J. 2019. Demonstration of a conformity assessment data model. 17th IEEE International Conference on Industrial Informatics (INDIN), Helsinki-Espoo, Finland, July 22–25, pp. 369–373.
- Linnosmaa, J., Pakonen, A., Papakonstantinou, N. & Karpati, P. 2020. Applicability of AADL in modelling the overall I&C architecture of a nuclear power plant. 46th Annual Conference of the IEEE Industrial Electronics Society (IECON 2020), Singapore, October 18–21, pp. 4337–4344.
- Linnosmaa, J., Hauge, A., Sechi, F. & Sirola, M. 2021a. Combining system architecture modelling with dynamic process simulation for early stage fault and effect analysis, 12th ANS Topical Meeting on Nuclear Plant Instrumentation, Control and Human-Machine Interface Technologies (NPIC&HMIT 2021), Providence, RI, USA, June 14–17, pp. 997–1006.
- Linnosmaa, J., Papakonstantinou, N., Malm, T., Kotelba, A. & Pärssinen, J. 2021b. Survey of cybersecurity standards for nuclear instrumentation and control systems, International Symposium on Future I&C for Nuclear Power Plants (ISOFIC 2021), Okayama, Japan, November 15–17.
- Linnosmaa, J., Papakonstantinou, N., Malm, T., Kotelba, A. & Pärssinen, J. 2022. Security and Safety Integration for the Nuclear Instrumentation and Control Systems, IEEE 27th International Conference on Emerging Technologies and Factory Automation (ETFA 2022), Stuttgart, Germany, Sep 6–9.
- Linnosmaa, J., Pakonen, A., Alanen, J., 2023. Demonstration of a model-based approach for formal verification of I&C logics, 13th International Topical Meeting on Nuclear Plant Instrumentation, Control and Human Machine Interface Technologies (NPIC & HMIT). To appear.
- NuScale 2022. Design Certification Application – NuScale small modular reactor. <https://www.nrc.gov/reactors/new-reactors/smr/nuscale.html>.
- NRC 2009. Diversity strategies for nuclear power plant instrumentation and control systems. NUREG CR-7007, United States Nuclear Regulatory Commission, <https://www.nrc.gov/docs/ML1005/ML100541256.pdf>
- OECD/NEA/CSNI 2015. Failure modes taxonomy for reliability assessment of digital I&C systems for PRA, OECD/NEA Working Group RISK report NEA/CSNI/R(2014)16.
- Ovsianikova, P., Buzhinsky, I., Pakonen, A. & Vyatkin, V. 2020, Visual counterexample explanation for model checking with Oeritte, 25th International Conference on Engineering of Complex Computer Systems (ICECCS 2020), Singapore, March 4–6, 2021, pp. 1–10.
- Ovsianikova, P., Buzhinsky, I., Pakonen, A. & Vyatkin, V. 2021a, Oeritte: User-Friendly Counterexample Explanation for Model Checking. IEEE Access, Vol. 9, 2021, pp. 61383–61397.

- Ovsianikova, P., Pakonen, A. & Vyatkin, V. 2021b. Change-based causes in counterexample explanation for model checking, 47th Annual Conference of the IEEE Industrial Electronics Society (IECON 2021), Toronto, Canada, October 13–16.
- Pakonen, A. 2021a. Model-checking infinite-state nuclear safety I&C systems with nuXmv, 19th IEEE International Conference on Industrial Informatics (INDIN 2021), Palma de Mallorca, Spain, July 14–17.
- Pakonen, A. 2021b. Model-checking I&C logics – insights from over a decade of projects in Finland, 12th ANS Topical Meeting on Nuclear Plant Instrumentation, Control and Human-Machine Interface Technologies meeting (NPIC&HMIT 2021), Providence, RI, USA, June 14–17, pp. 792–801.
- Pakonen, A. 2021c. Oops! Examples of I&C design issues detected with model checking, International Symposium on Future I&C for Nuclear Power Plants (ISOFIC 2021), Okayama, Japan, November 15–17.
- Pakonen, A., & Buzhinsky, I. 2019. Verification of fault tolerant safety I&C systems using model checking, 20th IEEE International Conference on Industrial Technology (ICIT 2019), Melbourne, Australia, Feb 13–15, pp. 969–974.
- Pakonen, A. & Mätäsniemi, T. 2021. Ontology-based approach for analyzing nuclear overall I&C architectures, 47th Annual Conference of the IEEE Industrial Electronics Society (IECON 2021), Toronto, Canada, Oct 13–16.
- Pakonen, A., Buzhinsky, I., & Vyatkin, V. 2018. Counterexample visualization and explanation for function block diagrams, 16th IEEE International Conference on Industrial Informatics (INDIN 2018), Porto, Portugal, July 18–20, pp. 747–753.
- Pakonen, A., Biswas, P. & Papakonstantinou, N. 2020. Transformation of non-standard nuclear I&C logic drawings to formal verification models. 46th Annual Conference of the IEEE Industrial Electronics Society (IECON 2020), Singapore, October 18–21, pp. 697–704.
- Pakonen, A., Buzhinsky, I. & Björkman, K. 2021, Model checking reveals design issues leading to spurious actuation of nuclear instrumentation and control systems. *Reliability Engineering & System Safety*, vol. 205, 107237.
- Papakonstantinou, N., Tommila, T., O'Halloran, B., Alanen, J. & Van Bossuyt, D.L. 2017. A model driven approach for early assessment of defence in depth capabilities of complex sosiotechnical systems. Proceedings of ASME 2017 International Design Engineering Technical Conference & Computers and Information in Engineering Conference (IDECT/CIE 2017), Saint Louis, MO, USA, August 16–19. 10 p.
- Papakonstantinou, N, Linnosmaa, J., Bashir, A. Z., Malm, T. & Van Bossuyt, D. L. 2020. Early combined safety - security Defense in Depth assessment of complex systems. 66th Annual Reliability & Maintainability Symposium (RAMS 2020), Palm Springs, CA, USA, Jan 27–30.

- Sechi, F., Hauge, A., Sirola, M., Olsen, S., Linnosmaa, J. & Sarshar, S. 2020. Early stage safety assessment using a system model as input. HWR-1287 OECD Halden Reactor Project. Institutt For Energiteknikk (IFE). Halden, Norway. 89 p.
- Tommila T, Alanen J. 2015. Conceptual model for safety requirements specification and management in nuclear power plants. VTT Technical Research Centre of Finland. VTT Technology No. 23.
- Wiśniewski, D., Potoniec, J., Ławrynowicz, A. & Keet, C.M. 2019. Analysis of ontology competency questions and their formalizations in SPARQL-OWL. Journal of Web Semantics, vol. 59, 2019, 100534.

3.5 Uncertainty management in fire risk analyses (URAN)

Jukka Vaari¹, Nikhil Verma¹, Timo Korhonen¹, Simo Hostikka²; Morteza Gholami Haghghi Fard²

¹VTT Technical Research Centre of Finland Ltd
P.O. Box 1000, FI-02044 Espoo

²Aalto University
P.O. Box 11000, FI-00076 AALTO

Abstract

Full-scale CFD simulations of cable fires were conducted in order to achieve better accuracy for predicting the heat release rate of these fires, and to understand and quantify the sources of uncertainty involved. Experimental data used for validation was collected in the OECD/NEA PRISME3 project.

Combustion of cylindrical fuels was studied by high-resolution CFD simulations to gain new and detailed information on the heat fluxes and pyrolysis rates of cables in a cone calorimeter experiment. Modelling involved detailed 3D heat transfer calculations inside the cable, taking into account the internal structure of the cable.

Ageing mechanisms of a typical cable jacket material, XLPE, were examined both numerically and experimentally in order to understand the effect of aging to the general fire safety of the NPP. Validation simulations of thermogravimetry and cone calorimeter experiments on aged polymers were conducted.

Introduction

A significant proportion of the overall core damage risk in nuclear power plants (NPP) is associated with internal fires. In addition, a NPP fire can cause large financial losses even when the reactor safety was not compromised. Therefore, the fire PRA plays an important role in the overall PRA of a power plant. Often, the most critical parts of the fire PRA, where conservative assumptions are not acceptable, utilize deterministic tools for the consequence analysis. These computational tools are also used routinely for the deterministic fire hazard analyses (FHA), and to calculate external fire incidents, such as aircraft impact induced fires.

The computational fire models have developed significantly over the last few decades: The deterministic analyses typically use CFD with fire-specific physical models and user-interface, and the probabilistic nature of the input values is treated with stochastic sampling (Monte Carlo), leading to an extensive computing project. Systematic validation of the fire CFD tools during the last two decades has quantified the model uncertainties in a range of applications. Unfortunately, these applications are largely limited to simple transport problems, whereas NPP fire analyses commonly require predictive capability of the most important boundary condition – *fire spread* – because the different physical phenomena are strongly

coupled. Model validations for such applications are still very incomplete, and the lack of suitable data is one of the reasons. Maintaining the computational infrastructure (tools, hardware and competence) requires continuous investments, and the research aiming at comprehensive, collaborative validation is the most effective way of competence development.

Ensuring accurate computations requires both phenomenological insight (correct physics/chemistry) and convergent (stable and consistent) numerical methods. Limitations of the experimental techniques in revealing the details of materials' behaviour in fires has turned the focus on computational chemistry as a means of increasing the insight. The long-term vision of multi-scale computational models for burning materials may be over-ambitious, but taking the steps to that directions enables us to act pro-actively when new materials and solutions are brought to the market for various reasons. The standardized testing protocols cannot guarantee the safety in complex applications with long desired lifespan, such as a modern NPP.

URAN-project covers three main themes: uncertainty quantification of fire models, modelling tool development and validation, and molecular-level investigation of aging effects. The first two themes will involve active participation to OECD PRISME 3 -project and utilization of the results. The third theme links the project to the other proposed SAFIR 2022 projects and applied and fundamental research projects outside the program.

Uncertainty quantification of fire models

The uncertainty of numerical simulations arises from three sources: input uncertainty, model uncertainty, and the user effect. Input uncertainty refers to the uncertainty of boundary and initial conditions in a real fire scenario. Model uncertainty is commonly quantified by comparing model results against experimental data, which means that the experimental uncertainty plays a role as well. User uncertainty in turn refers to the ability of the user to use the software in question correctly.

OECD/NEA PRISME projects have produced a significant amount of excellent quality, large scale experimental data of fire related phenomena for the past 15 years. This data has been utilised in some previous safety assessments, but one goal of URAN is to make more extensive and systematic use of the data.

A great venue for exploring the capabilities of fire models and associated uncertainties is the Analytical Working Group (AWG) of the PRISME3-project. The analytical working group of PRISME3 proceeds in three phases:

1. An open simulation study of a PRISME2 experiment,
2. A semi-blind simulation study of an experiment to be conducted in the PRISME3 project, and
3. A blind simulation of a real NPP fire incident picked from the OECD FIRE database.

Phase 1 of the AWG exercise provides opportunities for model uncertainty quantification and documentation of best practices through the open simulations. Phase 2 and Phase 3 are a semi-blind and truly blind simulation excercises that provide insight into the user effect and input uncertainty.

Two simulations were prepared for the first phase of the benchmark using Fire Dynamics Simulator (FDS) version 6.7.1. Two different methods were used in the simulations to model the fire propagation. In the first simulation (a prescribed simulation), the heat release rate (HRR) of the fire was directly taken from the experiments. In the second simulation (a predictive simulation), the fire propagation was modelled utilizing a pyrolysis model and Lagrangian particles. The capabilities to predict the fire growth and the prevailing conditions in the fire room were assessed.

The simulation domain (Figure 1) consisted of two rooms connected with a door. Length of a single room was approximately 5 meters, width was approximately 6 meters and height was approximately 4 meters. Stack of five (5) cable trays was present in the fire room. The first tray was approximately 90 centimetres above the floor and the spacing between the trays was 30 centimetres. Width of a single tray was 2.4 meters and depth 0.45 meters. Height of the trays was from 5 to 10 centimetres. In the prescribed simulation, the cable trays were modelled as solid geometries. In the predictive simulation, the cables were modelled with Lagrangian particles. In the experiment, the cables were ignited with a burner, which was turned off after a pre-selected value of heat release rate was reached.

The room was mechanically ventilated with the air supply located in the fire room and the air exhaust located in the adjacent room. The air exchange rate of the rooms was 15 1/h, which is equivalent to ventilation volume flow of 1 m³/s. To capture the effect of the fire on the ventilation system, the system was modelled using the HVAC submodel of the FDS program.

The assumed combustion reaction was a single step reaction with pure polyvinyl chloride (PVC) reacting with oxygen. Numerically the combustion reaction was assumed infinitely fast after mixing of gaseous fuel and oxygen. The default flame extinction model of FDS was used.

In the prescribed simulation, the cable trays were modelled as solid geometry. The real width of the trays was used. As the modelled geometry has to be compliant with the numerical mesh, depth of 40 centimetres and height of 10 centimetres were used for each tray. The solid geometries were given the material properties from the benchmark instructions, meant to represent the combustible cable material. The experimental heat release rate was applied as a boundary condition to the top sides of the modelled cable trays. All of the trays were assumed to ignite at the same time and all of the surface area was utilized at all times.

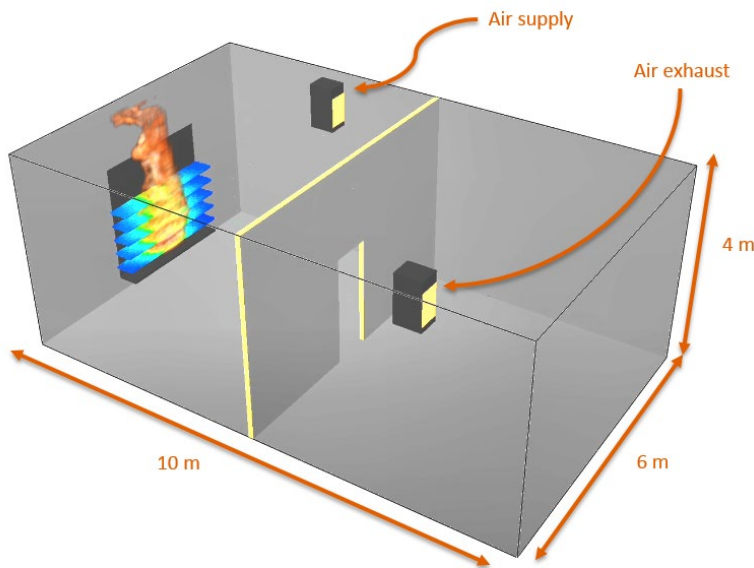


Figure 1. Simulation domain for the PRISME3 AWG benchmark exercise step 1.

In the predictive simulation, the cables were modelled using a pyrolysis model and Lagrangian particles. The particles were used to represent the trays in the simulation, and the formulated pyrolysis model was applied to the particles to be able to simulate thermal decomposition at elevated temperatures. The pyrolysis model for the cables was constructed based on the experimental results and the available information regarding the cable and material compositions. The sheath and insulation materials were assumed to consist of three components each based on the experimental thermogravimetric analysis (TGA) results.

The experimental and simulated heat release and mass loss rates are presented in Figure 2. As the heat release rate in the prescribed simulation was directly taken from the experiment, the simulated HRR was an exact match for the experimental value, i.e., the curves are on top of each other in the figure. The predictive simulation in the other hand predicted qualitatively quite different heat release rate in comparison to the experiment, but quantitatively the simulated result was on the same scale as the experimental values.

In terms of mass loss rate, the prescribed simulation differed from the experimental values. The mass loss rate in the prescribed simulation was equal to the heat release rate scaled by the heat of combustion, which was constant in the simulation. However, the peaks in the heat release rate were considered to be caused by accumulated, unburnt fuel gas combusting at a later time. No accumulation occurred in the simulation. The predictive simulation behaved in the same manner, i.e., all of the produced fuel gas combusted instantly.

The total heat release in the prescribed simulation was approximately 0.25% greater than in the experiment, and the total mass loss in the prescribed simulation

was approximately 8% greater than in the experiment. The total heat release in the predictive simulation was approximately 2% greater than in the experiment, and the total mass loss in the prescribed simulation was approximately 25% greater than in the experiment. The total heat releases and mass losses were obtained by numerically integrating the simulated and experimental heat release rates and mass loss rates. It can be concluded that the heats of combustion utilized in the simulations were smaller than the effective heat of combustion in the experiment, as for both simulations the difference between the simulated and experimental mass loss was greater than the difference between the simulated and experimental heat release.

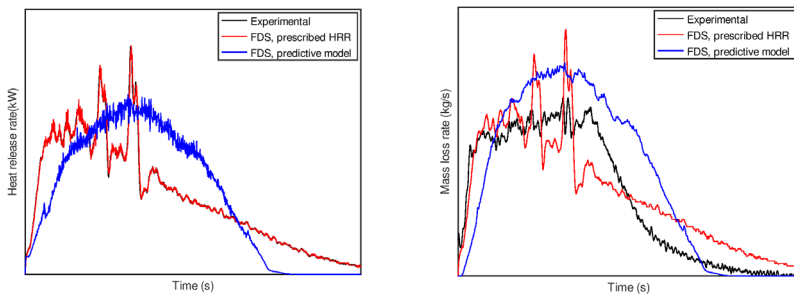


Figure 2. Experimental and simulated heat release (left) and mass loss (right) rates.

The scenario simulated in the benchmark step 2.1 corresponds to the CFP-D1 test from the experimental CFP campaign of PRISME 3. The scenario was simulated blindly, i.e., the experimental results were not known beforehand. Limited information regarding the scenario was available in the benchmark instructions. The scenario is very similar to the scenario simulated in the first stage of the benchmark (CFS-2 experiment from OECD PRISME 2) and to the CFS-4 experiment from OECD PRISME 2. In comparison to these experiments, the ventilation layout is reversed, i.e., in previous experiments the supply point was located in the fire room and the exhaust point in the adjacent room. In comparison to the CFS-2 experiment, the type of the cables is also different in the CFP-D1 test. In the first phase of the benchmark the cable was PVC based, whereas the cable type used in both CFP-D1 and CFS-4 tests is of same HFFR material.

The used FDS software requires that geometries conform to the rectilinear numerical grid. This limits the accuracy of geometrical descriptions of objects with complex shape. Cable trays are often represented as single solid geometries, which causes issues in simulating fire spread. If a tray of cables is simplified as a single solid geometry, the geometry prevents the rise of hot gases through the cables, which is important for vertical fire spread. Openings can be added to the solid geometry, but their size and location remains arbitrary.

Here a stochastic approach for making the simplified cable tray geometry is introduced by making an estimate for how many openings are required in the CFD cable tray geometry. First, a volume corresponding to the known tray volume is

considered, and it is represented by an auxiliary three-dimensional grid (Figure 3). Cables corresponding to the known tray loading are divided into smaller units, which are equivalent to pieces of cable with length equal to the grid cell length. The units of the individual cables are sequentially placed in the grid. Their path along the tray is random, but continuity is enforced (Figure 4, top). After all cable units have been placed, the generated three-dimensional array is made two-dimensional by summing over z. Using the two-dimensional array, an estimate can be made for the area of the openings. The estimated opening fraction, which is given as a percentage of the surface area, is saved. This procedure is repeated sufficient number of times to produce a statistical distribution. The average opening fraction is then used to calculate equivalent number of CFD grid cells (Figure 4, bottom).

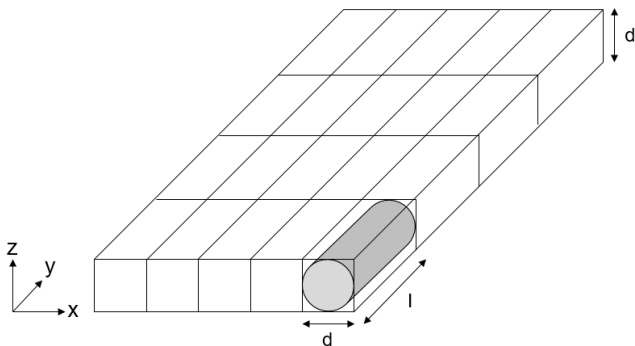


Figure 3. Schematic visualization of the auxiliary 3D grid and the coordinate system for the stochastic approach for cable tray modelling.

The original Flame Spread over Horizontal Cable Trays, abbreviated as FLASH-CAT, model was developed during the CHRISTIFIRE project (McGrattan et al. 2012) and originates from the model proposed in NUREG/CR-6850, Appendix R (EPRI 2005). The model was developed to prescribe the fire behaviour of a cable tray set in the open atmosphere. The original model proposes that the tray ignition occurs in a V-shaped pattern with a spread angle of 35° and that the ignition of each tray occurs at a given time.

In this work, modifications were made to the original FLASH-CAT model to better account for the difference between open and confined environments. As in the original model, tray ignition was assumed to occur in a V-shaped pattern. Instead of using the original model values for ignition times and spread angle, the values evaluated from an open atmosphere experiment for the same cable type and tray loading, PRISME 2 CFSS-2 test, were utilized. This modification was motivated by better capturing the behaviour of the specific cable type and cable arrangement.

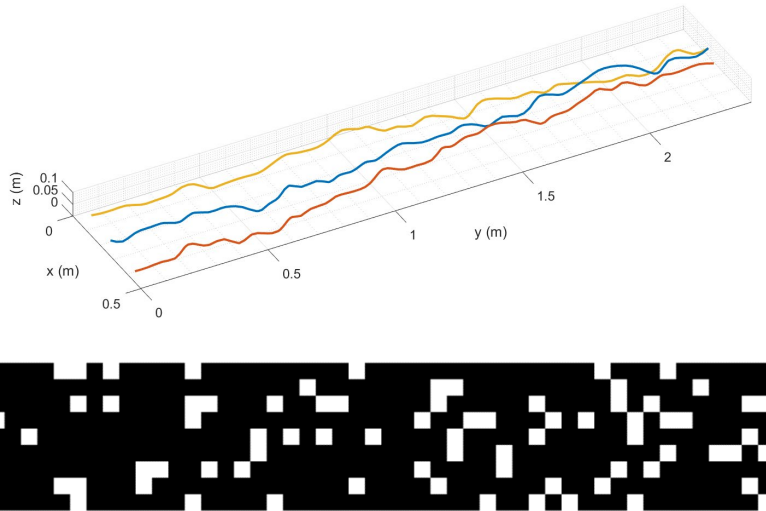


Figure 4. Top: Three examples of cables that have been generated using the developed stochastic process. The curves have been drawn through the cell centres where the cable pieces have been positioned. Bottom: A cable tray geometry generated with stochastic approach. Tray is shown from above. Black area is solid cells.

As the experimental results for the CFP-D1 are not currently in the public domain, the simulated heat release rate is compared to an earlier similar experiment and the simulated flame spread is qualitatively assessed. The simulated heat release rate for the benchmark step 2.1 is presented in Figure 5. The experimental heat release rate from the CFS-4 experiment is shown for reference. The CFP-D1 and CFS-4 tests are otherwise identical, except for the reversed ventilation. The simulated maximum heat release rate is almost 30 % greater than the experimental maximum. The fire also begins to grow rapidly at a later time, and the heat release rate decreases at a faster rate in the simulation than in the experiment.

Simulated flame spread during the first 15 minutes is shown in Figure 6. Shown times correspond to approximately 60 seconds after prescribed ignition of each tray. Room geometry has been excluded from the figures. At approximately 800 seconds, the uppermost tray is not burning yet, but the flames are passing through the openings in the tray geometry. The fire is slightly asymmetric in respect to the centreline, assumedly due to the ventilation conditions.

Simulated flame spread after the first 20 minutes is shown in Figure 7. Room geometry has been excluded from the figures. The predicted fire propagation seems realistic: flame spreads to the end of the trays, and the spreading occurs faster in the upper than in the lower trays. The fire remains slightly asymmetric.

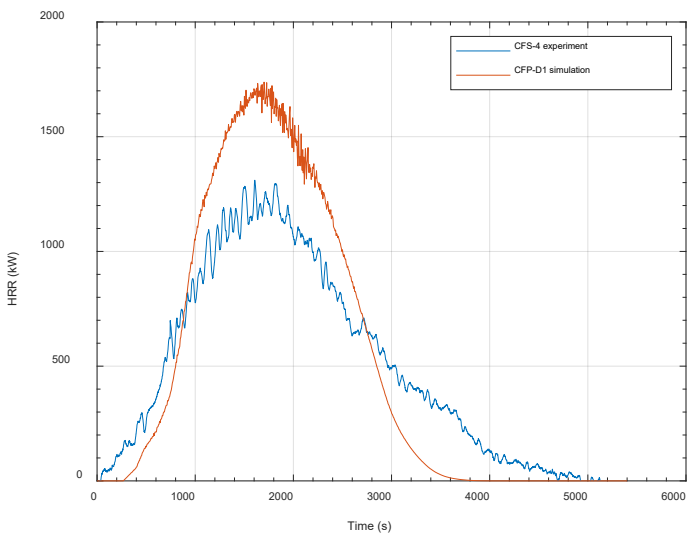


Figure 5. Simulated heat release rate for the benchmark step 2.1. The experimental heat release rate from the CFS-4 experiment is shown for reference.

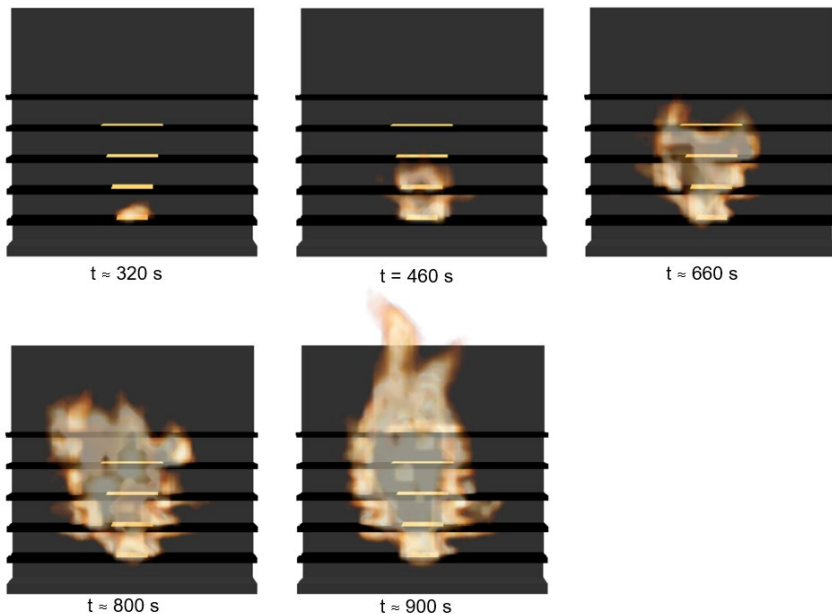


Figure 6. Simulated flame spread during the first 15 minutes. Shown times correspond to approximately 60 seconds after prescribed ignition of each tray. Room geometry has been excluded from the figures.

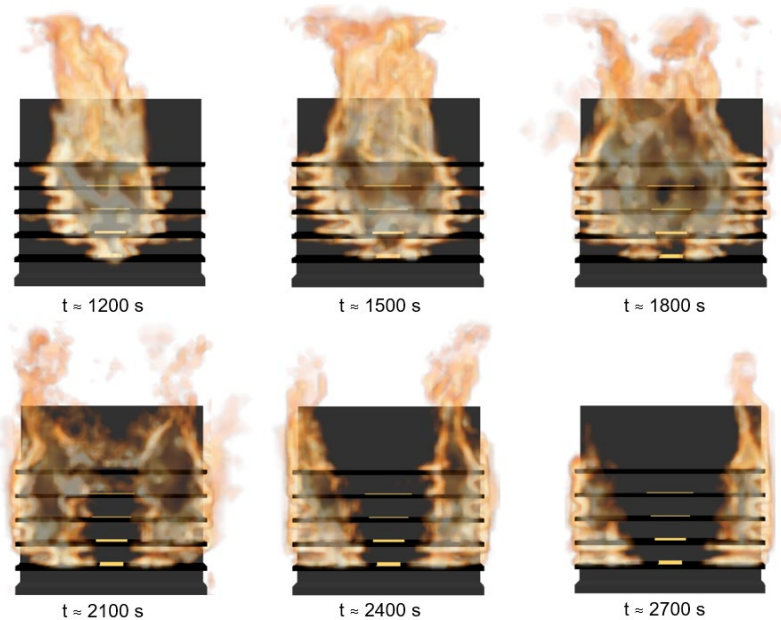


Figure 7. Simulated flame spread after the first 20 minutes. Room geometry has been excluded from the figures.

The studied scenario in benchmark step 2.2 corresponded to an experiment where two stacked, horizontal cable trays set against an insulated side wall were burned in a large-scale calorimeter (Figure 8). The trays included a large number of PVC (polyvinyl chloride) cables, which were arranged loosely in the trays. The trays were ignited simultaneously at two different locations.

Two different approaches to modelling fire spread were used. The approach based on modified FLASH-CAT model was the same as applied for Step 2.1. The other approach was a pyrolysis model taken from the FDS Validation Guide simulation models for the CHRISTIFIRE (Cable Heat Release, Ignition, and Spread in Fire Test Program) experiments. The specific models have been developed to simulate small- and bench-scale experimental tests, i.e., thermogravimetric analysis (TGA), microscale combustion calorimeter (MCC) and cone calorimeter. The chosen model corresponds to experimental results for cable known as 701 in the CHRISTIFIRE tests, which is reported to have a jacket of PVC and insulation of PE. Of the available models, the version v1 was chosen as it had the simplest reaction scheme.

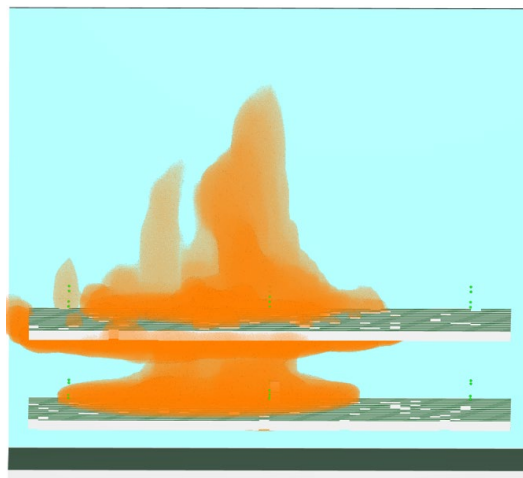


Figure 8. Simulated scenario for the PRISME3 AWG benchmark exercise step 2.2. Flame visualization corresponds to the simulation with modified FLASH-CAT model at $t = 0.5$ s/s.

Simulated heat release rates with both modified FLASH-CAT and pyrolysis models are shown in Figure 9. Results are presented in such manner that the confidentiality of the information used is maintained. Due to this, all heat release rates are expressed as normalized values where the value of 1 is equal to the peak heat release rate when two such cable trays were burnt in an open atmosphere in an experiment. Whereas the value of 1 for time represents the estimated time at which the sprinkler got activated during the accident studied in benchmark step 3. The value used for normalization was the same in both benchmark steps.

Both models captured the growth phase and the peak value quite well. The simulation with the pyrolysis model captured the growth phase more correctly, whereas the simulation with the modified FLASH-CAT model captured the peak value more closely. Both models were unable to capture the decay phase correctly, but the duration of the fire was longer in the simulation with the modified FLASH-CAT model and thus more correct.

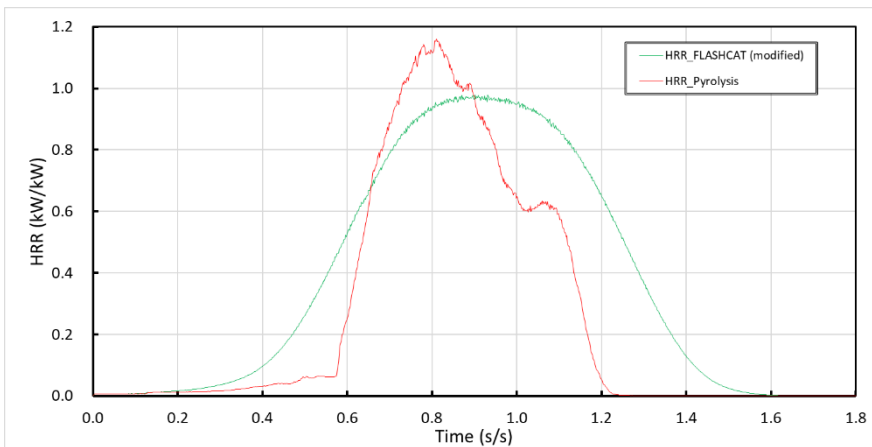


Figure 9. Simulated heat release rates, results corresponding to both modified FLASH-CAT and pyrolysis models shown.

In the benchmark step 3, a similar fire source as in step 2.2 was simulated in an enclosure (Figure 10). The studied scenario corresponded to a real accident which has occurred in an NPP. As the scenario corresponds to an accident, the information required for modelling is both limited and uncertain. Similarly, there is only a limited amount of information for assessing the results. The identified and considered uncertainty concerned the method of ignition, position of the obstruction above the trays, (which affects the flow of hot gases), sprinkler parameters (relevant to FDS software), extinguishment parameters of cables (relevant to FDS software) and area adjustment factor (relevant to FDS software). As an example of the effect of uncertainties, Figure 11 shows the change in the results when the location of the burner between the cable trays was varied.

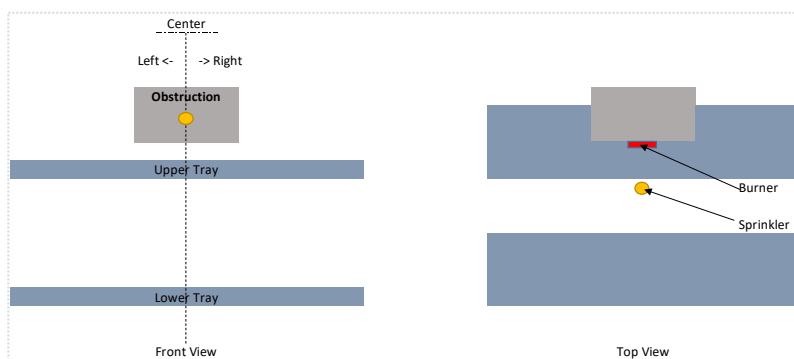


Figure 10. Schematic of trays, burner and the obstruction for the PRISME3 AWG benchmark exercise step 3.

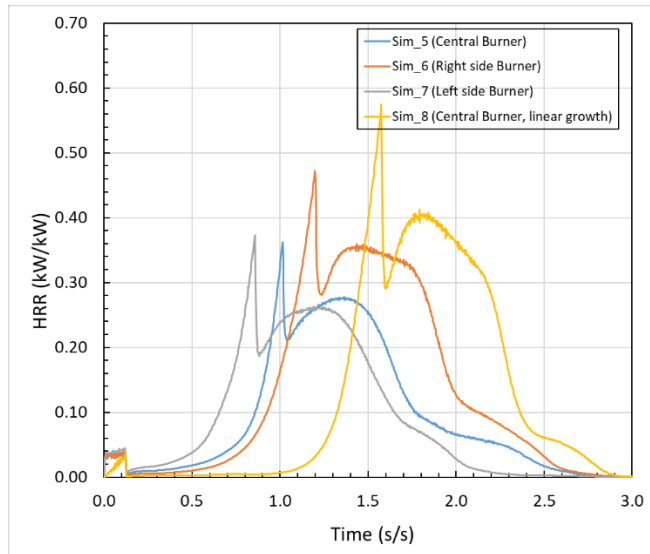


Figure 11. Heat release rate with the burner on the cable trays at different locations.

Over the last two decades, several stochastic fire analyses of the Finnish NPPs have been carried out using both zone (Hostikka & Keski-Rahkonen 2003) and CFD models (Keski-Rahkonen et al. 2007). The work included the development of the Probabilistic Fire Simulator (PFS) tool to serve as a Monte Carlo engine and interface for the fire models. Similar tools were developed in France (SUNSET by IRSN) and Germany (SUSA by GRS). In their analysis of the TVO cable tunnel, Matala and Hostikka (2011) were able to calculate the failure probability of the redundant cabling system using a full Monte Carlo simulation with complex CFD involving both solid pyrolysis and two-phase flows for water suppression. Yet, only the input uncertainties were investigated, and the possible contribution of the model uncertainty in the probability estimates was not evaluated. Theoretical (Paudel and Hostikka 2019a) and experimentally tested (Paudel and Hostikka 2019b) methods for the model uncertainty correction in Monte Carlo simulations were developed in the SAFIR 2018 -programme, but the large scale cable tunnel simulations have remained unvalidated.

Probabilistic fire spread simulations were carried out for quantification of the effect of input uncertainties, model bias and model uncertainties on outputs. The work was done using a cable fire scenario relevant for a nuclear power plant (NPP) (Figure 12, top). The systematic approach to address the uncertainties were exemplified through two separate cases. Case 1 covered a new cable fire scenario where numerous Monte Carlo simulations were carried out based on different input parameters' probabilistic distributions (Figure 12, bottom).

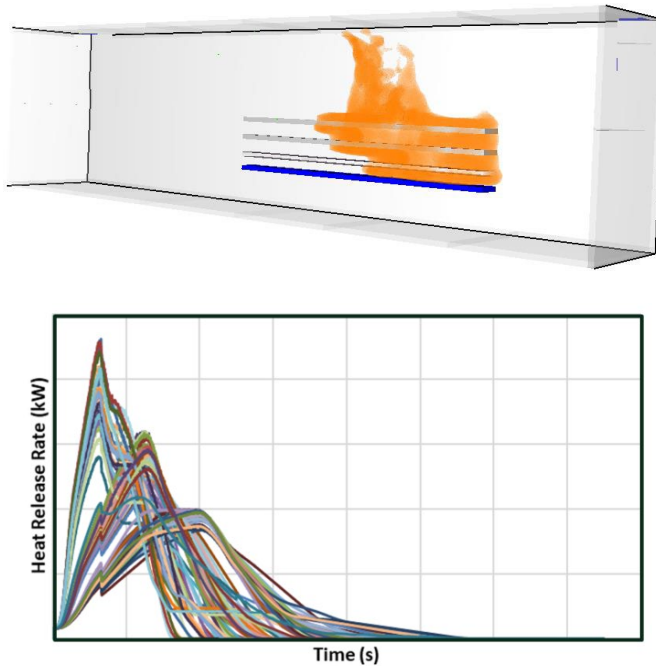


Figure 12. Top: cable fire scenario used for probabilistic fire spread simulations. Bottom: heat release curves from a set of simulations with inputs chosen by a Monte Carlo algorithm.

When model bias and uncertainty correction was applied to the heat release rate data of Figure 12, the following conclusions could be drawn.

- In 100% of simulations, peak HRR exceeds 0.05 MW, and that happens before 4500 seconds (75 minutes).
- In 91% of simulations, peak HRR exceeds 0.5 MW, and that happens before 4500 seconds (75 minutes). However, in 30% of simulations, peak HRR exceeds 0.5 MW, and that happens before 1500 seconds (25 minutes). It should be noted that if peak HRR exceeds 500 kW, it becomes more difficult to extinguish for one pair of firefighters.
- In 48% of simulations, peak HRR exceeds 1 MW, and that happens before 4500 seconds (75 minutes). However, in 23% of simulations, peak HRR exceeds 1 MW and that happens before 1500 seconds (25 minutes).
- In 9% of the simulation, peak HRR exceeds 1.5 MW before 3000 seconds (50 minutes). However, in 6% of cases, peak HRR exceeds 1.5 MW and that happens before 1500 seconds (25 minutes).

Case 2 involved correcting the estimates of cable failure probabilities in the Olkiluoto NPP cable tunnel fire. The failure probabilities, as reported in VTT-R-00655-09 for a non-sprinklered case, were based on input uncertainties only, through Monte-Carlo simulations using probability distributions for inputs. The corrections applied

in this work are based on adding the effect of model uncertainty. It was found that in the non-sprinkler case, the revised probability of at least one IC cable failure is between 0.35-and 0.42 (old estimate 0.60). For power cables, the revised failure probability is between 0.56 and 0.61 (old estimate 1.0). The available operating time for the fire brigade ranged from 15 to 30 minutes. However, with a high probability, the fire size would become difficult to extinguish sooner than that.

Development of modelling tools

Throughout the past few decades, vast attention has been given to assessing the flammability of polymers. The great extent of the work has been devoted to slabs and flat geometries due to their omnipresence. In spite of that, polymeric materials in the cylindrical configuration are dominant fuels in many household, industrial, aeronautical, and wildland fire scenarios.

The flammability of polymeric materials is commonly studied by following a hierarchy. Firstly, micro-scale decomposition measurements, such as Thermo-Gravimetric Analysis (TGA), are used to determine the temperature, form, and kinetics of the pyrolysis reactions. Gram-scale experiments, such as the cone calorimetry measurements, are employed to measure the rates of mass loss and heat release. These micro- and gram-scale measurements are then used to support efforts for analytical, empirical, or numerical modelling of the material pyrolysis.

Quite often, the numerical simulations of cone calorimetry (or similar experiments) need to be computationally inexpensive to enable their use as a part of the optimization process to estimate the model's parameters. As the speed is commonly achieved by strong geometrical simplifications and low numerical resolution, the numerical models cannot resolve neither the detailed radiator geometry, nor the flame heat feedback to the sample. For the simulations of flat samples, homogeneous radiator irradiance can be assumed, and empirical models can be applied for the flame heat fluxes. However, almost no methods exist for measuring heat fluxes on the surfaces of cylindrical samples. Hence, the necessary information must be obtained through detailed numerical simulations, which is the main motivation of the current work. This study targets for (a) characterizing the flammability of cylindrical polymer objects under cone calorimetry, (b) implementing a detailed modeling framework that can resemble the nature of the problem in a more realistic manner, and (c) providing robust support for the interpretation of the cable test results, to achieve a perception that can be used in the simplified models. Hence, the current work investigates the fire performance of non-charring polymeric rods with cone calorimeter firstly with experiments.

The cone calorimeter tests provide reference mass loss and energy release of the samples, and measurements are recorded with a thermal camera to supply material shrinkage data. A numerical methodology is employed to simulate the problem, which serves as the tool for obtaining comprehensive thermophysical data in the vicinity of the samples. This numerical framework is constructed with a two-dimensional resemblance of the actual geometry of the conical heater and

cylindrical objects, while the solid phase solution is based on two-dimensional pyrolysis and heat transfer implementations. After validating the methodology, the numerically obtained distribution of the thermal data on the rods is used to explain the observed shrinkage patterns.

Degradation of PMMA rods was first experimentally analyzed under 50 kW/m^2 irradiation of a standard cone calorimeter in both gasification and flaming conditions. Two sample layouts, namely single rod and five rods, were utilized in the measurements. Cross-sectional shape change in the experiments were recorded with an IR thermal camera to serve as reference for model verification. A 2D numerical framework was proposed for modeling of non-charring cylindrical objects in the cone calorimetry scenarios, and its applicability was validated with the experimental results (Figure 13).

Chemical decomposition of the PMMA was modeled with two-step Arrhenius reactions, kinetic parameters of which were fit to account for the TGA measurements. The solid-phase solution was based on the 2D heat transfer and pyrolysis algorithms of the FDS tool. Literature values for the thermophysical properties of the pyrolysis reaction were utilized. A surrogate of cylindrical rods were generated with putting together multitude small (1 mm^3) PMMA obstructions, leading to an almost realistic geometry. The geometry of the conical heater was tailored to a 2D stair-like model, and it was shown that it produces a flux distribution on the samples in an excellent agreement with the literature data. A symmetrical LES solution was employed for the gas-phase flow simulation, while a single-step, mixing-controlled reaction model defined the chemistry of the monomer combustion. The applied framework endows the modeler with new features, such as the capability to extract time resolved material deformation and thermodynamic variables on the surface of cylindrical rods.

The predicted mass loss rates in the single rod and five rods gasification tests are compared against their corresponding experimental results in Figure 14. In both cases, the model shows an excellent capability of predicting the time dependency of the material pyrolysis, considering the level of experimental and parameter uncertainties. In the experiments with five rods, some melting of PMMA was observed during the last minutes of the tests. Also, small amounts of material close to the outer sides of the sample holder started disintegrating and tumbling down at about $t = 1000 \text{ s}$ in all tests. Most repetitions were seized at about $t = 1100 \text{ s}$ to prevent any damage to the cone calorimeter parts from melted hot PMMA. The applied numerical model cannot reproduce this disintegration, and we expect this constitutes the main reason for the deviation of model result from the experimental curve from $t = 1000 \text{ s}$ onward in Figure 14. The fluctuations in numerical results originates from the burn away feature of the solution. When the PMMA inside a solid cell evaporates completely, the corresponding cell vanishes from solid domain, turning into a gas cell.

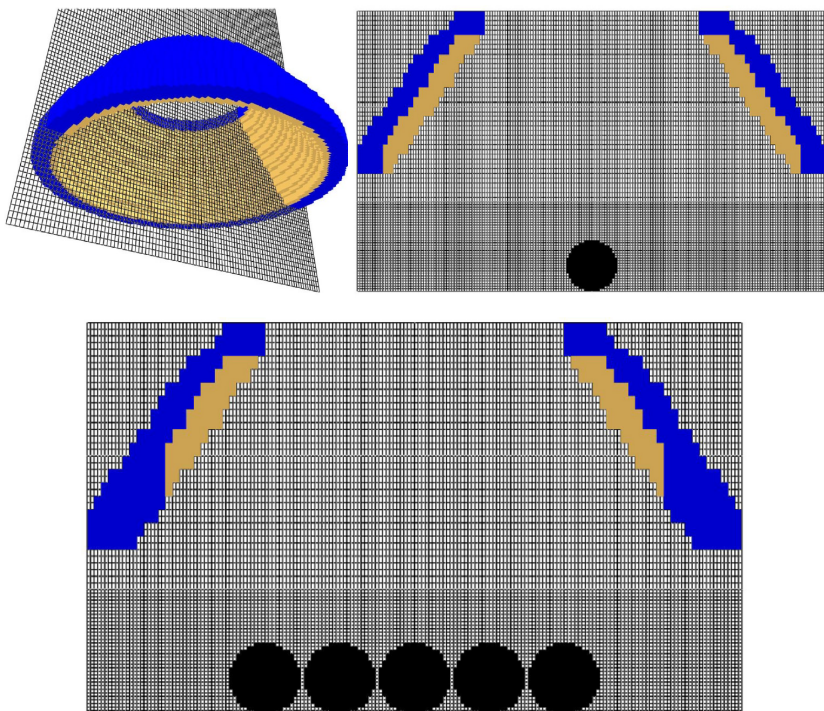


Figure 13. Top left: full 3D model. Top right: a vertical plane passing midway through the 3D cone geometry, along with the presence of a single PMMA rod. Bottom: modified 2D cone heater geometry used in the current study, along with the presence of five PMMA rods.

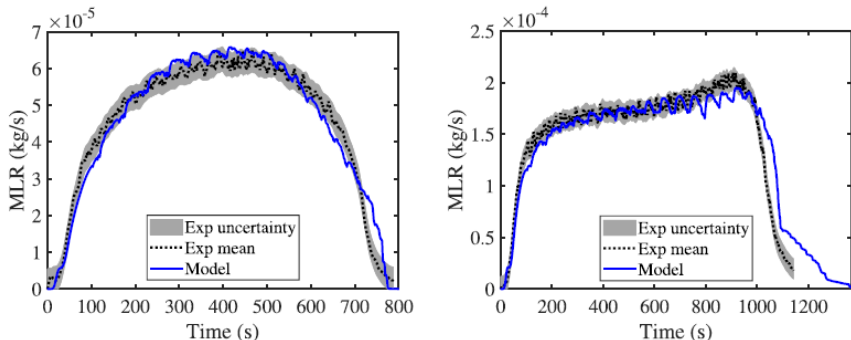


Figure 14. Comparison of mass loss rates between experimental and model prediction for single (left) and five rods (right) gasification test cases.

The predicted MLR and HRR of the five rods flaming case are compared against the experimental results in Figure 15. Here, the differences between the simulated

and measured curves are significantly greater than in the gasification tests or the flaming test with just one rod. One prominent difference is the model's increasing trend after ignition, while the experiments retain the decreasing trend in both MLR and HRR. The integrals of the model and the mean experimental MLR curve match with less than 0.1% difference, but there is a 16% difference in the HRR integrals. Qualitative differences in HRR may partly stem from the flame physics far away from the sample. We did confirm that the simulation domain was tall enough to enable the combustion of all gas phase MMA, but the effects of the reduced numerical resolution towards the top of the domain remain unclear. Figure 16 illustrates the propagation of the pyrolysis front across the fuel array.

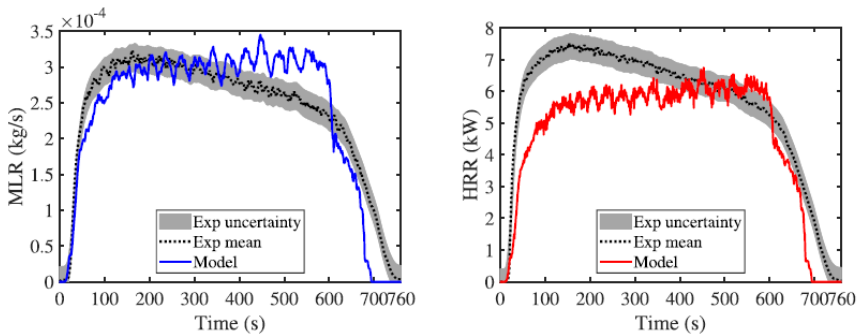


Figure 15. Comparison of mass loss (left) and heat release (right) rates between experimental and model prediction for five rods flaming test cases.

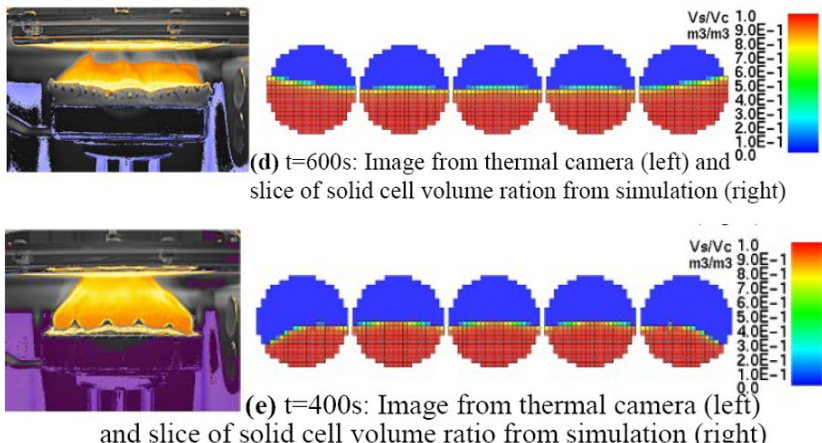


Figure 16. Comparisons of snapshots from thermal camera to the FDS prediction of pyrolysis front in a non-flaming (top) and flaming (bottom) five-rod cone calorimeter scenario. The effect of flame on the shape of the pyrolysis front is captured by the model.

Molecular modelling of ageing effects

A significant problem hampering our ability to perform predictive CFD simulations, particularly fire spread simulations, is the uncertainty in input data. The modeller already faces a considerable challenge in trying to find a suitable pyrolysis reaction mechanism, and associated kinetic parameters, for fresh materials. An additional component to the uncertainty comes through ageing, which may affect both the physical and chemical composition of the materials. The main chemical modifications for the base polymeric materials involve chain scissions and cross-linking reactions. It is expected that the modifications to the molecular weight distribution by these reactions inherently lead to changes in the burning properties. There is experimental evidence to suggest this is true, but the evidence is conflicting in the sense that in some cases ageing can enhance burning, while in other cases it can reduce burning (Vahabi et al. 2015). No systematic theoretical or numerical analyses to explain these effects exist.

In FIRED, we started the ground-breaking research of using Reactive Molecular Dynamics (RMD) to predict the kinetic parameters needed for flame spread. The idea in reactive molecular dynamics is to simulate chemical reactions within a classical MD framework, but using an interaction potential between atoms that has been formulated and trained such that chemical connectivity changes between atoms are possible. The ReaxFF potential (van Duin et al. 2001), used in FIRED, is a sophisticated and versatile potential for RMD. While computationally significantly cheaper than quantum mechanical calculations, it is still much more expensive than traditional classical MD potentials where connectivity remains fixed.

Recently, we have performed MD modelling of crystallisation, cross-linking, and bond-scission of polyethylene using an approach, where each CH₂ repeat unit is described as one particle. While this united-atom approach has been known for some time, we have modified the approach to include chemical reactivity.

In URAN, we have performed united-atom MD simulations of thermal decomposition of fresh and aged polyethylene in order to look for effects of ageing on the thermal decomposition process. The focus is entirely on the polymer matrix, so that additives, anaerobic ageing, radiation, and humidity are not considered. The simulations were performed using the MD software LAMMPS (Thompson et al. 2022). Chemical bonding and van der Waals interactions between particles were described by the TraPPE-UA force field (Martin and Siepmann 1999). Additives (antioxidants, plasticizers, fire retardants, colorants, fillers, etc) are not considered. The main chemical modifications for the base polymeric materials due to ageing involve chain scissions and cross-linking reactions. The hypothesis for this study is that the modifications to the molecular weight distribution by these reactions inherently lead to changes in the burning properties.

The MD model was built to include the main mechanisms of the free-radical pyrolysis scheme for polyethylene, which are random scission, unzipping, and backbiting (Poutsma 2003). To validate the model, we employed experimental data from the study by De Witt and Broadbelt (2000). They studied isothermal decomposition of polyethylene at 420 °C, measuring the yields of decomposition products (all

gaseous products plus solid-state decomposition products up to a carbon number of 34) at conversions 0.05, 0.21, and 0.34. The MD simulation of the data involved a polydisperse system with a weight-averaged mean chain length of 9000 repeat units and a dispersity of 1.79. It was prepared by first generating a random-walk MD model for a single chain of 90000 repeat units long, followed by random scission of 17 bonds. The dispersity deviates from a value of 2 because of the statistically small number of scissions.

Figure 17 presents the comparison of experimental and simulated data as the logarithm of the molar product yield vs the carbon number. Experimental data for carbon numbers 6 and 7 is missing due to experimental reasons. Data for the lowest conversion at high carbon numbers suffers from poor resolution. However, linearity of the plot for conversions 0.21 and 0.34 shows that for carbon numbers 8 to 30, the random scission mechanism is in effect. Clear deviation from linearity is seen in the data for carbon numbers 1–6, indicating that unzipping and back-biting effects are important, and they significantly increase the yields of these light species compared to pure random scission mechanism.

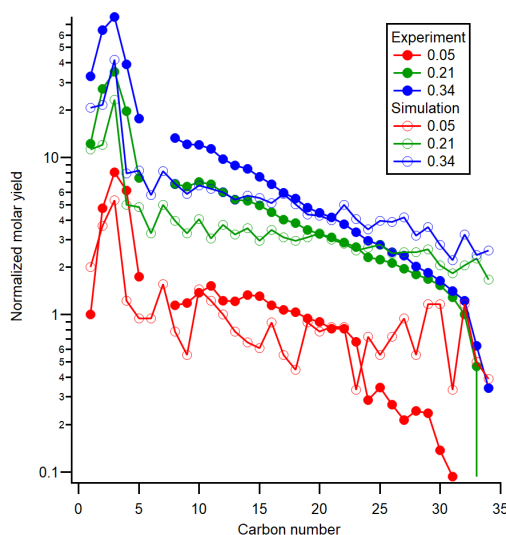


Figure 17. Experimental and simulated product yields for three conversions.

Regarding the random scission process, the simulated results for high carbon numbers show a linear trend on a logarithmic scale, but for each conversion the slope of the simulated data is smaller compared to experiments. Two explanations could be proposed. First, a general feature of the logarithmic plot is that the slope of the plot increases as a function of conversion. Therefore, it is possible that there is an unintended mismatch between the experimental and simulated conversions due to uncertainty in estimating the conversion. Second, the radical transfer processes may affect bond scission probabilities tens of bonds from the chain end,

and taking all of these processes into account in modeling (Levine and Broadbelt 2009) can quite accurately reproduce the experimental data, suggesting that the slope is sensitive to the details of the reaction mechanism.

We then used the united-atom MD model for simulating TGA curves for fresh and aged PE and XLPE systems listed in Table 1. The results are presented in Figure 18 for a heating rate of 3 K/ps. The general conclusion from the results is that neither the degree of aging, nor the degree of cross-linking have any significant effect on the results. There is a slight tendency of the TGA curves to move towards lower temperatures as a function of ageing, which might be an indication of better burning, but the effect is very small. It follows therefore that ageing is not expected to have a notable effect on the burning properties of an aged base polymer. It should be stressed, however, that this result only concerns the base polymer, and not the possible additives.

Table 1. PE and XLPE systems used in this work for studying the effect of ageing.

Linear PE		XLPE, gel fraction 0.71			XLPE, gel fraction 0.85		
Broken bonds		M _n	Broken bonds		M _n	Broken bonds	
number	%		number	%		number	%
182	0.06	637	355	0.12	679	367	0.12
365	0.12	459	566	0.19	459	566	0.19
570	0.19	349	1065	0.36	261	1054	0.35
765	0.26	285	1784	0.59	161		
1079	0.36	219	2258	0.75	129		

We also performed an isoconversional analysis for selected fresh and aged systems in order to quantitatively check the effect of ageing on the pyrolysis kinetics. Specifically, the systems were the fresh linear PE and the aged PE with Mn=219, and fresh XLPE with a gel fraction of 0.71, and aged XLPE with Mn=129. Figure 19 presents the conversion-dependent activation energies for these cases. The results indicate a slight increase (about 2 kcal/mol) of the activation energy due to ageing. Again, the effect of ageing is next to non-existent, but if real, it would suggest that ageing makes the pyrolysis process more difficult, suggesting reduced burning. This result runs contrary to the conclusion drawn from Figure 18, and currently it is not clear how these two results should be understood together. More work would be required to resolve the controversy, possibly using systems that are much more radically (and perhaps unphysically) aged so that the effects on the shape of the TGA curves and on the activation energies would become more pronounced. Nevertheless, for the moment the main conclusion from Figures 18 and 19 remains that the effect of ageing on the pyrolysis behaviour of PE and XLPE is minimal.

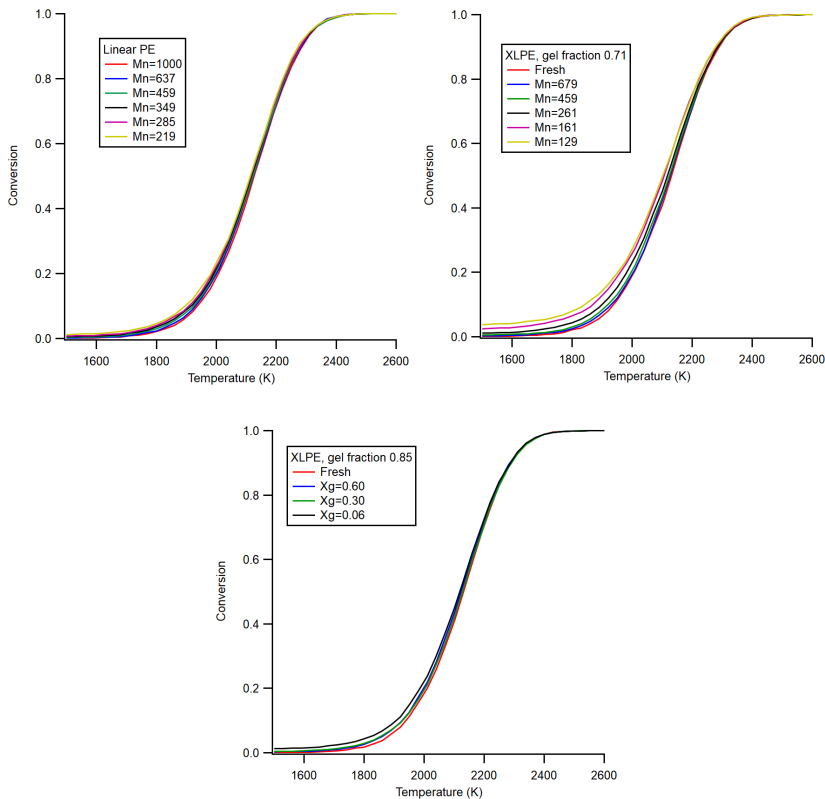


Figure 18. Simulated TGA curves for aged PE and XLPE systems at 3 K/ps heating rate.

Even though our united-atom MD approach was able to reproduce TGA curves, the fundamental problem of molecular dynamics related to available time scales remain: unrealistically high temperatures are required to accelerate reaction rates so that all interesting events occur in the microsecond scale. In order to access realistic time scales and reaction rates, we developed a coarse-grained approach to simulate TGA curves.

In coarse-grained models, a small selection of repeat units is used to represent different chemical groups, and only a limited set of non-elementary reactions are considered. To simplify the solution of the kinetics, a reaction probability-based Kinetic Monte Carlo (KMC) method can be used instead of solving systems of rate equations to track the chemical transitions due to the reactions (Gillespie 1977, Voter 2007).

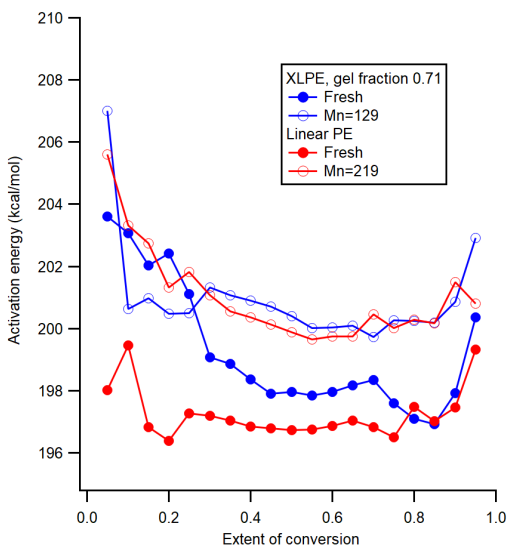


Figure 19. Conversion-dependent activation energies for selected fresh and aged systems.

We propose a coarse-grained graph representation of fresh and thermally degraded cross-linked polyethylene (XLPE) combined with analytical and numerical models to study the evolution of connectivity and volatile fraction during aging and pyrolysis. Disregarding local chemical changes and only considering topological evolution allows for studying very large systems and predicting network-dependent properties (mechanical etc.) and quantitatively predicting the TGA curves. Our analytical expressions allow rapid fitting to data while our numerical KMC models offer the flexibility to study more complicated systems and several types of reactions. We apply our models to identifying the aging states from experimental TGA results.

For model validation, we obtained XLPE material from Nexans NRC. The raw material was linear low-density polyethylene, and it was cross-linked at 65 °C using a silane cross-linker. The density and gel fraction of the resulting Si-XLPE were about 0.912 g/cm³ and 0.71, respectively. Thermo-radiative ageing was performed in the Panoza facility at UJV Rez, Czech Republic, with a 60Co γ -ray source. The average temperature was 47 °C, and the average dose rate was 77.8 Gy/h. TGA experiments were conducted at VTT under a nitrogen atmosphere using a heating rate of 10 K/min. Char yield was checked by switching to air atmosphere and heating the crucibles up to 1000 °C.

The thermogravimetric data for fresh and thermo-radiatively aged XLPE is presented in Figure 20 (solid lines). For the fresh material, the decomposition occurs in a single step in the 400-500 °C temperature range, with a peak degradation rate at 470 °C. In aged samples, a low-temperature tail develops in the curves at temperatures above 150 °C. For the longest ageing duration of 210 days, the low-

temperature tail includes about 30% of the total mass. No char yield is found after the degradation. Figure 20 also shows the results of fitting our theoretical model to the data.

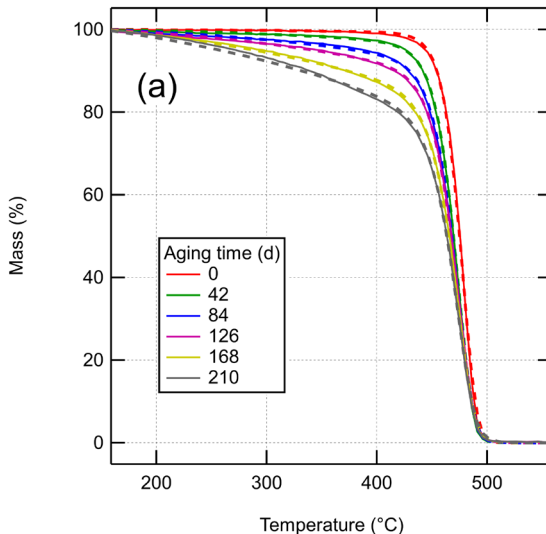


Figure 20. TGA curves. Solid lines show experimental TGA curves, while dashed line show the fitted model curves.

Prompted by these observations, work was carried out to investigate how such aging effects could be implemented in the Fire Dynamics Simulator (FDS). FDS simulations were first performed to develop a material model that would lead to replication of the cone calorimeter experiment (Figure 21). During this step it was observed that basing the FDS pyrolysis model on TGA measurement in N₂ resulted in a significant delay in the time to ignition. No TGA data in air atmosphere was measured in the project, so literature data was used to build a pyrolysis model for XLPE in air. Experimental TGA curves in air demonstrate mass loss at much lower temperatures than in N₂, which improved the prediction of the time to ignition. A significant observation from the experimental cone calorimeter data is that the heat release rate for aged material is lower than for fresh material, which is explained by a lower effective heat of combustion due to the presence of oxygen in the polymer chains due to aging.

In the second step, the material models were applied to two full-scale cable fire scenarios to investigate the effect of aging on fire spread. One of these was a scenario of two cable trays against a wall in open air, with ignition below the bottom tray (Figure 22, left). Fire spread was simulated using material models for virgin and aged cables. The results (Figure 22, right) showed that aged cables lose their mass faster than virgin cables. The time to get fully combusted is also faster for aged cables than for virgin cables. It indicates that fire spread for a given combustible

mass is faster in aged cables compared to virgin cables. Moreover, the aged cables have also shown the tendency for higher peak heat release rate compared to virgin cables. A higher peak heat release rate will be a matter of concern for firefighting personnel as they may require reassessing fire risk from aged cables when they burn in greater mass. However, such conclusions must be checked with more test cases and material models.

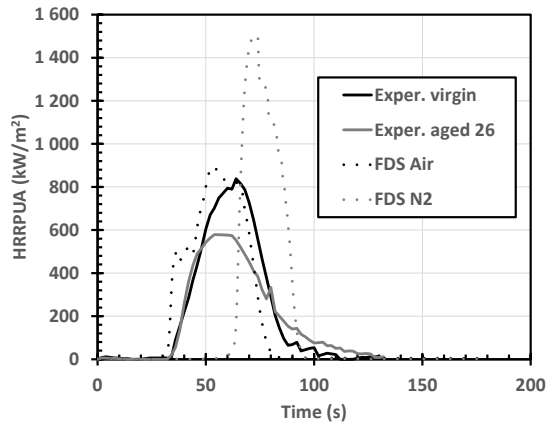


Figure 21. Experimental and simulated HRR curves for virgin and aged XLPE materials in cone calorimeter.

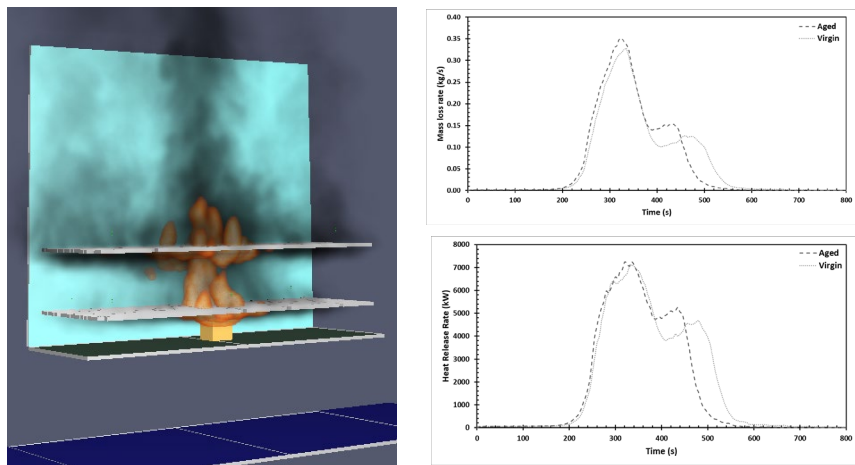


Figure 22: Left: a two-tray cable fire scenario for studying the effect of aging on fire spread. Right: mass loss rate (top) and heat release rate (bottom) from the simulations.

References

- De Witt, M.J. & Broadbelt, L.J. 2000. Binary Interactions between High-Density Polyethylene and 4-(1-Naphthylmethyl)bibenzyl during Low-Pressure Pyrolysis. *Energy & Fuels* vol. 14 pp. 448-458.
- Electric Power Research Institute (EPRI) and U.S. Nuclear Regulatory Commission Office of Nuclear Regulatory Research (RES), EPRI/NRC-RES Fire PRA Methodology for Nuclear Power Facilities: Volume 2: Detailed Methodology. EPRI TR-1011989 and NUREG/CR-6850. 2005.
- Gillespie, D.T. Exact Stochastic Simulation of Coupled Chemical Reactions. *J. Phys. Chem.* 1977, 81, 2340–2361. <https://doi.org/10.1021/j100540a008>
- Hostikka, S. & Keski-Rahkonen, O. (2003) Probabilistic simulation of fire scenarios. *Nuclear engineering and design*, 224(3):301–311.
- Keski-Rahkonen, O., Mangs, J., Hostikka, S. & Korhonen, T. (2007) Quantitative application of Monte Carlo simulation in Fire-PSA. *Kerntechnik*, 72(3):149-155.
- Levine, S.E. & Broadbelt, L.J. 2009. Detailed mechanistic modeling of high-density polyethylene pyrolysis: Low molecular weight product evolution. *Polymer Degradation and Stability* vol. 94 pp. 810-822.
- Martin, M.G. & Siepmann, J.I. 1999. Novel configurational-bias Monte Carlo method for branched molecules. Transferable potentials for phase equilibria. 2. United-atom description of branched alkanes. *The Journal of Physical Chemistry B* vol. 103 pp. 4508-4517.
- Matala, A., Hostikka, S. (2011) Probabilistic simulation of cable performance and water based protection in cable tunnel fires. *Nuclear Engineering and Design*, 241(12):5263-5274.
- McGrattan, K. et al., Cable Heat Release, Ignition, and Spread in Tray Installations During Fire (CHRISTIFIRE) Phase 1: Horizontal Trays, NUREG/CR-7010, Vol. 1, 2012.
- Paudel, D., Hostikka, S. (2019a) Propagation of modeling uncertainty in stochastic heat-transfer simulation using a chain of deterministic models. *International Journal of Uncertainty Quantification* vol. 9, issue 1, pp. 1-14.
- Paudel, D. Hostikka, S. (2019b) Propagation of model uncertainty in the stochastic simulations of a compartment fire. *Fire Technology* vol. 55, pp. 2027–2054.
- Poutsma, M.L. 2003. Reexamination of the Pyrolysis of Polyethylene: Data Needs, Free-Radical Mechanistic Considerations, and Thermochemical Kinetic Simulation of Initial Product-Forming Pathways. *Macromolecules* vol. 36 pp. 8931-8957.
- Thompson, A.P., Aktulga, H.M., Berger, R., Bolintineanu, D.S., Brown, W.M., Crozier, P.S., in't Veld, P.J., Kohlmeyer, A., Moore, S.G., Nguyen, T.D., Shan, R., Stevens, M.J., Tranchida, J., Trott, C., Plimpton, S.J. 2022.

- LAMMPS - a flexible simulation tool for particle-based materials modeling at the atomic, meso, and continuum scales. Computer Physics Communications 271, 108171. <https://doi.org/10.1016/j.cpc.2021.108171>
- Vahabi, H., Sonnier, R. & Ferry, L. 2015. Effects of ageing on the fire behaviour of flame-retarded polymers: a review. Polymer International vol. 64 pp. 313-328.
- van Duin, A.C.T, Dasgupta, S., Lorant, F & Goddard III, W.A. 2001. ReaxFF: a reactive force field for hydrocarbons. Journal of Physical Chemistry A vol. 105 pp. 9396-9409.
- Voter, A. Introduction to the Kinetic Monte Carlo Method. Radiat. Eff. Solids 2007, 235, 1-23.

4 Reactor and fuel

4.1 Coupled analysis of transient scenarios (CATS)

Rebekka Komu¹, Riku Tuominen¹, Jussi-Pekka Ikonen¹, Ville Valtavirta¹, Ville Hovi¹, Veikko Taivassalo¹

¹VTT Technical Research Centre of Finland Ltd
P.O. Box 1000, FI-02044 Espoo

Abstract

System code TRACE was adopted into use for transient analyses by calculating several benchmarks alone and together with a 3D neutronics code. TRACE was integrated with VTT's computational framework Kraken for future safety analyses, and couplings with nodal neutronics code Ants and fuel solver SuperFINIX were implemented and tested. VTT's tool Sensla was utilized for uncertainty and sensitivity analyses, and it was transferred to Kraken to be used within the framework.

A PWR core with a blocked fuel assembly was analysed with a two-phase porous CFD simulation. The results demonstrate the usefulness of porous CFD in coupled transient analysis applications. The methodology was also used within the Kraken framework with a coupled Ants-SuperFINIX-OpenFOAM simulation.

Introduction

The objective of the CATS project is to develop the modelling of transient events and accidents so that we can give more reliable answers to the safety requirements set in the YVL guides. To achieve this, CATS utilizes computational transient analysis tools that have been in use for decades, adopts new independent analysis tools into use as well as participates in the complete renewal of the VTT's reactor analysis system as a part of the ongoing effort to develop the Kraken computational platform. An important part of the project is generating and maintaining expertise for transient analysis calculations.

The focus in CATS is to further improve the analysis of transient scenarios using coupled thermal-hydraulics and reactor core modelling. The researched areas include both the computational tools as well as uncertainty and sensitivity analyses of the modelling. In addition, CATS includes exploratory research topics such as porous computational fluid dynamics (CFD) modelling of transient scenarios. These aid in developing both the modelling tools and the modelling expertise of future.

Plant modelling with neutronics coupling

The transient behaviour of reactor cores have been traditionally modelled at VTT by the in-house reactor dynamics codes TRAB3D [1] and HEXTRAN [2]. These are coupled to the system code SMABRE [3] to form a toolset for deterministic analysis of transient scenarios. However, there is an ongoing work at VTT to develop a new computational framework Kraken [4] for reactor analysis. This includes developing and adopting a new generation of simulation tools for Kraken. As a part of this development process, it was decided that Kraken needs an independent system code for transient analyses. This is especially important for providing an alternative for the use of Apros [5] or the system code SMABRE, where an independent alternative is needed. It was decided that the USNRC's system code TRACE [6] is very suitable for this role. It is an independent tool which can be used for modelling LOCA cases as well as other transients and accidents. A significant goal of CATS is the comprehensive adoption of the system code TRACE into use producing expertise in use of TRACE.

Work on adopting TRACE has been carried out by modelling VVER-1000 benchmarks, which familiarizes experts with the new code as well as different transient types. The work started in 2019 as a TRACE model for VVER-1000 was received from Karlsruhe Institute of Technology. At first, USNRC neutronics code PARCS [7], which comes together coupled with TRACE, has been used to solve the core power distribution in these calculations. The goal has been to produce reference results for future calculations. OECD/NEA's Kalinin-3 benchmark featuring a main coolant pump trip transient [8] and V1000CT-2 benchmark Exercises 1 and 2 [9] focusing on a main steam line break transient and vessel mixing have been calculated with TRACE-PARCS [10][11].

In 2021, one of major goals in CATS was completed when coupling between TRACE and VTT's nodal neutronics code Ants was implemented [12]. The aim is to use this code sequence in future safety analysis. The coupling validation was done in the LONKERO project.

Ants-TRACE was used to model V1000CT-2 benchmark Exercise 3, which is a main steam line break transient using the full VVER-1000 plant model with coupled neutronics [13]. The focus was on the steam lines modelling. Some stability and numerical issues were encountered in the secondary circuit, which will be reported to TRACE developers, but the main issues were resolved. Figure 1 shows the fission power from the transient compared to VTT's legacy codes HEXTRAN-SMABRE. Figures 2 and 3 show the break mass flow and steam generator pressure

in the broken loop calculated with Ants-TRACE and HEXTRAN-SMABRE. The results show good agreement between the codes.

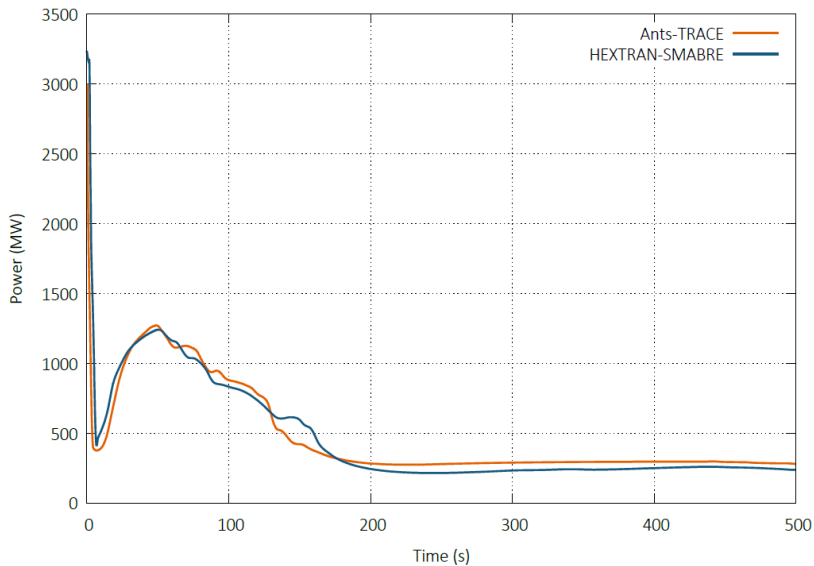


Figure 1. Total power from main steam line break transient calculated with Ants-TRACE and compared to HEXTRAN-SMABRE.

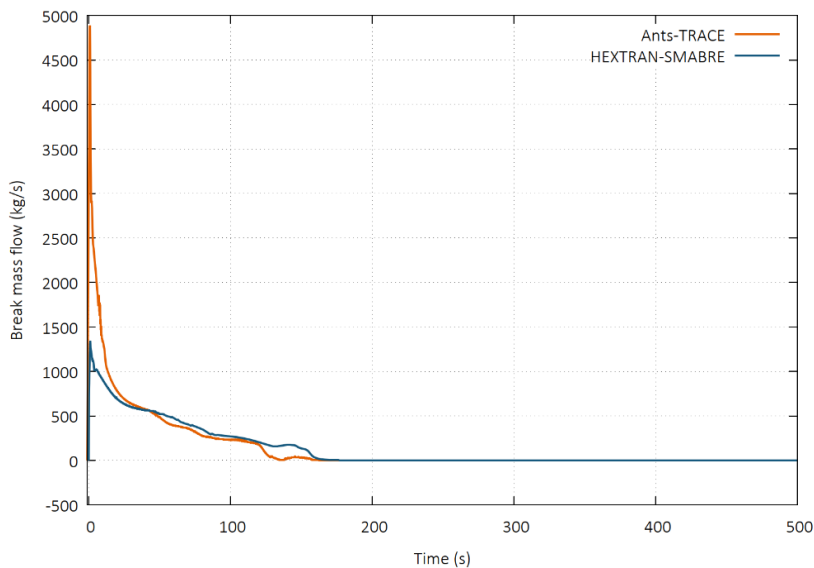


Figure 2. Total break mass flow from main steam line break transient calculated with Ants-TRACE and compared to HEXTRAN-SMABRE.

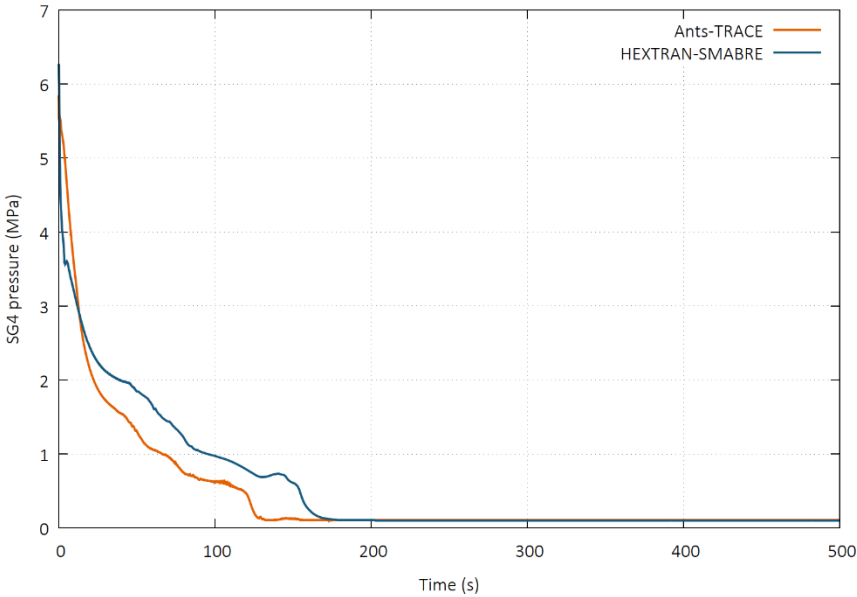


Figure 3. Steam generator (SG) pressure in the broken loop during main steam line break transient calculated with Ants-TRACE and compared to HEXTRAN-SMABRE.

The transient analysis capabilities were extended further by creating a coupling between TRACE and VTT's fuel solver SuperFINIX [14]. In the coupling, TRACE solves the thermal-hydraulics and Ants neutronics, and SuperFINIX solves the fuel behaviour. Using an in-house fuel solver has many benefits: including the thermo-mechanical behaviour of the fuel, allowing source code level development of fuel modelling, enhancing the modularity of Kraken, and restarting the fuel solution based on a preceding fuel cycle simulation to better represent the initial fuel state in the transient. This enhances safety by giving more accurate solutions in transient safety analyses. V1000CT-2 Exercise 2 – the main steam line break transient with vessel boundary conditions – was calculated with the new coupling and compared to earlier calculations with TRACE-PARCS and Ants-TRACE (Figure 4). Based on the results the coupling seems to work as expected and good agreement between the different code sequences is shown.

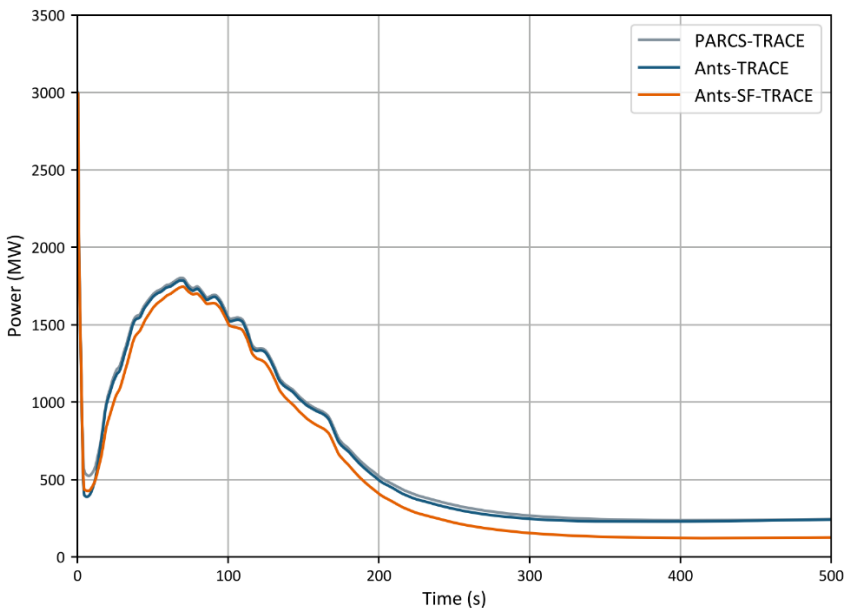


Figure 4. Total power from V1000CT-2 main steam line break benchmark with vessel boundary conditions calculated with TRACE-PARCS, Ants-TRACE and Ants-SuperFINIX-TRACE.

With these benchmarks, the modelling capabilities of TRACE has been investigated concerning the reactor pressure vessel mixing, the primary circuit, and the secondary circuit. Modelling benchmarks works as a way to familiarize experts with the new code as well as different transient types. Several bugs were found from PARCS regarding the VVER-1000 benchmark cross-section files, and TRACE as well. These bugs were reported to the TRACE and PARCS developers and their fixes will be distributed to all code users in the upcoming versions, which will benefit the whole international community. The work on validating Ants-TRACE for safety analysis has started and will be continued in the future.

Uncertainty and sensitivity analysis

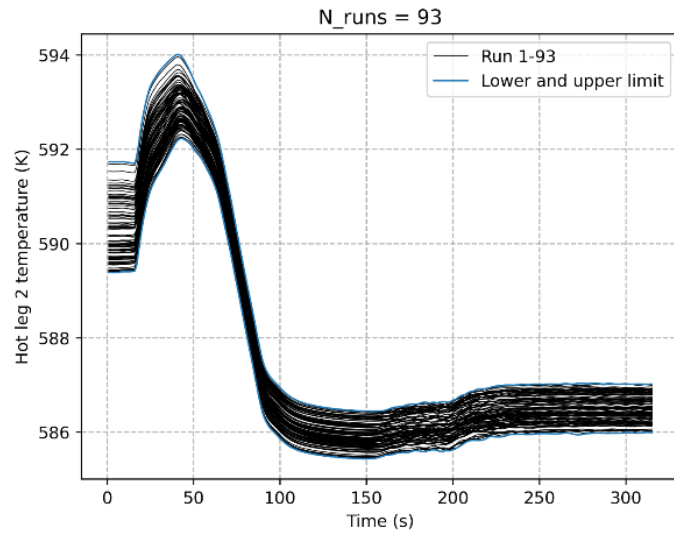
For comprehensive deterministic analyses, an additional layer of sensitivity and uncertainty analysis is needed on top of reactor dynamics simulation capabilities. Uncertainty and sensitivity analysis is an irreplaceable part of best estimate modelling and simulation. By analysing different uncertainties, the most impactful variables and parameters of deterministic analyses can be found. This ensures more reliable answers to the safety requirement questions.

Master's Thesis [14] on uncertainty and sensitivity analysis of nuclear reactor core and thermal-hydraulic system models was completed in 2019. The thesis examined a coolant pump transient from Kalinin-3 reactor, which is a part of the

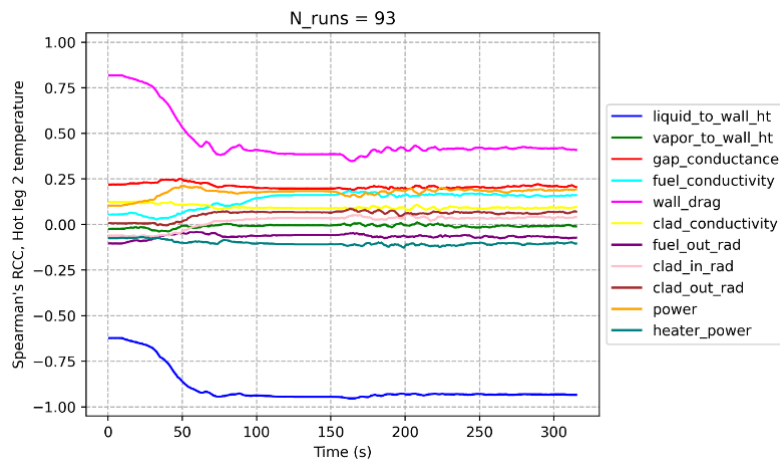
OECD/NEA LWR-UAM (Uncertainty Analysis in Best-Estimate Modelling for Design, Operation and Safety Analysis of Light Water Reactors) benchmark. Analyses were performed for a separate code model with HEXTRAN, for a thermal-hydraulics model with TRACE and for a coupled core and system model with HEXTRAN-SMABRE. VTT's own uncertainty and sensitivity analysis tool Sensla was used for simulations with HEXTRAN-SMABRE and DAKOTA tool was used for stand-alone TRACE simulations.

In 2020, these developments in uncertainty and sensitivity analysis were combined with the efforts in adopting TRACE-PARCS. The previously used sensitivity analysis tool for TRACE was not capable of comprehensive uncertainty and sensitivity analysis for the coupled TRACE-PARCS code system. Thus, Sensla was expanded for use with TRACE-PARCS and the first sensitivity analyses using TRACE-PARCS with Sensla were performed [15]. This was a continuation and replication of the earlier work using HEXTRAN-SMABRE. In addition, a partial rank correlation coefficient calculation routine external to Sensla was developed and taken into use. This increased the extent of uncertainty and sensitivity analyses that can be performed with both TRACE-PARCS and HEXTRAN-SMABRE.

During the final year, the goal was to integrate the uncertainty and sensitivity analysis methodology into Kraken. Sensla was converted into a Python script and transferred to KrakenTools. It can be now used for stand-alone TRACE calculations and can be later extended to other Kraken solvers as well. The tool automates the creation of input variables and code inputs, running the simulations on a computational cluster, and analysing sensitivity and uncertainty variables from the outputs as well as plotting the results. Figure 5 shows example outputs from the tool: TRACE hot leg temperatures from 93 runs and calculated Spearman's rank correlation coefficients (RCC) between the input variables and the hot leg temperature. The modelled case is a main coolant pump trip transient from the Kalinin-3 VVER-1000 coolant transient benchmark. A tutorial was created for the Kraken wiki about the use of the tool. The tool is user-friendly, flexible and can be easily modified for purpose. In the future, methodology on calculating thermal margins [16] with uncertainties can be included in the tool.



a)



b)

Figure 5. a) Hot leg 2 temperature and b) Spearman's rank correlation coefficient (RCC) from 93 TRACE runs of Kalinin-3 main coolant pump transient, where some input variables have been varied with the uncertainty and sensitivity analysis tool implemented in Kraken.

Porous CFD modelling and core clogging

Exploratory research in CATS aims to highlight shortcomings of current modelling tools and to examine the limitations of high fidelity approaches for transient calculations. For 2019-2021, the examined case for porous CFD modelling was a blockage in a fuel assembly in an European Pressurised Water Reactor (EPR) core.

The EPR primary loop is modelled with the system code SMABRE, the neutronics of the reactor core with the reactor dynamics code TRAB3D and the thermal hydraulics of the reactor pressure vessel and the reactor core with the porous CFD software PORFLO [17][18]. This division is presented in Figure 6 and a closeup of the PORFLO mesh in Figure 7.

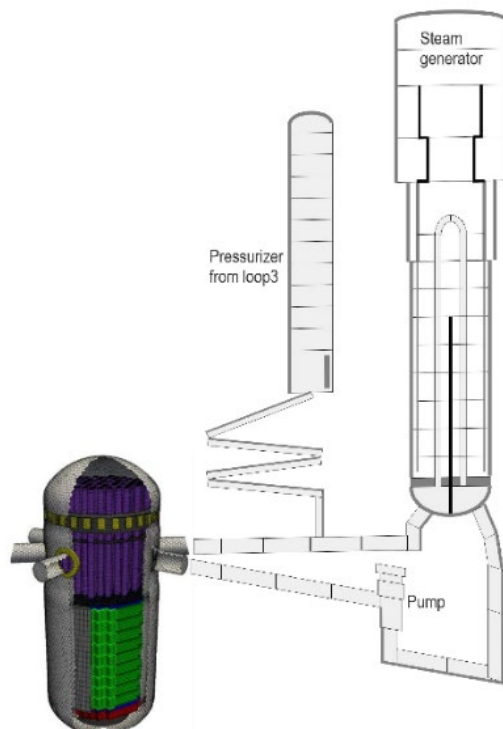


Figure 6. Nodalization of a single EPR primary loop for SMABRE and schematic representation of the couplings between SMABRE and PORFLO models.

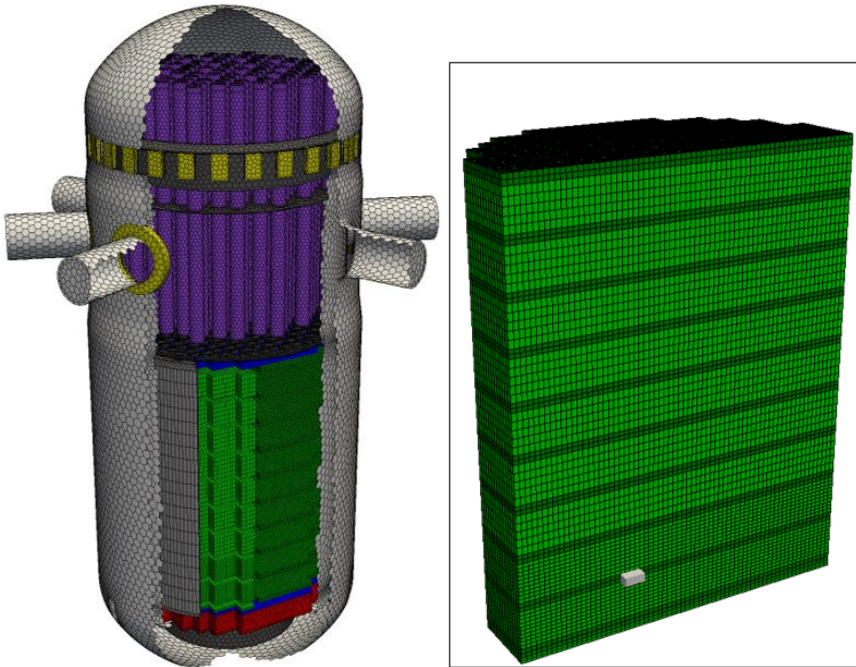


Figure 7. A closeup of the computational mesh for the porous CFD calculation. The clogged spacer grid is visible as a gray slate in the cross-sectional view of the reactor core.

The blockage has the cross-sectional area of a single assembly and represents a clogged spacer grid. The blockage locally restricts the flow of coolant. The blockage is partially porous, but has a higher resistance to flow than the surrounding area. Compared to a corresponding case with no blockage, coolant temperature rises more at the location of the blockage, as expected. Above the blockage, the coolant flow rate returns close to the unblocked case flow rate (Figure 8). Together with mixing, this reduces the influence of the blockage higher up in the core and in the upper plenum. It was noticed that the coolant temperature still rises above its saturation point in a small area of the core [19]. The CFD code was modified for two-phase applications [20]. The calculation was repeated with two-phase porous CFD using one-way coupling with the neutronics and system codes, and the same mesh. The temperature and void formation above the blockage are shown in Figure 9.

The results are more qualitative than quantitative in nature, because of the coarse mesh and lack of feedback for the neutronics power calculation, but the analysis highlights the feasibility and advantages of the porous-CFD approach in transient analyses. It is worth noting that these results should not be considered representative of any specific EPR. The computational model was based on publicly available material for different EPRs planned to be built in different countries.

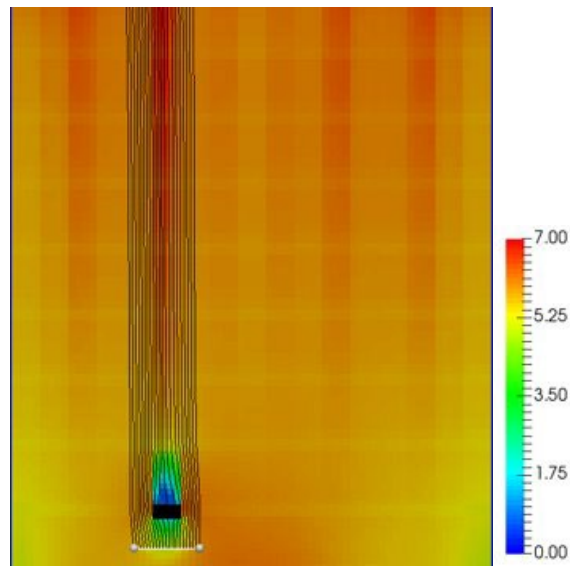


Figure 8. Velocity (m/s) and streamlines of the coolant flow around the blockage.

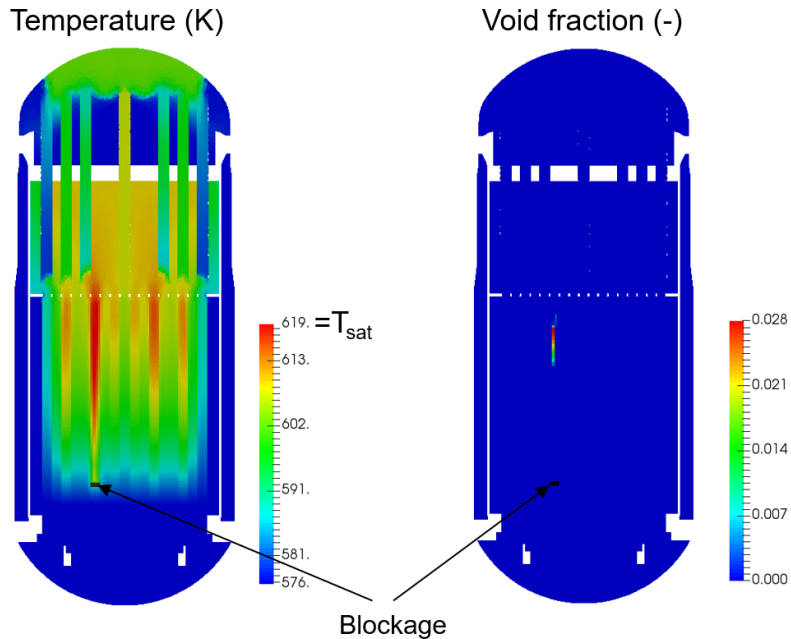


Figure 9. Cross-section of the reactor pressure vessel in an EPR with a blocked fuel assembly. Coolant temperature is on the left and void fraction on the right. The blockage causes the temperature to increase locally to saturation temperature and some void formation above the blocked assembly.

In 2022, coupled porous CFD methodology was also demonstrated with Kraken solvers [21]. Data transfers between Ants, SuperFINIX and OpenFOAM are demonstrated in Figure 10. The modelled case was the end state of Kalinin-3 main coolant pump trip transient. The results show that coupling works and is ready to be used in further applications. The next steps are to couple OpenFOAM with the system code TRACE for full plant-scale simulations, and to use the coupling in time-dependent transient simulations.

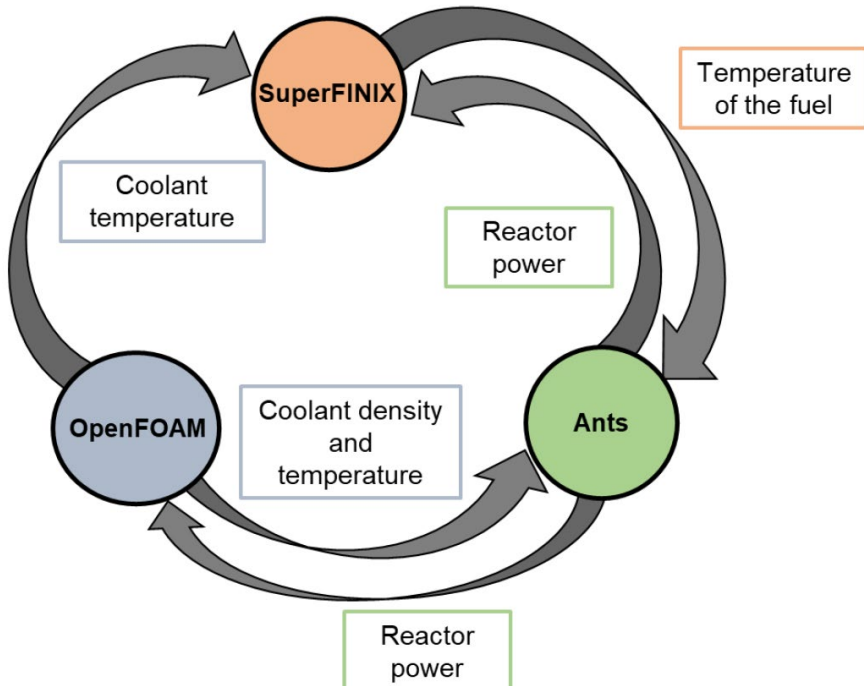


Figure 10. Data transfer between solvers in the Ants-SuperFINIX-OpenFOAM coupling.

International co-operation

Cooperation and information exchange on VVER safety within the AER framework together with other countries which use VVER reactors is an important part of the international co-operation and networking in the CATS project. In 2019, the AER working group D meeting was organized as a joint meeting with the OECD/NEA Rostov-2 Benchmark meeting in Munich, Germany [22]. In 2021, the AER working group D meeting was organized online due to the COVID-19 pandemic. After February 2022 all AER activities were ceased.

Participation in the meetings of the NEA Working Party on the Scientific Issues of Reactor Systems (WPRS), is also within the scope of CATS. WPRS is

responsible for the organization of the reactor dynamics benchmarks among other activities. Participation in NEA working groups and benchmarks is important for validating methods used in transient analysis. OECD/NEA WPRS & Expert Groups meetings in February 2019 in Paris, France, was attended [23].

The adoption of the system code TRACE and the reactor analysis code PARCS have created a new avenue of international cooperation for the CATS project. An online CAMP Fall meeting 2022 was attended and the coupling between TRACE and Kraken was presented, which raised a lot of interest. Ongoing work on adopting the codes requires active communication with the TRACE and PARCS developers regarding the bugs and issues found. This co-operation of CATS and the developers of TRACE and PARCS benefits all Finnish actors who wish to use them as independent analysis tools as well as the whole international TRACE-PARCS user community.

Summary and conclusions

The system code TRACE was adopted as a reactor analysis tool by calculating several OECD/NEA VVER-1000 coolant transient benchmarks. TRACE was coupled with the Kraken framework and the couplings with different solvers were tested. During the four-year project, CATS also produced a considerable amount of non-tangible results through training of new experts in the use of TRACE and on conducting transient analyses. Identifying and reporting several significant bugs and issues with TRACE and PARCS benefits the international CAMP code user community.

CATS is and remains at the forefront of examining new ways to model transient scenarios. While porous CFD simulation of a blocked assembly as a part of a PWR is at the limits of modern modelling capability, that is also the limit where new qualitative insights can be found.

Acknowledgements

We thank the development teams of the system code TRACE and the reactor analysis code PARCS for their cooperation with the CATS project.

References

- [1] Kaloinen, E and Kyrki-Rajamäki, R. "TRAB-3D, a new code for three-dimensional reactor dynamics," in CD-ROM Proceedings of ICONE-5, 5th International Conference on Nuclear Engineering. Nuclear Advances through Global Cooperation, Nice, France, May 26-30 1997.
- [2] Kyrki-Rajamäki, R. "Three-dimensional reactor dynamics code for VVER type nuclear reactors," Technical Research Centre of Finland, DrTech Thesis. VTT Publications 246, 1995.

- [3] Miettinen J. and Hämäläinen A, "Development and Validation of the Fast Running Thermohydraulic Model SMABRE for Simulator Purposes," ICONE-8: Eight International Conference on Nuclear Engineering. Baltimore, USA, 2-6 April, 2000 [CD-ROM]. New York: American Society of Mechanical Engineers. Paper ICONE8-8188, 12 p. ISBN 0791819922.,2000
- [4] Valtavirta V., Hovi V., Loukusa H., Rintala A., Sahlberg V., Tuominen R., Leppänen J., "Kraken – An upcoming Finnish reactor analysis framework". International Conference on Mathematics and Computational Methods Applied to Nuclear Science and Engineering, M and C 2019. United States, 25th-29th August 2019. Pages 786-795.
- [5] Webpages of Apros Process Simulation Software. <http://www.apros.fi/en/>
- [6] Office of Nuclear Regulatory Research, 2009. TRACE V5.0 Theory Manual. Field Equations, Solution Methods, and Physical Models. USNRC, Washington, DC.
- [7] Webpages of Purdue Advanced Reactor Core Simulator (PARCS) <https://engineering.purdue.edu/PARCS>
- [8] Tereshonok, V. et al. Kalinin-3 coolant transient benchmark – switching-off of one of the four operating main circulation pumps at nominal reactor power specification- First Edition 2008.
- [9] Kolev, N., Petrov, N., Donov, J., Angelova, D., Aniel, S., Royer, E., Ivanov, B., Ivanov, K., Lukanov, E., Dinkov, Y., Popov D. and Nikonorov S., VVER-1000 Coolant Transient Benchmark PHASE 2 (V1000CT-2) Vol. II: MSLB Problem – Final Specifications. Technical Report NEA/NSC/DOC(2006)6, OECD/NEA, 2006.
- [10] Komu, R., Kalinin-3 model for TRACE-PARCS, VTT Research Report VTT-R-01588-20.
- [11] Komu, R., Mixing modelling capabilities of TRACE – V1000CT-2 Benchmark Exercises 1 and 2, VTT Research Report VTT-R-00904-21.
- [12] Tuominen, R., Komu, R. & Valtavirta, V., Coupling TRACE with Nodal Neutronics Code Ants Using the Exterior Communications Interface and VTT's Multiphysics Driver Cerberus. International Conference on Physics of Reactors 2022 (PHYSOR 2022), Pittsburgh, PA, USA, May 15-20, 2022
- [13] Komu, R. V1000CT-2 benchmark Exercise 3 – MSLB transient with Ants-TRACE, VTT Research report VTT-R-00927-22
- [14] Komu, R., Tuominen, R. & Valtavirta, V., Coupling TRACE with VTT's Fuel Solver SuperFINIX for Transient Analysis, M&C 2023 - The International Conference on Mathematics and Computational Methods Applied to Nuclear Science and Engineering, Niagara Falls, Ontario, Canada, August 13 – 17, 2023

- [14] Komu, R., "Uncertainty and Sensitivity analysis for Nuclear Reactor Core and Thermal-Hydraulic System Models". Master's Thesis, University of Oulu, 2019.
- [15] Komu, R., "Implementing the uncertainty and sensitivity analysis tool Sensla for TRACE-PARCS", VTT Technical Research Centre of Finland, Research report VTT-R-00048-21.
- [16] Räty, H., "On the methodology of calculating thermal margins", VTT Technical Research Centre of Finland, Research report VTT-R-00197-20.
- [17] Ilvonen M., Hovi V. and Taivassalo V., 3D Core thermal hydraulics with the PORFLO code – turbulence modelling and porous medium with porosity steps, in proceedings of 22nd International Conference on Nuclear Engineering ICONE-22, Prague, Czech Republic, July 7-11, 2014.
- [18] Taivassalo, V., "Feasibility study on the applicability of TRAB3D-PROFLO-SMABRE in analyses of core clogging in a PWR", VTT Technical Research Centre of Finland, Research report VTT-R-00195-20.
- [19] Taivassalo, V., Hovi, V., Hämäläinen, A., Räty, H., Preliminary study on the applicability of TRAB3D-PORFLO-SMABRE in analyzing the effects of a fuel assembly blockage in a PWR, VTT Research Report VTT-R-00171-21.
- [20] Taivassalo, V. & Hovi, V., Feasibility study on the two-phase flow modelling for a fuel assembly blockage in a PWR, VTT Research Report VTT-R-00179-22
- [21] Ikonen, J.-P. Ants-SuperFINIX-OpenFOAM simulation of Kalinin-3 reactor, VTT Research report VTT-R-00029-23
- [22] Sahlberg, V., Travel report, AER working group D meeting and OECD/NEA Rostov-2 Benchmark meeting, 24.-27.6.2019, Munich, Germany.
- [23] Syrjälähti, E., Travel report, OECD/NEA WPRS & Expert groups meeting, 19.-22.2.2019, Paris, France

4.2 Interdisciplinary fuels and materials (INFLAME)

Janne Heikinheimo, Asko Arkoma, Henri Loukusa[†], Jussi Peltonen, Markus Hirvensalo[†], Caitlin Huotilainen[†], Konsta Sipilä, Rami Pohja, Sami Penttilä[†], Teemu Kärkelä

VTT Technical Research Centre of Finland Ltd

P.O. Box 1000, FI-02044 Espoo

[†]currently working elsewhere

Abstract

The INFLAME project focuses on nuclear fuel behavior during its irradiation in a nuclear reactor, including steady-state, transient and design basis accident conditions. The behavior of nuclear fuel is studied both by means of modelling and experiments. In the first part of the project, the modelling items of fuel behavior in reactivity-initiated accident (RIA) conditions has included CABRI international program pre-test simulations, and an RIA sensitivity analysis with Sobol' variance decomposition method. Code development work has continued with the in-house fuel performance module FINIX and SuperFINIX with performance optimization and MPI parallelization.

In the experimental work packages of the project, experimental studies have been performed for both, cladding and pellet materials. For the cladding samples, creep testing, autoclave testing and steam furnace testing capabilities have been developed. Tests and material characterizations have been done for conventional and accident tolerant cladding concepts. For the pellet materials, experimental capabilities at the VTT Centre for Nuclear Safety have been developed for iodine release experiments and scanning electron microscopy analyses.

One DSc thesis was finalized in 2020 based on the fuel thermochemical behavior analyses made in this and the preceding SAFIR fuel projects. One Master's thesis work has been completed within the INFLAME project.

Introduction

Nuclear fuel is the most central physical element of the nuclear reactor, as the energy used in power production is produced within the fuel. Nuclear fuel in light water reactors (LWR) currently in operation consists of ceramic uranium oxide fuel pellets within a metallic cladding tube. The cladding tube, and in some sense the fuel pellet, act as the first release barriers of radioactivity in accidental conditions. Nuclear fuel performance modeling is used to predict fuel behavior and thus ensure both efficient and safe operation of nuclear power plants, where one of the most important issues is to ensure the integrity of the cladding. For most accurate modeling of nuclear fuel, close connection between modeling and experiments must be maintained. The INFLAME project contains both experimental and modelling

work packages, and the objective is to have close contact between the experimental and theoretical research during the project for maximum impact.

In the INFLAME project, several current issues regarding fuel behavior under irradiation are investigated. These include integral fuel behavior modeling and participation to international research projects from which data for validation can be obtained, as well as experimental work on both fuel cladding and pellets.

Validation and capabilities for more advanced data processing

OECD NEA is currently building a new database for integral fuel experiments called DATIF (DATabase for IFpe) to enhance accessibility to the IFPE legacy collection of integral fuel performance experiments data, jointly put together by the NEA and the IAEA. DATIF currently contains data for 165 fuel rods corresponding to 15 experiments. This is to be compared with the full IFPE collection which contains ~ 1500 rods from ~90 experiments. Although initially developed to host the IFPE collection, DATIF has been considered from the start as a potential repository for other sources of data. Such sources could cover data from IAEA FUMEX/FUMAC exercises, legacy data from the Halden Reactor Project (HRP), and new data resulting from the FIDES programme of work.

The future development of fuel performance codes depends on the new DATIF and its utilization. With this scope in mind, a new lightweight python validation tool VAST (Validation tool for fuel performance software) has been developed in 2021-2022 for efficient validation and comparison of all fuel performance codes at VTT's disposal. Currently the tool utilizes only local data, but in the future this tool can be extended for DATIF applications as well.

The newly categorized data in DATIF calls for critical evaluation of current fuel performance model correlations. Therefore, a machine learning (ML) approach for thermal conductivity surrogate models has been developed in 2022 to allow efficient re-evaluation of the current correlations. The ML approach uses the Kernel Ridge Regression (KRR) and a generic fit function as the model concept. KRR is a flexible ML method that is suitable for the model training, and the use of a fit function provides a rigid profile for the thermal conductivity model. In this work IFA-677 was used for demonstrating the new concept. At the current development state, the model correlation can be trained for fuel pellet average thermal conductivity. In the future development the training should be able to address the temperature dependent fuel thermal conductivity profile.

Design basis accident analyses

In addition to normal operation of nuclear power plants, several other design basis scenarios must be taken into account in nuclear safety analysis. The YVL guides, i.e., the Regulatory Guides on Nuclear Safety of STUK (STUK, 2019) classify these as:

- (i) anticipated operational occurrences,

- (ii) postulated accidents, and
- (iii) design extension conditions.

Of postulated accidents, the reactivity-initiated accident (RIA) and loss-of-coolant accident (LOCA) are the two main types of accidents considered in fuel performance analyses.

The LOCA analyses performed in 2019 were related to pre-calculations of a planned hotcell LOCA test of a VVER rodlet tested previously in Halden IFA-789.

In an RIA, the reactivity of the core or part of it is abruptly increased, inducing a sharp power pulse. The event may cause fuel rod failures and consequent release of radioactive material to the coolant. The shattered fuel pellet fragments give rise to steam generation. In the worst case, this initiates a pressure pulse which can damage the surrounding fuel assemblies and possibly the whole core. The extremely narrow time scale of the reactivity-initiated accident, in the order of tens of milliseconds, sets additional demands on fuel modelling codes. For detailed thermo-mechanical modelling of fuel rod during RIA, VTT applies the SCANAIR computer program, developed by the French research organization IRSN. Models in SCANAIR are specifically developed for modelling RIAs.

In the current YVL guides, RIA-relevant enthalpy limits for loss of fuel rod integrity and fuel melting are stated. These historical figures may not be applicable for the fuels currently operated in the reactors. Over the years, the fuel burnup has increased, making the cladding more brittle and susceptible to failure in RIA. In several countries, including USA and France, RIA criteria have been or are currently being revised.

In the OECD/NEA CABRI International Project (CIP), the CABRI research reactor in France has been refurbished and equipped with a water loop for RIA testing. The experimental campaign began with the CIP-Q test in 2018, and after delays, the testing continued in late 2022 with the CIP1-2B test. Information obtained from CIP will be used to improve knowledge on the behavior of current fuel materials in RIAs, taking into account the confidentiality limitations of the CIP data. The first CABRI International Project (CIP) Analytical Group Meeting was participated in 2020 and the results reported during the annual VTT review of international fuel research projects held as a half-day seminar. VTT participated in the pre-calculations of CIP1-2B and CIP3-1R with SCANAIR, and the preceding steady-state operation histories were simulated with the VTT-ENIGMA code. CIP1-2B test will use a high burnup UO₂ fuel with M5 cladding to study especially the boiling crisis and fission gas contribution to the cladding loading. CIP3-1R test focuses on PCMI failure and fuel ejection.

During years 2010–2019, OECD/NEA/CSNI Working Group on Fuel Safety (WGFS) organized a series of RIA fuel codes benchmarks, Phases 1–3. As an in-kind item to fulfil the requirements of the SCANAIR license agreement, VTT participated in 2019 in a writing group which summarised the three phases into a single document.

SCANAIR in-kind work of 2020 consisted of calculation of 1st order (main effect), 2nd order and total effect sensitivity indices with the Sobol' variance decomposition

method for a fresh fuel case from the OECD/NEA RIA fuel codes benchmark Phase 2 (OECD/NEA, 2017). The existing Python and Matlab scripts by Ikonen and Tulkki (2014) were extended for SCANAIR. In the analysed case, the interaction effects were found to be negligible (2nd order indices were close to zero).

The work continued in 2021 with calculation of 2nd order and total effect sensitivity indices with the Sobol' variance decomposition method for OECD/NEA RIA fuel codes benchmark Phase 3 – CABRI CIP0-1 performed in a sodium loop. In this case, the interaction effects were found to be small except for cladding hoop stress, fission gas release and the cladding failure indicator by fracture mechanical approach. Figure 1 shows example of the comparison of 1st order and total effect sensitivity indices with correlation coefficients for clad hoop stress.

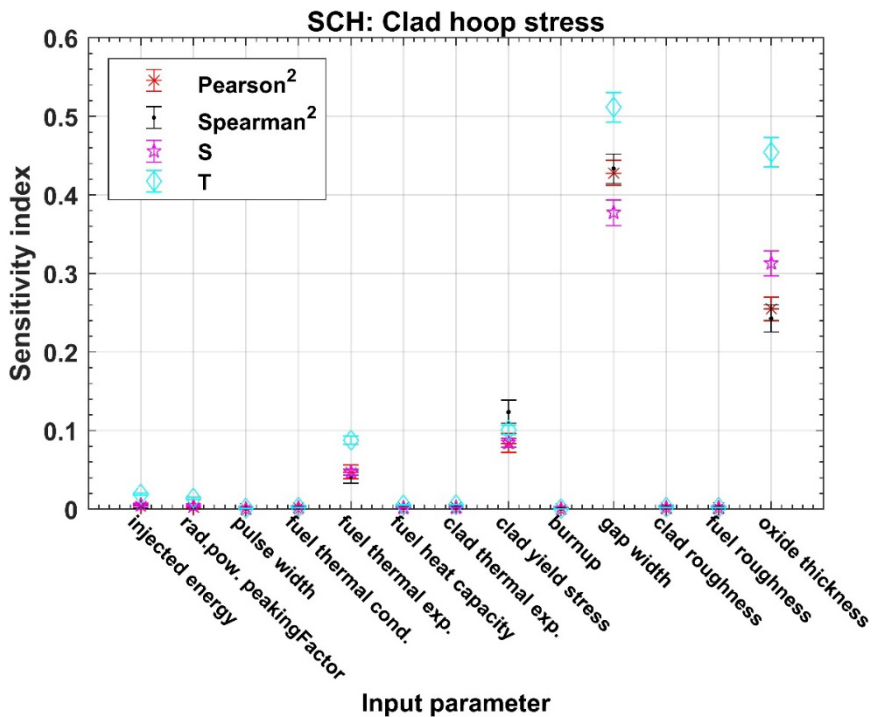


Figure 1. Comparison of 1st order and total effect sensitivity indices with correlation coefficients for clad hoop stress of irradiated fuel. If the first order Sobol' index "S" is equal to the total effect index "T", the underlying model is additive.

FINIX development

From initial basic modelling of the temperature distribution in fuel, FINIX currently can model many mechanical phenomena in fuel cladding, such as elastoplasticity and creep, and many complex phenomena in the pellet, such as fission gas release,

pellet densification and swelling. The approach of the development of FINIX is to be simple in modelling and in usage so that the code may find applications in a wide range of other codes. This is in contrast to many other multiphysics codes that strive for information in utmost detail from all possible sources to perform mechanistic predictions (e.g. BISON), or others that are simply modelling a specific phenomenon intended to be implemented within a certain code (Pizzocri et al., 2020).

In the years 2019–2020, the vast majority of effort put into FINIX has focused on enabling its performance in coupled applications. As such, two methods of FINIX restart were introduced with which the I/O of all FINIX data structures either via binary or ASCII files are possible, and as such the wrapper software SuperFINIX can run multiple FINIX simulations in steps at the same time while transferring files between FINIX simulations and the rest of the solvers in the Kraken calculation framework developed in the LONKERO project.

Improvements were done in error reporting and input checking functionality. Option to change rod internal gas contents within a simulation and the possibility to use cmake to compile the code were added. Other improvements consisted of implementations of new cladding material (FeCrAl), modified thermal property models for analysis of erbia-doped fuel pellets, modified cladding models for stress and strain, bug fixes, and computational optimizations. Figure 2 shows cladding inner surface temperature in CABRI REP-Na1 RIA test with FINIX, FRAPCON and FRAPTRAN with different variations in the base irradiation and transient modelling.

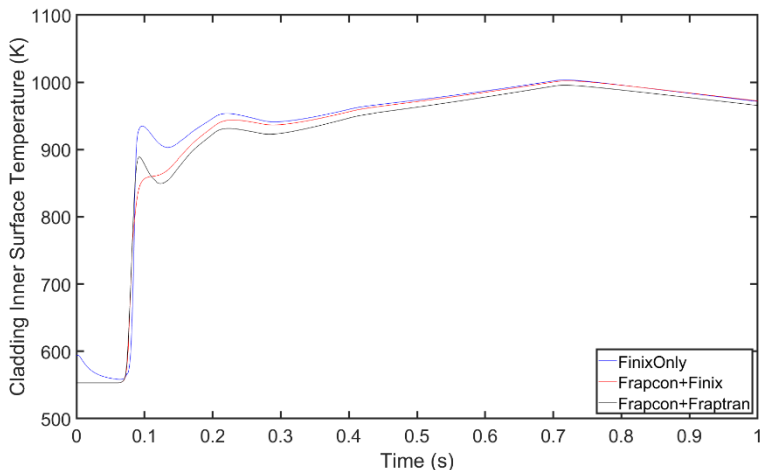


Figure 2. Cladding inner surface temperature in CABRI REP-Na1 RIA test with different code systems: base irradiation with FRAPCON and transient with FRAPTRAN as a reference, and base irradiation with FRAPCON or FINIX when transient is calculated with FINIX.

In 2021, MPI parallelization has been introduced to the coupled SuperFINIX calculations, thus reducing the computational bottlenecks of fuel performance

modelling in the coupled calculation chain. Optimization tests on stand-alone FINIX and coupled SuperFINIX were performed. The effect of different sub-models was studied on the computational time and on the output parameters. The work was performed as Markus' Master's thesis / diploma work for Aalto University.

A non-rigid pellet modelling was initiated to support mechanical modelling of fuel rods with harder cladding materials, such as ATF cladding materials. This will be further tested under the ATF-TS IAEA coordinated research project. In 2022, material correlations for LOCA were implemented into FINIX. Ballooning model was studied based on similar model in FRAPTRAN.

Modelling of Jules-Horowitz Reactor with Serpent

The research visit to CEA Cadarache was postponed due to the VTT travel ban caused by COVID. The original date of the secondment period was in the beginning of October. In January 2021 the project began in Finland, with the primary goalpost being the development of initial Serpent model for JHR. This model will be used for benchmarking purposes between Tripoli-4, MCNP and Serpent, after which the studies on the neutronic designs of JHR testing devices will be commenced. Among other topics, the optimization of OCCITANE experimental device will be performed with the Serpent model by calculating estimates for the spectrum ratio, fast neutron flux and gamma heating associated with the device. Figure 3 depicts the initial attempt at modelling JHR geometry with Serpent by utilizing the French GADGET-input script, whereas figure 4 depicts the relative capture cross section of JHR core with homogenized and simplified fuel rod assembly.

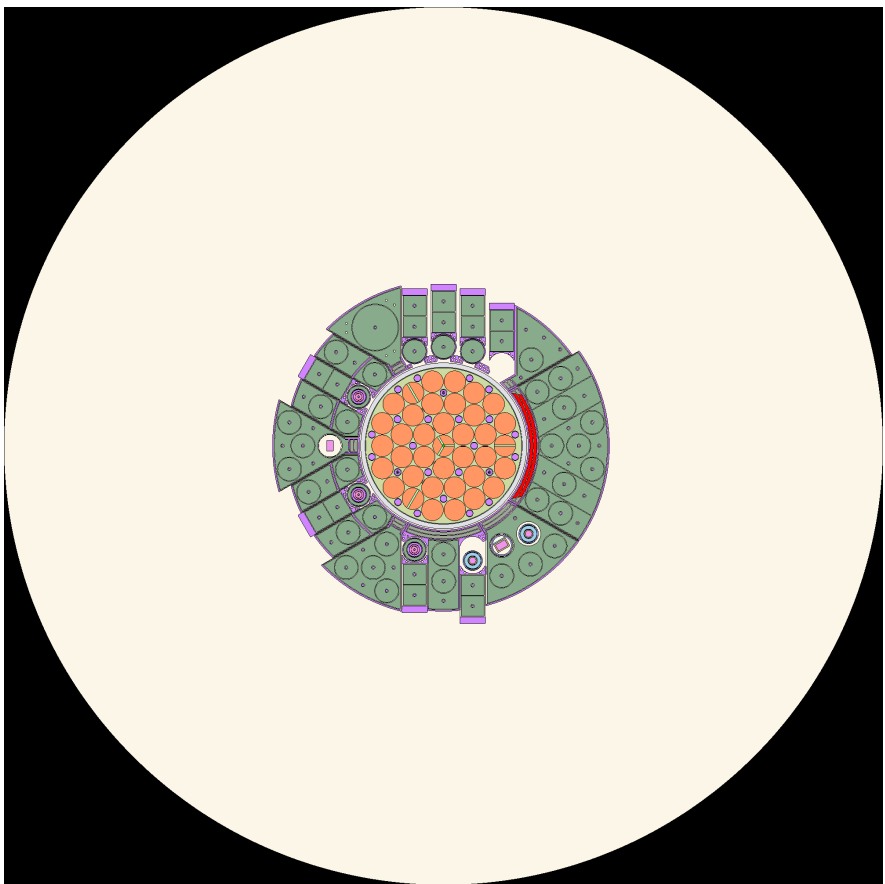


Figure 3. The initial attempt at modelling JHR geometry with Serpent by utilizing the French GADGET-input script.

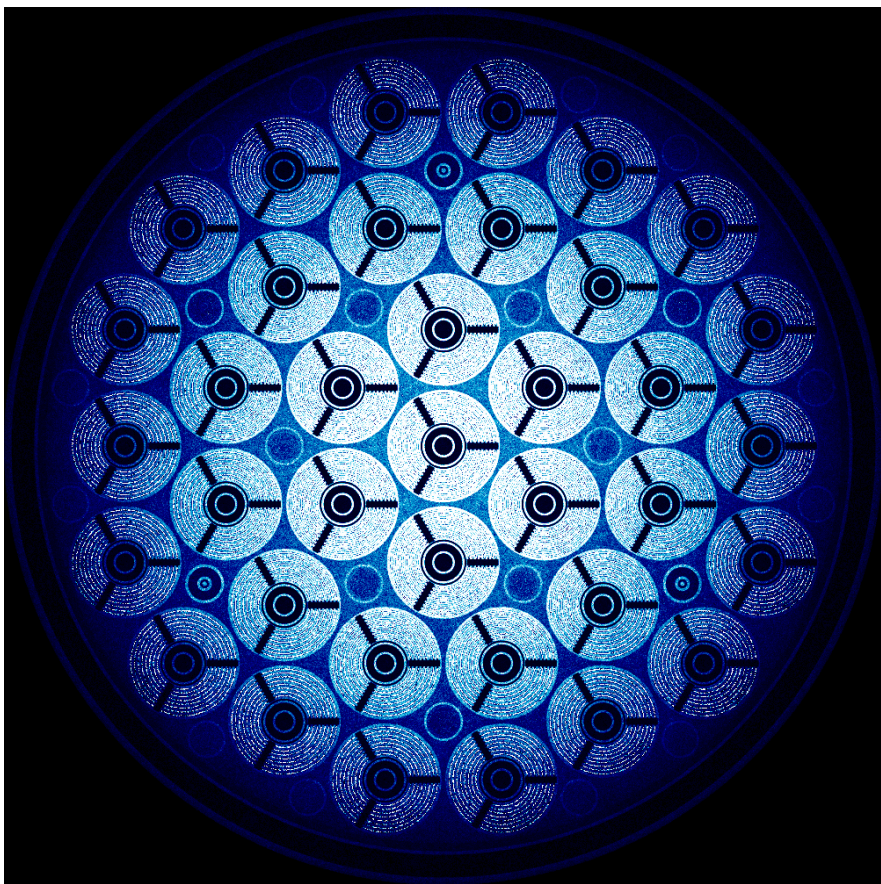


Figure 4. The relative capture cross section of JHR core with homogenized and simplified fuel rod assembly.

Mechanical tests

Creep, due to high temperature, stresses, radiation or a combination of these, is a significant degradation mechanism for nuclear fuel cladding during reactor operation and repository conditions. The fuel cladding material creep propagation may be affected also by other factors, e.g. waterside corrosion and hydrogen pick-up. ATF claddings, such as austenitic stainless steels and oxide dispersion strengthened (ODS) alloys, are designed to exhibit better creep resistance than zirconium-based alloys, which are widely used in currently operating light water reactors (Massey et al., 2016).

Creep testing of cladding materials is typically performed using internal pressure tests for thin-walled samples at elevated temperature. Although very significant creep is not expected for most ATF cladding types at normal operation conditions,

the current situation is that there is still inadequate amount of data available on the strain evolution in axial and hoop direction during creep.

A device for mechanical creep testing is already in use at VTT. In this project, the focus of the research is to use the device to perform creep tests on available advanced cladding material samples. At the first stage in 2019, the thermal creep experiments were carried out with DIN 1.4970 type austenitic stainless-steel claddings. In 2020, experiments continued with transient tests using DIN 1.4970 stainless steel. Tests were done with alternating pressure, hoop-axial pressure ratio and temperature.

The creep tested specimen was visually inspected and measured before and after the test (figure 5). No signs of significant damage were found from the specimen during the visual inspection and the dimension measurements did not indicate any significant creep evolution, e.g. ballooning in the middle of the gauge section.

The creep-to-rupture behavior of the specimen was assessed using the Larson-Miller modelling method. Figure 6 shows the hoop (circumferential) stress versus Larson-Miller parameter correlation for data from literature (Cautaerts et al., 2017), earlier VTT test data and the result of the test performed in 2020 (at 500 °C) together with Larson-Miller predictions and scatter bands of the assessed data. Because the latest test was performed with load transients, time weighted average hoop stress (364 MPa) was calculated for consumed creep exposure. The test was interrupted before rupture after 7359 h at the hoop stress level of 392 MPa. The model predicts that the creep to rupture for the test would have been 37178 h if the hoop stress of 392 MPa would have been maintained until the rupture. However, the increased axial stress level (due to additional axial load by the bellows) compared to the situation where the stress state would have been emerging solely from the internal pressure would have probably shortened the remaining time to a creep rupture.

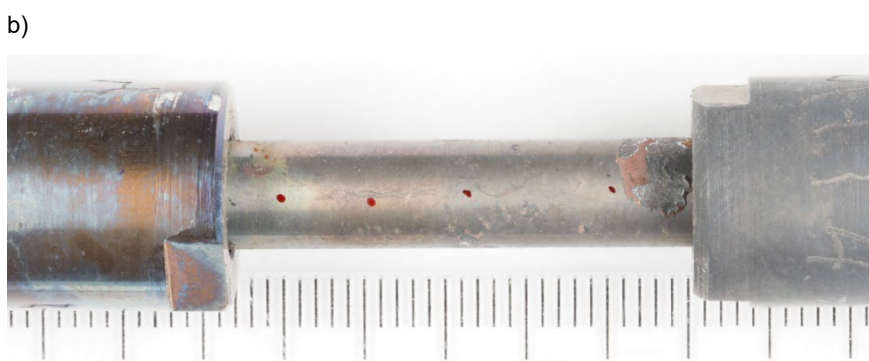


Figure 5. The creep specimen with length measurement in a) red dots indicating the diameter measurement locations in b) and black dots indicating the diameter measurement locations in c).

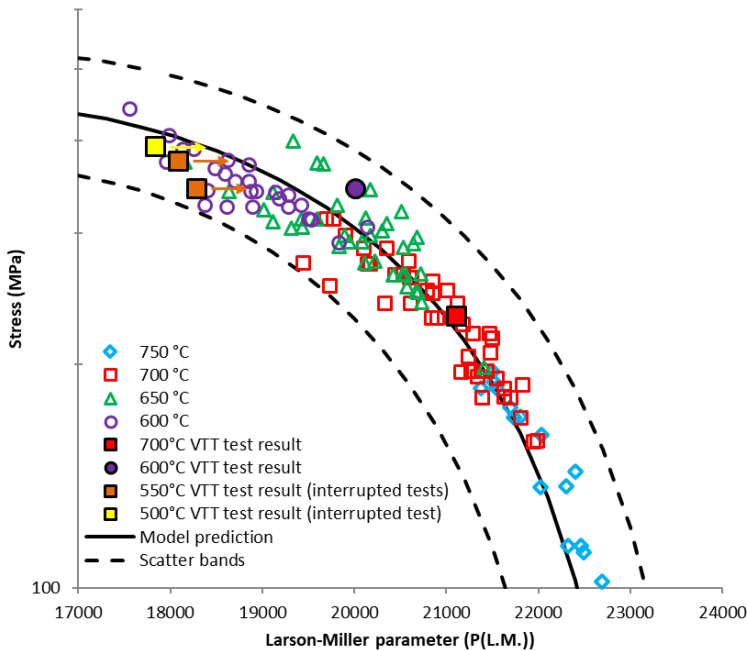


Figure 6. The hoop stress versus Larson-Miller parameter correlation for DIN 1.4970 material with data from literature (Cautaerts et al., 2017), earlier VTT test data and the result of the test performed in 2020 (at 500 °C) together with Larson-Miller predictions and scatter bands of the assessed data.

In 2021–2022, the goal of the task was to evaluate the thermal creep characteristics of the ATF cladding material with chromium-aluminium coating on the zirconium-based substrate tube. A similar plugging applied for a DIN-1.4970 tube failed for this kind of specimen. As a consequence, a new plugging technique based on welded joints was developed and tested, but unfortunately the new plugging method of the internal pressure creep test specimen was still unable to withstand the pressurizing, necessitating the termination of the experiment. A triple conical compressive joint and a supporting sleeve were included in the design for the next stage of the new mechanical plugging at the end of 2022, however the INFLAME project ran out of time to test this specimen.

Autoclave oxidation tests

VTT has developed a high temperature recirculation loop that has been previously used to study the corrosion of steam generator (SG) tubes under normal operating conditions (Huutilainen et al., 2018). The high temperature hot recirculation loop (figure 7) was adapted to simulate the relevant environment, in terms of thermal-hydraulic conditions and primary coolant chemistry, for fuel cladding. The effect of neutron irradiation has not been studied nor simulated with the high temperature

hot recirculation loop. The oxide's behavior and growth is monitored by online electrochemical measurements, such as electrochemical impedance spectroscopy (EIS) and linear polarization. EIS is a powerful technique for evaluating corrosion processes and providing invaluable data concerning the oxide, electrolyte and electric double layer properties.

A hot loop for testing material samples in controlled water chemistry and online oxidation measurement with electrochemical impedance spectroscopy already exists at VTT. However, the available heat flux over the sample in the existing device was only comparable to a low linear heat generation rate of the fuel. In 2019, the autoclave equipment was updated so that a linear heat generation rate of over 20 kW/m could be achieved with the apparatus. This enables testing of cladding materials in conditions relevant to a nuclear power reactor. The testing apparatus was verified by experiments on E110 cladding alloy material at around 300 °C. The impedance measurement performed well and the growth of the oxide layer could be distinguished from the test results. The connection of the impedance results to the oxide layer thickness were studied with the equivalent circuit (EQC) models. Boiling conditions were also investigated, and coolant boiling could also be distinguished from the impedance measurements, extending the applicability of the method.

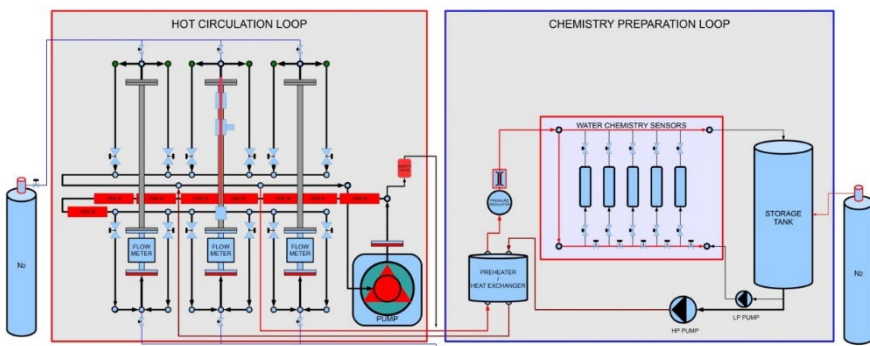


Figure 7. Schematic illustration of the high temperature hot recirculation loop (left side) and chemistry preparation loop (right side) used in this study.

In 2021 and 2022, the test results were further analysed, and EIS results were compared to scanning electron microscopy (SEM) images and oxidation correlations applied in fuel performance codes. Even though the EQC model can be tuned to represent the oxide thickness at the end of the experiment, the behavior of the oxidation growth rate remained spurious. It should be noticed that irradiation was absent in the experiments, which makes direct comparison of the oxidation rates impossible. Comparison of an EQC model and the oxidation correlations is shown in Figure 8.

Further, it is suspected that EQC model smaller thickness predictions are due to the sensitivity of the oxide capacitance parameter in the model towards the overlapping time constants in the EIS data. A more sophisticated EQC model and/or

a method for extracting the effects of the overlapping time constant would be required in order to improve the model predictions.

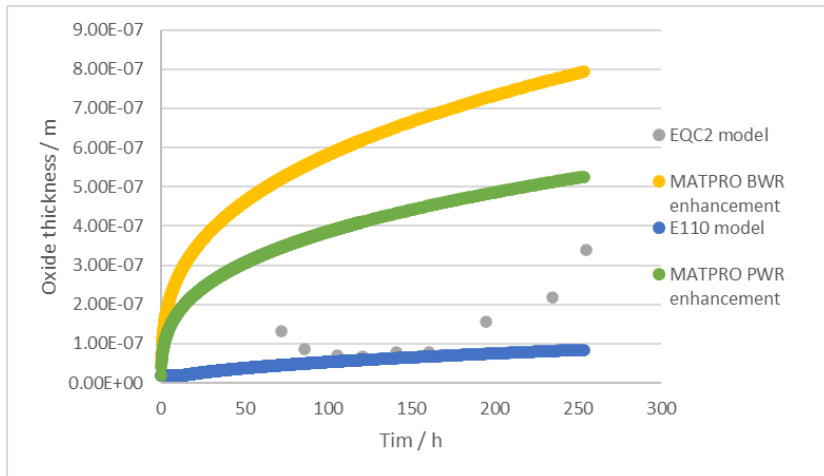


Figure 8. Comparison of oxide thicknesses based on EIS measurement and the computational models.

Steam furnace oxidation testing

High temperature steam testing are being performed for the selected ATF cladding materials in this part of the project. Cladding exposures are performed at different temperatures (1000–1600 °C) for different exposure times/experiment durations (from minutes to hours) to produce data on the oxidation of the tested materials with high temperature steam furnace system in VTT's Research Hall (figure 9). The test specimens are characterized using Light Optical Microscope (LOM) and SEM techniques, and the oxidation products will be analysed using SEM-EDS (energy dispersive spectroscopy). Test data is used for oxidation process modelling. Data on the oxide layer can also be obtained with glow discharge optical emission spectroscopy (GDOES), if necessary. The data can be used to improve the prediction capabilities of simulations in accident analyses and to increase understanding of accident evolution. Although the aim is to improve the cladding behavior in accident conditions, the materials are also studied to verify that the new claddings are not inferior compared to zirconium alloys during normal operation. A deeper understanding on oxidation mechanisms is created together with tests in normal LWR operating conditions. The exposure tests in LWR conditions are continued, with focus based on the most promising cladding solutions. Steam test samples are further characterized and modelling of oxide film thickness and hydrogen content as a function of depth is performed with the mixed-conduction model. Additional hydrogen pickup and desorption tests will be performed to gain a better understanding of uptake mechanisms and the behavior of hydrogen in

traditional and ATF cladding materials. The essential part of this activity is to contribute round-robin testing of new cladding material solutions within a new IAEA Coordinated Research Project (CRP) named Testing and Simulation for Advanced Technology and Accident Tolerant Fuels (ATF-TS). The scope is to test potential ATF cladding solutions in numerous international institutes with identical tests parameters.

Hot steam testing is a viable method for investigating the oxidation characteristics of cladding materials. Tests are performed at temperatures between 1200 and 1600 °C with variable exposure time, which gives data on oxidation behavior. This data can further be used in model development and validation. The technique is especially good for screening materials and for improved understanding of the oxidation mechanisms, but also for investigations under LOCA conditions.

VTT participated in the IAEA coordinated research program ACTOF (Analysis of Options and Experimental Examination of Fuels for Water-Cooled Reactors with Increased Accident Tolerance) with steam furnace oxidation testing of several advanced cladding materials in the past years. The results obtained at VTT in the research program were published in an IAEA TECDOC. From 2020 on, the experiments in steam environment continued for Zr-based coated claddings held at 1200 °C for 5 and 30 min. The coatings were pure Cr, CrN, CrAl and TiN. Many of the samples did not survive from the tests. Sample conditions after steam exposures with different hold times are shown in Figure 10. The weight gains measured for the samples are shown in Figure 11. In addition, sample pieces were inserted in hot loop with LWR primary water conditions at 320 °C for 500 hours. The behavior of the coatings was similar and indicated far less corrosion than the Zr1Nb reference sample.



Figure 9. High temperature steam furnace system in VTT's Research Hall.

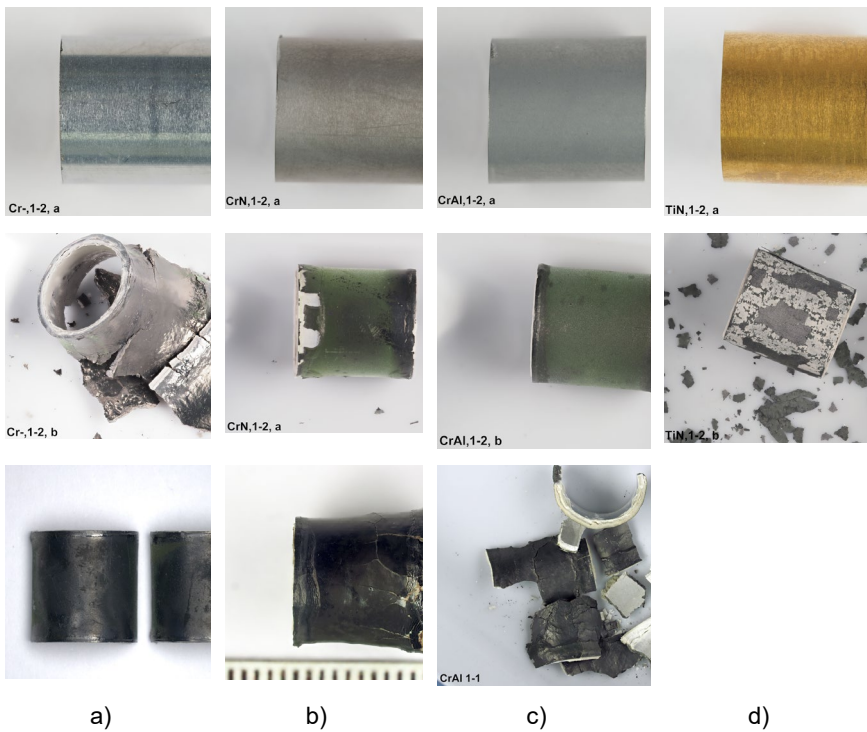


Figure 10. Columns represent a) Cr coated, b) CrN coated, c) CrAl coated, and d) TiN coated ZIRLO samples. Top row: before exposure; middle row: after 5-minute exposure; bottom row: after 30-minute exposure.

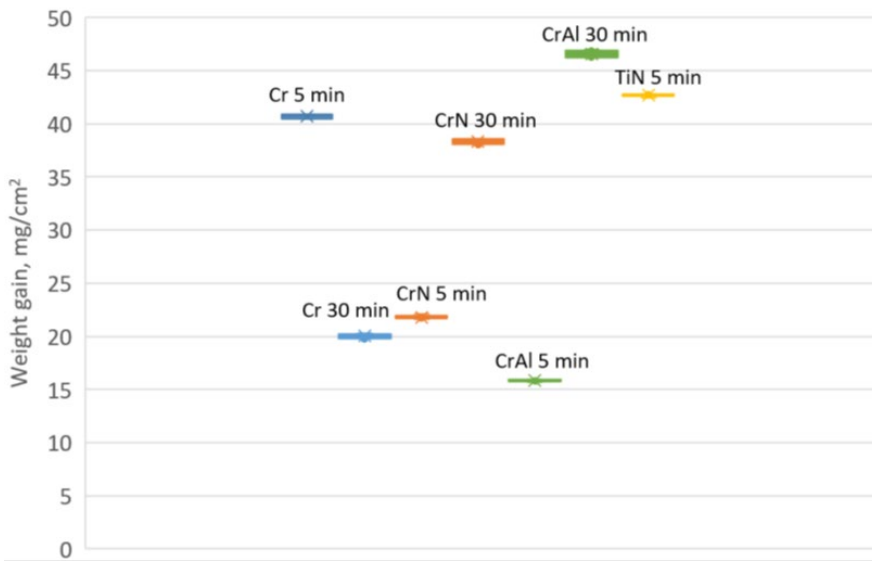


Figure 11. Weight gains of the coated ZIRLO samples after 5- and 30-minute exposures to 1200 °C flowing steam. TiN coated sample was not exposed for 30 minutes as the coating was fully delaminated already after the 5-minute exposure. It must be noted that due to breaking and flaking already in the furnace, all pieces could not be collected for weighing so the weight gains are more or less arbitrary.

Pellet annealing test equipment

The influence of chemical processes on the in-pile behavior of nuclear fuel is not very well understood. With increasing burnup, various chemical phenomena take place in the fuel rod, such as diffusion of fission products, formation of separate solid phases from an initially homogeneous material and vaporization of volatile elements from fuel. These chemical processes influence not only the material properties of the fuel but also of the cladding via gas phase diffusion and especially during hard contact between the pellet and the cladding. The possibility of damage to fuel due to pellet-cladding interaction (PCI) is a complex process involving both mechanical stress and active chemical processes. For example, iodine forms gaseous zirconium iodide (ZrI_4) which erodes the cladding and aids stress corrosion cracking (Cox, 1990). Additionally, in case of a defective fuel rod or in accident conditions, the chemical and physical properties determine the release behavior of radionuclides from the fuel.

An annealing furnace was obtained in 2019 for future testing of pellet materials at VTT (figure 12). During the course of the project, the furnace was tested at the VTT Centre for Nuclear Safety. A remote controller system was established for the furnace and temperature calibration tests were performed in 2020. The heating series up to 1700 °C is illustrated in figure 13.



Figure 12. Furnace opened prior to the acceptance tests. The MoSi₂ resistive heating elements are attached to the furnace top cover. The sample tube lies on the bottom part of the furnace.

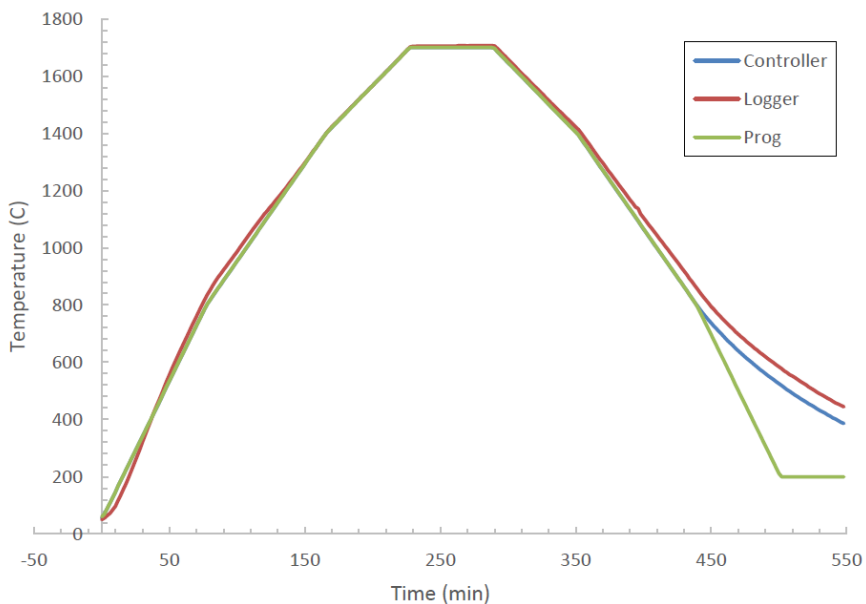


Figure 13. Temperature evolution during the programmed temperature cycle. The target temperature was 1700 °C and the ramp rate below 800 °C was 10 °C/min, at 800 °C < T < 1400 °C, 7 °C/min, and at 1400 °C < T < 1700 °C, 6 °C/min. The final temperature was 200 °C. The temperature cycle “Prog” was followed with the “Controller” thermocouple. The actual temperature inside the specimen tube was measured with a separate thermocouple “Logger”.

Non-radioactive CeO₂ has been previously applied in fuel pellet related experiments due to the same crystallographic structure and similar mechanical properties as UO₂ (García-Ostos et al., 2016; Khafizov et al., 2019; Pakarinen et al., 2015; Yablinsky et al., 2015). Under the pellet task, we applied CeO₂ powder as surrogate material for UO₂. The CeO₂ powder was mixed with CsI powder and pressed into pellets. Annealing experiments were performed for non-sintered and SPS sintered pellets.

In 2020, the first tests for CsI doped CeO₂ pellets were performed at high temperatures, and iodine and particle release were monitored. Sample for the calibration measurements was prepared with a cylindrical die and applying compression of 6 kN. The sample contained 30w% of CsI and 70w% of CeO₂ powder. First, two sample pellets were annealed to 1100 °C and cooled down. Iodine and particle measurements were applied during the heating cycle. The same samples were heated again to 1300 °C, while applying iodine and particle measurements. The goal was to observe sensitivity limits for the iodine on-line measurements as well as monitor iodine release during conventional sintering procedure. The second set of samples were sintered with the spark plasma sintering (SPS) device. The samples contained 1mol% of CsI and they were sintered at 900 °C, 1000 °C and 1100 °C. Annealing experiments for iodine release were performed up to 1500 °C while monitoring iodine and particle release via their transport through the experimental setup. The densities of the samples were 0.70%, 0.75%, and 0.76% of the theoretical maximum density, respectively. The spark plasma sintering procedure of the pellets and the density measurements were performed at Charles University (Czech Republic). Figure 14 represent the iodine release behavior measured with Inductively Coupled Plasma Mass Spectrometry (ICP-MS) for the SPS samples.

Finally in 2021 and 2022, the SEM imaging and sample preparation procedure was taken in use for UO₂ pellet samples. This includes grain characterization with SEM and preparation of cross-cut specimens for microscopy analyses. Different kinds of UO₂ pellets were imaged with SEM. A CsI doped CeO₂ sample was cut, and the following polishing procedure was estimated from the sample surface quality point of view. As a result, detailed SEM imaging can be performed for unirradiated UO₂ samples at VTT's Centre for Nuclear Safety building.

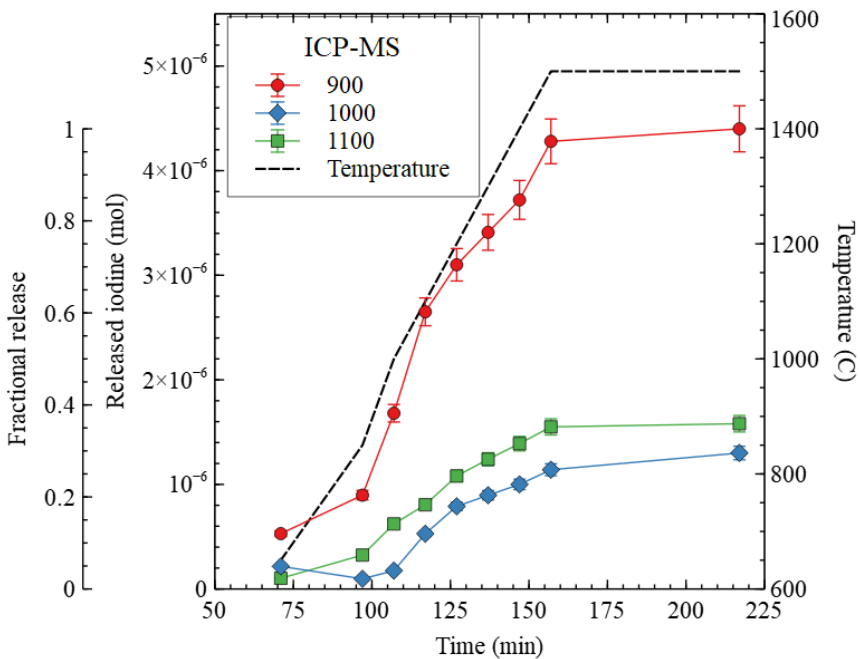


Figure 14. Released iodine measured with the ICP-MS method with sample outer surface-to-volume ratio and mass normalized against the SPS-900 sample data. The complete fractional release of 1 is set for the SPS-900 series maximum.

References

- Cautaerts, N., Delville, R., Dietz, W., Verwerft, M., 2017. Thermal creep properties of Ti-stabilized DIN 1.4970 (15-15Ti) austenitic stainless steel pressurized cladding tubes. *Journal of Nuclear Materials* 493, 154–167. <https://doi.org/10.1016/j.jnucmat.2017.06.013>
- Cox, B., 1990. Pellet-clad interaction (PCI) failures of zirconium alloy fuel cladding - A review. *Journal of Nuclear Materials* 172, 249–292. [https://doi.org/10.1016/0022-3115\(90\)90282-R](https://doi.org/10.1016/0022-3115(90)90282-R)
- García-Ostos, C., Rodríguez-Ortiz, J.A., Arévalo, C., Cobos, J., Gotor, F.J., Torres, Y., 2016. Fabrication and characterization of CeO₂ pellets for simulation of nuclear fuel. *Nuclear Engineering and Design* 298. <https://doi.org/10.1016/j.nucengdes.2015.12.026>
- Huutilainen, C., Ikäläinen, T., Peltonen, S., Saario, T., Sipilä, K., 2018. In-situ monitoring of stainless steel AISI 316L corrosion behavior under PWR secondary side thermal hydraulic and heat transfer conditions, in: 21st Inter-National Conference on Water Chemistry in Nuclear Reactor Systems.

- Khafizov, M., Pakarinen, J., He, L., Hurley, D.H., 2019. Impact of irradiation induced dislocation loops on thermal conductivity in ceramics. *Journal of the American Ceramic Society* 1–10. <https://doi.org/10.1111/jace.16616>
- Massey, C.P., Terrani, K.A., Dryepondt, S.N., Pint, B.A., 2016. Cladding burst behavior of Fe-based alloys under LOCA. *Journal of Nuclear Materials* 470, 128–138. <https://doi.org/10.1016/j.jnucmat.2015.12.018>
- Ikonen, T., Tulkki, V., 2014. The importance of input interactions in the uncertainty and sensitivity analysis of nuclear fuel behavior. *Nuclear Engineering and Design*, Vol. 275, pp. 229-241.
- OECD/NEA, 2017. Reactivity-initiated Accident Fuel-rod-code Benchmark Phase II: Uncertainty and Sensitivity Analyses. NEA/CSNI/R(2017)1.
- Pakarinen, J., He, L., Hassan, A.-R., Wang, Y., Gupta, M., El-Azab, A., Allen, T.R., 2015. Annealing-induced lattice recovery in room-temperature xenon irradiated CeO₂: X-ray diffraction and electron energy loss spectroscopy experiments. *Journal of Materials Research* 30, 1555–1562. <https://doi.org/10.1557/jmr.2015.13>
- Pizzocri, D., Barani, T., Luzzi, L., 2020. SCIANTIX: A new open source multi-scale code for fission gas behaviour modelling designed for nuclear fuel performance codes. *Journal of Nuclear Materials* 532, 152042. <https://doi.org/https://doi.org/10.1016/j.jnucmat.2020.152042>
- STUK, 2019. Nuclear fuel and reactor, 15.3.2019, YVL B.4, <https://www.stuklex.fi/en/ohje/YV рLB-4> (visited 19 Feb 2021)
- Yablinsky, C.A., Devanathan, R., Pakarinen, J., Gan, J., Severin, D., Trautmann, C., Allen, T.R., 2015. Characterization of swift heavy ion irradiation damage in ceria. *Journal of Materials Research* 30, 1473–1484. <https://doi.org/10.1557/jmr.2015.43>

4.3 Developing the working arms of Kraken, the next generation computational framework for reactor design and licensing analyses (LONKERO)

Ville Valtavirta,
Jaakko Leppänen, Markus Hirvensalo, Ville Hovi, Rebekka Komu,
Topias Kähkönen, Unna Lauranto, Jussi Peltonen, Antti Rintala,
Ville Sahlberg, Riku Tuominen

VTT Technical Research Centre of Finland Ltd
P.O. Box 1000, FI-02044 Espoo

Abstract

A modern Finnish reactor analysis framework, Kraken was developed for light water reactor analyses. The capabilities of Kraken were demonstrated by validating the framework for VVER-1000 fuel cycle and coolant transient analyses using international benchmarks with measured data from real world reactors. Kraken development provides the tools and expertise for future safety analyses of Finnish reactors.

In addition to developing Kraken as a whole, the nodal neutronics program Ants was extended in the project from static neutronics calculations to fuel cycle and transient simulations considering feedback effects from thermal hydraulics and fuel behaviour solvers. Ants is now also able to predict spent fuel nuclide compositions and the activation of in-core structural materials.

Small modular reactor models were routinely utilized in the testing and demonstration of modelling capabilities, including the evaluation of licensing relevant data during operating cycle analyses.

Introduction

The excellence project LONKERO answers the need stated in the SAFIR2022 Framework Plan regarding the development of a new set of advanced codes for reactor and nuclear power plant analysis. The focus in LONKERO is especially on developing a new computational reactor analysis framework leveraging the new generation of Finnish solvers for reactor core physics such as the Serpent Monte Carlo particle transport code, the Ants nodal neutronics code and the FINIX fuel behaviour module. This Kraken-framework is developed in LONKERO for future use in deterministic safety analyses of current and upcoming reactor concepts. Furthermore, Kraken is to be usable as a research and design tool that can be applied to a wide variety of reactor core related research problems including the design of new reactor concepts.

Kraken needs to be able to conduct steady state, operating cycle and transient analyses both at the core level and coupled to system codes that model the

feedback of the power plant itself. Achieving this goal in only four years when starting from separate solver codes in various states of development requires a significant amount of effort. Furthermore, the benchmarking and validation of the different capabilities of Kraken also need to be started as soon as the implementation of each capability is finished.

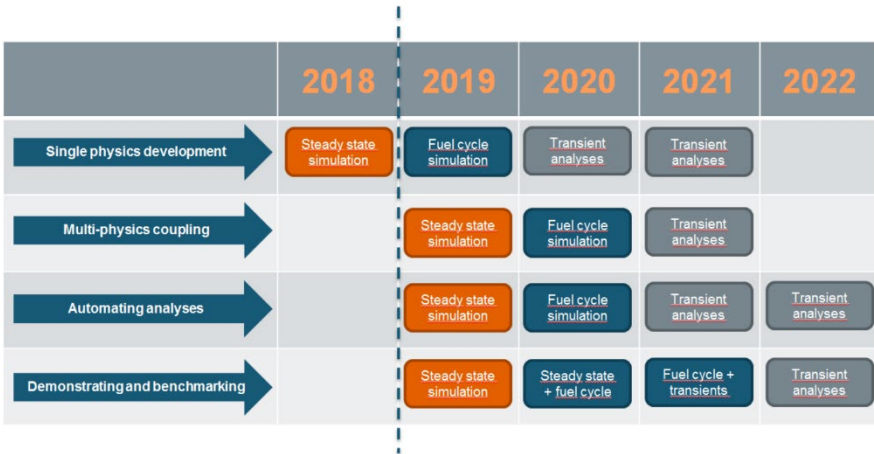


Figure 1. A high level overview of the four year plan for the development, demonstration and benchmarking of the Kraken framework.

In order to manage the construction of a complete reactor simulator in such a tight schedule, a rapid development pace has been set in the LONKERO project. An overview of this development schedule is given in Figure 1. The first year of the project focused on the coupled reactor core level solution in steady state while the second year had its focus in creating a core simulator capable of operating cycle simulations. Years 2021 and 2022 focus on extending Kraken's capabilities to transient analyses, initially at the core level and then coupled to a system code.

One of the design goals for the Kraken framework was to construct the framework in a modular fashion so that the solver for one core physics can be swapped to another with minimal effect on the other solvers and on the simulation model as a whole. This enables the verification of reduced order solutions (e.g. nodal diffusion neutronics) against high fidelity solutions of the same physics (e.g. Monte Carlo neutronics) without having to change the simulation models for the two other physics (thermal hydraulics and thermal mechanics). Figure 2 shows a schematic of the planned couplings for the Kraken framework: Solver modules for the three reactor core physics (neutronics, thermal hydraulics and thermal mechanics) are coupled together via a reactor core level interface to create a core simulator. This core simulator is further coupled with system codes in the future in order to simulate transients with system level feedbacks. While Kraken is mainly built on the new

generation of Finnish solvers, the coupling to existing national and international state-of-the-art solvers is also enabled by the design choices.

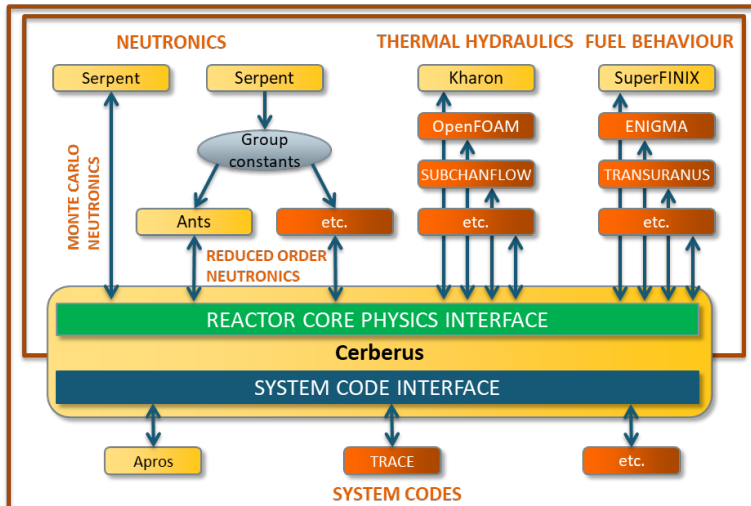


Figure 2. A schematic representation of the plans for the completed Kraken framework. Finnish solver modules developed at VTT are shown in yellow, while potential state-of-the-art third party solvers to be coupled are shown in orange.

At the beginning of the four-year excellence project, the individual core physics solver modules were available in various states of development, but could not be used together to solve the coupled problem between neutronics, coolant flow and fuel behaviour. Therefore, the first goal of the project was to establish a common communication syntax between the solvers and the multi-physics driver module Cerberus and implement basic communication capabilities in the individual solver modules. This was achieved for stationary applications in 2019, for burnup calculations in 2020 and for transient simulations in 2021. A 37 fuel assembly small modular reactor core model was widely utilized in the testing and demonstration of the framework, with validation against data from large LWRs conducted towards the end of the project.

Developing the nodal neutronics program Ants

The nodal neutronics code acts as the neutronics workhorse in a wide range of reactor core level analyses such as fuel cycle simulations and transient calculations. Before LONKERO, a wide range of application specific Finnish nodal neutronics codes had been used such as

- HEXBU for VVER-440 burnup calculations.
- HEXTTRAN for VVER-440 transient calculations.
- TRAB3D for BWR transient calculations.

- ARES for BWR and EPR burnup calculations.

As an answer to the giant effort needed to maintain both the wide set of separate legacy codes and the expertise related to them and to have a capable solver applicable for new reactor types such as upcoming SMRs and the AES-2006 a modern nodal neutronics program **Ants** began its development in 2017, before LONKERO.

At the start of the project, Ants included nodal models for stationary multigroup calculations of rectangular lattice and hexagonal lattice problems. Missing were the burnup and transient capabilities as well as couplings to thermal hydraulics and fuel behaviour required for analyses concerning real world reactors. LONKERO invested significant effort into the further development of both Ants itself and the group constant generation process that uses Serpent to evaluate the homogenized few group neutronics input data required by Ants.

Pin power reconstruction for Ants

In order to evaluate fuel rod level power peaking and eventually thermal margins, pin power reconstruction capabilities were implemented in Ants for rectangular lattice and hexagonal lattice. The rectangular lattice were verified against Serpent reference solutions in the fresh core Westinghouse type PWR of the BEAVRS benchmark:

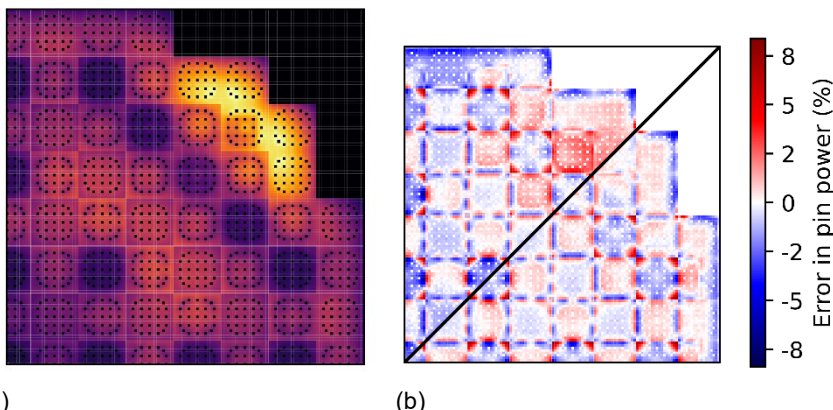


Figure 3. Results from computational validation for pin power predictions at hot-zero-power of the BEAVRS core in the beginning of cycle 1 (seven control rod banks inserted). (a) Serpent predictions for pin powers. (b) Pin power errors ($\text{Ants}/\text{Serpent} - 1 \times 100\%$) including (top left) and cleaned of (bottom right) assembly power errors.

The square lattice pin power results of Figure 3 were first published in a conference paper and later in an invited journal article as a part of a wider range of hot zero

power validation of Kraken for square lattice PWRs using data from the BEAVRS benchmark.

The hexagonal lattice pin power reconstruction capabilities were implemented later in the project together with the methodology in the KrakenTools Python package to evaluate the hexagonal lattice pin power form functions (input data for Ants) using a combination of data from Serpent and Ants. Verification work for the hexagonal lattices pin power reconstruction covered both VVER-440 and VVER-1000 full core models.

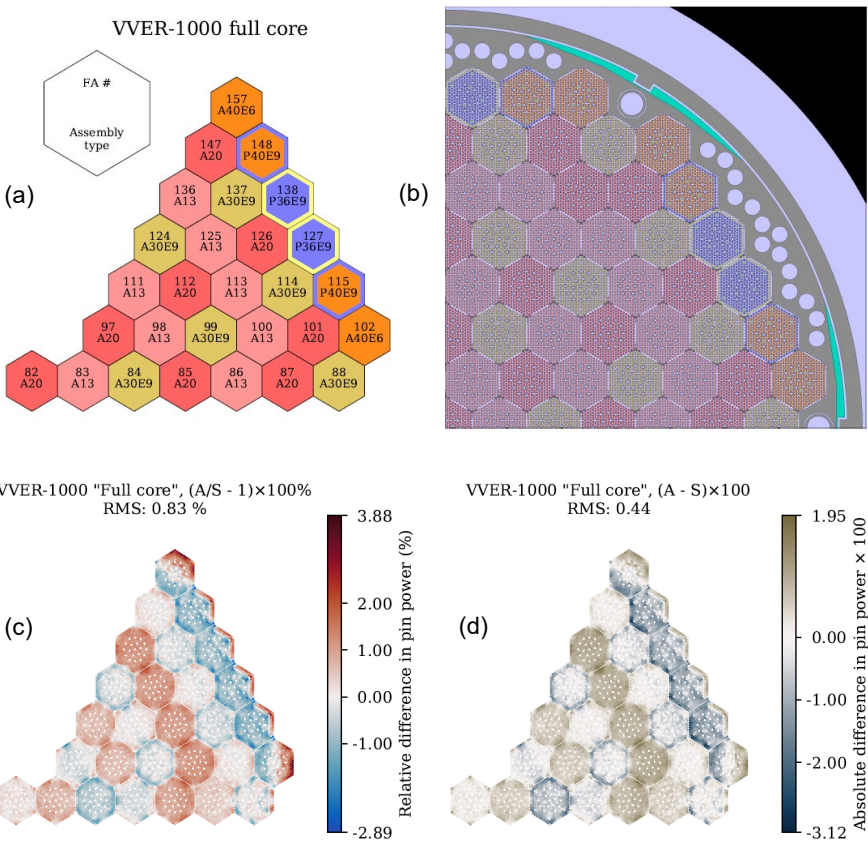


Figure 4. Results from computational validation for pin power predictions using the VVER-1000 “Full core” benchmark. (a) Core loading (1/6 shown). (b) Serpent geometry plot of the model. (c) Relative pin power errors ($\text{Ants}/\text{Serpent} - 1 \times 100\%$). (d) Absolute pin power errors ($\text{Ants} - \text{Serpent}) \times 100\%$

The results of the hexagonal pin power capabilities of Ants were published as a journal article with Figure 4 giving an example of the results. In these fresh core hot zero power models, Ants performed very well against the Serpent reference.

Evaluating rod level thermal margins

As Ants was able to evaluate the reactor power distribution at the level of individual pins and as the SuperFINIX fuel behaviour module could model each fuel rod in a reactor individually, it became possible to calculate rod level data required for thermal margin evaluation. A subchannel level thermal hydraulic solution was still needed and was obtained by coupling the SUBCHANFLOW solver to Kraken.

The Ants-SuperFINIX-SUBCHANFLOW calculation sequence of Kraken was then applied to modelling the first fuel cycle of the PWR in the BEAVRS benchmark, evaluating rod level data during the calculation. Maximum fuel temperatures, minimum cladding temperatures and minimum departure from nucleate boiling ratios (DNBRs) were evaluated at each point in the fuel cycle.

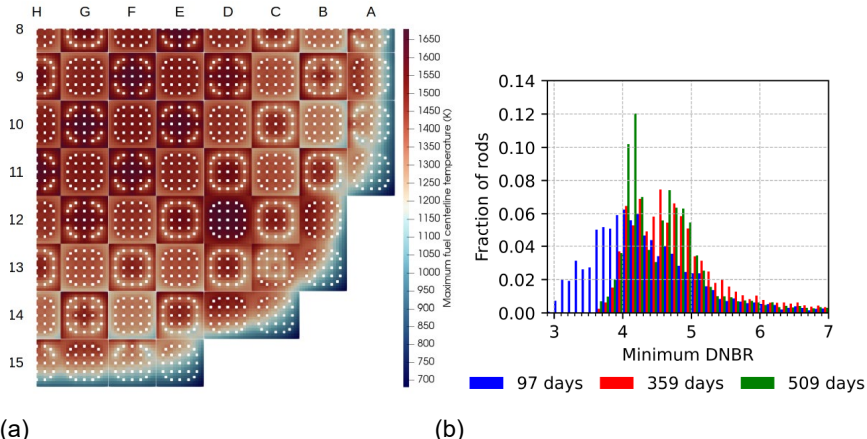


Figure 5. Evaluation of rod level data for the BEAVRS PWR using Ants-SuperFINIX-SUBCHANFLOW. (a) Maximum fuel rod centerline temperatures at 97 days. (b) Evolution of rod level minimum DNBR distribution during the fuel cycle, three time points shown.

Figure 5 shows the maximum fuel rod centerline temperatures early in the first fuel cycle of the BEAVRS reactor as well as the evolution of the rod level minimum DNBR distribution between 97 calendar days and 509 calendar days. Clearly the DNBR margins are lower early in the cycle, owing largely to the more aggressive power peaking in the beginning of the cycle, which is reduced with the accumulation of burnup. The pin level BEAVRS results were published as a journal article and the work continued by investigations to the use of a hybrid fidelity model where only certain regions of the core were solved at pin level, leading to a reduced computational effort.

Extending Ants to time dependent simulations

The neutronics solution for fuel cycle simulations could be solved with the time independent nodal models of Ants, but the modelling of reactor transients required time dependent nodal models. The development of such models to an advanced multi group code such as Ants was not a trivial task but was successfully achieved. This allowed Ants to solve time dependent neutron kinetics and neutron dynamics problems using any of the nodal models in Ants (rectangular, hexagonal and triangular).

The capabilities were validated against well known international benchmark considering both square lattice and hexagonal lattice cases first as a Master's thesis and later extended to a journal article.

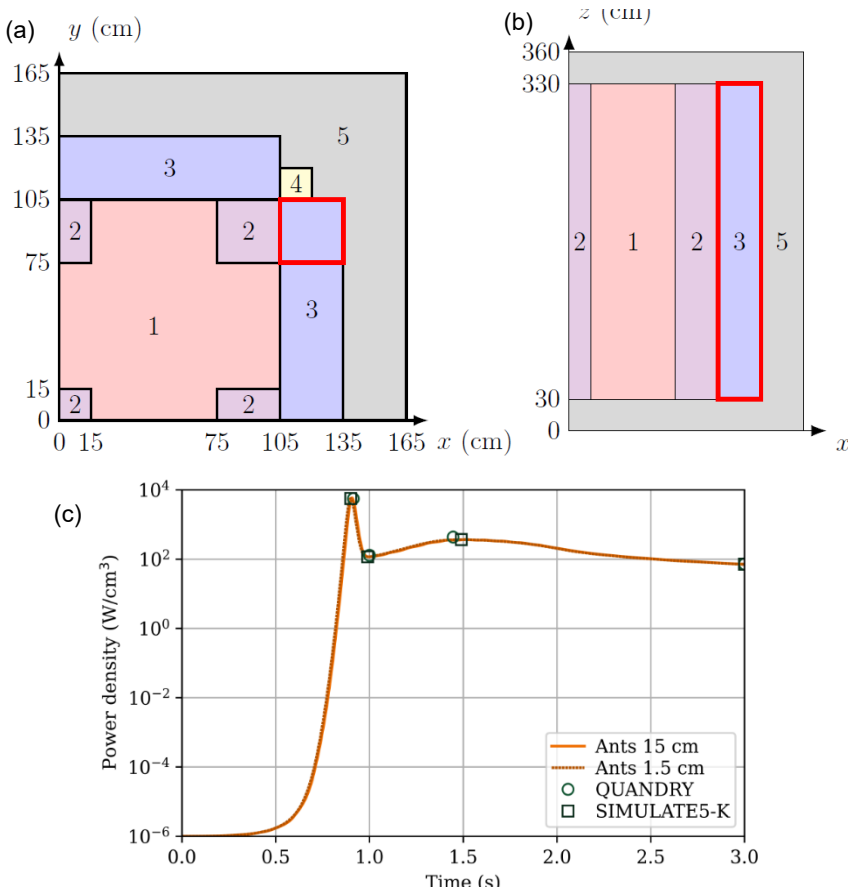


Figure 6. Horizontal (a) and vertical (b) geometry of the LRA BWR control rod drop benchmark. The position of the dropped control rod is indicated with a red box. The time dependent power after the control rod drop (four rod case) evaluated by Ants and two other nodal codes are shown in (c).

An example of the time dependent validation of Ants is shown in Figure 6, in the LRA computational benchmark mimicking a control rod drop in a BWR. The time dependent nodal models of Ants generally performed very well, but the results of the AER-DYN-001 benchmark highlighted the need to develop a robust and accurate treatment for control rod cusping in the code.

AER-DYN-001 is a control rod ejection reactor kinetics benchmark problem in which one control rod is ejected from a VVER-440 core followed later by reactor scram. The correct treatment of axial discontinuities such as that between the VVER-440 control rod and fuel follower in nodal codes requires either very detailed nodalization or additional runtime treatment such as axial homogenization.

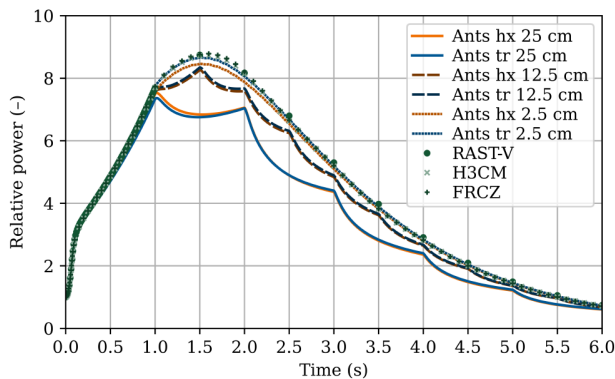


Figure 7. Solutions to the AER-DYN-001 VVER-440 control rod ejection benchmark by Ants (different nodal models and node heights) as well as other nodal codes.

Figure 7 shows nicely that Ants could model the transient well if a small enough node height was used, but larger node heights led to a clearly visible cusping effect with reduced predictive accuracy. During the last project year, a significant effort was put into developing a robust axial homogenization model for Ants, a process still ongoing at the end of the project.

Predicting spent fuel compositions with Ants

The nuclide composition of spent fuel and the activation of fuel assembly structural materials need to be evaluated in order to plan for the safe handling, transport and final disposal of spent fuel. Before LONKERO, the main Finnish tool for such analyses was the Monte Carlo code Serpent, an accurate but computationally costly high fidelity tool which meant that the evaluation needed to be conducted using 2D single assembly infinite lattice models applying some limiting case operating history data from a reactor simulator code. This makes it difficult to estimate 3D effects or correlations between different fuel assemblies coming from the same reactor core.

Building on the treatment of important fission products (^{135}Xe and ^{149}Sm) as well as the treatment of history effects in Ants, a generic microscopic depletion

(microdepletion) approach was implemented in the Serpent-Ants calculation chain. This allowed Ants to track a chosen set of nuclides, modelling their production and loss in neutron induced reactions as well as their radioactive decay resulting in the capability to evaluate nuclide inventories for spent fuel and related structural materials.

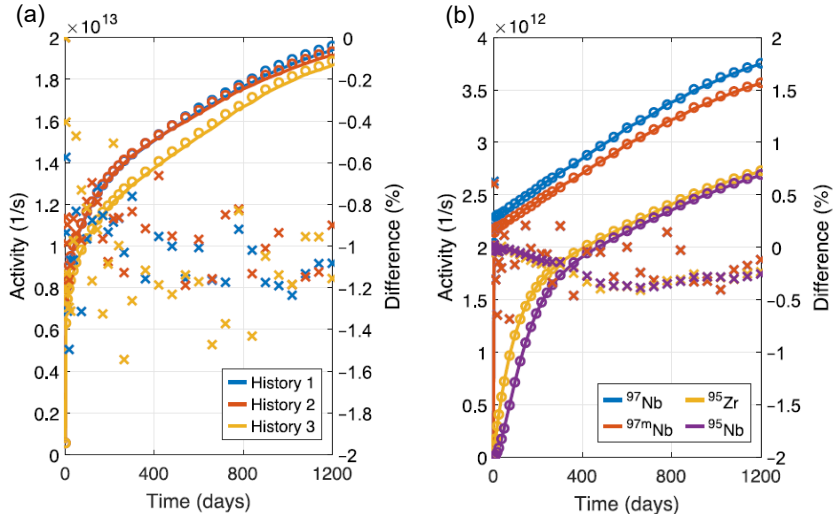


Figure 8. (a) Total activity of cladding material in a PWR assembly model in different historical operating conditions. (b) Activity of specific important nuclides in the PWR cladding (historical conditions 1).

Ants (solid line), Serpent reference (circle) and relative difference (x).

The development and implementation work as well as the initial verification against a Serpent reference solution for cladding activation in PWR conditions were published as a journal article. Figure 8 shows an example of the performance of Ants (solid lines) against Serpent (circles) in the PWR cladding activation evaluation.

The cladding activation did not require Ants to consider fission products and was overall a simpler problem than the prediction of spent nuclear fuel compositions. The latter problem was tackled during the final year of the project in a Master's thesis (together with SAFIR-RACSA and KYT-KÄRÄHDE), in which the methodology and its demonstration were extended to PWR spent fuel compositions, first in a single assembly 2D case and then in a full core 3D SMR problem.

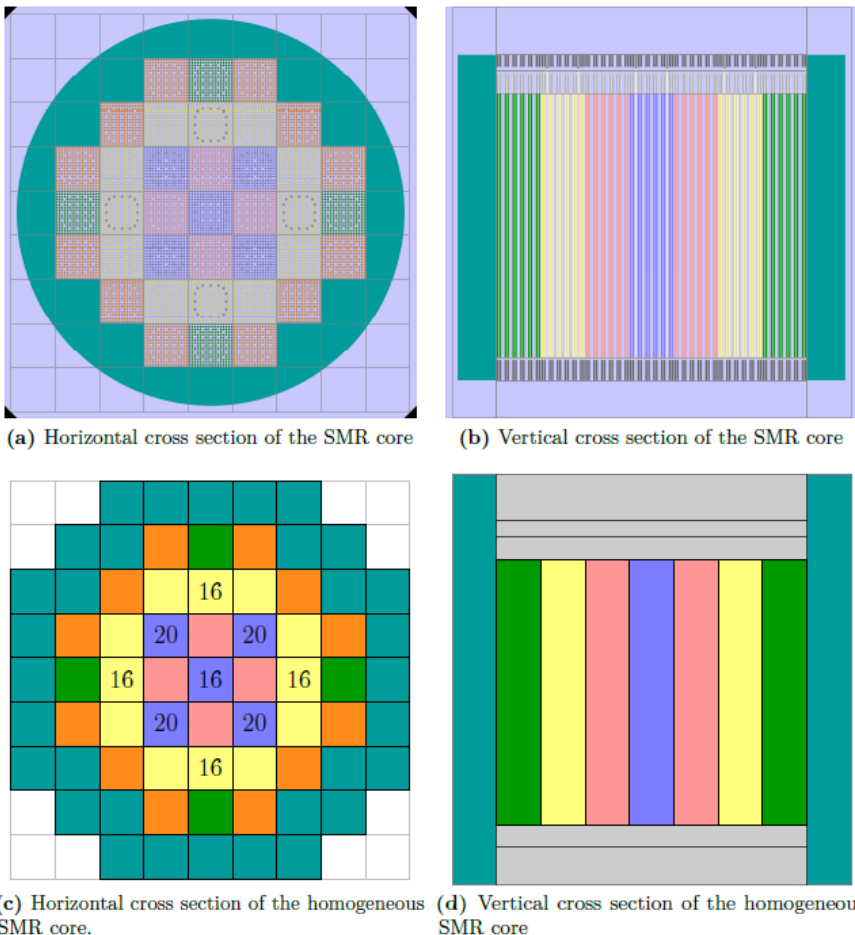


Figure 9. Heterogeneous (Serpent) and homogeneous (Ants) geometry models of the 37 fuel assembly SMR core used for the fuel microdepletion verification.

The 3D SMR problem utilized a two metre active height 37 fuel assembly model widely used in Kraken demonstration and verification during the project. The geometry of the core is shown in Figure 9 for both the Serpent reference model and the Ants model being verified. The required microdepletion input data was generated for Ants as a part of the normal group constant generation process with Ants following the concentrations of 1463 nuclides, 376 of which had evaluated data for their neutron interaction cross sections. Overall, 4346 reactions transmuting nuclides to others were modelled. The reactor core was depleted up to 640 days with 160 MW thermal power.

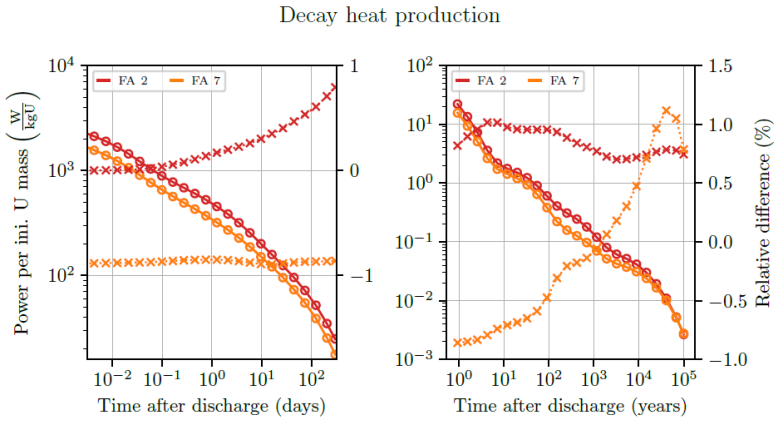


Figure 10. Decay heat production in fuel assemblies 2 and 7 of the SMR core, comparison between Ants (solid lines) and Serpent (circles), showing relative difference in the predictions (x).

A thorough verification of the Ants microdepletion model was conducted in the thesis with comparisons of the reactivity and fluxes between the Ants and Serpent calculations to provide baseline information of the to-be-expected differences. The total activity, decay heat production (Figure 10), gamma source rate and spontaneous fission rate were compared between Ants and Serpent at full core level and for two specific assemblies in the core. Ants had a very good accuracy in predicting the decay heat production at assembly level with differences below 1.2%.

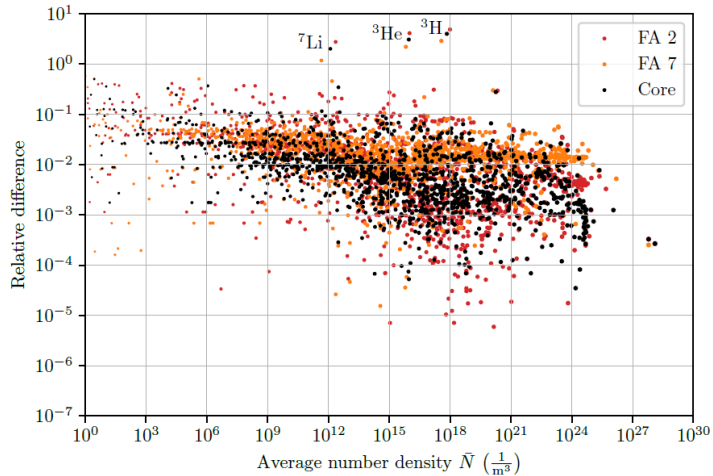


Figure 11. The average number density of each nuclide species calculated with Ants and their relative difference compared to the Serpent reference calculation in fuel assemblies 2 and 7 of the SMR core, comparison between Ants (solid lines) and Serpent (circles), showing relative difference in the predictions (x).

The spent fuel compositions were also compared at the level of individual nuclides (Figure 11) showing a generally good agreement between Ants and Serpent. Large differences were seen for a few light nuclides, but these have since been found to be a result of a programming error, with those differences greatly reduced after fixing the error.

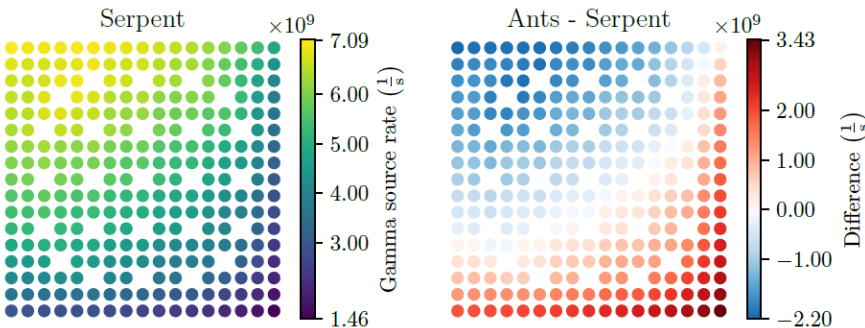


Figure 12. Reference spatial gamma source rate and the absolute difference resulting from assuming the Ants nuclide distribution to be spatially homogeneous inside the calculation node. A peripheral assembly from the SMR case.

The thesis work highlighted the fact that microdepletion approach of Ants does not consider the spatial distribution of the nuclides inside the Ants calculation nodes. When utilizing the Ants predictions in secondary Serpent analyses, a methodology for which was developed in the work, the simplest assumption to make related to the spatial distribution is to assume it homogeneous. This evidently leads to errors in e.g. the gamma source rate (Figure 12) that would be used in shielding calculations related to the spent fuel handling. The effects of this approximation on calculated unshielded gamma dose rates one metre from the assembly were evaluated as a part of the thesis work. Distributing the nuclides with the help of e.g. pin burnups obtainable from Ants could be a better approximation to be investigated in the future.

Validating Kraken for VVER-1000 fuel cycle simulations

LONKERO aimed to develop a new Finnish reactor analysis framework that can be used for the safety analyses of current and future Finnish NPPs. To demonstrate the capabilities required for such analyses, both the fuel cycle simulation capabilities and the transient capabilities of Kraken were validated using real world reactor data. The focus during the project was on showing capabilities applicable to the Hanhikivi 1 AES-2006 project that was underway during SAFIR2022.

Fuel cycle simulations of power plants are required both for ensuring the fulfilment of design criteria during normal operation as well as for producing the initial state for transient analyses. These simulations involve modelling the three

reactor core physics (neutronics, thermal hydraulics and fuel behaviour) during multiple fuel cycles, considering the loading of fresh fuel into the core and the shuffling of the remaining old fuel assemblies to new positions in the core.

LONKERO validated the capabilities of Kraken for such work using data from the Khmelnitsky NPP unit 2 reactor, which entered commercial operation in 2005. The X2 benchmark is based on the first four cycles of Khmelnitsky unit 2, providing history data for reactor power, control rod movements etc. and measured data for boron letdown, reconstructed power distributions from the core monitoring system and results for the start up tests at the beginning of each fuel cycle.

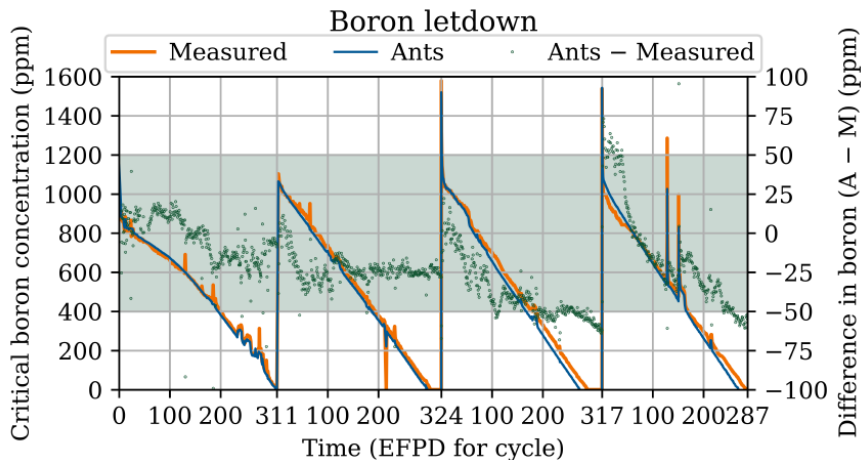


Figure 13. Kraken (Ants) prediction for boron letdown during the first four fuel cycles of Khmelnitsky NPP unit 2 reactor. Comparison to measured data from the plant.

The Ants-SuperFINIX-Kharon calculation sequence was used to model the four fuel cycles including the reloading of fuel between the cycles with the results submitted to be published as a journal article. Ants predicted boron letdown was compared to measured data (Figure 13). The accuracy of Ants critical boron predictions compared favourably with that of other nodal codes such as SIMULATE, RAST-V and DYN3D.

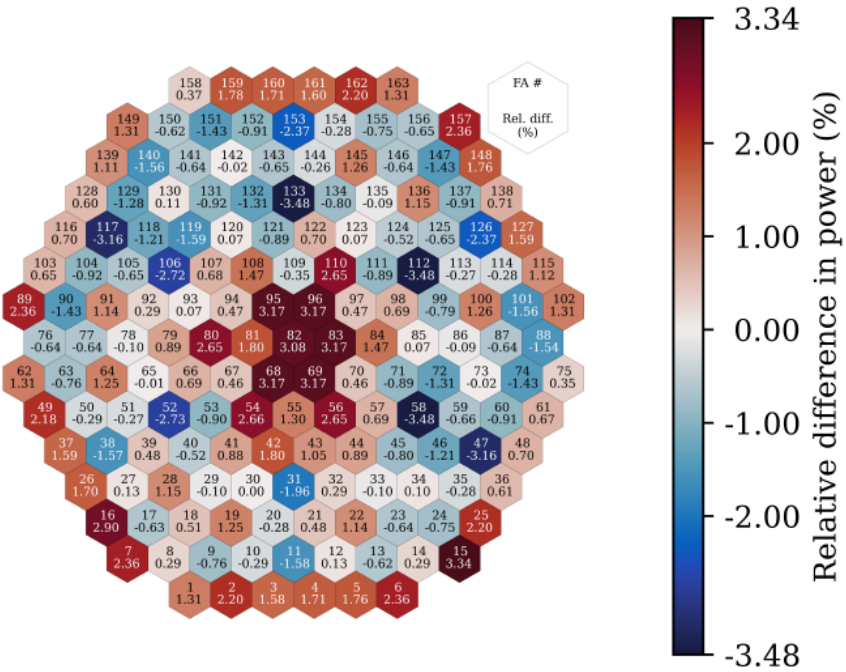


Figure 14. Relative difference between normalized power distribution predicted by Kraken and reconstructed by the core monitoring system based on self powered neutron detector measurements at 29 EFPD of cycle 2 at Khmelnitsky NPP unit 2 reactor

The assembly power distributions predicted by Kraken at different points of the four fuel cycles were compared to reconstructed data from the core monitoring system. An example in Figure 14 shows the relative difference between Kraken prediction and reconstructed data early during the second fuel cycle of the reactor. Axial power comparison for a peripheral fuel assembly 102 at the same time is shown in Figure 15.

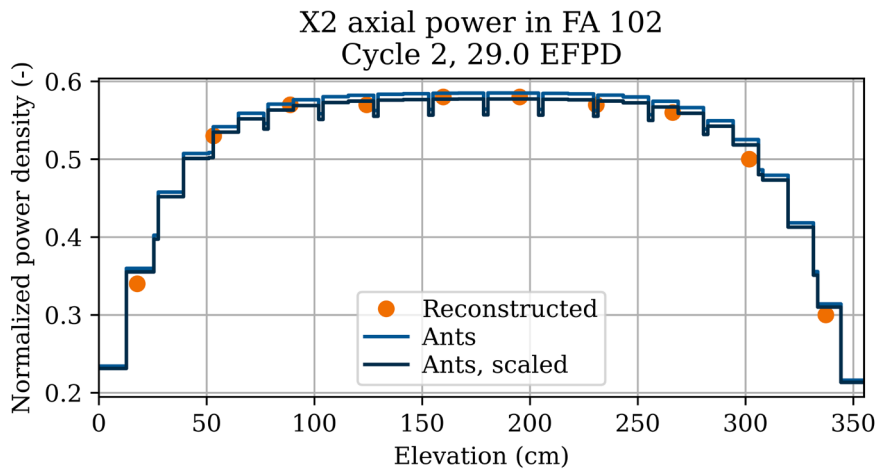


Figure 15. Normalized axial power distribution in fuel assembly 102 at 29 EFPD of cycle 2 of Khmelnitsky unit 2 reactor. Kraken prediction (Ants) vs. data reconstructed from the core monitoring system.

A range of zero power startup tests was conducted for the reactor at the beginning of each fuel cycle. These tests measured the reactivity (critical boron concentration) of the core at different conditions, the isothermal reactivity coefficient of the core, control rod worth curves and the net and gross scram worths of the control rod system.

Kraken was used to model each of the startup tests with comparisons made between the Kraken predictions and measured data. The accuracy of Kraken was contrasted with that of other modern nodal codes. One example of the evaluated data is shown in Figure 16 in the form of differential worth curves of control rod group 10, which was used to control the axial offset during the fuel cycles.

Overall, the X2 benchmark results of Kraken showed that the framework is capable of predicting the operation of VVER-1000 plants over multiple cycles with good quantified accuracy.

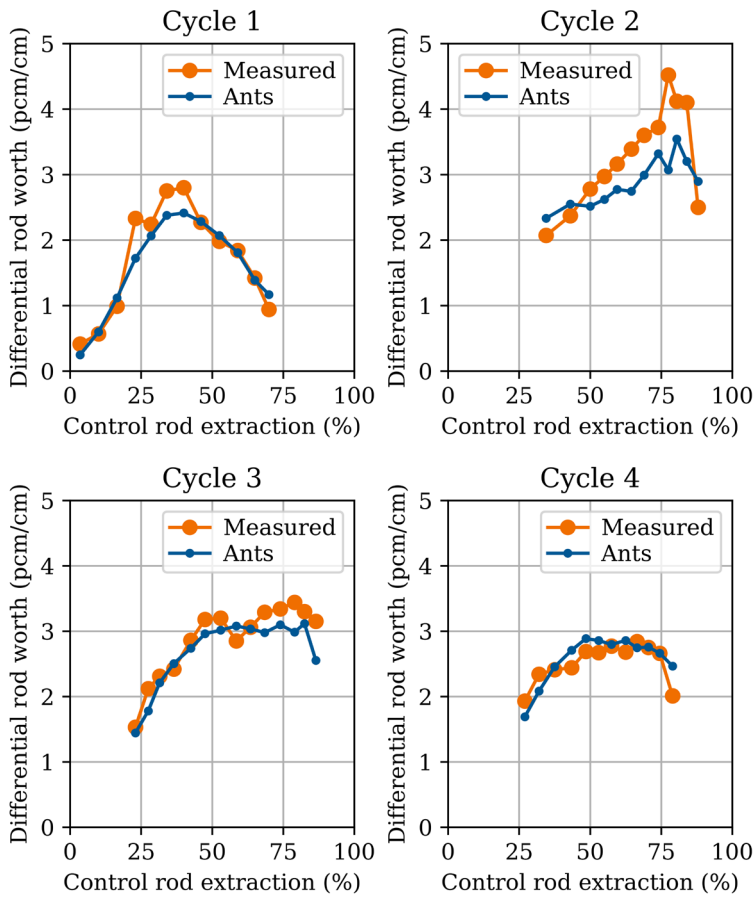


Figure 16. Differential reactivity worth curve of the working control rod group (#10) during the startup tests of each cycle.

Validating Kraken for VVER-1000 coolant transients

The transient capabilities of Kraken were validated using data from the Kalinin NPP unit 3 commissioning tests and the V1000CT-2 computational benchmark with the results submitted to be published as a journal article. The Kalinin 3 test was the stopping of one main circulation pump (MCP) at full power followed by a reduction of reactor power by the reactor control system and stabilization at a lower power level. This transient was modelled using the Ants-TRACE sequence of Kraken including a large VVER-1000 plant model for the system code TRACE. The V1000CT-2 Exercise 2 computational benchmark was also modelled with Ants-TRACE, this time using vessel boundary conditions specified in benchmark. The scenario was a simulated main steam line break (MSLB) in a VVER-1000 plant.

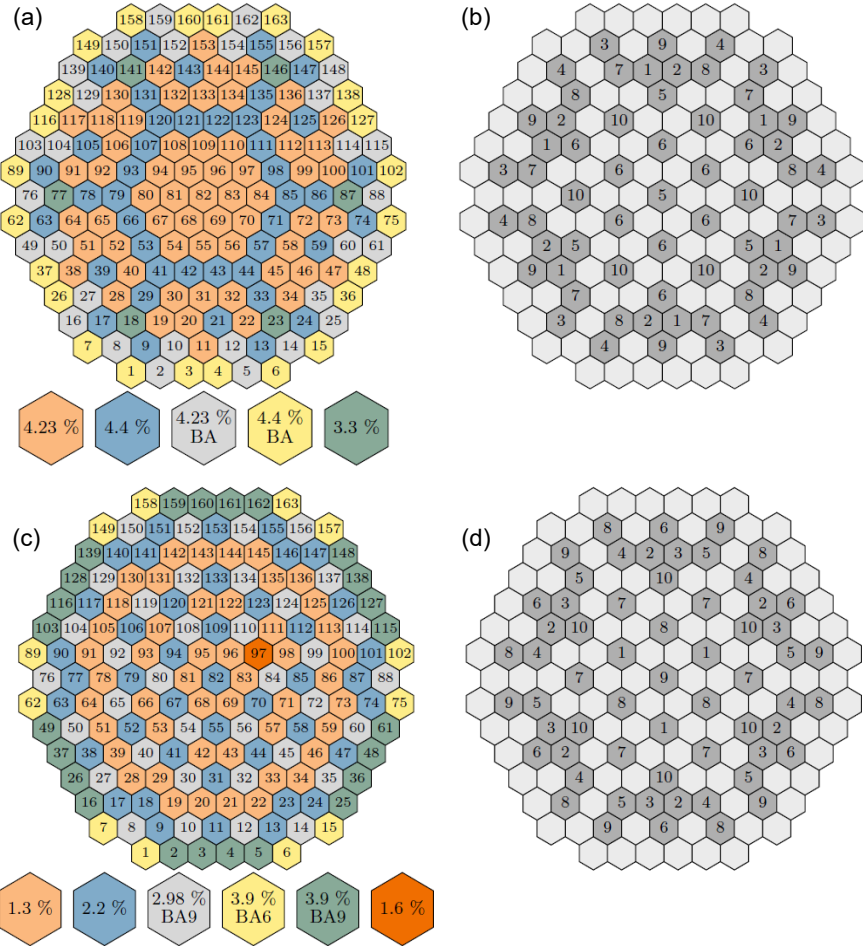


Figure 17. Core loading and control rod group numbering in the V1000CT-2 Exercise 2 (a & b) and the Kalinin 3 reactor (c & d).

Both benchmarks were based on a typical VVER-1000 core shown in Figure 17 indicating also the control group positions in the two cores. The Kalinin 3 core had one fuel assembly (#97) replaced before the MCP trip test.

The MSLB event in the modelled V1000CT-2 exercise included a realistic scenario (scenario 1) where the MCP in the failed loop trips as expected followed by the successful shut down of the reactor via scram and a pessimistic scenario (scenario 2) where the MCP fails to trip resulting in the overcooling of the core. The pessimistic scenario also reduces the scram worth, which combined to the overcooling leads to a recriticality and return to power at the later part of the transient.

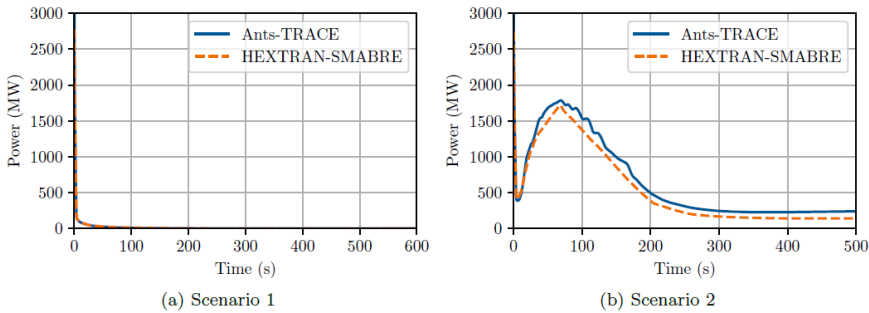


Figure 18. Total reactor power in the realistic (a) and pessimistic (b) main steam line break scenarios in the V1000CT-2 Exercise 2. Ants-TRACE vs. HEXTRAN-SMABRE.

The Ants-TRACE solution for the initial state of the V1000CT-2 transient was compared to other benchmark participants from the point of view of initial reactivity (k_{eff}), power peaking as well as core radial and axial power distributions. The transient power in the two scenarios was compared to earlier predictions by the legacy calculation chain HEXTRAN-SMABRE (Figure 18). System scale thermal hydraulic quantities such as hot leg temperatures (Figure 19) were also compared between the two solutions.

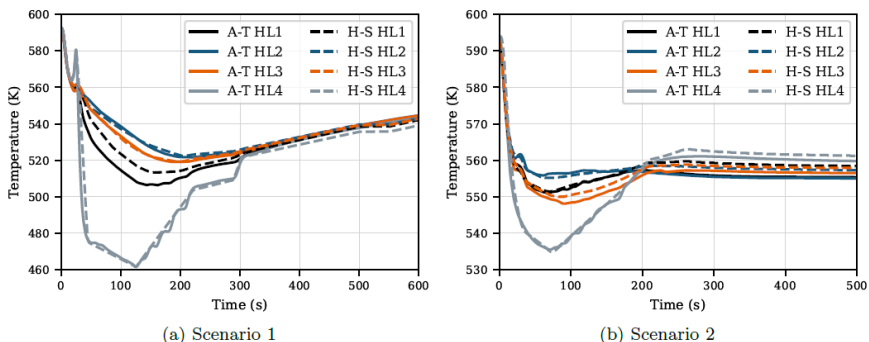


Figure 19. Hot leg temperatures in the realistic (a) and pessimistic (b) main steam line break scenarios in the V1000CT-2 Exercise 2. Ants-TRACE vs. HEXTRAN-SMABRE.

Validation against the Kalinin 3 pump trip test data started with a comparison of the initial assembly power distribution (Figure 20) and axial power distribution against reconstructed data from the reactor. The fresh assembly in the core has the largest local error in the predicted power as with other benchmark participants. The neutronics input data was given as a part of the benchmark and the power distribution is closely a results of the input data.

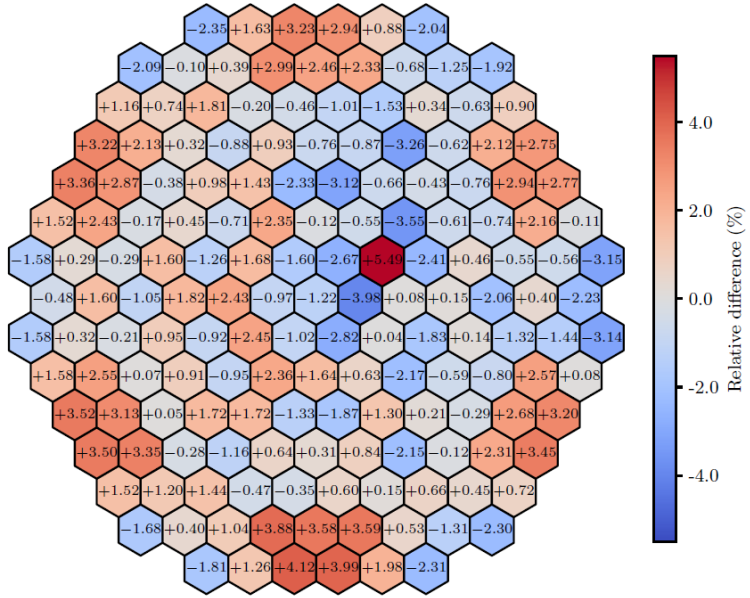


Figure 20. Relative error in predicted fuel assembly power distribution in the initial state of the Kalinin 3 pump trip transient. Ants-TRACE vs. reconstructed from measurements.

The pump trip experiment was modelled with Kraken including the control rod movements in response to the trip with good results. Agreement between Kraken prediction and measured value for the reactor total power during the transient is very good (Figure 21). The TRACE based system scale thermal hydraulics of Kraken catch the relevant thermal hydraulics phenomena well (Figure 22).

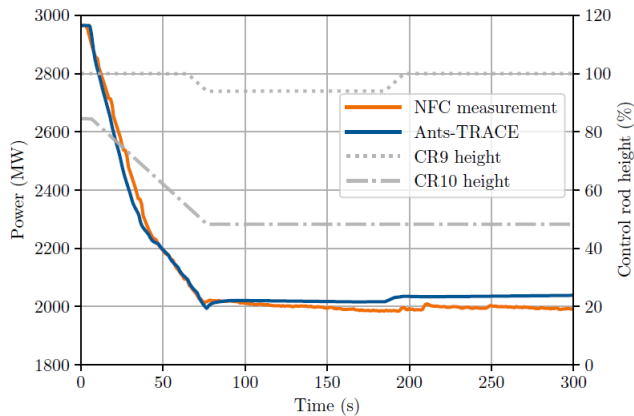


Figure 21. Total reactor power during the Kalinin 3 pump trip transient.

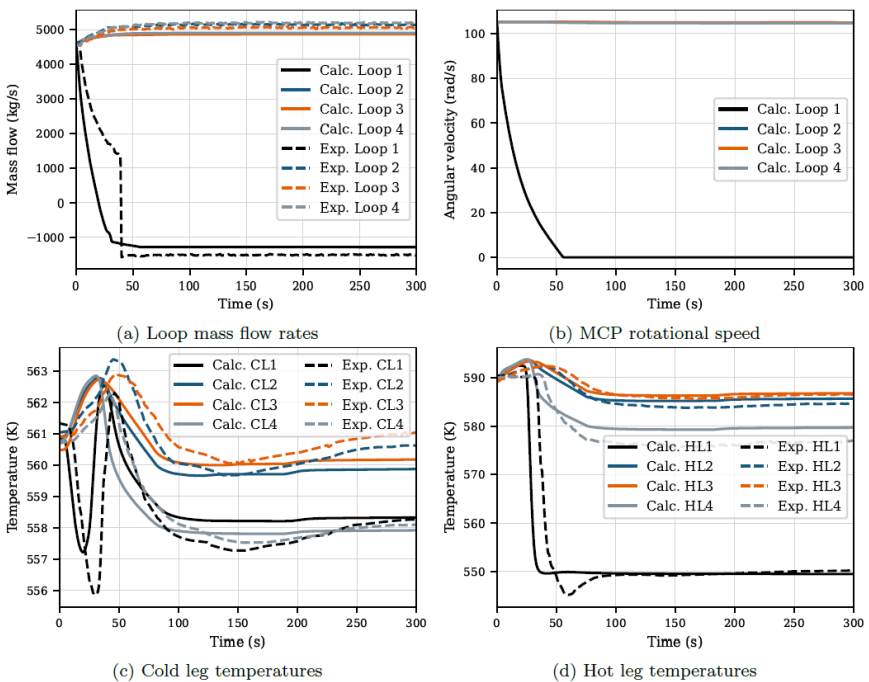


Figure 22. Calculated vs. measured system scale thermal hydraulic data for the Kalinin 3 pump trip transient.

4.4 Radiation shielding and criticality safety analyses (RACSA)

Pauli Juutilainen, Eric Dorval¹, Ville Valtavirta¹, Lauri Vaara¹, Topias Kähkönen¹

¹VTT Technical Research Centre of Finland Ltd
P.O. Box 1000, FI-02044 Espoo

Abstract

The main project target was to produce validated tools for radiation shielding, dosimetry and criticality safety analyses. New radiation shielding cases provided increased confidence in the Serpent Monte Carlo Code by validating its photon transport functionality. The dosimetry capabilities were improved in two ways: by validating Serpent 2 against eight benchmarks, and by developing the new deterministic code REMS as a reduced-order solver. The validation package for criticality safety analyses for fresh fuel was extended with a few new experimental series. Sensitivity and uncertainty-based methods were adopted to identify those experiments most neutronically similar to the target application. A Total Monte Carlo calculation environment was established to study the impact of nuclear data uncertainties from a burnup credit preparedness perspective.

Introduction

The RACSA project was established around the theme of particle transport for applications elsewhere than in a reactor core. This covered photon transport for gamma shielding cases, reactor dosimetry to evaluate the damage to reactor pressure vessel due to fast neutron irradiation and criticality safety. The general objective has been to improve computational tools and methods, as well as expertise in these fields. The work in the project has been computational only, with Monte Carlo codes Serpent (Leppänen et al., 2015a) and MCNP (Werner et al., 2018) as the main tools. As these fields somewhat differ between each other in practical working contents, they have formed the highest level division into work packages. The WP division also acts as a basis for main sections of the present report.

The main aim of the dosimetry WP in RACSA was the verification and validation (V&V) of Serpent 2 for reactor dosimetry applications. Even though during the previous SAFIR programme a first test with Serpent yielded promising results (Viitanen & Leppänen, 2016), a considerably wider and more systematic approach was adopted in SAFIR2022. The main step of the V&V effort required identification of all benchmark problems to be modelled. The U.S. NRC guide 1.190 provided a good starting point for this. Taking such document as a reference, the effort was then targeted at obtaining detailed information that would permit setting up 3-D computational models. It became evident that the data for some of the benchmark

problems was not straightforward to obtain, and consequently the candidate benchmark list had to be updated accordingly. In total, two computational benchmarks for code-to-code comparison between MCNP and Serpent 2 were selected, in addition to five experimental benchmarks. Except for the computational benchmarks (Carew et al, 2001), the rest of the specifications was sourced from the SINBAD database (Kodeli et al, 2006). The Belakovo-3 benchmark problem listed in SINBAD but not in the NRC guide 1.190 was added to the validation set, given the importance of VVER reactor types in Finland.

In parallel to the V&V of Serpent 2, work on a new, reduced-order deterministic dosimetry code was initiated in 2020. The purpose of such a code is to allow faster calculations than Monte Carlo codes can perform, for situations in which the ultimate accuracy is not the primary objective. The new code is called REMS. Prior to its development, scoping work was carried out to identify what would be the most promising methodology to solve the underlying neutron transport problem. Once a response-matrix formalism had been chosen, the work that followed was aimed at extending Serpent 2 in order to generate all the necessary response-matrix set data needed by REMS (Dorval, 2020b). From there onwards, the full-blown development of REMS was started. In 2021, an important milestone was reached when the VENUS-3 benchmark was solved using Serpent 2 as well as REMS (Dorval, 2021). Changes in project resource allocations dictated that further validation of REMS had to be put on hold. The rest of the dosimetry work focused on the simulation of all remaining benchmark problems with Serpent 2 and the preparation of the corresponding validation report (Dorval, 2022).

The photon transport functionality is required in a particle transport code in order to enable gamma shielding analyses to be performed with it. The physical photon transport models relevant for computational modelling had been mostly implemented to Serpent prior to the initiation of the SAFIR2022 programme, but almost all testing and validation of the functionality was still missing. Therefore, a proper validation of Serpent for gamma shielding calculations was determined as the first priority target in the topic. Also, it was seen desirable that Serpent would be capable of modelling entire nuclear facilities so that it could be used for licencing purposes and other for required analysis. Demonstrating this kind of performance was another main objective.

The work to improve criticality safety analysis preparedness practically meant development of tools and methods to assess appropriate safety margins for such analysis. For fresh fuel applications, the project continued the work on the validation package that has been constructed over a few SAFIR programmes already. The major topic in RACSA was the introduction of nuclear data sensitivity and uncertainty -based approach assisting the user in selection of most similar critical experiments for each target application. For criticality safety analysis with spent fuel, the concept of burnup credit requires additional topics to be considered compared to fresh fuel applications. One of them is the set of uncertainties related to burnup calculation, such as nuclear data uncertainty propagation and various modelling and computational assumptions. As the main achievement, Total Monte Carlo environment was set up for Serpent at VTT's computing cluster.

Reactor Dosimetry

A reactor dosimetry benchmark has several constitutive parts. In addition to accurate geometrical and material definitions, information about target responses (for example, nuclide activities at end-of-irradiation in the case of experimental benchmarks, or neutron fluxes/fluences in the case of computational benchmarks) at selected locations are required. Moreover, accurate information about the irradiation history, as well as the neutron source, are needed. The neutron source is often overlooked, but we must bear in mind that dosimetry problems are seldom solved in criticality source mode, because the irradiation often features a long history during which considerable isotopic changes take place. Consequently, dosimetry benchmarks also include carefully evaluated neutron sources which are often procured from reactor simulator output (in such cases, we talk about pin powers) or from more careful experimental determinations based on activation detectors. The latter approach is mainly feasible in research reactors. Whatever the case, we need a means to provide Serpent 2 with the source space-energy information needed to properly represent the neutron source with the same degree of detail as supplied in the benchmark specification. Considering that we are dealing with quite diverse benchmark geometries, a common external source format and the associated external source routines in Serpent to read from that format were implemented. The source is specified at two levels: assembly and pin. Even though the approach adopted is not fully general, it was found to be sufficiently flexible for the benchmark problems simulated. The main fixed source options are presented in Table 1.

Table 1. Fixed neutron source options available in the new routine (Dorval, 2020a).

1 st level (assembly)	2 nd level (pin)	Pin type	Axial	Angular	Energy
Cartesian, hexagonal	Cartesian, hexagonal	Square, (hollow) cylindrical, rectangular, (bent) MTR plate	Piece-wise constant	isotropic	Histogram, Watt fission spectrum, Maxwell fission spectrum

Benchmark results for problems calculated during the period 2020–2021 have been reported in the Interim Report (Hämäläinen & Suolanen, 2021). Since then, the following experimental dosimetry benchmarks have been simulated:

- NESDIP-3
- VENUS-3
- Balakovo-3

The 18/20 NESDIP-3 Benchmark Experiment (ASPIS) was carried out in 1985. The aim was to study neutron transport in a shield simulating the radial shield of a PWR, including the cavity region and the backing shield. The source was a fission plate constructed of 93% enriched uranium aluminium alloy driven by a thermal flux from

the extended graphite reflector of the NESTOR reactor. Neutron dosimeters were placed along the fission plate centreline at varying distances from the plate. The activity of products of the following nuclear reactions were measured: $^{32}\text{S}(\text{n},\text{p})^{32}\text{P}$ and $^{103}\text{Rh}(\text{n},\text{n}')^{103\text{m}}\text{Rh}$.

In Serpent, the case was simulated using Weight Windows as a Variance Reduction (VR) technique. The overall layout of the problem as well as the importance maps generated by Serpent 2 (from which the weight-window bounds are derived) are presented in Figure 2. The comparison between calculated and experimental activities for the aforementioned reactions is given in Figure 3.

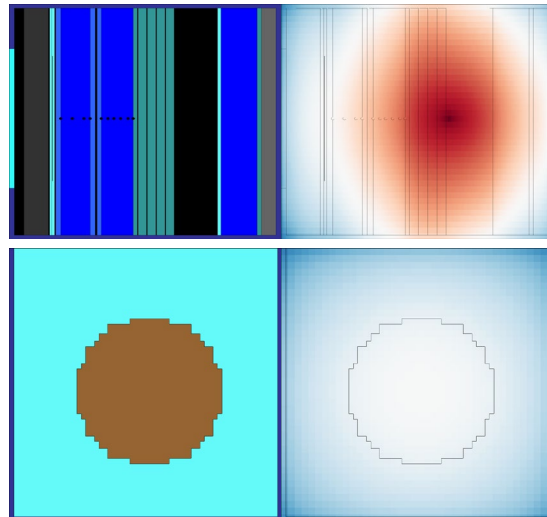


Figure 2. Top views (upper row) and fission plate views (bottom row) of the NESDIP-3 model. The left column depicts the problem geometry, whereas the right row presents the importance map produced by Serpent 2.

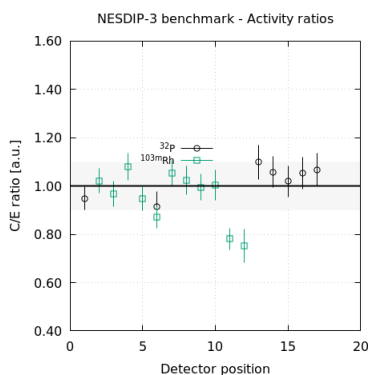


Figure 3. NESDIP-3 benchmark results. The low C/E ratios for locations 11 and 12 are in line with findings by other authors (Milocco et al, 2013).

The VENUS-3 benchmark of Figure 4 was also simulated in Serpent 2 using weight windows. The results of Figure 5 indicate a good agreement with experimental activities for three threshold reactions. Moreover, this benchmark problem was also calculated with REMS (Dorval, 2021).

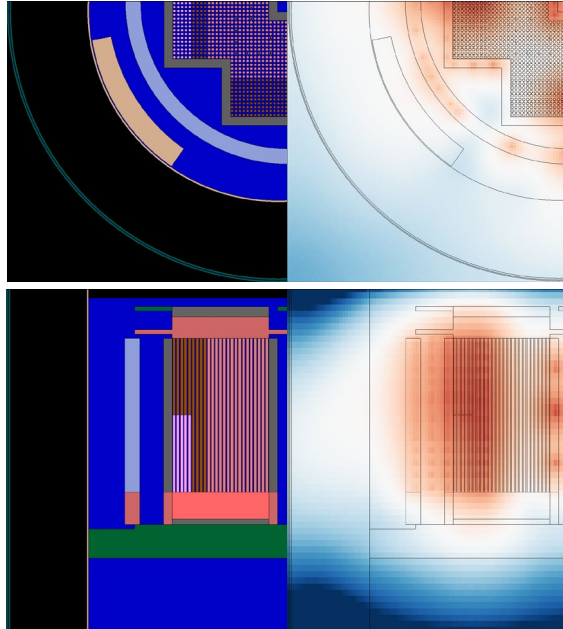


Figure 4. Top views (upper row) and side views (bottom row) of the VENUS-3 model. The left column depicts the problem geometry, whereas the right row presents the importance map produced by Serpent 2.

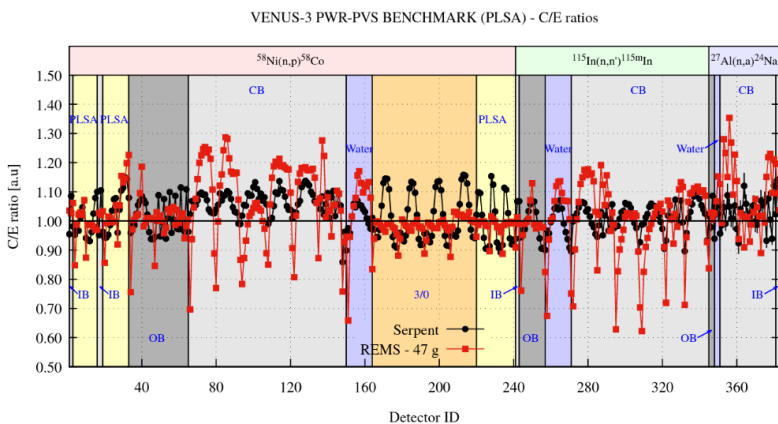


Figure 5. VENUS-3 benchmark results calculated by Serpent 2 and by REMS for three threshold reactions at various axial and radial locations (Dorval, 2021).

The last benchmark problem to be simulated was Balakovo-3: a neutron dosimetry experiment using activation and fissionable detectors carried out at Russian NPP Balakovo, unit 3 (Balakovo-3), during cycle 5, from March 1994 to January 1995. The detectors were installed in the ex-vessel cavity near the outer RPV surface. Top views of the Serpent 2 model and its importance map are presented in Figure 6, whereas the comparison of nuclide activities at various axial and azimuthal locations is presented in Figure 7 for two different approaches: one where the same neutron source (average) was used throughout the cycle; and another one where six different neutron transport steps were calculated. In all cases, the powers were scaled and activities decay-corrected to cater for the 27 power steps that reflect the operation of the reactor during cycle 5.

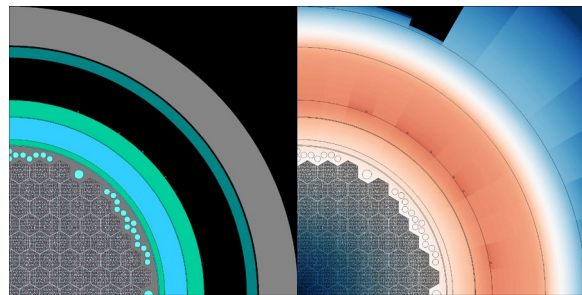


Figure 6. Top view of Balakovo-3 geometry (left) and importance map (right).

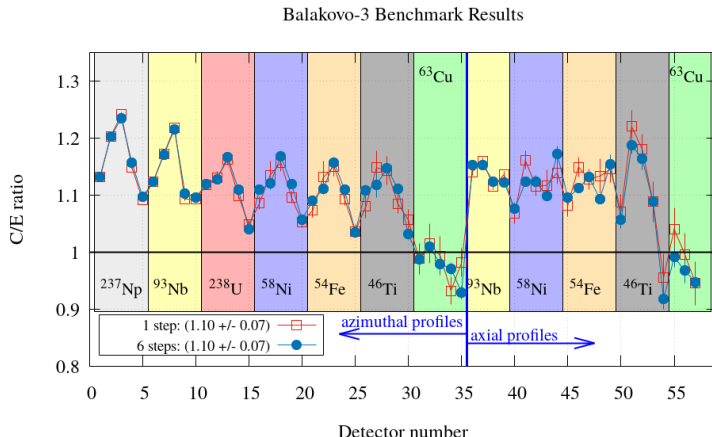


Figure 7. Balakovo-3 benchmark results calculated by Serpent 2 for seven dosimetry reactions at various axial and radial ex-vessel locations.

The development of REMS has reached an important milestone with the calculation of the VENUS-3 benchmark, but the code development and validation are still far from complete. As of this writing, (some of) the main features and capabilities of rem are:

Multi-file, keyword-based input	Multi-group neutron transport
Multi-cycle activation calculations	Sparse matrix storage/operations
Embedded profiler	Command-line steering options
Statistical checks on RESMAT sets	Formatted output
Versatile, built-in plotter	Cartesian transformations
Parallel calculations (OMP)	60-degree boundary conditions (HEX)
Acceleration scheme (CMRM)	Stochastic volume calculations
Criticality source calculations	Source spectral components
Adaptive topology option	

At present, the work on REMS is aimed at the production of a User's Manual for the current version (0.9).

Radiation shielding

The implementation of a photon transport mode in the Serpent Monte Carlo code first began outside of the SAFIR projects with the original target to account for gamma heating in coupled multi-physics simulations (Leppänen et al, 2015b). Since then, the photon transport mode has been developed to the level where it is capable of modelling all the relevant photon interactions, related to primary and secondary gamma radiation (Kaltiaisenaho, 2020a).

As an important part of shielding applications, variance reduction methods have been implemented to Serpent (Leppänen, 2019). Also known as non-analog Monte Carlo method, such methodology is practically necessary when the particle population differs significantly in various parts of the modelled configuration. This is obviously the case or at least the primary and only target of all shielding configurations. The above-described reactor dosimetry is an other field of applications where variance reduction techniques are required.

The method development has been mostly frozen in the RACSA project and the focus has been on validating and testing these previously developed functionalities. In case of gamma transport, the validation efforts have been based on the shielding benchmark presented in the Shielding Integral Benchmark Archive Database (SINBAD, Kodeli et al, 2006) and International Criticality Safety Benchmark Evaluation Project (ICSBEP, OECD/NEA 2019). It would be desirable to calculate benchmarks with variety of physical phenomena and throughout the energy spectrum. However, it turned out during the project that such a broad coverage various types of experiments may not be available.

The validation process was started with the OKTAVIAN benchmark from SINBAD (Kaltiaisenaho, 2020b). In the experiment, D-T fusion reaction generates a neutron beam, whose energy is peaked around 14 MeV. The neutron source is surrounded by various shielding materials and the photons and neutron leaking from the sphere are measured. The experiments were repeated computationally by Serpent 2.1.32

and MCNP-6.2. The computational agreement between these codes was mainly good, but the agreement between calculations and measurements strongly depended on the shielding material.

Similar outcome was obtained with the ALARM-CF-FE-SHIELD-001 and ALARM-CF-PB-SHIELD-001 benchmarks (Häkkinen, 2021). These experiments involved a Cf-252 source inside iron or lead spherical shield whose thickness was varied. The outgoing neutron and photon flux was measured. The energy spectrum was weighted in the low-energy end, with highest-energy particles slightly below 10 MeV. Again, MCNP and Serpent yielded rather similar results, when the same ENDF/B-VII.1 -based nuclear data was applied. However, Serpent calculations were also run with JENDL data, with which considerable discrepancy was observed in some cases against the ENDF/B data. Varying agreement was obtained between calculated and measured results, an example of which is shown in Figure 8. Additionally, the significance of a few such Serpent functionalities that have been preliminary implemented to a development version, but not integrated to official distribution versions, was tested. Particularly, the Gaussian Energy Broadening showed some importance at least with these benchmark experiments.

A Serpent model was constructed and preliminarily tested for a subcritical weapon-grade plutonium source with shielding sphere (SINBAD experiment NEA-1517/92), but it was not possible to fully analyse the case or build and run an MCNP or other reference model for it (Räty, 2022). The Pu source was surrounded by polyethylene reflector and stainless steel shielding. The outgoing neutron and photon flux were measured. The benchmark tests somewhat high-energy photons (up to 11.8 MeV) created in (n, γ) reactions.

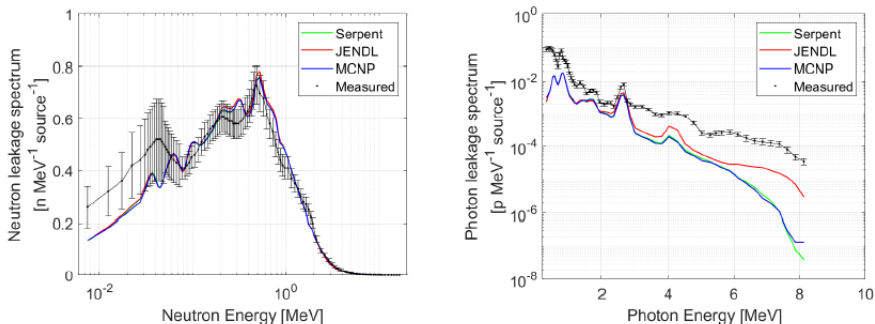


Figure 8. Neutron (left) and photon (right) spectra from Cf-252 source through a lead sphere shielding with radius of 20 cm.

In order to test Serpent's capability of modelling demanding configurations, a radioactive storage vault at VTT's Centre for Nuclear Safety was modelled (Leppänen & Jokipii, 2021). A Co-60 was located in the vault. The resulting dose rates around the vault were measured and calculated with Serpent. The configuration and calculated dose fields are depicted in Figure 9. Despite having the C/E component, the study was mainly aimed to demonstrate the computing

performance of Serpent with CAD-based geometry description and its variance reduction techniques in a complicated geometry. The computational process performed well, although it was also demonstrated that the non-optimized weight window generation reduced the computational efficiency for some detectors. The computational and measured results showed rather large discrepancy. It was probably due to various modelling simplifications and uncertainties, and also due to the relatively low accuracy of the used dosimeters with respect to the needs of a proper C/E comparison.

The functionality of reading CAD-based geometry descriptions had been developed to Serpent previously. It was fully documented during RACSA in a journal article (Leppänen, 2022).

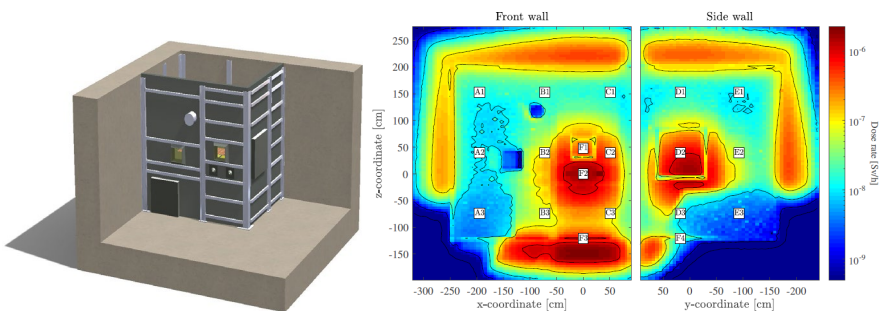


Figure 9. Left: CAD figure of the modelled geometry. Right: dose rate fields from two angles calculated with Serpent.

As a student project, the applicability of Serpent for detector modelling was studied with a passive gamma emission tomography (PGET) configuration. As a specific development item, a new variance reduction functionality was implemented to improve the photon transport in collimated detector modelling (Kähkönen, 2022). Improvement by factor 13 or more was achieved with respect to the analog simulation of the respective environment.

Criticality safety

In order to enable the use of the Monte Carlo codes Serpent and MCNP to be used for criticality safety analyses at VTT, a criticality safety validation package for these codes has been constructed over several years. The work has been performed mainly following the guidelines by (Dean and Tayloe, 2001). The package consists of

- a large collection of input models for MCNP and Serpent of critical experiments documented in the International Handbook of Evaluated Criticality Safety Benchmark Experiments (ICSBEP) (OECD/NEA, 2019)
- tools and processes for similarity analysis with sensitivity and uncertainty (S/U) -based methods to identify the most suitable experiments for each validation case and

- a dedicated Perl-package to run the validation analysis.

The purpose of the validation package is to determine the computational safety margin of the platform when it is used for criticality safety analyses for a target application. The package is applicable for for fresh or fresh-assumed fuel configurations. The analyses for spent fuel utilizing burnup credit (BUC) require additional validation items, such as the depletion calculation and critical benchmarks with spent fuel. Whilst some actions have been taken to address these, the validation package in this context refers to the one with fresh fuel. The steps to promote BUC capabilities will be described later in the text.

As a result of previous work, hundreds of Serpent and MCNP inputs modelling benchmark critical experiments have been integrated to the benchmark collection of the validation package. Many of these have been obtained from other institutions, but since the end user is always obliged to verify that they are correct, they cannot be added to the collection directly. In RACSA, the work expanding the collection has focused on inspection of such inputs. In the end of SAFIR2022, the package contains 507 inputs for Serpent and 275 for MCNP such that they can be considered as confirmed part of the benchmark collection. Additionally, 192 cases would be available for Serpent and 283 for MCNP, but not without review.

However, the number of modelled experiments is not the full story. First, the benchmarks to be used in a validation for a certain application needs to share similar neutronics properties. Second, the current international regulatory view is that only a few experiments per experimental series can be used for validation. For Serpent, the modelled experiments belong to 27 series, whilst the number of represented series is 19 for MCNP. The numbers of modelled benchmarks and experimental series are provided in Table 2. Figure 10 presents the distribution of modelled experiments and experiment series according to the U-235 enrichment. It is noteworthy that the class “<3 wt-%” practically means experiments with 2.5 wt-% enriched U-325 and they can be used for fuels with less than 4.0 wt-% U-235 according to the guidelines by (Dean & Tayloe, 2001).

Table 2. The number of experimental series/experiments modelled for Serpent and MCNP per facility.

Site	Serpent	MCNP
Pacific Northwest Laboratories (USA)	11/183	5/83
CEA Valduc (France)	3/44	2/22
Russian Research Centre Kurchatov Institute, SF-9 and P	6/49	5/55
Central Research Institute for Physics of the Hungarian Academy of Sciences, ZR-6	1/151	1/23
Nuclear Research Institute Rez, LR-0 (Czech)	2/35	2/35
Others	4/45	4/57

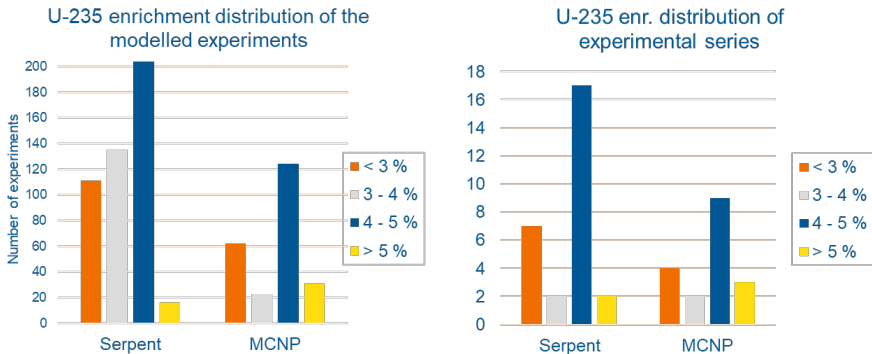


Figure 10. Number of modelled experiments (left) and represented series (right) per U-235 enrichment. The experiments with various enrichment levels in same core are not counted in the figure.

The selection of appropriate benchmarks has traditionally been based on various qualitative guidelines with some quantitative elements, but ultimately the selection relies heavily on expert judgement. In order to bring numerical support to the selection, sensitivity and uncertainty (S/U) method -based approach for similarity evaluation has been studied within RACSA. In the first year, the functionality of MCNP with its Whisper module was tested. Whisper (Kiedrowski et al., 2015) automatically selects the most similar cases for the given application and runs the statistical analysis to define the safety margins.

The similarity evaluation uses correlation coefficient c_k between each experiment and the application as the measure of similarity. It requires the sensitivity vectors to describe the sensitivity of the system k_{eff} on various perturbations in nuclear data items and the covariance matrix representing the nuclear data uncertainties. The sensitivity vectors can be calculated by both MCNP (Kiedrowski et al., 2011) and Serpent (Aufiero et al., 2015). The covariance matrix is based on information available in the nuclear data evaluations, but it is a non-trivial task to process it into a correct and usable format for calculations.

The functionality to evaluate the c_k :s with Serpent was developed within RACSA and integrated to the KrakenTools Python package. Whilst the latest MCNP distributions contain the automatized functionality to define the safety margins with the help of similarity evaluation, the process is still somewhat manual with Serpent. It is still up to the user to choose the right benchmarks and run the analysis with the Perl package that was constructed several years ago and has been slightly upgraded along with the work on the topic. It is, however, noteworthy that the similarity analysis is subject to the quality of the uncertainty data. Since it is known that the uncertainties are somewhat too large, it is still important for the user to put some expert judgement to the selection.

The driver script package has been upgraded to be able to set multiple user-defined thermal scattering data libraries to Serpent inputs, instead of the single one

in the earlier version. The use of multiple cross-section data files was also enabled for Serpent. For MCNP, the current implementation does not enable more than one thermal scattering data source definition, but an assistant script has been built to identify the inputs in which various thermal scattering data entries exist. In order to support the traditional trend analysis to define the area of applicability, various case parameters were added to MCNP inputs and the script was updated to read them, as well as related neutron spectrum metrics from the output files.

As stated above, the processing of covariance data from the original nuclear data is a somewhat complicated task and requires expertise. Currently, the Serpent/KrakenTools similarity analysis relies on covariance data distributed with the SCALE code package. During the last half of RACSA, effort was put to develop in-house expertise for covariance data processing (Valtavirta & Juutilainen, 2022)(Valtavirta, 2023). The nuclear data processing code NJOY2016 (Macfarlane et al., 2017) was used for the purpose. The first objective was to replicate the 56-energy-group data based on ENDF/B-VII.1 nuclear data and is distributed with the SCALE package.

For the fundamentals, KrakenTools was extended with a set of required pre- and postprocessing scripts driving NJOY. Other first steps were to study the use of applicable NJOY modules and identify the input choices that need to be made in the processing. In order to verify the processed data, the covariance data of four nuclides (H-1, Pm-147, Gd-155 and U-235) were analysed more carefully in the first phase. An example comparison of the processed and SCALE data is shown in Figure 11, in which the Gd-155 radiative capture covariance matrix were compared. The first results were generally acceptable to allow further progress.

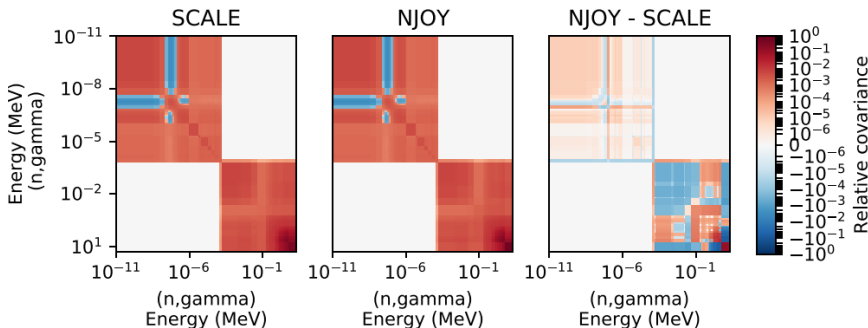


Figure 11. Relative covariance matrices for the Gd-155 radiative capture (mt 102–mt 102): the one from SCALE package (left), the one processed with NJOY (middle) and the absolute difference of the two.

In the next phase, the self-produced NJOY covariance data was tested against the 44- and 56-group data sets of SCALE. The same VVER-1200 assembly wet storage model as used in all previous similarity tool tests acted as the target application. The correlation coefficients between the application and each of the critical

experiment modelled for Serpent were calculated with SCALE-based and self-produced 56-group covariance data.

The data sets are not fully comparable in addition to the different energy group resolution, but also e.g. the underlying nuclear data evaluations differ to some extent. The results were analysed based on comparison of the ranking of each case achieved with various covariance versions. An example is provided in Figure 12, where the ranking of each experiment obtained with other evaluation are plotted as a function of the correspondent experiment's ranking of the top-100 experiments by SCALE 56-group data. In case of full agreement, all the dots would be on the $x = y$ line, and the extent of the dot spread indicate the level of disagreement between the data sets.

Part of the disagreements were likely explained by the differences in the base nuclear data versions, as the SCALE 56-group data contains contribution from the ENDF/B-VII.2 data. The NJOY processing of ENDF/B-VIII data improved the agreement on the most distinct outliers. However, unexplained discrepancies were still left for further studies, and they should be solved before taking the in-house produced data in the production use.

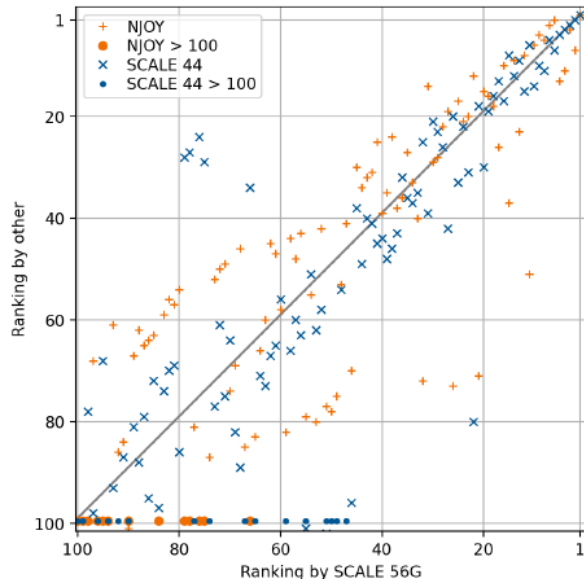


Figure 12. Comparison of rankings between SCALE 56G data and other data sets. Points on diagonal indicate equal ranking between data sets. Points below diagonal indicate lower ranking using other dataset. Points above diagonal indicate higher ranking using other set.

In the field of developing burnup credit capabilities, the work of RACSA 2021-22 mainly consisted of testing the nuclear data uncertainty propagation through burnup calculation using the Total Monte Carlo (TMC) approach with Serpent in tight co-

operation with the KYT2022/KÄRÄHDE project. With smaller volume, we have contributed to the OECD/NEA benchmark on uncertainty quantification in burnup calculation.

Considering the on-going benchmark, the first phase consisted of plain burnup calculation with a 15 x 15 PWR assembly characterized by 4.1 wt-% enriched U-235 fuel and 52.5 MWd/kgU discharge burnup. The calculations revealed a few unexpected discrepancies between the users of same codes and libraries. Work has been done to identify the user effects and other possible explanations and the report should be completed later in 2023. However, it may take significantly longer to get the report published. The work will be described also in an ICNC 2023 conference paper (Carmouze and Ichou, 2023). The actual uncertainty quantification is planned for the next phase of the benchmark.

Considering the RACSA/KÄRÄHDE activities for the spent fuel inventory uncertainty quantification, the TALYS (or T6) code package was tested and introduced to run the Total Monte Carlo together with Serpent. The TALYS package (Koning & Rochman, 2012) creates the randomized cross-section and fission yield data sets. The process starts from the fundamental physics models and experiment database and utilizing the incorporated uncertainty evaluations and correlations. As a result, the TENDL nuclear data file and the created set of randomized data sets are obtained. After processed by NJOY to the ACE format readable by Serpent, the uncertainty evaluation for spent fuel characteristics can be obtained by Serpent burnup calculation with every data set. The process is illustrated in Figure 13.

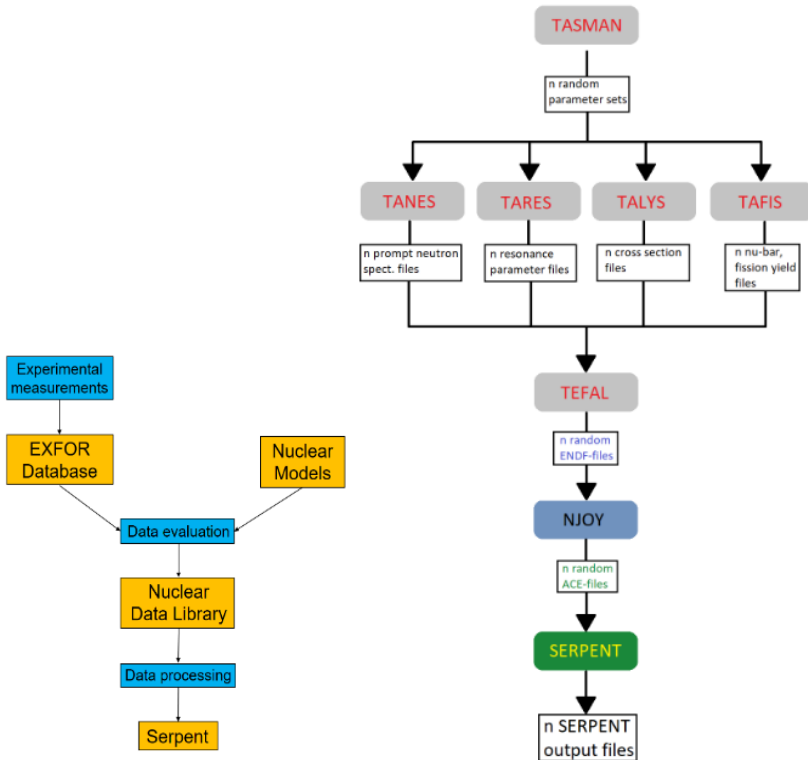


Figure 13. Flow chart TALYS/T6 package in producing the TENDL library and the randomized data sets, overview on the left and the code-wise representation on the right (Vaara, 2022).

The first installation and test package of the TALYS package was performed within a M.Sc. thesis (Vaara, 2022). As a demonstration case, a BWR 6 x 6 assembly with mostly 2.53% and some pins 1.87% enriched U-235 was calculated in 2D infinite lattice. The calculations were run up to 80 MWd/kgU, though the real discharge burnup for the modelled assembly was at ~23 MWd/kgU. The observed uncertainty ranges in the results naturally varied a lot between nuclides. Two examples results are shown in Figure 14: the uncertainty range for k_{eff} and Pu-239 concentration as a function of time.

The second phase in the Total Monte Carlo process was to extend the range of randomized data to larger number of nuclides. Additionally, the full TENDL 2019 has been processed for use and the randomized fission yield data has been installed. Several processing scripts have been written to enable and facilitate the TMC calculations on VTT's high-performance computing cluster.

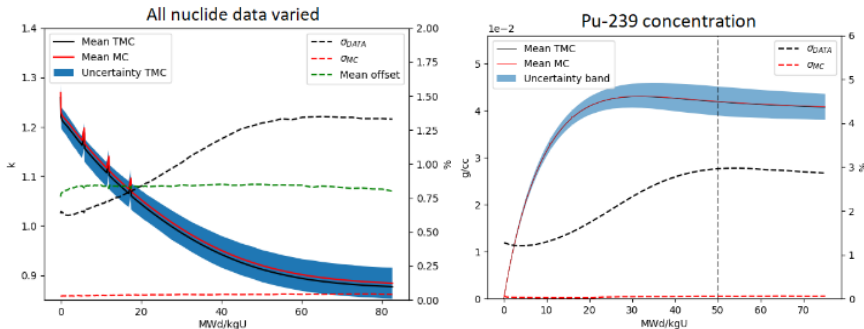


Figure 14. Examples of the results of uncertainty quantification with Total Monte Carlo and Serpent on a 6×6 BWR assembly. On the left, the uncertainty band of K_{eff} is illustrated, whilst the concentration of Pu-239 is depicted on right, both as a function of burnup. The left y-axis presents the absolute values and the right one relative uncertainties. Sigma_data refers to nuclear data uncertainties and sigma_MC to stochastic uncertainty of the Monte Carlo simulation. (Vaara, 2022).

After the improvements to the TMC environment, a new demonstration case was calculated. It is a VVER-440 assembly provided in the SFCOMPO burnup credit benchmark database with measured spent fuel nuclide inventory. The results are to be published in a journal article that is under construction at the moment of writing the present report, so the results cannot be published yet.

References

- Aufiero, M., Bidaud, A., Hursin, M., Leppänen, J., Palmiotti, G., Pelloni, S. & Rubiolo, P. 2015. A collision history-based approach to sensitivity/perturbation calculations in the continuous energy Monte Carlo code SERPENT. Annals of Nuclear Energy. Volume 85. Pages 245-258. 2015. <https://doi.org/10.1016/j.anucene.2015.05.008>.
- Carew, J., Hu, K., Aronson, A., Prince, A., & Zamonsky, G. 2001. PWR and BWR pressure vessel fluence calculation benchmark problems and solutions. Technical Report NUREG/CR-6115, Brookhaven National Laboratory.
- Carmouze, C., Ichou, R., Overview of Spent Nuclear Fuel Inventory results for the ARIANE GU3 sample, abstract submitted to ICNC 2023 – The 12th International Conference on Nuclear Criticality Safety, October 1st – 6th, 2023 in Sendai, Japan
- Dean, J. C. and Tayloe, R. W. 2001. Guide for Validation of Nuclear Criticality Safety Calculational Methodology. Technical report, U.S. Nuclear Regulatory Commission, 2001.
- Dorval, E. 2020a. Validation of the Serpent 2 Monte Carlo code for reactor dosimetry applications. Abstract accepted for participation in the 17th Symposium on

Reactor Dosimetry (ISRD-17), Lausanne, Switzerland. Postposed to 2023 due to the Covid-19 pandemic.

- Dorval, E., 2020b, On the generation of response-matrix data with Serpent 2. VTT Research report VTT-R-01489-20.
- Dorval, E., 2021, Calculation of the VENUS-3 benchmark experiment by response-matrix and Monte Carlo methods. Ann Nucl Energy, 178:109351.
- Dorval, E., 2022, Validation of Serpent 2 for reactor dosimetry applications. VTT Research report VTT-R-01056-22.
- Häkkinen, S. 2021. Serpent 2 Validation for Radiation Shielding Applications. ASME J of Nuclear Rad Sci., <https://doi.org/10.1115/1.4051614>
- Hämäläinen, J. & Suolanen, V., 2021, SAFIR2022 – The Finnish Research Programme on Nuclear Power Plant Safety 2019-2020 Interim Report. VTT Technology 383.
- Kaltiaisenaho, T. 2020a. Photon transport physics in Serpent 2 Monte Carlo code. Computer Physics Communications. Volume 252. <https://doi.org/10.1016/j.cpc.2020.107143>
- Kaltiaisenaho, T. 2020b. Validation of the coupled neutron-photon transport in Serpent 2 with OKTAVIAN benchmarks. VTT Research report VTT-R-00005-20.
- Kiedrowski, B.C., Brown, F.B. & Wilson, P.P.H. 2011. Adjoint-Weighted Tallies for k-Eigenvalue Calculations with Continuous-Energy Monte Carlo. Nuclear Science and Engineering, 168(3):226–241, 2011.
- Kiedrowski, B.C., Brown, F.B., Conlin, J.L., Favorite, J.A., Kahler, A.C., Kersting, A.R., Parsons, D.K., & Walker, J.L. 2015. Whisper: Sensitivity/Uncertainty-Based Computational Methods and Software for Determining Baseline Upper Subcritical Limits, Nuclear Science and Engineering, 181:1, 17-47, DOI: 10.13182/NSE14-99
- Kodeli, I., Sartori, E. & Kirk, B. 2006. SINBAD - Shielding Benchmark Experiments - Status and Planned Activities, Proceedings of the ANS 14th Biennial Topical Meeting of Radiation Protection and Shielding Division, Carlsbad, New Mexico (April 3-6).
- Koning, A. J., Rochman, D., Nuclear Data Evaluation with the TALYS Code System. Nuclear Research and Consultancy Group NRG, Netherlands, Petten, 2012.
- Kähkönen, T., Variance reduction for collimated gamma detector geometry in Serpent, Aalto University, School of Science, PHYS-E0441 - Physics Special Assignment V, 2022, <http://urn.fi/URN:NBN:fi:aalto-202206234186>
- Leppänen, J., Pusa, M., Viitanen T., Valtavirta, V. & Kaltiaisenaho, T. 2015a. The Serpent Monte Carlo code: Status, development and applications in 2013. Ann Nucl Energy, 82:142–150.

- Leppänen, J., Hovi, V., Ikonen, T., Kurki, J., Pusa, M., Valtavirta, V. and Viitanen, T. 2015b. The Numerical Multi-Physics project (NUMPS) at VTT Technical Research Centre of Finland. *Ann. Nucl. Energy*, 84 (2015) 55-62.
- Leppänen, J. 2019. Response Matrix Method-Based Importance Solver and Variance Reduction Scheme in the Serpent 2 Monte Carlo Code. *Nucl Technol*, 205:1416–1432.
- Leppänen, J., Jokipii, M., Radiation Shielding Calculations at VTT Centre for Nuclear Safety Using the Serpent 2 Monte Carlo Code, In Proceedings of ANS M&C 2021 - The International Conference on Mathematics and Computational Methods Applied to Nuclear Science and Engineering, Raleigh, North Carolina, USA, October 3 – 7, 2021 (virtual meeting) dx.doi.org/10.13182/M&C21-33721
- Leppänen, J., Applications and Performance of the CAD-based Geometry Type in the Serpent 2 Monte Carlo Code. *Annals of Nuclear Energy*, Volume 176, 2022, <https://doi.org/10.1016/j.anucene.2022.109259>
- Macfarlane, Robert, Muir, Douglas W., Boicourt, R. M., Kahler, III, Albert Comstock, and Conlin, Jeremy Lloyd. *The NJOY Nuclear Data Processing System, Version 2016*. United States: N. p., 2017. Web. doi:10.2172/1338791.
- Milocco, A., Trkov, A. & Kodeli, I. 2013. Quality Assessment of Evaluated Experiments Nesdip-2, Nesdip-3, Janus-1, Janus-8. 22nd International Conference Nuclear Energy for New Europe, Slovenia.
- OECD/NEA. 2019. International Handbook of Evaluated Criticality Safety Benchmark Experiments. NEA/NSC/DOC(95)03.
- Räty, A., Serpent gammatransportin validoinnin valmistelu, VTT Research Report VTT-R-00089-22 (2022, in Finnish).
- U.S. NUCLEAR REGULATORY COMMISSION (NRC), 2001. Regulatory Guide 1.190 - Calculational and dosimetry methods for determining pressure vessel neutron fluence.
- Vaara, L., Nuclear Data Uncertainty Propagation with Total Monte-Carlo Method, Aalto University, School of Science, Master's thesis, 2022, <http://urn.fi/URN:NBN:fi:aalto-202209045290>
- Valtavirta, V., Juutilainen, P., Development of criticality safety analysis capabilities at VTT - status report 2021, VTT Research Report VTT-R-00253-22 (2022)
- Valtavirta, V., Processing multigroup covariance data for similarity analyses, VTT Research Report VTT-R-00019-23 (2023).
- Viitanen, T. & Leppänen, J. 2016. Calculating Neutron Dosimeter Activation in VVER-440 Surveillance Chains with Serpent. 26th Symposium of AER on VVER Reactor Physics and Reactor Safety, Helsinki.
- Werner, C.J, et al., "MCNP6.2 Release Notes", Los Alamos National Laboratory, report LA-UR-18-20808 (2018).

4.5 Enhanced multi-physics calculation capabilities for fuel behaviour and reactor analyses (EMBER)

Rintala Ville¹, Suikkanen Heikki¹

¹LUT University
P.O. Box 20, FI-53851 Lappeenranta

Abstract

EMBER aims at reducing uncertainties in reactor and fuel analyses via development of advanced coupled multi-physics calculation capabilities that account for the reactor core neutronics, thermal hydraulics and fuel thermo-mechanic behavior. Existing solvers are used in the coupling including the Monte Carlo type code Serpent for the reactor physics and burnup solution, the subchannel code SUBCHANFLOW for the thermal-hydraulic solution, and TRANSURANUS for the fuel thermo-mechanic solution. Starting from a coupling between Serpent and TRANSURANUS established earlier, new capabilities and features were developed during EMBER including the transfer of Serpent-calculated nuclides to enhance TRANSURANUS fuel simulations, addition of SUBCHANFLOW as the thermal hydraulic solver and initial capabilities for coupled transient analyses. The developed capabilities can be used to reduce and quantify uncertainties in reactor and fuel related safety analyses.

Introduction

Nuclear reactor core is a textbook example of a multi-physics problem where several interdependent physical and chemical processes take place. The accurate numerical solution of the reactor core thus calls for a coupled calculation methods that consider at least the most relevant connected processes in a coupled manner.

Most importantly, the neutron induced reactions and radioactive decay responsible for the thermal power production as well as the depletion and conversion of the fuel materials and the build-up of fission products in the reactor need to be considered. The solution of this part of the core problem is handled by neutronic and burnup calculation codes. The neutronic solution is strongly affected by material temperatures of especially the fuel and the moderator via the Doppler and the moderator density feedbacks, respectively. On the other hand, the temperatures are dependent on the produced power and thus the total solution of neutronics and material temperatures is coupled. The fuel temperature solution requires a code that can solve the fuel rod internal heat transfer, preferably considering various other physico-chemical interdependencies and changes in thermal conductivities along the fuel burnup. Thus, a dedicated fuel thermo-mechanic behaviour code is a preferred choice for obtaining the fuel temperature solution, more so, as it also provides the solution for various important fuel integrity

-relevant parameters. The solution of the water moderator/coolant is obtained with a thermal-hydraulic solver that considers the fluid flow and heat transfer. Dedicated, so called, subchannel codes exist specifically for solving reactor core thermal hydraulics.

EMBER focused on developing couplings between codes handling these main reactor core solution areas. As a starting point, an initial coupling between the Monte Carlo reactor physics code Serpent (Leppänen et al., 2015) and the fuel behaviour code TRANSURANUS (Lassmann, 1992) was established in earlier projects. Within EMBER, this initial coupled calculation system was further extended with new capabilities and the addition of the thermal hydraulic code SUBCHANFLOW (Imke and Sanchez, 2012).

Coupled calculation framework

The coupled calculation system developed at LUT University before the EMBER project consisted of Serpent and TRANSURANUS that exchanged power, fast neutron flux, fuel temperature and fuel pin radius data between each other (Suikkanen et al., 2020). The coupling was established by developing a separate coupling code written in Perl that handles the solution process and data transfer between the codes. During EMBER, the calculation system was developed into a more comprehensive framework by the addition of the thermal hydraulic code SUBCHANFLOW and implementation of new data transfer and solution process features, such as the transfer of nuclide data from Serpent to TRANSURANUS, predictor-corrector scheme for burnup calculations and preliminary capabilities for transient calculations.

The developed coupled calculation scheme in the case of burnup calculations is shown in Figure 1. The general solution process inside each burnup step consists of iterations between Serpent, SUBCHANFLOW and TRANSURANUS, which are sequentially executed with data transfer in between. This iteration loop is continued until pre-determined convergence criteria are fulfilled. In the first round, initial guesses are provided for solution variables that have not yet been solved. The burnup solution process can be performed either with or without the corrector phase. After a burnup step has reached convergence, the solution process moves to the next burnup step for which solution fields from the previous burnup step are used as the initial guesses.

The data that the codes exchange between each other are also indicated in Figure 1. SUBCHANFLOW provides Serpent the temperature and density fields of the coolant and TRANSURANUS the coolant temperature and the cladding-coolant heat transfer coefficient in slices corresponding to the axial nodalization of the TRANSURANUS rod model. Serpent provides both SUBCHANFLOW and TRANSURANUS the rod axial power distribution and for TRANSURANUS also its radial distribution as well as the fast neutron flux in the cladding. It can also provide TRANSURANUS nuclide data as obtained from the burnup calculations.

TRANSURANUS returns Serpent the fuel axial and radial power distributions as well as the radial dimension changes in the axial rod slices.

Coupled transient simulation capabilities were not fully completed during EMBER, but in such simulations the burnup loop is replaced by a time loop that progresses the simulation with short time steps. The transient solution needs to account for the delays in heat transfer and the accumulation of heat, thus requiring to separate the rod thermal solution solely to TRANSURANUS and the coolant solution to SUBCHANFLOW. Thus, the solution process of the complete coupled transient calculations will be slightly different from what is shown in Figure 1.

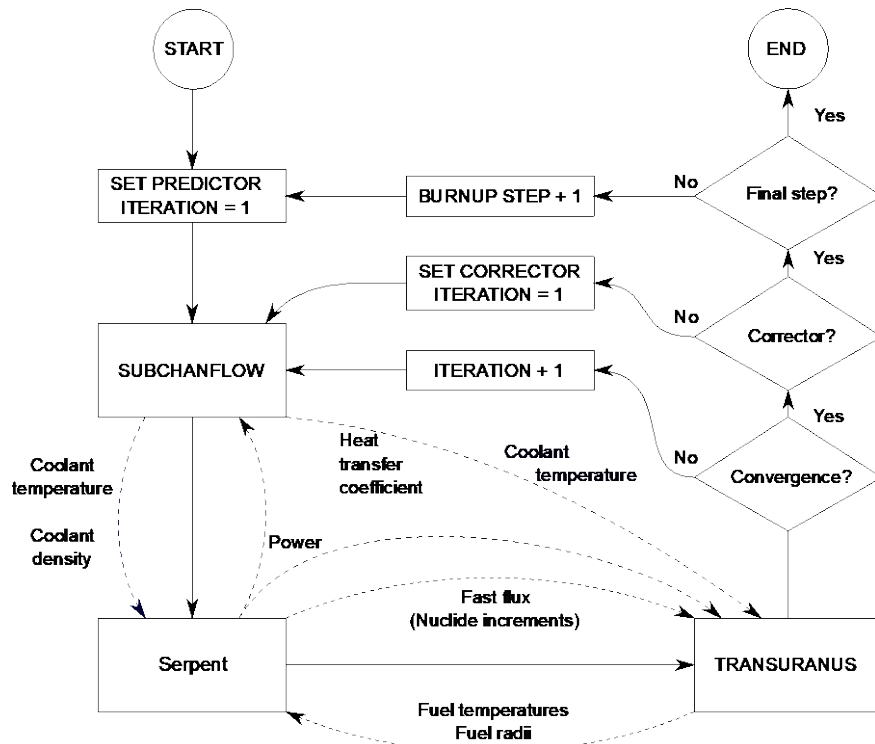


Figure 1. Scheme for coupling Monte Carlo neutronics and burnup (Serpent) with subchannel thermal-hydraulics (SUBCHANFLOW) and 1.5D fuel thermo-mechanic behaviour (TRANSURANUS).

Capabilities developed during 2020–2022

During 2020, a capability to utilize Serpent-calculated nuclide compositions in TRANSURANUS during coupled calculations between the two codes was developed (Rintala et al., 2022; Rintala, 2022). This work included collaboration with the European Commission Joint Research Centre, Institute for Transuranium Elements (JRC ITU) who maintains and distributes the TRANSURANUS code. The

goal was to utilize the more accurate burnup modeling of the Monte Carlo reactor physics code to produce more accurate nuclide concentrations for the fuel behavior code. The coupling code was modified in such a way that nuclide data was collected from the nuclide files written by Serpent and the corresponding nuclides in TRANSURANUS were incremented based on the data at each burnup step. In a demonstration calculation, the fission products of interest to TRANSURANUS were transferred from Serpent, and the differences between coupled and standalone TRANSURANUS for the fission gases xenon and krypton are shown in Figure 2. The short demonstration calculation did not result in major differences but further investigations should be performed for higher burnups and different fuels. While the demonstration only considered the fission gases currently handled by TRANSURANUS, the developed capability allows the transfer of practically any nuclide available in Serpent results to TRANSURANUS, which would facilitate further development of models in TRANSURANUS, e.g., for solid fission product swelling. Furthermore, in TRANSURANUS side the capability was implemented as a new data transfer interface that allows the input of any node-wise quantities, not just nuclide data, during the coupled simulations. This can open up further development possibilities not yet identified. In addition, the coupling code was implemented the capability to perform the coupled burnup calculations using the predictor-corrector scheme of Serpent for improved accuracy.

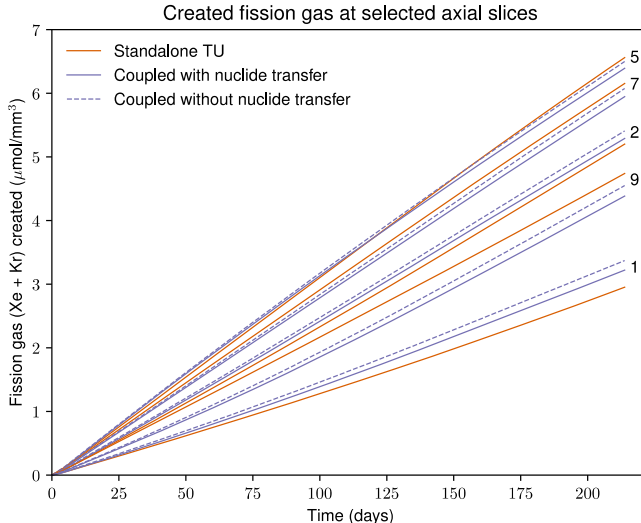


Figure 2. Fission gases created in the fuel obtained with the developed capability (solid blue line) and compared to results from a regular coupled calculation (dashed blue line) and a standalone TRANSURANUS calculation (orange line).

During 2021, a thermal-hydraulic solver was incorporated to the coupled calculation framework (Suikkanen and Rintala, 2022). For this purpose, the subchannel thermal

hydraulic code SUBCHANFLOW was obtained from Karlsruhe Institute of Technology (KIT). SUBCHANFLOW solves the coolant flow and heat transfer part of the coupled solution. The coupling was modified to provide the pin axial power distributions solved by Serpent as inputs to SUBCHANFLOW while SUBCHANFLOW provides the coolant temperature and density distributions to Serpent and the rod-adjacent coolant temperatures and heat transfer coefficients to TRANSURANUS. All these data transfers were established utilizing the existing data output and interface features of the codes. A specific development that needed to be made for data transfer was a separate Python tool that first creates the specified subchannel geometry and then further a corresponding 3D mesh in the OpenFOAM file format that Serpent uses via its multi-physics interface for input of coolant temperature and density data. With the Python tool, the user can first generate the geometry input files for SUBCHANFLOW calculations and then map the result data to the 3D data transfer mesh. The coupled calculation functionality with the solution obtained in iterations between the three codes was established for steady-state and burnup calculations. Figure 3 presents the pin powers (a), (b), and (c) and pin maximum temperatures (d), (e) and (f) at three stages of the cycle calculated for a single VVER-440 fuel assembly with six pins containing gadolinium oxide as the burnable absorber. With the inclusion of SUBCHANFLOW the coupled calculation framework was completed for steady state and burnup analyses considering the three major core solution areas.

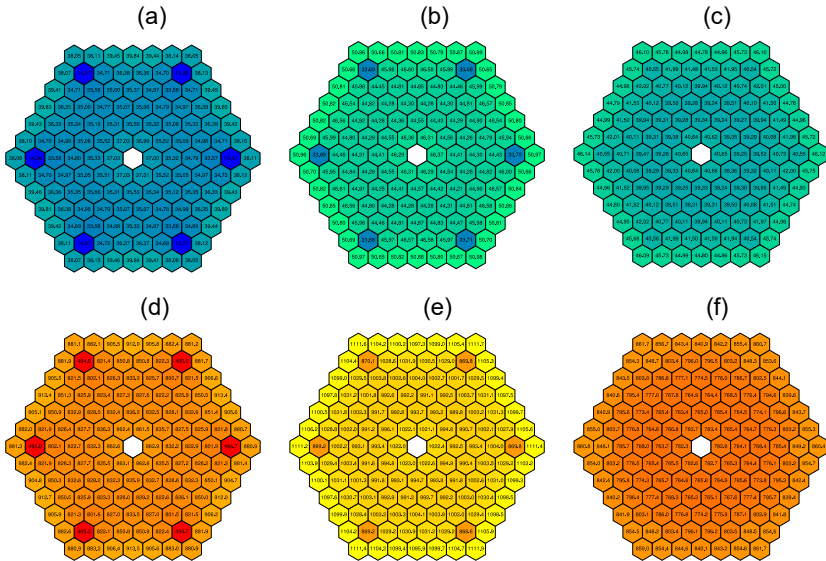


Figure 3. Fuel pin powers in kW (a), (b), (c) and maximum temperatures in °C (d), (e), (f) at 0 days (left), 102 days (middle) and 331 days (right) obtained in a Serpent-SUBCHANFLOW-TRANSURANUS coupled calculation.

Development in 2022 focused on adding transient analysis capabilities to the framework. All the three codes on themselves have transient calculation capabilities and the developments required for running coupled transient calculations mainly involves modifications to the coupling code that is used to run the codes in a coupled manner. As the first step, it was necessary to implement a proper restart functionality to the coupled calculation system. This is needed as the transient calculations will need to be started from an already established steady state condition with the core possibly burned to a desired phase of the cycle. Moreover, the restart functionality also allows steady-state and burnup calculations to be continued from a saved restart point, which is an essential feature for large and time-consuming coupled simulations. For coupled transient simulations, initial functionality between Serpent and TRANSURANUS was established as well as a control routine for running SUBCHANFLOW as a shared library during coupled simulations. This was found necessary as contrary to steady state simulations, the thermal hydraulic solution now needs to retain information of the heat that is received by the coolant during the short time steps, while in steady state all heat generated in the fuel can be considered to be transferred to the coolant during a state point. Thus, in earlier steady-state simulations, each SUBCHANFLOW iteration was started as a fresh run.

Conclusions

The work in EMBER resulted in a tool for performing highly detailed coupled calculations where the high-fidelity neutronic solution obtained with the Monte Carlo method based neutronics is used in conjunction with subchannel type thermal-hydraulics and 1.5D fuel thermo-mechanics to provide information on the behaviour of the fuel and the reactor at a very high level of detail and accounting for the relevant couplings between the neutronics, thermal-hydraulics and fuel thermo-mechanics. The toolset can in principle be used at various resolution levels and for problems spanning from a single fuel pin to the whole reactor core. However, mainly due to the use of the Monte Carlo based neutronics, the toolset is computationally expensive and thus has its main use in research or special purposes rather than in production-level calculations at power plants. The main expected benefit of the coupled toolset is that with the detailed approach, that also considers the couplings between the three major solution areas, it can be used to reduce and quantify uncertainties of the less detailed solution approaches more commonly used in reactor and fuel related safety analyses.

Acknowledgement

The authors would like to acknowledge Fortum Power and Heat Oy for providing power history data of the Loviisa NPP for use in this research. The authors would like to acknowledge the European Commission Joint Research Centre (JRC) Institute for Transuranium Elements (ITU) for collaboration related to the coupling

of TRANSURANUS. The authors would like to acknowledge Karlsruhe Institute of Technology (KIT) Institute of Neutron Physics and Reactor Technology (INR), the reactor physics and Dynamics Group (RDP) for providing the subchannel solver SUBCHANFLOW for use in this research.

References

- Imke, U. & Sanchez, V. H. 2012. Validation of the subchannel code SUBCHANFLOW using the NUPEC PWR tests (PSBT). *Science and Technology of Nuclear Installations* 2012, 465059.
- Lassmann, K. 1992. TRANSURANUS: a fuel rod analysis code ready for use. *Journal of Nuclear Materials* 188, 295-302.
- Leppänen, J., Pusa, M., Viitanen, T., Valtavirta, V. & Kaltiaisenaho, T. 2015. The Serpent Monte Carlo code: status, development and applications in 2013. *Annals of Nuclear Energy* 82, 142-150.
- Rintala, V., Suikkanen, H., Schubert, A. & Van Uffelen, P. 2022. Supplementing fuel behaviour analyses via coupled Monte Carlo neutronics and fission product solution. *Nuclear Engineering and Design* 389, 111668.
- Rintala, V. 2022. Coupling Monte Carlo neutronics with thermal hydraulics and fuel thermo-mechanics. *Acta Universitatis Lappeenrantaensis* 1059, Lappeenranta-Lahti University of Technology LUT, 63 p.
- Suikkanen, H., Rintala, V., Schubert, A. & Van Uffelen, P. 2020. Development of coupled neutronics and fuel performance analysis capabilities between Serpent and TRANSURANUS. *Nuclear Engineering and Design* 359, 110450.
- Suikkanen, H. & Rintala, V. 2022. Development of a calculation framework coupling Monte Carlo neutronics, subchannel thermal-hydraulics and 1.5D fuel thermo-mechanics. In *Proceedings of International Conference on Physics of Reactors 2022 (PHYSOR 2022)*, May 15-20, 2022, Pittsburgh, PA, 566-575.

5 Thermal Hydraulics

5.1 CFD methods for reactor safety assessment (CFD4RSA)

Timo Pätkangas¹, Ville Hovi¹, Juho Peltola¹, Ari Silde¹, Ulla Ojaniemi¹,
Jouni Syrjänen¹, Veikko Taivassalo¹, Tommi Rämä², Timo Toppila²

¹VTT Technical Research Centre of Finland Ltd
P.O. Box 1000, FI-02044 Espoo

²Fortum Power and Heat Oy
P.O. Box 100, FI-00048 FORTUM

Abstract

The overall objective of the CFD4RSA project has been to improve the usability and reliability of Computational Fluid Dynamics (CFD) calculations in nuclear Reactor Safety Assessment. The work consisted of five Work Packages, where topics important in safety assessment were studied. First, coupled CFD-Apros calculations were validated against experiments performed at the LUT University. Second, uncertainty quantification methods in CFD calculations were tested and taken into use. Third, coarse-mesh CFD models were developed for reactor pressure vessel and validated against international benchmark results. Fourth, CFD models for fuel rod bundles of boiling water reactors were validated against available experimental results. Fifth, thermal stratification in pressure suppression pools of BWRs were studied and Apros models for stratification were investigated.

Introduction

Computational Fluid Dynamics (CFD) is gradually becoming more important in Nuclear Reactor Safety (NRS) assessment. Increasing computing power and better understanding of the uncertainties and limitations of CFD methods are making use of CFD in NRS more appealing. Emerging coarse-mesh CFD methods reduce the computational cost of CFD but on the other hand increase the need of model

development. In the CFD4RSA project, some of the topics, where CFD is most useful for safety assessment, were developed and validated.

In WP1, coupled CFD–Apros simulations were performed for the PASI test facility of LUT University. The PASI test facility is a model of a passive cooling system of a containment, where natural circulation is used for cooling and pressure suppression of the containment vessel. Experiments performed in the PAHE project were modelled in co-operation with the THACO project, where an Apros model for the PASI facility was constructed. In the CFD4RSA project, the Apros model of the cooling circuit was coupled with a CFD model of the containment. An experiment of PAHE project was simulated, where steam had been injected into the containment. The coupled CFD–Apros calculation included the modelling of the condensation of steam on the heat exchanger, formation of mist in the gas space of the containment and the removal of condensate from the containment.

In WP2, Uncertainty Quantification (UQ) of CFD calculations was addressed. A test performed with the ROCOM test facility was used for testing UQ methods for CFD. The ROCOM test facility is a model of a PWR pressure vessel. In the experiments, hot water has been injected into the downcomer of the pressure vessel from one of the loops. In the experiment, mixing of hot water with cold water from other loops has been measured. The ASME method for UQ was tested by analyzing CFD results for temperatures at the core of the pressure vessel. In addition, the mixing of hot and cold water in the downcomer of the pressure vessel was studied. In both cases, the reliability limits for the CFD results were determined.

In WP3, coarse-mesh CFD models for reactor pressure vessels were developed and validated. The coarse-mesh CFD methods provide three-dimensional analysis for situations, which cannot be properly described with lumped parameter models. In the coarse-mesh approach, the computational cost is smaller than in traditional CFD calculations, but some additional sub-grid-scale modelling of the flow is necessary. Multiphase solver of OpenFOAM was developed for the coarse-mesh simulations, where the NuScale SMR reactor was used as the test case. Benchmark simulations for the Kalinin VVER-1000 reactor were performed by using two-way coupled OpenFOAM – Hextran-Smabre codes.

In WP4, fuel rod bundles of BWR were modelled with CFD calculations, where both OpenFOAM and ANSYS Fluent were used. The CFD results were compared to the measurements performed in the NUPEC BWR Full-size Fine-mesh Bundle Test (BFBT) Benchmark. The challenge was to find CFD models that can be used all the way from the bottom part of the fuel rod bundle to the top part. The interfacial friction and heat and mass transfer are drastically different in different parts of the fuel rod bundle. An important part of the work was the modelling of the size distribution of the vapor bubbles.

In WP5, CFD and Apros tools for the analysis of the thermal stratification of pressure suppression pools of BWRs were developed and validated. At the Royal Institute of Technology (KTH), an Effective Heat Source (EHS) and Effective Momentum Source (EMS) model were recently developed for the description of the thermal stratification, when steam is injected into a pressure suppression pool through sparger or vent pipe (Gallego-Marcos, 2018; Gallego-Marcos et al., 2018).

The possibility of implementing an EHS/EMS based model to the lumped parameter/system code Apros was tested.

Coupled CFD-Apros simulations of the PASI experiment

The PASI facility, located at the Lappeenranta-Lahti university of Technology, is designed for studies concerned with the functioning of a gravity-driven Passive Containment Cooling System (PCCS) (Kouhia et al., 2018). Such a system typically consists of several heat exchangers inside the containment building, connecting pipelines, and one or several water reservoirs outside the containment building. As the naming implies, coolant flow between the heat exchangers and coolant reservoirs is based on natural circulation. The design goal of the PASI facility is to study the performance characteristics of and to detect issues that could prevent the operation of a PCCS. In addition to providing valuable insight to the performance of PCCSs during post-accident conditions, the available measurement data can be used to validate existing computer codes and model combinations.

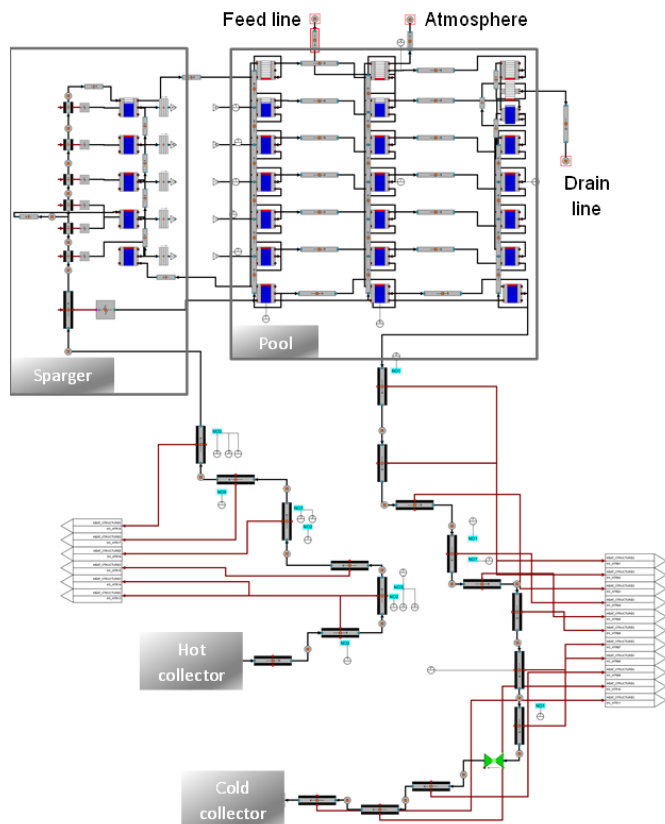


Figure 1. Main part of the Apros model.

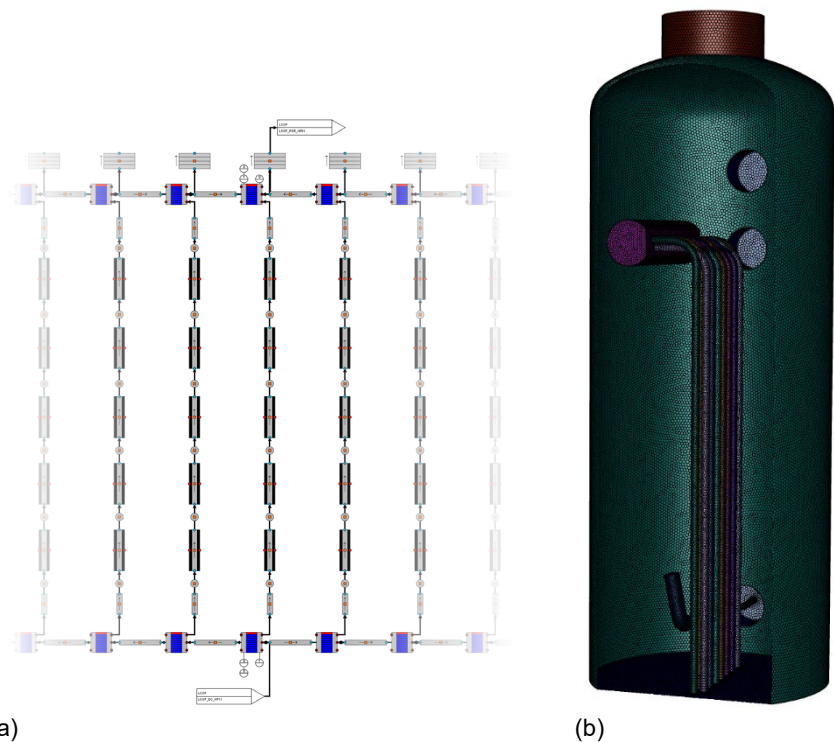


Figure 2. Nodalization of the PASI heat exchanger (a) and an overview of the surface mesh for the containment vessel (b).

The Apros model, provided by project THACO, contains the whole PASI facility: the containment vessel, heat exchanger, water pool, sparger, and the interconnecting pipelines (riser and downcomer). Main parts of the Apros model are illustrated in Figure 1. To facilitate the coupling, the original model was modified by removing the containment vessel and rebuilding the heat exchanger with a higher resolution. The nodalization of the heat exchanger is shown in Figure 2(a).

A CAD model of the PASI containment vessel was created based on the facility description provided by Kouhia et al. (2018). The internal structures included in the model are the steam inlet pipe, the heat exchanger tubes, and the hot collector. A CFD mesh, consisting of ~1.9 million polyhedral cells, was created based on the CAD model. Two shell conduction layers were added on the containment vessel exterior walls to better account for the heat losses to the laboratory room, which increases the total amount of cells to ~2.1 million cells. An overview of the surface mesh for the containment vessel is shown in Figure 2(b).

The computational models are combined at the outer surface of the heat exchanger tubes, where coupled heat transfer between the models is solved. Apros provides the surface temperature distribution for the heat exchange tubes, the

resulting heat flux is calculated by the CFD model, and the integrated heat transfer rates for each heat structure node are returned to Apros.

A bespoke experiment, VTT-01, was conducted at the PASI facility with a modified steam inlet pipe. The experiment starts from an initial state close to ambient conditions. At the beginning of the experiment, steam injection to the containment vessel is started with a mass flow rate of 10 g/s. During the experiment, steam mass flow rate is increased in a stepwise manner. However, due to time constraints, only the first mass flow rate step was simulated with the coupled model.

A comparison of containment temperature [$^{\circ}\text{C}$] at four measurement locations is presented in Figure 3(a) and Figure 3(b), where the measurements are plotted with continuous lines and the simulation results are plotted with markers. The measurement locations are shown in Figure 3(c).

When comparing the containment temperature in the two lowermost measurement locations, T5041 and T5042 in Figure 3(b), the results are quite close to the measurements. The wiggling in both the measured and simulated value of T5041 suggests that the location of the thermally stratified front is accurately captured and near the measurement location during the early stages of the experiment. A more noticeable difference exists in the containment temperatures at the two highest measurement locations, T5043 and T5044 in Figure 3(a). The simulated temperatures remain ~ 5 $^{\circ}\text{C}$ higher than the measured values during the early stages of the experiment.

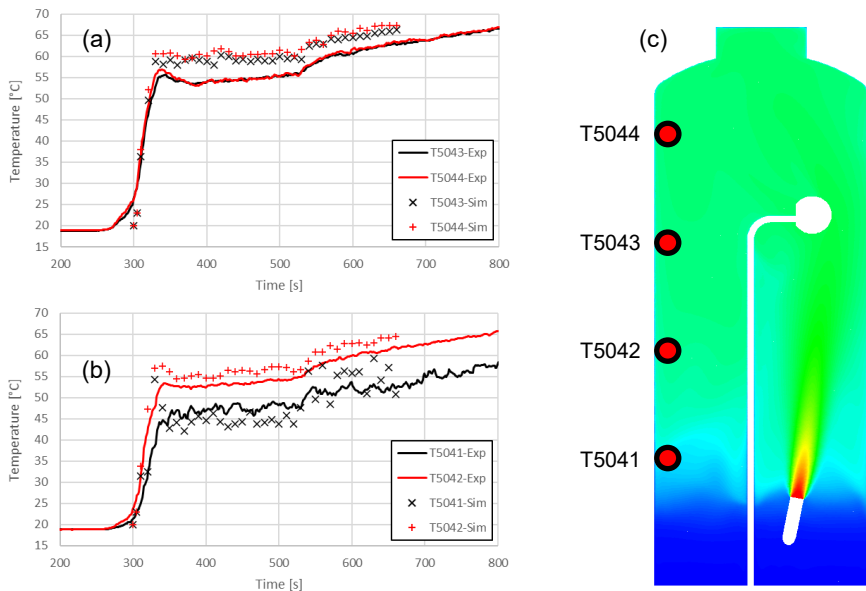


Figure 3. Containment temperature [$^{\circ}\text{C}$] at four measurement points (c): Measurement points T5043 and T5044 (a) in the upper half of the vessel and T5041 and T5042 (b) in the lower half of the vessel.

Uncertainty Quantification in CFD

The uncertainties of CFD simulation were explored in comparison with the experimental results made with the test facility ROCOM (Rossendorf Coolant Mixing Model). The experiments with ROCOM concerned the influence of the coolant mixing in the reactor pressure vessel on the Natural Circulation Interruption (NCI). NCI occurs as a result of the balance between the buoyancy driving forces in the primary loop downcomer, core, SG U-tubes, loop seal (Kliem and Franz, 2016).

The ROCOM tests considered in this work were designed to address the fluid/fluid mixing of hot and cold water in the RPV downcomer and in the lower plenum and the temperature distribution at the core inlet. The reactor consisted of four cooling loops. The coolant was fed into the reactor vessel from three loops, and from the Loop 3, the water/ethanol solution prepared to describe the hot water density was injected. The injected fluid was labelled with NaCl, which changes the conductivity of the fluid. The concentration was determined by measuring the conductivity. At the low concentrations applied in the experiments, the direct proportionality of conductivity and concentration is ensured. Therefore, the mixing in a reactor was measured by the conductivity of the fluid and the degree of mixing was followed with a mixing scalar determined based on the conductivity of the slug water fed from the Loop3. In the turbulent flow field, temperature differences between different parts of the coolant can be treated in a similar way as difference in salt concentration (Kliem and Franz, 2016). Therefore, the coolant mixing can be described on the basis of the mixing scalar determined in the ROCOM experiments.

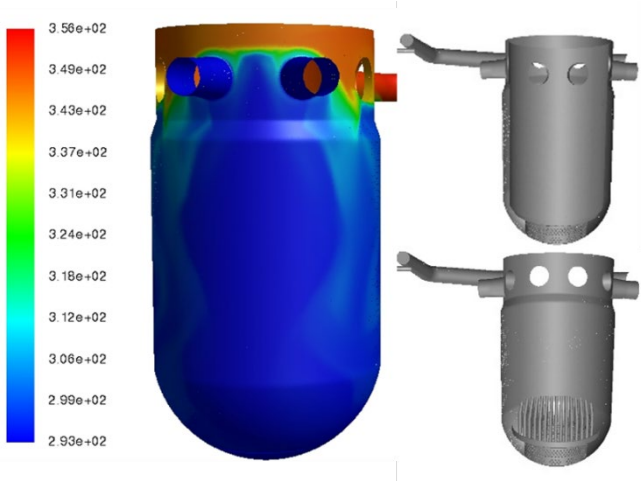


Figure 4. Geometry applied for the experimental facility of ROCOM. On the left: Simulated temperature distribution on the outer surface (K), On the right: internal structure of the computational domain.

In Figure 4, the geometry of ROCOM test facility is presented. On the left, the simulated temperature is shown on the outer surface of the RPV. On the right, the internal structure of the reactor is presented: at the top, the computational domain is presented between the inner and outer downflow walls, and at the bottom, the core of the reactor is presented. The computational domain was decreased by describing the pipes in the core partially by pressure drop. The experimental measurement plane for core inlet is located in the middle of the pipes shown in the core. In Figure 4 on the right, Loop3 is located on the back left.

ASME Verification and Validation (V&V) method was chosen for the uncertainty quantification (UQ). According to the ASME methodology, the overall uncertainty in CFD consists of three types: the numerical, the input, and the model uncertainty (NEA, 2016; Rakhimov et al., 2019). The model uncertainty represents the uncertainty introduced by the physical models that are used in the CFD simulation, such as turbulence models. The numerical uncertainty represents the combined effect of the mesh resolution, the convergence level and, in case of unsteady problems, time discretization. The input uncertainty is related to the data provided by the user in the code, such as initial conditions, boundary conditions, and physical properties of the materials. Uncertainties in these inputs is propagated through the solution process to the outputs. The propagation of the uncertainty in the input parameters was sampled with the Deterministic Sampling method DS-bin. The basic idea behind Deterministic Sampling (DS) is that a continuous Probability Density Function (PDF) can be substituted by a set of discrete weighted samples, called Sigma Points (SP), that have to represent the same statistical moments of the PDF. These SP are few in number, hence the number of required simulations for input ensemble propagation reduces substantially (Rakhimov et al., 2019).

Simulated cases for uncertainty quantification were carried out variating the size of the time step, and the spatial discretization method. Further, the inlet temperature and mass flow rate at Loop 3 were variated. In here, with two input parameters, there was required only four sample cases simulated with CFD for input ensemble according to DS-bin. The k- ω Shear Stress Transport (SST), wall resolved model with full buoyancy effects was applied for modelling the turbulence. The turbulent intensity values in the inlets were kept constant in the tested cases. As well, the amount of iterations during a time step was kept constant, 80. Increasing the amount did not improve the convergence of the computation further. In here, uncertainties due to mesh resolution were not considered. All the cases were initialized with the same state comparable with experimental arrangement, that was started only with coolant feed during the time period of 100 seconds.

The reliability limits for the CFD results were determined for the core inlet and for the downcomer of the test facility of ROCOM. In Figure 5, the results at core inlet are presented, and in Figure 6, the results are presented for the downcomer. At the bottom of the figures, the results of UQ are presented at several cross-sections over the computational domain. The simulated results are shown with the black lines, and the pink lines present the asymmetric uncertainty bands.

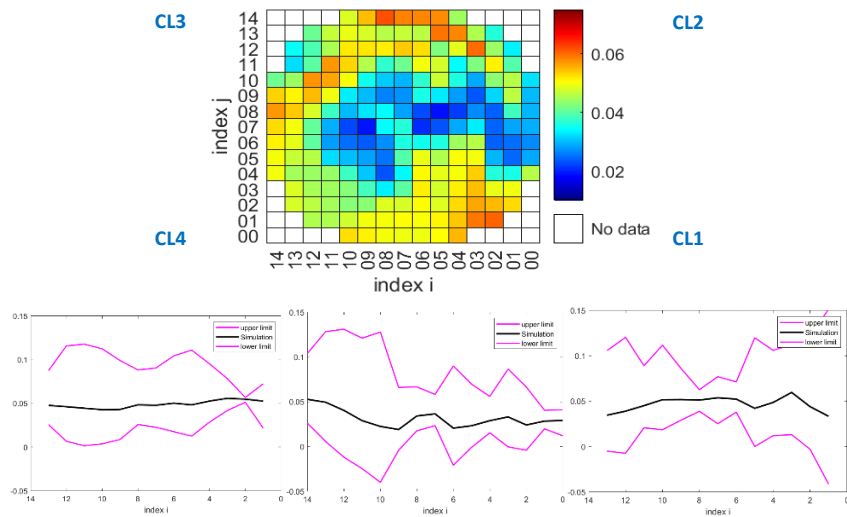


Figure 5. On the top: Simulated temperature distribution by mixing scalar at the core inlet. At the bottom: Results of UQ at the 2nd, 7th and 12th, row from the figure on the top.

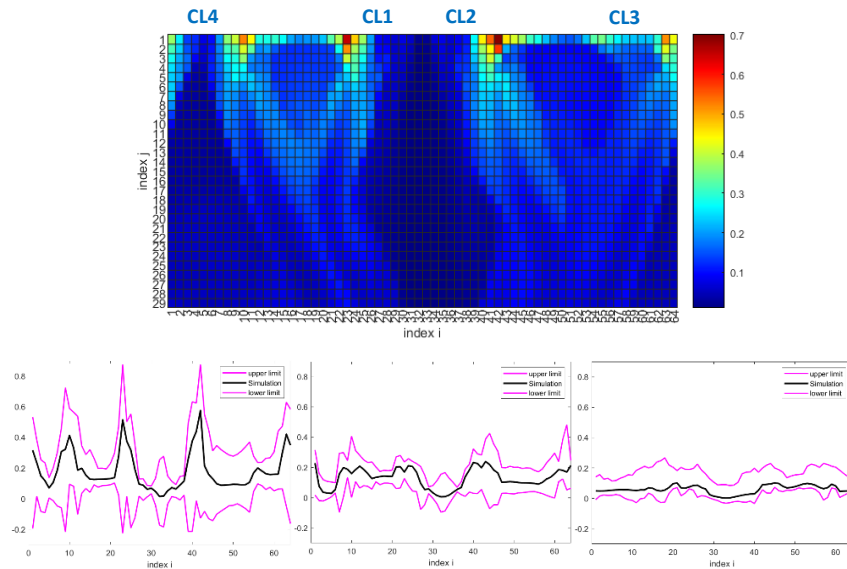


Figure 6. On the top: Simulated temperature distribution by mixing scalar at the downcomer. At the bottom: Results of UQ at the 2nd, 7th and 25th row from the figure on the top.

Coarse-mesh CFD models for pressure vessels

The OpenFOAM multiphaseEulerFoam framework and subsequently the present multiphaseEuler solver module was extended for the purposes of coarse-grained simulation of nuclear safety applications. The concept is based on using stationary phases of the multiphase solver to represent abstracted physical structures as porous medium. The approach can be used for both single and multiphase flow applications.

The required extensions have been tightly integrated to the framework, minimizing code duplication to decrease future maintenance load and to benefit from ongoing development of the framework for other purposes. The solver and implemented functionality have been continuously tested in open medium subcooled nucleate boiling simulations and in RPV simulations of an SMR design similar to NuScale, and also in simulations of VVER-1000 RPV.

The interfacial model framework was found to be inadequate to support the targeted coarse-grained reactor pressure vessel simulation model and a custom extended version of the framework was implemented and tested. The project participated in specification and funding of large restructuring of the interfacial modelling framework, which is now available in the OpenFOAM Foundation release (Bainbridge, 28 January 2022) and has been applied in the recent simulations, rendering the earlier custom implementation unnecessary. Similarly, the recent addition of turbulence model stabilization (Weller, 16 February 2022) serves to make the previous implementation in this project obsolete. Preparation of the volumetric wall boiling models for integration into the public OpenFOAM Foundation release led to a restructuring of the existing wall boiling functionality and implementation of a more robust solution algorithm for wall temperature (Bainbridge, January 2023). Integration of cavitation modelling outside of this project led to improved implementation of the pressure implicit phase change algorithm, which also benefits present thermal phase change simulations. The RPV simulations presented here led to changes in the latent heat treatment of the solver in thermal phase change simulations (February 2023). All-in-all, the solver is now significantly more robust in thermal phase change simulations than it was even one year ago.

The present extensions that are not currently available in the public OpenFOAM Foundation release consist of porous medium induced turbulence model, interfacial model wrappers that introduce regional modelling filtering options as well as new porous medium specific interfacial models, notably a volumetric wall boiling model and support for anisotropic drag modelling. The wall boiling model uses the same runtime selectable sub models as the open medium wall boiling wall functions previously developed in SAFIR programs. To enable this, the phase system has been modified to add coupling to interfacial models that are able to trigger nucleation. Further integration of the functionality to the OpenFOAM Foundation release is targeted in near future, although the present project has ended.

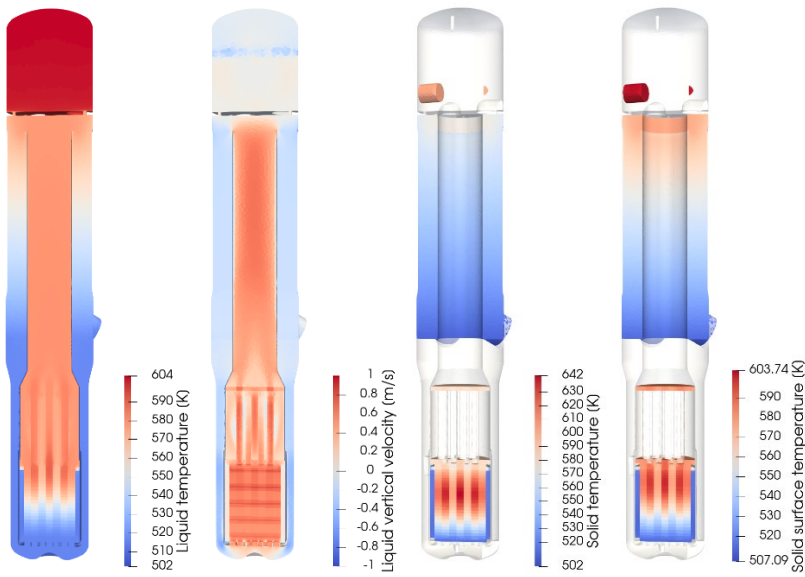


Figure 7. Illustration of results for the NuScale RPV simulation: liquid temperature (K), liquid vertical velocity (m/s), solid temperature (K), and solid surface temperature (K).

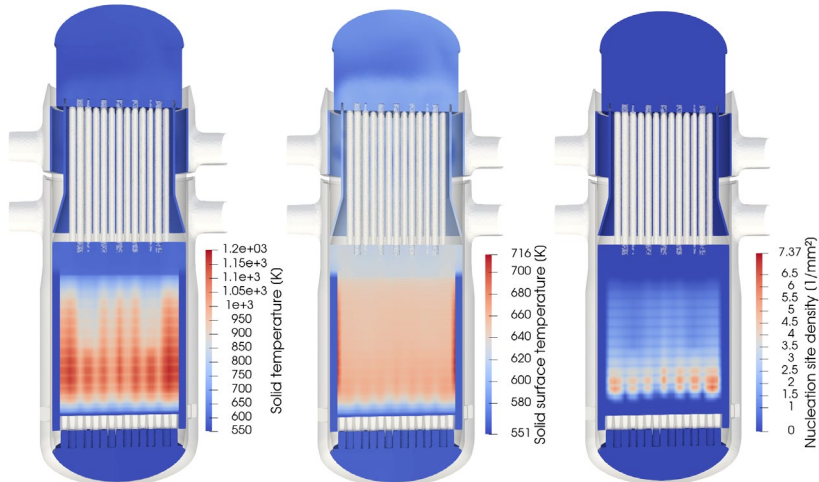


Figure 8. Illustration of the developed VVER-1000 model: solid temperature (K), solid surface temperature (K), and nucleation site density ($1/\text{mm}^2$).

A major improvement for the applicability of the solver to nuclear safety applications was the recent (Autumn 2022) change in the architecture of the OpenFOAM Foundation release to move from standalone solvers to solver modules that can be

coupled together in arbitrary combinations. This enables conjugate heat transfer (CHT) simulations beyond porous regions with the present solver. Not to mention any combinations of coupled single-phase, Volume-of-Fluid (VoF) multiphase and Eulerian multiphase solvers in different regions of a simulation.

Coupling to other nuclear safety simulation tools was demonstrated by implementing and testing a coupling to VTT in-house Kraken simulation framework. The extended framework was used for steady state simulation of a reactor pressure vessel that resembles a NuScale SMR reactor design with coupling to nodal neutronics code ANTS. In stable condition shown in Figure 7, the reactor core is cooled by natural circulation. The temperatures of the stationary solid phase regions and the solid structure surface temperature are shown separately. The surface temperature is coupled to a wall boiling model. There is no apparent nucleation in the core with the applied heat transfer models. Slight nucleation occurs on the surface for the pressurizer heater elements and interfacial phase change on steam-water interface in the pressurizer.

The framework has also been applied to OpenFOAM-ANTS-SuperFINIX simulation of the VVER-1000 reactor in project CATS. For those simulations the multiphase capability of the solver was not needed. The same VVER-1000 case was, however, used as the test case for the solver development both in single phase and two-phase configurations. Figure 8 shows results for a solver stress test simulation of the VVER-1000 with core heating power increased to create strong boiling in the core region.

In its present form, the solver module provides a feature rich, extendable and transparent platform for many nuclear safety simulations. Clear remaining development items include adoption of the interval splitting algorithm also for the volumetric wall boiling model, surface condensation models, extension of the new anisotropic solid phase thermal conduction modelling to stationary phases. Further integration of the functionality to the public release is necessary to avoid maintenance and development of duplicate functionality amongst the collaborators in this project and in the wider nuclear safety community.

Coarse-mesh CFD models for VVER-1000

The coarse-mesh models were also applied to the VVER-1000 reactor, which was selected because of the experimental data available. Exercise 1 in Phase 2 of the VVER-1000 Coolant Transient Benchmark (V1000CT-2), also known as the VVER-1000 vessel mixing problem (Kolev et al., 2010), was chosen as the first test case. The primary objective of this exercise was to test the performance of the thermal-hydraulics models in reproducing the single-phase mixing in a reactor pressure vessel. The exercise was based on experiments in the Kozloduy-6 reactor and its purpose was to model thermal-hydraulics with given boundary conditions for the pressure vessel and with a pre-described power distribution. Experimental results exhibit a significant angular shift of the coolant flow between the inlet nozzles and

the core. This phenomenon is a characteristic feature of the VVER-1000 V320 reactors.

A set of meshes with different spatial discretizations were created and applied in the coarse-mesh simulations with an OpenFOAM solver. A one-way coupling of the neutronics code HEXTRAN and the OpenFOAM solver was employed and the coolant heating power field from a pre-calculated HEXTRAN-SMABRE simulation was applied in the computations with OpenFOAM.

Computationally the coolant flow rotates in the downcomer if a small bias is applied in the velocity profile at the cold leg inlets. A reasonable turbulent intensity at the inlets further improves the agreement with the experimental data. In addition, when the turbulent viscosity is increased from the $k-\epsilon$ model prediction calculated with a coarse mesh, computational mixing is in a good agreement with the experimental results and an excellent agreement with the experimental data is obtained (Figure 9). Computational results for meshes with different spatial discretizations indicate the insensitivity of the modelling approach to the mesh density.

The OpenFOAM solver with the coarse-mesh models was also applied to another VVER-1000 benchmark, to the OECD/NEA/NSC Kalinin-3 benchmark (Tereshonok et al., 2009). This benchmark provides reactor-scale experimental results for testing and validation of reactor analysis tools. The primarily focus is in the reactor behaviour during an asymmetric transient following the switching-off of one main circulation pump.

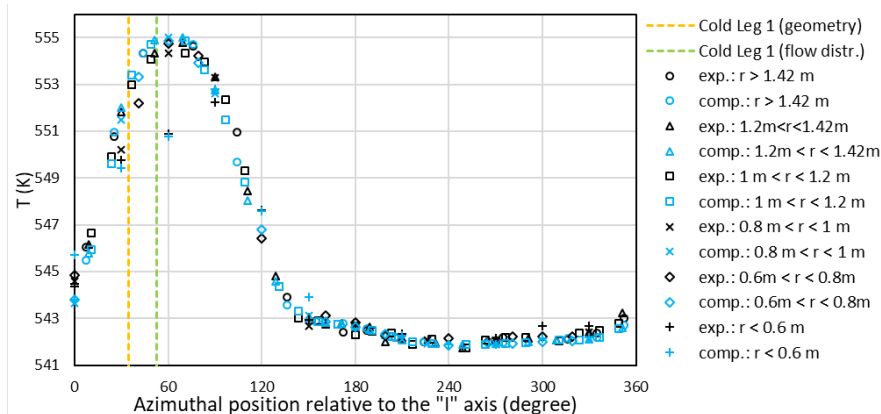


Figure 9. Computed and experimental coolant temperature at the assembly inlets for different radial zones in the final state of the VVER-1000 Coolant Transient Benchmark.

In the studied Exercise 3 of the benchmark, the transient behaviour of the whole nuclear power plant was predicted in challenging flow conditions. A coarse mesh was created for the reactor pressure vessel and OpenFOAM computations were performed applying models and methods developed and tested previously for

coarse-mesh modelling of the VVER-1000 pressure vessel. The SMABRE model covers the rest of the power plant. In a transient simulation for Kalinin-3, two-way couplings of the neutronics code HEXTRAN and the system code SMABRE with the OpenFOAM solver were employed.

The OpenFOAM modelling of the reactor pressure vessel improves the agreement with the experimental data compared to the HEXTRAN-SMABRE simulation (Figure 10). For the initial and final stages, the computed differences between the coolant temperatures in the hot and cold legs are significantly closer to experimental values than in the HEXTRAN-SMABRE simulation and the deviations are well within the experimental uncertainties. Simulations predict an earlier reversal of flow in Loop 1 than interpreted for the experiment, which causes some timing deviations in the transient stage. Figure 11 shows the coolant temperature on the cross sections of the legs in the final state with the reversed flow in Loop 1. The good agreement of the coolant heat-up with experimental data in the final asymmetric stage indicates that heat production in the core as well as mixing in the pressure vessel are satisfactorily modelled.

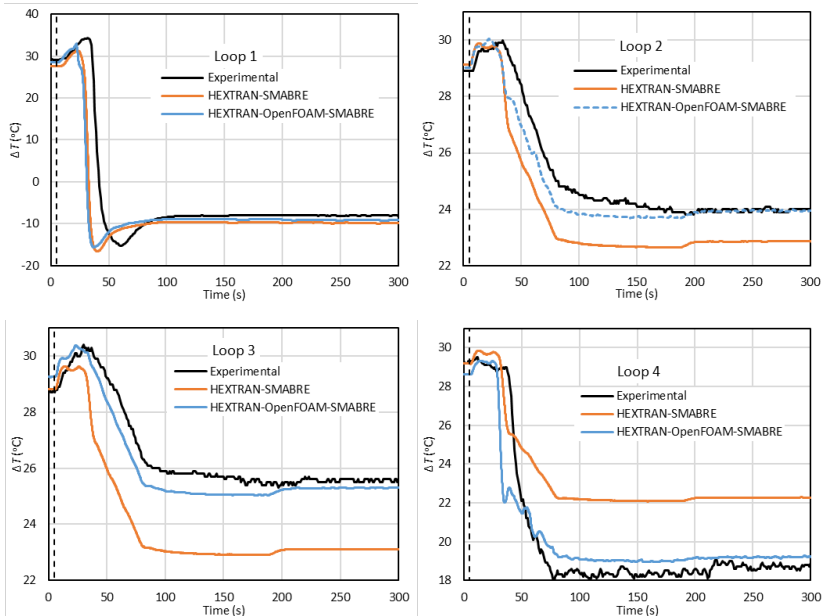


Figure 10. Experimental and computed differences of the coolant temperatures between the hot and cold legs in the Kalinin-3 benchmark. The broken vertical lines mark the time of the pump stop.

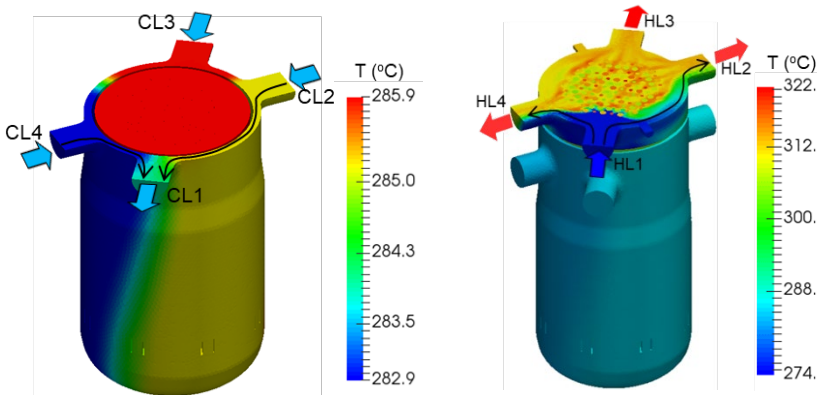


Figure 11. Computed coolant temperature for the pressure vessel on the horizontal planes of the cold and hot legs as well as in the outer cells of the mesh under the planes in the final state of the Kalinin-3 benchmark.

CFD simulations of BWR fuel rod bundle

CFD simulations of a BWR fuel rod bundle using the NUPEC BWR Full-size Fine-mesh Bundle Test (BFBT) Benchmark as the test case were conducted with ANSYS Fluent (Fortum) and OpenFOAM (VTT).

BFBT experiment 0011-53 was simulated utilizing the multiphase models developed in the present SAFIR2022 and earlier SAFIR2018 and SAFIR2014 research programmes. The applied models are all publicly available as part of the OpenFOAM Foundation release. The goal was to assess suitability, performance and shortcoming of the existing models primarily intended for PWR conditions in simulation of a BWR bundle. The case setup and sub model selection were largely based on the wall boiling tutorials of OpenFOAM Foundation release.

The simulations were carried out for a single subchannel and a half of the bundle geometry utilizing diagonal symmetry of the bundle. The applied solver was OpenFOAM-dev (21 November 2021 version) multiphaseEulerFoam. The model was a two-fluid model with an inhomogeneous class method population balance for the vapor bubbles and an extended RPI wall boiling model. The present study was limited to simulation of a 2% exit equilibrium steam quality experiment 0011-53.

The results indicated that with a suitable bubble diameter prediction the void distribution at the end of the heated section can be relatively well predicted with the selected interfacial models. A key is the bubble diameter prediction. With the present coalescence and breakup models the inhomogeneous population balance did not predict large enough bubbles to reproduce the central void peak to the degree observed in the experiment. The model was able to reproduce the

simultaneous wall and central void peaks observed in the experiment when inhomogeneous population balance was used, Figure 12.

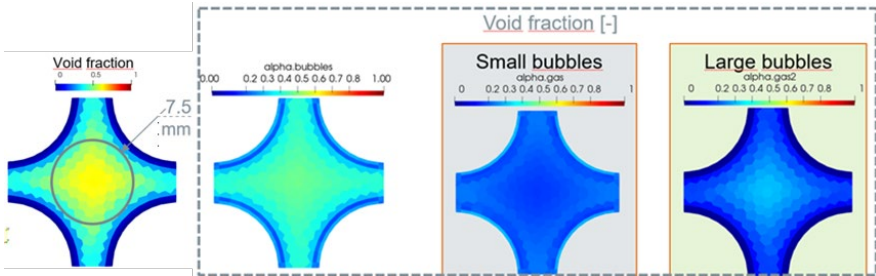


Figure 12. Predicted void fraction distribution of the subchannel simulation with algebraic bubble diameter model using near constant 7.5 mm bubble diameter at the cross-section (far left). Predicted void fraction distribution of the subchannel simulation with population balance with combined void fraction (centre left) and separated result for the small and large bubbles (centre and far right).

In the bundle simulations the results did not show the large variations between adjacent subchannels observed in the experimental result. Possible reasons for the difference include geometric simplifications like the neglected spacer grids. Weaknesses in turbulence and interfacial force modelling and numerical diffusion may also contribute and further investigation was needed to improve the model.

The simulations were stable, and performance was good enough for practical simulation of fuel rod bundles with the presented case setup models, including the inhomogeneous population balance model. Simulation results for a bundle could be obtained in roughly three days of computation on a 64 CPU core node.

Based on observations of too high average void fraction in the simulations, a swarm correction was added to increase the slip velocity between the phases. The modified drag modelling improved the simulation results of local steam bubble void fraction maximum values in subchannels on outlet surface of the channel qualitatively, presented in Table 1. Overall void fraction peak distribution prediction on the outlet remained uniform unlike found in the experiment (see Figure 13).

Inclusion of spacer grids in the simulation improved the void fraction distribution to more realistic non-uniform configuration, shown in Figure 13, although the present simulations with the spacer grids were carried out with slightly simplified set of closure models. Taking account of bubble break-up when passing the spacer grids and coalescence above them is important feature in the modelling of the test case, as is illustrated in Figure 14. Average void fraction on the outlet surface remained higher than in the experiments, though.

Simulations of the BFBT experiment were also done with ANSYS Fluent in by Rämä (Rämä, 2022). In those simulations, ANSYS Fluent's boiling model with constant saturation temperature was used. For the evaluation of the capabilities of the used CFD tool for BWR bundle simulations, REFPROP based real-gas property

tables, provided as beta-feature in ANSYS Fluent 2021R2 (Ansys 2021), were implemented. The simulations were hampered by convergence difficulties.

Table 1. Comparison of effect of swarm correction of drag on bubble velocities and void fractions.

Swarm correction parameter	Average bubble velocity (m/s)	Maximum bubble velocity (m/s)	Average bubble void fraction	Maximum bubble void fraction
$L = 1.5$ (no correction)	3.21	3.7	0.32	0.40
$L = 1$	3.24	3.8	0.31	0.45
$L = 0.5$	3.28	4.0	0.31	0.53
$L = 0$	3.32	4.8	0.30	0.81

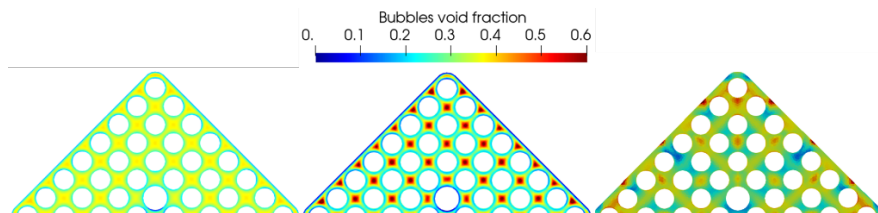


Figure 13. Void fractions on outlet surface on top of the channel, without swarm correction or spacer grids (left); with swarm correction and without spacer grids (centre); and with swarm correction and spacer grids (right).

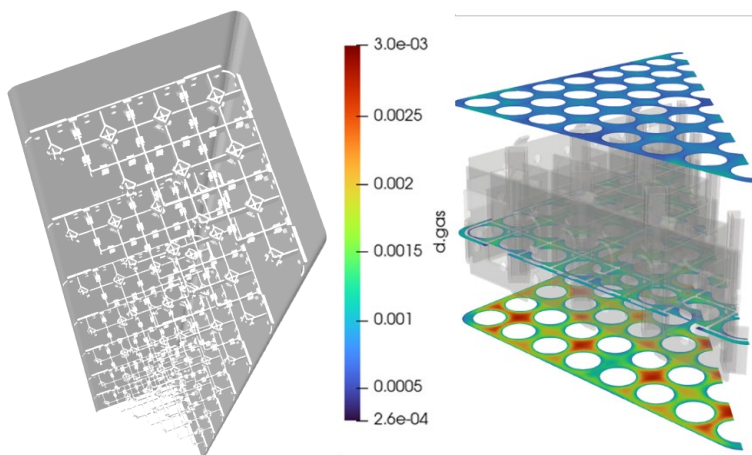


Figure 14. Geometry of spacer grids in the simulated half of the rod bundle channel (left), and bubble diameters (m) below and above the topmost spacer grid illustrating bubble break-up due to it (right).

Stratification in pressure suppression pools

The pool thermal stratification phenomena were investigated by Apros model and the ANSYS Fluent code by calculating the POOLEX stratification tests SPA-T3 and SPA-T8R. Puustinen et al. at the LUT University performed the pool thermal stratification and mixing experiments with the PPOOLEX test facility (Laine et al., 2014) (Figure 15 and Figure 16). The facility simulates the BWR containment system consisting of the drywell and wetwell gas volumes with interconnecting pipes between them and the pressure suppression pool in the wetwell.

Initial free volumes of the PPOOLEX drywell and wetwell are 13.3 m^3 and 5.5 m^3 , respectively. Total height and diameter of the facility are 7.45 m and 2.4 m, respectively. Water initial elevation in the wetwell in PPOOLEX tests under consideration was 3.0 m. The initial pressure, and gas and water temperatures were 1 bar and 21°C , respectively. The PPOOLEX tests SPA-T3 and SPA-T8R were calculated with the Apros code. The Fluent code was applied in SPA-T8R test calculation.

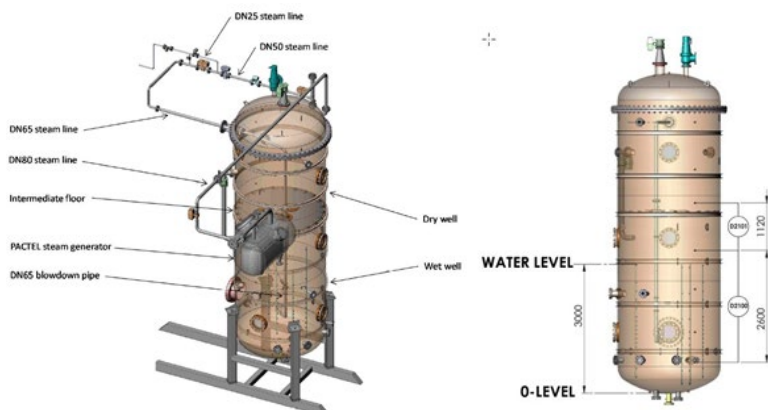


Figure 15. PPOOLEX test vessel (Laine et al., 2015).



Figure 16. Sparger of the PPOOLEX test facility (Laine et al., 2015).

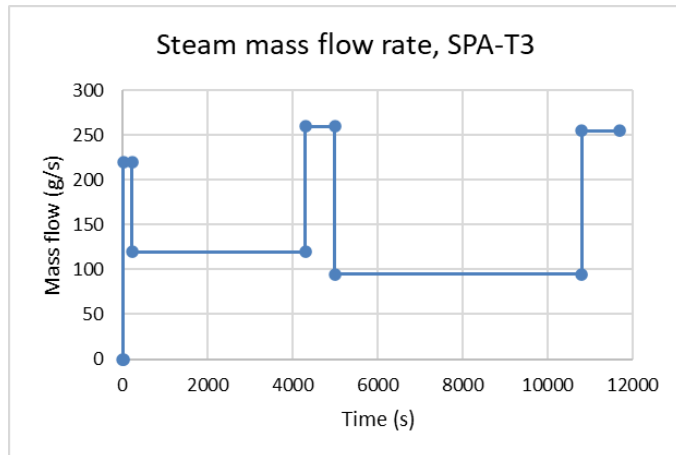


Figure 17. Steam mass flow rates in PPOOLEX SPA-T3 experiment.

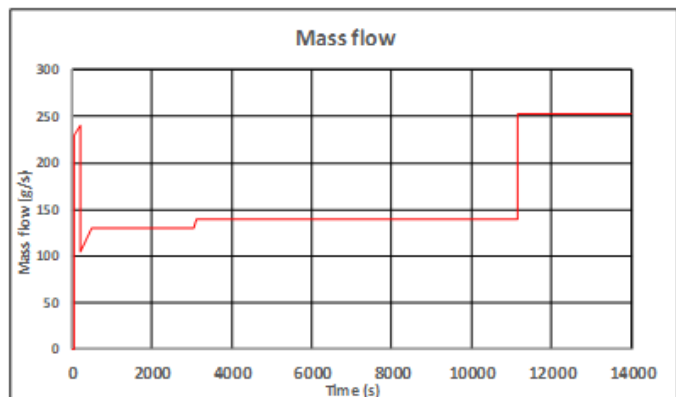


Figure 18. Steam mass flow rates in PPOOLEX SPA-T8R experiment.

The steam was injected into the pool through sparger holes at around 1.2 m elevation from the pool bottom. The steam injection rate was varied during both tests under consideration and the pool stratification and pool mixing phases alternated during the tests (Figure 17 and Figure 18).

The goal of the Apros analyses was to study the modelling capabilities of Apros for pool stratification and mixing. In addition, it was studied whether the implementation of KTH EHS/EMS model in Apros would be worthwhile (Silde, 2022), (Gallero-Marcos, 2018). The drywell and wetwell gas spaces of the PPOOLEX facility and the environment node were modelled with the Apros LP containment model, whereas the steam pipeline and the sparger, and the suppression pool was modelled with the six-equation thermal hydraulic model. Pseudo-2D nodalization schemes were used for the suppression pool. The best

estimate nodalization consisted of three node columns and 21 axial node levels. Therefore, the height of one node level was 0.1 ... 0.2 m. Sensitivity studies were also performed for the discretization scheme used between pool nodes (upwind or second order) and effect of steam mass flow rate on pool mixing/stratification.

The measurements and simulation results of pool temperatures obtained with the Apros 3-column nodalization are shown in Figure 19. The measurements are along the measuring bar L4 which is located at 0.8 m distance from the sparger vertical pipeline. The legends of the figures indicate the distance from the pool bottom. The plot on the top shows the measurement values and the bottom plot shows the Apros calculation results. The pool temperatures are in fairly good agreement with measurements at +0.82 m and above it. In this area the pool is relatively well mixed vertically through the test. The mixing of pool bottom at +0.16 m is overpredicted beyond 11 000 s, but at elevation of +2.2 m and above the mixing is also well simulated. Use of 3 node columns instead of 2 in the Apros model attenuates the pool vertical mixing above the sparger elevation, and correspondingly strengthens the natural circulation flow, also in the lower parts of the pool. It is worth noting that in Apros the pool mixing takes place only due to natural circulation flow, not by turbulence, which is not modelled at all.

The results of the Apros calculation showed that the 2-column model could simulate the pool vertical stratification reasonably, but the global pool mixing phase could not be simulated realistically. The 3-column model could predict the stratification phase very well. The better results of the 3-column model are probably caused by the way how the model is able capture the main natural circulation flow inside the pool. Use of higher order discretization scheme did not give any advantages for pool stratification and mixing simulations. The 3-column nodalization used in the work is promising and the model concept should be further studied by simulating some full-scale experiment, such as PANDA pool stratification test. Apros results also indicated that an implementation of the KTH EHS/EMS models in Apros would probably give advantages for pool mixing/stratification calculations, since enhanced momentum improved the Apros results in this work. However, it is worth noting that the 1D modelling approach of Apros (even when using pseudo 2D nodalization) cannot model all detailed 2D/3D pool phenomena accurately.

The stratification and mixing phases of the SPA-T3 condensing test performed in the PPOOLEX test vessel were also simulated with ANSYS Fluent v.19.5 by using the volume of fluid (VOF) model for free surface and $k-\omega$ turbulence model. The VOF model was included to describe the water surface elevation and to improve the heat transfer on the water surface, which issues were noted in the earlier simulation (Pätkangas, 2020). The steam jets of the SPA-T3 test were modelled with the effective momentum source and the effective heat source (EMS/EHS) models, which simplifies the CFD modelling task and saves computational resources.

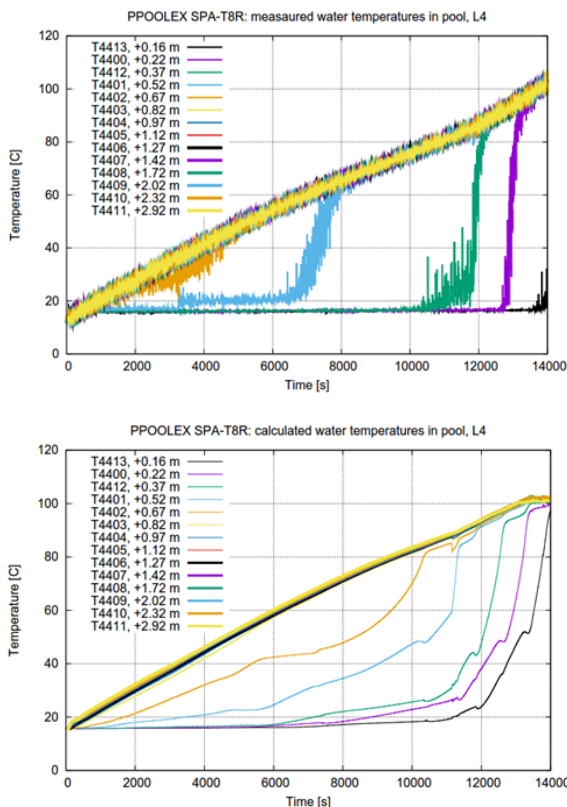


Figure 19. Pool temperatures: measurements (top) and calculation with 3-column model (down).

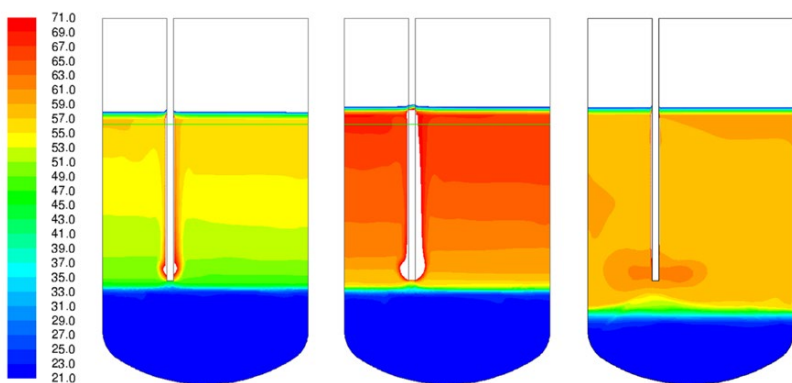


Figure 20. Simulated water temperature ($^{\circ}\text{C}$) in the end of stratification phase (4303 s) at left, and in the end of mixing phase (5000 s) with original steam source location (centre) as well as with extended steam source location (right).

The CFD simulations underpredicted the mixing of pool water to some degree. It suggested stronger stratification of temperature both in stratification and mixing phases of the experiment than observed. When the EMS/EHS source location was extended for the mixing phase simulation, the mixing improved considerably, illustrated in Figure 20.

The weaker than expected mixing might have been caused partly by less accurate discretization schemes, which were used for convergence or compatibility reasons. Also, $k-\omega$ turbulence model may predict lower level of turbulence and thus weaker heat transfer than $k-\varepsilon$ model used in the earlier simulation (Pätkangas, 2020). Extending the EMS/EHS source location, if necessary, could be done in more optimal way. Including heat losses from the steam pipe to the EHS model and through the vessel wall would further improve the model, the latter by enhancing circulation from the top of the vessel to the bottom.

References

- ANSYS, ANSYS Fluent 2021R2 Fluent Beta manual section (2021).
- Gallero-Marcos, I. 2018. Steam condensation in a water pool and its effect on thermal stratification and mixing. KTH School of Engineering Sciences. Doctoral thesis.
- Kliem, S., Franz, R., 2016. OECD PKL3 Project – Final Report on the ROCOM Tests, Institute Report HZDR\IFWO\2016\01.
- Kolev N.P., Aniel, S., Royer, E., Bieder, U., Popov, D., Topalov, Ts., 2010. VVER-1000 Coolant transient benchmark Phase II (V1000CT-2), Vol. 1, Final specifications of the VVER-1000 vessel mixing problem, NEA/NSC/DOC (2007)22, OECD.
- Kouhia, V., Riikonen, V., Telkkä, J., Partanen, H., Räsänen, A., Kauppinen, O., Kotro, E., Saure, I., Tielinen, K., Karppinen, J., 2018. General description of the PASI test facility, 2nd edition. Technical Report, Lappeenranta-Lahti University of Technology LUT.
- Laine, J., Puustinen, M., Räsänen, A. 2014. PPOOLEX mixing experiments. Nordic Nuclear Safety Research, NKS-309.
- NEA, 2016. Review of Uncertainty Methods for Computational Fluid Dynamics Application to Nuclear Reactor Thermal Hydraulics. NEA/CSNI/R(2016)4.
- Pätkangas, T. 2020. CFD analysis of pressure suppression pool by using effective heat and momentum source models. VTT Technical Research Centre of Finland, Research report VTT-R-00228-20.
- Rakhimov, A.C., Visser, D.C., Komen, E.M.J., 2019, Uncertainty Quantification method for CFD applied to the turbulent mixing of two water layers – II: Deterministic Sampling for input uncertainty, Nuclear Engineering and Design 348 (2019) 146–158.

- Rämä, T. Safe&Efficient operations R&D 2021, CFD modelling of BFBT experiment 0011-53. Fortum Report NUCL-4677. Fortum Power and Heat Oy, Espoo. 25.2.2022.
- Silde, A. 2022. Simulation of POOLEX SPA-T8R and SPA-T3 pool stratification experiments using the Apros thermalhydraulic model. VTT Research Report VTT-R-00264-22. 9.3.2022.
- Tereshonok, V. A., Nikonov, S. P., Lizorkin, M. P., Velkov, K., Pautz, A., Ivanov, K., 2009. Kalinin-3 coolant transient benchmark – switching-off of one of the four operating main circulation pumps at nominal reactor power – Specification - First Edition 2008. NEA/NSC/DOC(2009)5. Final draft. OECD/NEA, 2009.

5.2 Passive heat exchanger experiments (PAHE)

Vesa Riikonen, Virpi Kouhia, Joonas Telkkä, Lauri Pyy

LUT University
P.O. Box 20, FI-53851 Lappeenranta, Finland

Abstract

The objective of the project was to improve understanding of the AES-2006 design PHRS-C passive heat removal system and to generate data for code validation. Carefully designed experiments are the most reliable way to obtain fundamental understanding and reliable data of the phenomena. Data can be used in the development and validation of system and CFD codes for the safety analyses of nuclear power plants.

Introduction

The main aim of the project was to ensure the operation and efficiency of the AES-2006 design PHRS-C passive heat removal system in accident and transient situations of nuclear power plants and to generate data for code validation. The goal was to identify physical mechanisms that can reduce performance or prevent the functioning of the loop, to help recognizing conditions in which the functioning of the system could be endangered and to suggest ways assuring the operation. Especially, flow oscillations in two-phase conditions were a topic of interest.

Different organizations can use data in the development and validation of system and CFD codes for the safety analyses of nuclear power plants. Computer analyses are needed also in the planning of the experiments as well as in post analyses to help understanding the physics in the experiments.

The project carried out research on topics relevant to the safety of Finnish nuclear power plants on a high scientific level and with modern methods and experimental facilities. It maintained and extended the research expertise needed for the experimental work and generated data for the validation of computational tools.

PASI facility

The AES-2006 design PHRS-C passive heat removal system is designed to operate without an external power source and to rely on relatively small gravitational pressure differences. The system operates at low near atmospheric pressure, meaning that it is susceptible to boiling oscillations due to large water-steam density difference. While oscillating flow may be an efficient heat removal mechanism, it may cause dynamic loads and consequent fatigue on system piping, containment penetrations, pipe supports, and associated vessels.

The PASI facility (Kouhia et al., 2018, 2020) is a one-loop model of an open passive containment cooling system. The applicable reference system for the PASI test facility is the passive containment heat removal system of the AES-2006 type pressurized water reactor. The design height scale of the PASI facility versus the reference system is 1:2. PASI (Figure 1) consists of a steam system, an open natural circulation system, and measurement and data acquisition systems. To the original design of the facility the higher sparger and water pool have been designed and installed.

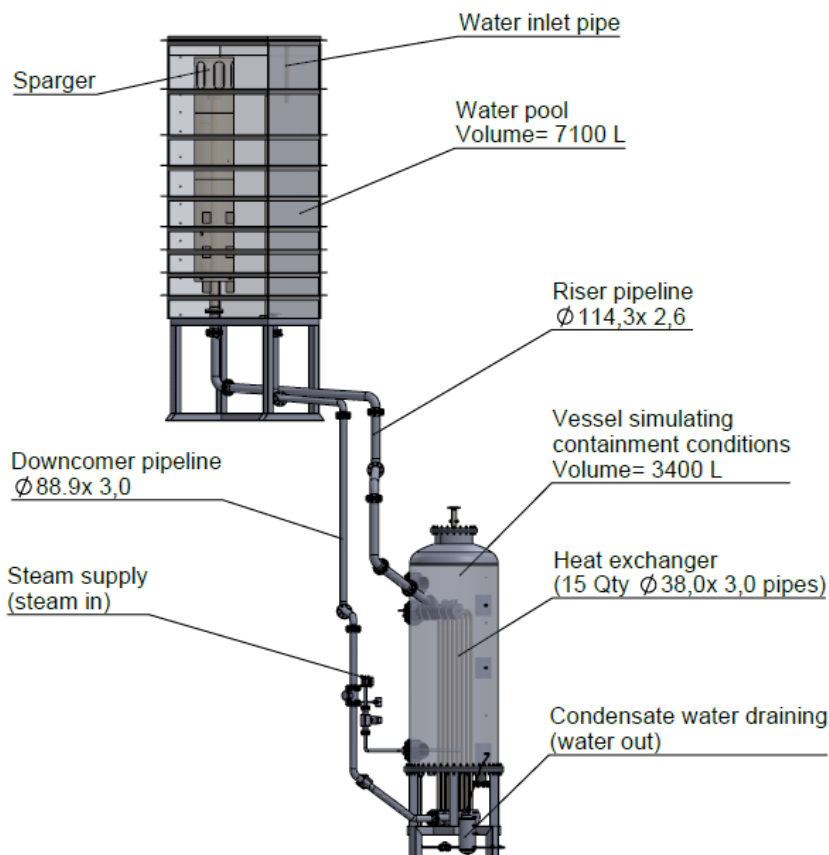


Figure 1. General view of the PASI test loop.

Natural circulation experiment

Seven characterizing experiments were performed with the PASI test facility in 2018 with the original low sparger and water pool (Kouhia, Riikonen, 2018, Kauppinen, 2019). One of these experiments was the natural circulation experiment, which was

performed to characterize the basic facility operation modes. Flow oscillations were observed in the experiment, which ended before the system reached quasi-steady two-phase flow conditions. It was expected that the oscillations would even out when the temperature in the system increases to the saturation temperature of the water pool. This was tested with a new natural circulation test in 2019 (Telkkä, Riikonen, 2019). Pre-test calculations with APROS were done with the PASI simulation model provided by VTT (Kolehmainen, 2018) to find experiment parameters.

In the experiment, the loop mass flow rate fluctuated strongly with the average oscillation frequency of about 0.01 Hz (Figure 2). The oscillation continued approximately for one hour, until the end of the experiment. Hence, the assumed attenuation of the flow oscillation was not achieved in this experiment.

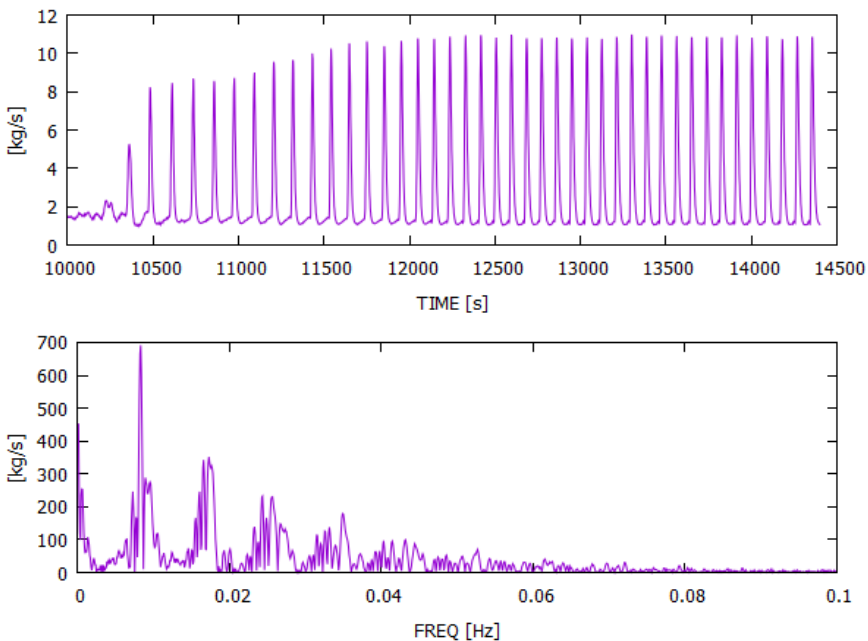


Figure 2. Flow oscillation period of the experiment and the results of the Fourier analysis for that period.

Experiments for VTT projects

In SAFIR2022, VTT proposed projects (THACO and CFD4RSA) where APROS-Fluent simulations are used for calculating the operation of the PASI facility. A test series with PASI was needed to fulfil these needs. In 2019 the tests were planned with VTT (Riikonen et al., 2019). The new experiments required some additional instrumentation and facility modifications to the vessel simulating containment

conditions. Specific goal was to produce as high-quality data as reasonable possible for APROS-Fluent simulation needs of VTT.

Two experiments were carried out with the high sparger and water pool (Telkkä, Pyy, Riikonen, 2020). In the first experiment, the goal was to observe the natural circulation behavior of the PASI facility under different steam mass flow rates to the containment and how much condensate can be collected from the bottom of the containment vessel and from the walls of the containment vessel. In the second experiment the heat losses from the containment were under investigation.

It was possible to measure the amount of condensate from the heat exchanger part of the containment where the bulk amount of condensate was created. The wall condensation was minimal (Figure 3). Most of the time it was below the measurement range of the smallest available flow measurement device.

Undesired stratification of temperatures in the containment was observed (Figure 4). The stratification was most likely due to the condensate in the bottom of the containment. A small layer of condensate will be always kept in the bottom of the vessel to ensure that pressure is not lost from the containment when draining the line.

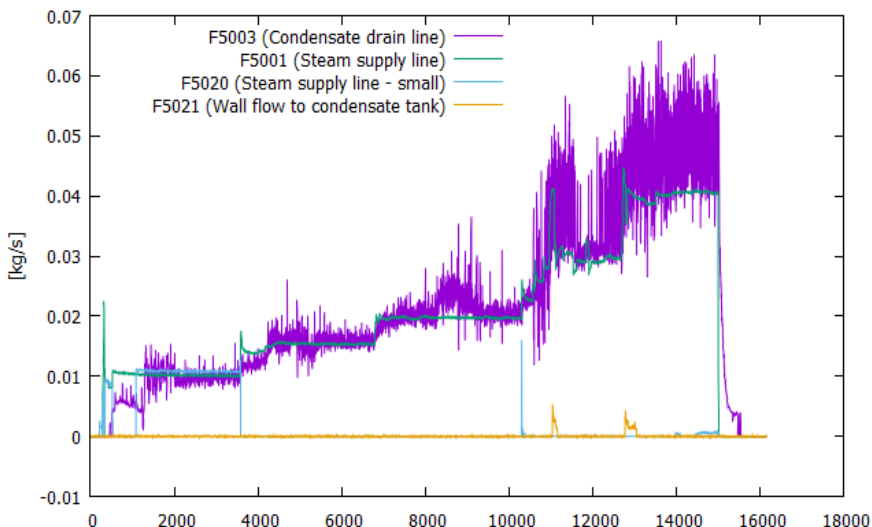


Figure 3. Mass flow rates for condensate drain line and wall flow in relation to steam supply line flows.

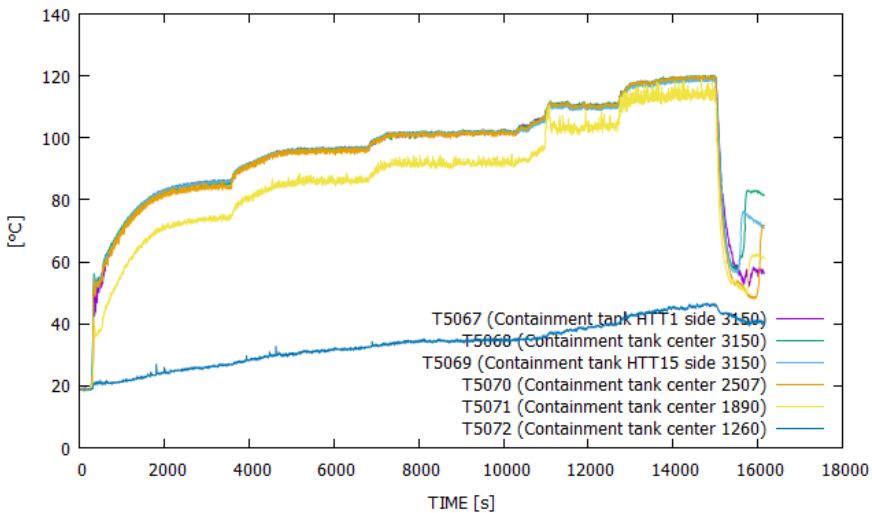


Figure 4. Temperatures inside the containment at different elevations.

The uncertainties in the defined heat losses and heat capacities of the PASI facility are relatively high. There is not any single source for the uncertainties. Mostly those are rising from the approximations made for the analysis and from the uncertainties in the measurements. The most significant source of uncertainty is the flow measurements. An additional heat loss experiment was carried out to clarify the situation. In this experiment, the loop was empty, and the vessel was heated up without steam supply but using electrical heaters inside the vessel instead.

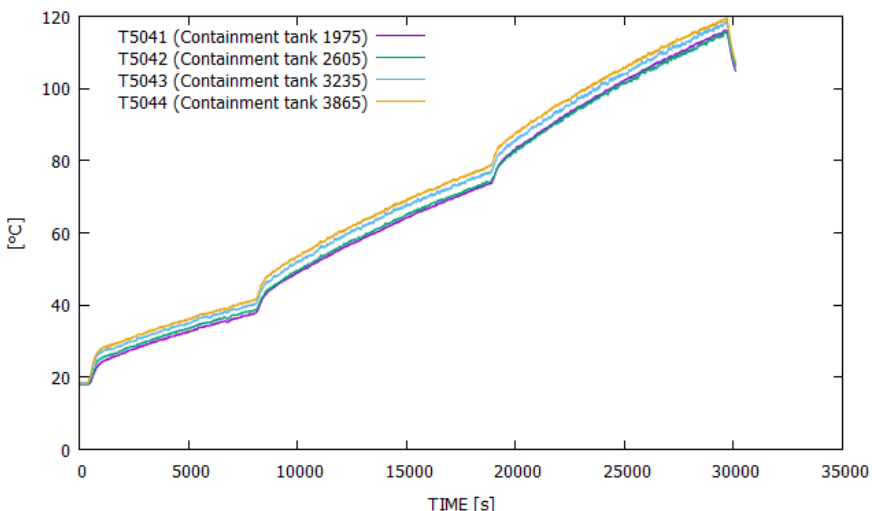


Figure 5. Temperatures at different elevations inside the containment tank.

Only minor temperature stratification inside the containment vessel was observed (Figure 5). Concerning the inner and outer wall temperatures, the temperature was clearly higher at the lowest elevation compared with the other elevations. The containment tank temperature at the lowest elevation was closer to the wall temperatures compared to the situation at the topmost elevation.

Acknowledgement

The Finnish Research Program on Nuclear Power Plant Safety 2019–2022 (SAFIR2022) has provided funding for the SAFIR2022 PAHE project. The authors are grateful for the support of this research task.

References

- Kauppinen O-P, TRACE model of PASI test facility. PAHE 1/2019, Research Report, LUT University, Nuclear Engineering, 2019, Lappeenranta.
- Kolehmainen, J., Apros simulations of the PASI characterizing experiments. Research report, VTT-R-04602-18.
- Kouhia V., Riikonen V., Telkkä J., Partanen H., Räsänen A., Kauppinen O-P., Kotro E., Saure I., Tiilinen K., Karppinen J., General description of the PASI test facility, second edition. INTEGRA 5/2018, Technical Report, Lappeenranta-Lahti University of Technology LUT, Nuclear Engineering, 2018, Lappeenranta.
- Kouhia V., Riikonen V., PASI facility – characterizing experiments. INTEGRA 3/2018, Research Report, Lappeenranta University of Technology, Nuclear Engineering, 2018, Lappeenranta.
- Kouhia, V., Riikonen, V., Kauppinen, O.-P., Telkkä, J., Hyvärinen, J., 2020. PASI – A TEST FACILITY FOR RESEARCH ON PASSIVE HEAT REMOVAL. Article in the proceedings of the International Topical Meeting on Advances in Thermal Hydraulics 2020 (ATH 2020).
- Riikonen V., Purhonen H., Kauppinen O-P., Kouhia V., Telkkä J., Räsänen A., Kotro E., Tiilinen K., PASI test plans. PAHE 2/2019, Research Report, LUT University, Nuclear Engineering, 2019, Lappeenranta.
- Telkkä J., Pyy L., Riikonen V., PASI tests for VTT projects. PAHE 1/2020, Research Report, LUT University, Nuclear Engineering, 2020, Lappeenranta.
- Telkkä J., Riikonen V., PASI natural circulation test NC-03. PAHE 3/2019, Research Report, LUT University, Nuclear Engineering, 2019, Lappeenranta.

5.3 PWR PACTEL tests (PATE)

Vesa Riikonen, Virpi Kouhia, Joonas Telkkä, Lauri Pyy, Antti Räsänen, Eetu Kotro

LUT University
P.O. Box 20, FI-53851 Lappeenranta, Finland

Abstract

The objective of the project was to improve the understanding of thermal hydraulic system behavior of EPR type PWRs by performing integral effects tests with PWR PACTEL. The project enhanced the Finnish nuclear safety assessment capability for solving future safety issues as they appear. It maintained and extended the research expertise needed for the experimental work and produced data for the validation of computational tools. Computer analyses were needed in the planning of the experiments as well as in post analyses to help understanding the physics in the experiments. The project had a significant international connection through the OECD/NEA PKL Phase 4 and OECD/NEA ETHARINUS projects training new researchers and familiarizing them with international networking.

Introduction

The PWR PACTEL facility has been designed and constructed at LUT University to gain experience on the behavior of EPR type PWRs and to study unique EPR accident management procedures. The research has focused on different phenomena in the main circulation loops and vertical steam generators. The main aim has been to ensure the operation of safety related systems or the efficiency of the procedures in accident and transient situations of nuclear power plants. The education of experts on EPR specific issues and the preservation of expertise on experimental research have been the major tasks of the PWR PACTEL related research. An integral test facility, such as PWR PACTEL, offers a good possibility to carry out tests that supplement test campaigns in the other facilities or make independent tests to study phenomena relevant to the safety of EPR type nuclear power plants.

The PATE project carried out research on the topics relevant to the safety of the Finnish nuclear power plants on a high scientific level and with modern methods and the experiment facility. The project enhanced the Finnish nuclear safety assessment capability for solving future safety issues as they appear. It also maintained and extended the research expertise needed for the experimental work and produced data for the validation of computational tools. Computer analyses were needed in the planning of the experiments as well as in post analyses to help understanding the physics in the experiments.

A part of the international efforts in enhancing the reactor safety is the OECD projects. The PATE project had a significant international connection through the

OECD/NEA PKL Phase 4 and OECD/NEA ETHARINUS projects training new researchers and familiarizing them with international networking, as well as developing their skills in communicating about their research. Most of the OECD countries using nuclear power have been participating in the projects. LUT University participated in the OECD/NEA PKL Phase 4 project and provided three integral tests with the PWR PACTEL facility. The experiments in the project investigated safety issues relevant for current PWR plants as well as for new PWR design concepts by means of systematic parameter studies on thermal hydraulic phenomena and transient tests under postulated accident scenarios.

Most of the organizations participating in the OECD PKL Phase 4 Project were doing analytical work with thermal hydraulic codes. LUT University participated also in the analytical work of the experiments with the PKL facility for educational purposes with the TRACE simulation model of the PKL facility. In 2018, a TRACE model of the PKL facility was made in the SAFIR2018 INTEGRA project. In the PATE project, the model was used in the simulation of the selected PKL experiment (Kauppinen, 2019). The OECD/NEA PKL Phase 4 project ended in autumn 2020.

The OECD/NEA ETHARINUS project began on 1st of December in 2020 and will continue at least to the end of November 2024. Finland participates in the project with two PWR PACTEL integral tests. The project objectives are to investigate phenomena where the knowledge base for safety assessment is not sufficiently developed and to provide valid data for thermal hydraulics code-model development and validation for the analysis of key safety issues. The experiments in the OECD/NEA ETHARINUS project are highly relevant to the improvement and validation of thermal hydraulics safety codes and their use, as well as maintaining competence and expertise in this field which is an important goal for the NEA member countries.

PWR PACTEL facility

The PWR PACTEL test facility (Kouhia et al., 2019) is designed for safety studies related to thermal hydraulic of the PWRs with the EPR type vertical steam generators. The facility consists of a U-shaped reactor pressure vessel model, two loops with vertical steam generators, a pressurizer, and emergency core cooling systems including nitrogen-driven accumulators.

The loops and steam generators of the EPR type construction enable the EPR-related experimental research. The reactor pressure vessel model in PWR PACTEL comprises a U-tube construction modeling the downcomer, lower plenum, core, and upper plenum. The core is not a direct model of the reference EPR core. The core rod bundle consists of 144 electrically heated fuel rod simulators arranged in three parallel channels. The heated length of the core is about 2 m shorter than in the EPR core. However, the center of the core is at the correct elevation. The core can be powered by a maximum of 1 MW electric power supply. The maximum core power corresponds roughly to the scaled residual heating power of the EPR reactor. The total height of the PWR PACTEL pressure vessel model corresponds to the

pressure vessel height of EPR. The volume ratio between the pressure vessels in PWR PACTEL and EPR is about 1/405. The pressurizer is shorter than in EPR. The volume ratio between the pressurizers of PWR PACTEL and EPR is 1/562.

The two primary loops with vertical steam generators are fully representative for PWR applications. Both loops have a steam generator with 51 full diameter inverted U-shaped heat transfer tubes arranged in five groups with different lengths, a hot leg, and a cold leg with a pump. The height of the steam generators is approximately 1/4 of the height of the steam generators in the EPR plant. The heat transfer area of the heat exchange tube bundles and the primary side volume of both steam generator scale down to the ratio of 1/400. The general view of the PWR PACTEL test facility is presented in Figure 1.

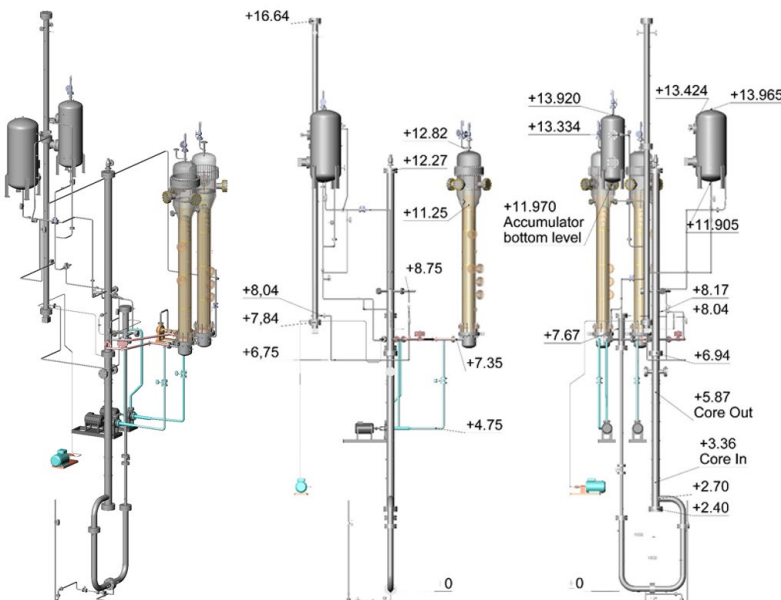


Figure 1. General view of the PWR PACTEL facility.

The instrumentation of the facility comprises temperature, pressure, pressure difference, and flow transducers. The core power and the power of the heaters in the pressurizer, and the power of the main circulation pumps are also measured. Signals from the measurement instruments are recorded with the National Instruments Compact FieldPoint distributed I/O system and then converted into engineering units using appropriate conversion equations and factors. Some parameters such as mass flow rates and collapsed liquid levels require calculation of the single-phase coolant density based on the local pressure and fluid temperature information using steam tables. The experiment data are checked manually. Data are reviewed for anomalous readings and mutually compared with readings of nearby instruments.

PWR PACTEL experiments in the OECD/NEA projects

In the OECD/NEA PKL Phase 4 project three PWR PACTEL experiments (Riikonen, 2019) were performed in 2018 and 2019. The experiments were planned in co-operation with the project partners and complemented the PKL experiments on IB/SB-LOCA. Nitrogen released into the primary cooling system can have a direct effect on reactor cooling conditions, such as on water distributions and condensation. In the earlier PWR PACTEL experiments (Riikonen et al., 2018), the piston effect of nitrogen (Figure 2) was studied. In these experiments, the connection line between the upper plenum and downcomer was open and the break location in the cold leg near the downcomer. Therefore, nitrogen escaped through the break and no clear piston effect was observed. In the PWR PACTEL experiments of the OECD/NEA PKL Phase 4 project, the break location was in the cold leg near the steam generator and the effect of the connection line between the upper plenum and downcomer was tested but was not observed. The experiments required a reference experiment where nitrogen was not released to the primary system. Two experiments where nitrogen was released to the primary system, were carried out in 2019 in the SAFIR2022 PATE project.

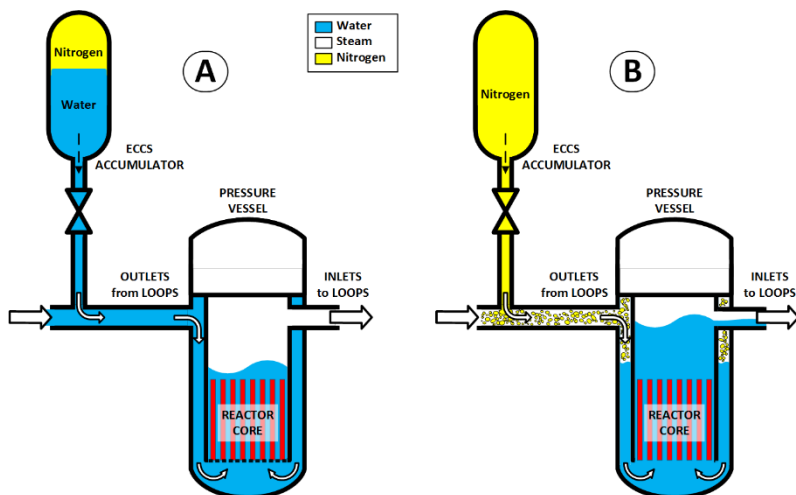


Figure 2. Anticipated behavior of the reactor cooling system during LOCA when nitrogen in the accumulator is released to the primary side.

In the event of a LOCA, when there is saturation at the core outlet, switching the low head safety injection from the cold to the hot leg is required on a long-term basis to stop the production of steam into the containment and reduce the boron concentration in the core. In the OECD/NEA ETHARINUS project, two PWR PACTEL experiments were done to test the effect of a common-cause failure of the cold leg safety injection system check valves and the planned actions when the cold leg safety injection was not possible (Riikonen, 2022a). The manual switch from the

cold leg to the hot leg safety injection in the power plant was originally specified to take place after one hour from the beginning of the secondary side depressurization. This evidently too long waiting period has been changed to 10 minutes as such a long time span could lead to a core damage if the safety injection system check valves fail. For the PWR PACTEL experiments, a conservative delay of 30 minutes was chosen to check if the hot leg injection can prevent a core damage if the manual switch to the hot leg injection begins 30 minutes after the beginning of the secondary side depressurization and there are not any physical phenomena that can prevent the core cooling. Against all expectations the cold leg break was more serious case than the hot leg break. Pre-test simulations with Apros were done to assist in planning the experiments.

Supplementary PWR PACTEL SBLOCA experiments with common-cause failures of cold side safety injection system check valves

Two supplementary PWR PACTEL experiments were done to test the effect of a common-cause failure of the cold leg safety injection system (SIS) check valves and the planned actions when the cold leg safety injection was not possible (Riikonen, 2022b). In the OECD/NEA ETHARINUS project, a conservative delay of 30 minutes was used to check if the hot leg injection can prevent a core damage if the manual switch to the hot leg injection begins 30 minutes after the beginning of the secondary side depressurization (SDE) and there are not any physical phenomena that can prevent the core cooling (Riikonen, 2022a). The manual switch from the cold leg to the hot leg injection in the power plant has been changed to take place 10 minutes after the beginning of the secondary side depressurization. The original one-hour delay was too long as that could lead to a core damage if the safety injection system check valves fail. With the supplementary PWR PACTEL experiments delay of 10 minutes was tested.

In both experiments, similar initial and boundary conditions as well as operational actions were used, except for the break location (Figure 3). The first experiment replicated a hot leg break and the second experiment a cold leg break transient. The hot leg break experiment showed that the manual switch to the hot leg safety injection 10 minutes after the beginning of the secondary side depressurization without a core heat-up is possible. When the hot leg injection began, the rising water levels in the primary side compressed steam in the upper plenum and pressurizer. The pressurizer safety release valve was opened twice to intensify the primary side pressure reduction below the level where the safety injection system can operate. The cold leg break experiment showed that the manual switch to the hot leg safety injection 10 minutes after the beginning of the secondary side depressurization can lead to a core heat-up (Figure 4) if the break is located so that an efficient single-phase water flow through the break is possible during the transient thus causing a significantly larger inventory loss than in the hot leg break case. Against all expectations the cold leg break was more serious case than the hot leg break.

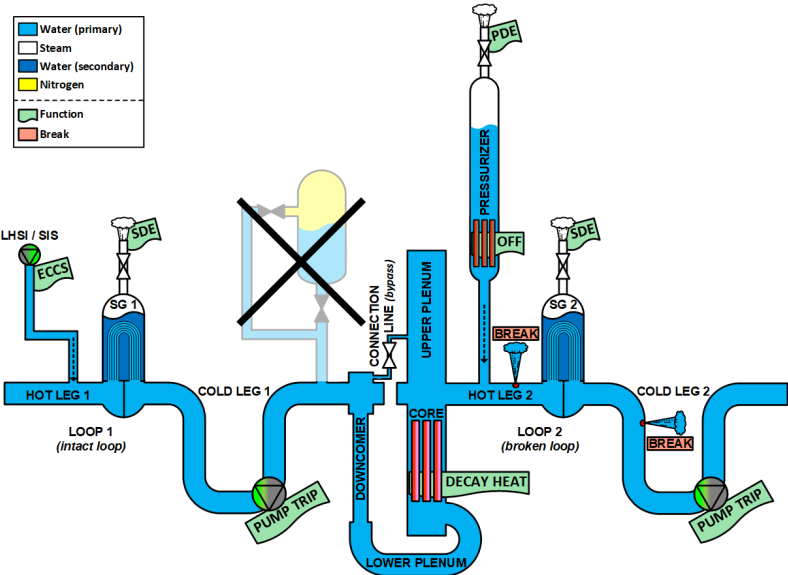


Figure 3. Test configuration.

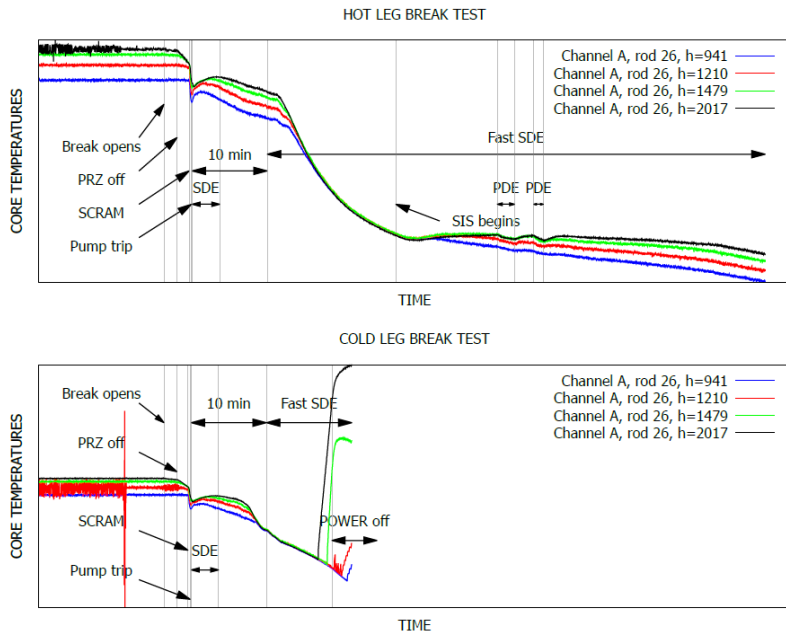


Figure 4. Core temperatures.

Apros simulation of the PWR PACTEL nitrogen experiment in the OECD/NEA PKL Phase 4 project

The Apros code version 6.08.23 was used in the post-test simulation of a PWR PACTEL nitrogen experiment, which was performed in the OECD/NEA PKL Phase 4 project. The simulation model of the PWR PACTEL facility utilizes the 6-equation thermal hydraulic model of the Apros code. The PWR PACTEL simulation model includes the main parts of the facility – the primary side, the secondary sides of the steam generators, and the ECCS as needed. The geometry is modelled in moderate detail, and the measurement elevations of the facility are considered in the nodalization. The simplified scheme of the simulation model is shown in Figure 5. The higher fidelity nodalization in the simulation model is not fully visible in the figure. The process components include more than one node in the calculation level and the division into nodes is not fully representative.

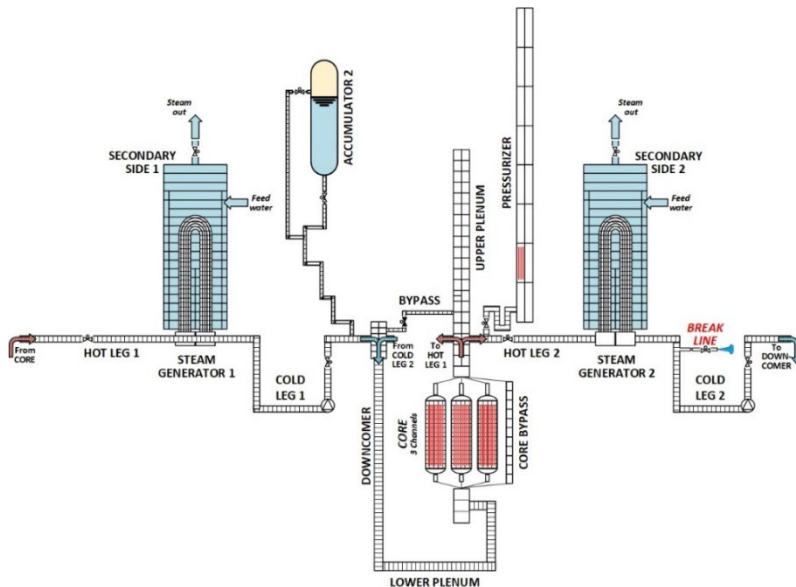


Figure 5. Schematic view of the PWR PACTEL simulation model for the Apros code.

In general, the simulation showed comparable results to the measured data (Kouhia, 2020). The overall trends and events during the transient were predicted. Yet, some discrepancies were found, connected to some local parameter values and the manometric behavior. The accumulator injection period was slightly prolonged in the simulation. The nodalization choices affected the mixing and parameter trends for example in the downcomer top parts. The accumulator model needed modification considering the efficiency of the liquid interface heat transfer

by increasing the multiplication factor from the default value of the code, similarly to what was presented by Kauppinen et al (2019). The transient calculation with nitrogen content included was consuming at certain periods the computer CPU time and prolonging the overall calculation time.

TRACE simulations of the PKL experiment in the OECD/NEA PKL Phase 4 project

In the OECD/NEA PKL Phase 4 project, the experiment results were analyzed by the organizations participating in the project. Extensive computational efforts were used in the OECD/NEA PKL Phase 4 project to analyze the transients ran in the test facilities and to transfer the data to the reactor scale. With the TRACE simulation model of the PKL facility, LUT University participated also in the analytical work of the experiments with the PKL facility.

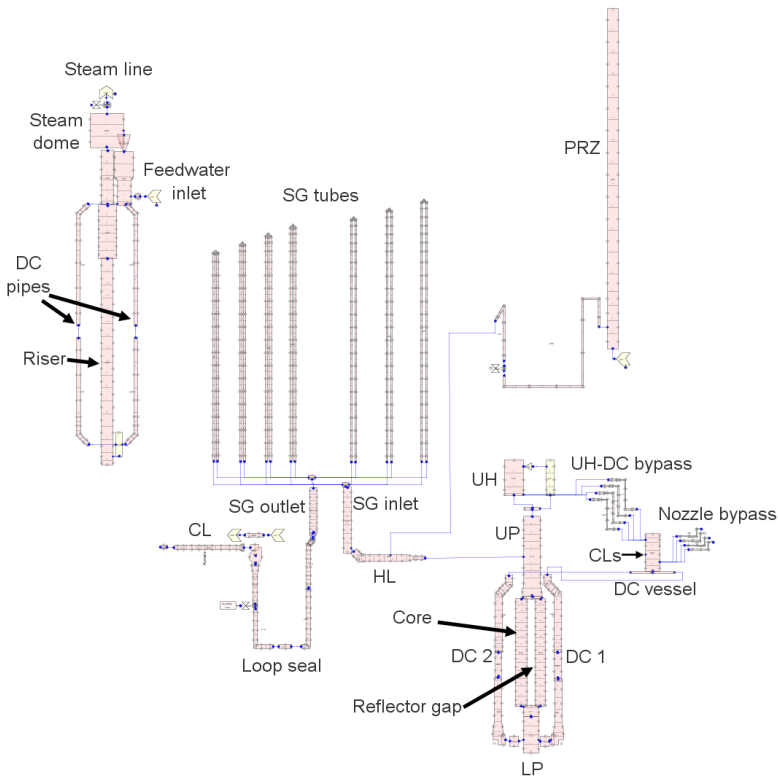


Figure 6. TRACE model of the PKL test facility. Only the reactor pressure vessel and Loop 2 with the pressurizer and steam generator secondary side are presented. All four loops are modelled similarly.

At LUT University, the TRACE model of the PKL test facility was constructed in the SAFIR2018 INTEGRA project in 2018. In the SAFIR2022 PATE project in 2019, the TRACE model was tested by calculating a transient test of the PKL facility (Kauppinen, 2019). The TRACE model of the PKL facility was constructed by using the Symbolic Nuclear Analysis Package (SNAP) and the calculations of the PKL test were performed with the TRACE version of 5.0 patch 5. Figure 6 presents the TRACE model of the PKL test facility. The model includes all the main components of the facility – the reactor pressure vessel, pressurizer, four loops with steam generators and primary coolant pumps, steam generator secondary sides, and accumulators. The pressure drops and heat losses of the model were adjusted according the PKL experiment results. The TRACE model was borrowed to VTT in 2021 when VTT made PKL simulations with Apros and TRACE related to the OECD/NEA ETHARINUS project (Alblouwy, Karola, 2021).

The calculated test at LUT University was the PKL test i2.2 run 3 which is a 17% cold leg IBLOCA experiment (Kauppinen, 2019). The HPSI and LPSI systems were used. Two of the eight PKL accumulators were active. The calculated initial conditions were mostly well predicted by TRACE. Also, the general progression of the transient was relatively well predicted, even though there were some discrepancies between the calculation and test. The leaked water mass was overestimated in the calculation. The direct outflow of the ECC water through the break seemed to be overestimated due the simple nodalization in the downcomer top part. The LPSI injection started much earlier in the calculation than in the test since the primary side pressure dropped at the lower level compared to the test. TRACE did not predict the two small core temperature deviations in the test. Also, there were discrepancies in the steam generator outlet collector and secondary side temperatures between the test and calculation.

During the TRACE calculations, the adjustments of the k-factors at the break throat, at the edges of the cold legs and downcomer, and at the accumulator injection line orifice were done for improving the model prediction. These adjustments improved the prediction of the leaked mass, the behavior of the primary side pressure, the accumulator injection flow rate, and the core cladding temperature behavior during the accumulator water injection.

Apros and TRACE simulations of the PWR PACTEL experiments in the OECD/NEA ETHARINUS project

The PWR PACTEL facility hot leg test in the OECD/NEA ETHARINUS project was simulated with the Apros code (Kouhia, 2022) to test the model capability to predict the transient conditions, observe possible discrepancies, and modify the model or make notes for needs for studies in the future concerning calculations. In general, the calculation task with the Apros code showed moderately comparable results to the measured data of the experiment. The overall trends and events during the transient were predicted reasonably well. Nevertheless, some discrepancies were found in the timings of the events and parameter values.

The new cooperation between LUT University and VTT that is intended to take place in SAFER2028 was piloted with the PATE and THACO projects. One VTT research scientist participated in the OECD/NEA ETHARINUS PWR PACTEL experiment at LUT University in 2022. Later the experiment was analyzed with Apros at LUT University and TRACE at VTT (Kouhia, Karola, 2022). As VTT had no TRACE model of the PWR PACTEL facility, VTT borrowed the PWR PACTEL TRACE-model of LUT University for the work.

The simulated test included a break in a cold leg of the broken loop with simultaneous operational actions, such as the secondary side depressurization periods and the emergency core cooling water injection to the hot leg of the intact loop. The main objectives of the task were to test the capability of the models to predict the transient conditions, observe possible discrepancies, modify the models, and make notes for needs for studies and improvements in the future. In general, the codes showed comparable results to the measured data of the experiment. The overall trends and events during the transient were predicted reasonably well. Though, discrepancies were found in the timings of the events and parametric values.

Nitrogen experiments

The PWR PACTEL nitrogen experiments with a hot leg break (Riikonen et al., 2018) showed that the accumulator nitrogen could stop the primary side depressurization and cause a core heat-up at a reactor pressure above or very close to a typical low-pressure safety injection shut-off head. System codes have difficulties to catch the phenomena. To map the range of the pressures at which the decoupling of the primary and secondary side pressures takes place more testing is needed, as a function of the break size, the number of the accumulators injecting (nitrogen mass) and the number of the steam generators participating in the secondary side depressurization (volume available for nitrogen). These nitrogen effect tests also generate data for the code validation of system thermal hydraulic codes. Pre-test simulations with Apros were done to plan the experiments. In the pre-test simulations the effect of break size and suitable break sizes in the experiments were studied.

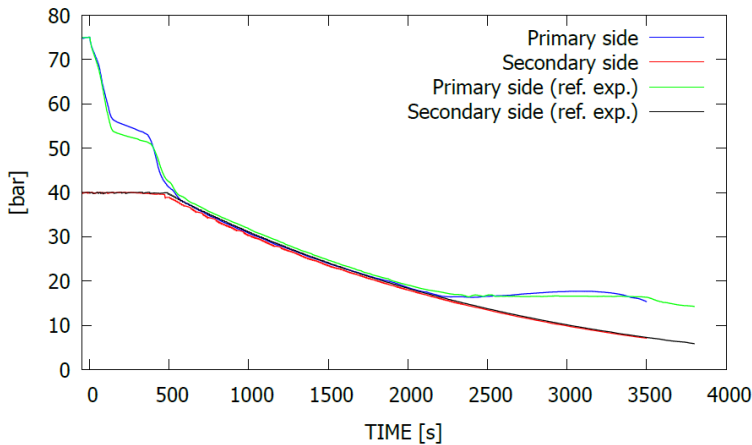


Figure 7. Pressures in the primary and secondary sides and accumulator.

The test to investigate the effect of the number of steam generators on the system was carried out in 2020 (Kouhia, Riikonen, 2020). In this experiment only one loop of the facility was used. The overall system behavior was as in the reference experiment with two loops. The progression of the main parameters was similar and the main event timings were relatively close to each other in the experiments, though the transient proceeded slightly faster with one loop. In the test with one loop, the core heat-up started slightly earlier than in the test with two loops, and the amount of water in the pressure vessel and loop was located slightly differently between the experiments. As the accumulator nitrogen release period started, the primary pressure decrease stopped. The results showed that the transient with either one or two loops and steam generators connected to the system had a similar effect on the appearance of the decoupling of the pressures, the pressure value level when the decoupling appeared, and the length of that period (Figure 7).

To study the effect of the amount of injected nitrogen, an experiment with the reduced amount of nitrogen was performed in 2021 (Riikonen, 2021). Also, the amount of injected water from the accumulator was reduced, respectively. The overall system behavior was as in the reference experiment from the earlier studies with the maximum available amount of nitrogen and water until the nitrogen injection began (Figure 8).

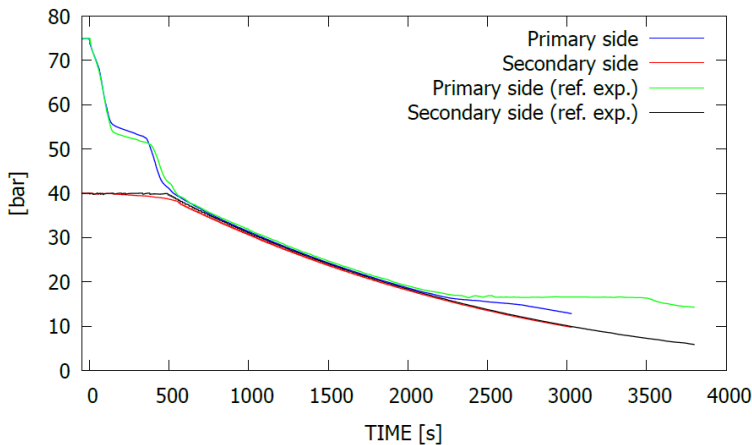


Figure 8. Pressures in the primary and secondary sides and accumulator.

The results showed that the amount of injected nitrogen affects the decoupling of the pressures. With the small amount of nitrogen, the decoupling began when the nitrogen reached the break. After that, the primary side pressure decreased slowly but did not follow the secondary side pressure. Still, the accumulator nitrogen caused a core heat-up at a reactor pressure close to a typical low-pressure safety injection shut-off head. In the reference experiment, the amount of the nitrogen release was bigger, and the decoupling of the primary and secondary side pressures began already when the nitrogen release began. That caused core heat-up at the higher reactor pressure. Some of nitrogen flowed out through the break but the results also indicated the presence of nitrogen in the steam generator heat exchange tubes. All the parameters affecting the decoupling of the pressures are not clear yet. The work is planned to continue in SAFRE2028 with the break size experiments.

The results of the tests on nitrogen effects are used for ensuring the computational capabilities in predicting the effect of nitrogen in the accumulator injection in plant analyses. The test data can be used in the development and validation of computer codes for the safety analyses of nuclear power plants.

Simulation of the PWR PACTEL nitrogen experiment

The Apros code version 6.11.32 was used in the post-test simulation of the PWR PACTEL nitrogen experiment performed in 2021. In the experiment, the effect of the amount of released nitrogen was studied. The experiment is part of the test series dedicated to studies on the effect of nitrogen released into the primary side coolant during LOCA situations. In this task, the simulation model utilizes the 6-equation thermal-hydraulic model of the Apros code and includes models of all main parts of the PWR PACTEL facility. The geometry of the facility is modelled in moderate detail, and the measurement elevations of the facility are considered

thoroughly in the nodalization structure. The simplified general scheme of the simulation model used in this simulation case is shown in Figure 9.

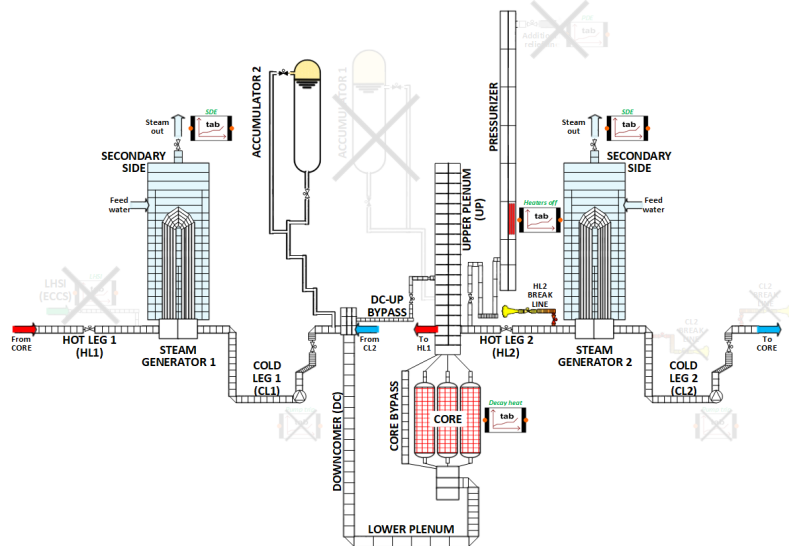


Figure 9. Scheme of the Apros simulation model of the PWR PACTEL facility.

In general, the simulation showed comparable results to the measured data (Kouhia, 2022). The overall trends and events during the transient were predicted reasonably (Figure 10). Though, discrepancies were found in the timings of the events, and in some parametric values. Yet, the observations on the simulation can assist in the evaluation of the favorable periods for flow propagation and paths also in the experiment.

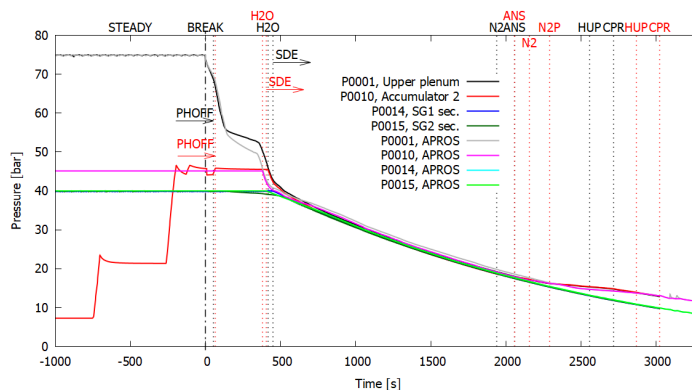


Figure 10. Pressures of the primary and secondary sides in the experiment and simulation.

Inadvertent opening of the pressurizer safety valve with a simultaneous opening of the main steam relief trains valves experiments

An inadvertent opening of the pressurizer pilot operated safety valve with a simultaneous spurious full opening of the valves in the main steam relief trains influences the departure from nucleate boiling ratio in the beginning of a LOCA. At the same time, the primary system is cooled down. This affects the core temperature and DNBR, but the magnitude of the effects is not clear. The goal of the experiments was to clarify the effect of the fast secondary side cooldown. The experiments were planned in co-operation with TVO in 2019 (Riikonen, Pyy, 2019). Pre-test simulations with Apros were done to get initial insight on the conditions during the experiment procedures.

Two experiments were performed (Riikonen, Pyy, 2020). In the first experiment, the opening of one pressurizer safety release valve was assumed. The second experiment was similar but the main steam relief valves were assumed to open at the same time as one pressurizer safety release valve. The expected behavior was observed. The general system behavior was similar in both experiments (Figure 10). The core temperatures never increased above the initial values. At the end, the core temperatures stabilized and decreased slowly.

The results of the experiments are used for clarifying the effect of the fast secondary side cooldown. The subject is relevant to validate I&C fault analysis. The test data can be used in the development and validation of computer codes for the safety analyses of nuclear power plants.

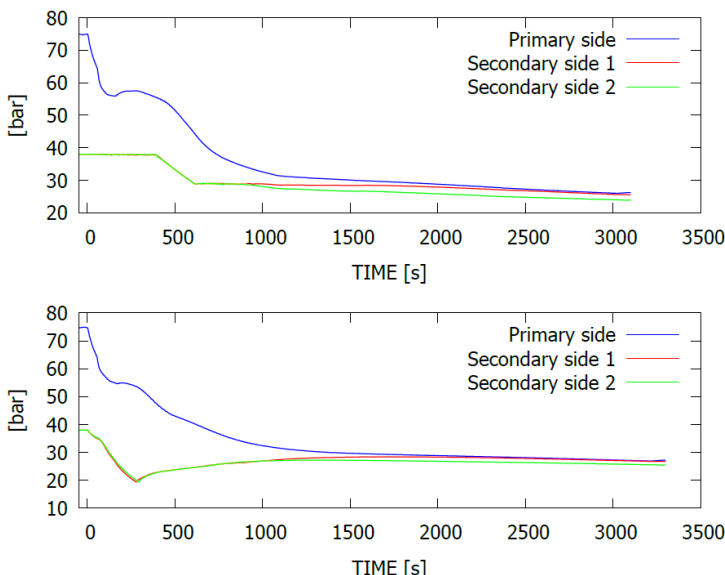


Figure 11. Pressures in the primary and secondary sides.

Summary and conclusions

The objective of the PATE project was to improve the understanding of thermal hydraulic system behavior of the EPR type PWRs by performing integral effects tests with the PWR PACTEL facility. The main aim was to ensure the operation of safety related systems or the efficiency of the procedures in accident and transient situations of nuclear power plants. The project carried out research on the topics relevant to the safety of the Finnish nuclear power plants on a high scientific level and with modern methods and the experiment facility. The work in PATE enhanced the Finnish nuclear safety assessment capability for solving future safety issues as they appear. The project maintained and extended the research expertise needed for the experimental work and produced data for the validation of computational tools. Computer analyses were needed in the planning of the experiments as well as in post analyses to help understanding the physics in the experiments.

The project had a significant international connection through the OECD/NEA PKL Phase 4 and OECD/NEA ETHARINUS projects training new researchers and familiarizing them with international networking, as well as developing their skills in communicating about their research. LUT University participated also in the analytical work of the experiments with the PKL facility for educational purposes with the TRACE simulation model of the PKL facility.

The experiments in the OECD/NEA ETHARINUS project are highly relevant to the improvement and validation of thermal hydraulics safety codes and their use, as well as maintaining competence and expertise in this field which is an important goal for the NEA member countries.

Acknowledgement

The Finnish Research Program on Nuclear Power Plant Safety 2019–2022 (SAFIR2022) has provided funding for the SAFIR2022 PATE project. The OECD/NEA ETHARINUS project was performed with the financial support of the Finnish Research Programme on Nuclear Power Plant Safety (SAFIR2022) and the partners participating in the OECD/NEA ETHARINUS project. The OECD/NEA PKL Phase 4 project was performed with the financial support of the Finnish Research Programme on Nuclear Power Plant Safety (SAFIR2018 and SAFIR2022) and the partners participating in the OECD/NEA PKL Phase 4 project.

We are grateful for their support to all the financiers of this research task, OECD Nuclear Energy Agency (NEA), the members of the SAFIR2018 and SAFIR2022 Reference Group 4, and the members of the Program Review Group and the Management Board of the OECD/NEA PKL Phase 4 and OECD/NEA ETHARINUS project. The data from the experiments in the OECD/NEA projects is available to the NEA member countries via their CSNI representative organizations three years after the end of the project.

References

- Alblouwy F., Karola E., Analysis of PKL III J2.1 and J2.2 with TRACE and Apros Codes, Research Report, VTT-R-00126-22, VTT Technical Research Centre of Finland Ltd, 2021, Espoo.
- Kauppinen O-P., TRACE calculations of PKL i2.2 run 3, Research Report, PATE 6/2019, LUT University / Nuclear Engineering, 2019, Lappeenranta.
- Kauppinen O-P., Kouhia V., Riikonen V., Hyvärinen J., System code analysis of accumulator nitrogen discharge during LOCA experiment at PWR PACTEL test facility, Nuclear Engineering and Design, Volume 353, November 2019, <https://doi.org/10.1016/j.nucengdes.2019.110288>.
- Kouhia V., APROS Simulation of PWR PACTEL Experiment SBL-63, Re-search Report, PATE 3/2021, LUT University / Nuclear Engineering, 2022, Lappeenranta.
- Kouhia V., Simulation of PWR PACTEL Nitrogen Experiment NCG-23 with APROS, Research Report, PATE 5/2019, LUT University / Nuclear Engineering, 2020, Lappeenranta.
- Kouhia V. (LUT University), Karola E. (VTT), APROS and TRACE Simulations of PWR PACTEL Experiment SBL-65, Research Report, PATE 3/2022, LUT University / Nuclear Engineering, 2022, Lappeenranta.
- Kouhia V., APROS simulation of PWR PACTEL Nitrogen Experiment NCG-31 Research Report, PATE 4/2022, LUT University / Nuclear Engineering, 2022, Lappeenranta.
- Kouhia V., Riikonen V., PWR PACTEL Nitrogen Experiment NCG-30, Research Report, PATE 1/2020, LUT University / Nuclear Engineering, 2020, Lappeenranta.
- Kouhia V., Riikonen V., Partanen H., Räsänen A., Kauppinen O-P., Telkkä J., Pyy L., Tielinen K., General Description of the PWR PACTEL test facility – fourth edition, Technical report, PATE 1/2019, LUT University / Nuclear Engineering, 2019, Lappeenranta.
- Riikonen V., The PWR PACTEL nitrogen experiments in the OECD/NEA PKL Phase 4 project, Research Report, PATE 2/2019, LUT University / Nuclear Engineering, 2019, Lappeenranta.
- Riikonen V., PWR PACTEL nitrogen experiment on the effect of the amount of injected nitrogen, Research Report, PATE 1/2021, LUT University / Nuclear Engineering, 2021, Lappeenranta.
- Riikonen V., PWR PACTEL SBLOCA experiments with common-cause failures of cold side SIS check valves, Research Report, PATE 1/2022, LUT University / Nuclear Engineering, 2022a, Lappeenranta.
- Riikonen V., Supplementary PWR PACTEL SBLOCA experiments with common-cause failures of cold side SIS check valves, Research Report, PATE 2/2022, LUT University / Nuclear Engineering, 2022b, Lappeenranta.

Riikonen V., Kouhia V., Kauppinen O-P., Sjövall H., Hyvärinen J., Experimental observation of adverse and beneficial effects of nitrogen on reactor core cooling, Nuclear Engineering and Design 332 (2018) 111–118, <https://doi.org/10.1016/j.nucengdes.2018.03.027>.

Riikonen V., Pyy L., Plans for the PWR PACTEL inadvertent opening of SV and MSRT tests, Research Report, PATE 3/2019, LUT University / Nuclear Engineering, 2019, Lappeenranta.

Riikonen V., Pyy L., PWR PACTEL experiments of inadvertent opening of SV and MSRT, Research Report, PATE 2/2020, LUT University / Nuclear Engineering, 2020, Lappeenranta.

5.4 Sparger separate effect tests (SPASET)

Markku Puustinen, Antti Räsänen, Lauri Pyy, Eetu Kotro, Kimmo Tielinne,
Giteshkumar Patel, Elina Hujala

Lappeenranta-Lahti University of Technology LUT
School of Energy Systems
Nuclear Engineering
P.O. Box 20, FI-53851 Lappeenranta

Abstract

The Sparger Separate Effect Tests (SPASET) project has increased knowledge of small-scale phenomena affecting the effective heat and momentum sources during steam injection through spargers. The effect of pool water sub-cooling, a transition from sub-sonic to sonic flow conditions, injection nozzle chamfer, and multi-hole injection on the effective momentum have been studied. The experiment results have been utilized in the development and validation of the simplified effective heat source (EHS) and effective momentum source (EMS) models proposed by KTH. They are also being used at LUT and VTT in the improvement of the computational fluid dynamics (CFD) models related to direct contact condensation (DCC).

Introduction

Steam injection through spargers induces heat, momentum, and mass sources that depend on the steam injection conditions and can result in thermal stratification or mixing of the pressure suppression pool (PSP). The development of thermal stratification in the PSP is of safety concern since it reduces steam condensation capacity of the pool, increases the pool surface temperature, and thus leads to higher containment pressures, compared with completely mixed pool conditions. A realistic evaluation of the steam condensation capacity of the PSP in different thermal stratification scenarios is therefore important and additional data on pool behaviour are needed for validation of computer models and realistic evaluation of safety margins.

The SPASET project has contributed to the validation of simulation tools, i.e. CFD codes such as ANSYS Fluent and OpenFOAM and system codes such as Apros, by increasing knowledge of small-scale phenomena affecting the effective heat and momentum sources during steam injection through spargers. The experiment results have been utilized for the evaluation of the simulation models in the SPASET project itself at LUT as well as in the related CFD4RSA project at VTT and in Nordic co-operation research efforts between LUT, VTT and KTH.

Prediction of the long-term thermal behaviour of a large water pool during steam injection through blowdown pipes and spargers with CFD codes is time-consuming and requires lots of computational capacity because the associated DCC

phenomenon needs to be solved. The simplified EHS and EMS models would reduce the needed computational capacity. The premise of these models is that due to the difference in spatial and time scales between the DCC phenomena and large pool behaviour, only the integral effects of DCC on the pool should be modelled. These effects are defined as heat and momentum sources, which determine the large-scale pool circulation and temperature distribution.

Validation of the EHS/EMS models has been done using experimental data from the drywell-wetwell suppression pool facility (PPOOLEX) and the separate effect facility (SEF-POOL) at LUT, Finland, and the PANDA facility at PSI, Switzerland [Li et al., 2014, Li et al., 2018, Gallego-Marcos et al., 2018a, Gallego-Marcos et al., 2018b, Gallego-Marcos et al., 2019a, Gallego-Marcos et al., 2019b, Gallego-Marcos et al., 2018c]. The validated models have been applied to the full-scale analysis of a Nordic BWR PSP during a steam injection through spargers [Gallego-Marcos et al., 2019c]. The results show that strong thermal stratification of potential safety importance can develop in the pool during prototypic steam injection conditions. The analysis results suggest that further development of the EHS/EMS correlations and computational models is necessary to enable modeling of regimes and conditions, which have not yet been studied in experiments, but are critically important and can completely change the PSP stratification and mixing behaviour.

LUT has studied the suitability of the large interface condensation and interfacial area models of the OpenFOAM code for steam injection through spargers in the SPASET project [Patel et al., 2019, Patel et al., 2020]. VTT has implemented the EHS/EMS models in the ANSYS Fluent code by using user-defined functions and performed simulations of DCC and thermal stratification experiments of LUT in a related CFD4RSA project [Pätkangas et al., 2018, Pätkangas, 2020]. Also, VTT has studied the possibilities to implement the approaches based on the EHS/EMS model in the Apros system code.

A combined experimental/analytical/computational program has been carried out during the SPASET project. With experiments in the SEF-POOL facility, a database for the development, improvement, and validation of numerical simulation models has been generated. Sophisticated, high-frequency measurements and high-speed video cameras have been used to get detailed enough data.

SEF-POOL test facility

The reference system for the SEF-POOL facility is an SRV sparger pipe of a BWR plant. Hence, the facility is designed in such a way that discharge of steam through injection holes at the sparger lower end into sub-cooled pool water can be simulated representatively [Tielinen et al., 2018]. The goal of the tests is to define the effective momentum for a given steam condensation regime, particularly for the oscillatory bubble regime. For this purpose, the design of the test facility is such that the effective momentum (liquid force carried by the condensate liquid) can be directly measured with a force sensor or it can be calculated based on measured steam momentum (steam force at the injection hole) (Figure 1).

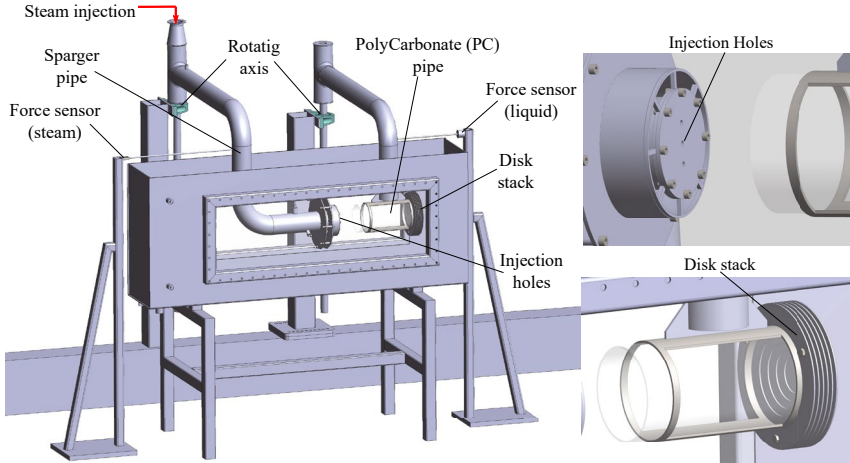


Figure 1. General view of the SEF-POOL facility configuration where the propulsion volume (PC pipe) is independent and attached to its own support arm.

For helping to recognize different flow regimes and for obtaining the bubble diameter as a function of time, the test facility allows high-speed video recordings of the DCC of steam through a window on the sidewall of the pool. The high-speed camera system consists of two monochromatic Phantom Miro M310 cameras. The maximum resolution is 1280x800 px, but in practise the picture area is cropped to increase the maximum amount of the images the internal memory can hold, thus increasing the total time of the recordings. The imaging system has evolved during the project and in the tests conducted in 2020 stereo viewing perspective, i.e. both cameras were in an angle towards the pool, was applied. Besides, the calibration procedure was improved by shifting from separate calibration images to recording a calibration video consisting in theory of thousands of calibration images.

An air injection system has been built for generating bubbles into the pool for visualizing flow fields. Figure 2 shows a stereo view of a cloud of rising small air bubbles generated with the system in a stagnant pool, i.e. there was no steam injection into the pool at that moment.

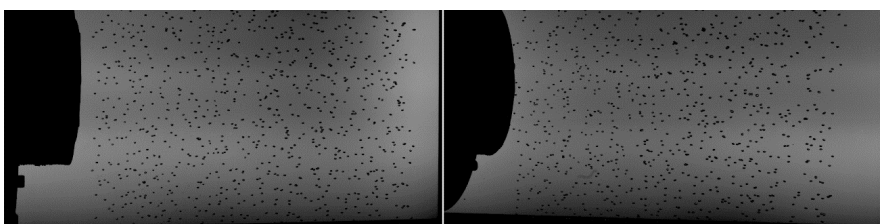


Figure 2. Cloud of intentionally generated air bubbles for tracking liquid movements in the SEF-POOL facility.

SEF-POOL tests

In BWRs, the development of thermal stratification or mixing during steam injection through spargers can affect the performance of the PSP. Prediction of the effective momentum induced by the oscillatory bubble regime is necessary for the modelling of the pool behaviour. To directly measure the effective momentum an extensive test series has been run in the SEF-POOL facility at LUT [Puustinen et al., 2019, Gallego-Marcos et al., 2019b, Puustinen et al., 2020, Puustinen et al., 2021]. Data on the characteristics of small-scale phenomena affecting the effective heat and momentum sources have been provided.

Effect of pool water sub-cooling on the effective momentum, effective momentum in the transition regime, i.e. effect of transition from sub-sonic to sonic flow conditions, effective momentum at mass fluxes higher than $300 \text{ kg/m}^2\text{s}$, the effect of nozzle chamfer and multi-hole injection have been studied in 2019-2020. Particular interest in the 2020 tests was in capturing good-quality high-speed camera stereo recordings of the steam jet behaviour and jet entrainment visualized with the help of air bubbles injected into the pool. Oscillatory bubble, partly the oscillatory cone jet, and partly the stable jet regimes have been the covered flow modes in the tests.

Steam injection into the initially highly subcooled pool in sub-sonic and sonic regimes revealed that both the Jacob and Mach number have a significant effect on the effective momentum coefficient C (i.e. the ratio of the liquid momentum rate to the theoretical value of the momentum rate of steam). Figures 3 and 4 present the time-averaged steam mass flow rates, force values, and pool temperatures from the tests done in sub-sonic and sonic conditions, respectively. In the sub-sonic case, the measured force curve has a low gradient shape during the initial phase of the test when the pool water is highly sub-cooled. In the sonic case, the measured force jumps more directly upwards as soon as the steam injection is started.

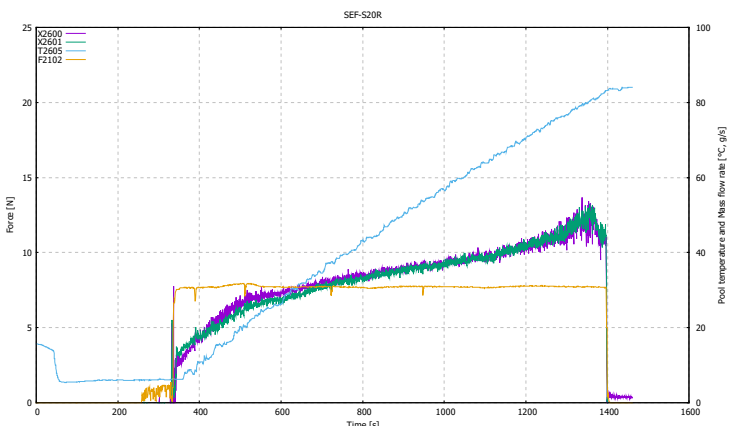


Figure 3. Measured forces (X2600, X2601), flow rate (F2102) and pool temperature (T2605) with sub-sonic steam injection into a highly sub-cooled water pool.

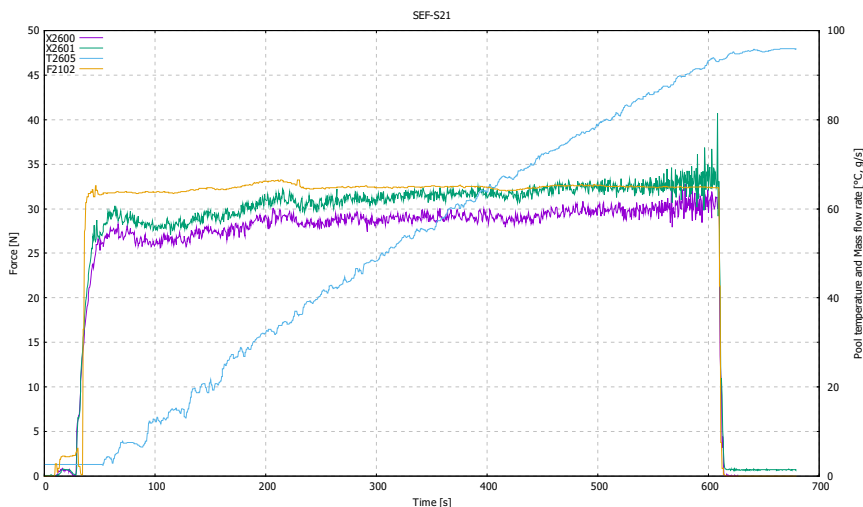


Figure 4. Measured forces (X2600, X2601), flow rate (F2102) and pool temperature (T2605) with sonic steam injection into a highly sub-cooled water pool.

Practically all the injection holes in plant spargers are drilled with chamfers, i.e. the outlet edge of the injection hole is specifically shaped. The effect of the chamfered injection hole was studied in the 2019 tests in SEF-POOL. The injection plate used in those tests was manufactured so that a 125° chamfer on the outlet edge of the 16 mm orifice was formed. The chamfer effect on the effective momentum magnitude was found to be almost insignificant both in the sub-sonic and sonic regime when compared to reference tests done with straight holes.

In the 2020 tests, steam injection through a three-hole plate seemed to produce slightly larger force measurement values than injection through a single-hole plate with the same steam mass flux. In addition, in the three-hole case, the measured force curve reached its peak value at the pool temperature of about 60 °C and then turned very slightly downwards while in the single-hole case the peak occurred at the pool temperature of about 80 °C.

As the sub-cooling of the pool water decreases, the size of the forming steam bubbles increases (Figure 5). The high-speed video clips reveal that at low sub-cooling detached bubbles can move a long distance from the injection hole and allow the formation of a new bubble before they collapse. Close to saturation conditions a new developing bubble can catch up with the previous detached bubble, which has not condensed completely yet, collide with it, and even merge with it.

Both in the single-hole and three-hole tests done with the smallest steam injection rate, incomplete condensation occurred as the pool temperature approached saturation conditions. The forming steam bubbles were large and they started to rise upwards due to buoyancy forces even when they were still attached to the injection plate. The detached bubbles continued the rising movement and seemed

to reach the pool surface before they collapsed. In these cases, the steam flow velocity was so small that the forming steam bubbles slowed down and were unable to travel horizontally far from the injection plate. Instead, the buoyancy forces took control and started to lift the bubbles upwards.

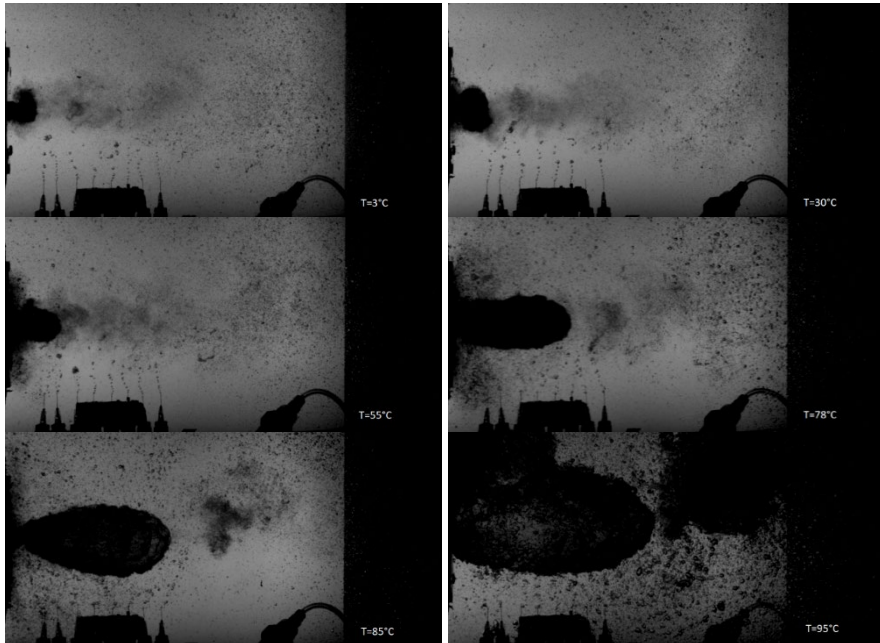


Figure 5. Effect of pool water temperature on the size of forming steam bubbles.

The most important outcome of the 2020 tests was the successful refining of the air bubble generator configuration and the high-speed camera set-up so that KTH can effectively use their in-house tools in the analysis of the recordings for tracking the movement of the air bubbles and thus ultimately assess the liquid velocity and the amount of jet entrainment.

OpenFOAM simulations and pattern recognition algorithm

The SEF-INF2 test was chosen as the reference case for the CFD simulations. In the test, the saturated vapour was injected by using an orifice of a diameter of 16 mm. A 2D-axisymmetric geometry containing a 1° sector of the whole SEF-POOL facility was generated including the condensation pool around the PC pipe. Two grid refinements (1 mm and 2 mm) were used in the PC pipe uniformly to study the effect of grid density on DCC rates. All the simulations were obtained by employing the compressible two-phase solver 'reactingTwoPhaseEulerFoam', which is based on the Eulerian-Eulerian two-fluid approach of the OpenFOAM-7 CFD code. The

Rayleigh-Taylor Interfacial (RTI) area model of Pellegrini et al. was included for the interfacial area modeling [Pellegrini et al., 2015]. The interfacial heat transfer between steam and water was modelled by using the Nusselt number formulation of the Coste continuous model of Coste [Coste, 2004]. Flow turbulence was solved by employing the $k - \varepsilon$ turbulence model.

The results showed that the velocity boundary condition yielded incorrect behaviour of the steam-water interface in the PC pipe. A pressure inlet boundary condition was suitable for this case and provided the average mass flow rate measured in the test. The formation and condensation of the bubbles were visible in the OpenFOAM simulations of the SEF-POOL test (Figure 6). The steam plume length and bubble size qualitatively were smaller in the 1 mm grid case than in the 2 mm grid case. The denser grid enlarged the total interfacial area, which increased the total DCC rate in the simulations. However, it is difficult to draw any further conclusions based on the simulated short transient. A longer simulated transient is needed to analyse the validity of the DCC and interfacial area models in sparger cases.

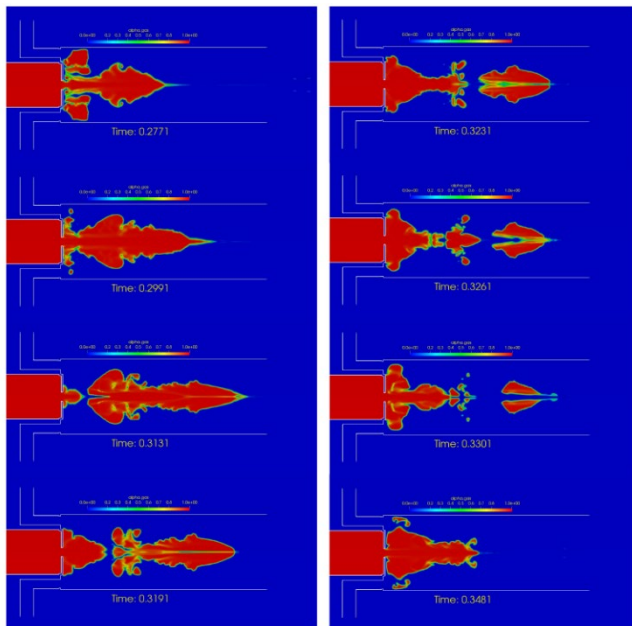


Figure 6. Instantaneous volume fraction fields showing the second bubble formation and condensation in the OpenFOAM simulation with 1 mm uniform grid size.

The same test was simulated with the 3D domain. The results show that a bubble formed at the sparger orifice and detached from there (Figure 7). It travelled forward oscillating and finally condensed rapidly in the pool water. The steam bubble

condensed inside the PC pipe. In the 3D simulation, the first bubble formation, and its detachment took a little longer time than in the 2D-axisymmetric simulations. Also, the total interfacial area and bubble volume in the 3D simulations were smaller than in the 2D-axisymmetric simulations.

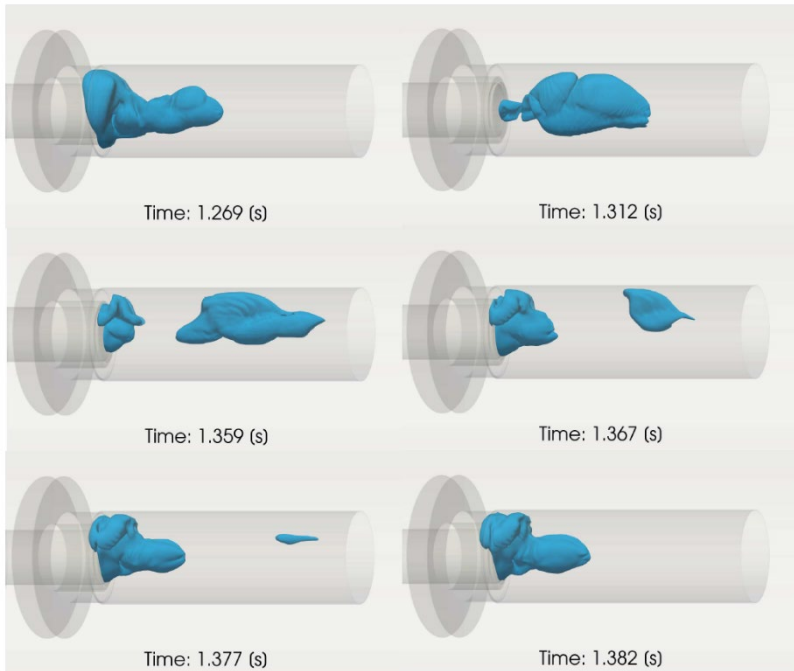


Figure 7. Instantaneous volume fraction fields showing the formation and condensation of a steam bubble in the 3D OpenFOAM simulation of the SEF-INF2 test.

Image analysis and pattern recognition have great potential in thermal-hydraulic research. The image analysis algorithm developed at LUT has been improved to cover cases where multiple bubbles travel at the same time in the frame being analysed and it now seems to work well with multiple bubbles tracking their whole lifetime (Figure 8). After constructing the tracks of the bubbles, different properties of the bubbles can be evaluated, such as mean bubble lifetime, the mean time difference between the bubble formations, the corresponding bubble formation frequency, surface velocities, and accelerations to different directions in the 2D plane. The algorithm was applied to the SEF-INF2 video recordings and the instantaneous volume fraction field images of the 2D simulation results. The modified pattern recognition-based image analysis algorithm represented the real bubble shape better than before. It yielded a good total bubble volume of the 2D-axisymmetric case with the 2mm grid size.

With suitable video recordings, the algorithm can be used with pipe flows too. Surface velocity and acceleration estimations at arbitrary angles give important knowledge, for example of the direction in which the condensation of the steam bubble begins, and will thus be a good aid for CFD validation purposes.

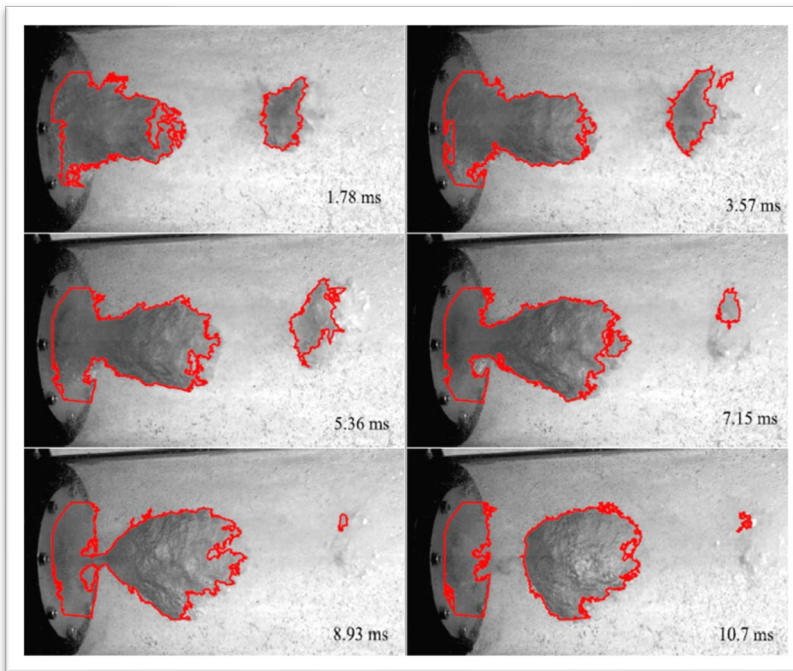


Figure 8. Application of pattern recognition algorithm to the SEF-INF2 test. Recognized steam bubble boundaries are marked as red.

Summary and conclusions

The SPASET project (2019–2020) has contributed to the validation of the simplified EHS/EMS models by increasing knowledge of small-scale phenomena affecting the effective heat and momentum sources during steam injection through spargers. Tests in the SEF-POOL at LUT have also supported the validation effort of the DCC and interfacial area models of CFD codes as well as the implementation of the EHS/EMS models to the Apros system code.

The effect of pool water sub-cooling, the transition from sub-sonic to sonic flow conditions, injection nozzle chamfer, and multi-hole injection on the effective momentum have been studied in 2019–2020. Good-quality high-speed camera stereo recordings of the steam jet behaviour and jet entrainment visualized with the help of air bubbles injected into the pool have been captured. KTH can effectively use their in-house tools in the analysis of the recordings for tracking the movement

of the air bubbles and thus ultimately assess the liquid velocity and the amount of jet entrainment.

OpenFOAM simulations of the SEF-POOL tests have been performed by using both 2D-axisymmetric and 3D geometries. The effect of interfacial area modeling has been studied by implementing the Rayleigh-Taylor Interfacial (RTI) area model of Pellegrini et al. (2015) The simulated 3D transient showed that the total DCC rate, interfacial area, and bubble volume were smaller in the 3D simulation than in the 2D-axisymmetric simulations. The improved pattern recognition-based image analysis algorithm has been successfully applied for tracking multiple steam bubbles at the same time for their whole lifetime. The algorithm was also applied to the instantaneous volume fraction field images of the 2D simulation results. The improved algorithm represented the real bubble shape better than before and yielded a good total bubble volume of the 2D-axisymmetric case with the 2mm grid size.

Acknowledgement

NKS and SSM have given financial supported for the work done under the SPASET project.

References

- Coste, P. 2004. Computational Simulation of Multi-D Liquid-Vapor Thermal Shock with Condensation. Proceedings of ICMF'04, Yokohama, Japan, May 30 - June 4, 2004.
- Gallego-Marcos, I., Villanueva, W., Kudinov, P. 2018a. Modelling of Pool Stratification and Mixing Induced by Steam Injection through Blowdown Pipes. Annals of Nuclear Energy 112 (2018), <https://doi.org/10.1016/j.anucene.2017.10.019>
- Gallego-Marcos, I., Kudinov, P., Villanueva, W., Kapulla, R., Paranjape, S., Paladino, D., Laine, J., Puustinen, M., Räsänen, A., Pyy, L., Kotro, E. 2018b. Pool Stratification and Mixing Induced by Steam Injection through Spargers; Analysis of the PPOOLEX and PANDA Experiments. Nuclear Engineering and Design 337 (2018), <https://doi.org/10.1016/j.nucengdes.2018.07.004>
- Gallego-Marcos, I. 2018c. Steam Condensation in a Water Pool and its Effect on Thermal Stratification and Mixing. Doctoral thesis, KTH Royal Institute of Technology, School of Engineering Sciences (SCI), Physics, Nuclear Engineering (2018), URN: urn:nbn:se:kth:diva-238732.
- Gallego-Marcos, I., Kudinov, P., Villanueva, W., Kapulla, R., Paranjape, S., Paladino, D., Laine, J., Puustinen, M., Räsänen, A., Pyy, L., Kotro, E. 2019a. Pool Stratification and Mixing Induced by Steam Injection through Spargers; CFD Modelling of the PPOOLEX and PANDA Experiments.

Nuclear Engineering and Design 347 (2019),
<https://doi.org/10.1016/j.nucengdes.2019.03.011>

- Gallego-Marcos, I., Villanueva, W., Kudinov, P., Puustinen, M., Räsänen, A., Tiilinen, K., Kotro, E. 2019b. Effective Momentum Induced by Steam Condensation in the Oscillatory Bubble Regime. Nuclear Engineering and Design 350 (2019), <https://doi.org/10.1016/j.nucengdes.2019.05.011>
- Gallego-Marcos, I., Grishchenko, D., Kudinov, P. 2019c. Thermal Stratification and Mixing in a Nordic BWR Pressure Suppression Pool. Annals of Nuclear Energy 132 (2019), <https://doi.org/10.1016/j.anucene.2019.04.054>
- Li, H., Villanueva, W., Puustinen, M., Laine, J., Kudinov, P. 2014. Validation of Effective Models for Simulation of Thermal Stratification and Mixing Induced by Steam Injection into a Large Pool of Water. Science and Technology of Nuclear Installations. Volume 2014, Article ID 752597.
- Li, H., Villanueva, W., Puustinen, M., Laine, J., Kudinov, P. 2018. Thermal Stratification and Mixing in a Suppression Pool Induced by Direct Steam Injection. Annals of Nuclear Energy 111 (2018), <https://doi.org/10.1016/j.anu-cene.2017.09.014>
- Patel, G., Hujala, E., Tanskanen, V., Puustinen, M. 2019. OpenFOAM Simulations and Pattern Recognition Analysis of the SEF-POOL Tests. Lappeenranta University of Technology, School of Energy Systems, Nuclear Engineering, Research Report SPASET 2/2019.
- Patel, G., Hujala, E., Puustinen, M. 2020. CFD Simulations and Pattern Recognition Analysis of the SEF-POOL Tests. Lappeenranta University of Technology, School of Energy Systems, Nuclear Engineering, Research Report SPASET 2/2020.
- Pellegrini, M., Naitoh, M., Josey, C., Baglietto, E. 2015. Modeling of Rayleigh-Taylor Instability for Steam Direct Contact Condensation. The 16th International Topical Meeting on Nuclear Reactor Thermal Hydraulics (NURETH-16), Chicago, IL, August 30 - September 4, 2015.
- Puustinen, M., Laine, J., Räsänen, A., Kotro, E., Tiilinen, K. 2019. SEF-POOL Tests. Lappeenranta: Lappeenranta-Lahti University of Technology LUT. School of Energy Systems. Nuclear Engineering. Research Report INSTAB 1/2018.
- Puustinen, M., Räsänen, A., Kotro, E., Tiilinen, K. 2020. SEF-POOL Tests on Small-Scale Phenomena of Steam Discharge into Sub-Cooled Water. Lappeenranta: Lappeenranta-Lahti University of Technology LUT. School of Energy Systems. Nuclear Engineering. Research Report SPASET 1/2019.
- Puustinen, M., Räsänen, A., Kotro, E., Tiilinen, K., Pyy, L. 2021. SEF-POOL Tests on Jet Entrainment. Lappeenranta: Lappeenranta-Lahti University of Technology LUT. School of Energy Systems. Nuclear Engineering. Research Report SPASET 1/2020.

- Pätkikangas, T., Hovi, V. 2018. CFD Simulation of Condensation of Vapor Jets. Research Report VTT-R-00993-18, Espoo, 2018.
- Pätkikangas, T. 2020. CFD Analysis of Pressure Suppression Pool by Using Effective Heat and Momentum Source Models. Research Report VTT-R-00228-20, Espoo, 2020.
- Tielinen, K., Räsänen, A., Kotro, E., Saure, I., 2018. General Description of SEF-POOL Test Rig. Lappeenranta University of Technology, School of Energy Systems, Nuclear Engineering, Research Report INSTAB 2/2017.

5.5 Safety through thermal-hydraulic analyses and cooperation (THACO)

Seppo Hillberg, Robert Airaksinen, Fares Alblouwy, Jarno Hiittenkivi, Tatu Hovi,
Eero Karola, Ismo Karppinen, Joona Kurki, Joona Leskinen, Afeef Murad, Sixten
Norrman, Ari Silde, Marton Szogradi

VTT Technical Research Centre of Finland Ltd
P.O. Box 1000, FI-02044 Espoo

Abstract

The goal of THACO was to improve nuclear safety through increasing the reliability of thermal-hydraulic deterministic safety analyses. Main part of the analysis work was carried out with, and related to, the system-scale safety analysis tool Apros that has been developed in Finland in cooperation between VTT and Fortum. Participation in international thermal hydraulics field research projects formed an essential part of the project. The most notable international cooperation task was the participation in OECD/NEA Rod Bundle Heat Transfer (RBHT) benchmark in all of its phases. Domestically, cooperation ties were tightened with LUT University. The project also included representation in multiple international OECD/NEA projects and in the U.S. NRC CAMP program.

Introduction

As thermal-hydraulic safety analysis tool Apros is used in the analyses of all the nuclear power plants in Finland, both the current one's and the one under construction, it is of the utmost importance that the simulation results obtained with the code are reliable, and that there are capable people available to carry out such simulations and to correctly assess the results.

Utilizing by younger researchers in the research work, under the supervision and guidance of senior experts, promotes a learning-by-doing approach to the education. This approach helps the younger researchers participating in the project to form a fundamental understanding of a thermal-hydraulic system-scale analysis code's capabilities and limitations from the nuclear safety point of view.

Participation in international research projects related to nuclear safety research in the field of thermal hydraulics, as well as domestic cooperation with LUT University, have formed an essential part of THACO project. Experimental data produced in these activities was directly utilized in the validation work carried out within THACO, and on the other hand, these validation activities supported the conduction of the experiments. In addition, they promoted international and domestic cooperation in the field of nuclear safety research.

The project comprised of three work packages: the first included the analysis work and the second international cooperation. The third work package contained only participation fees of international programs.

Assessment of Apros and TRACE against RBHT reflooding experiments

Rod Bundle Heat Transfer (RBHT) calculations began in 2019 with both Apros and TRACE calculations (Leskinen and Hovi, 2020). Experiments 1143, 1096, 1196, 1108 and 1383 were calculated and the results were compared against the corresponding experimental data. The interest in these experiments was related to the new OECD/NEA RBHT project but, as the new data project data was not yet available, older experiments were calculated in preparation for the soon expected open-phase benchmark cases. The experiments are listed Table 1, model data in Figures 1 and 2, and quench front propagation results in Figure 3.

Table 1. Summary of the experiments calculated with Apros and TRACE.

Run condition	Experiment index				
	1143	1096	1196	1108	1383
Upper plenum pressure [MPa]	0.138	0.138	0.276	0.138	0.276
Initial peak clad temperature [°C]	870.85	759.85	870.85	759.85	759.85
Rod peak power [kW/m]	2.3	1.31	2.3	1.31	1.31
Flooding rate [m/s]	0.1524	0.0254	0.1524	0.0254	0.0254
Inlet subcooling [°C]	83	11	53	83	11

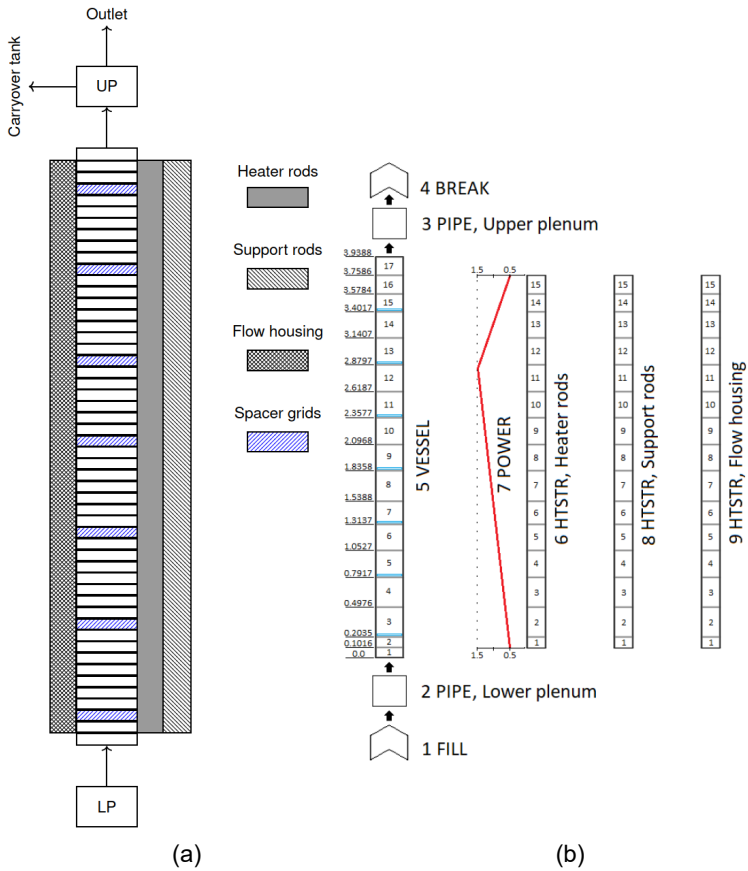


Figure 1. (a) Apros and (b) TRACE nodalizations of the RBHT test section.

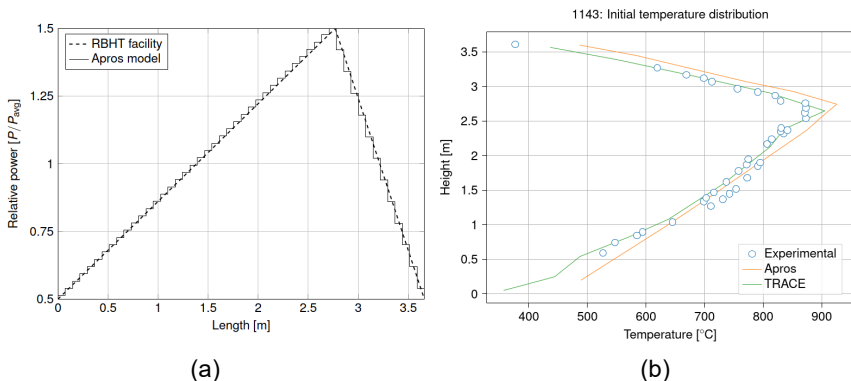


Figure 2. (a) Axial power distribution and (b) initial temperature distribution in one of the tests.

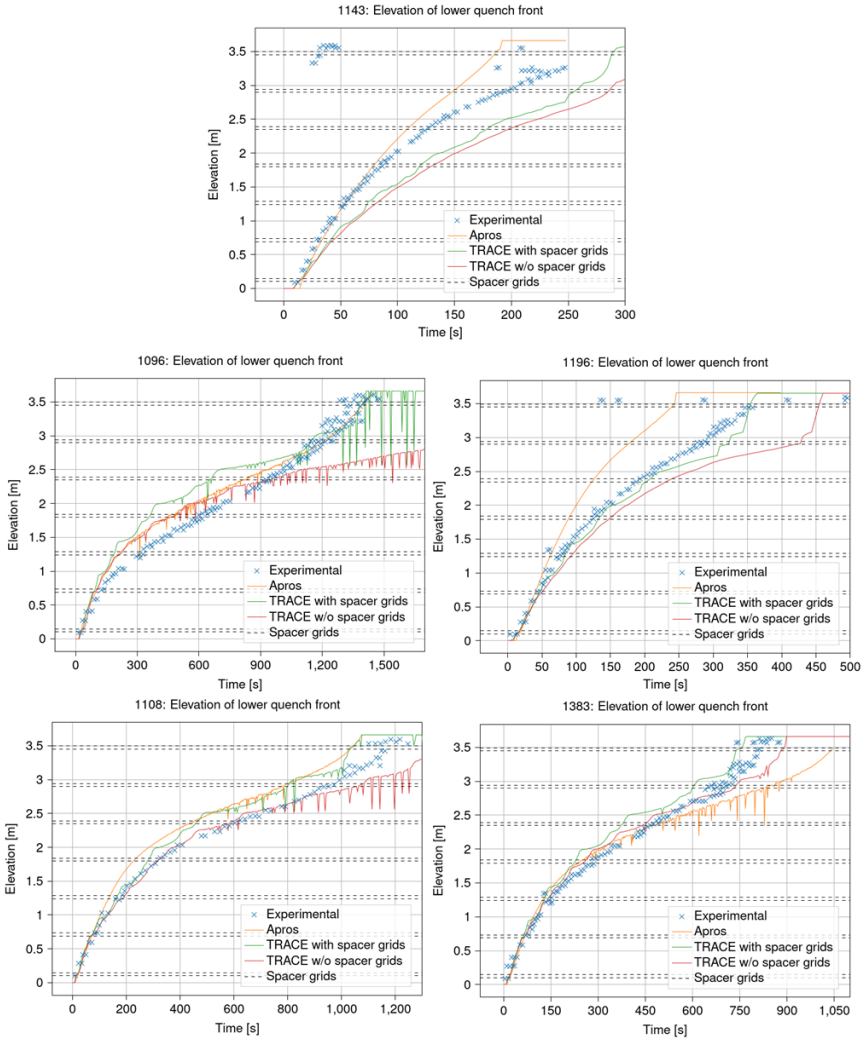


Figure 3. Lower quench fronts in the simulated cases.

Apros and the TRACE model with spacer grids predicted the reflooding phenomena with reasonable accuracy. As expected, the TRACE model with spacer grids provided an enhanced heat transfer compared to the model without spacer grids. Overall, in most cases Apros predicted the early stages of reflooding more accurately than TRACE. On the other hand, TRACE gave a better estimation for the total quench time. Both codes provided mainly conservative estimates for heater rod peak temperatures, but Apros generally gave a more accurate temperature profile behavior. TRACE significantly overestimated the peak temperatures, especially at higher elevations.

Assessment of Apros and TRACE against open phase RBHT reflooding experiments

In 2020 OECD/NEA RBHT project was starting in full with open phase experiment data open for project participants. The performed experiments focused on the impact of rod peak power, inlet subcooling and most notable, different reflooding rates and types such as oscillatory reflooding. Two experiments 9014 and 9015 had higher reflooding rates whereas seven experiments had low reflooding rates. In addition, two experiments 9011 and 9043 had extremely low reflooding rates. While these experiments can be used for code validation on their own, their other purpose was to provide modelling data in preparation for the incoming blind phase code benchmark.

These experiments were calculated with both Apros and TRACE (Hovi, 2020a, Hovi, 2020b). Machine learning was utilized and the Apros model was calibrated for the incoming benchmark according to these results. With Apros, also BEPU analysis was used for some of the cases. Normalized results are presented in Table 2, quench front progression in Figure 4 and one of the steam temperature measurements in Figure 5.

Table 2. Normalized Apros and TRACE peak cladding temperature (PCT) results.

Experiment	Apros				TRACE			
	PCT	PCT time	PCT elevation	PCT quench	PCT	PCT time	PCT elevation	PCT quench
9005	1.002	0.401	1.079	1.017	0.982	5.921	1.043	1.042
9011	0.966	1.317	1.074	1.145	1.004	0.944	1.149	N/A
9012	0.953	0.035	1.019	1.043	1.010	0.808	1.015	1.376
9014	1.007	0.780	1.079	0.860	0.982	1.007	1.043	1.183
9015	1.008	0.224	1.019	1.033	0.980	0.537	0.985	1.511
9021	0.963	0.386	1.019	1.063	1.015	0.603	1.015	1.013
9026	0.941	0.698	1.019	0.939	1.003	1.013	1.015	1.001
9027	0.953	0.596	1.019	0.960	1.008	0.975	1.015	1.006
9029	0.971	1.015	1.019	0.958	1.039	1.127	1.007	0.964
9037	1.023	0.488	1.019	0.993	0.989	5.131	0.985	1.019
9043	0.966	0.824	0.982	1.080	0.947	0.976	1.108	1.064

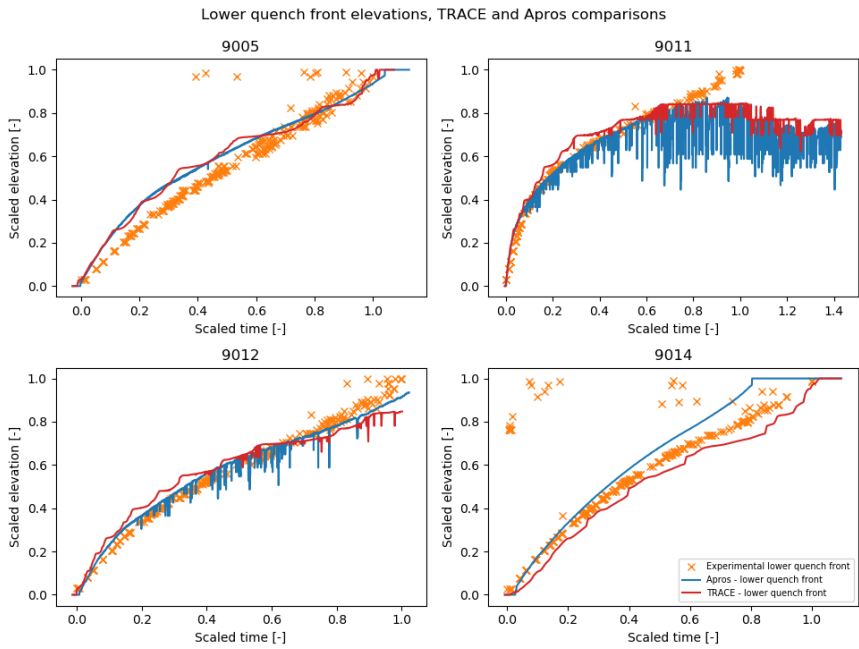


Figure 4. Quench front progression in some of the experiments.

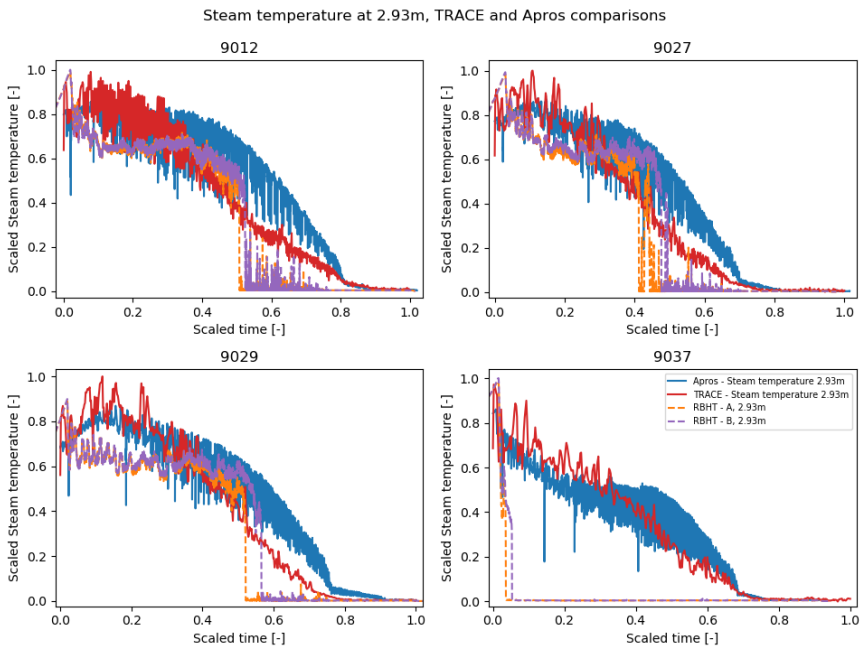


Figure 5. Steam temperature in some of the experiments.

In overall, the calibrated Apros model produced more accurate results. Quench front propagation and rod surface temperature estimations were good. As the benchmark was to be participated only with Apros, the TRACE model did not go through similar calibration. The TRACE results, however, were still quite good. Especially steam exhaust rates and bundle pressure drop gave reasonably accurate estimations.

Participation in the RBHT blind phase benchmark and the post-test analyses

In 2021 the RBHT project continued with a blind benchmark and five blind phase experiments were conducted in the RBHT test facility (Table 3). The benchmark was participated and Apros calculation results were submitted to the organizers. Later, once the experimental results were published, the data was compared with the results obtained with Apros (Hovi, 2022). Simulated results were compared with Figures of Merit (FoM) values which include quench front elevations during the reflooding, rod surface temperatures and heat transfer coefficients at two different elevations, steam temperature, droplet sizes, pressure drop across the bundle, carryover fractions, steam exhaust rates and peak cladding temperature (PCT) related values. All the simulated blind experiments by Apros also included uncertainty analysis for the FoM values. In addition to the RBHT experimental data and Apros simulation comparisons, post-test analysis was conducted for two RBHT blind experiments and a separate investigation was conducted for quench front propagation during extremely low reflooding rates.

Apros predicted most of the FoM values in good agreement. Including the post-test analysis, uncertainty bands successfully captured the majority of the experimental FoM values. Apros had most trouble estimating carryover fractions where the values were continually overestimated. Extremely low reflooding rates caused lot of numerical oscillation for the quench front propagation (Figure 6). Peak cladding temperature and quenching at PCT results are shown in Figure 7.

Calibrated Apros model enhanced heat transfer by greater margin that resulted in earlier quenching times in higher reflooding experiments. These higher reflooding experiments were chosen for post-test analysis and yielded better results when the uncertainty analysis was included (Figure 8). Default uncertainty coefficients were used in these cases.

A separate investigation mapped out the impact on the oscillation when varying uncertainty coefficients, adaptive nodalization option, simulation timestep and the amount of thermal hydraulic nodes in the simulation model. The cause for the oscillation was found to be the quench front detection logic in cases where the calculation transfers temporarily out of wetted-wall calculation at multiple locations at the same time. This behaviour doesn't affect the main quench front prediction and can be described as mostly visual. The best way to reduce the oscillations during low reflooding was to increase the number of thermal hydraulic nodes in the model and to slightly increase the timestep.

Table 3. Summary of the blind phase experiments (Hanson and Lowery, 2021).

Run condition	Experiment index				
	B1-9047	B2-9053	B4-9056	B6-9059	B3-9064
Upper plenum pressure [kPa]	275.8	275.8	137.9	413.7	275.8
Initial peak clad temperature [K]	1144.26	1144.26	1144.26	1000.0	1000.0
Rod peak power [kWm ⁻¹]	2.3	2.3-1.31	2.3-1.20	1.31	1.31
Flooding rate [ms ⁻¹]	0.10	0.10	0.10	0.025	0.025 ± 0.025, t=2.0s
Inlet subcooling [K]	10.0	5.0	5.0	30.0	10.0

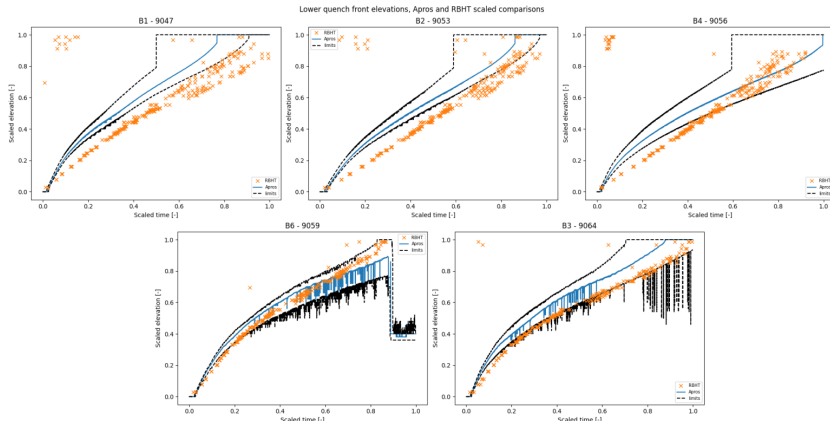


Figure 6. Lower quench front elevations and uncertainty bands in the blind RBHT experiments.

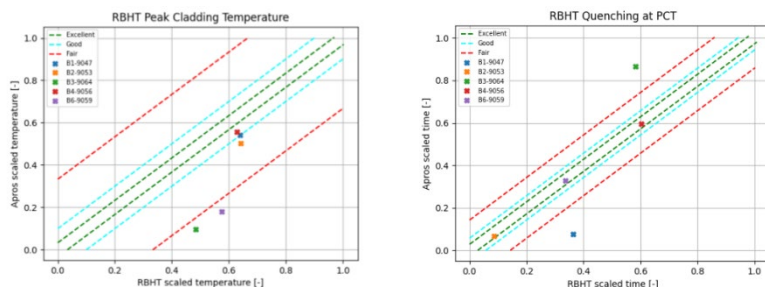


Figure 7. Peak cladding temperature (left) and quenching at PCT (right) in the post-test calculations. The limits were decided in a RBHT workshop. Low reflooding cases were difficult to calculate for everyone and Apros performed quite well in the benchmark.

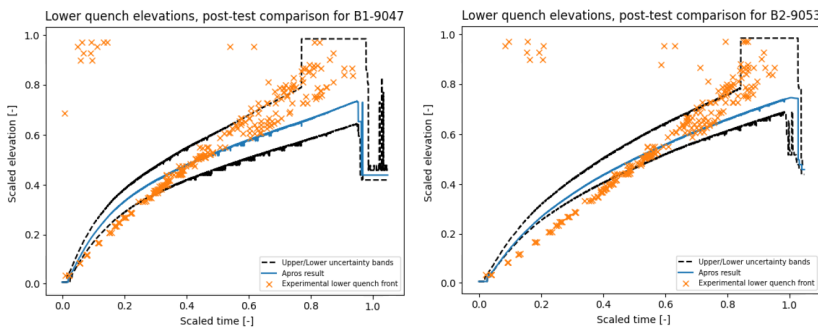


Figure 8. Lower quench front elevations and uncertainty bands in the RBHT post-test calculations.

LUT cooperation pilot

This task piloted the new planned closer cooperation between VTT and LUT that will take place in the SAFIR2022 continuation programme SAFER2028. VTT research scientist participated the LUT experiment execution and post-test calculation with TRACE was performed. The goal was to study the capability of TRACE to calculate such transient as well as compare the results with Apros simulation of the same test. The used TRACE model was borrowed from LUT and it was refined to correspond to the test. PATE project calculated the same post-test case with Apros. The TRACE results made in THACO were reported in the PATE deliverable (Kouhia and Karola, 2022).

Examination of interfacial drag modelling in hexagonal geometry

This task focused on interfacial drag in hexagonal geometry (Murad, 2022). The work was divided into two parts. The first one is the analysis of the interfacial drag modelling of hexagonal fuel rod bundles. This was started by conducting a literature review on the interfacial drag modelling in different thermal-hydraulics system codes with a more detailed analysis of the Apros interfacial drag models. This was done in order to identify the most suitable model to be used when modelling hexagonal fuel bundles. The most mature and up to date model in Apros interfacial models was chosen (improved Bestion correlation for fuel bundles). Then by analysing the different parameters used in the model equations, it was found that the parameter to be modified when modelling hexagonal fuel bundles is related to the vapor friction on the liquid films along the fuel rods. The interfacial drag model chosen was validated by simulating three different boiloff experiments that were conducted in the separate effect test facility VEERA.

The three calculated VEERA cases showed that the identified parameter had only a minor effect on the results. As a result, it can be concluded that the Bestion correlation can be assumed to perform reasonably. In order to assess the suitability for hexagonal geometry more thoroughly, more experimental data would be needed and there is very little of it available.

The second part of this work was a simulation of a reflooding experiment that was conducted in a IVO separate effect test facility. The main goal of this simulation was to study Apros capabilities when it comes to modelling counter current flow limitation (CCFL) by trying to reproduce the flooding curve. Apros respected the curve and the CCFL model is working as intended.

A joint publication on the PASI VTT-01

The PASI facility, located in and operated by LUT, is a one-loop model of an open passive containment cooling system. The reference system of the PASI test facility is the passive containment heat removal system of the AES-2006 type pressurized water reactor. In the recent years multiple PASI experiment have been performed at LUT. This test facility was first modelled and simulated at VTT in SAFIR2018 COVA. In 2020 this existing model was updated to contain the larger condensation pool and VTT-01 experiment, performed in SAFIR2022 PAHE, was calculated (Hillberg, 2020). In 2021 this model was further fine-tuned and handed over to SAFIR2022 CFD4RSA for Apros-Fluent coupling. The Apros stand-alone model utilizes 6-equation model for modelling the pool and the circulation loop. The heat exchanger connects to a Apros containment node which represents the containment. The Apros model is shown in Figure 9. In 2022 CFD4RSA replaced the Apros containment node calculation with CFD calculation. A joint publication is being written of this cooperation between THACO, PAHE and CFD4RSA.

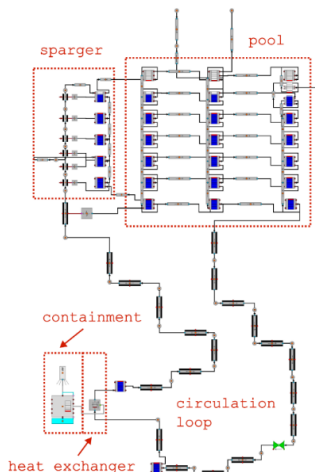


Figure 9. Apros model of the PASI facility.

A master's thesis on critical flow modelling

A masters thesis on critical flow modelling was produced (Airaksinen, 2021). The aim of this thesis was to examine the recently updated critical flow calculation in the Apros program by comparing the predictions of different critical flow models to empirical data. A model of Marviken Critical Flow Test facility was created with the Apros program, and a total of 26 blowdown experiments were simulated. The tested nozzle geometries varied in diameter and length in range representative of the primary circuit of a typical water-cooled nuclear reactor. Moody and Henry-Fauske critical models with local average pressure and stagnation pressure were compared with experimental data.

The work suggested the Henry-Fauske model with stagnation pressure to be the recommendable option when underprediction must be strictly avoided. For best estimate calculation, the models of Henry-Fauske with static pressure and Moody with stagnation pressure seemed more accurate.

Analyses of other experimental facilities

Additionally, several PKL facility steady-state and IBLOCA experiments (Szogradi and Karppinen, 2020, Alblouwy and Karola, 2021), were calculated. A double-ended FIX-II facility LBLOCA case was analysed with Apros (Hillberg, 2019) and pool stratification in PERSEO facility was studied in (Karppinen, 2021).

International cooperation

International cooperation was heavily represented in the project. Multiple research projects were being actively followed. In addition to the new validation data, these programs also contributed to knowledge transfer between organizations. The following programs or projects were followed (Table 4) during the four years of THACO:

- OECD/NEA Hydrogen Mitigation Experiments for Reactor Safety Phase 2 (HYMERES-2) was aimed on detailed analysis of the containment phenomenology during postulated severe accidents with the release and distribution of hydrogen.
- OECD/NEA Rod Bundle Heat Transfer (RBHT) is a experimental research project with an objective of conducting new experiments and evaluating system hydraulics codes in the simulation of reflood tests in a full height rod bundle for complex inlet flows. The facility is operated by Pennsylvania State University/U.S. Nuclear Regulatory Commission.
- OECD/NEA PKL-4 project investigated safety issues relevant for current PWR plants as well as for new PWR design concepts by means of systematic parameter studies on thermal-hydraulic phenomena and transient tests under postulated accident scenarios.
- Experimental Thermal Hydraulics for Analysis, Research and Innovations in NUclear Safety (ETHARINUS) project investigates phenomena where the knowledge base for safety assessment is not sufficiently developed and

of providing qualified data for thermal-hydraulics code model development and validation for the analysis of key safety issues. It utilizes PKL, PWR PACTEL and PSB-VVER experimental facilities.

- OECD/NEA CSNI Working Group on Analysis and Management of Accidents (WGAMA) aims to advance the current understanding of the physical processes related to reactor safety.
- U.S. NRC's Code Applications and Maintenance Program (CAMP) is formed to exchange information on thermal-hydraulic safety related issues between U.S. NRC and its international partners. TRACE, PARCS, RELAP5 codes and the graphical interface SNAP are made available through this program.

Table 4. Type of representation in the international cooperation programs.

Project or program	Type of representation
OECD/NEA RBHT	MB member
OECD/NEA HYMERES-2	PRG member
OECD/NEA PKL-4	PRG member
OECD/NEA ETHARINUS	PRG member
OECD/NEA WGAMA	country representative
U.S. NRC CAMP	country contact person

References

- Airaksinen, R. 2021. Simulation of Marviken two-phase critical flow tests. Master's thesis, Aalto University School of Engineering, Mechanical Engineering. <http://urn.fi/URN:NBN:fi:aalto-202106207459>
- Alblouwy, F., Karola, E. 2021. Analysis of PKL III J2.1 and J2.2 with TRACE and Apros codes. VTT Research Report. VTT-R-00126-22.
- Hanson, M. K., Lowery, B. R. 2021. Rod Bundle Heat Transfer Reflood Data from Bundle 2 Experiment, Quick Look reports RF2-9047 / RF2-9053 / RF2-9056 / RF2-9059 / RF2-9064. Pennsylvania State University, Applied Research Laboratory.
- Hillberg, S. 2019. Analysis of FIX-II experiment 5052 with Apros. VTT Research Report. VTT-R-00914-19.
- Hillberg, S. 2020. Apros analysis of PASI natural circulation experiment VTT-01. VTT research report. VTT-R-00054-21.
- Hovi, T. 2020a. Assessment of Apros against open phase RBHT reflooding experiments. VTT research report. VTT-R-01349-20.
- Hovi, T. 2020b. Assessment of TRACE against open phase RBHT reflooding experiments. VTT research report. VTT-R-00032-21.

- Hovi, T. 2022. Post-test assessment of Apros against blind phase RBHT reflooding experiments. VTT research report. VTT-R-00950-22.
- Karppinen, I. 2021. PERSEO Test 7 simulation with Apros. VTT Research Report. VTT-R-00229-22.
- Kouhia, V., Karola, E. 2022. APROS and TRACE Simulations of PWR PACTEL Experiment SBL-65. LUT University Nuclear Engineering Research Report. 360/322/2018.
- Leskinen, J., Hovi, T. 2020. Assessment of Apros and TRACE against RBHT reflooding experiments. VTT research report. VTT-R-00033-20.
- Murad, A. 2022. Examination of interfacial drag in hexagonal fuel bundles and the CCFL model verification in Apros. VTT Research Report. VTT-R-00980-22.

5.6 Containment safety research (CONTSA)

Ari Silde, Tuomo Sevón, Ville Hovi, Arina Värä, Ismo Karppinen

VTT Technical Research Centre of Finland Ltd
P.O. Box 1000, FI-02044 Espoo

Abstract

The general objective of the 2-year CONTSA project was to study important thermal-hydraulic containment safety issues and validate analyses methods to improve their reliability for containment deterministic safety analyses. CONTSA was mainly relied on the test program of the international OECD/NEA HYMERES-2 projects by using related experiments as code validation cases. CONTSA also followed closely both the OECD/NEA HYMERES-2 and the following PANDA project findings and delivered them to the SAFIR2022 organisations.

Multi-nozzle spray and containment cooler system tests performed at Panda facility in Switzerland were analysed using the Apros, MELCOR and CFD Fluent codes. The calculation results were compared with the measurement data and also code benchmark was conducted. Suitable modelling approach and nodalisation concepts with related sensitivity studies were also investigated.

CONTSA rounded up the containment know-how across relevant research areas such as DBA thermal-hydraulics, severe accidents and CFD method. One goal of the project was also to exchange knowledge from the older to younger experts and educate new experts in area of containment safety. One Master's thesis was finalized in this project.

The Finland's participation fee for the international OECD/NEA PANDA co-operation program was paid through CONTSA.

The research report of this work is restricted according to the OECD/NEA project restrictions. The duration of the non-disclosure period is 3 years starting from the date when the final project report including all experimental data has been sent to the HYMERES-2 partners. The report is available from the project contact person but signing of an NDA is required. Please contact Ari Silde (ari.silde@vtt.fi) for receiving the report.

Introduction

The general objective of the 2-year CONTSA project was to study important thermal-hydraulic containment safety issues and validate analysing methods to improve their reliability for containment deterministic safety analyses, and hence, to increase containment safety. CONTSA has mainly relied on the test program of the international OECD/NEA HYMERES-2 and PANDA projects by using related experiments as code validation cases. CONTSA also followed the OECD/NEA project results and delivered the main findings to the SAFIR2022 organisation.

CONTSA has rounded up the containment know-how across relevant research areas such as DBA thermalhydraulics, severe accidents and CFD method. The essential goal was also to exchange knowledge from the older to younger experts and educate new experts in the area of containment safety. One Master's thesis was finalized in this project.

The Finland's participation fee for the international co-operation program OECD/NEA PANDA was paid through CONTSA.

Function of two containment safety system has been considered: containment spray and cooler system. The aim of the spray analyses was to clarify, whether lumped parameter (LP) methods are valid for analysing a single-nozzle and more representative multi-nozzle spray phenomena. The HYMERES-2 spray experiment series H2P5 was analysed with the Apros and MELCOR codes. The containment cooler function was studied using both lumped parameter codes (Apros and MELCOR) and the CFD methods (Fluent) by calculating HYMERES-2 experiment series H2P6. The Apros analyses against the cooler tests were made as a Master's thesis, where also suitability of different heat transfer correlations were investigated. Both the H2P5 and H2P6 test series under consideration have been conducted by PSI at the Panda facility in Switzerland. In general, the calculation results were compared with measurement data and also code benchmark were conducted. Suitable modelling approach and nodalisation concepts with related sensitivity studies were also investigated.

The research report of this work is restricted according to the OECD/NEA project restrictions. The duration of the non-disclosure period is 3 years starting from the date when the final project report including all experimental data has been sent to the HYMERES-2 partners. The report is available from the project contact person but signing of an NDA is required. Please contact Ari Silde (ari.silde@vtt.fi) for receiving the report.

Spray-analyses

The work aimed to study the capabilities of Apros (version 6.11.05) and MELCOR (version 2.2 revision 18019) codes to model containment phenomena with spraying including different number of spray nozzles in a pressurized mixture of air, steam and helium. Two experiments of the HYMERES-2 H2P5 series were modelled: a nine-nozzles and a single-nozzle tests (Paladino et al, 2021). In the nine-nozzle test, the spray covered almost the whole test vessel, and a significant part of the droplets hit directly the vessel wall because the nozzles were located relatively close to the side walls. In the single-nozzle test, the nozzle was located at the centre axis and the spray covered only a part of the test vessel, and the droplets did not hit the side walls.

The H2P5 tests were performed with Vessel 1 (Drywell 1) of PANDA large-scale facility that is based on 670 MW Simplified Boiling Water Reactor by General Electric (Paladino et al, 2021). The facility has full-scale heights and 1:25-scale in volume. There are two drywells in the facility that are connected with a pipe. For

H2P5 tests, the connecting pipe is sealed. Vessel 1 has a height of 8 m and a diameter of 4 m. The volume is about 89.9 m^3 . The vessel is made of stainless steel, and it is thermally insulated with a 20 cm layer of rock wool.

Schematic picture of the test configuration can be seen in Figure 1 (Paladino et al, 2021). Tests started with creating specific air-steam mixture in the Vessel 1. Wanted temperature was reached by heating the walls of the vessel. Helium was injected, which created helium-rich gas mixture in the upper part of the vessel, and helium-free lower part. Test H2P5_1 used nine spray nozzles (Figure 1) and H2P5_2 test used a single spray nozzle. The nine-nozzle ring-arrangement is more representative for real NPP's. Other initial conditions for both tests were the same. The total spray flow rate was also the same, the flow was divided evenly to nine nozzles in H2P5_1. The spray water was taken from the GDCS tank, where it was heated to specific temperature. After the spray period, Vessel 1 conditions were let to become steady.

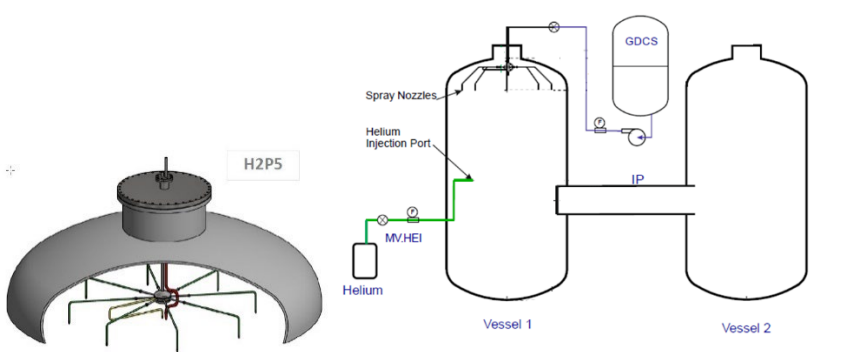


Figure 1. Test configuration in Vessels 1 and 2 for H2P5_1 (Paladino et al, 2021).

The Apros nodalisation for Vessel 1 of PANDA facility was based on the pseudo 3D approach used for many earlier applications where the gas stratification is assumed to take place such as in the HYMERES PANDA HP6_1 test (Silde, 2018). The vessel was divided into vertical levels, which then were divided into 5 nodes, radially and azimuthally (Figure 2). The bottom level was an exception, as it was modelled only with one node. Each level contained five nodes, one of which was the center node and the four others were surrounding it forming a cylindrical level. Walls, including floor and roof, of the vessel were modelled as heat structures that were connected to nodes. For comparison purposes, also a one cell nodalisation was created.

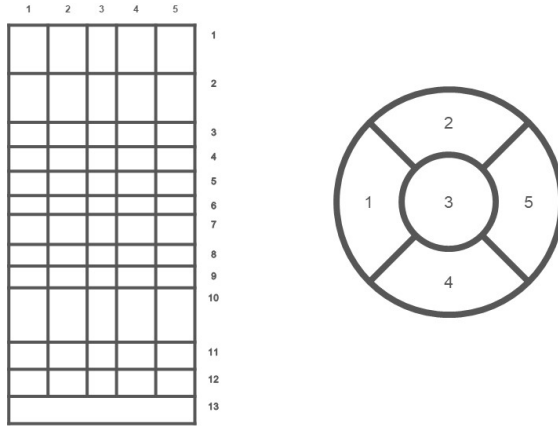


Figure 2. Nodalization of Apros model. The left picture represents the node levels, and the right picture shows how the node levels from one to twelve have been divided using pseudo 3D approach (Sevón and Karola, 2022).

In the MECLOR analyses, both the nine-nozzle and the one-nozzle tests were firstly modelled with one control volume, representing the entire test vessel. This is the normal practice for MELCOR models of nuclear power plants, so that one control volume represents one room in the containment. The one-volume model did not give good results for the one-nozzle test because the spray covered only a part of the vessel. Therefore, also a four-volume model was developed for the one-nozzle test. In the four-volume model (Figure 3), the sprayed part was modeled as a cone with 30° angle. It represents 22% of the total vessel volume. The sprayed part and the dry part were both divided into two parts in the vertical direction, in order to model the helium stratification. A spray junction was defined so that when the droplets reach the bottom of the upper control volume, they are carried over to the lower volume. The upper part was connected to the lower part with two vertical flow paths. The sprayed part was connected to the dry part with three horizontal flow paths at different elevations. The third flow path was added because the scoping calculations with the GOTHIC code (Vázquez-Rodríguez et al., 2021) showed that there will be an eddy that has a stagnation point less than 2 m from the vessel bottom. The third flow path turned out to be very important because it increased the flow velocity in the lower dry volume, which in turn increased the heat transfer coefficient from the wall to the gas. MELCOR calculates the flow velocity in each control volume, based on the volumetric flow rates in and out of the volume. The flow path areas were set to the interfacial areas between the volumes, calculated from the geometry. The flow path lengths were calculated from volume center to center. The form loss coefficients were set to zero.

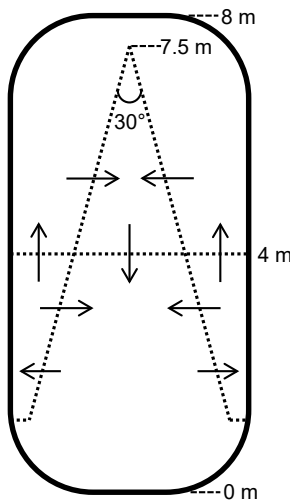


Figure 3. Four-volume MELCOR nodalization of the one-nozzle test. The arrows are flow paths. (Sevón and Karola, 2022).

Figure 4 presents the pressure comparison between the code calculations and measurement in the nine-nozzle test. Similar one cell nodalisation with the rough assumption that 22% of the spray droplets hit directly the side walls was used in the both code calculations. The agreement between the code results is good that hints that the spray cooling effect is calculated consistently by the codes. In general, the agreement between the measurements and code results is also fairly good, but the codes have a tendency to underestimate pressure.

Corresponding results in the single-nozzle test is shown in Figure 5. The multi-node LP nodalisations presented in Figures 2 and Figure 3 are used. The codes underestimate pressure more than in the nine-nozzle test. When the nodalization is different between the codes, some other mechanisms than the spray cooling power, such as gas mixing phenomenon and heat transfer from warm walls to the gas region are of importance resulting in deviations of the code results. Further analysis explained that MELCOR models the higher gas flow rates than Apros, which clearly affect the wall heat transfer. Slower flow rates in Apros occur likely due to more complex nodalization. This implies that a simpler nodalization would work better for spray calculation like this.

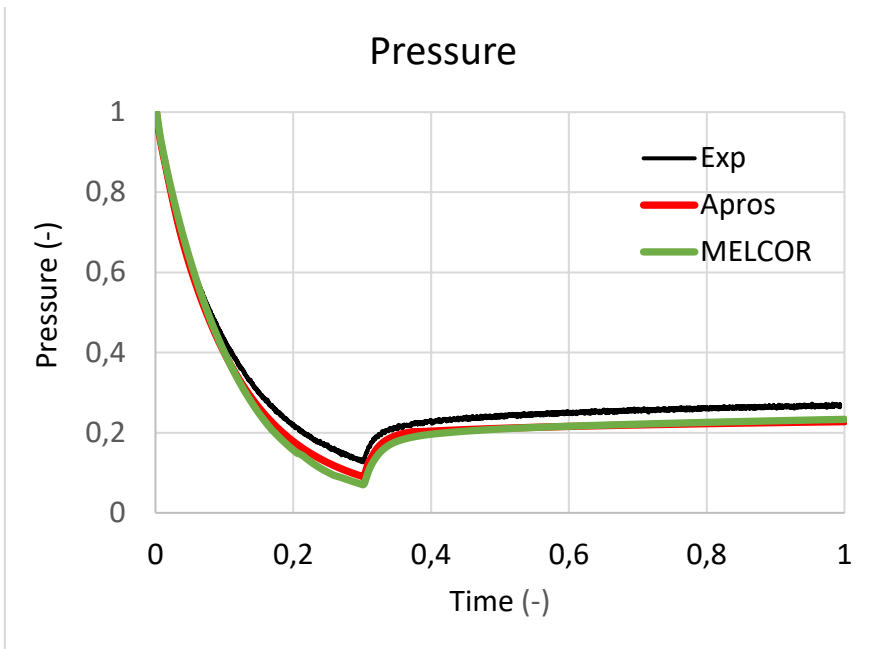


Figure 4. Vessel pressure in the nine-nozzle test. Values are scaled (Sevón and Karola, 2022).

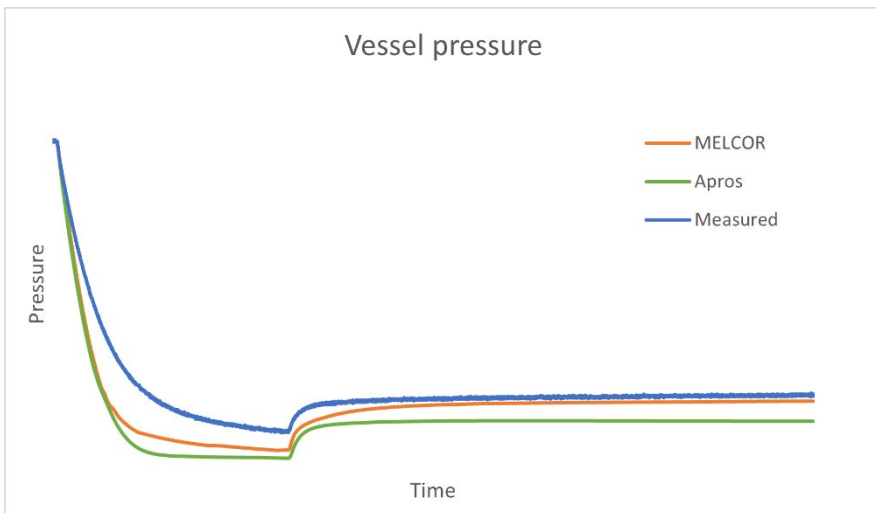


Figure 5. Vessel pressure in the single-nozzle test (Sevón and Karola, 2022).

Containment cooler analyses

The cooler tests were performed in the drywell 1 vessel of the PANDA facility (Kapulla et al., 2021). Three coolers were installed to the vessel (Figure 6). Each cooler consisted of 18 vertical heat exchange tubes. Water was pumped to the lower end of the tubes through an inflow hose and inlet collector. The warm water flowed out of the upper end of the tubes through the outlet collector and outflow hose. Before the beginning of the tests, the test vessel was pressurized with steam and air, and helium was injected to form a helium-rich layer to the upper part of the vessel. In test H2P6_1, all three coolers were in operation. In test H2P6_2, only one of the three coolers was operated. The both test series were calculated by the Apros (as Master's thesis) and MELCOR code. The CFD Fluent code was applied only for three-cooler test (Väärä, 2022; Sevón&Hovi, 2023).

The Apros nodalisation was otherwise similar pseudo 3D nodalisation to one presented in Figure 2, except that the vertical node levels 3 to 6 (where the cooler units were located) were merged. With MELCOR, several different nodalisations of the test vessel were investigated. The best results were obtained with the eight-volume nodalisation (Figure 7, left picture). The vessel was divided into four levels in the vertical direction and into two halves in the horizontal direction. The helium-rich layer at time zero was above the 4 m elevation. Nodalisations with six and ten volumes were tested, but the eight-volume nodalization was the best at reproducing the timing of the helium mixing. For comparison, also a one-volume model was made because the normal practice in MELCOR models is to have one volume per one containment room. Naturally, the one-volume model ignores the helium stratification and mixing. For Fluent, a fairly coarse polyhedral mesh, consisting of ~3.6 million cells, was created based on the CAD model (Figure 7, right picture). The surface mesh on the containment vessel exterior walls is shown in the top right, the surface mesh on the cooler modules in the top left, and a close-up of the surface mesh near one of the cold collectors is shown on the bottom. Mesh resolution was kept high in the vicinity of the cooler modules, to properly resolve the heat transfer tubes. Elsewhere, the mesh was kept coarse to decrease the total amount of cells. Two wall cell layers were created for the heat transfer tubes and the collectors to facilitate the Eulerian wall film solution. A single wall cell layer was created for the containment vessel walls. Thin slivers were created on horizontal sections of the heat transfer tubes (and collectors) to prevent pooling of the Eulerian condensate film. Instead of forming a thick film and separating into droplets, the film is removed from simulation when it encounters the sliver sections.



Figure 6. Test arrangement in the Panda cooler tests (Paladino et al., 2022).

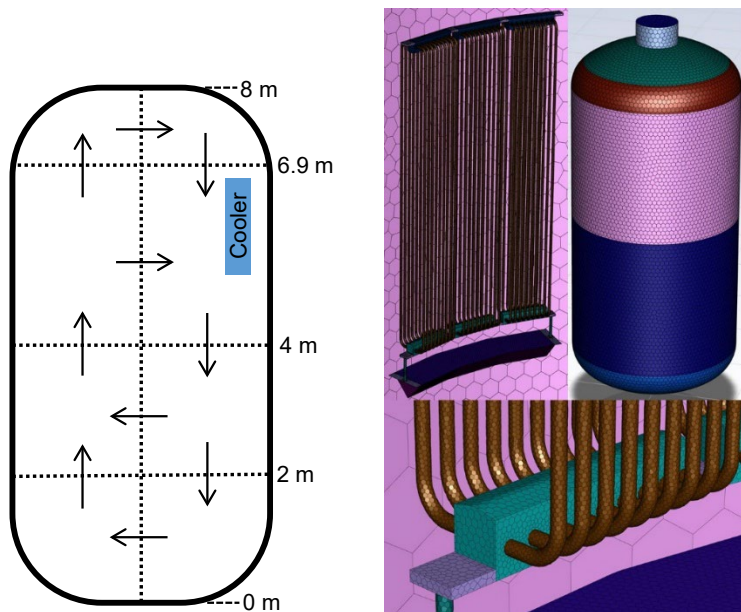


Figure 7. Code nodalisation concepts for the three-cooler H2P6 test: MELCOR (left) and Fluent (right) (Sevón and Hovi, 2023).

The measured and calculated vessel pressure behaviours in the three cooler test are shown in Figure 8. Figure 9 shows the cooler water temperature difference corresponding to the cooling power of cooler. The pressure behaviour is dependent on the cooling power, which is further dependent on gas temperature and gas composition i.e. gas stratification and mixing phenomena are also of importance. Generally speaking, all codes can model the pressure behaviour qualitatively reasonably, but there are quantitative differences between the calculations and measurements. The differences in the calculated pressures may be partly caused by the way how the cooling power and gas stratification/mixing are modelled. Several control volumes are needed for modelling gas stratification and mixing qualitatively soundly when using the Apros and MELCOR lumped parameter codes. MELCOR calculates the beginning of the test correctly, but at later times when the gas stratification breaks MELCOR overestimates slightly the pressure decrease rate and cooling power, and underestimates slightly the final pressure. Apros underestimates the pressure and overestimates the cooling power until the break of stratification, after which the pressure decay rate is slightly underestimated, but however, the final pressure is well predicted. Containment pressure in the Fluent analyses is slightly overestimated throughout the simulation, since the heat flow to the cooler unit (cooling power) is underestimated. The Fluent results also show that erosion of the helium stratification layer may be too slow in the simulation. Neither the top of the cylindrical section is not mixed properly in the Fluent simulation.

The experimental findings proved that the number of used coolers is unimportant from the point of cooling efficiency of one cooler unit. However, it was not possible perfectly replicate this finding in the Apros and MELCOR analyses (Fluent code was only applied in the three-cooler test). This is possibly due to limitations of the lumped parameter method in modelling the gas flow pattern correctly. This highlights that modelling mixing phenomena with lumped parameter codes is difficult, as the results depend on the chosen nodalisation and flow path settings.

The cooler that was utilized in the experiment resembles the passive containment condenser of the AES-2006 design. However, the coolant flow in the experiment was not passive. The water was pumped to the condenser, and its flow rate was used as a boundary condition in the calculations. Modelling a real reactor accident would be more challenging because the coolant flow rate depends on density differences. In later phases of an accident, the coolant may start to boil, causing two-phase flow, which has its own challenges from modelling point of view.

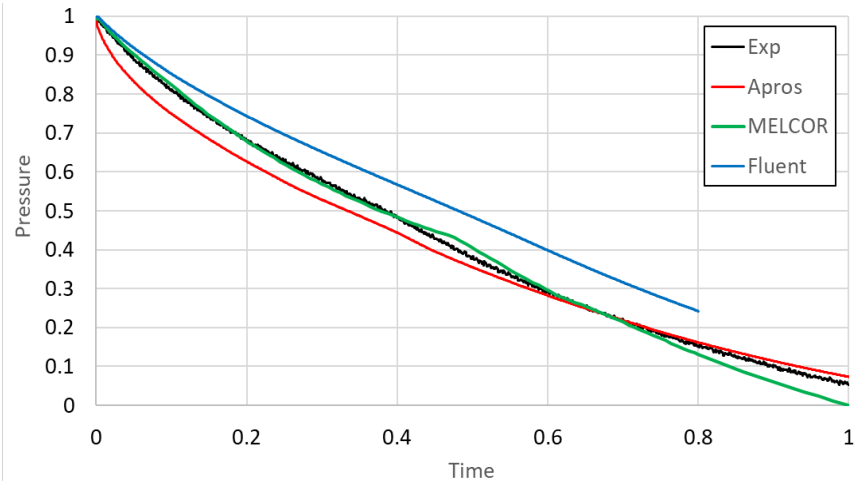


Figure 8. Measured and calculated pressures in a three-cooler test (Sevón and Hovi, 2023).

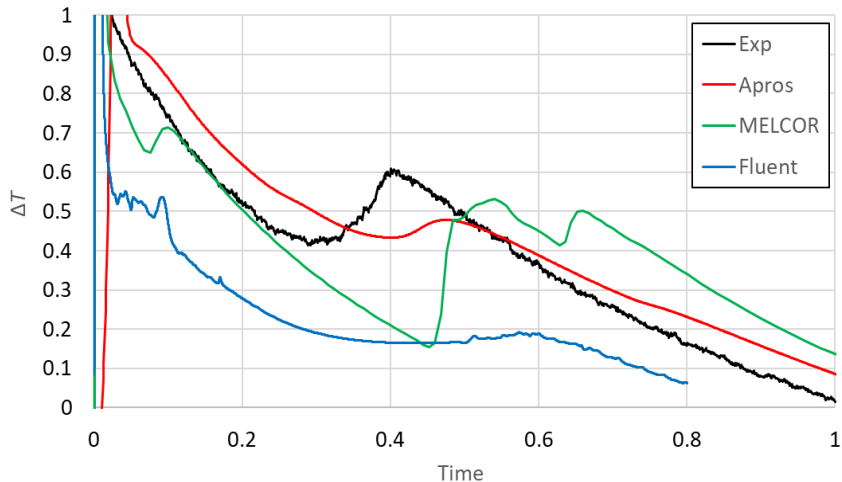


Figure 9. Measured and calculated water temperature difference in a three-cooler test (Sevón and Hovi, 2023).

International cooperation

A substantial part of the CONTSA work was the participation in the international OECD/NEA HYMERES-2 (Hydrogen Mitigation Experiments for Reactor Safety) and PANDA (Advanced Knowledge on the Nuclear Power Plant Containment Thermal-Hydraulics) co-operative research programs. Selected tests of these research projects were used as code validation cases in CONTSA. CONTSA also

followed the OECD/NEA project findings and delivered them to the SAFIR2022 organisation.

Change of knowledge and education of new experts

CONTSA has rounded up the containment expertise across relevant research areas such as DBA thermalhydraulics, severe accidents and CFD method. The essential goal was also to exchange knowledge from the older to younger experts and educate new experts in the area of containment safety. One Master's thesis was finalized in the project.

References

- Kapulla R., et al. 2021. The effects of activated cooler power on the transient pressure decay and helium mixing in the PANDA facility. Nuclear Engineering and Technology. DOI: <https://doi.org/10.1016/j.net.2021.12.032>
- Paladino, D. et al. 2021. Spray nozzle ring – H2P5 Series and Data Report. OECD/NEA HYMERES-2 Project. TM42-21-22-0. HYMERES-2-21-22-0. 27.8.2021.
- Paladino, D., Kapulla, R., Paranjape, S., Suter, S. and Andreani, M. 2022. PANDA experiments within the OECD/NEA HYMERES-2 project on containment hydrogen distribution, thermal radiation and suppression pool phenomena. Nuclear Engineering and Design 392 (2022) 111777.
- Sevón, T and Hovi Ville. 2023. Modelling of PANDA H2P6 cooler test with MELCOR and Fluent. VTT Research Report VTT-R-00034-23.
- Silde, A. 2018. Calculation of the HYMERES/PANDA natural circulation test HP6_1 with Apros containment software. VTT-R-06500-17. VTT Technical Research Centre of Finland 31.1.2018.
- Vázquez-Rodríguez C., Andreani M., Jiménez G. 2021. H2P5 Scoping Calculations: Main differences between the single nozzle and multi nozzle configurations for PANDA. PRG6/MB6 Meeting of the HYMERES phase 2 project, March 23–24, 2021.
- Värä, A. 2022. Nuclear Power Plant Passive Containment cooling System Simulation in Apros. Master's Thesis. Aalto University. 25.9.2022.

5.7 Critical flow separate effect test facility (CRITFLOW)

Lauri Pyy¹

¹LUT University
P.O. Box 20, FI-53851 Lappeenranta, Finland

Abstract

CRITFLO was a one-year project conducted in 2022. In the original project proposal, LUT University proposed to design and commission a separate-effect-test facility that would enable critical flow experiments in a primary-to-secondary guillotine break scenario. The motivation for the critical flow experiments was the result of LUT University's roadshow conducted in 2021 aiming for the future research needs of the Finnish nuclear safety community. Talks were organized with all the Finnish power companies (TVO, Fortum, Fennovoima), VTT, and STUK. In the talks, the general conclusion was that more phenomena-based research was preferred. SET facilities can provide an easier approach to the experimental study of the phenomena where it can be isolated compared to integral facilities. Due to the funding reduction of the original proposal, a literary review of recent critical flow experimental work was conducted instead.

The literary review: "state-of-the-art report on experiment work on critical flow" included an introduction of the theoretical background and a short description of two-phase critical flow (TPCF) models used in system thermal-hydraulics (SYS-TH) codes. The experiment work presented was divided into two parts. First part focused on critical flow experiments conducted with key large-scale experimental facilities and second part to more recent experiments. The recent work was divided between experiments in pipes, cracks and valves.

As a part of CRITFLO, SILENCE meetings considering TPCF model development were attended where valuable information about experimental needs for the future TPCF model development was acquired.

Introduction

CRITFLO was originally a project where the initial goal was to design and commission a separate effect-test facility capable of critical flow studies at LUT University. The funding proposal of the CRITFLO was accepted for the last year of SAFIR2022. However, the scope of the project was thought of as being too ambitious. Thus, the funding was accepted only for a literature review of the state-of-the-art of critical flow studies. Two-phase critical flow modelling has still large uncertainties in SYS-TH codes which are in the range of several tens of percents depending on the mechanical and thermal non-equilibrium state of the discharging phases as identified by the FONESYS network's study published in 2020 (Landfredini, 2020).

In the past, many researchers have studied critical flows. The scale of these classical experimental facilities and instrumentation is unmatched with more recent experimental works conducted for critical flow studies. The classical experiments are still very state-of-the-art considering these facts. However, novel information was found in the more recent experimental works including new phenomena like double-choking or using actual steam generator tube cracks as the test samples. So-called advanced measurement systems are not yet applied even in recent experiments except for visualization with cameras. As part of CRITFLO, SILENCE (Significant Light and Heavy Water Reactor Thermal Hydraulic Experiments Network for the Consistent Exploitation of the Data) network's meetings aiming at TPCF model development and how to implement advanced measurement systems for critical flow measurements were attended.

Original proposition

CRITFLO was originally proposed as a larger volume project where a separate effect test facility (SET) capable of critical flow discharges were proposed. The preliminary sketch of the SET is presented in Figure 1.

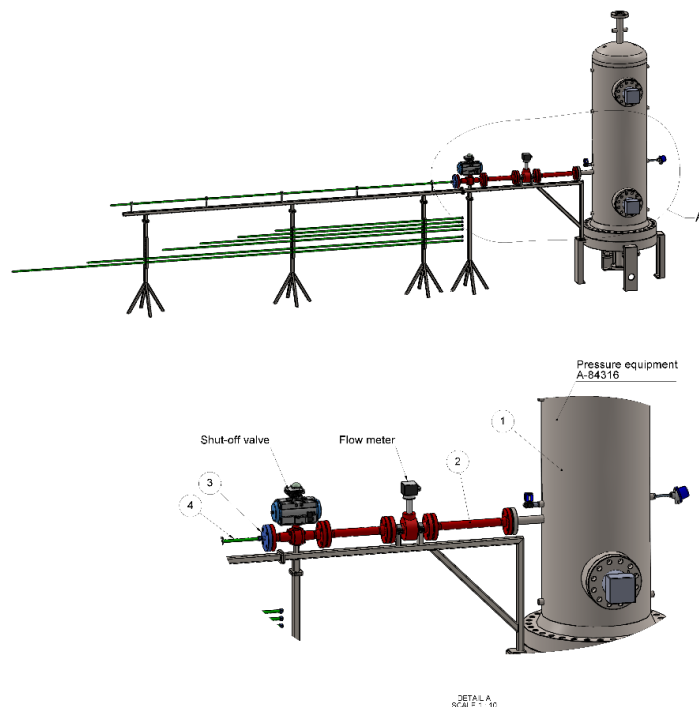


Figure 1. Preliminary sketch of the separate effect test facility (SET).

The SET consisted of an upstream pressure vessel, a larger instrumentation tube (in red) and interchangeable tubes with varying length-to-diameter (L/D) ratios. The SCRAM tank used in the prior experiments at LUT University will be repurposed as the upstream pressure vessel to reduce overall costs. The maximum pressure of the tank is 10 MPa and the maximum temperature is 270 °C (41 °C subcooling at maximum pressure). The maximum temperature is set by Finnish pressure vessel standards. The instrumentation tube with a larger diameter would have housed the volume flow meter and the shutoff valve. The discharge tubes would be the representative diameter of Finnish PWR steam generator tubes ($d = 13\text{--}16$ mm). The modelling scenario is a primary-to-secondary guillotine break.

Changed proposition

CRITFLO was granted funding for the last year of SAFIR2022 but with a sizable reduction to the originally applied funding. The overall volume measured in person months was reduced from 11 to 3.5. The Steering Group commented on the proposal that due to the extent, the project as it was proposed would be more fitting for following the national research program SAFER2028. There was also the suggestion to complete a literary study on what has been done prior in the field of critical flow experiment studies. Considering these recommendations CRITFLO's Work Package 1 Task 1.1 was changed for a literary review. This was also considered useful from LUT University's side if the proposition for the commission of the SET would be proposed again in the SAFER2028. The change was accepted also in Research Group 4 (RG4) where CRITFLO was part. The modification to the project is presented in Figure 2.

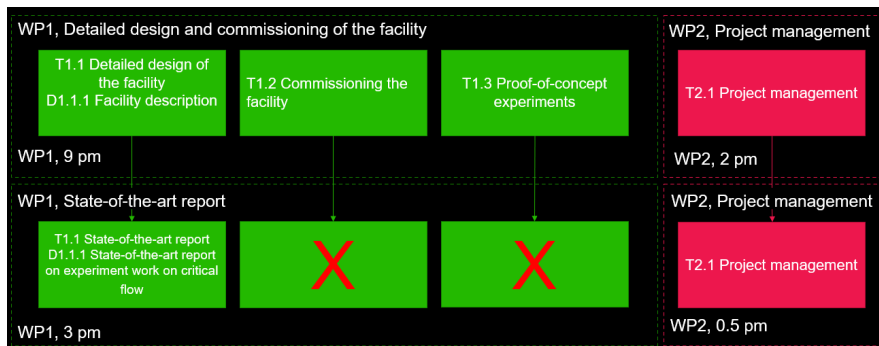


Figure 2. The changes made to original project proposal.

In addition, the SILENCE network started discussions on TPCF model development and the applicability of so-called advanced measurement systems in TPCF experiments in 2022.

The literary review

Modification to the original proposal was made for T1.1. The original T1.1 was titled “detailed design of the facility” and it was changed for the literary review named “state-of-the-art report on experiment work on critical flow”. The review included an introduction to critical flow and TPCF as phenomena, a short description of TPCF models used in SYS-TH codes, examples of older “classical” critical flow experiments, like Marviken, and more recent experimental work conducted in critical flow studies.

TPCF models used in SYS-TH codes

Critical flow models can be divided into three types: simplified analytical models, fitted functions and numerical models based on analytical functions and differ by:

1. The number of conservation equations used takes into account mass, momentum and energy conservation.
2. The number of state equations that describe the state of the system through variables like pressure, temperature, enthalpy, etc. and/or the transformation equations which outline the state exchange of the system by given criteria.
3. The number of constitutive equations is usually empirical equations derived either from dimensionless analysis or from assumptions regarding the system's behaviour.
4. The number of analytical conditions added to the models.
5. The necessity of semi-empirical parameters for problem solution (D'Auria, 1980).

A common way of categorizing different models is whether the model assumes thermal equilibrium or non-equilibrium between the phases. These models can be divided into homogenous and non-homogenous models depending on whether the phases are considered to have equal velocities or not. The four main categories from the simple to complex are homogenous equilibrium model (HEM); non-homogenous equilibrium model (NHEM); homogenous non-equilibrium model (HNEM); and non-homogenous non-equilibrium model (NHNEM) as presented in Table 1 (Liao&Lucas, 2020).

Table 1. Four main categories of two-phase critical flow models.

Models	Phase features
HEM	equal velocity equal temperature
NHEM	unequal velocity equal temperature
HNEM	equal velocity unequal temperature
NHNEM	unequal velocity unequal temperature

FONESYS network updated the state-of-the-art of TPCF modelling with a benchmark of eight system codes against TPCF experiments. The benchmark revealed large error prediction, especially in sub-cooled upstream conditions which can be as large as 40%. APROS was one of the SYS-TH codes that were used in the benchmark (Landfredini, 2020). In the benchmark, the Delayed Equilibrium Model (DEM) was utilized. DEM is a 1D three-field model with saturated steam, saturated liquid and metastable liquid. The benchmark showed that it performed better than any other model in low subcooling conditions. The maximum absolute error of DEM was about 10% whereas SYS-TH codes showed a maximum relative error of 35%.

Classical critical flow experiment

In 1993, the OECD CSNI published “Separate Effects Test Matrix for Thermal-Hydraulic Code Validation” which identified the best available sets of data for assessment, validation and improvement of code predictions of the individual physical phenomena including critical flows. The report was the continuation of the original CSNI Code Validation Matrix which consisted almost entirely of integral tests however, it was seen that there was a need to develop a distinct Separate Effect Test matrix. In the OECD test matrix, the facilities were categorized into breaks ($L/D < 1$), pipes ($L/D > 5$) and valves (Aksan, 1994).

One distinctive feature in the older experimental facilities is the scale. The efforts put into critical flow studies prior were probably hard to match nowadays. Test facilities like Marviken (see Figure 3) and HDR Vessel were originally built for power generation but not taken into operation for that purpose. Instead, they were repurposed as experimental facilities.

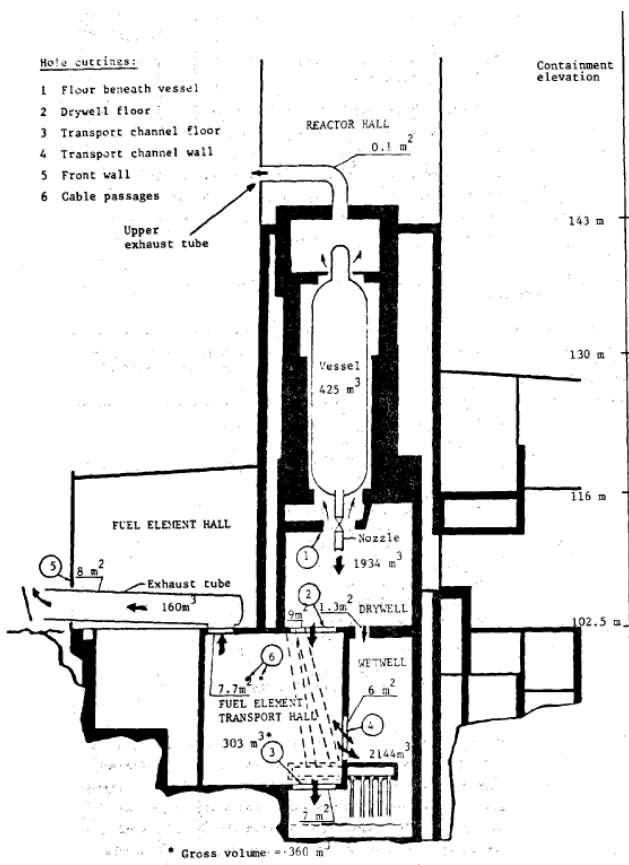


Figure 3. Marviken experiment test facility.

The review showed that very thorough instrumentation was used in all the experimental facilities presented. One distinct difference between the older and newer experimental facilities was that void fraction measurements were only used in the older experiments.

One problem with relying on older experimental data is data preservation issues. The review showed that finding information about the older facilities is somewhat difficult. In addition to not having open publication of data, the publications and reports made can be in their respective languages of the authors. One major issue is that most of the experimental facilities presented in the OECD test matrix are dismantled. It is not possible to replicate the experiments with updated instrumentation or novel measurement systems. In addition, the know-how of commissioning and running demanding tests are not easily adapted by the newer generation of experimentalists and modellers as the details are neither thoroughly recorded, nor available. Also, the personnel and their know-how are retired from the field.

The literary review presented the following older test facilities: Marviken, Super Moby Dick, Super CANON, Battelle RS16B, and HDR Vessel. The facilities, instrumentation, operating conditions, and how the experiments were run were presented whether the information was available.

Recent critical flow experiments

The experimental work conducted after the publication of the OECD test matrix was considered "recent" in the literary review. The classification of the experimental facilities followed the OECD test matrix, and the experiments were divided into three categories: pipes, cracks and valves. The majority of the experimental work had been conducted in the break category e.g. cracks, holes and slits. The experiment works within cracks, holes and slits that are closely related to the leak-before-break (LBB) concept. Generally in LBB, if a small leak can be detected with activity release per time unit, then further growth or rupture can be prevented. Thus leak rate of postulated leakages is an important parameter when assessing the activity release. In the review, the test facilities, instrumentation, operating conditions, how the experiments were run and condensed results were presented. In pipe geometry, three different experiments were presented. Novel information, like the double-choking phenomenon, was identified. In the category of cracks, holes and slits three experiments were presented in more detail and three additional experiments were shortlisted. Novel information, like using actual cracks of steam generator tubes for critical discharges were utilized. In valve geometry, two experiments were presented in detail. In general, critical flow experiments in valve geometry are very rare and are focused on the effect of disk lift of a safety valve on critical flow discharge rate. Novel information, like imaging the critical flow patterns qualitatively in critical discharge was presented. In the following chapters one example of each category is presented with condensed information and the reader is advised to see the literary review for additional information (Pyy, 2022).

In 2000, Attou, A. et al. published the experimental results for a steady-state critical steam-water flows through a horizontal relief line involving an abrupt cross-sectional area change. Two geometrical singularities were tested, one with sudden enlargement and one with a circular orifice. The stagnation pressure was fixed at 0.6 MPa and the stagnation temperature varied between 100 °C–150 °C with varying back pressure. Relief lines were located downstream from safety devices like safety valves and rupture discs which were installed for protecting pressurized vessels or reactors. Relief lines involved several singularities such as abrupt area changes (enlargements or contractions) and abrupt direction changes (elbows or tee junctions). The study aimed to present original experimental results over a steady-state flashing water flow through a discharge line which involved one geometrical singularity. A sketch of the experimental facility is presented in Figure 4.

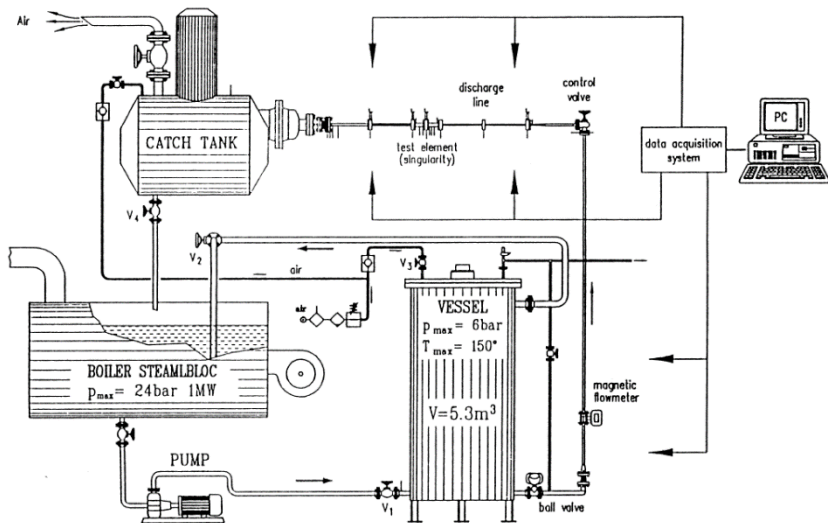


Figure 4. The sketch of the experimental facility for critical flashing flow studies.

In the experiment, a double-choking phenomenon was occurred. Double-choking was identified from the evolutions of different measured parameters presented in Figure 5.

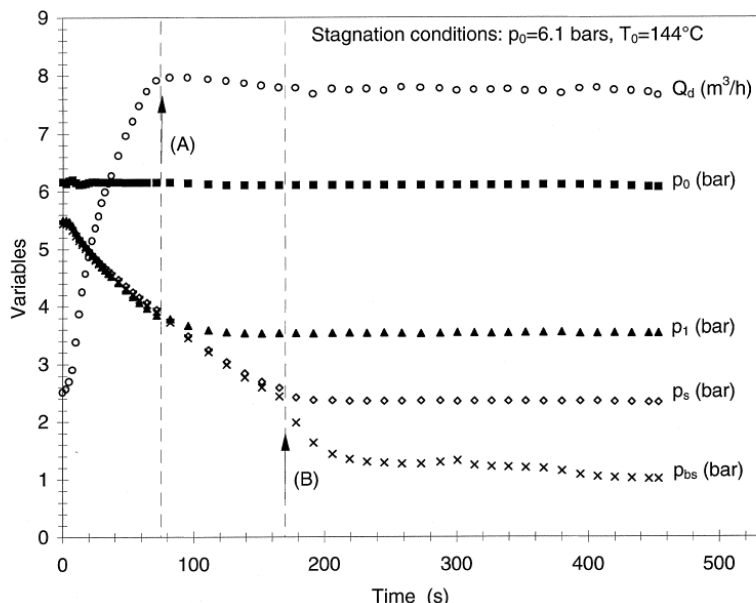


Figure 5. Evolution of flow variables during the decrease of back-pressure using sudden enlargement test section and stagnation subcooling of 9 °C.

In figure 5 back-pressure, p_{bs} , is gradually decreased. At point (A), the pressure at the outlet of the test section in the upstream part, p_1 , becomes independent of p_{bs} , and the critical flow condition is achieved. At point (B) also the pressure in the outlet of the relief line, p_s , just before the catch tank becomes independent of p_{bs} . The second critical section does not influence the maximum value of the mass flow rate. It is only determined by the first critical cross-section. The double-choked occurrence is explained as follows: The averaged flow velocity decreases downstream from the first critical section after the flow again adheres at the pipe wall, and the flow becomes subcritical. After the establishment of the wall shear stress, the flow through the downstream pipe becomes of the Fanno type, i.e. adiabatic flow of compressible fluid through a duct with a constant cross-section area. Accordingly, for a small enough value of back-pressure, the Fanno effects along the downstream pipe can produce a strong acceleration of the fluid up to reach again the local velocity of sound at the exit of the relief line.

It was concluded that the double-choked flow phenomenon occurred for both singularities, abrupt enlargement and the circular orifice, with a small enough back-pressure value. The maximum flow rate was limited by the first critical section only (Attou, 2000).

In 2019, Revankar and Riznic published the experimental results of a two-phase choked flow of initially subcooled water through a stress corrosion crack (SCC) on the steam generator tube. Five different samples were studied with axial SCC. Three of the samples (samples 1, 2 and 4) were artefacts from the CANDU steam generator. Two samples (samples 3 and 5) were obtained from the SG integrity research program conducted at Argonne National Laboratory, and they resembled US PWR steam generator tubes. The used test samples are presented in Figure 6.

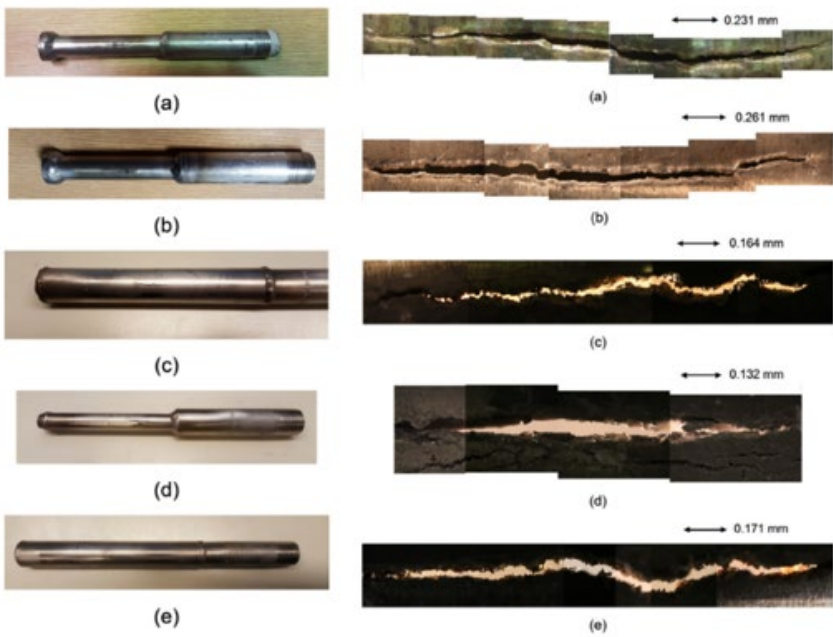


Figure 6. The used test specimens (on left) and microscopic images of the test sample cracks (on right): (a) sample 1, (b) sample 2, (c) sample 3, (d) sample 4, and (e) sample 5.

Samples 1 and 2 were Incoloy 800 tubes with an outer diameter of 15.9 mm and a wall thickness of 1.2 mm. Sample 4 was Inconel 600 tube with an outer diameter of 12.7 mm and a wall thickness of 1.1 mm. Samples 3 and 5 were Inconel 600 tubes with an outer diameter of 22.2 mm and a wall thickness of 1.3 mm. The axial cracks for samples 3 and 5 were artificially generated. The test sample dimensions are presented in Table 2.

Table 2. Test sample dimensions.

Samp le	Crack's opening area [m^2]	Length of the channel, L [m]	Crack's hydraulic diameter, D [m]	L/D
1	$5.216 \cdot 10^{-6}$	$1.200 \cdot 10^{-3}$	$4.501 \cdot 10^{-4}$	2.7
2	$8.381 \cdot 10^{-6}$	$1.200 \cdot 10^{-3}$	$6.472 \cdot 10^{-4}$	1.9
3	$1.712 \cdot 10^{-6}$	$1.270 \cdot 10^{-3}$	$2.087 \cdot 10^{-4}$	6.1
4	$2.450 \cdot 10^{-6}$	$1.100 \cdot 10^{-3}$	$3.721 \cdot 10^{-4}$	3.0
5	$2.801 \cdot 10^{-6}$	$1.127 \cdot 10^{-3}$	$3.137 \cdot 10^{-4}$	4.1

The mass flux through the different specimens in room temperature and in sub-cooled condition ($T_{\text{sub}} = 40 \text{ }^{\circ}\text{C}$) with different stagnation pressures was investigated and the results are presented in Figure 7.

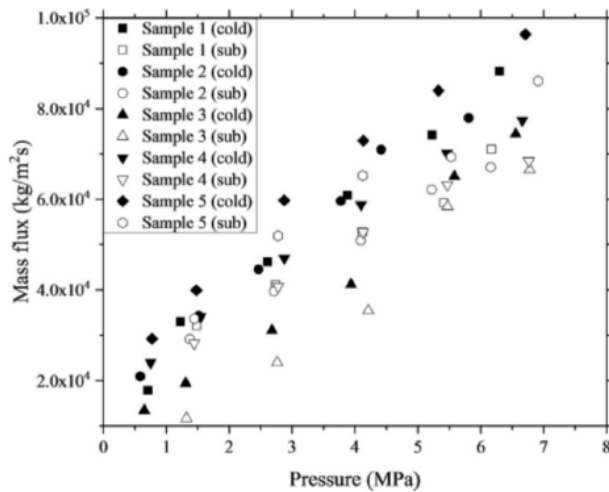


Figure 7. Mass fluxes of different test samples with discharge in room temperature or in subcooled conditions with different stagnation pressures.

The authors stated that the increase in L/D caused by the increase in channel length strongly affects the flashing location. Liquid going through a very short channel length was subjected to a very high depressurization rate which makes the liquid superheated and the flashing was delayed. The dependence of mass flux on L/D indicated a significant influence of friction on the choked flow (Revankar, 2019).

In 2001, Kim S.W. and No H.C. published an experimental investigation on critical flow phenomenon in a safety valve. Different subcooling levels at around 1 MPa inlet pressure were investigated with three disk lifts of 1 mm, 2 mm, and 3 mm to find the relation between subcooling level and disk lift level. The critical flow patterns were also visualized. The test section used in the study is presented in Figure 8.

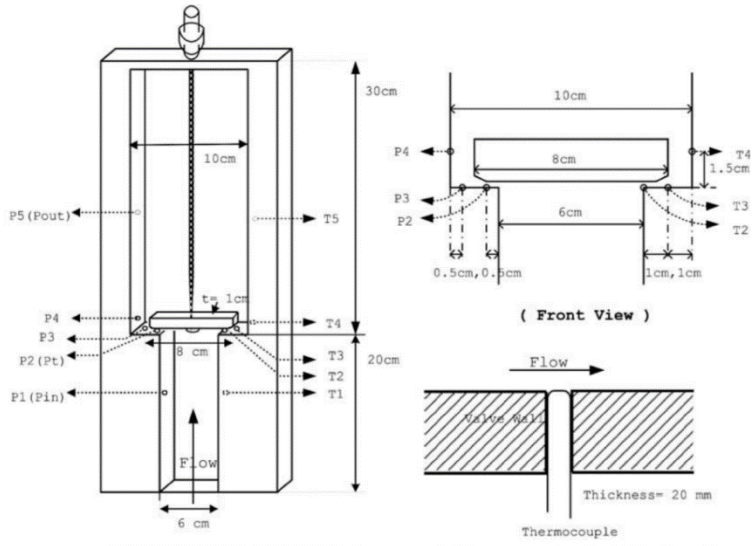


Figure 8. The test section with temperature and pressure measurement locations.

It was found that the upstream flashing of the throat took place when the throat inlet temperature, T_{in} (measurement location T2 in Figure 7), was greater than the saturation temperature of the throat critical pressure, $T_{sat}(P_{cr})$. The results from this temperature difference between different disk lifts are presented in Figure 9.

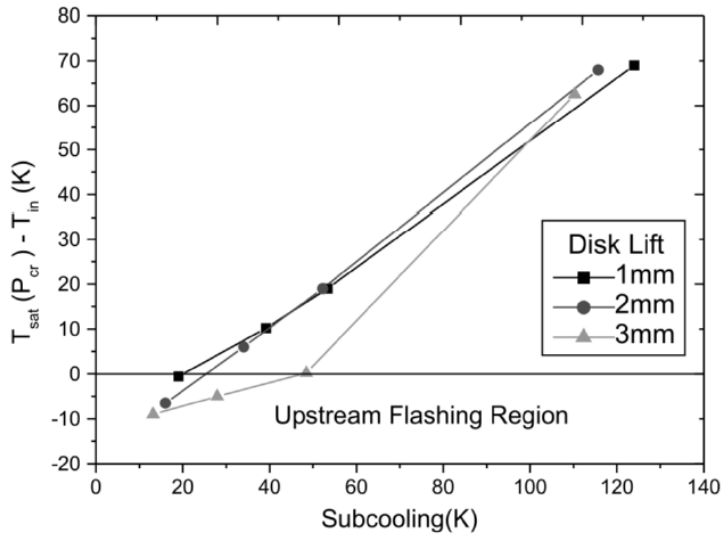
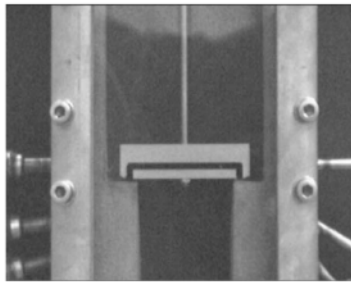
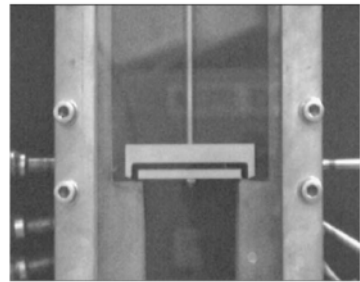


Figure 9. Effect of subcooling on upstream flashing at different disk lift.

The throat critical pressure was measured at location P2. Sufficient subcooling was needed to avoid the flashing at the throat. The required subcooling for 1 mm disk lift was 19 °C, for 2 mm disk lift 22 °C, and for 3 mm disk lift 49 °C. A transparent wall was used in the test section to visualize the flow. The authors presented one example of critical flow pattern evolution when the back pressure was gradually lowered, and it is presented in Figure 10.



$(P_{in} = 0.89, P_t = 0.72, P_{out} = 0.76, \text{ MPa})$



$(P_{in} = 0.85, P_t = 0.6, P_{out} = 0.66, \text{ MPa})$



$(P_{in} = 0.85, P_t = 0.56, P_{out} = 0.59, \text{ MPa})$



$(P_{in} = 0.85, P_t = 0.55, P_{out} = 0.55, \text{ MPa})$



$(P_{in} = 0.86, P_t = 0.51, P_{out} = 0.43, \text{ MPa})$



$(P_{in} = 0.9, P_t = 0.505, P_{out} = 0.26, \text{ MPa})$

Figure 10. Critical flow patterns from one experiment.

Flashing starts when a critical pressure ratio is achieved at the throat. The authors concluded through visual observation, that the first critical flow condition occurred when the downstream region of the disk is filled with subcooled water and the

second one when the same region is filled with large amounts of voids. The first critical throat pressure condition in low subcooled water flow is established by cavitation with one constant throat pressure. When the downstream pressure is decreased further, cavitation in the downstream section would be decreased due to the perturbation of the flow field resulting in the existence of many voids. The further decrease of back pressure affects the critical pressure ratio at the throat (Kim, 2001).

SILENCE co-operation

SILENCE network started in 2022 and talks about TPCF model development and way to implement new measurements with advanced measurement systems in future experiments were done. In the meetings, LUT University and the interest in the Finnish nuclear safety community considering critical flow experiments and model development were presented. In addition, the proposed SET was presented to the experts of the SILENCE network. The interest in building a new SET capable of critical flow studies got positive feedback from the network. For the state-of-the-art experiment work to bring real benefit for model development and validation it would need to produce the following measurement information:

- mass flow rate
- pressure evolution along the axis of the break section, $P(z)$
- void-fraction evolution along the axis of the break section, $\alpha(z)$
- liquid temperature along the axis of the break section: integration of liquid energy evolution and liquid temperature allows determining the liquid mass flow rate evolution and with void-fraction evolution liquid and vapor velocities could be determined
- when the transition to froth flow occurs and what is the slip ratio between the phases
- when the transition from annular-mist flow to pure mist flow occurs
- bubble size or at least bubble size at the detachment
- film thickness, droplet size and droplet velocity

The required information could partly be achieved with the help of high-speed imaging coupled with pattern recognition and infrared thermometry. The break section should use transparent materials. A constant diameter pipe is the best geometry to implement measurements and to derive the flashing models.

Project management

The project management was a separate work package (WP2). Within the work package, RG4 and SILENCE network's meetings were attended, and the final seminar of SAFIR2022 was attended. In 2022, two SILENCE meetings were attended which provided a valuable information on TPCF model development needs and insights into the current state-of-the-art of TPCF, and communication channel

to the very broad knowledge base that is held within the SILENCE network and its experts in the field of thermal-hydraulics.

Acknowledgement

The author would like to thank the members of SAFIR2022 RG4 for constructive talks and support, the members of the SAFIR2022 Steering Group 2 for feedback on the project and funding recommendation and the SAFIR2022 Management Board for funding recommendation, and VYR for the funding. In addition, the author would like to thank all the members of the SILENCE network for valuable discussions on the topic of TPCF.

References

- Aksan, N. et al., OECD/NEA-CSNI Separate Effects Test Matrix for Thermal-Hydraulic Code Validation, 1994, 680 p.
- Attou, A. et al., Experiment study of the critical flashing flow through a relief line: evidence of the double choked flow phenomena, International Journal of Multiphase Flow, Vol. 26, 2000. 27 p.
- D'Auria, F., Vigni, P., Two-phase critical flow models, CSNI Report No.49, OECD, 1980. 277 p.
- Kim, S.W., No, H.C., Subcooled water critical pressure and critical flow rate in a safety valve, International Journal of Heat and Mass Transfer, Vol.44, 2001. 11 p.
- Lanfredini, M. et al, Critical flow prediction by system codes – Recent analyses made within the FONESYS network, Nuclear Engineering and Design, Vol. 336, 2020. 8 p.
- Liao, Y., Lucas, D., A review on numerical modelling of flashing flow with application to nuclear safety analysis, Applied Thermal Engineering, 2020, 64 p.
- Pyy, L., State-of-the-art report on experiment work on critical flow, CRITFLO 1/2022, 2022, 64 p.
- Revankar, S.T., Riznic, J., An experimental investigation of subcooled choked flow in actual steam generator tube cracks, Nuclear Engineering and Design, Vol. 354, 2019. 9 p.

6 Mechanical Integrity

6.1 Advanced materials characterisation for structural integrity assessment (AMOS)

Laura Sirkia¹, Sebastian Lindqvist¹, Juha Kuutti¹, Pentti Arffman¹, Antti Forsström¹,
Timo Veijola²

¹VTT Technical Research Centre of Finland Ltd
P.O. Box 1000, FI-02044 Espoo

²University of Oulu
P.O. Box 4300, FI-90014 University of Oulu

Abstract

The AMOS project focuses on development of numerical and experimental testing methods in fracture mechanics for the purpose of structural integrity assessments. Five main topics were identified: 1) development of quality criteria for miniature C(T) specimens, 2) development of improved methods for assessing the constrain effect on transition temperature, 3) development of verified and validated methods for determining the effect of transient loads in the upper shelf region to fulfil YVL requirements, 4) validation of crack arrest testing techniques for small specimens, and 5) methods for applying fracture toughness in structural integrity analyses and aging management.

Introduction

The structural analysis of nuclear power plant (NPP) safety class 1 components is based on fracture mechanics (Figure 1). The AMOS (Advanced materials characterisation for structural integrity) project focuses on development of numerical and experimental testing methods for fracture mechanical assessment of safety class 1 components: the reactor pressure vessel (RPV) and the dissimilar metal welds (DMW) of the pipe nozzles. The analyses of safety class 1 components are

mandatory according to Finnish YVL E4 guidelines. The aim is to develop methods so that fracture can be understood, explained, predicted, and controlled better than before. An important part of the project is also training of new experts in the research field of fracture mechanics, as several retirements have occurred during the past years at VTT.

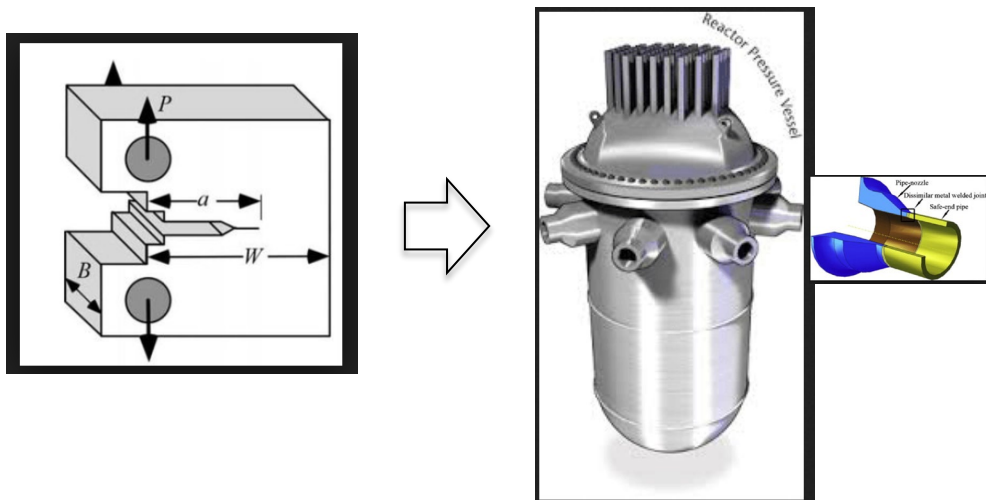


Figure 1. Fracture toughness data obtained with suitable specimens is utilized for assessing safety on the component level.

Since the introduction of fracture mechanics for safety analysis of components, the assessment methods have evolved, and different applications have been introduced. The fracture toughness in the ductile-to-brittle transition region as a function of temperature can be described statistically with the Master Curve method. The Master Curve enables a probabilistic description of material's lower boundary fracture toughness. Based on current testing practices, fracture toughness is obtained with specimens with relatively deep cracks loaded in bending, which causes a high constraint condition in the specimen leading to a conservative estimate of fracture toughness.

The progress of fracture mechanics has enabled the development of miniature-sized specimen testing techniques. Development of miniature specimen testing techniques is crucial for modern day surveillance programmes as the amount of available material for assessing irradiation embrittlement by means of fracture mechanics is limited. It enables reuse of larger specimens for continued evaluation and ensures the cost-efficiency of the testing programmes. The focus is also on developing capabilities in Finland to analyse and interpret results from surveillance programmes and to determine the actual material performance.

In AMOS project, five main topics related to analytical and experimental fracture mechanics are identified: 1) development of suitable quality criteria for miniature

C(T) specimens, 2) development of improved methods for assessing the constrain effect on the obtained transition temperature, 3) development of verified and validated method for determining the effect of transient loads in the upper shelf region to fulfil YVL requirements, 4) validation of crack arrest testing techniques for small specimens, and 5) methods for applying fracture toughness in structural integrity analyses and aging management.

WP1: Miniature testing techniques

The overall objective of WP1 is to develop and validate quality criteria for the miniature C(T) specimens. Both, experimental and numerical analysis support alleviating the quality criteria in the standard for miniature sized C(T) specimens.

The miniature C(T) specimen technique (Figure 2) has been developed for the last 10 years. However, for historical reasons surveillance programmes have been typically based on Charpy-V specimens. On the other hand, miniature specimen testing techniques and reconstitution techniques enable obtaining fracture toughness data from the already tested Charpy-V specimens. Thus, the miniature C(T) specimen testing technique is under development in several countries. In Japan, USA, France and Russia, the technique has gained interest since fracture mechanical data is required to demonstrate the safety of continued operation of the NPP fleets.

The method is being validated for base materials, welds, irradiated materials, and for materials from different depth locations relative to the inside surface of the RPV. However, more development is required to make the technique more applicable. Currently, the standards that are used for C(T) specimens and the quality criteria that those standards apply have been developed for 25 mm thick specimens and thus, can be too strict for miniature-sized specimens. The thickness of the miniature specimens is typically 4 mm. If the quality criteria are not fulfilled, the test result should be discarded, which is unfavourable for surveillance programmes when the amount of material available is restricted.

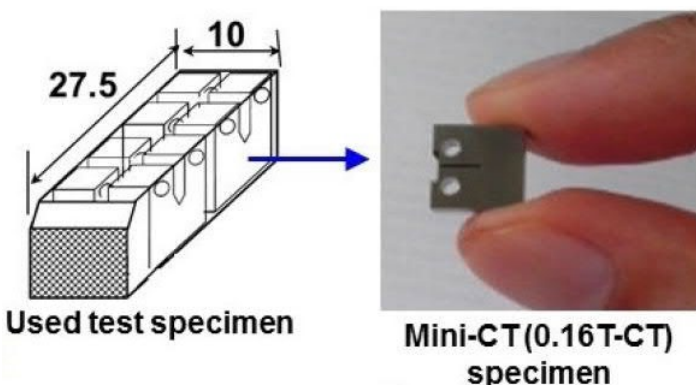


Figure 2. Miniature C(T) specimens, extracted from a larger Charpy-V specimen.

In WP1, the focus has been in assessing the effects of eccentric pinholes on test data obtained with miniature-sized C(T) specimens as part of developing quality criteria for miniature-sized specimens. Experimental results obtained with specimens with eccentric pinholes were compared to reference results obtained with standard specimens. The test series show similar results, which substantiates the postulate that miniature C(T) specimens, even with eccentric pinhole locations, give reliable results for assessment of the transition temperature. Additionally, comparison of load-displacement charts supports this assumption; slopes, either determined from COD measured from the load-line or from the front face, between the series are either identical or have no more than five percent of difference.

Numerical analysis of specimens with eccentric pinholes was performed with three different finite element (FE) models; namely 'nominal', 'mean' and 'max' models, applied in Abaqus. In addition to the displacements and loading pin forces, the stress intensity factors, and J-integrals were evaluated using the default Abaqus contour integral calculation routine. The simulated load-line and front face displacement data was converted into stress intensity factors and J-integrals, which allowed the evaluation of the accuracy of the ASTM E1921 standard formulae in the eccentric pinhole case.

Depending on the model, the obtained slopes gave a disparity of two to three percent when compared to experimental data. The calculated slope affects the standard-based evaluation of the plastic work done to the specimen, affecting also the calculated J-integral. The difference between the simulated J-integrals and those obtained with the ASTM E1921 formulae was approximately five percent, when the elastic simulations of the stress intensity factors were in good agreement with the standard. All in all, numerical analysis further confirms the postulate that eccentric pinholes do not have a great effect on the reliability of the test data.

Effects of curved crack fronts of miniature-sized C(T) specimens were also assessed. The results suggest that it may be possible to loosen the crack curvature criterion for miniature C(T) specimens as the scatter of the data is not markedly increased by small deviations from the current criterion when the crack length-to-width ratio (a_0/W) is standard 0.5. The current curvature criterion is not dependent on a_0/W , but it may be justified to include the effect of a_0/W in the criterion. This is because lower a_0/W may require a stricter curvature criterion than higher a_0/W .

Reduction of miniature C(T) specimen thickness from 4 mm down to 3 mm was studied, and it was found that there are some contradictions on what comes to the use of experimental fracture mechanical standard and interpretation of results. According to the current ASTM E1921 standard, dimensioning of the test specimens is proportional, and thus, the use of 3 mm thick specimen is allowed. The standard also allows the use of so-called censored data points; if a single data point exceeds the limits set for a fracture toughness value, it can still be used as a censored data point with half a weight and included in the analysis. But then, when determining the plastic zone size ahead of the crack tip (Figure 3) through equations for plane stress and plane strain state (Figure 3), some contradictions were found. Although the standard accepts these fracture toughness results to be used as censored data points (Figure 4, marked with a red circle), the plastic zone size in these specimens

is too large in relation to the specimen dimensions, and the loss of constraint is inevitable since the triaxial stress state no longer holds. Figure 4 shows the maximum stress intensity site ahead of the crack tip (calculated) versus the crack initiation location (determined with a scanning electron microscope (SEM)). It is seen that data points (specimens) with higher fracture toughness (processed as censored in the analysis) have a larger difference between the maximum stress intensity site and the crack initiation location. In addition, these same specimens have such a large plastic zone size, that the use of these results in the analysis is highly arguable. This is further discussed in a scientific article to be published.

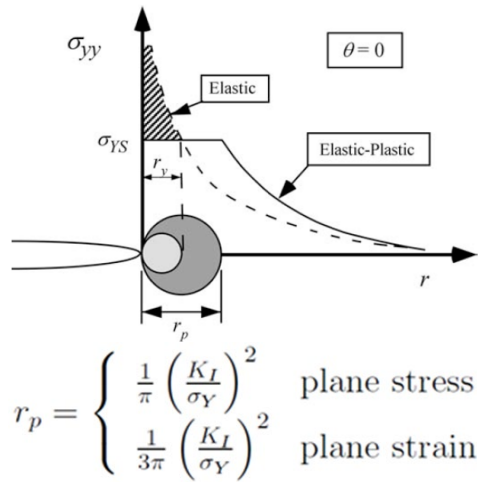


Figure 3. Illustration of elastic and elastic-plastic regions ahead of the crack tip, and equations for plane stress and plane strain state.

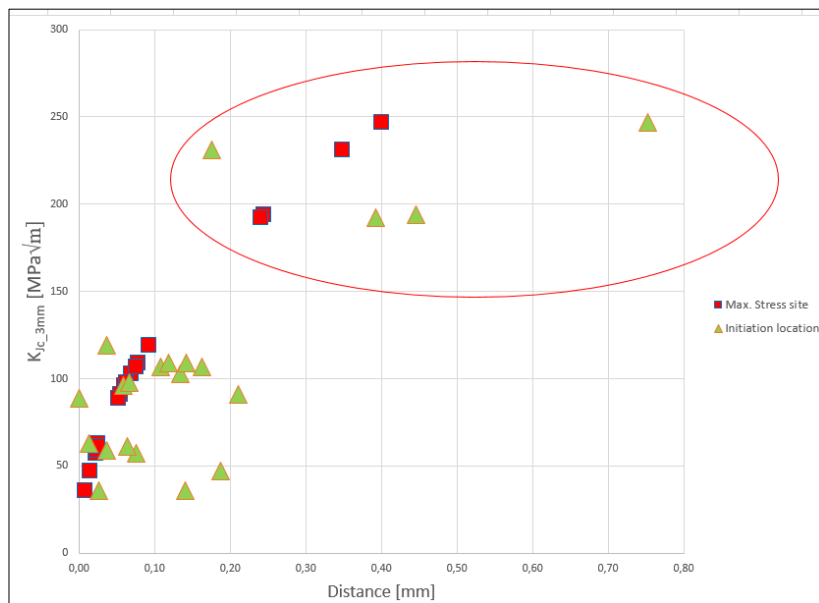


Figure 4. Maximum stress- intensity site vs. initiation location of fracture of the miniature C(T) specimens with 3 mm of thickness.

WP2: Constraint effects

WP2 deals with assessing effects of constraint on the obtained fracture toughness and transition temperature. Numerical methods for assessing the constraint effect were developed. Large deformations and other non-proportional loading effects cause the near-tip contour to be path-dependent, whereas it should be path independent. However, it was concluded that J-integrals may be calculated using the small-strain assumption. Constraint effects can be quantified using crack tip triaxiality, elastic T-stress, and Q-parameter, calculated from crack tip stress fields, when large deformations are present. The constraint state varies between specimen types, and crack and component geometries. Large deformation analysis is needed for accurate constraint quantification. Constraint trends can be obtained with small-deformation calculations.

In 2022, a Master's thesis was written on "Evaluation of constrain effect on the T_0 temperature of miniature SE(N)T specimens". The thesis explores the fracture toughness values derived using miniature SE(N)T specimens using the Master Curve method as described in the standard ASTM E1921. By comparing the results to previous experiments conducted on the ASTM A533B Class 1 pressure vessel steel designated JRQ, the effects of size and especially the constrain effect on fracture toughness were investigated.

The experimental section consisted of 12 $a_0/W = 0.5$ and 11 $a_0/W = 0.2$ crack length-to-width ratio SE(N)T specimens tested at -85 °C. The effect of constraint on

the T_0 temperature was investigated by comparing the toughness values between the two crack length-to-width ratios. The $a_0/W = 0.5$ specimens produced a T_0 temperature of -54°C which is on the brittle side for the reference material. The $a_0/W = 0.2$ specimens had an uncensored T_0 temperature of -113°C and a censored T_0 temperature of -98°C . Both were tougher than the comparison values used. The difference in the T_0 temperatures reflect a change in toughness between the specimen types due to the constrain effect. The constraint effect was evaluated with an Abaqus CAE FEM model, from which Q-parameters were derived using the HRR field as a reference. The modelled difference between the specimen types was 29°C which is within the margin of error of the experimental results but indicates further experimental factors contributed to the toughness values obtained. The SE(N)T specimens were observed to be sensitive to constraint effects with respect to the crack length-to-width ratio. The effect of specimen size could not be evaluated due to limited number of experiments. The reliability of the measurement results was estimated using a partial derivatives method and Sobol's indices. The results were supplemented with microscopy and hardness analyses.

WP3: Transient loads

Currently, there are no test methods for analysing transient loads in the upper shelf region to fulfil the YVL guide. The objective in AMOS is to develop such methods. The transient loads should be investigated in two ways: 1) the effect of transient loads on fracture toughness when the material behaviour is completely ductile and 2) the effect of transient loads on fracture toughness when decreasing temperature shifts the material behaviour from the ductile regime to the brittle regime, see Figure 5.

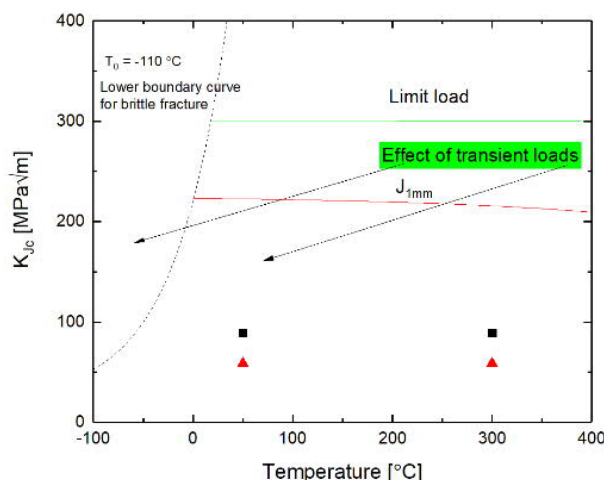


Figure 5. Effect of decreasing temperature transients on ductile fracture toughness properties.

WP3 focuses on developing methods for assessing the effect of transient loads on crack growth in the upper-shelf region and investigation of ductile fracture mechanisms. Due to the unfortunate COVID-19 situation the European Conference of Fracture, ECF, was cancelled in 2021, but it was held in 2022. A conference paper entitled "The effect of cooling transients on tearing resistance of rolled steel" was presented as part of the conference.

80 specimens with different a_0/W (0.1 and 0.5) were tested at VTT in Finland and at KTH in Sweden. The temperature was varied between 300 °C and 20 °C during testing. No brittle fracture occurred in the upper-shelf region during the cooling transient. If no other information is available, it is recommended to use lowest fracture toughness properties in the investigated temperature range.

Sixteen AMOS NKS SE(B) specimens were tested in WP3 for transition temperature T_0 with a_0/W of 0.1 and 0.5. The specimens were preloaded in room temperature to about -18 kN, cooled down to -85 °C, and tested. T_0 transition temperatures of $-90 \pm 8^\circ\text{C}$ and $-70 \pm 8^\circ\text{C}$ were obtained, respectively. For a combined data set, the transition temperature was $-84 \pm 6^\circ\text{C}$. The combined result is similar to results obtained by the Swedish partners.

Application of digital image correlation (DIC) for fracture mechanical J-R curve determination was investigated in 2022. DIC was applied to J-R tests of five SE(B) specimens made of WB36 steel. Similar J-R curves were obtained with DIC virtual extensometer method and standard clip-gauge method for measuring the crack mouth opening displacement (CMOD). The tests confirm that it is possible to determine J-R curves reliably with DIC. The advantage is that DIC is a non-contact displacement measurement method, and therefore using DIC may enable use of non-standard specimen configurations, such as specimens without a cut-out for the traditional clip-gauge. This in turn may help with studying low crack length-to-width ratios ($a_0/W < 0.2$), as there is more material left in the specimen for the shallow surface crack to grow in.

WP4: Crack arrest toughness

The crack arrest toughness is sometimes applied as a lower boundary toughness value in analysis of NPP safety class 1 components. Arrest toughness describes the stress intensity at crack arrest, see Figure 6. For highly irradiated materials, the crack initiates relatively easily, but crack arrest can be more difficult. Thus, it is recommendable to use the crack arrest toughness to describe the lower boundary fracture toughness. Additionally, the arrest toughness properties of high-Ni pressure vessel steels are typically equal to the crack initiation properties. The arrest toughness can be used as a secondary safety margin. The challenge with determining arrest toughness is that large specimens, impractical for surveillance programmes are required. A small specimen test technique relying on Charpy-V sized specimens and instrumented impact loading has been developed. However, due to lack of arrest toughness results for different materials, the instrumented impact toughness testing technique to determine arrest toughness has not been

validated for many materials. In AMOS project, more results for materials with varying strength are obtained to validate small specimen crack arrest toughness testing techniques.

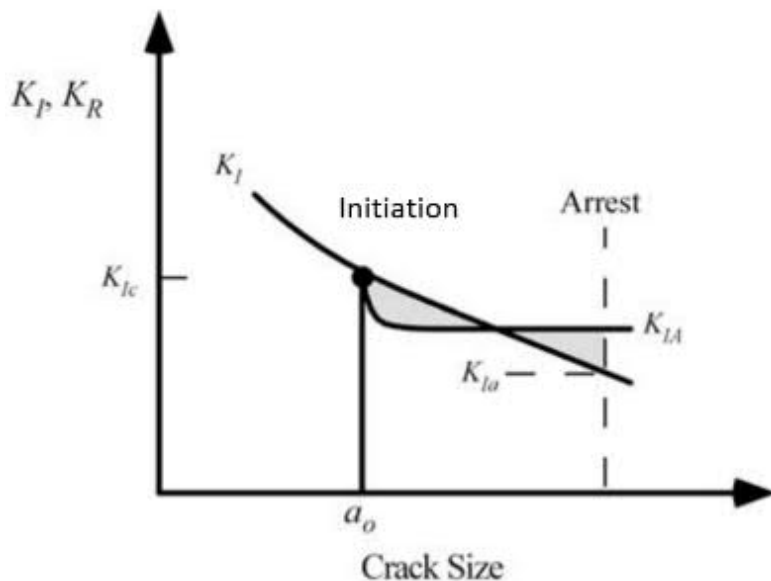


Figure 6. Crack arrest toughness.

WP4 focuses on validating a model that enables characterization of crack arrest toughness of materials in surveillance programmes. Although crack arrest toughness is a tempting alternative for a minimum fracture toughness of the material, the current testing methods are quite complicated and require very large specimens. This makes them unappealing for surveillance programs. To make crack arrest toughness more useful, it is essential to be able to use smaller specimens. Sub-sized impact specimens, such as KLST with dimensions of 3x4x27 mm³, are investigated as possible alternative to standard sized 10x10x55 mm³ Charpy-V specimens. The correlation of small specimen data to standard data is established. International research programme material JRQ was chosen as test material in 2020, due to abundance of previous results and availability of the material.

The tests were commenced after machine issues were solved in January 2021. Data analysis methods for the instrumented impact toughness tests were developed for the sub-sized KLST specimens. Several filtering and smoothing methods for the oscillating impact force-displacement data were identified, of which a low-pass filter offers simplicity and good quality, and a DTCWT filter offers excellent quality, but with complex parametrization. A journal paper on data analysis methods for instrumented impact test data obtained by KLST specimens was written in 2022 and submitted for review.

WP5: Structural integrity and aging management

In structural integrity analysis, the lower boundary fracture toughness curve obtained experimentally is compared to the crack driving force, and if the crack driving force is lower than the determined fracture toughness, the component is safe to use. Different guidelines (ASME, RCC-M, YVL) provide various methods for assessing the lower boundary curve. An understanding of the various methods, their differences and use is not easily obtained. Additionally, related to aging management, an important part is to determine the embrittlement behaviour of the material.

By obtaining the ductile-to-brittle transition temperature with varying fluence or thermal aging time, an embrittlement curve can be generated to predict the effect of irradiation or thermal embrittlement on fracture toughness. The embrittlement trend curves are used for assessing the remaining lifetime of the component. The mechanisms causing the shift in the ductile-to-brittle transition temperature need to be understood to be able to predict the embrittlement. The goal in AMOS, is to review the different methods to obtain a lower boundary fracture toughness curve according to ASME, YVL etc. and factors causing the shift in the ductile-to-brittle transition temperature.

WP5 focuses on reviewing the methods for structural integrity analysis and aging management through fracture mechanical means. The different methods used to assess the lower boundary energy curve, e.g., the Master Curve, in the ductile-to-brittle transition region are examined and the process for assessing the experimental uncertainty in these analyses is established. In addition, a review is done on different factors affecting the shift in transition temperature due to irradiation and thermal aging. The microstructural reasons for materials to behave differently due to embrittlement are reviewed and the physics behind the developed irradiation embrittlement models are described.

A paper was written to ASTM symposium on radiation embrittlement trend curves and their use for RPV integrity evaluations. In the paper, the experience of using embrittlement trend curves in Finland is discussed.

The ASTM E08 workshop was attended on Wednesday, November 2nd, 2022, with 19 people participating. The objective of the workshop was to serve as a strategic planning session to identify current and future uses of Appendix X5 in the ASTM E1921 standard and associated technical gaps. There were 8 scheduled presentations as well as a supplementary presentation. During the workshop, attendees discussed the clarity and usability of the appendix, possible modifications, and other analysis methods that are not addressed in the appendix. Several topics related to the future evolution of the appendix were discussed by the workshop participants after the formal presentations were completed.

Applications

The structural analysis of safety class 1 components shall be based on fracture mechanical properties of the materials. The AMOS project results in development of methods for basing the safety analysis on fracture mechanics. The methods can be applied for design of new power plants or extension of lifetime of current plants.

The developed quality criteria for miniature C(T) specimens will reduce the material consumption due to less invalid test results. The miniature specimens will be utilized in surveillance programmes, either as such or for obtaining fracture toughness related information from already tested Charpy-V specimens. They can also be used for obtaining T_0 from other critical regions e.g., the dissimilar metal welds of pipe nozzles. The investigation is relevant for the whole nuclear sector in Finland (STUK, FORTUM, FENNOVOIMA, TVO) as fracture mechanics-based data is required for demonstrating the safety of the RPVs.

The methods that are developed for accounting the constraint effect in structural integrity analysis can also be used for safety assessment of RPVs or pipe nozzles. The method can be used either for assessing the conservatism of the obtained fracture toughness results, or it can be applied as a reference value of T_0 for the component, shifting the irradiation embrittlement trend curve to a lower level. The shift may justify prolongation of operation.

The method that is developed for determining the effect of transient loads in the upper-shelf region can be applied to RPV steels so that the plant owners can show that the YVL requirements are fulfilled. The small specimen testing technique for obtaining crack arrest toughness can be applied for RPV steels to obtain a more reliable assessment of how and when the crack arrests. The lower boundary crack arrest toughness curve can be used for demonstrating the safety of the RPVs. It is particularly applicable and interesting for NPPs with high-Ni RPV steels and steels subjected to high irradiation.

Summary and conclusions

Five main topics were identified in the AMOS project: 1) development of quality criteria for miniature C(T) specimens, 2) development of improved methods for assessing the constrain effect on transition temperature, 3) development of verified and validated methods for determining the effect of transient loads in the upper shelf region to fulfil YVL requirements, 4) validation of crack arrest testing techniques for small specimens, and 5) methods for applying fracture toughness in structural integrity analyses and aging management.

The overall objective of WP1 was to develop and validate quality criteria for miniature C(T) specimens. Both, experimental and numerical analysis support alleviating the quality criteria in the ASTM E1921 standard for miniature sized C(T) specimens. The current criteria are too strict for miniature C(T) specimens, which results in unnecessary disqualification of test results due to the requirements.

Adjusting the requirements for miniature C(T) use would be beneficial, for example, to save valuable reference material.

In WP2, the constraint effect was studied. Constraint in this context means that strain in certain directions is constrained by geometry or microstructure, which in turn increases triaxiality of the local stress state. High constraint then means that stress triaxiality is high and brittle fracture may initiate more easily. With low constraint, stress triaxiality is low and brittle fracture does not initiate as easily. Constraint effects can be quantified using crack tip triaxiality, elastic T-stress, and Q-parameter, calculated from crack tip stress fields, when large deformations are present. The constraint state varies between specimen types, and crack and component geometries. Constraint effect on the T_0 temperature was investigated. The SE(N)T specimens and the obtained T_0 were sensitive to constraint effects with respect to the crack length-to-width ratio.

In WP3, a conference paper was prepared on thermal effects and transient loads and the results were presented in ECF23 conference.

In WP4, crack arrest toughness determination by miniature KLST specimens was studied. Several filtering and smoothing methods for the oscillating impact force-displacement data were identified, of which a low-pass filter offers simplicity and good quality, and a DTCWT filter offers excellent quality, but with complex parametrization. A journal paper on data analysis methods for instrumented impact test data obtained by KLST specimens was written.

WP5 considers structural integrity assessments. In structural integrity analysis, the lower boundary fracture toughness curve obtained experimentally is compared to the crack driving force, and if the crack driving force is lower than the determined fracture toughness, the component is safe to use. A paper was written to ASTM symposium on radiation embrittlement trend curves and their use for RPV integrity evaluations. In the paper, the experience of using embrittlement trend curves in Finland is discussed.

Acknowledgements

The authors would like to thank the Finnish authorities for providing the funding for the research. The contribution of Senior Research Technician Jorma Hietikko is also highly appreciated for conducting many of the tests in the project, as well as Senior Research Technician Taru Lehtikuusi for her assistance in imaging fracture surfaces and preparing microsections.

References

- Arffman, P. 2022. Improved analysis of instrumented Charpy-V impact curves.
Submitted to Engineering Fracture Mechanics.
- Arffman, P. 2020. VTT report: Overview of crack arrest toughness K_{Ia} . VTT-R-00105-20.

- Forsström, A. & Lindqvist, S. 2022. J-R curve determination with digital image correlation for side-grooved SE(B) specimens. Submitted to International Journal of Fracture.
- Lindqvist, S. & Kuutti, J. 2022. Sensitivity of the Master Curve reference temperature T_0 to the crack front curvature. Theoretical and Applied Fracture Mechanics 122, 103558.
- Lindqvist, S., Seppänen, T. & Sirkiä, L. 2022. The effect of cooling transients on tearing resistance of rolled steel. 23rd European Conference in Fracture – ECF23.
- Lindqvist, S. & Peltonen, V. 2021. VTT report: NKS: Fracture toughness behaviour in the ductile-to-brittle transition region – small and large specimens and shallow and long cracks, VTT-R-00053-21.
- Seppänen, T. & Lindqvist, S. 2022. Embrittlement trend curves in Finland. International review of nuclear reactor pressure vessel surveillance programs. ASTM international: Selected technical papers. To be published.
- Sirkiä, L., Cronvall, O. & Virkkunen, I. 2022. Miniature C(T) specimens - Reduction of specimen thickness from 4 mm down to 3 mm and its effect to the applicability according to the experimental fracture mechanical standards. To be submitted to a scientific journal.
- Sirkiä, L., Kuutti, J. & Virkkunen, I. 2022. Miniature C(T) specimens – Pinhole eccentricity and the effect of crack opening displacement measurement location. Journal of Testing and Evaluation 51(2).
- Sirkiä, L. 2021. VTT report: A literature survey on miniature testing techniques – the past and present, VTT-R-00762-21
- Sirkiä, L. & Kuutti, J. 2020. VTT report: Experimental investigations on the effect of pinhole location on fracture toughness, VTT-R-01183-20.
- Sirkiä, L. 2020. VTT report: The effect of measuring the crack opening displacement from the load line vs. front face and the effect of side grooving of miniature specimens, VTT-R-00126-20.
- Veijola, T. 2022. Evaluation of constraint effects on the T_0 temperature of miniature SE(N)T specimens. Master's thesis. University of Oulu.

6.2 Effect of long-term operation on aging and environmentally assisted cracking of nuclear power plant component materials (ELIAS)

Caitlin Huotilainen¹, Pekka Nevasmaa¹, Petteri Lappalainen¹, Zaiqing Que², Ulla Ehrnsten¹, Iikka Virkkunen², Gaurav Mohanty³

¹VTT Technical Research Centre of Finland Ltd [*Font: Arial 9*]
P.O. Box 1000, FI-02044 Espoo, Finland

²Aalto University
P.O. Box 11000, FI-00076 Finland

³Tampere University
FI-33014 Tampere, Finland

Abstract

During the first two years of the ELIAS project the main focus has been on reactor pressure vessel embrittlement mechanisms (2019) and reactor pressure vessel repair welding techniques and approaches (2019–2020). The reactor pressure vessel repair welding research work has been performed in close collaboration with the FEVAS Project.

Introduction

Nuclear power plants (NPP) must be operated in a safe and cost-effective manner. Central to the safety and reliability goals of these plants is effective materials degradation management. Effective materials degradation management must include the maintenance of operating plants, extension of the lifetime of plants, and choice and use of materials in new plants. (Wright 2017)

The long-term behaviour of the nuclear power plant component materials is of particular interest in Finland, because there are nuclear power plants that are at critical stages of their lifetime: either in the beginning of their operation or reaching the planning phase for lifetime extensions. Understanding of the materials' aging phenomena and the most important degradation mechanisms are of utmost importance in order to ensure safe plant operation and effective lifetime management for lifetimes that can reach 60 years or even beyond that.

The project focused on two main technical topics: (i) the identification of reactor pressure vessel (RPV) embrittlement mechanisms and (ii) the development of RPV repair welding techniques and approaches. In addition international collaboration and the dissemination of international projects to the Finnish community.

Identification of RPV Embrittlement Mechanisms

As the current fleet of NPPs approach the end of their original design lifetime, long-term operation (LTO) becomes an increasingly important topic and the integrity of safety-critical components must be ensured. While the RPV demonstrates excellent mechanical properties, in terms of hardness and fracture toughness and room and elevated temperatures in its “as fabricated” state, exposure to neutron irradiation can result in the embrittlement and, thus, degradation of the RPV base material and weld metal in the long term.

The embrittlement of pressure vessel materials consists of the hardening response from two separate mechanisms: (i) matrix damage (MD) mechanism and the (ii) formation of copper-rich precipitates (CRP). Neutron irradiation embrittlement is a result of three main mechanisms, i.e., matrix damage (vacancies and interstitials), segregation and formation of clusters, i.e., Cu-rich and MnNiSi - rich clusters. The dominating cluster type is dependent on the chemical composition of the material. Cu-rich clusters are frequently referred to as copper rich precipitates, CRPs, although they affect the properties of the RPV material also before becoming precipitates. CRP saturates at relatively low fluences ($1 \times 10^{19} \text{ n/cm}^2$, $E > 1 \text{ MeV}$) and full saturation occurs before typical pressurized water reactor (PWR) end of life fluences. MD cannot be characterized by conventional microscopic methods as the size of the formations is beyond the resolution of small-angle neutron scattering, atom probe tomography, and transmission electron microscopy. Segregation of especially phosphorus to grain boundaries, and possibly also other surfaces (e.g. precipitates and inclusions), typically results in an increased amount of grain boundary cracking. MD formations are small in size and they anneal much faster than the CRPs and hence they can be separated by annealing studies.

During thermal annealing of an RPV material, most of these CRPs are dissolved back into matrix, while some of may grow larger (coarsening). The level (mechanical properties) of recovery depending on (i) the annealing temperature relative to the irradiation temperature, (ii) the annealing time, (iii) the impurity and alloying elements and (iv) type of product (e.g. plate, forging, weldment, etc.). Re-irradiation embrittlement is defined primarily by the MD term because the amount of Cu-rich cluster formation during re-irradiation is small. In low-Cu, high-Ni RPV materials, NiMnSi clusters are more decisive for the embrittlement, than Cu-rich clusters. Very little is known about the behavior of these clusters during annealing and re-irradiation.

The Russian norm for embrittlement (PNAE-G7-002-86) describes only total embrittlement, hence it does not separate MD, segregation and CRP. Further, it is an upper boundary description without confidence limits and the norm has not been revised since its first issue. The US power reactor embrittlement database (PR-EDB) including 855 transition temperature shift values has been recently reanalyzed (Easton et al. 2006). These analyses consist of MD and CRP terms, but the MD term can be considered incomplete, as it is based on data for low or no-copper materials. The full effect of MD can only be derived from annealing studies with real impurity content materials. The PR-EDB analysis also defines the flux effect for low

flux irradiations, which is relevant for boiling water reactors (BWR). The PR-EDB analysis is compared with the Irradiation Variable Database (IVAR) created by UC-Santa Barbara and Oak Ridge National Laboratory (ORNL) including tensile specimens of 33 alloys irradiated in well-controlled experiments. IVAR indicates the existence of a flux effect also for high flux irradiations, which is expected based on physical arguments (retardation of irradiation enhanced diffusion by recombination of primary defects).

Preliminary annealing studies were performed with several VVER440 materials approximately (Valo & Lappalainen 2015). The results are very promising but the analysis is restricted by the relatively small number of studied materials (12 samples) and the relatively large number of candidate variables and their combinations. A larger number of data points with varying P, Cu, Ni, Mn and Si contents and varying neutron fluence and fluence rates would enable increasing the parameters to be defined and would add confidence to the results. Preliminary annealing data give very good descriptions for the MD and CRP terms as a function of Cu, Ni, P, Mn and neutron fluence and Ni, Cu, P and neutron fluence.

In 2019, within the ELIAS project, studies on a larger set of specimens aiming to (i) increase the size of the database, (ii) include low flux data and (iii) widen the parameter range of the data were started. Specimens have been prepared from irradiated and tested Charpy V-notch (CVN) specimens, see Figure 1. Vickers hardness measurements (HV5) were performed to identify the initial condition, as well as any hardness gradients present in the materials, see Figure 2.

Future investigations will focus on (i) data analysis and the evolution of (ii) hardness and (iii) electrical resistivity as a function of annealing time (at 450 °C) and complementary microstructural characterizations. By employing these three complementary techniques information and insight to the embrittlement mechanism in RPV steels and welds can be obtained. Hardness measurements will provide information on changes and the evolution of mechanical properties, while resistivity measurements and microstructural characterizations will provide insight on the deformation of the crystal lattice of the material (e.g. due to the dissolution and/or precipitation of impurity elements in the matrix) and identify the impurities (precipitation, segregations) within the matrix as a function of annealing time, respectively.



Figure 1. Photo of (a) a tested CVN specimen to be machined for investigations and (b) a 10 mm×10 mm×2 mm sample blank machined using electrical discharge machining (no hardness measurements performed yet).

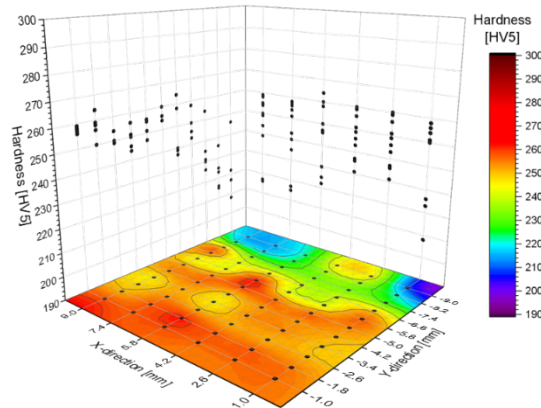


Figure 2. Representative reference hardness profile for a weld material sample presented as a contour map and as XZ and YZ reference point hardness value projections. Measured hardness indentations are shown as black dots on the map.

Development of RPV Repair Welding Methodology

As plants continue to age, there is an increased probability for the need of repairs due to extended exposure to a harsh environment (neutron flux, high temperature, high pressure, water chemistry). It is paramount that qualified and validated solutions are readily available, and that such methods are validated proactively, at a stage when they are not yet needed. In ELIAS, joint with FEVAS, a repair method for a postulated through cladding crack into the low alloy steel of a nuclear power plant's reactor pressure vessel has been investigated (Keinänen et al. 2020, Virkkunen et al. 2020, Huutilainen et al. 2021).

Repair welding (RW) is thought to represent the “worst-case” scenario where a postulated linear crack-like defect exists beneath the cladding and might extend across the interface into the RPV steel side. This postulated defect is then removed by machining, and the thereby machined groove will be filled by repair welding using a nickel-base superalloy filler metal and using mechanized/robotized arc welding process. While FEVAS focused on computational support for mock-up design and weld procedure tests, ELIAS performed the repair procedure design and characterization of the mock-up microstructures. The mock-up was welded at Aalto University as a joint effort between the projects.

In the project, a RW mock-up has been produced using an automated gas metal arc welding (GMAW) utilizing Cold Metal Transfer (CMT) method. As an alternative to conventional gas tungsten arc welding process, the use of automated GMAW-CMT mode offers many advantages, such as good weld quality, exceptionally stable arc, easy automation and very low heat input along with narrow heat-affected zone (HAZ). A postulated crack was excavated from a cladded and thermally embrittled low alloy steel base material (BM) and repaired using a nickel base filler metal by gas metal arc welding-cold metal transfer. No pre-heating or post-weld heat treatment (PWHT) was applied, as it would be nearly impossible to apply these treatments in a reactor pressure vessel repair situation. One cladded plate was welded, meaning two excavations were filled, see Figure 3. One excavation was filled with 100 beads along the long side, while the second excavation was filled halfway (5 layers) the long side, followed by a 45° hatch pattern (6 layers) for a total depth of 40 mm.

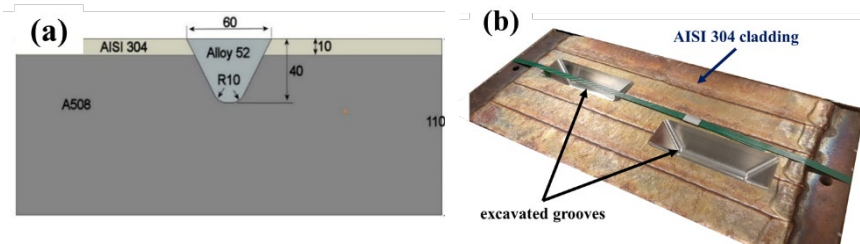


Figure 3. (a) Schematic diagram of the RW and (b) photograph of the two excavated grooves.

The mock-up RW was sectioned and a metallographic samples were prepared to study the weld quality and microstructure. Light optical microscopy (LOM) observations of the LAS HAZ can be seen in Figure 4. The HAZ is characterized by a coarse-grained structure of mixed lower-bainite and martensite, see Figure 4(a). There appears to be a band of upper-bainite and polygonal ferrite close to the weld interface. Near the LAS BM, a fine-grained area of bainite with some ferrite can be seen Figure 4(b). No indications of austenite were observed in the LAS HAZ.

Therefore, it can be presumed that the HAZ has not experienced significant heating during the RW by GMAW-CMT. (Huutilainen et al. 2021)

The thermal embrittlement treatment of the LAS has resulted in significant changes in the ferritic steel's microstructure, compared to a typical as-supplied (quenched and tempered) LAS. The thermal embrittlement treatment has also led to coarsening of the grains, see Figure 4(c). The LAS is predominately bainite, and the long tempering time and slow cooling rate, may have favored secondary carbides and/or the re-precipitation of carbides and may have affected carbide coarsening. Some crack-like lack of inter-pass fusion defects and pores were observed in the RW. The observation of these defects indicates that further optimization of the RW parameters is required. Additional microstructural characterizations are required to completely assess the quality of the RW. (Huutilainen et al. 2021)

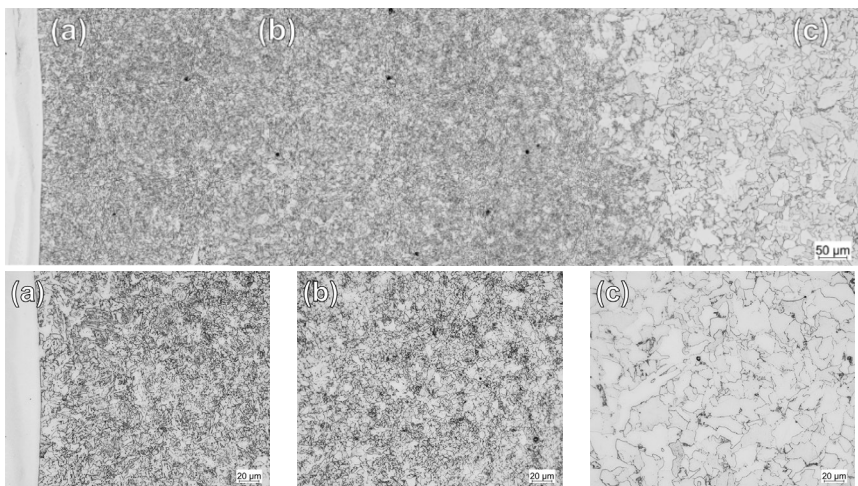


Figure 4. LOM images of the microstructure across the LAS HAZ of the 45°-hatch pattern RW after etching.

The hardness across the HAZ was measured by Vickers microhardness. Two loads were applied, (a) HV_{0.3} and (b) HV_{0.1}, to evaluate the hardness in the LAS HAZ and very locally near weld interface, respectively. The results can be seen in Figure 5 (Huutilainen et al. 2021). A maximum hardness was measured locally in the LAS HAZ close to the FB. The hardness is within the acceptable range of values for a RW, even without the application of a pre-heating treatment or PWHT (Ohms et al. 2005, Bruomovsky et al. 2007, Yurioka & Horii 2006, Yu et al. 2014, Matejova, Jandova & Kask 2015).

In addition, micromechanical fracture toughness testing was performed on the RW produced in 2019 by Tampere University. This was the first time this method has been demonstrated on this material in Finland. A total of eight notched micro-

cantilevers ($\approx 10 \mu\text{m} \times \approx 2 \mu\text{m} \times \approx 2 \mu\text{m}$) were ion-milled, in the WM and across the HAZ, and tested, see Figure 6. Data analysis of the fracture toughness behaviour of the HAZ is ongoing.

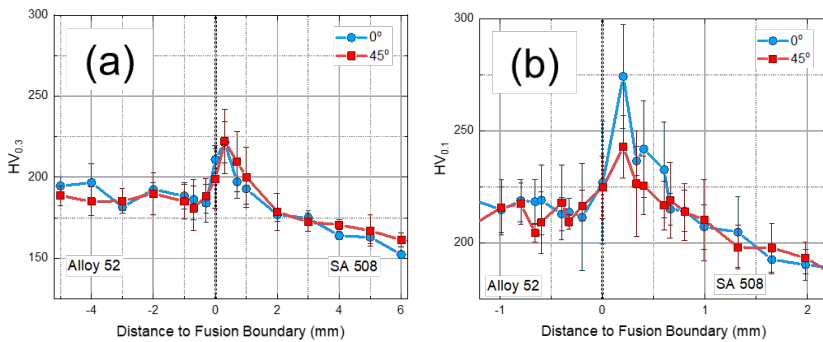


Figure 5. Measured microhardness ((a) HV_{0.3} and (b) HV_{0.1}) across the HAZ of the RWs. The FB location is indicated by the dotted vertical line in the plots.

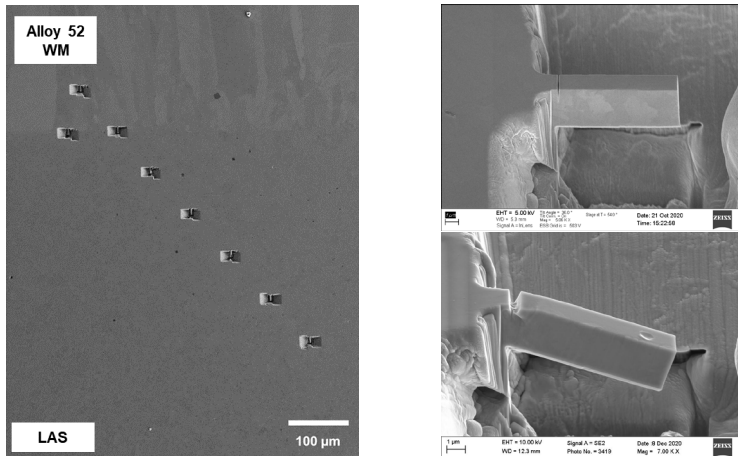


Figure 6. (left) Placement of microcantilevers in the RW and SEM images of micromechanical testing of the RW; (right-above) as-milled (focus ion beam) microcantilever before fracture mechanical testing and (right-below) post-test microcantilever.

The RW was simulated using a finite element method with in-house welding simulation methods. This work is described in more detail within the FEVAS Project.

Complementary experimental and numerical evaluations have been used to investigate a RW method for a postulated through cladding crack in to the RPV of an NPP using automated GTAW-CMT mode and a Ni-base superalloy weld metal. While the results are very promising, additional work is required in order to fully characterize the weld interface, investigate the welding residual stresses and fully optimize the welding parameters, in terms of, for example, heat input, travel speed, bead placement, etc.

Closing remarks

This research presented here has been performed within the ELIAS project in 2019 and 2020. The ELIAS project will not continue in 2021, but the development of RPV repair welding methodology will continue the FENIX project.

Acknowledgements

The authors would also like to thank Taru Lehtikuusi (VTT), Johanna Lukin (VTT), Jari Lydman (VTT), Asta Nurmela (VTT), Hannu Hänninen (Aalto University), Mikko Peltonen (Aalto University), Henrik Sirén (Aalto University), Laura Tiainen (Aalto University), Mari Honkanen (Tampere Microscopy Center) and Aloshious Lambai (Tampere University) for their valuable contributions to this work.

References

- Brumovsky, M., Brynda, J. & Ellinger, J. 2007. Welding Repair Procedure of Defects in WWER Reactor Pressure Vessels. Proceedings of the ASME 2007 Pressure Vessels and Piping Conference (PVP2007), 22–26 July 2007, San Antonio, Texas, USA, American Society of Mechanical Engineers, New York, pp. 907–911.
- Eason, E.D, Odette, G.R., Nanstad, R.K. & Yamoto, T. 2006. A Physically Based Correlation of Irradiation-Induced Transition Temperature Shift for RPV Steels. ORNL/TM-2006/530.
- Huotilainen, C. et al. 2021. Evaluation of an Alloy 52 / Cladded Carbon Steel Repair Weld by Cold Metal Transfer, PVP2021-61981. To be published in the Proceedings of the ASME 2021 Pressure Vessels & Piping Conference PVP2021, July 12-18, 2021, virtual conference.
- Keinänen H. et al. 2020. A52M/SA52 Dissimilar Metal RPV Repair Weld: Evaluation of Different Techniques, PVP2020-21233, Proceedings of the ASME 2020 Pressure Vessels & Piping Conference PVP2020, July 20-24, 2020, virtual conference.
- Matejova, M., Jandova, D. & Kasl, J. 2015. Structure Analyses of Experimental Welds Designed for Repair Welding of VVER 1000 Pressure Vessel, Key Engineering Materials, Vol. 647, pp. 131–140.

- Ohms, C. et al. 2005. ENPOWER - Investigation by Neutron Diffraction and Finite Element Analysis on Residual Stress Formation in Repair Welds Applied to Ferritic Steel Platers. Proceedings of the ASME 2005 Pressure Vessels and Piping Division Conference (PVP2005), 17–21 July 2005, Denver, Colorado, USA, American Society of Mechanical Engineers, New York, pp. 385–393.
- PNAE-G7-002-86, Standards for Calculating the Strength of Equipment and Pipelines in Nuclear Power Plants, Energoatomizdat, Moscow.
- Valo, M. & Lappalainen, P. 2015. Electrical resistivity response to annealing of VVER440-type weld material in irradiated, post-irradiation annealed and re-irradiated conditions, VTT Research Report VTT-R-00163-15. Espoo: VTT.
- Virkkunen I. et al. 2020. A52M&SA52 Dissimilar Metal RPV Repair Weld: Experimental Evaluation and Post-weld Characterizations, PVP2020-21236, Proceedings of the ASME 2020 Pressure Vessels & Piping Conference PVP2020, July 20-24, 2020, virtual conference.
- Wright, M. 2017. Preface of Proceedings of the 18th International Conference of Environmental Degradation of Materials in Nuclear Power Systems-Water Reactors. Portland, Oregon, USA, August 13-17, 2017.
- Yu, L. et al. (2014). Hardness Prediction for Temper Bead Welding of Non-Consistent Layer Technique. In: 8th Int. Conf. on Processing & Manufacturing of Advanced Materials (THERMEC 2013), 2–6 December 2013, Las Vegas, USA, Materials Science Forum/Trans Tech. Publications, Switzerland.
- Yurioka, N. & Horii, Y. (2006). Recent developments in repair welding technologies in Japan, Science and Technology of Welding and Joining, Vol. 11, pp. 255–264, No 3.

6.3 Extended lifetime of structural materials through improved water chemistry (ELMO)

Konsta Sipilä¹

¹VTT Technical Research Centre of Finland Ltd
P.O. Box 1000, FI-02044 Espoo

Abstract

Optimizing the water chemistry to mitigate corrosion and maximize the lifetime of the structural components is essential as the lifetime of nuclear power plants are considered. In ELMO project several topics related to this field were studied.

Regarding hydrazine replacement chemicals, their high temperature oxygen scavenging efficiency were determined. Carbohydrazide seemed to be the most efficient chemical in this sense. Decomposition products and effects on corrosion of structural materials were studied as well. The decomposition analysis indicated that erythorbic acid interferes the acidic conductivity measurement so severely that it does not seem to be a good candidate for the plant trials.

Impurity deposition is steam generator conditions were studied by validating the use of "Hot loop" facility. The facility enables online chemistry monitoring and performance of electrochemical measurements. It was shown that the effects of boiling to corrosion are only moderate and in a large extent reversible. Similarly to the validation of the "Hot loop" facility, high temperature zeta potential measurement setup based on streaming potential technique was validated. In addition, the dissolution of cobalt in simulated primary chemistry was estimated.

Finally, the stress corrosion cracking susceptibility of A690 in alkaline and Pb containing crevice chemistry was assessed. It was shown that in these kind of crevice environments the presence of Pb can be beneficial for A690 as it improved the protectivity of the oxide layer.

Introduction

The most important part of operating a nuclear power plant is ensuring radiation safety throughout the operating years. The integrity of the nuclear power plant structures, components and piping, which act as radiation barriers, is deteriorated by various degradation and aging mechanisms. The primary reason for most of these mechanisms is material-environment interaction caused by contact with the process medium. This material-environment interaction can result in the manifestation of numerous different corrosion phenomena including stress corrosion cracking (SCC), wear, denting and pitting. Corrosion phenomena are linked to materials, component designs, the used water chemistry and in some cases, irradiation. Since especially for older plants, materials and designs are already selected, the easiest way to affect corrosion is to alter water chemistry. In

fact, the prevalence of failures caused by corrosion has been closely associated to the water chemistry used [IAEA, 2011]. Therefore, water chemistry design, monitoring and optimisation is a subject of the utmost importance.

Alternative oxygen scavenging chemicals

The most effective way of corrosion protection is controlling water chemistry and one topical issue related to it is to find a suitable replacement chemical for hydrazine. Hydrazine is an excellent oxygen scavenger and used routinely in PWR and VVER plants during both operational and shutdown periods. During power operation, the concentrations are typically below 100 ppb. Preservation of SGs during outages requires much higher concentrations of hydrazine. Hydrazine is currently considered to be hazardous to health and environment. There is a distinct possibility that, because of the health and environmental risks related to the use of hydrazine, the EU will in the future pass a directive restricting and even forbidding its use [Betova et al. 2016]. Already at the moment, the Finnish environmental regulations have been tightened so that the use of high concentrations of hydrazine during outages is becoming more and more challenging. Thus, alternative water chemistries need to be studied broadly which is one of the aims in this project as well. [Betova et al. 2017] Three aspects were studied, including oxygen scavenging efficiency, formation of decomposition products and effects on corrosion of structural materials.

The efficiency of a range of hydrazine alternatives (carbohydrazide (CH), diethyl-hydroxylamine (DEHA), erythorbic acid (EA) and methyl-ethyl-ketoxime (MEKO)) as oxygen scavengers in simulated PWR steam generator inlet conditions are quantitatively compared. Kinetic parameters of oxygen reaction are estimated for the first time in such conditions using both an oxygen and a redox sensor. The results are displayed in Table 1. The initial rate of oxygen reaction at eight-fold excess of the scavenger estimated from both oxygen and redox sensors allows for the following ranking of additives: CH > hydrazine \approx EA > DEHA >> MEKO. The oxygen reaction is found to be first order with respect to hydrazine, EA and DEHA. The order with respect to CH is estimated to be 0.6, whereas that with respect to MEKO as 0.5. The increase of the rate of oxygen consumption with concentration is the fastest for carbohydrazide, i.e. the desired effect is the largest.

Electrochemical impedance measurements were performed to investigate the effect of studied alternatives on carbon steel corrosion. Using a quantitative interpretation of the impedance data by the Mixed-Conduction Model (MCM), the influence of hydrazine and its alternatives on charge transfer reactions at the oxide/solution interface and film growth/dissolution processes were evaluated. A pronounced decrease of the impedance magnitude at low frequencies upon addition of the oxygen scavengers to the electrolyte was observed. This decrease is the most evident for EA, CH and DEHA, to a certain extent smaller for MEKO and the smallest for N₂H₄.

To discriminate between different processes responsible for this decrease, the EIS data for 22K steel were interpreted with the MCM in terms of film growth and restructuring, as well as charge transfer reactions at the film/solution interface. It can be concluded that the charge transfer reaction of scavengers is first order with respect to EA and CH, close to first order (with a power of 0.8) for DEHA, and 0.5 for MEKO. The order estimated for hydrazine is close to 2, i.e. the effect of this additive is considerably smaller.

The influence of scavengers on the reaction of film growth and dissolution (increase of the corrosion rate) is once again much more pronounced for the hydrazine alternatives (EA, CH and DEHA) than for hydrazine itself, indicating a much more efficient interaction of the alternative scavengers with the oxide layer on steel.

Table 1. Summary on the efficiency of various oxygen scavenging chemical.

Oxygen scavenger	Concentration dependence	Rate constant	Initial rate at scavenger concentration $25 \mu\text{mol dm}^{-3}$ / $\mu\text{mol dm}^{-3} \text{s}^{-1}$
Hydrazine	No	$1.39 \pm 0.01 \text{ dm}^3 \text{ mmol}^{-1} \text{ s}^{-1}$	0.103
Erythorbic acid	No	$1.18 \pm 0.005 \text{ dm}^3 \text{ mmol}^{-1} \text{ s}^{-1}$	0.093
Carbohydrazide	Yes	$0.52 \pm 0.01 \text{ dm}^{1.8} \text{ mmol}^{-0.6} \text{ s}^{-1}$	0.171
Diethyl-hydroxylamine	No	$0.45 \pm 0.05 \text{ dm}^3 \text{ mmol}^{-1} \text{ s}^{-1}$	0.031
Methyl-ethyl-ketoxime	Yes	$0.027 \text{ dm}^{1.5} \text{ mmol}^{-0.5} \text{ s}^{-1} (\text{E-t})$ $0.014 \text{ dm}^{1.5} \text{ mmol}^{-0.5} \text{ s}^{-1} (\text{O}_2\text{-t})$	0.015 (E-t) 0.008 (O ₂ -t)

Reaction kinetics and decomposition products of five different oxygen scavenger chemicals were analysed at 228 °C and room temperature. The kinetic rate constant k values were determined for the oxygen scavenging reactions for every scavenging chemical. It was noticed that there was discrepancy between the k values whether they were calculated based on the commercial oxygen sensor or Pt-Pt electrode pair data.

Carbohydrazide had similar decomposition products as hydrazine. The oxygen scavenging reaction with carbohydrazide resulted in decrease of pH and slight increase of the acidic conductivity. This is most likely due to the formation of CO₂ during the scavenging reaction.

The decomposition of erythorbic acid resulted in several different type of organic acids. Identifying individual effects of these species to e.g. corrosion of the structural materials would be laborious. These decomposition products had an effect to the acidic conductivity (see Figure 1) and pH. The effect to acidic conductivity was significant and might interfere the impurity monitoring performed at plants.

Decomposition product analysis of DEHA resulted only in reliable values for ammonia and acetaldehyde. Acetic and formic acids are formulated as well as

diethylamine in the studied conditions. However, the detected amounts were below the reliable detection limits of the analyses methods and defining accurately concentrations for these species remain to be challenge. Approximates for nitrate and nitrite were obtained. In the tests, DEHA had an effect to conductivity and pH but it should be emphasized that the applied concentration was high, 100 ppm, and in real application several times lower concentrations would be applied.

Electrochemical measurements performed to samples in MEKO environment indicated that higher dissolution rates and thinner oxide formation is anticipated on the stainless steel samples compared to A690. These results were in good agreement with the GDOES analyses.

Corrosion rates based on weight loss could be determined for the stainless steel samples studied for most of the studied chemicals. DEHA and MEKO seemed to cause smaller corrosion rates compared to CH, N₂H₄ and NH₃ environments. No corrosion rates based on weight loss could be calculated for A690 as all A690 samples gained weight during the exposure. Longer exposure times at higher temperature is suggested to obtain more reliable corrosion rate estimations.

FAC test setup for low alloyed steel 22K was constructed and calibrated for the future FAC tests. It was shown that the FAC setup is sensitive to temperature and reasonable FAC rates can be obtained with the setup after eight days of high temperature testing.

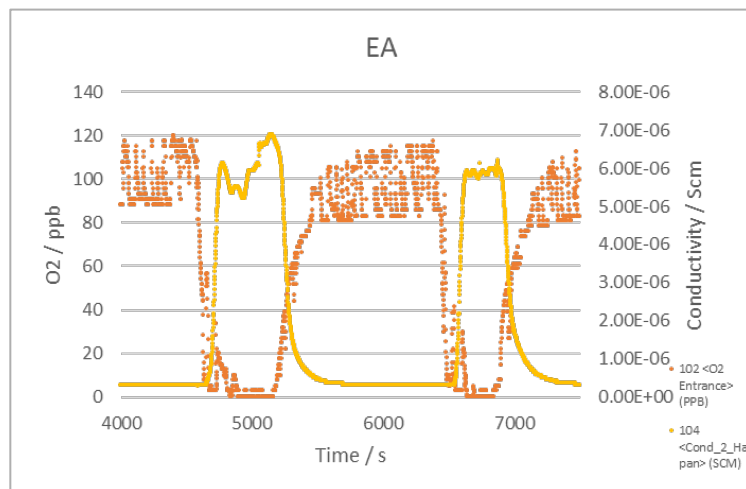


Figure 1. The measured oxygen content (orange) and acidic conductivity (yellow) after injections of EA in the measurement cell.

Estimation of impurity enrichment onto a simulated steam generator tube

Water is boiling in the SG due to the heat transfer from the primary to secondary circuit. Boiling is taking place on the SG surface and additionally, evaporation is also occurring beneath the deposits and within the pores of deposits. As water flows into the crevices and pores within the deposits, the impurities concentrate within them as the water is evaporated out from the crevices as almost pure steam. Increasing impurity concentration results in a higher boiling point and thus a longer time is required for the water to deliver impurities to the vicinity of deposit. [Green et al. 1995] The concentration of impurities can be very high, even a million times higher than the impurity concentration in the bulk water [IAEA, 2011]. Impurities can also return to the water from the deposits during transients, this effect being called hide-out return (HOR). Impurity concentration will change the local chemistry in the vicinity of deposits, and especially under the deposits, to worse. For example, the pH can shift locally into acidic or alkaline (depending on the impurities in the bulk water). [Turner 2011] It has been shown that extremely acidic or alkaline conditions cause corrosion problems in SG materials, even in reducing conditions [IAEA, 2011]. There is a need to study the kinetics of impurity enrichment into the crevices (and inside the deposits), particularly in view of possible impurity in-leakage due to seawater heat exchanger breaches or accidental breakdown of ion-exchangers. There is also a need to study the kinetics of impurity re-entrainment, out of the crevice or deposit back into the coolant water. This data is needed in order to evaluate the risks involved in such in-leakages, and also, in setting time limits for corrective actions.

The deposition of impurities on steam generator tube surface during boiling and their effect on corrosion of Alloy 690 was studied by conductivity, ICP-MS and EIS measurements. The following conclusions can be drawn based on the experimental and calculational results:

- 1) The form of the added impurity affects to its deposition on a boiling surface. Impurities added in a salt form (NaCl and Na_2SO_4) tend to deposit on a boiling surface, whereas those in acid form (HCl and H_2SO_4) did not deposit on the boiling surface most probably due to higher solubility.
- 2) Deposition and release rates estimated from both conductivity and HR ICP-MS measurements are affected by the concentration of impurities in the system (see Figure 2) and follow a quasi-first order kinetics with respect to concentration of the impurity added as a sodium salt.
- 4) EIS analysis revealed four different physical processes in the studied electrochemical system that are only moderately affected by boiling, the effect being to a large extent reversible.
- 5) The rate constants of the hydrogen evolution/oxidation reaction are not influenced by the impurity concentration within the experimental error, indicating that neither sulfate nor chloride participate in this reaction. The apparent reaction orders of the alloy oxidation reactions with respect to chloride and sulfate are rather small (0.11-0.13), indicating an indirect participation of both chloride and sulfate in

the particular reaction steps. On the other hand, the effect of impurity concentration on rate constants of cation ejection and oxygen incorporation via vacancy filling at the film/solution interface is much more pronounced (the respective reaction orders range from 0.5 to 1.0). It can be argued that chloride and/or sulfate adsorbed on the film surface accelerate cation ejection from the oxide and can compete with water for filling oxygen vacancies.

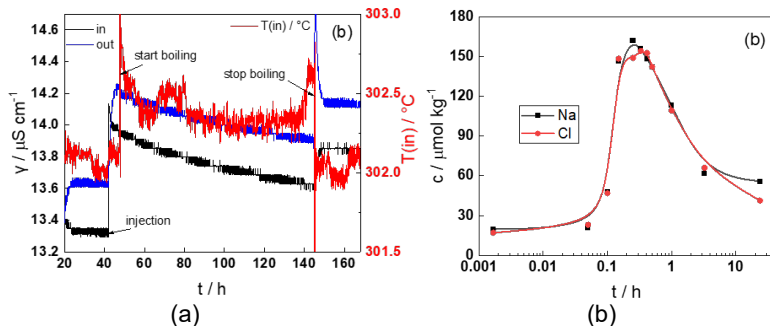


Figure 2. (a) Conductivity and temperature data during a boiling test when 200 ppm Cl was added into the simulated secondary side environment as NaCl. (b) Na and Cl analysis results after the boiling of the sample tube had been stopped.

Zeta potential measurements

Impurities can accumulate extremely well within and beneath magnetite deposits. One of the properties that has been thought to have an effect to magnetite deposition in SGs has been the surface charge, or zeta potential, of the magnetite particles in the process water. The theory of deposition is based on that if the charge of the magnetite particle is opposite to that of a surface in its vicinity, deposition occurs. If the surface charges of the particle and surface are similar, no deposition occurs. VTT has been developing a special measurement equipment for zeta potential and provided measurement results for magnetite and stainless steel in various secondary side chemistries.

High temperature zeta potential measurements based on streaming potential technique were performed for magnetite as a function of temperature in simulated PWR primary water chemistries. The calibration test without magnetite showed that the contribution of the ceramic filter to the overall zeta potential measurement result is negligible. The zeta potential measurement results obtained in the beginning of cycle chemistry did not seem to be reliable. It is suspected that a by-pass flow between the ceramic filter and the sealant have been occurred during the test affecting the pressure drop along the magnetite column and repetition of the measurements would be required. The zeta potential measurement results obtained in the end of cycle chemistry seemed to be very similar to the values reported in literature (see Figure 3). This would indicate that the measurement setup can provide reliable zeta potential measurement results in the studied temperature

range. Finally, some improvements for the future measurements can be suggested based on this work.

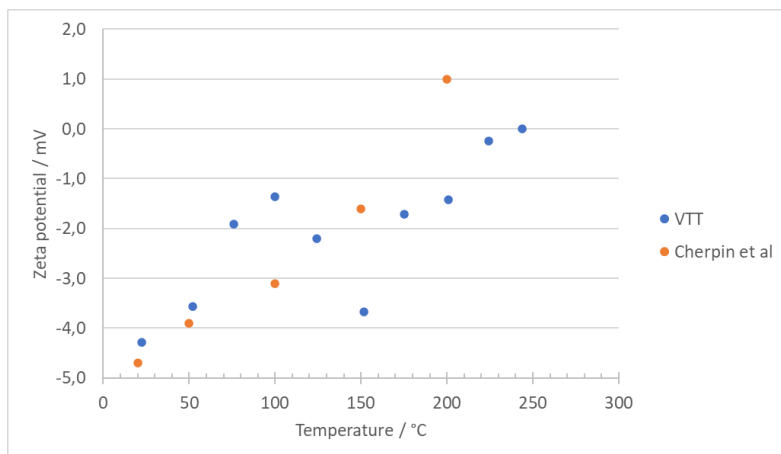


Figure 3. Obtained zeta potential values for magnetite in simulated primary chemistry and comparison to literature values.

PbSCC in Ni-based alloy A690

Pb has been observed in tube-supports, crevice deposits and surface scales of SGs [McGarvey et al. 1998]. Typical concentrations are 100 to 500 wppm, but in some plants, concentrations as high as 2000-10 000 wppm have been detected [Kim et al. 2009]. Pb might get into the system from radiation shields used during maintenance work, from impurity in various materials, certain turbine or pump parts or some greases, oils, lubricants or paints. Lead is presumed to induce cracking in SG tubes, although there is no consensus as to its critical concentration or material-environment combinations for Pb-induced stress corrosion cracking (PbSCC) to occur [Staeble 2003]. The cracking susceptibility has a strong dependence on redox potential of the crevice environment. Redox potential, on the other hand, is strongly affected by e.g. copper content in the crevice solution [Kim et al. 2005].

The hindered dehydration process during passivation is one of most important mechanisms of lead-induced passivity degradation, and it will result in the formation of anodic films containing more amorphous hydroxides and less crystalline (spinel) oxides [Lu et al. 2013]. The hindrance of dehydration is enhanced by increasing solution pH. In acidic crevice chemistry, the addition of 2.2 mmol dm^{-3} (500 ppm) lead contamination does not affect the dehydration at 300°C . Owing to the strong hindered dehydration effect of lead contamination in the alkaline crevice chemistry, the chromium species in the anodic film are mainly hydroxides, with the consequence that the anodic film is less protective, although the chromium content is increased. The presence of lead contamination promotes hydrogen incorporation

into the anodic films. This effect is most significant in alkaline chemistries, less marked in acidic and near neutral environments, changing the semiconducting properties of oxides in a complex manner.

Lead (Pb) addition (2.2 mmol kg⁻¹, or 500 wppm) to acidic and alkaline crevice solutions studied in this work was found to affect markedly the electrochemical behavior of Alloy 690 tube material at 278 °C. In the current-voltage -curve, the anodic peak just above the corrosion potential increased in magnitude by a factor of ca. 3 upon the addition of Pb (see Figure 4). On the other hand, the impedance magnitude at the lower end of the frequency spectrum increased considerably in the passive range. Quantitative interpretation of the EIS data using a recent version of the MCM developed especially for Alloy 690 indicates that the oxidation processes at the alloy/inner layer interface are accelerated in the presence of Pb, however, the charge transfer reactions at the oxide/solution interface are slowed down. Further, significantly larger thicknesses are observed for films formed in the presence of Pb, as evidenced by both calculations based on EIS and estimations from compositional in-depth profiles measured by GDOES. Concerning the cation composition of the surface and especially Pb(II) content, there is a semi-quantitative agreement between GDOES and XPS. Electronic properties of the oxide are also markedly influenced by Pb addition to alkaline crevice electrolyte, as inferred by the significant differences in both absolute values and potential dependences of the space charge capacitance. The fracture strain of the Alloy 690 tube material studied in this work was found not to be affected by addition of 500 ppm of Pb into the crevice environments. Based on the results gained, Alloy 690 tube material studied here appears not to be susceptible to SCC in the present crevice conditions at 278 °C. XPS analyses of the films on the strained and unstrained parts of the SSRT specimens exposed Pb-containing alkaline electrolyte indicated the presence of Ni(II), Fe(II) and (III), PbO and PbSO₄ (the latter after 2–8 nm of sputtering).

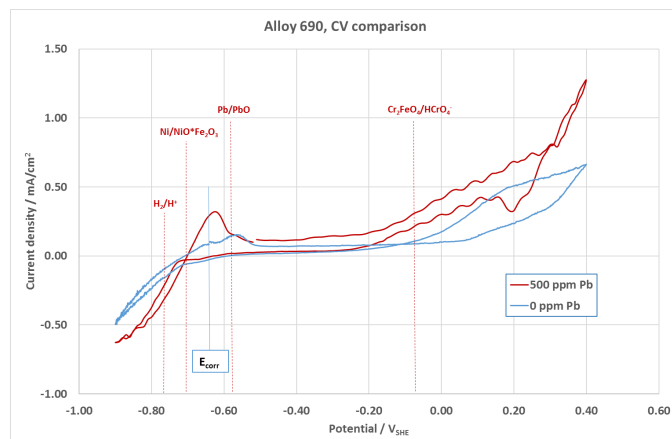


Figure 4. Cyclic voltammetry curves for alkaline crevice environment with and without Pb addition.

State of the art of monitoring the corrosion product dissolution and transport

According to the literature study on the corrosion product dissolution and transport monitoring methods it seems that there are some promising solutions available, but there might be some limitations that restrict the devices to be used in the power plant environment, at least not *in situ*. Most promising solutions for corrosion rate monitoring seem to be electro-chemical measurements systems, and some of them (corrosion potential, ECP, and linear polarization resistance, LPR) are used in power plants. In addition to them, also electrochemical impedance spectroscopy (EIS) measurements are very informative, though since they need experienced users, they might be restricted to laboratory use only. Out of the physical, non-electrochemical, corrosion rate monitoring methods, the most usable might be electrical resistance (ER) measurements, ultrasonic testing or acoustic emission measurements, but their sensitivities are not as high as the ones of the electrochemical measurement systems. Electrochemical measurement systems can even be used in the high-temperature low conducting solutions, at least in the laboratory environment, where traditionally physical methods have been preferred. This can be accomplished by using a controlled-distance electrochemistry (CDE) - arrangement.

What comes to the corrosion product transport rate or corrosion product concentration monitoring, there are several methods available, even though their on-line or *in-situ* nature can be questionable. Problems of traditional grab sampling can be minimized by using devices based on integrated sampling. Especially the ones working with an internal XRF analysis seem promising and can be used in power plant environments. Their sampling interval is still so long that they are not real on-line monitoring systems. There are available colorimetric methods for iron and copper detection, but their sensitivity is rather poor for at least condensate and feedwater applications. Turbidimeters/nephelometers and particle counters could provide a real on-line monitoring option, but their problem is that they are more qualitative devices and the correlation to the real particle concentration might be difficult. Dynamic light fluctuation monitors might have better sensitivity than traditional particle counters, but they are more novel technology and not so commonly used. All of these turbidity or particle counting based technologies still are a promising option, at least in the low temperature regions, where they are already used in some power plants. Development of a suitable window material for these methods, a material which would withstand high pressures and temperatures and still remains clear, could greatly enhance their usability at high temperature process environments. Acoustic detection is also a promising technology, currently used in the oil and gas industry, but the minimum particle size is a little high for corrosion applications.

High-temperature corrosion of cobalt and Stellite-6

Isotopes of cobalt, especially ^{60}Co and ^{59}Co , have a relatively long lifetime and are one of the main contributors to the radioactive dose in nuclear power plants. Cobalt is utilized in hard-facing alloys called Stellites in nuclear power plants and exists also as an impurity in structural materials. Stellite alloys have been extensively studied for their tribological properties as they are typically used in valves and other applications where hard-facing surfaces are required. However, general corrosion and release of cobalt from these alloys have been studied to a smaller extent. In this study, general corrosion of pure cobalt and Stellite-6 alloy was investigated in nuclear power plant primary loop water with boric acid and potassium hydroxide at 300 °C.

Open circuit potentials (OCP) of the samples were close to the hydrogen line for both samples and in CoO boundary region for pure cobalt and CoCr_2O_4 and Cr_2FeO_4 boundary region for Stellite-6, according to E-pH diagrams. Neither of the materials showed an anodic peak at potentials above the OCP, probably due to the passive film formed on the samples prior to the LSV measurements. The corrosion rate of pure cobalt at 300°C varied from 105 to 215 $\mu\text{m}/\text{y}$ and Stellite-6 from 35 to 58 $\mu\text{m}/\text{y}$ according to the linear polarization resistance (LPR) and linear sweep voltammogram (LSV) measurements (see Figure 5). The corrosion rates were confirmed by measuring the samples with electrochemical impedance spectroscopy (EIS) at the end of the test and these results were in good agreement with the voltammetric results.

There is very limited information on the general corrosion of cobalt-containing alloys in high-temperature water and therefore further tests are recommended to evaluate the corrosion rate of this alloy in primary circuit water chemistry. In addition to the electrochemical measurements, weight loss coupons and/or cross-sectional analysis of the samples should be used for the analysis of the corrosion rates, corrosion products and passivation. The relative proportions of cobalt released from high-cobalt alloys and impurities of other alloys should be estimated based on the corrosion rates of high-cobalt alloys and other alloys where cobalt is an impurity.

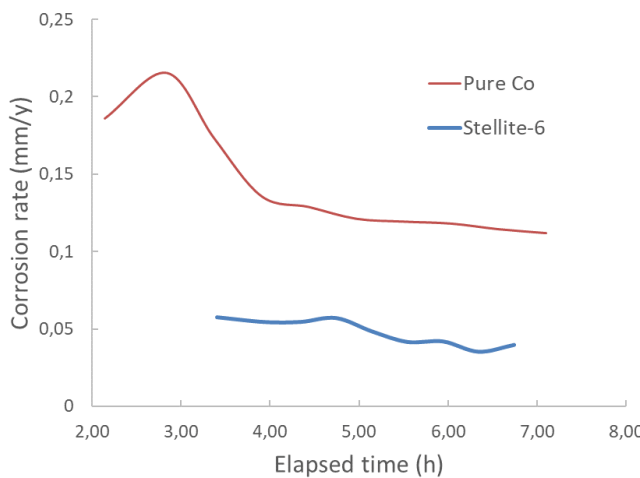


Figure 5. Measured corrosion rates for Co and Stellite-6 in simulated primary side chemistry.

Water chemistry and corrosion issues in PWR and WWER steam generators

The corrosion issues in PWR and VVER plants were studied in a form of a literature survey. The results obtained in the field of PWRs can be summarized as follows:

- Issues concerning previously used Alloy 600(MA): all corrosion related degradation modes encountered in SGs.
- Issues concerning Alloy 600TT: all modes, but in a lesser scale than in Alloy 600(MA).
- Replacement of alloys 600 and 600TT by 690TT has resulted in a notable decrease in corrosion related issues in SG heat exchanger tubes. However, possible incubation period is not known (was 10–12 years in Alloy 600).
- Alloy 800: very good service behavior (used in, e.g., some German PWRs and Candus). However, in recent years pitting, SCC, and IGA encountered – thermal ageing and influence of sulphur suspected.

The obtained VVER field experience indicates that the austenitic steel heat exchanger tubes can operate for a long time without essential degradation due to corrosion. However, the effect of deviations from normal water chemistry and the surface quality of SG tubing to the different modes of localized corrosion should be examined in more detail.

Some cases of ODSCC of austenitic steel heat exchanger tubes at locations where deposition of corrosion products occurs has been reported. ODSCC has been mitigated by replacing components made of carbon/low-alloyed steel that act as a source of depositing particles (condensers, feed-water distributor and high

pressure pre-heaters) by ones with higher Cr content, removal of copper containing parts, cleaning procedures and applying elevated secondary side pH.

General corrosion and FAC are typical phenomena for VVER type plants and cause dissolution, transportation and deposition of corrosion products. The main concern is the aggressive environments that may form underneath the deposits and can locally promote other forms of corrosion (such as SCC). Mitigation measures are well known.

SCC has been observed in dissimilar metal welds of VVER-1000 and VVER-440 steam generator collector pockets. The main factors leading to the occurrence of delayed deformation stress corrosion cracking was related to deposition formation, prevailing electrochemical conditions and the driving force for crack propagation from thermal and external stresses. This mechanism cannot occur in the absence of plastic deformation and/or oxidizing medium. A much better stress state of the headers has been achieved in new projects of NPPs. In addition, eliminating the use of copper-containing materials and using modern water chemistries create conditions for excluding the occurrence of oxidizing medium at all stages of SG operation.

SMR materials and water chemistries

A summary of the known water chemistries and construction materials used in advanced SMRs (marine and submarine small reactors were excluded, as they probably do not fulfil the present day safety requirements for civil use) was done within SAFIR2018 project GENXFIN in 2016. At that time, not much information was publicly available on these and they survey was updated in 2019.

Very little specific information is available (as of 2019) concerning the construction materials of SMRs. However, where available, the materials used in the main components in present day designs of SMRs seem to be mainly the same materials that are used in generation 3 large reactors: low carbon or stabilized austenitic stainless steels (e.g. 304L, 316L, 321, 347), low alloy steels (e.g. RPV: SA-508 Grade 3 Class 1 type pressure vessel steel), and better SCC resistant nickel base or high nickel alloys than Alloy 600 (e.g. 690, 800).

As seen in many cases, reactivity control of the reactor core takes place most often apparently without soluble boron (boric acid). The benefits of a soluble boron free core are [Hidayatullah et al 2015]:

- No boron dilution
- Less corrosion
- Reduces volume of liquid radwaste
- Strong negative moderator temperature coefficient
- Boron monitor and adjustment systems eliminated

No mention of primary side corrosion potential control by dissolved H₂ (except on the case of SMART) nor pH control was found in open literature. The applied secondary side water chemistries have neither been revealed. However, it can be

assumed that the latest chemistry and corrosion control methods used in large nuclear power plants are applied in the secondary side.

Summary and conclusions

ELMO-project aimed to improve nuclear safety in the field of water chemistry and corrosion of structural materials. The main results can be summarized as follows:

- Hydrazine replacement studies provided new information on the high temperature scavenging efficiency of alternative chemicals. Work on decomposition products and corrosion have been performed too.
- Validation of "Hot loop" facility have been performed which enables us to study the effect of boiling to impurity enrichment and corrosion of SG materials.
- High temperature zeta potential measurement setup has been validated.
- Pb is beneficial for A690 in alkaline crevice conditions when its susceptibility to corrosion is considered.
- There is very limited information on the general corrosion of cobalt-containing alloys in high-temperature water and therefore further tests are recommended to evaluate the corrosion rate of this alloy in primary circuit water chemistry.
- The current PWR VVER corrosion issues in secondary circuits were listed.
- Very little specific information is available (as of 2019) concerning the construction materials of SMRs.

Acknowledgement

Finnish Nuclear Waste Management Fund VYR, VTT Technological Research Centre of Finland Ltd, Fortum Power and Heat Oy and Teollisuuden Voima Oy are greatly acknowledged for funding this work.

References

- Betova, I., Bojinov, M. and Saario, T. 2016. Hydrazine replacement in nuclear power plants - alternative substances and techniques. VTT Research Report VTT-R-03426-16.
- Betova, I., Bojinov, M. and Saario, T. 2017. Kinetics of oxygen removal by hydrazine alternatives in conditions of steam generator preservation during outage. VTT Research Report VTT-R-05209-17.
- Green, S. J. and Hetstroni, G. 1995. PWR steam generators. International Journal of Multiphase Flow, Vol 21, suppl. pp. 1-97.
- Hidayatullah, H., Susyadi, S. & Hadid Subki, M. 2015. Design and technology development for small modular reactors-Safety expectations, prospects and impediments of their deployment, Progress in Nuclear Energy 79 (2015), p. 127-135.

- IAEA, International Atomic Energy Agency. 2011. Assessment and Management of Ageing of Major Nuclear Power Plant Components Important to Safety: Steam Generators. 2011 Update. International Atomic Energy Agency, Vienna. IAEA-TECDOC-1668. ISBN 978-92-0-121410-2. ISSN 1011-4289.
- Kim, D.-J., Kim, M.A., Kwon, H.C., Hwang, S.S., Kim, J.S., Hong, J.H., Kim, H.P. 2009. Oxide investigation formed on Alloy 600 in leaded aqueous solutions. 14th International Conference on Environmental Degradation of Materials in Nuclear Power Systems, Virginia Beach, Virginia, USA, American Nuclear Society, 2009, pp. 1148-1156.
- Kim, U.Ch., Kim, K. M. & Lee, E.H. 2005. Effects of chemical compounds on stress corrosion cracking of steam generator tubing materials in caustic solution. Journal of Nuclear Materials 341 (2005) pp. 169-174.
- Lu B.T., Luo J.L., Lu Y.C. 2013. Effects of pH on lead-induced passivity degradation of nuclear steam generator tubing alloy in high temperature crevice chemistries. *Electrochimica Acta* 87, pp.824-838.
- McGarvey, G.B., Ross, K.J., McDougall, T.E. and Turner, C.W. Lead Corrosion and Transport in Simulated Secondary Feedwater. Proc. 3rd International Steam Generator and Heat Exchanger Conference, Toronto, Canada. 1998. pp. 617-627.
- Staehle, R.W. 2003. Clues and Issues in the SCC of High Nickel Alloys Associated with Dissolved Lead, Proc. 12th International Conference on Environmental Degradation of Materials in Nuclear Systems – Water Reactors, T.R. Allen, P.J. King, and L. Nelson, Eds., TMS, Warrendale, PA. pp. 1163-1209 (2003).
- Turner, C. 2011. Implications of Steam Generator Fouling on the Degradation of Material and Thermal Performance. 15th International Conference on Environmental Degradation of Materials in Nuclear Power Systems – Water reactors. Colorado Springs, USA, August 7 – 11, 2011.

6.4 Fatigue and evolving assessment of integrity (FEVAS)

Juha Kuutti¹, Jarno Hiittenkivi¹, Heikki Keinänen¹, Pekka Nevasmaa¹, Ahti Oinonen¹, Tommi Seppänen¹, Henrik Siren², Iikka Virkkunen²

¹VTT Technical Research Centre of Finland Ltd
P.O. Box 1000, FI-02044 Espoo

²Aalto University
P.O. Box 11000, FI-00076 AALTO

Abstract

The project FEVAS focuses on the structural integrity aspects of the pressure vessel and primary circuit with special emphasis on developing novel models, tools and techniques that help to ensure safe plant operation over the whole plant lifetime. The project has focused on the development of a F_{en} model to take into account the effect of the environment and temperature on the fatigue endurance of the primary circuit, conducted a study of surface crack behavior under cyclic thermal loads followed development of experimental and numerical techniques to capture it and developed techniques needed for the assessment of pressure-pulsation induced piping vibrations. Additionally, the project concentrated on the development of surface crack repair welding techniques through mock-up manufacturing, its material characterization and numerical simulations of the welding process.

Introduction

The emphasis of the FEVAS project is the research and development of the methods to assess the long-term structural integrity of the pressure vessel and primary circuit. The overarching aim of all research in the project to provide advanced and calibrated integrity assessment methods and input information required in these methods and to identify and quantify the uncertainties and errors of the structural integrity analyses performed to demonstrate the integrity of the primary circuit. The project improves the overall safety of NPPs by providing information on the state-of-the-art integrity assessment methods and their relations to conventional norm-based methods, including the inherent safety margins of the conventional methods.

The project focused in three topics: fluid-induced loads on piping, fatigue usage of primary circuit and development repair welding approaches.

Fluid-induced loads on piping

The coupling of primary water acoustics and piping vibrations is considered in the project. Suitable efficient analytical and numerical modelling capabilities are

developed and the possible excitation sources are studied. The emphasis is on i) creating understanding of the most important acoustic-structural phenomena in the primary circuit and ii) having efficient methods which can account for the fluid-structure-interaction (FSI) between the acoustics and the piping. The coolant water necessarily affects the dynamic behaviour of piping and components. At simplest, the effect can be modelled through the added mass. More complex two-way FSI effects result e.g. when the acoustic and structural natural frequencies are similar (Oinonen, 2019). For the coupled cases FSI modelling methods are necessary, such as 1D or 3D acoustic-structural codes or even coupled computational fluid dynamics (CFD) and structural analyse. A literature review was conducted on analytical and numerical methods for modelling coupled acoustic-structural piping vibrations. The current emphasis of the work is on 1D tools which enable efficient modelling of the whole circuit and on analytical methods which can be used for assessing the significance of different acoustic-structural phenomena.

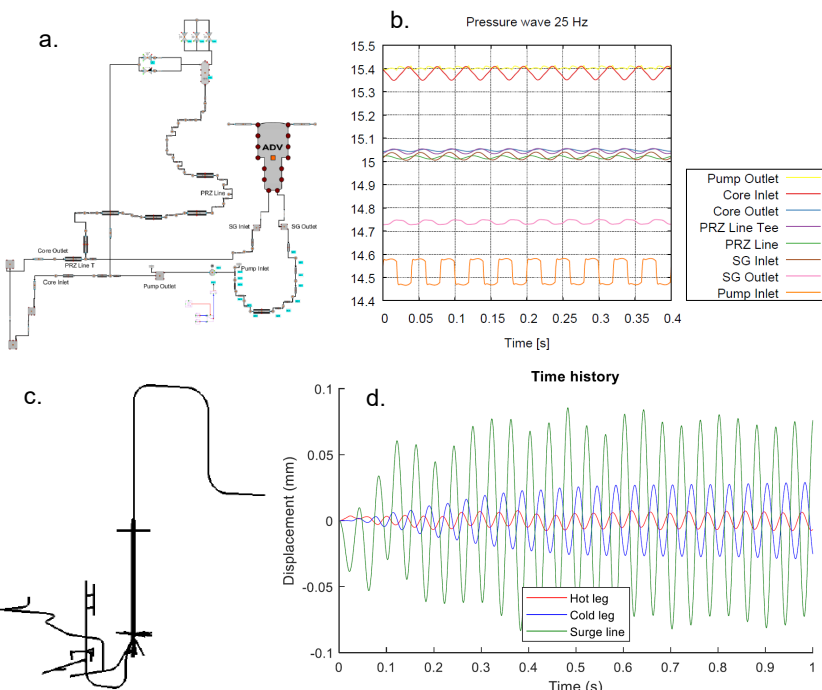


Figure 1. Apros model of a PWR primary circuit (a) and pump-induced pressures at different locations (b). Abaqus structural model of a PWR primary circuit (c) and vibration time histories in the model caused by pump pressure pulsations (d).

Apros was seen as a suitable modelling tool and it was used to calculate the acoustic pressure propagation in a PWR example primary circuit (Hiittenkivi 2019). Cyclic pressure pulsation was produced by the main circulation pump in the model. Figure 1a-b presents how the pressure propagates through the system and

attenuates due to the flow resistances in the circuit. The amplitude of the pulsation generally diminishes but some amplifying phenomena is observed at specific excitation frequencies. The excitations were used as input for the structural piping vibrations analysis with Abaqus FE software (Kuutti & Hiittenkivi, 2020). Figure 1c-d shows the structural piping model and the resulting hot leg, cold leg and surge line vibrations. The assessment was performed one-way coupled such that the feedback effects of structural deformations were not considered in the thermal hydraulic assessment. The results show that this idealization was sufficient in the studied case as the structural vibration amplitudes remained low.

This part of the project also focused in combining new experimental NDT techniques with fracture mechanics simulations to study the behavior of a surface crack under cyclic thermal loading (Koskinen et al., 2021). As an improvement to conventional techniques, nonlinear ultrasound measurement techniques make it possible to detect partially closed cracks. Such a scenario may occur for example due to residual stresses or thermal contraction (Kuutti & Virkkunen, 2020). Together with the RACOON project, an experiment was performed where a surface crack in a thick steel plate was subjected to cyclic thermal loading. The specimen was instrumented with ultrasonic sensors, which performed on-line monitoring of the crack response during the loading. The scenario was simulated using the finite element method to obtain the crack opening displacements and contact pressure distributions on the crack face over the full loading cycle. Figure 2a-d shows the numerical predictions of the temperature history, crack opening displacements and contact stresses. The crack response signal measured using nonlinear ultrasonic techniques is shown in Figure 2e. The ultrasonic response is qualitatively in line with the crack opening state distribution.

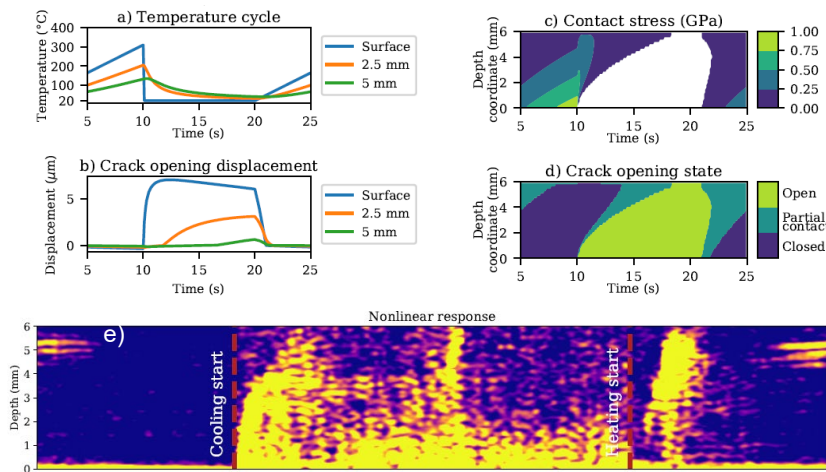


Figure 2. a-d: The temperature histories, crack opening displacement histories, contact stress and crack opening displacement over the load cycle obtained from the finite element simulation. e: Nonlinear ultrasonic response over the load cycle.

Fatigue usage of primary circuit

The project also focuses in the research on the environmental factor affecting the fatigue life of components subjected to the primary water environment and cyclic loading. Fatigue design curves are based on testing in air, but for four decades it has been observed that a reactor coolant environment degrades fatigue life. The greatest challenge in environmentally-assisted fatigue (EAF) has been quantifying the effect through a reduction factor, F_{en} . The work has two specific goals: to generate valid EAF data in support of a plastic strain rate based F_{en} model which can be applied in cumulative usage factor evaluation of plant components and to complete development of a relevant F_{en} model (Seppänen et al. 2019, 2020).

Environmental effects of LWR coolant need to be factored in when defining cumulative fatigue usage of primary circuit components. The basis is a set of codified design rules and fatigue design curves, based on experimental data. To accurately quantify environmental effects, the reference curve in air to which fatigue life in water is compared shall be as reliable as possible. Literature studies and accumulated data at VTT reveal that the use of common reference curves for a wide range of austenitic stainless steel alloys and temperatures is unreliable. Some design codes already include measures to consider this but ASME III is not yet among them. The ASME III design curve is adopted from NUREG/CR-6909 and contains no consideration for dependence of temperature or stainless steel grade.

Two different stainless steel grades, AISI 304L and 347, have previously been used in environmentally-assisted fatigue experiments at VTT. The experimental work in FEVAS focused in providing additional baseline fatigue data for the development of the F_{en} model.

The results from the test series performed at 25 °C and 325 °C is shown in Figure 3. The project provided reference curves for the AISI 304L heat at room temperature and 325 °C to complement the curves already available for AISI 347. In Figure 4, demonstration of realistic environmental effect quantification is done using these reference curves as an alternative to the NUREG methodology. (Seppänen et al. 2019, 2020).

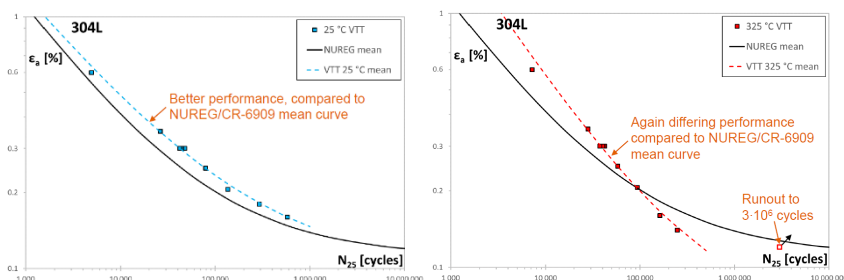


Figure 3. Low-cycle fatigue tests results for AISI304L at RT and 325 °C.

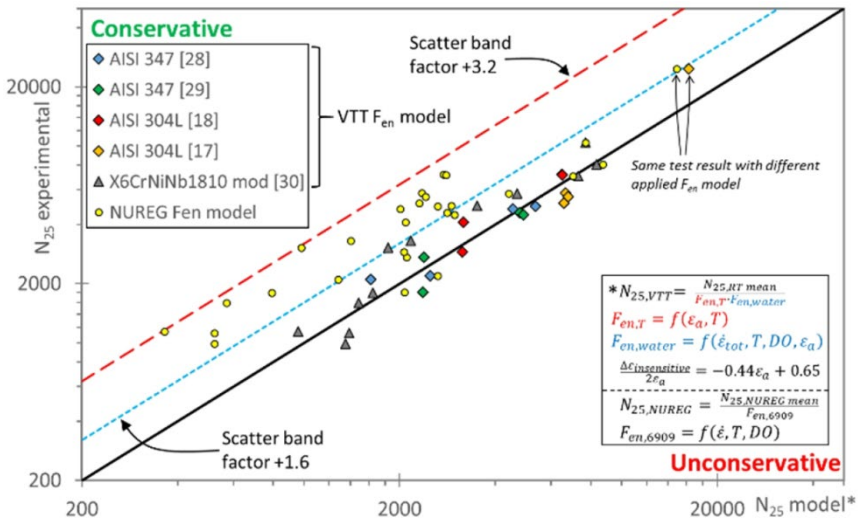


Figure 4. Fatigue life from application of VTT and NUREG F_{en} models.

Development of repair welding

As plants continue to age, there is an increased probability for the need of repairs due to extended exposure to a harsh environment (neutron flux, high temperature, high pressure, water chemistry). It is paramount that qualified and validated solutions are readily available, and that such methods are validated proactively, at a stage when they are not yet needed. In FEVAS (joint with ELIAS), a repair method for a postulated through cladding crack into the low alloy steel of a nuclear power plant's reactor pressure vessel has been investigated.

Repair welding is thought to represent a 'worst-case' scenario where a postulated linear crack-like defect exists beneath the cladding and might extend across the interface into the RPV steel side. This postulated defect is then removed by machining, and the thereby machined groove will be filled by repair welding using a nickel-base superalloy filler metal and using mechanised/robotised arc welding process. While FEVAS focused on computational support for mock-up design and weld procedure tests (Keinänen et al. 2020), ELIAS performed repair procedure design and characterization of the mock-up microstructure (Virkkunen et al. 2020). The mock-up was welded at Aalto University as a joint effort between the projects.

In the project, a repair weld mock-up was produced with CMT welding. As an alternative to conventional gas tungsten arc welding (GTAW) process, the use of automated gas metal arc welding (GMAW) utilizing Cold Metal Transfer (CMT) mode offers many advantages, such as good weld quality, exceptionally stable arc, easy automation and very low heat input along with narrow HAZ (Virkkunen et al., 2020). A postulated crack was excavated from a cladded and thermally embrittled low alloy steel material and repaired using a nickel base filler metal by gas metal

arc welding-cold metal transfer. No pre-heating or post-weld heat treatment was applied, as it would be nearly impossible to apply these treatments in a reactor pressure vessel repair situation. One cladded plate was welded (Figure 5), meaning two excavations were filled. One excavation was filled with 100 beads along the long side, while the second excavation was filled halfway (5 layers) the long side, followed by a 45° hatch pattern (6 layers) for a total depth of 40 mm.

The mock-up weld was sectioned and a metallographic sample prepared to study the weld quality. This part of the research and its results are described in more detail by the ELIAS project. (Huutilainen et al., 2021)

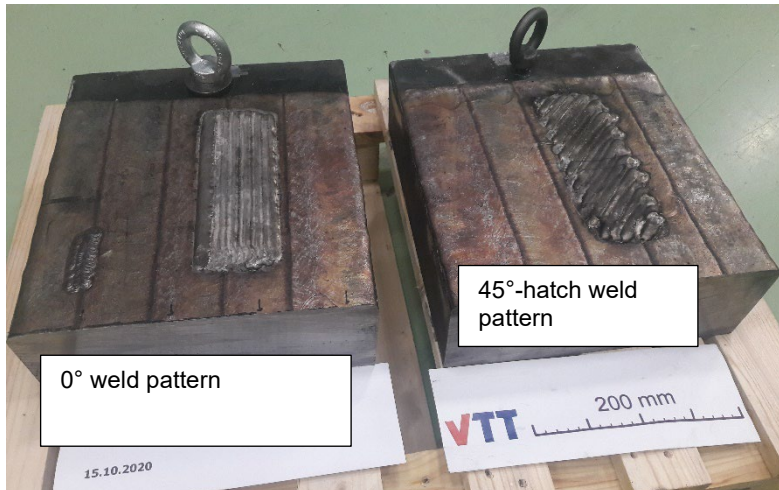


Figure 5. Repair weld mock-ups after welding.

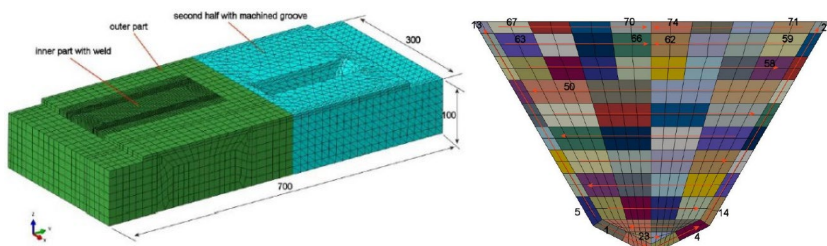


Figure 6. Finite element model for the mock-up welding simulation and bead order in the weld cross-section.

The welding was simulated with the finite element method using in-house welding simulation methods (Figure 6, Keinänen, 2019). The aim of the simulations was to scope the effects of different welding parameters and bead orders on the residual stresses, HAZ extent and cooling curves (Huutilainen et al. 2021). The computed longitudinal residual stresses show maxima at the surface of the weld, Figure 7. A

particular interest in the simulations was the computational prediction of the hardness distributions around the weld location. Based on an empirical correlation formulae and the simulated $t_{8/5}$ cooling time parameter, the as-welded hardness distribution in the base metal is shown in Figure 8.

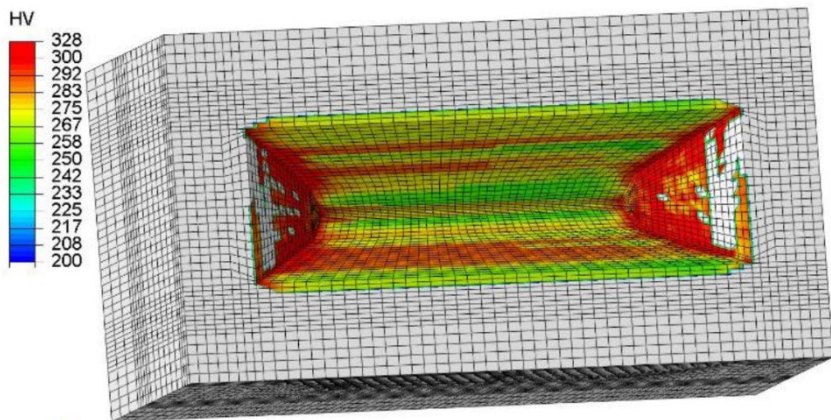


Figure 7. Hardness predictions in the base metal after welding as predicted from the $t_{8/5}$ cooling time.

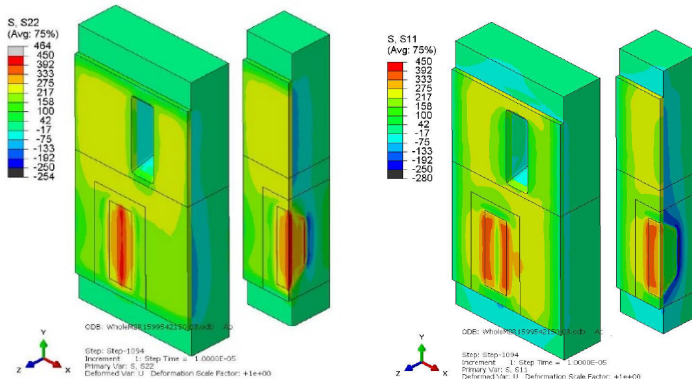


Figure 8. Computational prediction of the longitudinal (left) and transverse (right) weld residual stress distributions after welding at room temperature.

Experimental and numerical evaluations have been used to investigate a repair welding method for a postulated through cladding crack in to the RPV. The work will continue to fully characterize the weld interface, investigate the welding residual stresses and fully optimize the welding parameters along with the development of tools and methods to numerically simulate the welding process and predict the deformations and residual stresses.

Closing remarks

The research described above summarizes the accomplishments in the FEVAS project in 2019 and 2020. In 2021-2022, the work focuses solely in the development of repair welding thought the FENIX project.

References

- Hiittenkivi, J. 2019. Vibration Induced by Pressure Waves in Piping. VTT Research Report VTT-R-01297-19. Espoo: VTT.
- Huotilainen et al., 2021. Evaluation of an Alloy 52 / cladded carbon steep repair weld by cold metal transfer. Submitted to the ASME 2021 Pressure Vessels & Piping Conference PVP2021, PVP2021-61981, Virtual, Online.
- Keinänen, H. 2019. Comparison between Abaqus Welding Interface and VTT inhouse welding codes. VTT Research Report VTT-R-00519-19. Espoo: VTT.
- Keinänen, K. et al. A52M/SA502 dissimilar metal RPV repair weld: Evaluation of different techniques, ASME 2020 Pressure Vessels & Piping Conference PVP2020, PVP2020-21233, August 3, 2020, Virtual, Online.
- Koskinen, T., Kuutti, J., Virkkunen, I. & Rinta-aho, J. 2021. Online nonlinear ultrasound imaging of crack closure during thermal fatigue loading. Journal article manuscript in preparation.
- Kuutti, J. & Hiittenkivi, H. 2020. An assessment of fluid-induced vibrations in a PWR primary circuit, Research Report VTT-R-01114-20. Espoo: VTT.
- Kuutti, J. & Virkkunen, I., 2020. Crack closure behaviour of semicircular surface cracks subjected to cyclic thermal loads. Fatigue and Fracture of Engineering Materials and Structures, 2020, 43(12), pp. 3063–3067.
- Oinonen, A. 2019. Fluid-Structure-Interaction analysis for a water hammer loaded piping elbow, SMiRT-25 Conference, Charlotte, NC, USA, August 4-9, 2019.
- Seppänen, T., Alhainen, J., Arilahti, E. & Solin, J. 2019. Strain-controlled low cycle fatigue of stainless steel in PWR water. ASME 2019 Pressure Vessels & Piping Conference PVP2019, July 14-19, 2019, San Antonio, Texas, USA.
- Seppänen, T., Alhainen, J., Arilahti, E. & Solin, J. 2020. Grade and temperature dependent reference curves for realistic Fen quantification of austenitic stainless steels. ASME 2020 Pressure Vessels & Piping Conference PVP2020, PVP2020-21136, August 3, 2020, Virtual, Online.
- Virkkunen, I. et al. A52/A502 dissimilar metal RPV repair weld: experimental evaluation and post-weld characterizations. ASME 2020 Pressure Vessels & Piping Conference PVP2020, PVP2020-21236, August 3, 2020, Virtual, Online.

6.5 Reactor pressure vessel repair welding collaboration (FENIX)

Juha Kuutti¹, Noora Hytönen¹, Pekka Nevasmaa¹, Iikka Virkkunen², Gaurav Mohanty³, Aloshius Lambai³, Suprit Bhusare³

¹VTT Technical Research Centre of Finland Ltd
P.O. Box 1000, FI-02044 Espoo

²Aalto University
P.O. Box 11000, FI-00076 AALTO

³Tampere University
FI-33014 Tampere University

Abstract

As nuclear power plants age, it becomes more necessary to repair safety-critical components that are difficult to replace such as the reactor pressure vessel. The reactor pressure vessel repair weld scenario is studied in the project by production of a mock-up with two surface excavations that were filled with repair welding with automated gas metal arc welding (GMAW) using cold metal transfer (CMT). Two different bead patterns, a conventional 0-degree welding direction and a 45-degree hatch pattern were used to optimize the residual stress state. No clear differences in the weld microstructure and fusion boundary were observed using SEM, EBSD and EDS between the two welds. The microhardness measurements indicated higher fusion boundary hardness in the 0-degree welding direction sample, but the indentation hardness measurements did not show any such differences. The measured residual stress profiles were similar for both welding patterns. Overall, the research showed that GMAW-CMT is a promising technique to perform surface repairs, due to its easy automation, good weld quality and stable arc and low heat input leading to a narrow heat affected zone, but the observation of both porosity and lack of inter-run fusion between weld beads indicated that there is a need to further optimize the welding parameters.

Introduction

As nuclear power plants age and their intended lifetimes are extended, there is a growing need to repair safety-critical and hard-to-replace components. One example of this is the repair of defects in the reactor pressure vessel that can occur due to exposure to high temperatures, pressures, corrosive environments, and neutron irradiation, which often need to be repaired using various welding techniques.

The FENIX project has developed repair welding techniques using robotized gas metal arc welding cold metal transfer to repair a linear crack like defect beneath the

cladding, which extended into the reactor pressure vessel steel. Here, the repair welding of a thermally embrittled and cladded low-alloy steel plate with two groove excavations filled using Alloy 52 with two different welding directions, 0-degree and 45 degree, and corresponding bead patterns is presented. The two welds were characterized with micrographs, microhardness measurements and residual stress measurements.

The research work developing repair welding techniques has been originally presented in ASME PVP conference papers (see the list of references). The latest publication is summarized here.

Description of mock-up welding

To simulate the inner surface of a reactor pressure vessel (RPV), a mock-up was made from a 100 mm thick low alloy steel slab. The mock-up was subjected to heat treatment to create thermal embrittlement similar to represent RPV ageing.

to that found in a used pressure vessel. The mock-up was then clad with stainless steel to match the surface conditions of an RPV. No stress-relieving was performed after cladding. Two excavations were machined into the mock-up to represent potential repair locations (Figure 1), and repair welding was performed using a nickel-based Alloy 52 filler metal and a partially robotized GMAW CMT (gas metal arc welding cold metal transfer) procedure. The use of a robotized GMAW process and the CMT procedure allows for easy automation and reduced heat input during welding, respectively, which can be beneficial for repairs in challenging conditions.

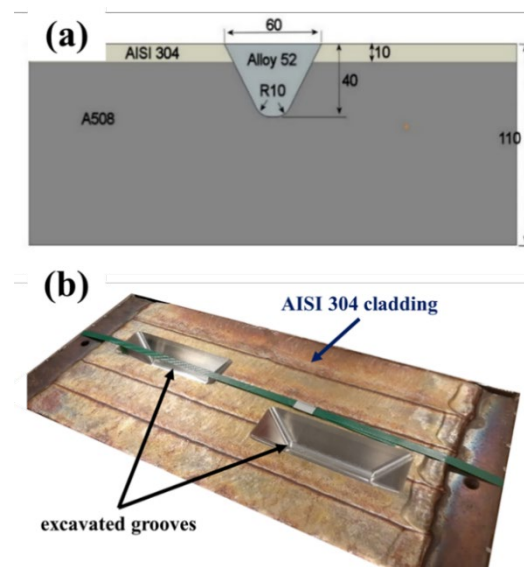


Figure 1. (a) weld groove schematic and (b) mock-up plate after groove excavation before repair welding.

In order to investigate the impact of various welding techniques on residual stress, two distinct welding bead configurations were tested. The first approach utilized a conventional setup where the beads were parallel to the main axis of the excavation, resulting in a minimal number of beads. The second approach employed a new technique where later layers were filled with 45 degree welding direction, with each successive layer being perpendicular to the previous one. This approach is similar to that commonly employed in additive manufacturing printing. It was hypothesized that the alternating bead direction would decrease the build-up of residual stress and also prevent the alignment of the highest longitudinal stress along the longitudinal axis of the repair excavation.

Residual stress measurements

Residual stress levels were measured for both repair-weld scenarios using the contour method. Samples were cut in half by making a single cut through the centre of the weld. As a result, the measured residual stresses were along the longitudinal axis of the repaired area. The residual stress contours obtained from the measurements are shown in Figure 2.

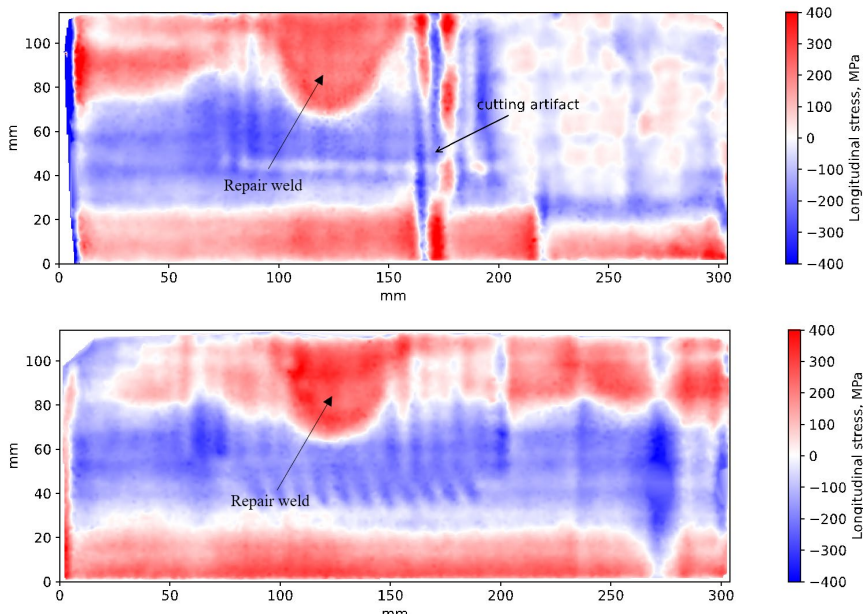


Figure 2. Residual stress contour for the repair with 0° (top) and 45° (bottom) bead arrangements.

Despite the weld bead order and the corresponding welding process were significantly different, the residual stresses were found to be quite similar. It was

expected that the crisscross pattern of the weld beads would lead to subsequent layers of welding creating stresses that would counteract the previous layers, reducing the overall residual stress field. But this was not the case and both weld areas had tensile stresses around 300 MPa, which is close to the yield stress of the weld material. Compressive stresses were induced to the base material with lower magnitude, peaking around 200 MPa. This suggests that the yield behaviour of the weld material is the primary factor governing the residual stress field.

Mock-up microstructural characterization

The microstructure of the two fusion boundary areas of the welds were studied using scanning electron microscopy (SEM) with detection of secondary electrons (SE) and backscattered electrons (BSE). The combined macro-image of the fusion line in Figure 3 shows the primary features of the microstructure around the fusion boundary. The LAS is composed of coarse-grained (CG) and fine-grained (FG) heat-affected zones (HAZ), which together are around 1 mm wide. The coarsening of the grains in the HAZ is more prominent in the corner area, which has been affected by both the cladding process and the welding process. Qualitatively, it also appears that in the 0-degree weld, the CG-HAZ extends to a wider width than in the 45-degree weld.

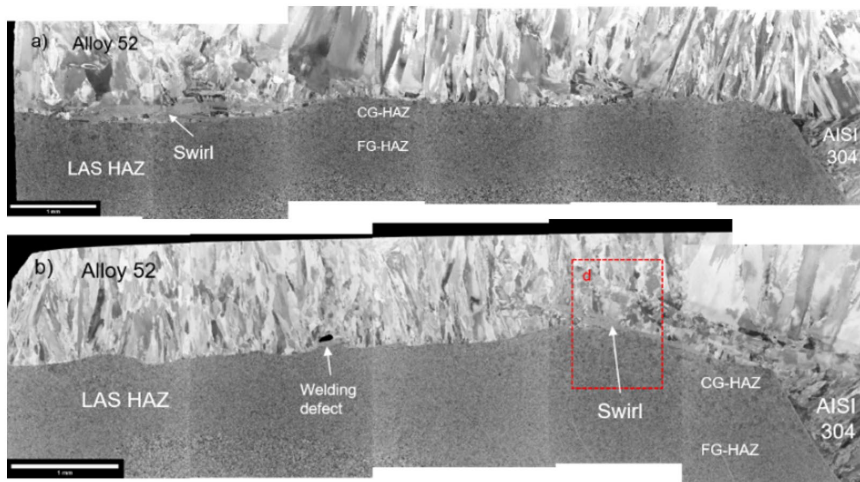


Figure 3. SEM-EBSD microstructure characterization of (a) 0-degree and (b) 45-degree mock-ups fusion boundary areas with Alloy 52 weld, LAS HAZ and a small part of the AISI 304 stainless steel cladding. The location marked by the red rectangle in (b) is presented at higher magnification in Figure 4(d-e). The micron marker shows the distance of 1 mm.

When looking at the microstructure of the weld, no significant differences are observed as a result of the orientation of the welding. Figure 4 shows typical microstructures of the fusion boundary. Typically, the fusion boundary is a narrow, fine line of fusion with a noticeable difference in the microstructure of the two dissimilar metals. In both weld fusion lines, a swirl pattern can be seen, which is commonly associated with the formation of weld passes, as seen in Figures 3(a,b) and 4(d-f). The swirl is caused by the melting of a small amount of base material that mixes in the weld pool with the A52 weld metal and solidifies with the weld bead into a partially mixed/melted zone (PMZ) composed of a mixture of A52 and LAS. Figure 4(d-f) shows a PMZ at higher magnification.

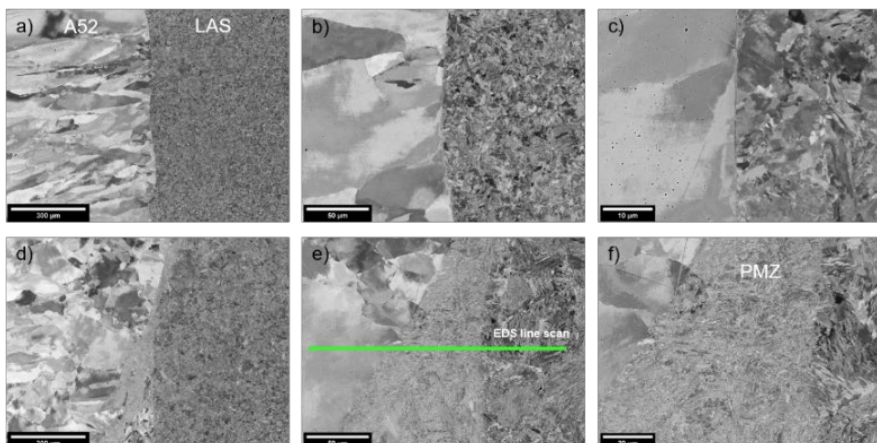


Figure 4. Microstructure of the 45-degree weld fusion boundary (a-c) showing the typical fusion boundary and (d-f) showing a wide swirl with partially melted microstructure.

The microstructure was analysed in more detail using the electron backscatter diffraction (EBSD) technique. Figure 5 shows a cross-section map of the 0-degree welding sample. The difference in grain size between the CG-HAZ and FG-HAZ observed qualitatively is clearly visible. In the upper right corner region, which is the area comprising both stainless steel cladding and Alloy 52 weld metal, the heat input from welding causes stronger grain coarsening in the HAZ. In the CG-HAZ, relatively large grains, up to tens of micrometres, of ferrite, bainite and martensite can be observed, but only up to a distance of about 200 micrometres from the fusion boundary. The grains are irregularly shaped and elongated, with a large variation in grain size. Many grains have diameters exceeding 20 micrometres, with some reaching up to 50 micrometres. The grain size decreases with increasing distance from the fusion boundary, and transitions to a grain size of a few micrometres. Specifically, this region has relatively smaller grain size variation, with an average grain diameter of 8 micrometres, and very few grains exceeding 15 micrometres. The fusion boundary between the LAS and stainless steel cladding is more mixed

compared to the narrow boundary between the LAS and weld. However, the HAZ in Figure 5 shows the effect of welding on the LAS only, and the heat effect from the preceding cladding cannot be determined.

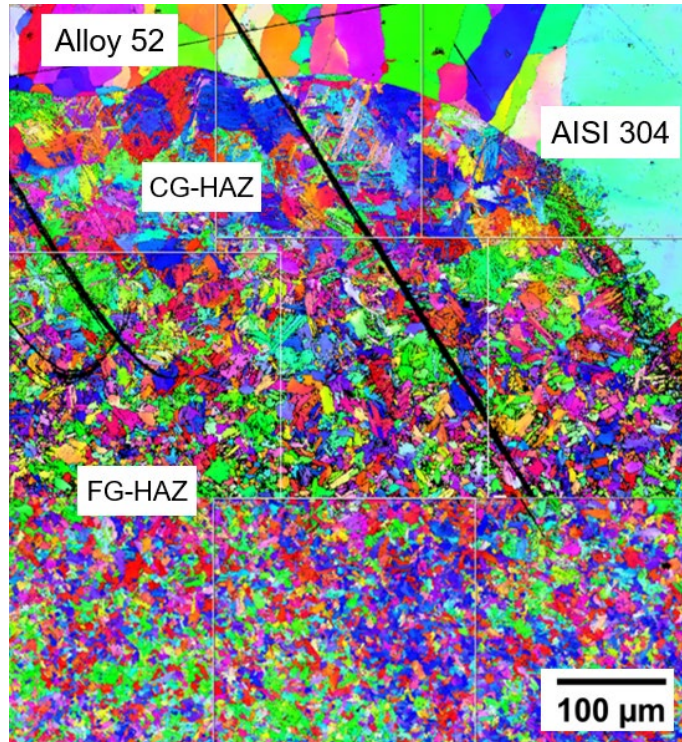


Figure 5. Combined EBSD image of the 0-degree sample microstructure in the corner with weld material, LAS HAZ and cladding.

To gain a deeper understanding of the mechanical properties of the LAS at elevated temperatures and to examine any potential differences in mechanical properties between the 0-degree and 45-degree samples, in-situ scanning electron microscope (SEM) nanoindentation tests were performed from room temperature up to 250 °C. Figure 6 shows the variation in indentation hardness of the LAS for both repair weld samples as a function of the test temperature. Both samples have similar initial hardness values of around 2.75 GPa at room temperature, suggesting that there is no apparent change in mechanical properties as a result of the bead arrangement during welding. The hardness drops by only a small amount (around 7%) at 250 °C in both cases. The temperature dependence of hardness is similar for both welding samples, which further indicates that there is no noticeable change in mechanical performance at elevated temperatures. Additionally, room temperature hardness measurements were taken again after the elevated temperature tests to determine if there were any microstructural changes due to

heating the sample. These hardness results, shown with open symbols in Figure 6, seem to be in agreement with the initial hardness data, suggesting that there were no major changes in the microstructure due to heating up to 250 °C.

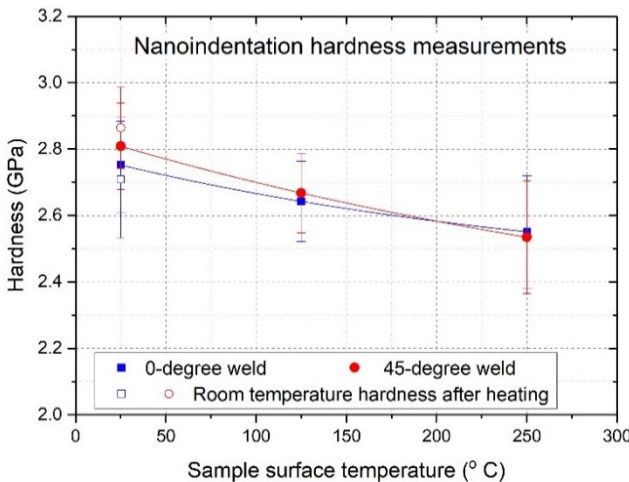


Figure 6. Room and elevated temperature hardness results for las from both 0- and 45-degree weld samples.

In addition, the microstructural characterization of the two welding orientations included determination of microhardness and nanohardness across the low alloy steel and Alloy 52 weld fusion boundary. The results showed that the microhardness peak was located in the coarse-grained heat-affected zone adjacent to the fusion boundary, with the peak being higher in the 0-degree weld than in the 45-degree weld, indicating that there is slightly higher mismatch in the properties. However, the nanohardness measurements did not confirm this. Furthermore, the microstructural analysis did not reveal any significant differences between the two welding orientations, with the exception of a few weld defects, particularly voids.

Discussion

The work studies the effects of welding direction in an RPV repair weld. Two welds were produced, one with a conventional 0-degree welding direction and one with a 45-degree welding direction using a crisscross bead pattern. The differences in the weld caused by the welding direction in terms of residual stresses, weld microstructure and hardness properties have been assessed.

The microhardness measurements suggested that the 0-degree weld had a higher hardness peak adjacent to the fusion boundary when compared to the 45-degree sample, indicating a higher degree of mismatch and/or hardened microstructure. To further investigate this, nanoindentations were performed across

the fusion line to detect any localized hardened grains and regions. The detected variations in both samples were found to be within the typical range for nanoindentation measurements, and no evident hardness peaks were observed. The nanoindentation results showed a decreasing trend in hardness with increasing temperature, as expected. To evaluate any potential effects of thermal aging, the hardness was measured again after cooling back to room temperature. There was no indication of aging-induced hardening, as the nanoindentation results remained within the variation of the initial state.

In the microstructure of the welds, no clear differences were observed as a result of the welding orientation. Both samples presented a typical fusion boundary which is a narrow, fine line of fusion with a noticeable difference in the microstructure of the two dissimilar metals. A similar ~1mm wide coarse-grained and fine-grained heat-affected zones (HAZ) were observed for both samples, despite the differing welding directions, although it appeared that the coarse-grained area in the 0-degree weld extended to a greater width than in the 45-degree weld.

A few weld defects were observed in the samples, most notably an inter-run fusion defect located in the cross-section cut from the 0-degree weld. This can be attributed to the welding parameters that were not optimized during welding. It is also expected that the 45-degree weld may be more susceptible to such defects because of the greater number of beads and the crisscross pattern. Only one defect was observed in the 45-degree microstructural sample.

The residual stress measurements using the contour technique indicate that the residual stresses in the mock-up are highly tensile throughout the 40 mm depth of the weld and exceed the 280 MPa yield stress of the weld material at room temperature. The measurements show that the residual stresses decrease to zero on the surface of the weld, which is likely due to the measurement uncertainty near the surface. The data also shows a sharp transition from tensile to compressive stresses at the root of the weld, and this transition can be observed all along the fusion boundary and partially melted zone. The measurements show variation in the residual stresses in the base material below the weld, which can be attributed to the potential presence of initial residual stresses in the cladding. The influence of the softer cladding material is evident in the residual stresses, even though a cladding layer was not included in the repair weld.

Summary and conclusions

The reactor pressure vessel repair weld scenario is studied in the project by production of a mock-up with two surface excavations that were filled with repair welding with automated gas metal arc welding (GMAW) using cold metal transfer (CMT). The differences in the residual stresses, microstructure and hardness properties in the welds made using two different bead patterns, a conventional 0-degree welding direction and a 45-degree hatch pattern, were studied. The general conclusion of these studies is that no significant differences caused by the welding direction and bead pattern can be observed. Specifically:

- No clear differences in the weld microstructure and fusion boundary were observed using SEM, EBSD and EDS.
- The microhardness measurements indicated higher fusion boundary hardness in the 0-degree welding direction sample, but the indentation hardness measurements did not show any such differences.
- The measured residual stress profiles were similar for both welding patterns. The simulated residual stress profiles differed below the surface due to higher tempering effect in the 45-degree welding simulation.
- The more complex bead pattern may render the weld more susceptible to more welding defects, such as lack-of-fusion and porosity, of which some evidence was found

Acknowledgement

This work was funded by the Finnish Nuclear Power Plant Safety Research Programme 2019-2022 (SAFIR2022) within the FENIX project. The authors would like to thank Taru Lehtikuusi (VTT), Jussi Loporanta (VTT), Johanna Lukin (VTT), Mika Jokipii (VTT) and Arto Nyholm (VTT) for their valuable contributions to this work. The EBSD and in-situ nanoindentation studies were performed using the Tampere Microscopy Center facilities at Tampere University.

References

- Huutilainen, C, Keinänen, H, Kuutti, J, Nevasmaa, P, Sirén, H, & Virkkunen, I. "Evaluation of an Alloy 52 / Cladded Carbon Steel Repair Weld by Cold Metal Transfer." Proceedings of the ASME 2021 Pressure Vessels and Piping Conference, PVP 2021. Volume 4: Materials and Fabrication. Virtual, Online. July 13–15, 2021. V004T06A048. ASME.
- Keinänen, H, Nevasmaa, P, Kuutti, J, Huutilainen, C, Virkkunen, I, Peltonen, M, & Sirén, H. "A52M/SA502 Dissimilar Metal RPV Repair Weld: Evaluation of Different Techniques." Proceedings of the ASME 2020 Pressure Vessels and Piping Conference, PVP 2020. Volume 6: Materials and Fabrication. Virtual, Online. August 3, 2020.
- Keinänen, H, Kuutti, J, Hytönen, N, Nevasmaa, P, Huutilainen, C, Virkkunen, I, Bhusare, S, Lambai, A, & Mohanty, G. "Effect of Welding Direction and Bead Pattern in Alloy 52 / SA508 Repair Weld." Proceedings of the ASME 2022 Pressure Vessels and Piping Conference, PVP 2022. Volume 4B: Materials and Fabrication. Las Vegas, Nevada, USA. July 17–22, 2022. V04BT06A053. ASME. <https://doi.org/10.1115/PVP2022-84662>
- Virkkunen, I, Peltonen, M, Sirén, H, Nevasmaa, P, Huutilainen, C, Keinänen, H, Kuutti, J, Lambai, A, Mohanty, G, & Honkanen, M. "A52M/SA52 Dissimilar Metal RPV Repair Weld: Experimental Evaluation and Post-Weld Characterizations." Proceedings of the ASME 2020 Pressure Vessels and Piping Conference, PVP 2020. Volume 6: Materials and Fabrication. Virtual, Online. August 3, 2020. V006T06A110. ASME.

6.6 Non-destructive examination of NPP primary circuit components and reliability of inspection (RACOON)

Ilikka Virkkunen¹; Arja Saarenheimo²; Tuomas Koskinen²; Oskar Siljama¹, Oskari Jessen-Juhler²; Qais Saifi²; Jari Rinta-Aho²; Yazemin Inc²; Mohammed Siddig²;

¹Aalto University
P.O. Box 14200, FI-00076 AALTO

²VTT Technical Research Centre of Finland Ltd
P.O. Box 1000, FI-02044 Espoo

Abstract

The project included studies relating to nondestructive evaluation (NDE).

NDE reliability was studied using virtual round robins (VRRs). The virtual round robin was a novel approach developed during the project, which enabled quantitative evaluation of NDE reliability in terms of probability of detection (POD) in the nuclear industry. The previous difficulties with POD evaluations and round robins were solved with the use of virtual flaws. Two virtual round robins were completed during the project and highlighted some important issues with NDE reliability in the challenging inspections of dissimilar metal welds.

Ultrasonic simulation was studied to enable more realistic ultrasound responses from difficult flaws to be simulated for use as virtual data or in AI/ML training. While marked advances were made, realistic ultrasonic simulation still requires further study and especially the computational burden associated with simulating 3D defects is still excessive.

Nonlinear ultrasonic techniques were studied to improve characterization of tight or closed cracks. Cracks were measured under varying thermal loading and compared with computational estimates of crack closure.

The applicability and reliability of machine learning in evaluating ultrasonic data was studied. Machine learning (ML) models were developed and trained to detect flaws in complex ultrasonic data. The results were compared with human performance. The results showed, that ML can reach human level performance in wide range of nuclear inspection cases and data-sets.

Finally, the ML results were compared with human responses collected in the second virtual round robin. Due to its consistency, the ML gave the best overall results in the VRR and showed that the use of ML as an aide to the inspector can help address some of the performance issues revealed by the VRR results.

Introduction

Efficient and reliable non-destructive evaluation (NDE) techniques support economical and safe operation of NPPs. The RACOON project, addressing “NDE on NPP primary circuit components and reliability of inspection” of the SAFIR2022

programme, focuses on the development and understanding of NDE methods with novel and state of the art approaches. The end goal is to increase reliability of inspections and find non-destructive approaches for aging monitoring. In 2020 small project ANDIE was merged to RACOON to provide machine learning (ML) aspect to non-destructive inspection. Since the feasibility study of the machine learning project proved successful the project has focused on developing the ML powered ultrasonic inspection as well as assessing and increasing the reliability of difficult inspections.

Reliability of non-destructive evaluation and probability of detection (POD)

WP1 focused on reliability of NDE. The goal for 2020 was to analyse and report the findings from the conducted virtual round robin (VRR). The participation for the VRR was good as 12 inspectors submitted back the results around the world.

In recent times, more and more of the inspections in the nuclear field are performed in a mechanized manner. This means, that the data acquisition and analysis, that were traditionally conducted simultaneously and interactively, are now separated to distinct steps. The analysis is often conducted in a different location after the data acquisition has been completed. This division can be carried over to the evaluation of NDT performance. While both successful data acquisition and evaluation are critical for the overall performance of the NDT, they can now be assessed separately. The quality of the data acquisition is, in general, far easier to evaluate. The potential sources of error include incorrect calibration of the equipment and failure to maintain sufficient probe coupling during scanning. These can often be evaluated without large mock-ups or representative flaws. In contrast, the data evaluation phase is challenging to evaluate because the evaluation procedures vary and may include significant human judgement. Thus, they necessitate relevant data and, traditionally, large mock-ups. Consequently, the primary interest for international round robin is for the evaluation and comparison of the data evaluation phase.

Transportation of the round robin mock-ups all over the world to NDT laboratories is costly and a slow process. While the round robin exercise gives valuable insight on the capability of the used NDT methods and procedures, they are seldom conducted due to fiscal and time constraints.

The use of virtual flaws (Virkkunen, Miettinen, & Packalén, 2014; Virkkunen, Rönnegård, Grybäck, Emilsson, & Miettinen, 2016; Svahn, Virkkunen, Zettervall, & Snögren, 2018) opened a possibility to conduct a virtual round robin exercise for mechanized data in a completely new way. The round robin was focused on the data analysis, where pre-acquired data was distributed around the world, making the exercise far more cost-effective than ever before. Moreover, as virtual flaws enable an ample flaw data generation a statistically meaningful sample could be generated to quantify the round robin performance with a POD. The VRR was

divided into two phases, manufacturing, scanning and augmentation of the flaws and result analysis.

In 2021 the work focused on creating a new VRR on the basis of lessons learned from the initial VRR. In the first VRR the available ultrasonic data was simplified and only B-scans were delivered to the inspectors to invite participation in ease of completing the VRR. In addition only one scan line with 45° was made at optimal angle in regards with the flaws. The instructors were also advised to use the same analysis procedure. The limitation of the ultrasonic data to one scan line, limited data to the inspectors differed from procedures used for actual inspections.

After participating in the first VRR it is assumed that the participation in the follow-up VRR would be more easily justified, even when the effort in participation is higher. So this VRR data was collected as rich multi-channel phased array data with industry standard acquisition procedures. This allows also the inspectors to use their own analysis procedures and possibility for flaw sizing as well. In the initial round robin the used flaws were mainly qualification flaws which are designed to be detectable, for POD also undetectable flaws are needed. This was alleviated by making synthetic changes to the available flaws in most importantly by reducing signal amplitude. This made the flaws quite repetitive and might have influenced the inspector responses. In addition the limited amount of raw canvas data might have exaggerated the repetitiveness. In the new VRR the data needed to be improved in flaw richness, flaw size distribution and more flaw free canvas data. (Meyer et al., 2021; Virkkunen, Koskinen, & Jessen-Juhler, 2021)

Generation of probability of detection curves was not directly possible from the available data due to limited amount of raw flaws, exceptional performance of some inspectors and lack of small flaws.

The work in 2021 started with acquisition of suitable DMW test blocks. The inspection target was selected to be VVER steam collector head provided by Fortum, while not exactly matching the western designs it was considered adequate for the purposes of this VRR. This is used to produce the raw canvas data. The flaw data was gathered from thermal fatigue cracks, by Trueflaw, produced into DMW plates provided by EPRI. A commonly understood best practice was used in gathering of the data. The flaw population was collected in a way that the DMW plates were initially scanned as clean data, and thermal fatigue cracks were grown into the plates. As the crack size was increased the plates were scanned multiple times to have a vast population of different sized cracks. As this was identified as one of the key improving points of the VRR a lot of effort was put into this, which in turn meant higher requirement of personnel resources as anticipated alongside with the reservation of the ultrasonic equipment. The eFlaw generation to the flaws was contributed by Trueflaw. Flaw data was extracted from the scanned data and re-introduced to the data.

In 2022, the generated files were distributed to international participants and results collected. As with the first virtual round robin, the results showed that inspectors display wide variability in performance. With the same exact data, the inspectors found between 17 and 64 out of the 66 potential flaws. With the complex multi-channel phased array data, new potential failure modes were revealed. The

misses were not well correlated with flaw size. This can be attributed to the flaw distribution, which emphasized very small and hard to detect flaws. Flaw saliency against background noise improved detection, but all the flaws exhibited sufficient saliency for detection. In addition, flaws only visible in “peripheral” channels were more often missed. This may indicate that the inspectors either used merge-views, which masked indications only present in some of the channels or focused their effort on the more central channels which can intuitively be considered more important. This tendency would decrease the benefit from using multiple channels in inspections and reduces the marginal advantage of adding more channels. The detection results are shown in Figure 1.

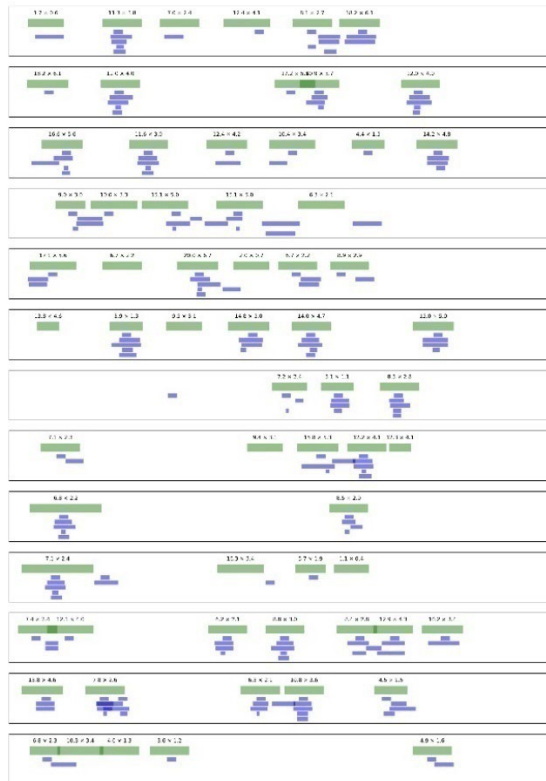


Figure 1. Detection results from the second virtual round robin. Top green bars show true flaw area (maximum changed area), annotated with nominal size (width x depth). Blue bars below show results from individual inspectors.

In the second virtual round robin, the data was sufficiently rich to allow meaningful sizing to be performed. Surprisingly, all the submitted sizing results were wildly inaccurate. In contrast to previous round robin, the inspectors did not voice concerns about the sizing accuracy due to limited data. The same physical cracks scanned

from slightly different distances and implanted in different data areas in the data were given very different sizing estimates that spanned the whole plausible range. Sizing results are shown in Figure 2.

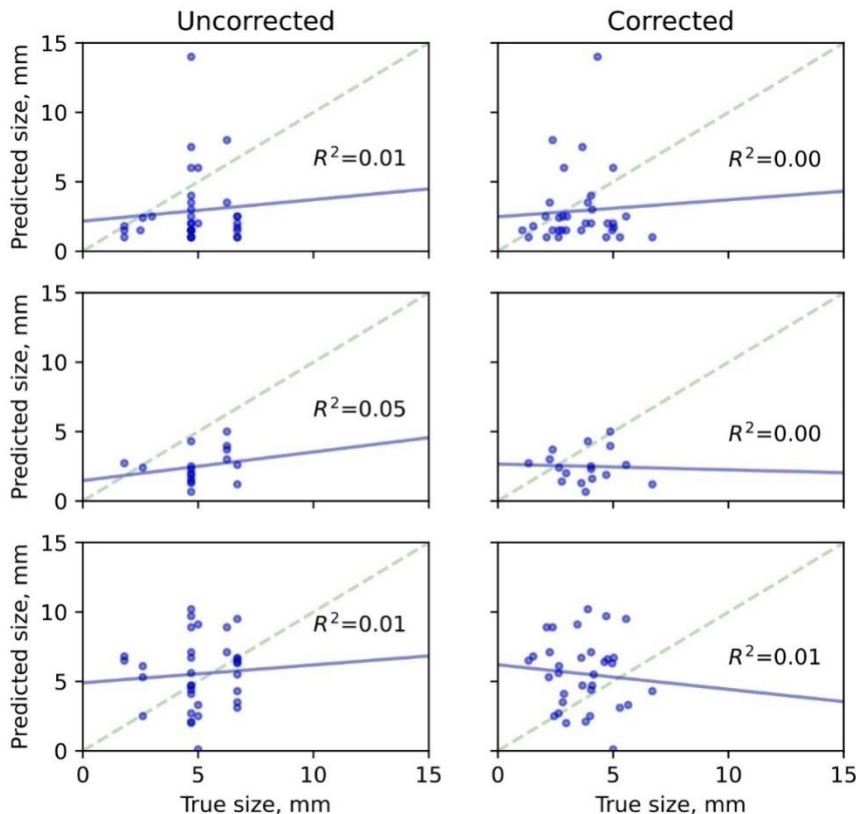


Figure 2. Sizing results showed poor correlation to the true sizing results. Even when considering the effect of amplitude change introduced for varied detectability in the eFlaw modification, the sizing results show no significant correlation with the flaw sizes.

Ultrasonic simulation

Ultrasonic simulation has been conducted in the WANDA project, predecessor to RACOON project (Koskinen & Virkkunen, 2018; Koskinen, Virkkunen, Papula, Sarikka, & Haapala, 2018) with CIVA simulation software. However, CIVA simulation approximates the signal widely and for anisotropic situations such as austenitic stainless-steel weld or dissimilar metal weld, the approximation might be too vague for proper use in reliability exercises or as training data for machine learning. (Virkkunen, Koskinen, Jessen-Juhler, & Rinta-aho, 2021; Siljama,

Koskinen, Jessen-Juhler, & Virkkunen, 2021; Koskinen, Virkkunen, Siljama, & Jessen-Juhler, 2021)

Finite element method FEM was speculated to give more accurate approximation for flaw signal generation and simulation efforts were started in 2D in 2019. As flaw signal generation was successful in 2D, the simulation model was extended to 3D shown in Figure 3a). The model was able to generate an A-scan show in Figure 3b). The simulations contained a simple phased array probe with a rexolite wedge. The wedge contained absorbing layers similar to a traditional wedge to reduce the noise from refracted ultrasonic waves. Unlike traditional ultrasonic probe, the transmitting and receiving elements do not have their own natural frequency, thus the recorded signal needs to be filtered digitally around this natural frequency to achieve the desired result. The material properties represented a homogeneous stainless-steel.

While both simulations in 2D and 3D were successful, the number of elements required made the computing time to exceed over 20 hours per single A-signal. As the simulated model was smaller than required for simulating a complete weld inspection the computation would take even longer with Abaqus based solver. Therefore, the time required to simulate a B-scan would take multiple these A-scans to be any use for reliability and machine learning exercises would be too great.

The next step for the simulation effort is to find a solution for this computation time issue. Since the Abaqus simulations did not scale with addition of computation power. One viable approach is to investigate other solvers, which might be more efficient in dealing with ultrasonic based problems.

For this work the Elmer solver was investigated. It was soon discovered that explicit solving is not possible in the Elmer solver and for a problem with a lot of small time steps implicit solving takes more time in the time steps. With GPU accelerated computing in the CSC supercomputers the issue might be overcome. However, within this project a novel numerical treatment is proposed to decrease the computation time. This is done with an in-house solver that utilizes the initial mass, stiffness and acceleration matrices produced by Elmer. In ultrasonic simulation problems the wave is propagating in only a small part of the complete model at each given time. In addition, the unwanted echoes originating from the borders of the simulation model cause problems to the interpretation of the results. In this treatment the model is discretized into rectangular elements with special node numbering. Then in the developed in-house solver with the special numbering the different regions can be activated and deactivated for the calculation according to the position of the wave propagation. This allowed the simulation time of 15 hours to be reduced to 10 hours when run with 1 cpu at the laptop computer.

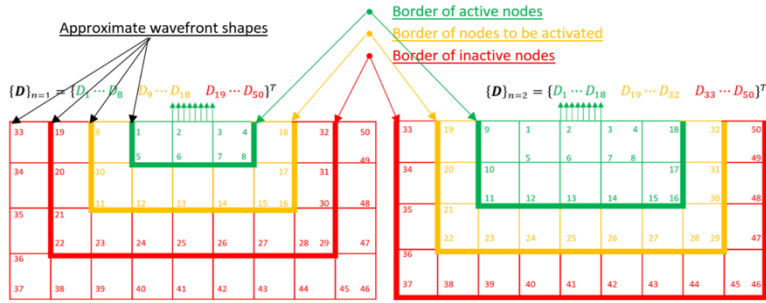


Figure 3. Discretization and special node numbering of the model in principle.



Node sets	Nodes		
	Start No.	End No.	Total
1	1	220291	220291
2	220292	399774	179483
3	399775	616561	216787
4	616562	801153	184592
5	801154	1019021	217868
6	1019022	1356935	337914
7	1356936	1708897	351962
8	1708898	2072647	363750
9	2072648	2351455	278808
10	2351456	2572836	221381
11	2572837	2846197	273361
12	2846198	3064484	218287
13	3064485	3216796	152312

Figure 4. Discretization and special node numbering in the model in practice.

FEM software	CPUs	Simulation time [hour]
Abaqus (notch 1 case)	12	14.75
In-house solver	1	~10

Figure 5. Reduce in the simulation time.

However, currently the simulation procedure requires a lot of expert knowledge and the activation and deactivation of the different node sets is done manually. A lot of work need to be done in order to get the model producing multiple flaw simulations. The project personnel had to be changed from the previously planned due to

personnel changes in VTT, this effected the focus of the work package. Due to the personnel change reasons and project budget reductions the simulation part was dropped from the 2022 project.

Machine learning for automated data evaluation

WP3 build on the existing knowledge of the feasibility and use of ML models in ultrasonic data analysis. The feasibility study carried out in 2019 showed that the virtual flaw system can be used to train the machine learning model to do weld inspection in austenitic stainless steel welds with simple ultrasonic data. The performance was also compared with human inspectors and human level performance was achieved (Virkkunen et al., 2021).

After the feasibility study a data rich multi-channel phased array data from austenitic stainless steel weld was inspected with the machine learning model. The model was trained with thermal fatigue flaws using the virtual flaw tool as well. Again, the results were compared with the human inspector using the VRR tool developed for the VRR in WP1 and human level performance was reached. (Siljama et al., 2021). This was also the case study selected in the discussions with TVO.

After studying the feasibility of thermal fatigue cracks and austenitic stainless steel a study in DMW was made using different flaws in simulated flaws, EDM notches and solidification flaws. In the study it was found out that the smallest detectable flaws are closely related to the smallest flaws used in training. Also, the flaw type used in training should represent the flaw type of the inspection object. The PODs of the different training sets were assessed with the VRR tool. (Koskinen et al., 2021)

For 2021 the DMW inspection target in the steam generator mock-up was identified with Fortum and the mock-up delivered by mock-up. However, the starting of the work was delayed due to VTT personnel changes and reductions and the ultrasonic equipment being reserved for WP1 scans. When the scans could be started a lot of difficulties occurred in the DMW scanning. The initial mock-up was too big for the VTT scanner and the scanner code needed to be modified to enable the scanning of larger component with a radius bigger than we can use in the rotational manipulator. This work was done for the training/qualification mock-up yd016. After scanning it the flaws were not very clearly visible and extraction of the flaws proved difficult, which caused extra work in the data augmentation. After scanning the mock-up for flaws the steam generator weld was scanned for the canvas data. However, due to the size of the mock-up it is impossible to fit it to the VTT scanner and the scanning had to be done manually. This caused time and resource delays as the scanning had to be re-done, because the movement of the probe could not be done slowly and steadily enough with the initial scanning procedure. The report on the performance of the inspection system is delayed as it is still in the data augmentation phase.



Figure 6. DMW steam generator mock-up.

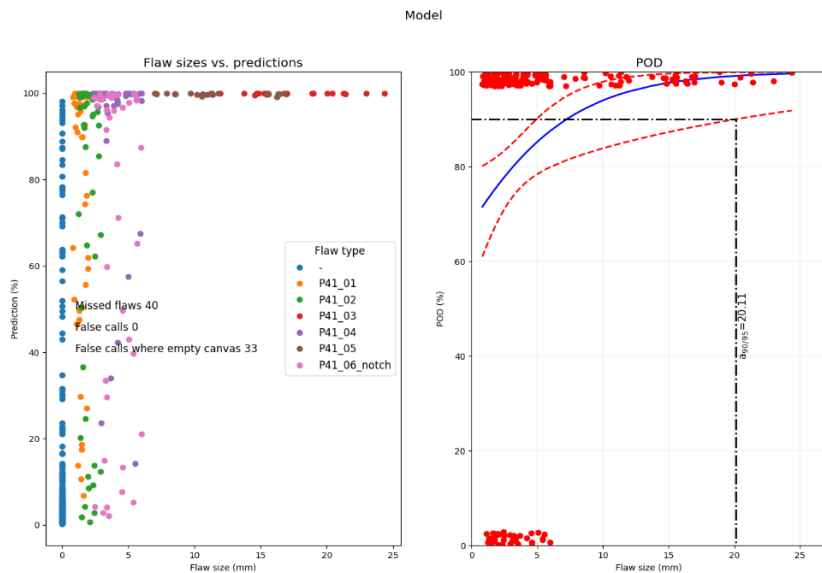


Figure 7. Performance of the austenitic stainless steel model in DMW.

In the scientific publication for WP3 transfer learning is studied. In the project the model developed for multi-channel ultrasonic analysis in austenitic stainless steel weld with thermal fatigue cracks is used for DMW weld inspection.

The initial results show that the model can generalize a little bit to the DMW but the results are very poor with $a_{90/95}$ of 20.11 mm and a lot of missed flaws and false calls are made. However, the model still can generalize to the DMW weld.

To improve the model is re-trained with a small DMW subset. The subset is too small in size for training the model completely and would lead to overfitting of the

model. The re-training only allows the alteration of the dense layer of the model (the decision layer).

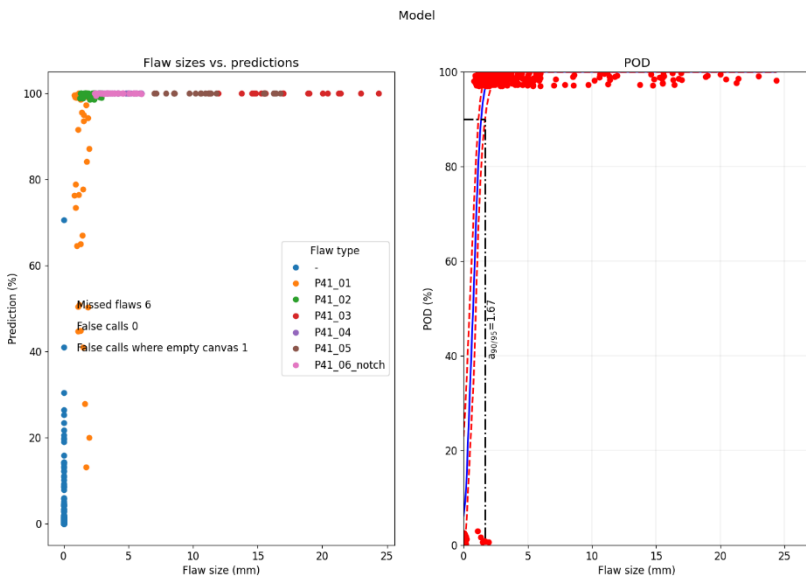


Figure 8. Results after DMW re-training.

After re-training with the DMW data set the results are very good the $a_{90/95}$ value of 1.67 mm and only 1 false call with 6 missed small flaws present.

In 2022, Machine learning model was developed for reactor pressure vessel inspection. The inspection made use of multi-channel phased array ultrasonic data. The data was carefully calibrated to maximize the benefit gained from multiple channels and to allow accurate merging of different channels without shadowing of small flaw signals. The mock-up proved challenging for the ultrasonic inspection and the data exhibited significant coupling variations and other data quality issues. Thus, part of the challenge was to train the model in a way to allow the model to gracefully degrade in the face of poor data quality.

Effects of ML on NDE reliability

While the virtual round robin was initially planned exclusively for human participation, the rapid development of ML models allowed us to also use it to test the potential effect of ML on the detection capability. To this end, the best available model was taken and adjusted to fit the data used in the second virtual round robin (i.e. the EPRI-Trueflaw model). The virtual round robin data was evaluated with the model.

Despite not being explicitly trained for this data type, the model performed quite well and exceeded the detection capability of the human participants. Thus, had a human participant used ML such as this model, it would have made it the best submission in the round robin. The limitations in the human participants' performance were, to certain extent, attributed to susceptibility to miss flaws only visible in small number of channels and/or peripheral channels. In contrast, the ML evaluates each channel identically and repeatably. Thus, it appears the ML addresses the very issues stemming from large data volume and highlighted by the second virtual round robin. The comparison of human participants to AI is shown in Figure 9.

While the ML model showed top detection performance, it also made somewhat more false calls than the human participants. The false call performance is still easily acceptable, especially when viewed as an assistive tool to a human inspector. In this setting, the human inspector can evaluate all the indications and disregard false calls as appropriate.

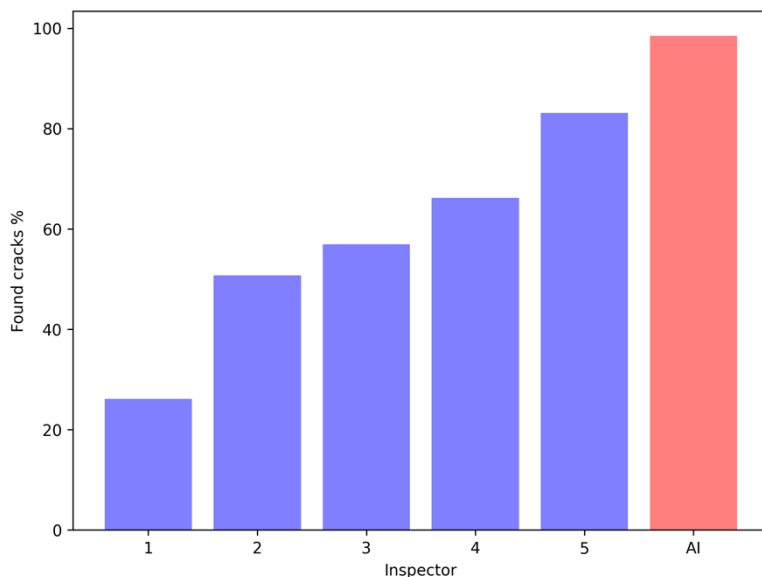


Figure 9. Comparison of percentage of detected flaws between human participants and ML evaluation. The ML shows the best detection rate.

Summary and conclusions

The RACOON project featured groundbreaking research in multiple fronts. In particular, the project oversaw the development and administration of a first-of-a-kind virtual round robin to study NDE reliability. The project also showed that Machine learning techniques are capable of handling modern data evaluation to

human level performance and show significant potential in improving NDE effectiveness and, in particular, addressing the human factors issues that are inherent in NDE data evaluation. The following contributions to nuclear safety are recognized:

- New tools developed (VRR) to assess NDE reliability
- VRR highlighted new areas of interest for NDE reliability; especially issues with DMW inspection and sizing
- Demonstrated human level AI/ML performance in NDE
- Demonstrated that AI can address some of the deficiencies highlighted in during the reliability studies.

Acknowledgement

EPRI provided test pieces used for some of data generation and (with Trueflaw) offered ML state-of-the-art models for comparing ML and human performance in the second virtual round robin. Trueflaw contributed eFlaw augmentation that allowed training of high performance ML models. Their support is gratefully acknowledged.

References

- Koskinen, T., Virkkunen, I., Papula, S., Sarikka, T., & Haapalainen, J. (2018). Producing a POD curve with emulated signal response data. The British Institute of Non-Destructive Testing. *Insight-Non-Destructive Testing and Condition Monitoring*, 60. *Insight-Non-Destructive Testing and Condition Monitoring*, 60(1), 42-48. Retrieved from <https://www.ingentaconnect.com/content/bindt/insight/2018/00000060/0000001/art00009>
- Koskinen, T., Virkkunen, I., Siljama, O., & Jessen-Juhler, O. (2021). The Effect of Different Flaw Data to Machine Learning Powered Ultrasonic Inspection. Springer Science and Business Media LLC. *Journal of Nondestructive Evaluation*, 40. *Journal of Nondestructive Evaluation*, 40(1). doi:10.1007/s10921-021-00757-x
- Koskinen, T., & Virkkunen, M. (2018). *Hit/Miss POD With Model Assisted and Emulated Flaws*. Proceedings from 12th ECNDT, Gothenburg, Sweden.
- Meyer, R., Virkkunen, I., Holmes, A., Morales, R., Seuaciuc-Osorio, T., & Lin, B. (2021). Results of a Virtual Round Robin Study to Estimate Probability of Detection for Dissimilar Metal Welds 48th Annual Review of Progress in Quantitative Nondestructive Evaluation. United States.
- Siljama, O., Koskinen, T., Jessen-Juhler, O., & Virkkunen, I. (2021). Automated Flaw Detection in Multi-channel Phased Array Ultrasonic Data Using Machine Learning. Springer Science and Business Media LLC. *Journal of Nondestructive Evaluation*, 40. *Journal of Nondestructive Evaluation*, 40(3). doi:10.1007/s10921-021-00796-4

- Svahn, P.-H., Virkkunen, M., Zettervall, T., & Snögren, D. (2018). *The use of virtual flaws to increase flexibility of qualification*. Proceedings from 12th European Conference on Non-Destructive Testing, Gothenburg 2018, June 11-15 (ECNDT 2018).
- Virkkunen, I., Miettinen, K., & Packalén, T. (2014). *Virtual flaws for NDE training and qualification*. Proceedings from 11th European Conference on Non-Destructive Testing, Prague 2014, Oct 6-11 (ECNDT 2014).
- Virkkunen, I., Koskinen, T., & Jessen-Juhler, O. (2021). Virtual round robin—A new opportunity to study NDT reliability. Elsevier. Nuclear Engineering and Design, 380. *Nuclear Engineering and Design*, 380, 111297. Retrieved from <https://www.sciencedirect.com/science/article/pii/S0029549321002491>
- Virkkunen, I., Koskinen, T., Jessen-Juhler, O., & Rinta-aho, J. (2021). Augmented Ultrasonic Data for Machine Learning. Springer Science and Business Media LLC. *Journal of Nondestructive Evaluation*, 40. *Journal of Nondestructive Evaluation*, 40(1). doi:10.1007/s10921-020-00739-5
- Virkkunen, M., Rönneteg, U., Grybäck, T., Emilsson, G., & Miettinen, K. (2016). *Feasibility Study of Using eFlaws on Qualification of Nuclear Spent Fuel Disposal Canister Inspection*. Proceedings from 12th International Conference on NDE in Relation to Structural Integrity For Nuclear and Pressurized Components, Dubrovnik, Croatia.

6.7 Fatigue Management for LTO (FATIMA)

Tommi Seppänen¹, Jussi Solin¹, Jouni Alhainen¹, Esko Arilahti¹, Petri Lemettinen²,
Rami Vanninen³, Erkki Pulkkinen³

¹VTT Technical Research Centre of Finland Ltd
P.O. Box 1000, FI-02044 Espoo

²Fortum Power and Heat Oy
P.O. Box 100, FI-00048 FORTUM

³Teollisuuden Voima Oyj
Olkiluoto, FI-27160 Eurajoki

Abstract

The general objective of FATIMA was to go beyond existing state-of-the-art in fatigue management for long-term operation, including accounting for environmental effects on fatigue life. In the longer term, improved methods can be adopted as alternatives to existing practices through a combination of scientifically solid justification and international acceptance.

The FATIMA project aimed to understand the current state-of-the-art in codified practices for environmentally-assisted fatigue. The project team joined an international collaboration group on the topic for visibility and active discussions.

Experimental project work consisted of fatigue studies on a stainless steel pipe manufactured to Olkiluoto 3 specifications. The results, which are limited to air environment, fully align with expectations and highlight benefits of material-specific understanding and application.

The planned experimental campaign in simulated reactor water could not be realized during the project timeframe. A modernized research facility for this purpose was designed and procured, but commissioning continues beyond the project.

Introduction

The general objective of FATIMA project, which started in 2020, was to go beyond existing state-of-the-art in fatigue management for LTO, accounting for environmental effects on fatigue life. The main body of work was divided into three work packages, identified in Figure 1. They focus on international state-of-the-art and collaboration activities (WP1), environmentally-assisted fatigue (EAF) (WP2) and fatigue studies in air (WP3).

Successful R&D on material performance and ageing mechanisms has made it possible to refine specifications for materials and plant operation to exclude many failure scenarios, but cyclic strains caused by thermal transients cannot be excluded

and fatigue remains a life limiting ageing mechanism. Mechanical loads and vibration excitation can also contribute to fatigue.

Monitoring and mitigation of Cumulative Usage Factor (normally for CUF ≤ 1) for fatigue is a challenge for long-term operation (LTO) and optimization of in-service inspection programs (RI-ISI). The priority of inspection correlates with codified calculation of component usage (CUF). Improved realism in fatigue management allows maintaining high load factors and economic competitiveness for ageing plants without compromising safety. In addition, improved timing and focus of non-destructive evaluation or repair reduces radiation doses of personnel.

Fatigue management is based on international practices, codes and standards. Improved methods can be adopted through scientifically solid justification and international acceptance, but consensus on current codes and state-of-the-art for environment assisted fatigue (EAF) has been lost. Together with the debated and evolving F_{en} models for accounting the effects of reactor coolant water, ambiguity and volatility in fatigue assessment rules may cause uncertainty in long-term fatigue management of primary piping components.

Such uncertainty requires mitigation through responsible experimental research and development of science-based EAF models which remain compatible with the design codes and transferable to NPP components. This is the aim and long-term goal of FATIMA. As our research capacity is limited, opportunity for collaboration with major international stakeholders is an attractive route for discussion and wider acceptance of proposed methodologies.

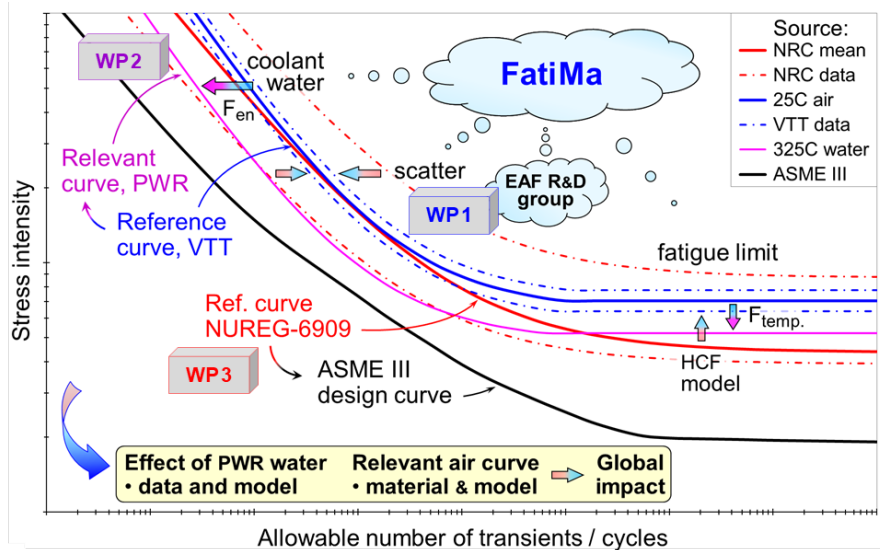


Figure 1. Research themes of the FATIMA project.

International state-of-the-art and collaboration

The original ASME III (ASME, 1963), first published in 1963, served as a common root for all design codes and standards currently used for design and safety assessment of NPP primary loop pressure boundaries. The Finnish YVL Guide E.4 (STUK, 2020) requires that the general safety level of ASME III shall be met, but also other Design Codes can be applied [e.g. RCC-M (AFCEN, 2016), KTA 3201.2 (KTA, 2013), PNAE G-7-002-86 (Energoatomizdat, 1989)].

Transferability of laboratory results to components in plants was a key target for the original ‘design by analysis’ fatigue assessment procedures, but ignored in some later adjustments. The current fatigue design curve for stainless steels in ASME Code section III is an example of this. The German KTA (KTA, 2013) and Japanese JSME (ongoing) make clear distance to fatigue rules in ASME III (ASME, 2010). The French RCC-M (AFCEN, 2016) aims to maintain partial compatibility with ASME III, but with some corrective measures.

Solin et al. (2020, 2021, 2022) reviewed the international state-of-the-art. The various challenges in management of fatigue and the evolving state-of-the-art in different codes, standards, rules and assumptions were discussed. The roots and current status of fatigue curves and design criteria applied in Finnish NPP’s were described in detail. The notable differences between the selected design codes are an interesting detail, when considering that all applicable design codes were originally rooted from the same ASME III code from 1963.

Challenges remain in developing common understanding and practical application(s) for management of EAF while avoiding unnecessary conservatism without compromising safety and operability of reactors. It was suggested that collaboration between major stakeholders and contributors is needed, if harmonization of the design criteria and regulation is sought for internationally. The suggestion is also a direct reference to the collaboration activities within FATIMA.

The specific goal of collaboration activities was membership and active participation in an international EAF R&D Collaboration Group, moderated by EPRI and formed by the major global stakeholders in EAF research. Meetings of the group are organized for ideation and discussion between leading experts in the world.

In 2020, Team Finland joint membership of VTT, Fortum and TVO entered the EAF R&D Collaboration Group as a new participant. The group has not met physically since the beginning of the global pandemic, but has kept discussion active in online webinars, including an introductory presentation of Finnish EAF activities in the past and present. The motto of Team Finland is “*solution-oriented continuous improvement based on state-of-the-art and scientific approach for LTO*”.

Research facility for simulated PWR water

Research on EAF for reactor materials can be divided in two main groups:

- Fatigue crack growth tests, typically using compact tension (CT) specimens. The tests aim to determine acceleration of crack growth rates due to hot water environment, and to solve the underlying mechanisms.

The results are applied for improving safety during reactor operation, determination of applicable inspection intervals and for assessment of safe operation before repair in cases of crack detected or assumed in a component.

- Axial low cycle fatigue (LCF) tests aiming to determine reductions of fatigue endurance due to hot water environment using smooth specimens. These results challenge the results of fatigue assessments and reduce the allowable fatigue cycles (transient budgets). During reactor operation assessed cumulative fatigue usages are multiplied by penalty factors (F_{en}).

VTT has performed both types of fatigue research in reactor coolant environment. The former type was adopted first, more than 40 years ago, as part of broad international collaboration and was directly linked to safety concerns and inspections according to the ASME XI (ASME, 2019). The laboratory data on crack growth rates is explicitly transferable to fatigue assessment during operation of plant.

The second type of environment assisted fatigue landed VTT laboratory about twenty years later, again amid broad international activity. A first prototype EAF device was developed for this purpose (Solin et al. 2003, 2005; Solin, 2006). At the time, the F_{en} factors were based on regression fits for partly questionable laboratory data without a science-based model or knowledge of underlying mechanisms. Transferability of the laboratory results to operating NPP components is complex, but this LCF type of testing in environment has become dominant and today, the term EAF typically refers to this type of experimental research.

VTT has a mission to provide the utilities and regulator with state-of-the-art technical support. This includes fatigue management and optimization of risk informed in-service inspection (RI-ISI) programs. Interest in experimental research on environmental effects in reactor coolant environment raised when new requirements on EAF were looming and even a reactor project (OL3) was in sight. Building an experimental facility was justified because readiness to perform appropriate EAF testing was missing in Europe. Direct strain control was set as the goal at VTT, because it would ensure obtaining unbiased LCF data directly applicable for fatigue assessment and for comparison with the design curves. This was achieved with the second EAF device, FaBello, in the SAFIR2010 FATE project (Solin et al. 2011).

The FaBello facility was tailored for researching the conservative edge of EAF with slow strain rates at reactor normal operation temperatures which lead to high predicted F_{en} factors approaching the saturation values according to the currently endorsed models (Chopra and Shack, 2007; JSME, 2006). The FaBello results indicate that the current models may be overly conservative in the studied range of test parameters. However, notable parts of fatigue usage in operation of NPP's originate outside of the studied range, namely of the strain rate parameter.

In aim to optimally serve needs of realistic fatigue data for long-term fatigue assessment of primary circuit components, capacity for higher strain rates and amplitudes, preferably including variable amplitudes and realistic time-based signals was desired. A typical set of fatigue relevant transients occurring in PWR

reactors' safety injection (SIS) and surge lines is illustrated in Figure 2. This kind of cycle cannot be simulated in the FaBello facility. A system upgrade was deemed necessary to perform experiments with better control and more relevant test parameters.

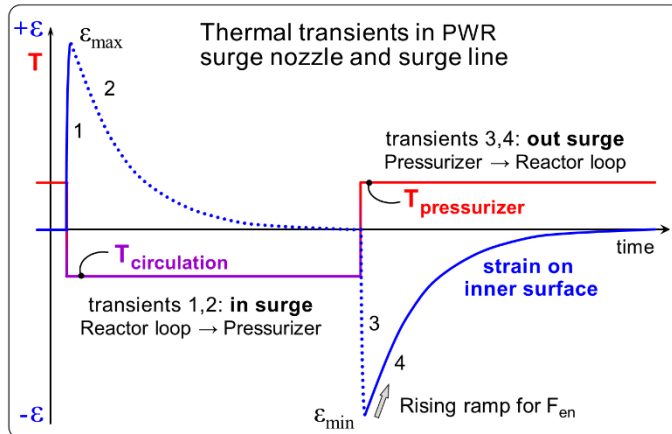


Figure 2. Example of fatigue transients including a broad range of strain rates.

The transformation from pneumatic servo-controlled FaBello to the third generation EAF facility “FaVite”, was near completed during the FATIMA project and will be finalized during 2023. The search for a new solution for the load train ended in selection of ball bearing screw driven linear actuators, which become the key components for the new load trains – outside the autoclave. The water circulation loop, autoclaves and eddy current sensors from FaBello are reused, but new lids for the autoclaves and mechanical parts have been redesigned. Much of the technical solutions will follow the model applied in FaBello and the lead through of the load train to the pressurized autoclave takes model and experience from the facilities where the external load was generated by servo hydraulic actuators.

The assembled components of the FaVite unit are summarized in Figure 3. As can be seen on the left, the assembly on top of the autoclave becomes high and heavy. New supporting and lifting devices had to be designed and manufactured (Monto, 2022). The parts submerged inside the autoclave play similar roles as in FaBello, but the load train arrives through the lid and the bellows are removed. However, every part is redesigned to improve the operability and accessibility to make mounting of the specimen and instrumentation easier. The openings in the load frame are broader, the weight of strain measuring devices is reduced and their attachment to the specimen gauge section is supported by jigs, which guide the contact points directly to the desired spots. The principle of coaxial strain measurement below the specimen and load frame is similar to that in FaBello. A more thorough technical description of the FaVite facility is given in a research report (Solin et al., 2023).

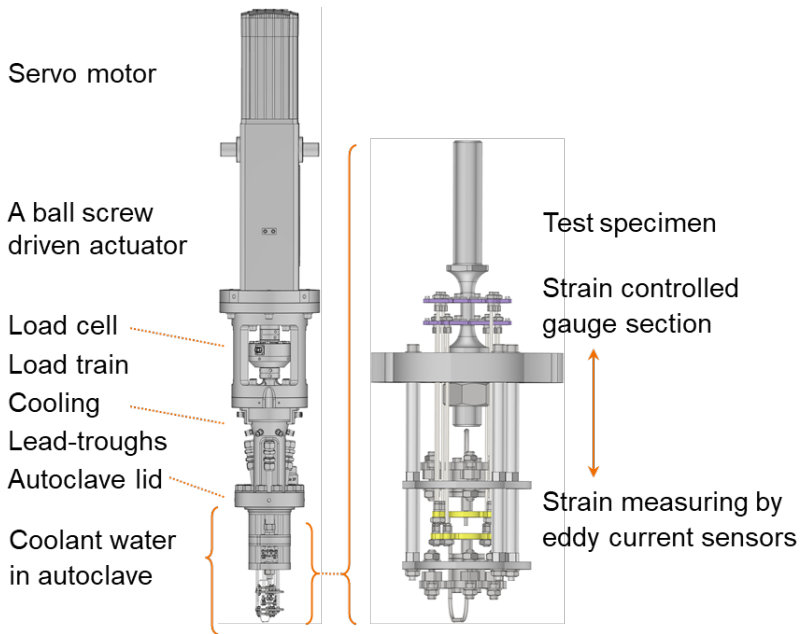


Figure 3. Assembly of FaVite for strain controlled axial fatigue in simulated reactor coolant water.

Experimental characterization of an EPR pipe material

In July 2021, nearly 7 meters of seamless 12" Schedule 140 pipe ($\varnothing 323.85$ mm x 28.58 mm thick) in the solution annealed and quenched condition was provided by TVO to VTT. The pipe, shown in Figures 4–5, fulfills the RCC-M Class 1 requirements for Z2CND1812 N2 which is roughly equivalent to AISI 316L austenitic stainless steel. The microstructure consists of a range of grain sizes with numerous twins, as seen in Figure 6 for the orthogonal plane of the pipe. The material report gives an average grain size G=6.

Round bar specimens were extracted around the circumference of the pipe, in the longitudinal direction. All specimens were manufactured by turning, after first cutting approximately 200 mm long rings. Three rings were sawed: two from the ends of the pipe (rings "A" and "ZZ") and one from the mid-length (ring "P"). Cutting plans were drawn up to evenly distribute tensile, cyclic stress-strain curve (CSSC) and LCF specimens. Specimens were taken close to the inner pipe surface, as shown in Figure 5 for ring "P".

Dimensions of the Ø8 mm specimen for LCF, CSSC and tensile tests are shown in Figure 7. Specimens were polished in several stages, up to 1 µm diamond paste. Visual examination was done to confirm absence of transverse machining marks.

Experimental program details and results are given in Seppänen et al. (2022, 2023). A summary is given below.



Figure 4. Seamless 12" Schedule 140 Z2CND1812N2 (\approx 316L) EPR pipe.

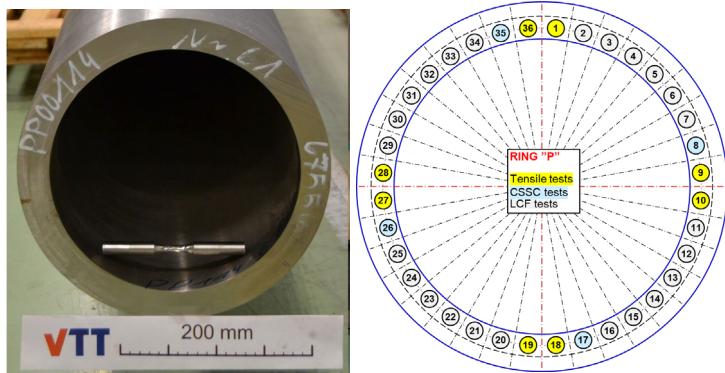


Figure 5. Z2CND1812N2 pipe cross-section with LCF specimen for scale (left) and specimen cutting plan from ring "P" (right).

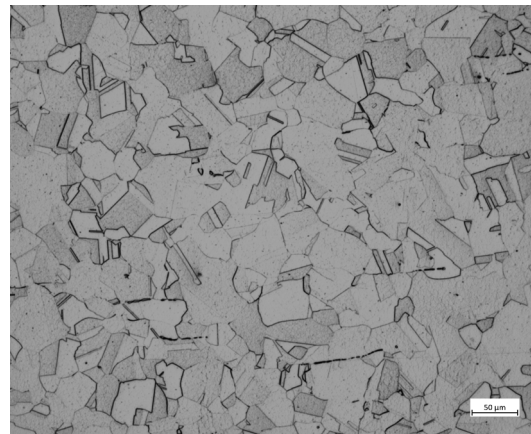


Figure 6. Orthogonal plane microstructure of the pipe in ring P.

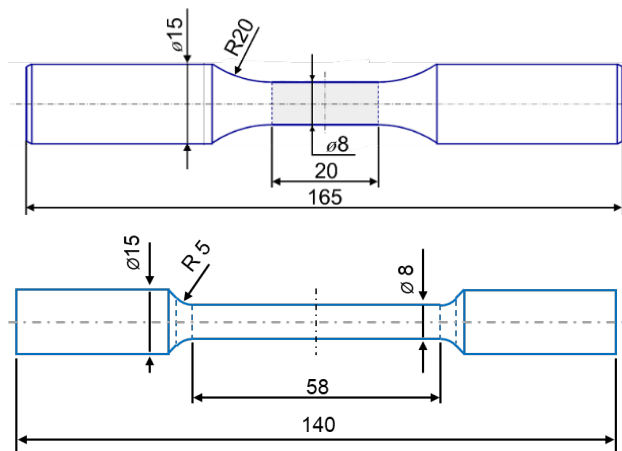


Figure 7. LCF, CSSC (top) and tensile test specimen (bottom) drawings in mm.

Tensile testing was performed at room temperature in an MTS 250 kN rig equipped with precision alignment grips, roughly in accordance with the ISO 6892-1:2019 standard (ISO, 2019). The alignment of the load train was performed prior to testing following the procedure in ASTM E1012-19 (ASTM, 2019a). Strain was measured and controlled using a 50 mm gauge length MTS extensometer. Digital image correlation (DIC) measurement was used in parallel to the extensometer in some experiments.

Strain rates between 0.0025–0.25 %/s were applied, 0.025 %/s up to 2% and continuation at 0.25 %/s being the ‘normal’. In all tests, a partial unloading was performed near the start of the test to measure elastic modulus. Some experiments were performed with multiple unloadings to evaluate the change of apparent modulus as a function of strain. True stress-strain curves were estimated based on instantaneous cross-section data obtained from DIC.

The average results of tensile tests are shown in Table 1 for each ring and separately for the slow strain rate tests performed from ring “P”. Stress-strain curves are shown in Figure 8. In general the results agree well with values from the material report and fulfill the minimum requirements for Z2CND1812 N2 indicated in RCC-M article M 3304.

Apart from the elastic modulus, there appear to be small but measurable differences between properties as a function of pipe location. Tenfold reduction of strain rates changes the response so that the yield strength and flow stress is reduced. However, the tensile strength is increased because of extended elongation at slow strain rate.

Table 1. Average room temperature tensile properties from experiments and material report.

	Ring				Material report
	A	P	P slow rate	ZZ	
E [GPa]	197	196	196	197	–
R _{p0.2} [MPa]	278	287	276	270	267
R _m [MPa]	586	585	592	571	574
A _s [%]	53	55	68	56	54
Z [%]	75	77	77	79	81

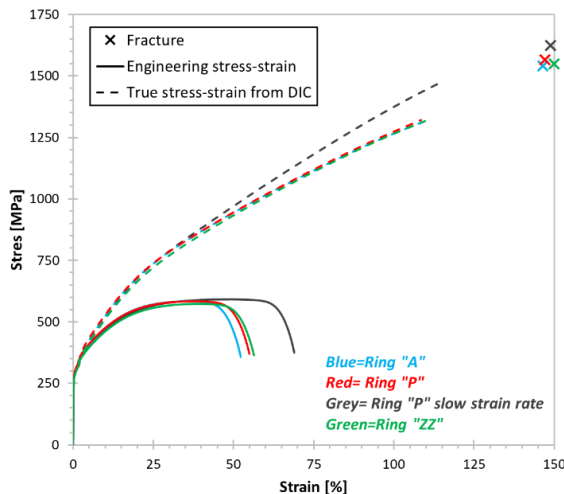


Figure 8. Summary of monotonic stress-strain curves at room temperature.

Strain-controlled ASTM E606-19 (ASTM, 2019b) LCF testing was performed at room temperature and elevated temperature in an MTS 250 kN testing machine equipped with precision alignment grips. Same alignment procedure was used as in tensile tests. At room temperature strain was controlled and measured using an 8 mm gauge length MTS extensometer. At 300 °C a 12 mm gauge length MTS extensometer, compatible with the MTS 653 high temperature furnace, was used.

All tests were performed using a triangular waveform at a constant strain rate 0.4 %/s for both tensile and compressive ramps. The definition of fatigue life N_{25} was chosen as the number of cycles to a 25% drop in peak stress from its absolute maximum value reached during primary hardening. N_{25} lives in these experiments are not particularly sensitive to the chosen reference point.

Cyclic stress-strain curves were defined using the spectrum straining method (Solin, 1986) with two different maximum strain amplitudes, 0.3% and 0.6%. This

method was previously successfully applied for studying stabilized stainless surge line piping (Solin et al., 2009).

Figure 9 shows all room temperature 316L strain-life data and best-fit curves plotted as elastic (blue), plastic (green) and total strain (black) amplitudes. Average strains until N_{25} were used. Regression of the elastic and plastic strain amplitudes was performed using power law equations suggested by Basquin (1910) and Coffin and Manson (Coffin, 1953;Manson, 1953), respectively. Comparison is made to the best-fit curve from NUREG/CR-6909 (Chopra and Shack, 2007) (red curve), which is the underlying technical basis document for the design fatigue curve in ASME III. Figure 10 shows all 300 °C strain-life data with the same regression principle and comparison as in Figure 9.

At room temperature, the best-fit curve to ring A, P and ZZ data differs considerably from the best-fit curve of Chopra (Chopra and Shack, 2007). For much of the LCF region, there is a near constant factor of about two conservatism in the latter, which is currently used to derive the ASME III design fatigue curve. Towards HCF, the curves appear to converge but more experimental results from the EPR pipe would be necessary to confirm this. At 300 °C, the general conclusions from a limited number of ring ZZ results are similar. The data suggests a change in the slope of the plastic strain regression curve. For LCF, this continues to mean a conservatism in the Chopra best-fit curve. In HCF, some data are underpredicted with the Chopra best-fit curve.

Overall, the level of scatter in the EPR pipe fatigue data appears very reasonable. Using the repeat tests at room temperature with 0.3% strain amplitude, a 5% lower bound with a factor of 1.4 on fatigue life has been estimated. For comparison, the ASME III stainless steel DFC is based on a factor of 2.3 for heat-to-heat variability, as suggested in NUREG/CR-6909 (Chopra and Shack, 2007).

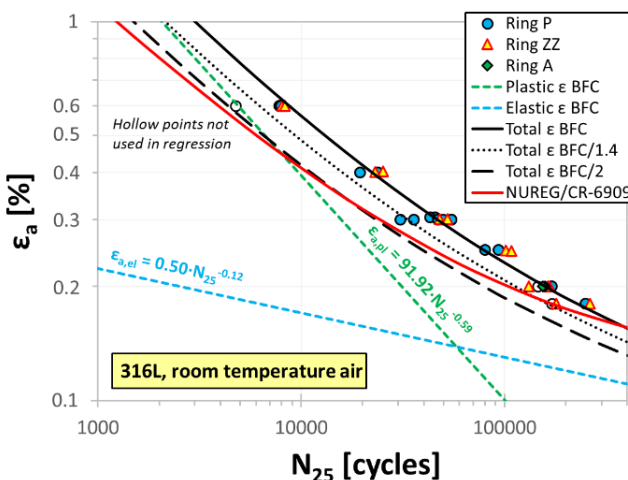


Figure 9. Strain-life best-fit curves for room temperature 316L data. Comparison is made to NUREG/CR-6909 best-fit curve.

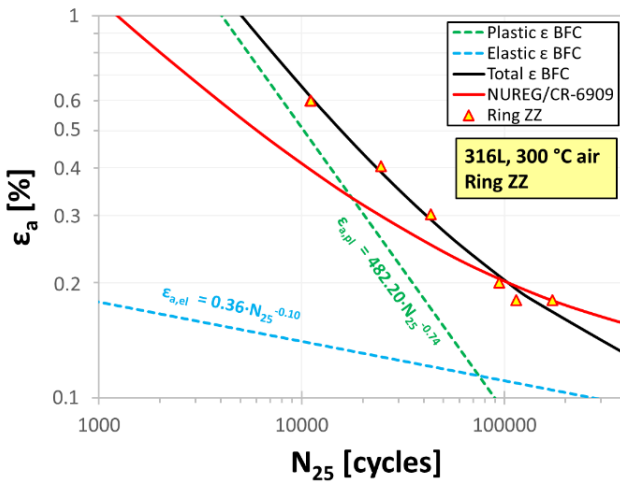


Figure 10. Strain-life best-fit curves for 300 °C 316L data. Comparison is made to NUREG/CR-6909 best-fit curve.

Figure 11 shows the stress responses at each chosen strain amplitude level. The plotted series of experiments was tested from a single 90° sector of ring P. Always, early cyclic hardening was followed by a lengthy period of cyclic softening. The cyclic hardening duration (in cycles) and measure (in MPa) was proportional to strain amplitude. Clear secondary hardening was not observed regardless of strain amplitude. The sudden upturn in the 0.18 % curve is a typical sign of crack initiation either outside the strain-controlled region or 180° to the extensometer, rather than material behavior. As such, these results should be treated with caution, particularly in HCF. For the Coffin-Manson-Basquin regression, these suspect points were not included.

Hysteresis loops of room temperature LCF experiments from one 90° sector of ring P are shown in Figure 12. Each loop is representative at approximately half-life, but note from Figure 11 that true stabilization of the stress response was typically not observed.

The cyclic stress response of ring ZZ at 300 °C is shown in Figure 13 for equivalent strain amplitudes as tested in room temperature. An obvious difference caused by temperature is the general softening. That is, the absolute stress amplitude is lower at 300 °C than room temperature. Beyond that, there is a higher tendency for secondary hardening at 300 °C, which is much less pronounced at room temperature or even non-existent at low strain amplitude. The onset of secondary hardening at 300 °C depends on the strain amplitude, taking many more cycles to show at $\epsilon_a=0.6\%$ than $\epsilon_a=0.18\%$. On the other hand, primary hardening at $\epsilon_a=0.6\%$ is more prevalent at 300 °C than at room temperature.

The secondary hardening of non-stabilized 316L at elevated temperature is in stark contrast to niobium stabilized X6CrNiNb1810, which secondary hardens at room temperature (Solin et al. 2009) but not at operating temperature. The

mechanisms responsible for such behavioral differences deserve more attention for a better understanding of primary piping materials. An immediate effect of secondary hardening, however, is a likely sharp endurance limit. The data at $\varepsilon_a=0.18\%$ results in finite life, but it is plausible that the endurance limit is not far off. In other words, secondary hardening would likely overcome the driving force necessary for crack growth when experimenting further at $\varepsilon_a<0.18\%$.

Room temperature CSSC curves are shown in Figure 14 along with representative monotonic tensile curves and constant amplitude LCF half-life data. Taking into account the higher strain rate for cyclic tests, the stress response during the first cycles matches well with the monotonic tensile curves. Short initial hardening phase is followed by cyclic softening, which leads the half-life stress response below the monotonic curve at low strain amplitudes. As seen in Figure 14, the softening phase is cut short during the tests at 0.6 % amplitude.

The 50 cycle block applied for spectrum straining CSSC tests contains one cycle with strain amplitude 0.6% and smaller cycles in random order. All amplitudes are divided by two for the second variant of test. For both variants, cyclic hardening occurs during two to three first repeats of the 50 cycle spectrum blocks. Peak hardening responses are shown for $40 \leq N_{\text{tot}} < 190$ in Figure 14. The following softening modifies the CSSC which differentiates notably from the monotonic response.

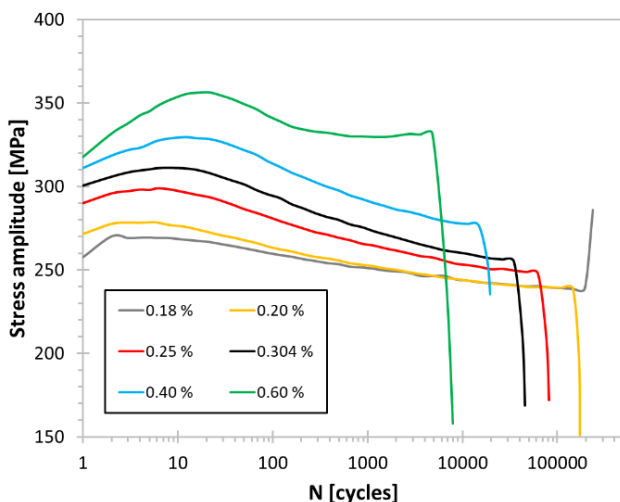


Figure 11. Representative stress response from ring P room temperature LCF experiments.

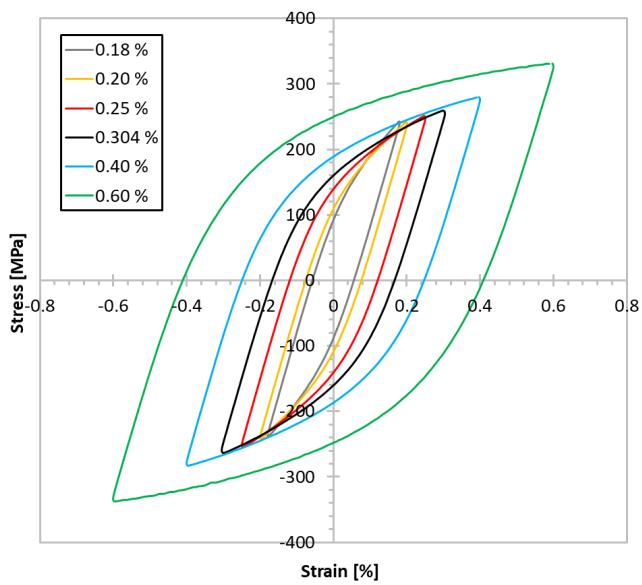


Figure 12. Selected half-life hysteresis loops from ring P room temperature LCF experiments.

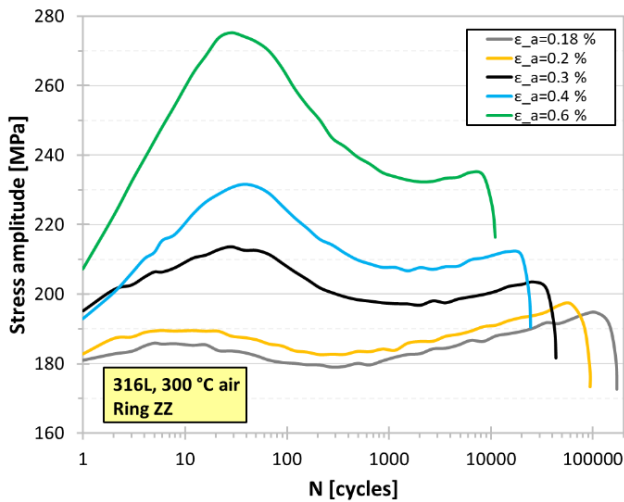


Figure 13. Representative stress response from ring ZZ 300 °C LCF experiments.

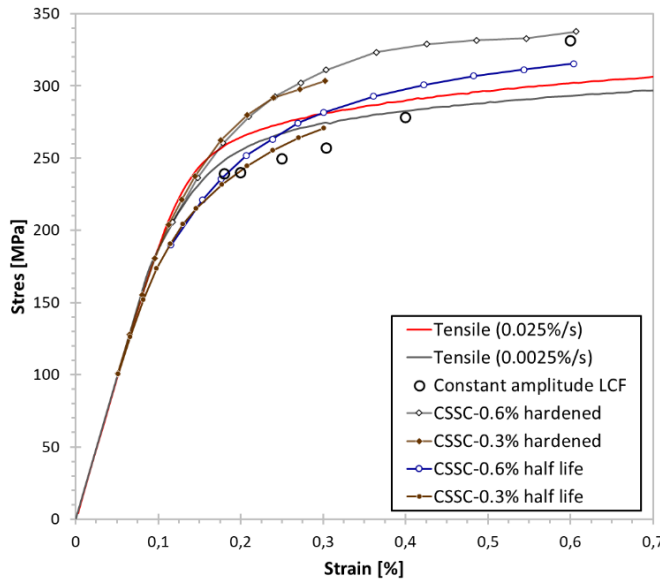


Figure 14. Comparison of room temperature cyclic and monotonic stress-strain curves with LCF half-life data from ring P.

Figure 15 shows the stress response of eight LCF tests from ring P with $\varepsilon_a=0.3\%$. This amplitude was selected for repeat experiments as it is typical for fatigue testing and lies reasonably close to the LCF/HCF crossover point as defined using elastic and plastic strain amplitudes. The circumferential location of these specimens is shown in Figure 16, with the same color coding as in Figure 15.

All repeat test stress amplitudes follow a common pattern: cyclic hardening for roughly the first 10 cycles, followed by a gradual softening which culminates in a rapid drop indicative of crack growth. However, there is an obvious offset of the curves in the stress direction. Between the extremes a difference of approximately 10 MPa persists throughout the fatigue life. When this same data is plotted into circumferential location of ring P, Figure 16 reveals a trend of hardening and softening when going around the pipe. This is probably linked to the manufacturing process and heat treatment history of the pipe.

Interestingly, the strength gradient appears to only show in cyclic loading as variation of strength measured in monotonic tensile tests from adjacent locations did not catch our attention. This suggests that the repeatedly back and forth moving dislocations in fatigue are able interact with the microstructure differently than in tensile tests, where the dislocations are unable to organize optimally in their single opportunity. Using similar argumentation, hardness testing would not be expected to reveal a circumferential gradient either.

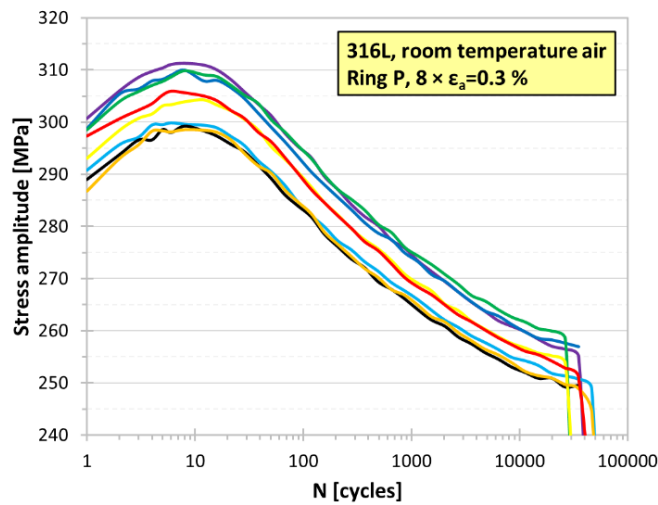


Figure 15. Stress response of eight ring P room temperature LCF experiments with 0.3% strain amplitude.

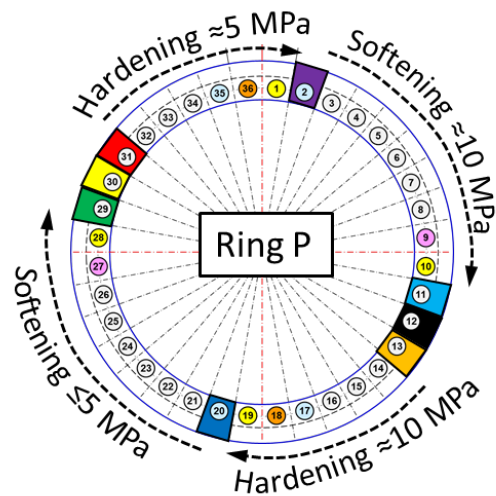


Figure 16. Circumferential cyclic hardening trend in ring P, based on Figure 14 results.

Summary and conclusions

The FATIMA project during 2020–2022 focused on building international collaboration, experimental readiness for EAF and performing experimental studies on representative material for a Finnish NPP.

Foundations for productive international research collaboration on fatigue and EAF have been established with Team Finland participating in R&D collaboration group activities moderated by EPRI. VTT's existing research facility FaBello for EAF was redesigned, though not yet applied, to face the experimental requirements for LTO support. Lastly, the characterization of an EPR pipe's mechanical properties has added to understanding of material specific behavior and arguments towards reducing unnecessary conservatism in some of the technical basis behind codified design fatigue curves.

Acknowledgement

In-kind contribution of significant NPP relevant materials for experimental studies by TVO is gratefully acknowledged.

References

- AFCEN (2016). RCC-M 2016 Règles de conception et de construction des matériels mécaniques des îlots nucléaires REP (in French). AFCEN.
- ASME (1963). ASME Boiler and Pressure Vessel Code, Section III, Nuclear Vessels. American Society of Mechanical Engineers.
- ASME (2010). ASME Boiler and Pressure Vessel Code, Section III - Rules for Construction of Nuclear Facility Components. American Society of Mechanical Engineers.
- ASME (2019) ASME Boiler and Pressure Vessel Code, Section XI - Rules for Inservice Inspection of Nuclear Power Plant Components, Division 1, Rules for Inspection and Testing of Components of Light-Water-Cooled Plants. American Society of Mechanical Engineers.
- ASTM (2019a) ASTM E1012-19, Standard Practice for Verification of Testing Frame and Specimen Alignment Under Tensile and Compressive Axial Force Application, ASTM International.
- ASTM (2019b) ASTM E606/E606M-19, Standard Test Method for Strain-Controlled Fatigue Testing, ASTM International.
- Basquin, O. H. (1910). The Exponential Law of Endurance Tests. Proceedings of the American Society for Testing and Materials, 10, part II, 625–630.
- Chopra, O. K., & Shack, W. J. (2007). Effect of LWR Coolant Environments on the Fatigue Life of Re-actor Materials (NUREG/CR-6909 Rev. 0, ANL-06/08). U.S. Nuclear Regulatory Commission.

- Coffin, L. F. (1953). A Study of the Effects of Cyclic Thermal Stresses on a Ductile Metal (KAPL-853). General Electric Company.
- Energoatomizdat (1989). PNAE G-7-002-86 Regulations of Strength Analysis of Equipment and Pip-ing of Nuclear Power Facilities. Energoatomizdat.
- ISO (2019) Metallic Materials. Tensile Testing. Part 1: Method of Test at Room Temperature (ISO 6892-1:2019), International Organization for Standardization.
- JSME (2006) Codes for Nuclear Power Generation Facilities: Environmental Fatigue Evaluation Method for Nuclear Power Plants, JSME S NF1-2006, The Japan Society of Mechanical Engineers. (comprehensive revision in 2009 as JSME S NF1-2009)
- KTA (2013). KTA 3201.2 Komponenten des Primärkreises von Leichtwasserreaktoren Teil 2: Auslegung, Konstruktion und Berechnung. Kerntechnischer Ausschuss.
- Manson, S. S. (1953). Behavior of Materials Under Conditions of Thermal Stress (NACA TN 2933). National Advisory Committee for Aeronautics.
- Monto, J. (2022) Väsytyiskoelaitteiston nostimen suunnittelu. Bachelor's thesis, Metropolia Ammattikorkeakoulu.
- Seppänen, T., Alhainen, J., Arilahti, E., Solin, J., Vanninen, R. and Pulkkinen, E. (2022) EPR Piping Material Study: Basic Characterization and Low Cycle Fatigue at Room Temperature, PVP2022-84007. ASME 2022 Pressure Vessels and Piping Conference, Las Vegas, Nevada, USA, July 17–22, 2022. 6 p.
- Seppänen, T., Alhainen, J., Arilahti, E., Solin, J. and Vanninen, R. (2023) EPR Piping Material Study: Effects of Sampling Location and Temperature on Low Cycle Fatigue, PVP2023-106439. Draft submitted to ASME 2023 Pressure Vessels and Piping Conference. 6 p.
- Solin, J. (1986) A Spectrum Straining Method for Low-Cycle Fatigue Resistance Determination, Paper C 245/86. Fatigue of Engineering Materials and Structures, Sheffield, United Kingdom, September 15–19, 1986. Vol 1, pp. 273–280.
- Solin, J., Karjalainen-Roikonen, P. and Moilanen, P. (2003). Fatigue Testing in Reactor Environments for Quantitative Plant Life Management. Materials Reliability Program: Second International Conference on Fatigue of Reactor Components (MRP-84) (1003536), 16 p.
- Solin, J., Karjalainen-Roikonen, P., Arilahti, E. and Moilanen, P. (2005). Low Cycle Fatigue Behaviour of 316 NG Alloy In PWR Environment. Materials Reliability Program: Third International Conference on Fatigue of Reactor Components (MRP-151) (1011958), 19 p.
- Solin, J. (2006) Fatigue of stabilized SS and 316 NG alloy in PWR environment, PVP2006-ICPVT11-93833. Proceedings of PVP2006-ICPVT11 2006

- ASME Pressure Vessels and Piping Division Conference, Vancouver, BC, Canada, July 23–27, 2006. 11 p.
- Solin, J., Nagel, G. and Mayinger, W. (2009) Cyclic Behavior and Fatigue of Stainless Surge Line Material, PVP2009-78138, Proceedings of the ASME 2009 Pressure Vessels and Piping Conference, Prague, Czech Republic, July 26–30. 2009. 9 p.
- Solin, J., Alhainen, J., Arilahti, E., Väinölä, J., Marjavaara, P., Järvinen, E., Halonen, M., Patalainen, M., Kaunisto, K. and Moilanen, P. (2011). Fatigue of Primary Circuit Components (FATE). In E. K. Puska & V. Suolanen (Eds.), SAFIR2010, The Finnish Research Programme on Nuclear Power Plant Safety 2007-2010 Final Report (VTT Research Notes 2571) (pp. 368–380). VTT.
- Solin, J., Seppänen, T., Lemettinen, P., Vanninen, R., Pulkkinen, E. and Faidy, C. (2020) Codes, Standards, Rules and Assumptions on Environment Assisted Fatigue for Fatigue Management of Primary Piping, PVP2020-21501. Proceedings of the ASME 2020 Pressure Vessels and Piping Conference, Virtual, Online, July 20-24, 2020. 9 p.
- Solin, J., Seppänen, T., Lemettinen, P., Vanninen, R. and Pulkkinen, E. (2021) Design By Analysis, Codes, Standards and Rules on EAF - Applicability to Stainless Steels in PWR Primary Piping, PVP2021-62187. Proceedings of the ASME 2021 Pressure Vessels and Piping Conference, Virtual, Online, July 13-15, 2021. 9 p.
- Solin, J., Seppänen, T., Lemettinen, P., Vanninen, R. and Pulkkinen, E. (2022) Environment Assisted Fatigue – Rules, Assumptions and Challenges for Fatigue Management of Primary Piping, PVP2022-84627. Proceedings of the ASME 2022 Pressure Vessels and Piping Conference, Las Vegas, Nevada, USA, July 17–22, 2022. 9 p.
- Solin, J., Arilahti, E., Moilanen, P., Alhainen, J., Juvalainen, J. and Seppänen, T. (2023) FaVite facility for fatigue research in reactor coolant environment. Research report VTT-R-00043-23.
- STUK (2020). YVL E.4e Strength Analyses of Nuclear Power Plant Pressure Equipment. Säteilytur-vakeskus.

7 Structures and materials

7.1 Additive manufacturing in nuclear power plants (AM-NPP)

Alejandro Revuelta¹, Tuomas Riipinen¹, Mika Sirén¹, Antti Vaajoki¹, Zaiqing Que¹,
Antti Förström¹, Konsta Sipilä¹, Sneha Goel¹, Yasemin Inc¹, Siddharth
Jayaprakash²; Niklas Kretzschmar²; Mika Salmi²; Markus Korpela³

¹VTT Technical Research Centre of Finland Ltd
P.O. Box 1000, FI-02044 Espoo

²Aalto University
P.O. Box 15500, FI-00076 Espoo

³Lappeenranta University of Technology
P.O. Box 20, FI-53851 Lappeenranta

Abstract

AMNPP has increased the knowledge of Finnish stakeholders regarding the use of Additive Manufacturing (AM), in particular Laser Powder Bed Fusion (PBF-LB), thus supporting the safe use of additively manufactured 316L components in the nuclear sector. As a relatively new manufacturing process, the first stages of the project focused on creating a roadmap on the use of the technology in Finland based on the landscape of existing standards as well as improving the understanding of the stakeholders on design issues and limitations. Additionally, the project has studied the expected level of quality which can be achieved for the reference material and demonstrated different quality control methods which can support the certification of AM parts for critical applications. Finally, the effect of novel higher temperature solution annealing heat treatments on the mechanical and stress corrosion cracking properties has been studied.

Introduction

Spare parts with additive manufacturing (AM, 3D printing) is a rising topic in different industries (Metsä-Kortelainen 2020). It has a potential for making spare parts on-demand, off- and onsite manufacturing and repairing existing parts (Salmi 2018, Chekurov 2017). It could also simplify the supply chains (Khajavi 2020). Based on different industries, distrust in quality, insufficient material and design knowledge among stakeholders and poor availability of design documentation on spare parts as the key barriers to adopting AM in the production of spare parts (Chekurov 2021). Also, limited build chamber volumes and the need of post-processing are technical challenges (Kretzschmar 2018). In some industries, the delivery time of spares can be long can challenging. AM could shorten this delivery times and be a solution for long tails of company spare parts (Chekurov 2018).

Due to the extremely long operating life of a nuclear power plant, power companies are facing the same problem as many other companies giving long service commitments for their products: how to ensure proper maintenance, repair and especially the availability of spare parts during the whole plant service life. Power plant maintenance is carried out during short annual service breaks. The maintenance is well planned, and many components have well scheduled exchange intervals either for the whole component or for part thereof. However, new, unexpected findings are also observed during the outage, and these may either require immediate action, or can be left as they are, for replacement or repair at a later stage, e.g. during the next outage. Some spare parts must thus be available during the outage, while others must have a reasonable delivery time. A well planned outage also include plans for both planned and possible repairs. However, there are many potential issues related to availability: very long lead times, lack of tooling needed to prepare the spare part, availability of appropriate contract manufacturer etc. One extremely potential answer to this demand are the extremely rapid developing and commercialising metal AM technologies, particularly powder-based processes that have matured on a wide front to production in extremely demanding applications, such as those of aerospace and medical industries. Additive manufacturing is also a very interesting in new reactor designs, e.g. small modular reactors (SMR).

Roadmap

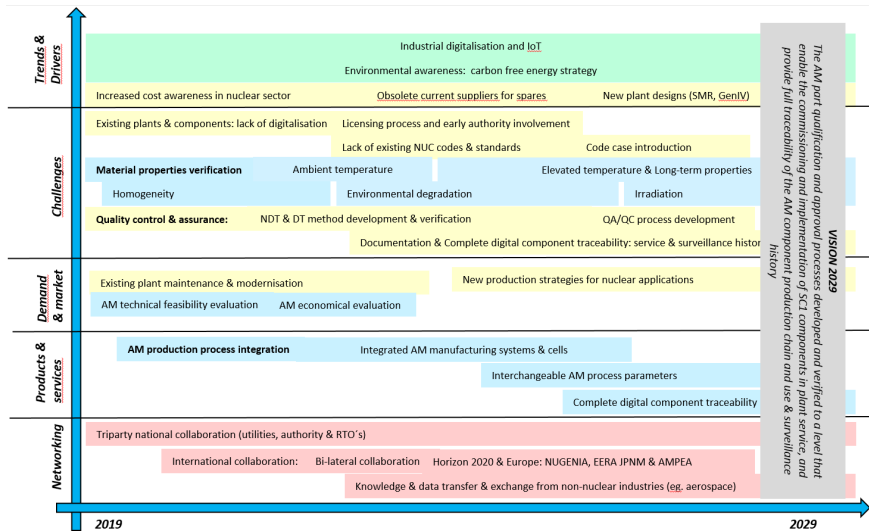


Figure 1. Overview of AM in nuclear power plants draft roadmap. (Sirén, 2019)

The initial task in the AM-NPP project was elaborating a draft of the roadmap for taking additively manufactured components in use in the Finnish nuclear energy sector. The final goal being introducing AM in nuclear design codes in Finland for 2029 at latest. In order to receive feedback from stakeholders, a workshop on this topic was arranged with participation of representatives of all licensees and also from the regulator. In this workshop, the state of the art of the technology was presented and attendants provided very constructive information regarding hopes and expectations (Korpela 2019). This information was the cornerstone of the work done on defining this initial draft of the roadmap. During the elaboration of the roadmap it soon became evident that, instead an actual roadmap, the outcome will be rather a proposition or a basis for one. The reason is that there are a number of decisions to be made by the stakeholders that have a fundamental effect on the realisation of AM process application. On Figure, the overall schematic of the roadmap is presented and the different to be considered and their implementation is further developed in (Siren 2019).

Component Identification

Another relevant task of AM-NPP was analysing the feasibility of printing parts using AM for a few characteristic components which can be found in nuclear power plant facilities (Jayaprakash et al., 2019). The stakeholders provided some of these components as examples, and others were modelled similar to prototypical components found on literature:

- Valve seat: Part of an emergency pump system for NPPs categorized under safety class 2.
- Water impeller: Water pump impeller which had become obsolete and required replacement no longer commercially available. Based on literature and publicly available press releases.
- Thimble Plugging Device: A crucial element to place nuclear fuel in the reactor core. Based on literature and publicly available press releases.
- Bearing Housing: Housing used in on electric motors used in NPPs. Based on literature and publicly available press releases.

The feasibility of these components was considered from both the technical point of view as well as from the safety perspective.

As an initial step, components have been assessed for printability of the component design. Even if AM provides great flexibility and potential for complexity, this is not guarantee that every component is printable. The screening has been performed using a software developed by Aalto University and using as an input part geometries and their material requirements. This process helps in gaining insights on design issues that impact the printing process, e.g., thin walls, and identifying potential postprocessing operations required to fulfil material quality requirements.

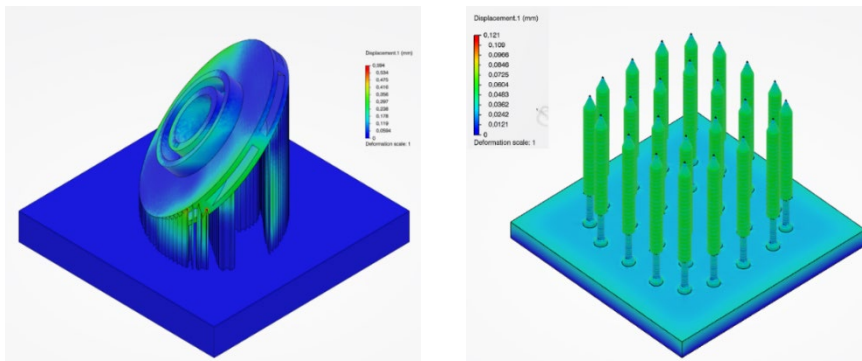


Figure 2. Example of simulations of representative AM components: a) water impeller, b) thimble plugging device. (Jayaprakash et al., 2019)

After this initial assessment was done, a simulation was performed to confirm printability of the parts and analyse displacements and associated re-coater collision risks that would induce print failure (Figure). The results of these simulations also contribute to gain insight on the necessity or redesign needs of support structures. As a result, it was identified that the valve impeller as initially configured for printing had a certain risk of collision; this would require a redesigned support structure, which would minimize the possible distortion.

Standardization

As of today, one of the major drawbacks for the adoption of additively manufactured components for critical applications is the need to ensure that those components are going to perform as expected, and that the whole quality assurance plan and quality control is carefully considered. This type of activities are typically supported by a collection of standards which provide instructions on what steps are required in order to ensure the proper level of quality. As PBF-LB is still a relatively new manufacturing process, there is a certain level of fragmentation in the different standards as well as some significant gaps. This has been clearly identified as part of the roadmapping exercise done during the first year together with all the stakeholders of the AM-NPP project and during the second year of the project effort has been made to clarify the status of the standardization landscape related to PBF-LB manufacturing of AISI 316L material, especially in the nuclear context. As a result, a report has been published summarizing the main findings (Riipinen, 2020).

On Figure, a summary diagram of some of the main existing and incoming standards (2020) related to PBF-LB is presented with a tentative organization around different stages of the manufacturing value chain for a component made of AISI 316L. And although some of the standards presented in Figure are generic for any material, different materials will require the development of specific standards. In addition, none of these presented in Figure are nuclear specific.

Two of the areas of special significance for the nuclear sector where there is still a gap in the existing standards, in addition to material behaviour under irradiation conditions, are fatigue and corrosion resistance properties (Riipinen 2020).

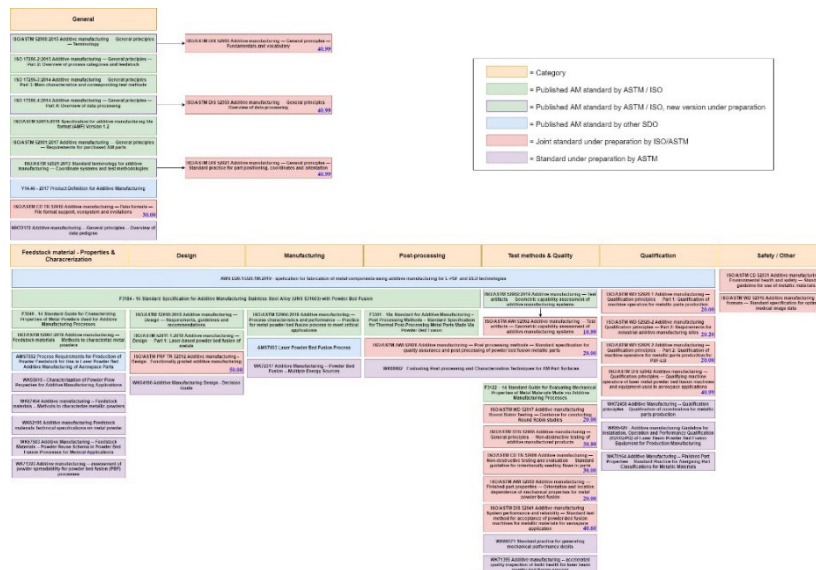


Figure 3. Overview of existing and incoming standards related to PBF-LB of AISI 316L (Riipinen 2020)

In 2019, the Nuclear Energy Institute published a roadmap for regulatory acceptance of advanced manufacturing methods in which it was described the existence of several ongoing code cases in the nuclear sector (Nuclear Energy Institute, 2019). In addition to these, there are several ongoing qualification activities done by European nuclear licensees to show the feasibility of AM in nuclear power plants. In 2020, the EURATOM project NUCOBAM (NUclear COmponents By Additive Manufacturing) started as a joint effort by industry, research institutes and academia to lay ground work for standardization efforts in the European Union in this field. As part of this project, different material experimental campaigns are being planned for material characterization; including behaviour of the material under irradiation conditions.

It can be easily seen that despite the still limited number of published standards, there is a wide range of standards in draft phase covering most topics of the manufacturing chain. Standardization organizations are being very active and many of these drafts will become approved standards in the short future. Once these standards are agreed and final, they will support the quality assurance plans of components used in nuclear power plants and will increase the confidence of the authorities and regulators, and overall safety of NPPs using AM components. Additionally the certification process of a component will become easier and faster as well as having a reduced cost.

Quality Assurance and Control

In order to produce safe AISI316L components manufactured by PBF-LB is necessary to have a very good understanding of the material properties that can be obtained from the process. Additionally, it is important to have solid quality assurance plans and quality control methods which will ensure that the performance of every component manufactured and put into service will be as expected.



Figure 4. Printed samples for quality evaluation. (Riipinen 2020)

As part of AM-NPP, some of the key steps to be considered for ensuring a metallic component is printed with good quality, and thus with improved safety, are

evaluated. Both from a general and practical level. These steps include, among others:

- Feedstock. Proper analysis and control of the raw material employed for the printing is the starting point of the manufacturing process. The material used has to ensure consistent values of powder chemistry, flowability and powder size distribution in addition to controlled storage conditions.
- Process monitoring. During recent years, several different systems to evaluate the progress of a build as the components are being printed have been developed. Although at the moment these process monitoring systems do not have closed loop control of the manufacturing process, they allow to analyze either in real-time or a posteriori the quality of a part with respect to a baseline/qualification component. These methods combined with possible Non Destructive Examinations, reduce the risk that a faulty part is accepted as valid. There are different types of process monitoring methods, being two of the most relevant the melt pool monitoring, which tracks the emissions of the melt pool continuously, and the so-called optical tomography, which analyse emissions of the whole building plate simultaneously typically from above the building plate.
- Non-Destructive Testing: Traditional NDT methods face difficulties for complex geometries making full use of the design freedom provided by AM. But, for many components, specially spare parts originally designed to be manufactured with a different process, they are still a valid testing method. For the most complex geometries, the X-ray Computed Tomography might be the only method technically capable of detecting flaws, especially in areas of difficult access.

It is concluded that in order to ensure the part quality and safety of the AM components used in the nuclear sector, a thorough part qualification framework should be in place. Especially considering the existing gaps in standardization.

To gain a hands on experience on how different quality control methods work together to improve the overall component quality and the variability of material properties within a manufactured batch, a set of 30 test cubes of 10x10x20mm was printed in an SLM125HL machine (125x125mm building platform) (Figure). All samples were printed with the standard parameters provided by the machine OEM and with powder previously analysed for chemical composition and particle size distribution. During manufacturing the process was monitored using a melt pool monitoring system (commercial PrintRite3D system from SigmaLabs Inc., with an approximate spatial resolution of 100µm) and a thermal camera (6 fps recording).

After the build job was finalized and an initial analysis was performed on the process monitoring data, the most interesting samples were scanned with an X-Ray Computed Tomography system with an approximate voxel size of 8.4µm and the rest were sectioned and further analysed using optical microscopy.

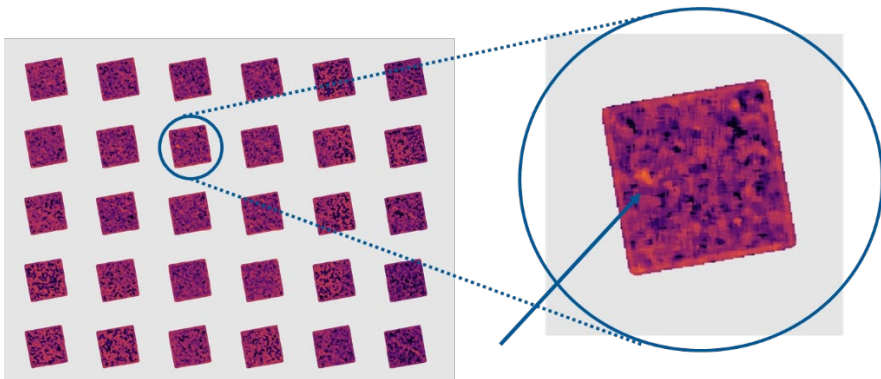


Figure 5. Example of defect prediction based on melt pool monitoring.

As this set of printed samples had simple geometries and well controlled and stable parameters, very few defects were detected by the MPM system, and a certain degree of manual evaluation by the final user was necessary. On Figure an example of the prediction of a possible defect using this method is presented.

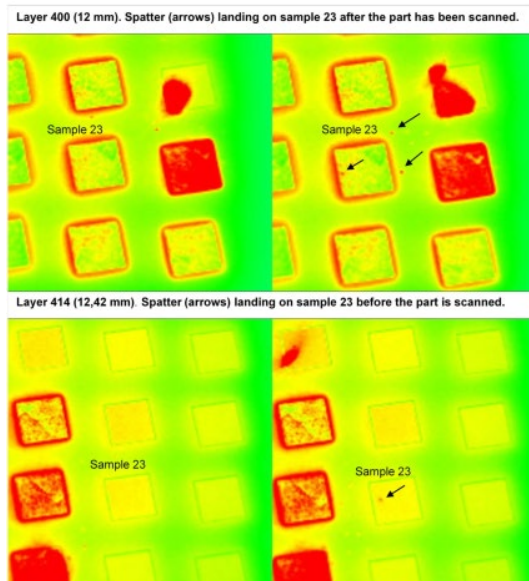


Figure 6. Infrared thermal image showing spatter during laser scanning near sample number 23 (Ripinen 2021). top) layer 400, bottom) layer 414.

Manual evaluation of the infrared images shows the existence of some spatter phenomena during the printing process which could lead to defects. In Figure two sequential frames for two different layers is presented. In these images, it can be

clearly seen the appearance of several hot spots which are indicative of spatter coming from the melt pool which could produce defects in the material.

Although X-Ray Computed Tomography is the NDT method which is better suited for the detection of small defects in complex metallic components, it is not completely hassle free. As it can be seen in Figure, even for a simple geometry as the one used in these experiments, there is a certain level of noise due to edge effects which can make more difficult the automated detection of defects. On the other hand, it still allows for an excellent level of detection of defects on a sample. Most defects detected in these samples had an average radius below 40 μ m. A few samples presented an increased number of defects on the top-most layers whose origin could not be determined. It was not possible to establish a correlation between the defects predicted by the process monitoring methods and the defects observed using μ CT.

The porosity calculated using optical microscopy was small (<0,03%) and there was no correlation on porosity level versus position in the building platform.

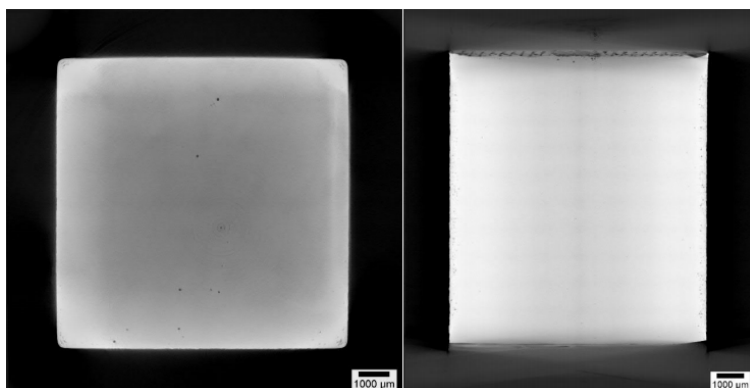


Figure 7. X-Ray Computer Tomography of one of the AISI316L samples. left) top view. right) vertical view. (Riipiinen 2021)

Although in this experimental work there was no clear correlation between the monitoring methods and the results of both NDT and optical microscopy examinations, it is important to remark that the final material had a very good overall density of >99.97%. This kind of comparative analysis should be repeated for a more representative component with more complex geometry which might be more likely to showcase defects. Is in that scenario where the potential of these process monitoring methods will better assessed.

In addition to the quality control of manufactured components, another important aspect of the components lifecycle is the ability of performing inspections in service; Accurate knowledge about sound propagation speed in the medium is crucial for the use of Ultrasonic Testing (UT) equipment, which is typically used for material's flaw characterisation. The anisotropic nature of additive manufacturing (AM)

products makes this especially relevant. For this purpose, a set of calibration blocks were printed during the project and velocity measurements of the ultrasonic longitudinal waves in different directions using the pulse-echo technique were done to quantify the effect of anisotropy on the sound velocity. In addition, the Distance-Amplitude Correction (DAC) curves for inspecting additively manufactured metallic parts were generated. The results of this work can be found from (Inc 2023).

New Heat Treatments

PBF-LB processed 316L is typically heat treated to alter the microstructure and material properties to erase the anisotropy induced by the manufacturing process, making the material more suitable for demanding applications. The heat treatments in current 316L AM standard (ASTM International, 2016) are adopted from practices in aerospace industry. While the HIP processing produces a microstructure close to conventional 316L the recommended solution annealing process does not produce homogenous microstructures and material properties.

The premise for using high temperature solution annealing is the possibility of having an alternative thermal processing method to the more traditional HIP process, which is considered as a suitable post processing route for AM 316L components for nuclear applications. The effect of high temperature solution annealing on the material properties of PBF-LB produced 316L were investigated and reported in (Riipinen, 2022).

Square bars for machining impact specimens and cylinder bars for tensile test specimens were additively manufactured from 316L powder using SLM 125HL machine at VTT.

All parts were stress relieved at 650°C for 2 hours and consequently subjected to one of three solution annealing cycles (vacuum): SA1 = 1066°C/1h, SA2 = 1150°C/1h, SA3 = 1200°C/1h. SA1 at 1066°C complies with the AMS 2759 standard and is used as the reference for the high temperature heat treatments. The printed parts and the heat treatment for each part are shown in Figure 8.

The top sections (length ≈ 2.5 cm) of the printed and heat-treated cylinders were cut and used for microstructure and composition analysis as well as for measuring porosity.

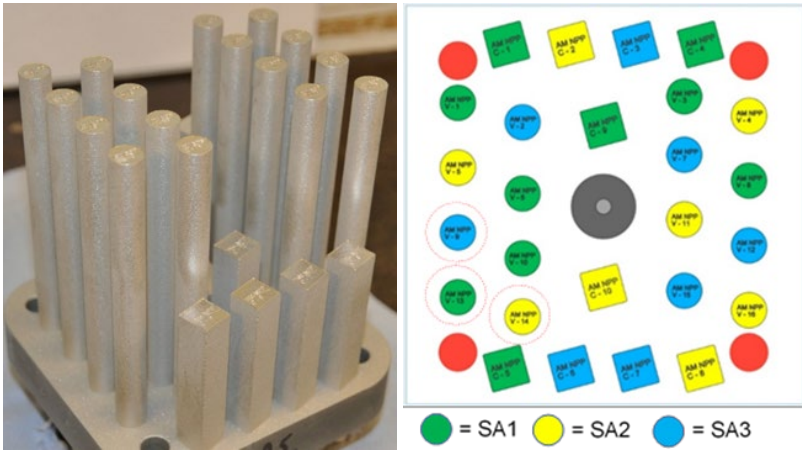


Figure 8. The printed test specimens and the heat-treatment for each part. (Riipinen, 2022)

Nearly identical experimental arrangement was implemented in DIVALIITO project (Metsä-Kortelainen et al., 2020) to obtain as comparable results to AM NPP specimens as possible. The DIVALIITO mechanical testing and characterization results were published in (Reijonen, 2021). The tensile properties of the AM NPP specimens decreased with increasing annealing temperature as expected for a material undergoing recovery, recrystallization and grain growth processes and the SA1 specimens from both projects had comparable tensile properties (**Figure**). All tested specimens fulfilled the minimum requirements for tensile properties in ASTM F-3184 (ASTM, 2016). The most obvious difference between the DIVALIITO and AM NPP specimens was the average impact energy, which were significantly lower for AM NPP specimens. The average impact energy of AM NPP SA1 was 58 J lower compared to DIVALIITO SA1 and the impact energies decreased with increasing solution annealing temperature.

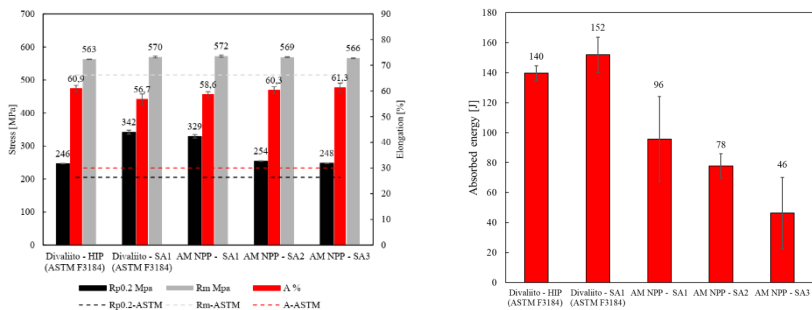


Figure 9. Tensile and impact properties from AM NPP and DIVALIITO projects (Riipinen, 2022)

Based on SEM / EBSD analysis the microstructure evolved from partially recrystallized anisotropic structure with high density of low angle grain boundaries after annealing at 1066°C to nearly fully recrystallized and stress free structure at 1200 °C (Figure 10). Inclusions, mainly oxides, were observed in large quantities in all samples and the size of the inclusion increased with higher annealing temperatures.

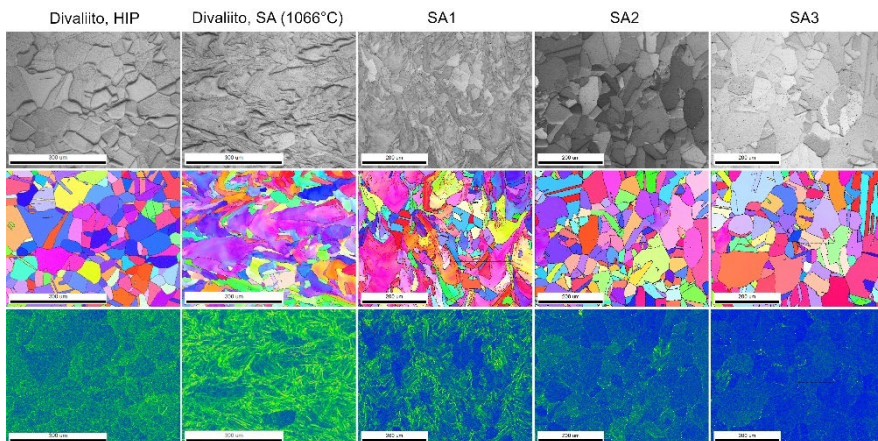


Figure 10. SEM and EBSD images of DIVALIITO and AM NPP specimen cross-sections (Riipinen, 2022)

Based on our research results, the high temperature solution annealing produced a nearly fully recrystallized and stress-free grain structure similarly to HIP processing. However, the impact energies were low for the solution annealed material, and high deviation of results indicate the microstructures vary between specimens with the same thermal processing history. Based on our findings the 1200 °C solution anneal did not result in satisfactory material properties as the impact energies were considered too low. However, annealing 1150 °C yielded higher strength and similar grain structure, and is therefore considered more optimal.

Corrosion properties

Heat treatments, surface condition and printing parameters can significantly influence the SCC response of AM 316L (Lou, 2017 & Cruz, 2022). A detailed investigation of high-temperature SCC behaviour of PBF-LB stainless steel 316L is very important for their applications in light water reactor environment during normal operation conditions and during an impurity transient.

Stress corrosion cracking (SCC) behaviour of laser powder bed fused stainless steel 316L was evaluated with U bend testing in oxygenated high-temperature water at 288 °C. The effects of solution annealing temperature (1066, 1150 and 1200 °C), surface finish (as-built and wire cut) and the sample orientations on the SCC

behaviour oxygenated high-temperature water with chloride addition at 288 °C were investigated and reported in (Que, 2023).

U-bend specimens were flat sheets with a geometry of 110×15×2 mm³ (L×W×H) that were additively manufactured using SLM Solutions 125HL powder bed fusion machine at VTT (Figure). The sheets were removed from the platform and heat treated at 650 °C for 2 hours for stress relieve and consequently subjected to one of three solution annealing cycles (vacuum): SA1 = 1066 °C/1h, SA2 = 1150 °C/1h, SA3 = 1200 °C/1h. Part of the U-bend specimens were given a surface finish by wire cutting and the rest remained in as-built condition. The as-built surface is an as-built surface from PBF-LB without further machining or cutting. The wire cut surface was prepared via an electrical discharge machining (EDM) process. (Que, 2023)

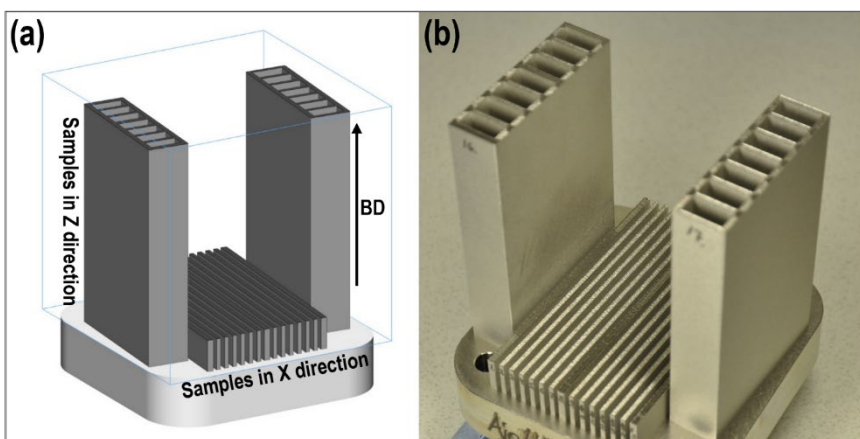


Figure 11. (a) Printed part layout and (b) photo of printed parts. (Que, 2023)

Altogether 24 U-bend samples were exposed to oxygenated high-temperature water with chlorides to study the effect of SA (SA1, SA2 and SA3), surface finish (PBF-LB as-built surface and the industry-prepared wire saw cut surface) and sample orientation (X and Z) on the SCC susceptibility. The U-bend specimens were exposed to the high-temperature water environment in the autoclave for a period of 2 weeks. Subsequently, all samples were bent to induce a nominal 10% strain, which was evaluated based on the curvature radius and specimen thickness (Figure 12). Visual inspection and liquid penetrant testing (Figure 13) were performed after the exposure to clearly discern the extent of cracking. The results of the U-bend test are summarised in Table 1. (Que, 2023)

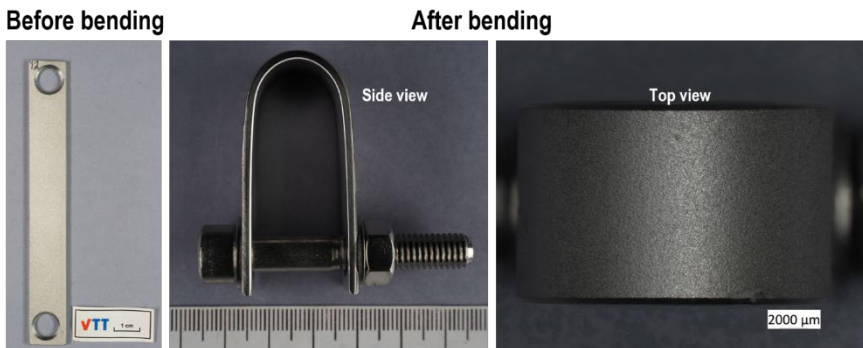


Figure 12. Example of the sample before and after the bending. (Que, 2023)

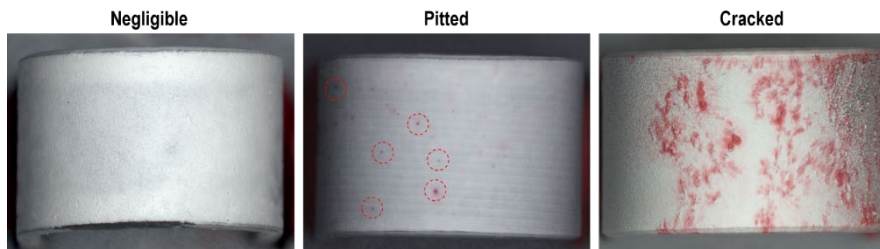


Figure 13. Examples of the non-cracked (negligible), pitted and cracked U-bend samples according to the liquid penetrant testing. (Que, 2023)

The applied high-temperature water environment is a simulated BWR water with ~10 wppm oxygen and ~100 wppm Cl (added as NaCl) at 288 °C. Redox and stainless steel electrode potentials were monitored versus a 0.05 M KCl/AgCl/Ag external pressure balanced reference electrode to ensure the presence of oxygen in the water (+0.1 VSHE). The high-temperature water environment chosen was based on the work of Gordon (Gordon, 1980) and this environment should heavily promote SCC. The presence of Cl⁻ ions in the test environment can increase the susceptibility of pitting and SCC. (Que, 2023)

Table 1. Summary of U-bend tests according to the liquid penetrant testing (Que, 2023)

Penetrant indication	Solution annealing	Surface finish	Sample amount	
			X orientation	Z orientation
Cracked	SA1	Wire cut	1	1
	SA2	As-built	0	2
	SA3	As-built	2	1
Pitted	SA1	Wire cut	0	1
		As-built	1	0

Penetrant indication	Solution annealing	Surface finish	Sample amount	
			X orientation	Z orientation
Negligible	SA3	As-built	0	2
	SA1	Wire cut	2	1
		As-built	2	3
	SA2	As-built	3	1
	SA3	As-built	1	0

For post-exposure characterization the upper bent surfaces and cross-sections of the upper part of the SA1, SA2 and SA3 U-bend specimens were examined with SEM. Figure shows the branching of the transgranular SCC cracks in the SA1 specimen with wire-cut surface. Locally some branching cracks followed the high-angle boundaries and the inclusions promote the crack propagation. In Figure (d,e) oxide layer with a high porosity can be seen at the crack initiation sites, which is not observed for the SA1 sample with the as-built surface. The SCC cracks were filled with oxides resulting from the dissolution and oxidation during the cracking. (Que, 2023)

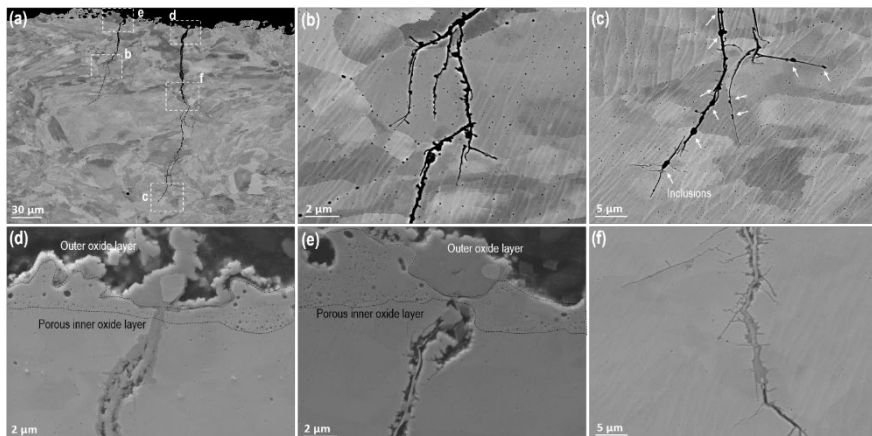


Figure 14. Cross-sectional SEM-BSE and SE images of the PBF-LB 316L specimen with SA1 treatment and the wire cut surface after the exposure to oxygenated high-temperature water environment. (a-c) SEM-BSE; (d-f) SEM-SE. (Que, 2023)

U-bend testing, liquid penetrant testing and post-exposure characterizations showed that a higher annealing temperature and the wire cut surface leads to a higher susceptibility to SCC in oxygenated high-temperature water with chloride addition. Sample orientation seems to play a minor role on SCC resistance in this study as SCC occurred in the dominating transgranular mode in all specimens. (Que, 2023)

The wire cut surface accelerates the SCC initiation due to formation of a porous passive film, indicating a higher corrosion rate and faster transportation of ions through the oxide film. (Que, 2023)

An annealing temperature around 1150 °C or slightly below this temperature might be optimal for applications in light water reactor environment. At such temperature, the anisotropic microstructure of the as-built material is largely removed, while the deterioration of mechanical properties and SCC resistance evident at higher annealing temperatures could be avoided. (Que, 2023)

Acknowledgements

The authors are grateful for the financial support received from the Finnish Nuclear Waste Management Fund (VYR), Aalto University, Lappeenranta University, VTT Technical Centre of Finland Ltd. and Teollisuus Voima Oy. In addition, we would like to acknowledge the active participation of Fortum Oy, Teollisuus Voima Oy, Fennovoima Oy and STUK in sharing their insights about the additive manufacturing process and its future in Finnish nuclear power plants.

References

- Metsä-Kortelainen, S., Reijonen, J., Riipinen, T., Vaajoki, A., Puukko, P., Salmi, M., Chekurov, S., Björkstrand, R., Kretzschmar, N., Akmal, J., Puttonen, T., & Partanen, J. 2020. New business from digital spare parts. VTT Technical Research Centre of Finland. <https://doi.org/10.32040/2020.978-951-38-8827-5>
- Sirén, M. 2019. Additive Manufacturing in Finnish Nuclear Sector - Roadmap for implementation, VTT Research Report, VTT-R-01270-19.
- Salmi, M., Partanen, J., Tuomi, J., Chekurov, S., Björkstrand, R., Huotilainen, E., Kukko, K., Kretzschmar, N., Akmal, J., Jalava, K., Koivisto, S., Vartiainen, M., Metsä-Kortelainen, S., Puukko, P., Jussila, A., Riipinen, T., Reijonen, J., Tanner, H., & Mikkola, M. 2018. Digital Spare Parts. VTT Technical Research Centre of Finland. http://www.vtt.fi/inf/julkaisut/muut/2018/DIVA_final_report.pdf
- Kretzschmar, N., Chekurov, S., Salmi, M., & Tuomi, J. 2018. Evaluating the readiness level of additively manufactured digital spare parts: An industrial perspective. *Applied Sciences*, 8(10), 1837.
- Chekurov, S., & Salmi, M. 2017. Additive manufacturing in offsite repair of consumer electronics. *Physics Procedia*, 89, 23-30.
- Chekurov, S., Salmi, M., Verboeket, V., Puttonen, T., Riipinen, T., & Vaajoki, A. 2021. Assessing industrial barriers of additively manufactured digital spare part implementation in the machine-building industry: a cross-organizational focus group interview study. *Journal of Manufacturing Technology Management*.

- Khajavi, S. H., Salmi, M., & Holmström, J. 2020. Additive Manufacturing as an Enabler of Digital Spare Parts. In Managing 3D Printing (pp. 45-60). Palgrave Macmillan, Cham.
- Chekurov, S., Metsä-Kortelainen, S., Salmi, M., Roda, I., & Jussila, A. 2018. The perceived value of additively manufactured digital spare parts in industry: An empirical investigation. International Journal of Production Economics, 205, 87-97.
- Korpela, M., Reijonen, J., Revuelta, A., Sirén, M. 2019. AM in Finnish Nuclear Sector - Workshop summary report, VTT Research Report, VTT-R-00741-19.
- Jayaprakash, Siddharth, Kretzschmar, N., Korpela, M., Salmi, M., Revuelta, A. 2020. WP2 Report. Aalto University Technical report.
- Riipinen, Tuomas. 2020. AM-NPP - Standardization in metal AM, VTT Research Report VTT-R-00617-20.
- Riipinen, T., Revuelta, A., Vaajoki, A. 2021. AM NPP - Configuration of Melt Pool Monitoring for tracking material quality. VTT-R-00090-21.
- Riipinen, T., Revuelta, A., Forsström, A., & Que, Z. (2022). AM NPP - High temperature solution annealing of AM 316L. VTT Technical Research Centre of Finland. VTT Research Report No. VTT-R-00119-22.
- Nuclear Energy Institute. 2019. Roadmap for Regulatory Acceptance of Advanced Manufacturing Methods in the Nuclear Energy Industry. Available at: <https://www.nei.org/resources/reports-briefs/roadmap-regulatory-acceptance-amm>
- ASTM International (2016) 'ASTM F3184 (2016) Standard Specification for Additive Manufacturing Stainless Steel Alloy (UNS S31603) with Powder Bed Fusion', Annual Book of ASTM Standards. West Conshohocken, PA 19428-2959, United States, pp. 1–9. Available at: <http://www.ansi.org>
- Reijonen, J. et al. (2021) 'Cross-testing laser powder bed fusion production machines and powders: Variability in mechanical properties of heat-treated 316L stainless steel', Materials and Design. The Author(s), 204, p. 109684. doi: 10.1016/j.matdes.2021.109684.
- Que, Z.; Riipinen, T.; Goel, S.; Revuelta, A.; Saario, T.; Sipilä, K.; Toivonen, A. 2023. SCC cracking behaviour of laser powder bed fused 316L stainless steel in high-temperature water at 288 °C. Submitted to Corrosion Science.
- X. Lou, M. Song, P. Emigh, M. Othon and P. Andresen, "On the stress corrosion crack growth behaviour in high temperature water of 316L stainless steel made by laser powder bed fusion additive manufacturing," *Corrosion Science*, vol. 128, pp. 140-153, 2017.
- V. Cruz, Y. Qiu, N. Birbilis and S. Thomas, "Stress corrosion cracking of 316L manufactured by laser powder bed fusion in 6% ferric chloride solution," *Corrosion Science*, vol. 207, no. 110535, 2022.

B. Gordon, "Effect of Chloride and Oxygen on Stress Corrosion Cracking of Stainless Steels: Review of Literature," *Materials Performance*, vol. 19, no. 4, pp. 29-38, 1980.

Inc, Y., "Calibration of PBF-LB 316L for Ultrasound Testing". VTT-R-00050-23, 2023

7.2 Critical studies in support of the ageing management of NPP concrete infrastructure (CONAGE)

Miguel Ferreira¹, Fahim Al-Neshawy², Elina Huttunen-Saarivirta¹, Edgar Bohner¹,
Pirkko Kekäläinen¹, Esko Sistonen², Abobaker Ba Ragaa²

¹ VTT Technical Research Centre of Finland Ltd.
P.O. Box 1000, FI-02044 Espoo, Finland

² Aalto University, School of Engineering, Department of Civil Engineering
P. O. Box 12100, FI-00076 Aalto, Finland

Abstract

The research topics being addressed in the CONAGE project are strongly linked by key aspects of ageing management, where critical input is needed to support decision-based actions, whether related to inspection and maintenance actions on existing concrete infrastructure, or the design of new concrete infrastructures.

The research topics are divided into three work packages, addressing i) the non-destructive evaluation of NPP concrete infrastructure (WP1); ii) the risk of internal expansive reactions for NPP concrete infrastructure (WP2); and iii) steel liner and anchor corrosion in contact with concrete (WP3).

In the following sections, a selection of research results from the four years of the project are briefly presented.

Introduction

Current Finnish nuclear power plants (NPP) have been designed for 40 years of operation. The concrete structures constructed before the starting of the NPP operation can be older than 45–50 years. There is evidence that ageing effects in some cases have been underestimated during the original design, construction and commissioning or have not been accurately taken into account during operation. It has also been recognized that the ageing of plants needs to be assessed, and an effective management strategy developed in a timely manner, to ensure the necessary technical basis for maintaining safety margins throughout the NPP operation [IAEA, 2016].

The CONAGE project addresses these ageing aspects of NPP structures, systems and components (SSC). The project identifies special aspects that are needed for long-term operation within the scope of ageing management. The topics of research addressed in this project are of interest not only for the concrete infrastructure of existing NPPs, but also especially for those in the design phase. According to an IAEA study, 90% of all ageing problems are initiated in design phase [IAEA, 2016].

NPP ageing management programmes should have access to relevant concrete related R&D. This is fundamental since new developments may contradict

assumptions made during a plant's design [IAEA, 2016] or highlight new issues previously unknown. Even though concrete has been extensively used as a construction material, the concrete used 40 years ago differs significantly from that commonly used today. The reinforced concrete structures of NPP (e.g. containment, spent fuel pools, water intake/outtake structures, foundations) perform multiple safety related functions (e.g. load carrying, radiation shielding and leak tightness). For many of these structures, it is neither technically nor economically feasible to have them replaced. For this reason, it is important that a comprehensive understanding of all possible ageing mechanisms, and their degradation consequence for the safety function of the structure, is achieved. This way, adequate considerations can be made during the design of existing NPPs, while mitigation measures can be planned for existing NPPs.

The research topics being addressed in CONAGE are strongly linked by key aspects of ageing management, where critical input is needed to support decision-based actions, whether related to inspection and maintenance actions on existing concrete infrastructure, or the design of new concrete infrastructures.

The research areas are divided into three main areas, addressing i) the non-destructive evaluation of NPP concrete infrastructure (WP1); ii) the risk of internal expansive reactions for NPP concrete infrastructure (WP2); and iii) steel liner and anchor corrosion in contact with concrete (WP3). In the following sections, the research undertaken during 2019-2023 is briefly presented.

The non-destructive evaluation of NPP concrete infrastructure

Testing of the hardened reinforced concrete structures in situ is often necessary to determine the suitability of a structure for its intended use. Non-destructive testing (NDT) methods are used to (i) evaluate concrete characteristic properties, (ii) determine of the location, diameter and depth of reinforcement steel and (ii) locate and categorize cracks, voids, honeycombing, and other defects in a concrete structures [AEA, 2015].

Various methods of NDT of concrete have been developed and are under development for examining different properties of concrete in addition to the necessary visual inspection. The popular (traditional) NDT tests for concrete used in this research include: (i) rebound hammer test, (ii) ultrasonic pulse velocity (UPV) test, (iii) combined method UPV, rebound hammer and core extraction for compressive strength test and (iv) concrete cover measurement using concrete cover meter. The advanced NDT techniques used include: (i) ground penetrating radar (GPR) and (ii) ultrasonic pulse echo (UPE) imaging using the MIRA – tomograph ultrasonic unit. For conducting this research work, data was obtained from testing the thick-walled reinforced concrete mock-up wall presented in Figure 1 [Al-Neshawy et.al., 2018].

Combined NDE for the Concrete Strength Evaluation.

A combined Ultrasonic Pulse Velocity and Rebound Number (SonReb) method gives a general relationship between compressive strength of concrete, rebound hammer number, and ultrasonic pulse velocity. The basis of SonReb technique is



Figure 1. Overview of the thick-walled concrete structure. [Al-Neshawy et.al., 2018]

given as tentative recommendations for “in-situ concrete strength estimation by combined non-destructive methods” published by RILEM Committee TC 43 CND, 1993 [RILEM, 1993].

SonReb method is an empirical correlation formula proposed to relate the concrete compressive strength to the rebound hammer number (RN) and the ultrasonic velocity (V).

$$f_c = f_0 \cdot e^a \cdot V^b \cdot RN^c \quad (1)$$

Where:

- f_c is the concrete compression strength, [MPa],
- f_0 is the unit conversion factor, [usually $f_0 = 1 \text{ MPa}\cdot\text{s}/\text{m}$],
- V is the ultrasonic pulse velocity [m/s],
- RN is the rebound number (either R -value or Q -value) and
- a, b, c are dimensionless correlation parameters.

Example of the compressive strength obtained by combining the UPV measurements and Rebound Hammer measurements for the west surface of the mock-up wall are represented in Figure 2. The improvement of the accuracy of the strength prediction using SonReb method is as shown in Table 1.

Table 1. Summary of the SonReb method estimated compressive strength results for the west surface of the mock-up wall.

Values	Rebound-hammer	UPV	Drilled specimens	SonReb (UPV+R)
Maximum strength	59,3	56,0	45,5	55,7
Minimum strength	32,3	30,3	34,9	40,3
Median	41,4	39,3	44,8	44,6
Average	39,1	42,2	45,4	45,0
Standard deviation	5,0	4,8	3,7	2,7
COV (%)	11,4	12,8	8,2	5,9

For the west surface example, the probability of the combination of rebound hammer and ultrasonic pulse velocity results in the peak probability 0.15. The coefficient of variation of concrete strength decreases from 11.4% by the original rebound hammer (R-value) to 5.9% when combined with the UPV measurements. It is very important to notice that the accuracy of each and every relationship depends on the calibration and correlation that is made with destructive tests, i.e., core samples.

Based on the example presented, SonReb results seems to be more accurate and reliable than any individual test performed on the same concrete surface. It can help to assess concrete performance more accurately and it will be easier to track concrete behaviour after long period of service.

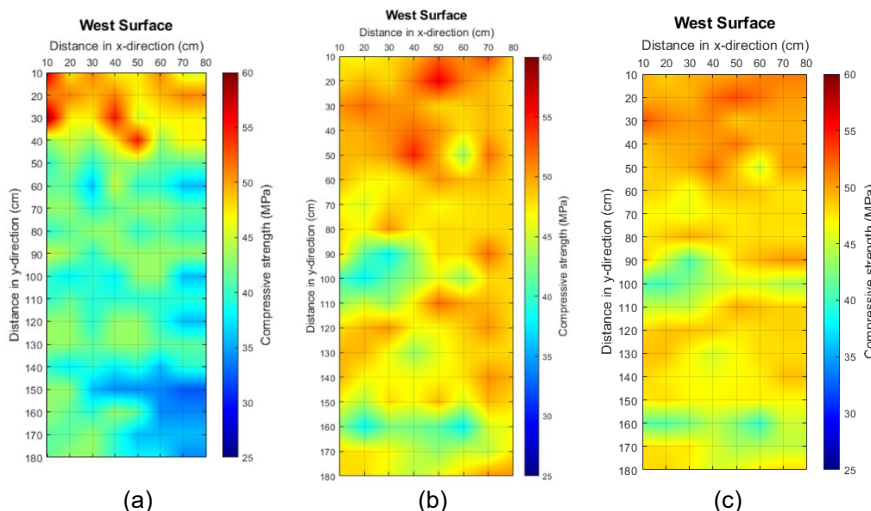


Figure 2. Compressive strength values for the west surface of the mock-up wall received by (a) R-Value hammer, (b) UPV measurements and (c) combining the results of the UPV and R-value Hammer.

Cover meter for the measurement of the concrete cover depth.

The cover meter was set to identify the clear cover above the rebar of 25 mm diameter. Examples of the concrete cover measurement obtained from the scans on the south side of the mock-up wall for horizontal and vertical reinforcement direction are presented in Table 2. The data show that cover meter can effectively be used to measure the cover depths. The concrete cover depths for the horizontal and vertical reinforcement bars. For the horizontal reinforcement bars, the mean (μ) of the verified concrete cover depth is about 43–44 mm with standard deviation (σ) is 1.6–1.7 mm and the coefficient of variation is 4,0–3,6% for left and right half side of the wall. The variation of the measurements was higher for the vertical reinforcement bars than the horizontal bars. The relative error in detection of the cover depth increases in the left half side where higher reinforcement density located.

Table 2. Details of the detected clear cover depth for both horizontal and vertical reinforcement scanning.

Reinforcement	Horizontal reinforcement bars		Vertical reinforcement bars	
South wall side area	Left half side	Right half side	Left half side	Right half side
Average detected cover, (mm)	43	44	50	52
Actual location of bar from top surface, (mm)	50	50	57,5	57,5
Accuracy (Relative Error), (%)	-14	-12	-13	-9,6
Standard deviation, (mm)	1,7	1,6	2,9	3,9
Coefficient of variation, (%)	4	3,6	5,8	7,5

GPR for the mapping of the reinforcement and the identification of general defects in the mock-up wall.

Ground Penetrating Radar (GPR) technique can be used to carry out imaging of reinforced concrete structure and make out assessment to the quality of concrete structure [Watt, 2007]. Interpretation of GPR data commonly helps to confirm the following main questions asked of a concrete structure:

- Concrete component thickness and reinforcement cover thickness (including variations from the original design)
- Existence, spacing, arrangement, and depth to embedded reinforcement
- Existence of other features such as prestressing cables, embedded conduits, and pipes

Examples of the Live concrete GPR scanner measurements are presented at Figure 3. At a depth of 4–6 cm, the near-surface primary reinforcement is visible, with the reinforcement on the left half side of the specimen being approximately twice as dense as on the right side. The secondary reinforcement surface is visible at the depth of 13–15 cm.

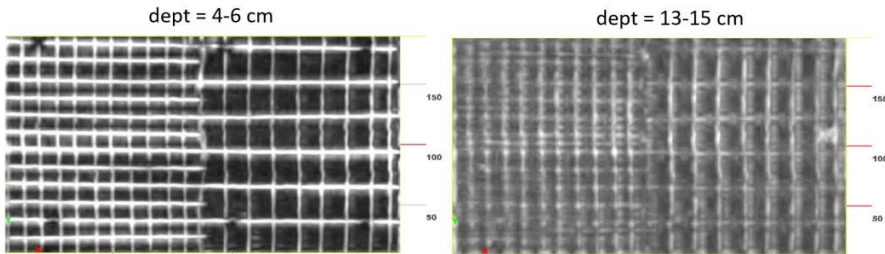


Figure 3. Depth sections, captured with the Live concrete GPR scanner on the south side of the mock-up (measuring field size = 330 cm x 180 cm).

Figure 4 presents the Hilti PS-1000 GPR scanning results of the scanning area (1200 x 1200 mm) on the middle of south direction. The estimated concrete cover depth is approximately 50 mm. Because of the data noise the exact value of concrete cover depth was difficult to determine. A dense reinforcement is shown in the scanning data. The concrete cover depth of the right scanning area is approximately 60 mm. The space between vertical steel rebar is about 150 mm at the right half side and 200 mm at the left half side. The space between horizontal steel rebar is about 150 mm at the right half side and 300 mm at the left half side.

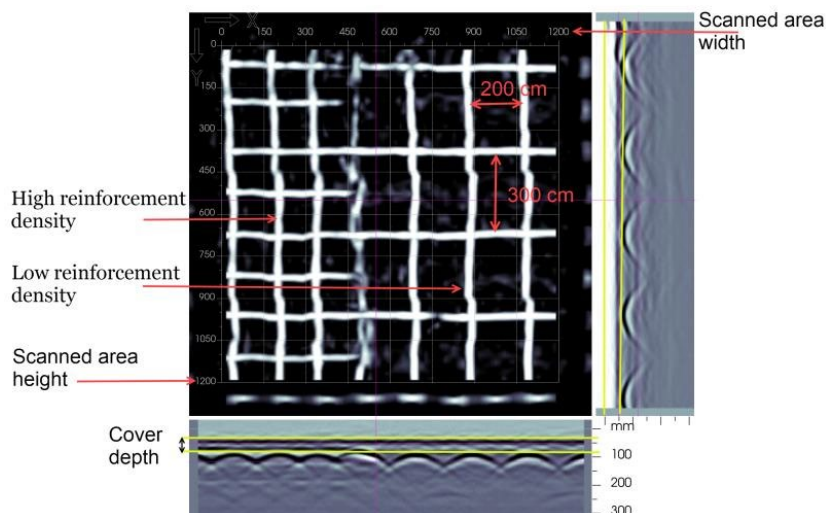


Figure 4. C-scan maps of the inspected area (depth $z = 5$ cm).

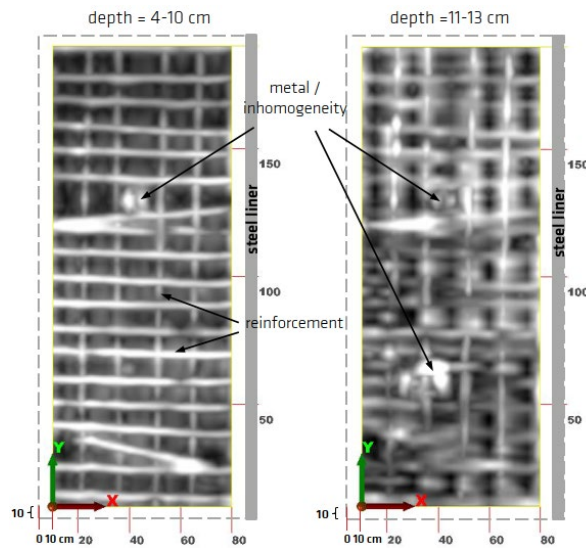


Figure 5. Depth sections from the reconstructed data set, captured with the GPR Live-system on the eastern side of the mock up wall (size of the measurement field = 80 cm x 180 cm) [Al-Neshawy, 2020].

The benefits of the application of the GPR technique to concrete include the identification and mapping of embedded reinforcement rebars. The data interpretation is technician (operator) dependent, and the human error is a factor of the reliability of the results. Example of the result images from the data set taken on the east side of the test specimen are shown in Figure 5. In addition to the structural reinforcement layer, a conspicuous area measuring approx. $15 \times 15 \text{ cm}^2$ is visible in the upper half of the image in the left depth section (depth range = 4–10 cm) (reflections from e.g. built-in components such as sensors, tendon heads, reinforcement or defects).

In the right depth section of the same dataset a further conspicuous area in the lower half of the picture is visible at a depth of 11–13 cm. This is also a clear reflection with a similar cause as mentioned above.

In summary, the GPR radar scanning system was used to take manual, area-wide measurements on the mock-up reinforced concrete wall. In the reconstructed data sets of each side surface the respective position of the existing structural reinforcement as well as conspicuous areas of e.g. tendon heads, built-in sensors, introduced defects or inhomogeneities were displayed.

Ultrasonic Pulse Echo (MIRA) tomograph ultrasonic unit for the identification of general defects in the mock-up wall.

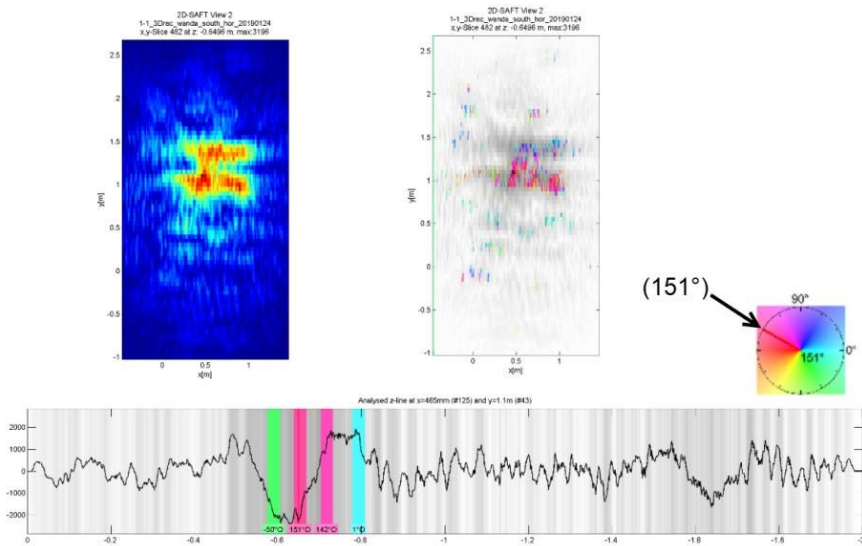


Figure 6. Phase processing of the measurements at the South side of the mock-up wall, horizontal measurement, $z = -0.5$ m (at 151°).

The reinforced concrete mock-up wall was investigated using a commercially available measuring MIRA device. The MIRA version incorporates 12 channels each comprised of 4 transducers in a multi-static array (type A1040 MIRA). The system works with transversal wave probes. The ultrasonic wave velocity used for the evaluation was $v_T = 2700$ m/s. The frequency was 55 kHz. For the evaluation, the imaging software InterSAFT was used.

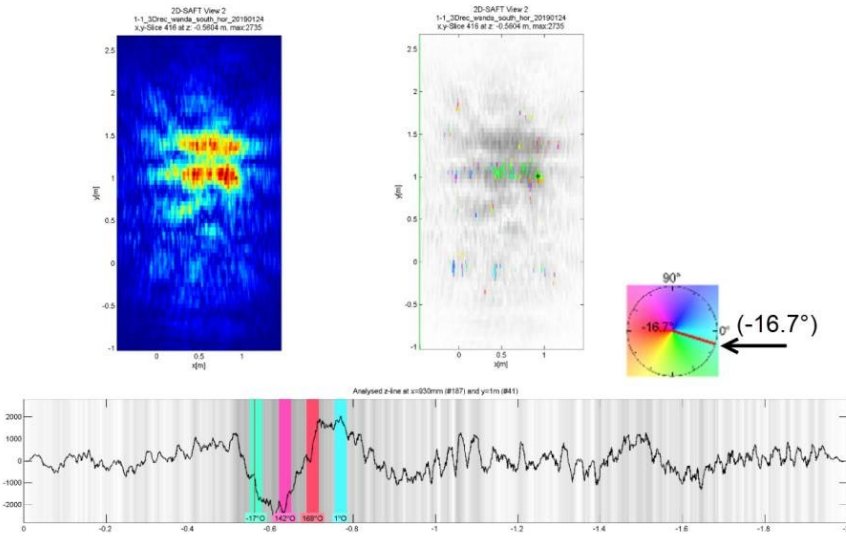


Figure 7. Phase processing of the measurements at the South side of the mock-up wall, horizontal measurement, $z = -0.5$ m (at -16.7°).

The measurement data was generated from the mock-up surface facing South. The area with the double reflectors shows inconsistent results. The phase evaluation in Figure 6 indicates an acoustically strong reflector (151°). The phase evaluation in Figure 7 shows a different acoustically reflector result (-16.7°). Here, the reflector shows acoustically weak properties. The large-surface reflector has strong and weak acoustically components and appears as two different objects (or one large object with two strong reflections). This could indicate an embedded acoustically strong reflector with injecting defects. It could also be an acoustically weak reflector with an acoustically strong coating. For the verification more, precise information from the construction plan would be needed. Verification could also be done with another non-destructive method.

Risk of internal expansive reactions of NPP concrete infrastructure

A significant number of problems related to concrete deterioration worldwide are due to the development of internal expansive reactions. These reactions diminish the affected structure's service life, may affect its function and, ultimately, can lead to its demolishing. Internal expansive reactions are mainly of two types: alkali-aggregate reaction (AAR) and delayed ettringite formation (DEF). Both deterioration mechanisms cause the hardened concrete to expand and thereby progressively inducing tensile stresses and cracking. This influences the mechanical properties of concrete, which in turn reduces the structural capacity influencing its fragility. The

research in this project focuses on AAR, or more specifically ASR (alkali-silica reactions, which are a subset of AAR that is more predominant in Finland) since it is more relevant to the Finnish utilities.

ASR related expansion in reinforced concrete structures has gained prominence in the recent past because of the widespread nature of the problem with in the nuclear community, and the potential adverse economic impacts that it may have [Snyder & Lwe, 2013; Chérnier et al., 2012, Manabe et al. 2018, Tang 2013]. Furthermore, the possibility of ASR occurrence in VTT's FiR 1 reactor containment structure [Orantie, 2014] and the many other documented cases in bridges and other infrastructure offer enough concern to address this issue in Finland.

For the occurrence of ASR, in addition to moisture, there should be enough alkalis and reactive aggregate. The source of alkalis can either be internal (constituent of the cement or the aggregate itself) or external (from the environment, e.g. from sea or ground water). Depending on the reactivity of the aggregate, concrete composition and the environment, damages can occur rapidly within the first years after construction, or slowly after decades. The cracking due to ASR leads to loss of function, durability, structural integrity and service life. ASR cannot be adequately stopped or repaired after it is found; only mitigated. NPPs and other nuclear infrastructures have been affected by ASR [Saouma & Hariri-Ardebili, 2014]. The risks are high in massive structures where a long service life is expected, if these are constructed with reactive materials. As well, certain structural members of nuclear facilities being exposed to increased temperature and humidity underlie a high damage probability. Since damages to nuclear structures can have large risks to the environment and society and are very costly to repair, strategies for preventing the use of improper concrete raw materials for the construction of new NPPs must be developed. Risk assessments regarding the inherent and residual swelling potential of the concrete subject to ASR needs to be assessed for existing NPP concrete structures, especial in the case of lifetime extension.

The main goal of this workpackage is to take initial steps in identifying the risk level of ASR for concrete used in Finnish NPPs. Furthermore, the project proposes to increase awareness of ASR as a potentially damaging mechanism and to initiate further actions to avoid ASR in newly planned or constructed nuclear structures. Subsequently, the gained knowledge on ASR in Finland will serve to increase the predictive accuracy when assessing service life extension of existing nuclear facilities and thus contributes to their operational safety in general.

The research conducted so far focuses on two aspects: i) Identify critical areas of Finnish NPP SSCs where ASR has the possibility to occur, based on concrete compositions and exposure conditions; and ii) study the reactivity of aggregates used in the construction of Finnish NPPs.

With this research the project contributes significantly to the current state of knowledge concerning ASR performance in Finland.

Critical areas of Finnish NPP SSCs where ASR has the possibility to occur.

This study relies on information about the concreting history (constituents of the compositions used if available) and the existing exposure conditions to which the

concrete infrastructure is subject to, provided by the utilities. This study is conducted to the component level, since a structure can be subject to unique variation in exposure (e.g. wall that is partially submerged). Key aspects considered are access to moisture, chemical composition of the concrete binder mixes, and geometry of the concrete elements.

The main reinforced concrete infrastructure of Finnish NPPs (OL1, OL2, OL3, LO1 and LO2) has been considered. Most of the information has been retrieved from the SERVICEMAN project [SAFIR 2010]. In addition, workshops were held with TVO and FORTUM to obtain additional insight and information to the NPPs in question. A detailed description of the work performed can be found in [Ferreira, 2019].

The exact compositions of the cement and supplementary cementitious materials used is not known, so the study is based on published literature for the same or similar cement of the years in which the NPPs where built.

The potential for occurrence of ASR is based on assessing the combined risk of two of the three factors needed to occur simultaneously: sufficiently high alkali content and high moisture content. Only the sufficiently reactive aggregate factor is not known, and therefore not considered.

The potential for occurrence is defined as being either LOW, MEDIUM, or HIGH depending on factors related to the moisture content in the concrete and the potential alkali level due to the type of cement and environmental exposure conditions [Ferreira, 2019].

A factor that has not been explicitly considered is the effect of temperature. At higher temperatures, the increase in reactivity results in ASR end product more quickly, i.e., the expansive gel.

The choice of "Source of Alkalies" is not straight forward as cement types can have both high and low alkali content. For this reason, it is very important to know what was the exact chemical composition of the cement used as well as any additions added to the mix, and whether the alkalies in their chemical composition are chemically bound, or available to contribute to the alkalinity of the pore structure.

Table 3. Classification of the potential for occurrence of ASR of NPP's reinforced concrete structures if the aggregate is found to be reactive [Ferreira, 2019].

Source of Alkalies*	Factors affecting RH	CS<0.2m RH<70%	0.2m<CS<0.5m 70%<RH<80%	CS>0.5m RH>80%
		Level	Low	Medium
CEM III	Low	LOW	LOW	MEDIUM
CEM I/II + SW CEM III + SW	Medium	LOW	MEDIUM	HIGH
CEM I, CEM II, CEM I/II + SW	High	MEDIUM	HIGH	(VERY) HIGH

SW – seawater; CS – thickness of the concrete structural element.

* – General indicator of cement types, but for confirmation exact binder composition should be known.

Table 3 presents the potential for occurrence of ASR on NPP reinforced concrete structures. By classifying, for a specific reinforced concrete structure/module, both the source of alkalis and the factors affecting relative humidity.

The results show that a large part of the concrete infrastructure of Finnish NPPs show medium to high potential of ASR occurrence, if the aggregate were to be found reactive [Ferreira, 2019]. This is due to the high alkali content in the concrete, and either the high relative humidity of the environment where the concrete element is situated, or due to the large cross section of the concrete element.

Reactivity of aggregates used in the construction of Finnish NPPs.

Various aggregates used for the production of concrete structure of NPPs were received from Finnish utilities TVO and FORTUM for testing.

From FORTUM, six sand samples were taken from independent sand extraction pits. These sands have been used for the construction of different structural elements at the Lovisa NPP and in the KJT repository. These aggregate samples were subject to the RILEM AAR-2.2 test. One of the aggregates (Malmgård) was also subjected to RILEM AAR4.1 and AAR 3.1 tests.

From TVO, eight rock samples taken from the surroundings of OL1 and OL2 where the excavated rock was used to make the aggregate for concrete were chosen to be tested for ASR. These aggregate samples were subject to the RILEM AAR-2.2 and the RILEM AAR-4.1 and AAR-3.1 tests.

In the RILEM AAR-2.2 method, prisms are moulded from mortar prepared with the aggregate to be tested. Prism dimensions 160mm x 40mm x 40mm were chosen. The prisms were demoulded after 24 ± 2 h and their initial length measured. The specimens were then placed in water, transferred to an oven at 80 ± 2 °C for 24 h, removed from the water, surface dried, and the length measured immediately before the temperature has dropped substantially (zero reading). The specimens were then placed in containers with a 1 Mol NaOH solution already at 80 ± 2 °C, which were sealed and placed in an oven at 80 ± 2 °C. Length measurements were taken periodically. The duration of the test is usually 2 weeks, but these tests were extended to 5 weeks to check for delayed expansion. The cement used was a CEM I 52,5 R (Paraisen Pikasementti from Finnsementti), with a $\text{Na}_2\text{O}_{\text{EQ}} = 1.77\%$. This value exceeds the minimum requirement of 1.0%. An absolute criterion for the interpretation of the results of AAR-2.2 have not yet been finally agreed, especially not for Finnish rock types. However, on the basis of trials carried out by RILEM on aggregate combinations of known field performance from various parts of the world, it seems that results in the test (after the standard 14-days, AAR-2.2) of less than 0.08 % are likely to indicate non-expansive materials, whilst results exceeding 0.16 % are likely to indicate expansive materials.

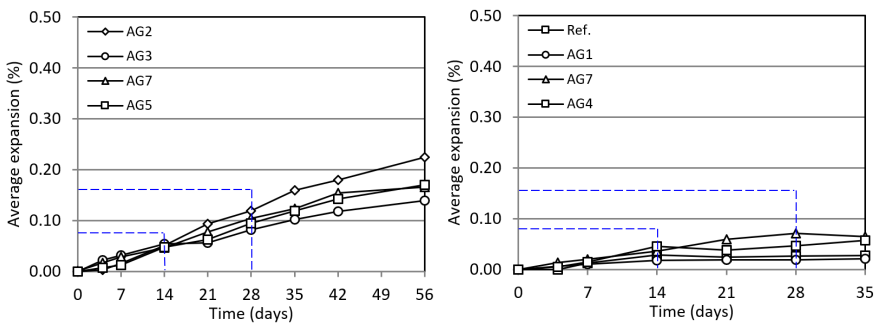


Figure 8. Expansion values for the AAR-2.2 test conducted on the sand aggregates from (a) Fortum [Ferreira, 2020b], and (b) TVO [Ferreira, 2020a].

The results of the tests for the FORTUM aggregate show expansion levels below 0.05% at 14 days, and expansion levels below 0.012% at 28 days. These results indicate that it is very likely that the FORTUM sands are non-expansive.

The results of the tests for the TVO aggregate show expansion levels below 0.05% at 14 days, and expansion levels below 0.08% at 28 days. These results indicate that it is very likely that the TVO rock aggregates are non-expansive.

In the RILEM AAR-4.1 method, prisms are moulded from concrete prepared with the aggregate to be tested. Prism size 280 mm x 75 mm x 75 mm was chosen. The prisms were demoulded after 24 ± 2 h and their initial length and weight are measured. The specimens were then placed in metallic containers with 35 ± 5 mm of water at the bottom. Each sealable container holds a maximum of three prisms. The sealed containers are placed inside an AAR reactor in which the temperature is at 60 ± 2 °C that contains an appropriate level of water to maintain 100% RH inside. Length measurements were taken periodically. The cement used was identical to that used in the RILEM AAR-2.2 tests. Criteria for the interpretation of the results of AAR-4.1 have not yet been finally agreed. However, on the basis of an initial assessment of the AAR-4.1 trials carried out by RILEM TC 191-ARP on aggregate combinations of known field performance from various parts of the world, it seems that a maximum expansion in the test of less than 0.03% at 15 weeks indicates a non-reactive aggregate or aggregate combination.

The results (Figure) of the tests for the TVO aggregate show expansion levels greater than 0.03% at 15 weeks, therefore inconclusive in relation to the nature of their reactivity.

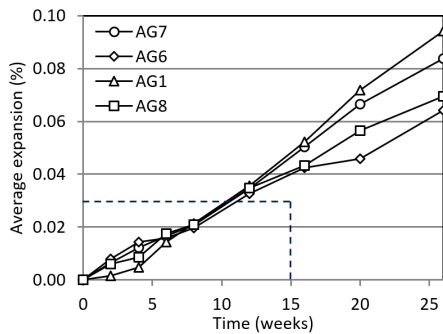


Figure 9. Expansion measurements for aggregate samples AG1, AG6, AG7 and AG8. The dotted line shows the expansion limit of 0.03% at 15 weeks [Ferreira, 2020b].

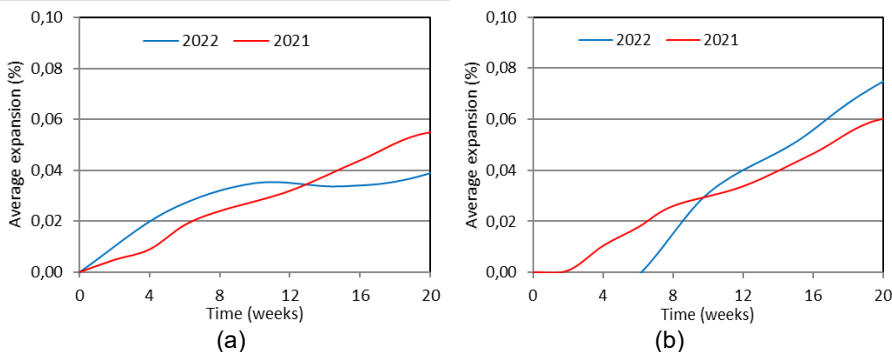


Figure 30. Olkiluoto TVO aggregate 3 (a) and 5 (b) average expansions in AAR4.1 test both in 2021 and 2022.

Since the results show expansion above the 0.03% at 15 weeks, and in the absence of local experience to the contrary, this indicates that it cannot be ruled out that the TVO rock aggregates are potentially expansive. These results are surprising as they contradict the AAR-2.2 tests conducted on the same aggregates. For this reason, the AAR-2.2 tests were repeated to confirm the result. Also, some of the AAR-4.1 results were repeated, namely the samples 4 and 5. The results were similar enough to earlier levels to confirm the results.

In the RILEM AAR-3.1 method, similar concrete prisms as in AAR-4.1 are produced. The sealed containers, containing the prisms, are placed inside an oven in which the temperature is at 35 ± 2 °C that contains an appropriate level of water to maintain 100% RH inside. Length measurements were taken periodically. The cement used was identical to that used in the RILEM AAR-2.2 tests. Criteria for the interpretation of the results of AAR-3.1 have not yet been finally agreed. However, on the basis of trials carried out by RILEM TC 191-ARP on aggregate combinations

of known field performance from various parts of the world, it seems that a maximum expansion in the test of less than 0.03% at 52 weeks indicates a non-reactive aggregate or aggregate combination. Since the beginning of this project a national guidance "by 74 Ohje betonin alkali-kivialainesreaktioon hallitsemiseksi 2022" has been published. In this publication aggregate is placed in two classes based on AAR-3.1 results: Reactivity unlikely (expansion \leq 0,04% at 52 weeks) or likely (expansion $>$ 0,04% at 52 weeks).

Fortum aggregate Malmgård and TVO aggregates 1, 2 and 8 are being tested with this method. The test is still ongoing and will not be terminated until May 2023. At 32 weeks (Figure) the expansion is, in all samples, still below suggested limits for potentially reactive aggregate. However, in most of the samples the expansion seems to continue and if the trend continues the expansion of some of the aggregate may exceed the suggested limits for reactivity.

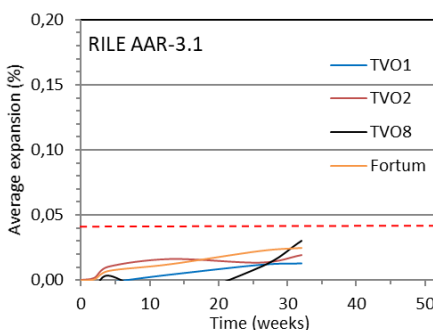


Figure 11. Expansion results from the ongoing AAR3.1 test for TVO aggregates, 2 and 8, and Fortum Malmgård aggregate.

In case of varying results from different test methods, a microstructural study on optical microscopy could give further evidence on actual behaviour of the aggregate during the test. The fact that the expansion in many cases has continued well beyond the evaluation age suggests, there's a need for longer testing times due to the possible slower reaction process that some aggregates exhibit.

Steel liner and anchor corrosion

Age-related degradation of steel components embedded in or in a direct contact with concrete, in particular corrosion of steel liner and anchors, is the subject of this research work. Corrosion experiments help to identify the electrochemical conditions and the mechanisms that allow for the corrosion of the steel liner plates at the interface of steel and concrete, i.e., in an area where the liner should be passive, thus protected from corrosion. Additional experiments will focus on corrosion and bond of anchors in concrete.

Steel liner corrosion

Corrosion of nuclear containment liner embedded in concrete structures has been observed at several occasions and at various NPPs globally [Petti et al., 2011]. Instances of steel liner corrosion have been reported also in Sweden and Finland (e.g. [Wegemar, 2006]). Figure 12 shows a corrosion damage in the steel liner, discovered in Ringhals 2 in 2004 [Aghili, 2007]. The liner materials are usually carbon steel, galvanised steel or stainless steel. Corrosion has been detected at the inner surface of the liner plates (direct exposure to the containment interiors), and in particular where the plates are in a direct contact with concrete (outer surface). Corrosion initiated on the outer containment surface has been associated with foreign material left embedded in the concrete, such as wood pieces or distance holders left in place at the time of concrete casting. Sometimes the cause of corrosion has been unclear, but the delamination of the steel plates from the concrete or liner bulging has been observed. At worst, corrosion has penetrated the thick plates of the liner, or led to a significant decrease of the liner cross-section.



Figure 12. Corrosion damage in the steel liner from Ringhals 2 [Aghili, 2007].

Of particular interest is the corrosion at the outer surface of the liner in direct contact to the concrete. The challenge is that the liner surfaces in contact with concrete cannot be checked by visual inspections, and there are also challenges in their location by traditional non-destructive test (NDT) methods. The alkaline concrete should in principle cause passivation of the steel surface, i.e., build-up a protective oxide film on the surface, and prevent any corrosion. However, according to the present understanding, corrosion is initiated where the local pH at the steel/concrete or steel/foreign material interface drops below the value necessary to sustain the passivity. The value is not a fixed quantity, as it depends, among other factors, on the concentration of aggressive species. Liner delamination and the presence of foreign materials in contact with the steel lead to the formation of a crevice. Additionally, a macro cell is formed between the small local anodic area, i.e., where active corrosion occurs, and a large cathodic surface surrounding the anode, in the presence of water or humidity. The passive sections of the liner act as cathodic

sites. Localised corrosion can propagate over the long time periods, e.g., many years, since massive concrete structures have sufficient water content and ionic conductivity to support the electrochemical corrosion reactions.

A detailed understanding of the factors responsible for the appearance and extent of the corrosion, the corrosion localisation and the electrochemical mechanisms is still lacking, but crucial for predicting possible future incidences, identifying the corrosion locations and the extent of attack as well as establishing best mitigation procedures. This is the motivation of the present work.

Experimental investigations aim at studying in detail and defining the corrosion mechanism of the steel plate and identifying which factors promote or impede the occurrence of corrosion. For this purpose concrete, corrosion specimens were designed [Bohner & Huttunen-Saarivirta, 2020] and manufactured to allow for electrochemical measurements during the course of the experiment and characterization of the liner surfaces afterwards.

The following two main corrosion scenarios have been presented in the literature review [Isotahdon et al., 2019] and will be the subject of the experiments: 1) loss of passivity, i.e., activation, and 2) delamination-induced corrosion. A schematic representation of the experimental setups used in the investigation of each corrosion scenario is given in Figure 13. Corrosion inlays were used to define the anodic area and introduce the reference electrode, necessary for electrochemical measurements.

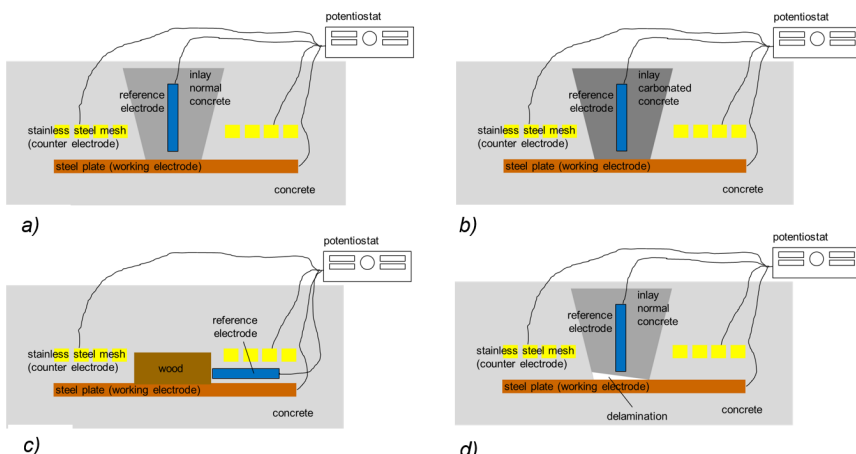


Figure 13. Schematic representation of the experimental setup for each corrosion scenario: a) Scenario 1, implemented with normal concrete; b) Scenario 1, implemented with carbonated concrete (low-pH concrete); c) Scenario 1, implemented with a piece of wood; d) Scenario 2, implemented with a gap between steel plate and concrete (delamination).

During the corrosion tests, electrochemical measurements were performed regularly. The measurements involved open circuit potential (OCP), linear

polarization resistance (LPR) and Tafel measurements. The combination of LPR and Tafel measurements enable the instantaneous corrosion rate to be determined. Figure 14 shows the derived instantaneous corrosion rates for the steel liner specimens in various test scenarios over the test duration.

In the case of specimens with the inlay of normal concrete or wood, the corrosion rate for the steel liner as a function of time is shown in Figure 14. In the specimens which did not contain chlorides (#1, #7, #9), the initial corrosion rate of the steel liner was somewhat higher than the stabilized value that was measured during most of the test duration. As expected, the lowest corrosion rate towards the end of the experiment, below 2 $\mu\text{m/a}$, was detected in the cases of reference specimens with normal concrete inlay, #1, and inlay with the delamination gap, #9. The use of wood inlay, #7, approximately doubled the steady-state corrosion rate, to the level of 4–5 $\mu\text{m/a}$, yet the initial value was almost ten times the stabilized value. The introduction of chlorides to normal concrete (#2) and normal concrete with delamination gap (#10) also slightly accelerated corrosion, with the corrosion rates about 5–6 $\mu\text{m/a}$ being detected. Among this batch of specimens, the highest corrosion rate for the steel liner was systematically detected in the tests with wood inlay with chlorides, #8. Here, the corrosion rate varied from 7 to 17 $\mu\text{m/a}$ during the test, yet for the majority of the test duration the corrosion rate of about 10 $\mu\text{m/a}$ was detected.

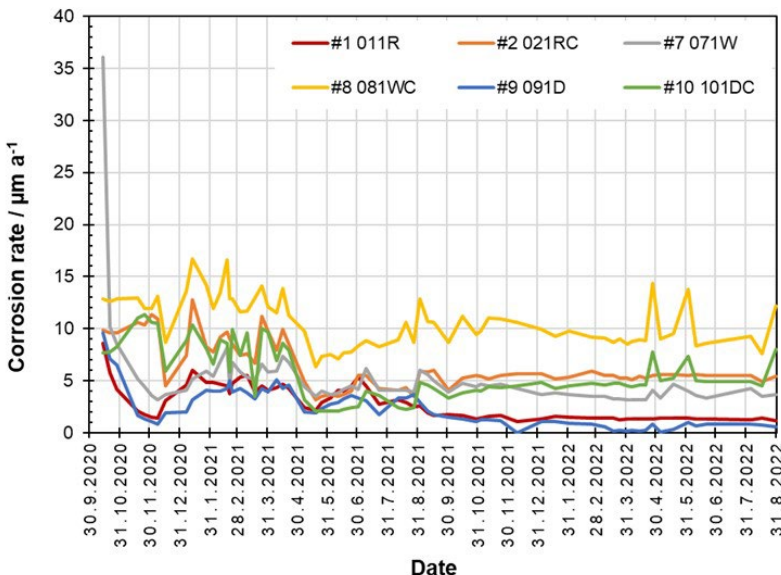


Figure 14. Corrosion rate of steel liner embedded in concrete. In the specimen identifiers, R refers to reference (“normal” concrete), C refers to chloride, W refers to wood and D refers to delamination.

In the case of specimens with the inlay of low-pH concrete in its all variants, corrosion rate for the specimens was, in most cases, much higher than in normal

concrete and wood. The exception was the case of low-pH concrete inlay, #3, in which the corrosion rate was retained at the level of $0.1 \mu\text{m/a}$ all through the test. In the case of low-pH concrete with chlorides, #4, the instantaneous corrosion rate of the steel liner varied between approximately $10 \mu\text{m/a}$ and $30 \mu\text{m/a}$, with an average of $20 \mu\text{m/a}$. This indicates that the presence of chlorides accelerates the corrosion rate of steel more significantly in low-pH concrete than in normal concrete. In the specimens with impressed current, #5, some differences between the two parallel specimens in the instantaneous corrosion rate were detected. In specimen 051PH, the instantaneous corrosion rate of the steel liner was retained below $10 \mu\text{m/a}$ until the impressed current was turned on, but increased systematically since then, up to above $100 \mu\text{m/a}$ towards the end of the experiment. In the specimen 052PH, the instantaneous corrosion rate of steel liner was in the range from 10 to $20 \mu\text{m/a}$ until the impressed current was applied, but increased then to values above $100 \mu\text{m/a}$. In the specimens with both chlorides and impressed current, the initial corrosion rates were in the range from 10 to $20 \mu\text{m/a}$, but the use of impressed current increased the rate up to several hundreds of $\mu\text{m/a}$, in the case of specimen 062PHCI even above $1000 \mu\text{m/a}$ (mm/a). These results demonstrate that the impressed current acted as planned, i.e., accelerated the corrosion rate of the steel. This enables us to evaluate the relative severity of corrosion between the various cases.

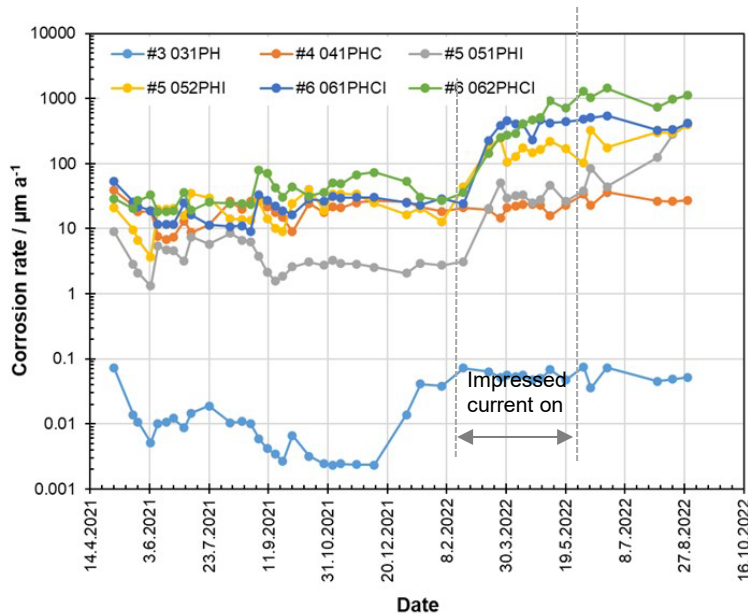


Figure 15. Corrosion rate of steel liner embedded in concrete. In the specimen identifiers, PH refers to low-pH concrete, C refers to chloride and I refers to impressed.

The steel liner specimens were photographed after the experiments. Examples of the photographs are shown in Fig. 16. In most cases, the surfaces of the three (#1-#4, #7-#10) or two (#5, #6) parallel specimens were well in agreement with each other with respect to the extent of corrosion. However, in the case of experiment #3 (low-pH concrete), there was slight variation in the extent of corrosion between the three parallel specimens. Based on visual examination, the specimens were categorized into the following four classes: *no corrosion*, *minor corrosion*, *moderate corrosion*, and *severe corrosion*. No corrosion category involved the specimens #1 and #9, i.e., normal concrete and normal concrete with the delamination gap. Minor corrosion category contained the specimens #2, #3 and #10, yet some of the parallel specimens of #3 (032PH and 033PH) also fell within moderate corrosion category. Moderate corrosion category covered, besides some of the specimens from #3, specimens #4, #7 and #8. Severe corrosion category contained all specimens that were subjected to impressed current, i.e., specimens #5 and #6.

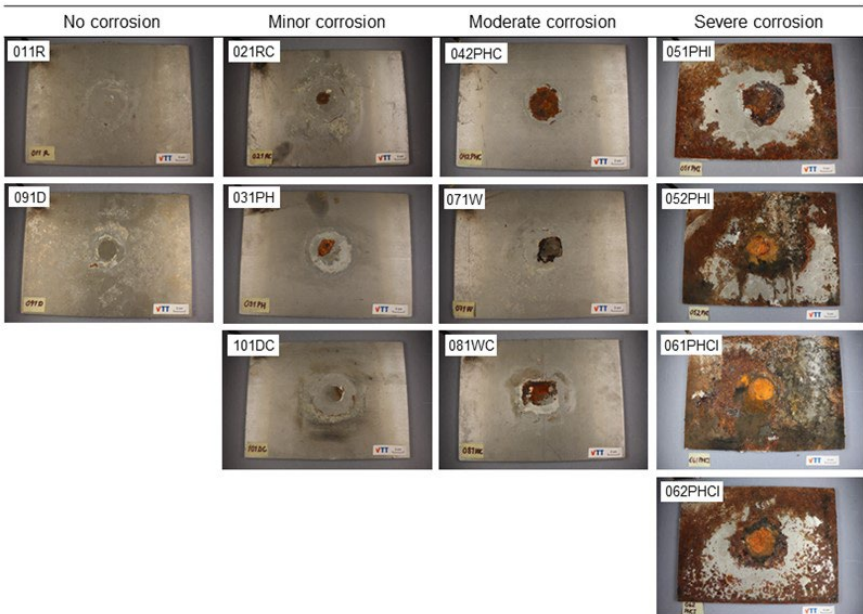


Figure 16. Photographs of steel liner specimens from the corrosion tests. Corrosion rate of steel liner embedded in concrete. In the specimen identifiers, R refers to reference (“normal” concrete), D refers to delamination, C refers to chloride, PH refers to low-pH concrete, W refers to wood and I refers to impressed.

The surfaces were further subjected to image analyses for defining the surface coverage (in cm^2 and %) by the corrosion products. The results are shown in Fig. 17. In the specimens with no corrosion, the corrosion products covered at maximum 0.1% of the surface area. This concerned the specimens with normal concrete, #1, with $0.6 \text{ cm}^2/0.1\%$ of the surface covered by corrosion products, and specimens

with normal concrete with delamination gap, #9, with $0.7 \text{ cm}^2/0.1\%$. In specimens falling within minor corrosion category, corrosion products covered at maximum 1% of the surface. This refers to specimens #2 with normal concrete and chlorides with $5 \text{ cm}^2/0.8\%$ surface coverage by corrosion products, specimens #3 similarly with $5 \text{ cm}^2/0.8\%$ surface coverage by corrosion products, and specimens #10 with delamination gap and chlorides, in which corrosion products covered $4 \text{ cm}^2/0.6\%$ of the surface. In the moderate corrosion category, the overall surface coverage by corrosion products was greater than 1% but less than 5%. In specimens #4 with low-pH concrete and chlorides, contribution by corrosion to the surface coverage was $23 \text{ cm}^2/2\%$. In the case of specimens #7 with wood, the corresponding figures were $14 \text{ cm}^2/2\%$, while in specimens #8 with wood and chlorides, the extent of corrosion on the surfaces was $21 \text{ cm}^2/3\%$. The results revealed by far the greatest surface coverage by corrosion products in the specimens #6 with low-pH concrete, chlorides and impressed current, amounting $568 \text{ cm}^2/86\%$ and $447 \text{ cm}^2/68\%$, and in the specimens #5 with low-pH concrete and impressed current, amounting $423 \text{ cm}^2/64\%$ and $388 \text{ cm}^2/59\%$. Indeed, these were the specimens under severe corrosion category, where the contribution by corrosion to the surface coverage was greater than 50%.

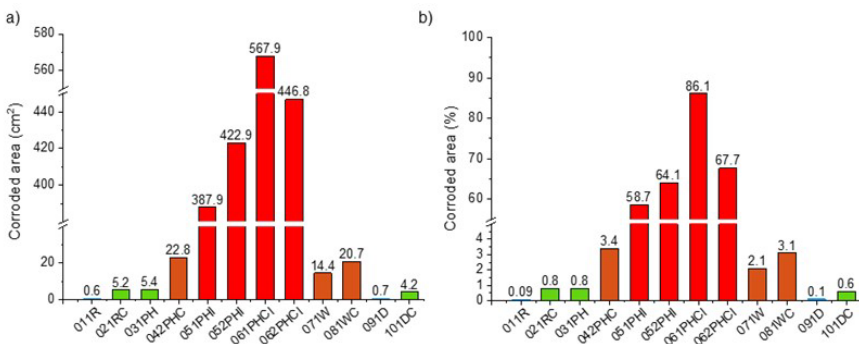


Figure 17. Results from image analyses of surface coverage in a) cm^2 and b) % by the corrosion products.

The surface profiles of the exposed surfaces were examined by 3D profilometry after the removal of corrosion products. The results are shown in Figure 13. In the case of normal concrete (#1, Fig. 13a) and normal concrete with the delamination gap (#9, Fig. 13b), profilometry investigations revealed negligible profile valleys. Only in occasional local points in the specimen #9, the results indicated penetration of the steel substrate. Profilometry investigations of the steel surfaces underneath the inlay of normal concrete with chlorides (#2, Fig. 13c) and normal concrete with the delamination gap and chlorides (#10, Fig. 13d) disclosed some profile valleys, thus material losses, which followed the periphery of the inlays. In the cases of low-pH concrete (#3, Fig. 13e) and low-pH concrete with chlorides (#4, Fig. 13f), profilometry investigations revealed uniform material losses in the steel liner all

through the area underneath the inlays (both in the absence and presence of chlorides). In comparison, the material losses in the liner underneath the wooden inlay (#7, Fig. 13g) and wooden inlay with chlorides (#8, Fig. 13h) were detected within narrow sections at and around the inlay edges. In the case of specimens subjected to impressed current, extensive material losses occurred underneath the concrete inlay. Corrosion attack was detected down to the depth of 0.37 mm (#5, Fig. 13i) and 0.5 mm (#6, Fig. 13j) below the original surface.

The obtained results enable the following conclusions to be drawn:

1. In the cases of normal concrete (#1, reference specimens) and normal concrete with the delamination gap (#9), the extent of corrosion detected on the steel liner surfaces was very low, and the measured instantaneous corrosion rates were of the magnitude of 1–2 $\mu\text{m/a}$. Under these conditions, the contribution of corrosion to the materials degradation can be considered negligible. Therefore, in the used experimental set-up, the presence of the delamination gap did not significantly change the corrosion behaviour of the steel liner in comparison to the corresponding flat surface of a normal concrete.
2. The loss of passivity explains the corrosion of steel liner embedded in concrete. This was observed both in the case of low-pH concrete and in the presence of the foreign matter: piece of wood. The electrochemical results obtained for the specimens and the results from surface coverage characterization refer to uniform corrosion of steel liner both in the case of low-pH concrete and of a piece of wood. However, 3D profilometry disclosed uniform corrosion only underneath the low-pH concrete. In the case of wooden inlay, 3D profilometry revealed that corrosion attack of the steel liner occurred within a narrow section at the inlay perimeter, being therefore more of localized than of uniform nature. We wish to emphasize that in practise, there may also be other reasons for the loss of passivity, such as flowing water, e.g., leakage, or large voids in the concrete in contact with the steel liner.
3. In the used experimental set-up, the presence of chlorides in the inlays accelerated the corrosion of steel liner. The presence of chlorides was systematically reflected to, e.g., higher corrosion rates and greater extent of corrosion on the steel liner surfaces both with respect to surface coverage by corrosion products and material losses in the steel liner revealed by 3D profilometry. However, based on the obtained results, we did not detect a significant change in the form of corrosion attack from uniform corrosion to pitting corrosion.
4. In the experiments, impressed current was used to accelerate the corrosion. The severity of corrosion was high in the experiments including impressed current, as expected.
5. The obtained results suggest that our approach of using the inlays for creating the anode under it is valid and applicable to the corrosion studies of steel liner in concrete.

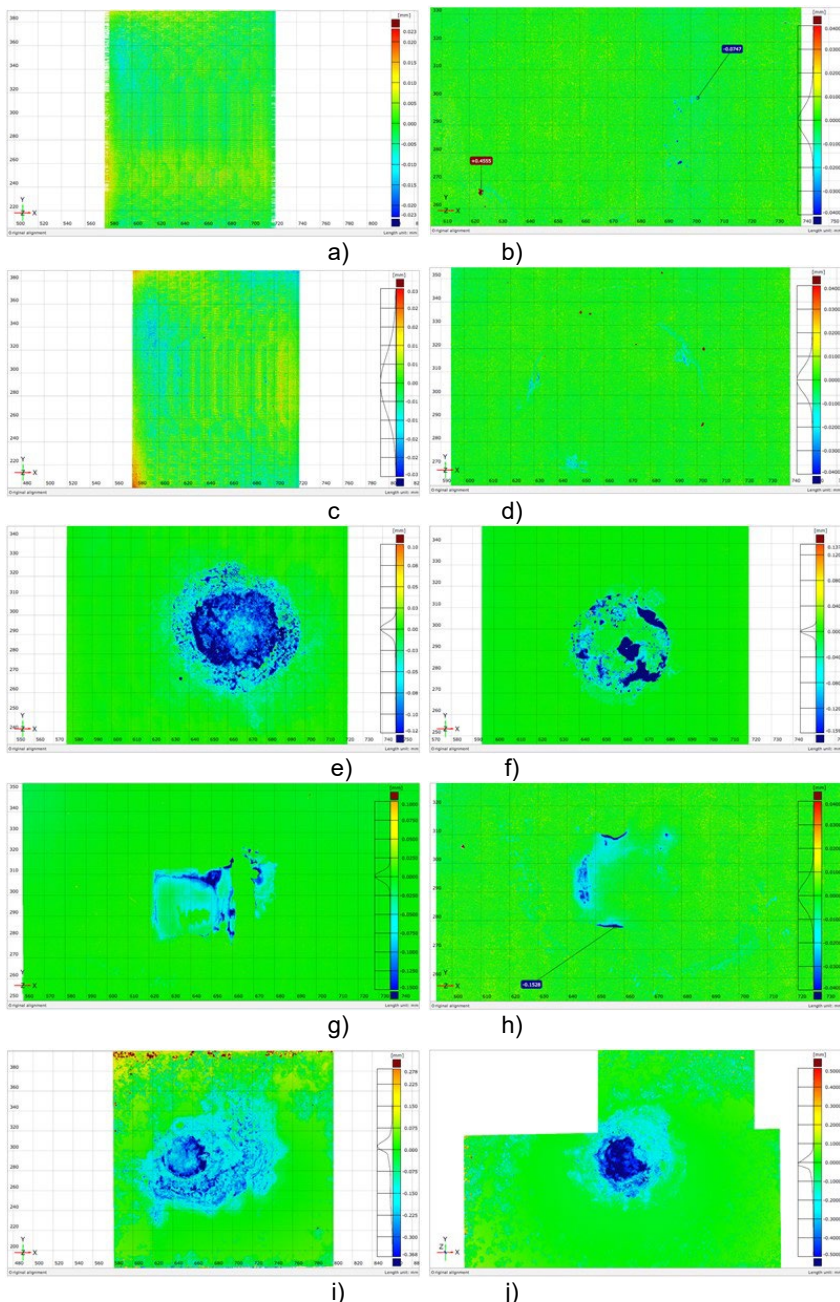


Figure 18. Results from 3D profilometry analyses of the surfaces after the removal of corrosion products. a) 012R. b) 092D. c) 022RC. d) 102DC. e) 033PH. f) 042PHC. g) 072W. h) 082WC. i) 052PHI. j) 062PHCl.

Post-installed anchor corrosion

The objective of the research was to define the influence of the anchor bar material and tensile stress-state on the durability of post-installed anchors in reinforced concrete structures. Studies were done to (i) estimate the extent of the corrosion after one and half years of exposure to wetting in sodium chloride solution and drying and (ii) to determine the probable corrosion mechanisms. The exposure conditions of concrete structures were simulated in the laboratory work.

Three different kinds of post-installed anchors were used: (i) undercut anchors, (ii) expansion (wedge) anchors, and (iii) chemical anchors. Three steel materials produced by Hilti Oy, expect ordinary threaded rod produced by Etra Oy were selected for each anchor type. The selected steel material were: (i) ordinary carbon steel, (ii) hot-dip or electro galvanised steel, and (iii) austenitic stainless steel (the grade of steel AISI 304 (A2), AISI 316 (A4), 1.4529 (A6)).

Table 4. Types and steel material of the different post installed anchors.

Anchor Code	Anchor type	Steel material
HST3	Expansion	Carbon steel
HST3-R	Expansion	Stainless steel, A4
HST-HCR	Expansion	Stainless steel, A6
HDA-P	Undercut	Hot-dip galvanised carbon steel
HDA-PF	Undercut	Carbon steel
HDA-PR	Undercut	Stainless steel, A4
TR-B	Chemical (threaded rod)	Tempered carbon steel
TR-ZN	Chemical (threaded rod)	Hot-dip galvanised carbon steel
HIT-Z-R	Chemical (anchor rod)	Stainless steel, A4

Self-compacting concrete was used for preparing the test specimens. The mix design of the self-compacted concrete was based on the C30/37 compressive strength class and SF2 consistency class. Maximum aggregate size used was #8 mm.

Table 5. Mix design of the self-compacting concrete.

The self-compacting concrete (SCC) mix design		(kg/m³)
Cement	CEM II/B-M 42.5 N	313
	CEM I 42.5 R	135
Aggregates	Filler – (0/1 mm)	48
	(0/8 mm)	1541
Water		228
Effective water content (SP)		228
Viscosity modifying agent (VMA)		0.45
Super-plasticizer		7.17
Target Air content		68.18

The specimens were carbonated 42 weeks in a carbonation chamber with 5% CO₂. As a result of the selected water-to-cement ratio of the specimens their permeability is rather low, which was assumed to result in the full carbonation of the specimens after the exposure. Target carbonation depth was the concrete cover 26 mm. Carbonation front after 42 weeks of exposure was approximately 30 mm. Propagation period of the corrosion tests simulates the exposure class XD3 (cyclic wet and dry). During wetting the samples are immersed to the sodium chloride solution (36.1% NaCl). Wetting time is one week, followed by three weeks of drying time.

The measured Half-Cell potentials were compared to the Pourbaix-diagrams for steel to estimate the state of corrosion of anchor. The reliability of the electrochemical measurements will be ensured with destructive tests and visual inspection of the corrosion state of the post-installed anchors.

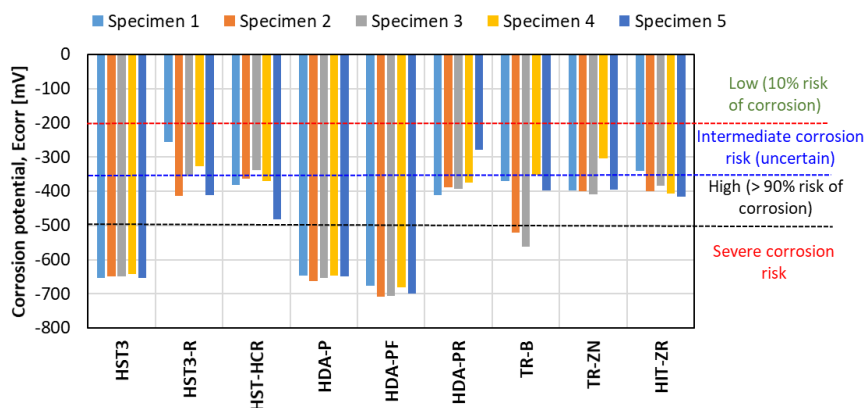


Figure 19. Corrosion potential for different post-installed anchor samples measured in 2022.

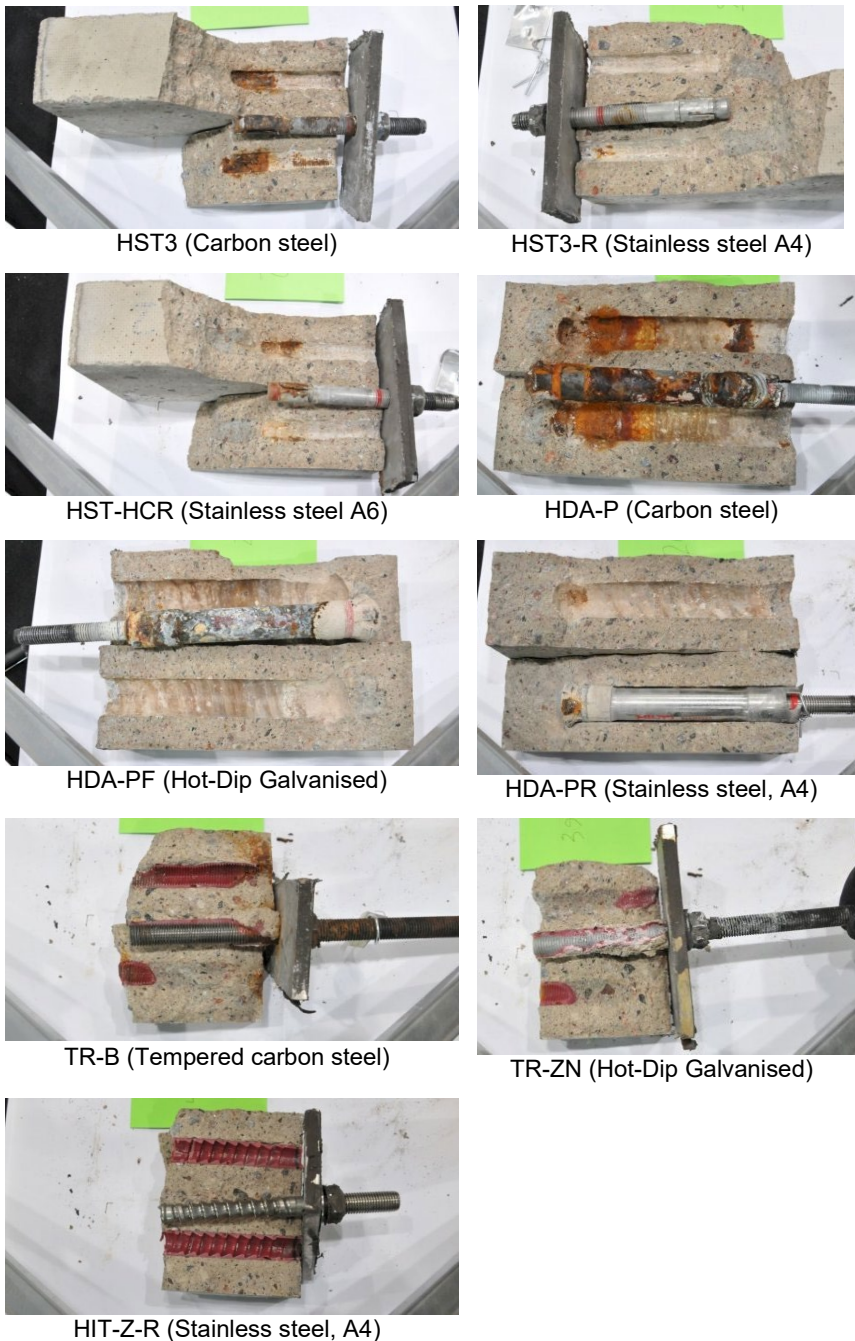


Figure 20. Visual inspection of the corrosion state of different post-installed anchors after performing the pull-out test

Figure 19 shows that the nine post-installed anchors started actively corroding within one year of exposure class XD3 (cyclic wet and dry) in the accelerated environment (36.1% sodium chloride solution). The carbon steel anchors were severely corroded as shown in the electrochemical potential measurements and also in the visual inspection. The average corrosion potential values for the HST3 expansion anchors, HDA-P and HDA-PF undercut anchors were -650 mV, -652 mv and -995 mV respectively. The average corrosion potential values indicate a severe corrosion state of the anchors which was also observed visually.

For the stainless-steel anchors, pitting corrosion was observed and also supported by the corrosion potential measurements. As shown in Figure 19, some individual measurements indicate a low 10% risk of corrosion, other measurements indicate uncertain intermediate and high risk of corrosion. The average corrosion potential values for the HST3-R and HST-HCR expansion anchors, the HDA-PR undercut anchors and the HIT-Z-R chemical anchors were -353 mV, -387 mv, -369 mV and -389 mV respectively. The average corrosion potential values indicate an intermediate (uncertain) corrosion state of the anchors which was also observed visually.

The chemical anchors were protected by the resin against the corrosion as shown in the case of TR-B, TR-ZN and HIT-Z-R anchors. The corrosion potential values for the chemical anchors varied between -304 mV to -563 mV, which indicate a low corrosion risk to severe corrosion risk in some points.

The visual inspection of the corrosion state of different post-installed anchors after performing the pull-out test is presented in Figure 20.

Final remarks

The results of CONAGE project can be exploited by all Finnish NPP's both operating and under construction and the information can be shared with foreign partners. The relevance of the objectives for NPPs, regulators, and the construction industry in general, is intrinsically linked to the correct understanding of deterioration mechanisms, their nature and consequences, how to address them in the design phase of new NPPs, and how to assess their current state and mitigate occurrence. As a result, it is expected that:

- Changes can be suggested to the current design procedure to take into account a performance based approach to design of new concrete structures and the assessment of existing concrete structures.
- Utilities will benefit from increased service life of their infrastructure. This is quite significant because the repercussions are directly linked to the sustainability of the sector: reduction in the consumption of natural resources; reduction in the production of construction and demolition waste; reduction in the production of CO₂ as a result of the previously mentioned factors;
- The risk for ASR in Finnish NPP concrete structures can be assessed and preliminary insight on avoidance of reactive material for the construction of new nuclear structures can be provided.

- Improved RI-ISI of liner and anchor bolt corrosion because of better understanding of the damage mechanisms and the likelihood of their occurrence.
- New knowledge for the education of new engineers (expert in NDE) for the Finnish NPPs and industry.

Acknowledgement

The authores woud like to acknowledge the funding received from SAFIR 2022, *The Finnish Research Programme on Nuclear Power Plant Safety 2019–2022*.

References

- Aghili, B. 2007. Ageing aspects of Concrete Containments from a Regulatory Point of View. Transactions, SMiRT 19, Toronto, August 2007. Paper # H02/3. 6 p.
- Al-Neshawy, F., Ojala, T., Ferreira, M., and Puttonen, J., 2018 "Mock-up wall for non-destructive testing and evaluation of thick reinforced concrete structures in nuclear power plants," The e-Journal of Nondestructive Testing & Ultrasonics, vol. 23, no. 8.
- Al-Neshawy, F., 2020. Ground Penetrating Radar (GPR) for use on thick-walled concrete structure. Research report, AALTO-R-002-2020.
- Bohner, E., Huttunen-Saarivirta, E. 2020. Report on the test setup for steel liner corrosion experiments. SAFIR2022 Conage Project, Deliverable 3.2.1. Research Report VTT-R-00069-20. March 2020, Espoo, Finland. 13 p.
- Chénier, J-O., et al., 2012. An approach regarding AMP for concrete containment structure at the Gentilly-2 NPP. Pro. 33rd Annual Conf. of the Canadian Nuclear Society, Saskatoon, Canada, June 10 -13, 2012, Vol. 1, 234-259.
- Ferreira, M., 2019. Assessment of the potential of AAR occurrence in NPP concrete structures. SAFIR 2022 - CONAGE Project, VTT Research Report VTT-R-00982-19, VTT Technical Research Centre of Finland Ltd. 34p.
- Ferreira, M., 2020b. Acquiring field experience concerning AAR in NPPs – Aggregates from Loviisa & Olkiluoto. SAFIR 2022 - CONAGE Project, VTT Research Report VTT-R-01287-20. VTT Technical Research Centre of Finland Ltd.
- Ferreira, M., 2020a. Acquiring field experience concerning AAR in NPPs – Aggregates from Olkiluoto. SAFIR 2022 - CONAGE Project, VTT Research Report VTT-R-00022-2, 28p. VTT Technical Research Centre of Finland Ltd.
- IAEA, 2002. Guidebook on non-destructive testing of concrete structures (Issue 17). IAEA-TCS-17, International Atomic Energy Agency. Vienna.

- IAEA, 2015. "Ageing management for nuclear power plants: International Generic Ageing Lessons Learned (IGALL)" Accessed: Jan. 22, 2023. [Online]. Available: <https://www.iaea.org/resources/safety-standards>
- IAEA, 2016. Ageing Management of Concrete Structures in Nuclear Power Plants. Nuclear Energy Series No. NP-T-3.5, Internat. Atomic Energy Agency. 372 p.
- Isotahdon, E., Bohner, E., Huttunen-Saarivirta, E., Sistonen, E. 2019. Corrosion of steel liners and anchors in concrete. VTT Research report VTT-R-01011-19. VTT Technical Research Centre of Finland Ltd. 49 p. + app. 7 p.
- Luodes, H., 2015. Ground penetrating radar and assessment of natural stone. Geological Survey Of Finland – GTK. Report of Investigation 223. 48 p.
- Manabe, R., Kawae, H., Ogawa, K., Matsuura, M., 2018. Maintenance management of turbine generator foundation affected by Alkali-silica reaction. Journal of Advanced Concrete Technology 16(4):179-190.
- Orantie, K. 2014. FiR 1 tutkimusreaktorin betonisen suojaon iljuusominaisuksien ja mikrorakenteen tutkimukset tarjouksen. VTT O-157037-14. VTT Expert Services Oy. 31 p.
- Petti, J. P., et al., 2011. Nuclear Containment Steel Liner Corrosion Workshop. Final Summary and Recommendation. Report. Sandia Report SAND2010-8718. Sandia National Laboratories
- RILEM TC 43-CND, 1993 "Draft recommendation for in situ concrete strength determination by combined non-destructive methods," RILEM Materials and Structures, vol. 26, no. 1. pp. 43–49, doi: 10.1007/BF02472237
- SAFIR 2010. The Finnish Research Programme on Nuclear Power Plant Safety 2007 – 2010. <http://virtual.vtt.fi/virtual/safir2010/>
- Samarin, A., 2004. Combined Methods. In V. M. Malhotra & N. J. Carino (Eds.), Handbook on Nondestructive Testing of Concrete.
- Saouma, V., Hariri-Ardebili, M., 2014. A proposed aging management program for ASR in a NPP. Nuclear Engineering and Design, Vol.277, 248-264.
- Snyder, K.A., Lwe, H.S. 2013. Alkali-Silica Reaction Degradation of Nuclear Power Plant Concrete Structures: A Scoping Study. NISTIR 7937 National Institute of Standards and Technology. Washington, USA. 48 p.
- Tang, T.M., 2013. Concrete Degradation of the Containment of Tihange 2 NPP in Belgium, OECD NEA/CSNI - WG1AGE – Concrete subgroup, 08 April 2013
- Watt, D. S., 2007. Building Pathology - Principles & Practice. Blackwell Publishing.
- Wegemar, B., 2006. Corrosion failure of a BWR embedded reactor containment liner. Journal de Physique IV, Vol. 136, Issue 1, pp. 257-262.

7.3 Modelling of aged reinforced concrete structures for design extension conditions (CONFIT)

Kim Calonius¹, Alexis Fedoroff¹, Oskari Jessen-Juhler¹, Kari Kolari¹, Antti Forsström¹, Miguel Ferreira¹, Edgar Bohner¹, Ludovic Fülöp¹, Reijo Kouhia²; Jani Vilppo²

¹VTT Technical Research Centre of Finland Ltd
P.O. Box 1000, FI-02044 Espoo

²Tampere University (TUNI)
Kalevantie 4, 33014 Tampereen yliopisto

Abstract

The CONFIT project uses a multi-disciplinary approach to investigate the various physical and chemical degradation mechanisms and how they affect the mechanical load bearing capacity of concrete in long term operation. Reinforced concrete structures are, indeed, of safety relevance in nuclear power plants due to the containment function of the reactor building and load bearing functions of the control building and shielding functions of specific concrete structures.

During the project, it was investigated how various external chemical and physical stressors affect the mechanical concrete properties as a material (Ferreira, M. and Fülöp, L., 2020) and in particular how corrosion of the reinforcement affects the load bearing capacity of a concrete structure (Calonius, et al., 2023b) and how this can be numerically simulated (Calonius, et al. 2021). For the simulation of full-scale loading scenarios on reinforced concrete structures involving physically, chemically or mechanically deteriorated concrete, specific material models for concrete were developed during the project. One of the advantages of such advanced concrete models is the ability to respond to anisotropic behaviour, which is inherent in damaged concrete (Vilppo, et al., 2021).

Since the calibration of the model parameters requires measurements of anisotropy in concrete under controlled multiaxial loading, a specific method using ultrasonic wave velocity measurement was developed (Calonius et al., 2022c). This method enables the computation of the damaged stiffness matrix components from the ultrasonic pressure and shear wave velocity measurements on the concrete sample in different directions.

As a result, the project has generated important findings in the domain of nuclear safety, some of which present novelty value of academic importance.

Introduction

The protective walls, containment and civil structures of Nuclear Power Plants (NPPs) are mainly reinforced concrete (RC) structures. Long term operation of NPPs requires structural integrity assessment of aged concrete structures in YVL

design extension conditions (DEC) e.g. external hazards like earthquakes and wide body aircraft crashes. These DEC have been introduced recently in NPP design in Finland. The DEC loads are considerably higher than the earlier design basis loads (DBL).

There is a need for a more universal material model which is more firmly based on physical phenomena and adequate for different types of loading cases, e.g. soft/hard impacts, earthquakes and resulting vibrations. Ageing of concrete has not been previously taken into account in DEC assessment. The material study including ageing and degradation mechanisms involves collaboration between structural analysis and concrete material experts at VTT. The material model development involves collaboration with Tampere University (TUNI).

Material model development (shown in Figure 1) is a trial and error process, which aims at finding the most appropriate mathematical description, such that the response of the model matches the response obtained from a number of experimental stress-strain situations. Due to the challenges that arise in the calibration of the material model against appropriate test results, it is of paramount importance to conduct proper validation simulations. In these small-scale validation simulations, the experimental test setup is modelled as accurately as possible using finite elements, and the measured macroscopic quantities are then compared to the simulated ones. In order to rule out artefacts due to discretization, a sensitivity study on the element mesh size has to be performed.

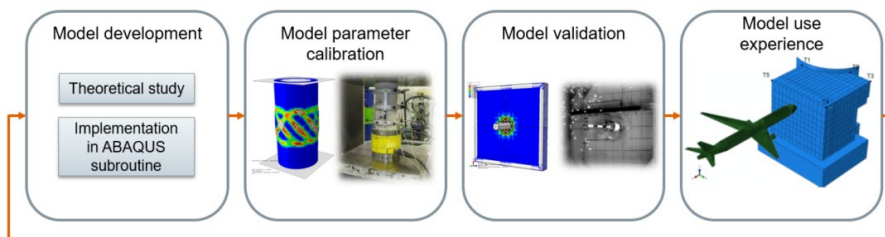


Figure 1. Concrete material model development chart.

The goal of the project is to develop understanding of the material modelling of concrete in the nonlinear domain by improving the use of existing material models, developing new material models and using calibration tests to stand at the basis of the development. Relatively new concrete material testing and measurement methods, such as DIC and ultrasonic methods, have also been further developed in the project. Methods and modelling techniques developed and validated here can directly be applied in safety assessment and design analyses of aged reinforced structures of NPPs under design extension conditions.

Impact simulation with Abaqus FE code

The Concrete Damaged Plasticity (CDP) model available in Abaqus finite element software has been implemented based on a theory developed in (Lubliner, et al., 1989) for monotonic loading cases and later enhanced in (Lee & Fenves, 1998) to encompass static cyclic behaviour. In order to extend the CDP model to dynamic behaviour, it is necessary to introduce rate dependency of concrete in the material model parameters. Based on the assumption that concrete compression strength increases with hydrostatic pressure, and that concrete tensile strength increases with strain rate, a VSDFLD Abaqus user subroutine has been written. This user-extended CDP model is described in (Fedoroff, et al., 2019). In addition to confinement pressure dependency of compressive strength and rate dependency of tensile strength, in hard missile impact simulations it is necessary to formulate an algorithm for element removal as a mean to materialize fragmentation of concrete during the impact process. The element removal algorithm is described in (Fedoroff & Calonius, 2020) and it is validated against experimental hard missile impact benchmark tests. The core of the work done for the implementation of the user-extended CDP model has been conducted in SAFIR2018 ERNEST project. Figure 2 shows an example where concrete confinement, shear cone formation and finally fragmentation of concrete can be observed.

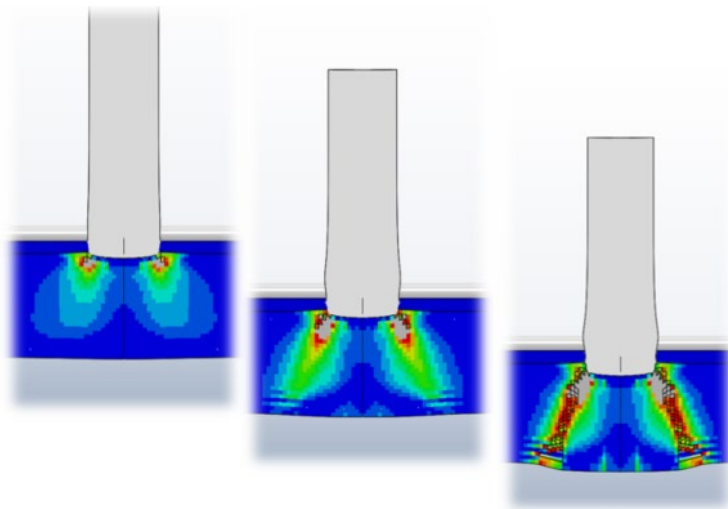


Figure 2. Example of hard missile impact simulation.

The focus was set on material model parameter calibration as described in (Calonius, et al., 2019). The proposed strategy for the material model parameter calibration is based on an iterative process where various concrete material tests (uniaxial compression, three point bending, split-tensile test, etc.) are simulated. At the end of each iteration, the model parameters are updated in order to obtain, on

the next iteration a stress-strain curve that matches the experimental one. The CDP model parameters are generated using an Excel-VBA script by entering values for Eurocode material parameters (such as stiffness modulus, compressive strength, tensile strength, fracture energy, etc.) as well as values for confinement pressure and strain rate dependencies.

In addition to the development and validation of the user-extended CDP model, some novel non-destructive concrete testing methods were evaluated (Calonius, et al., 2021). Digital Image Correlation (DIC) was tested in a concrete cube compressive test and compared to strain gauge measurement results, Figure 3, and to Abaqus simulation results using the CDP material model, Figure 4.

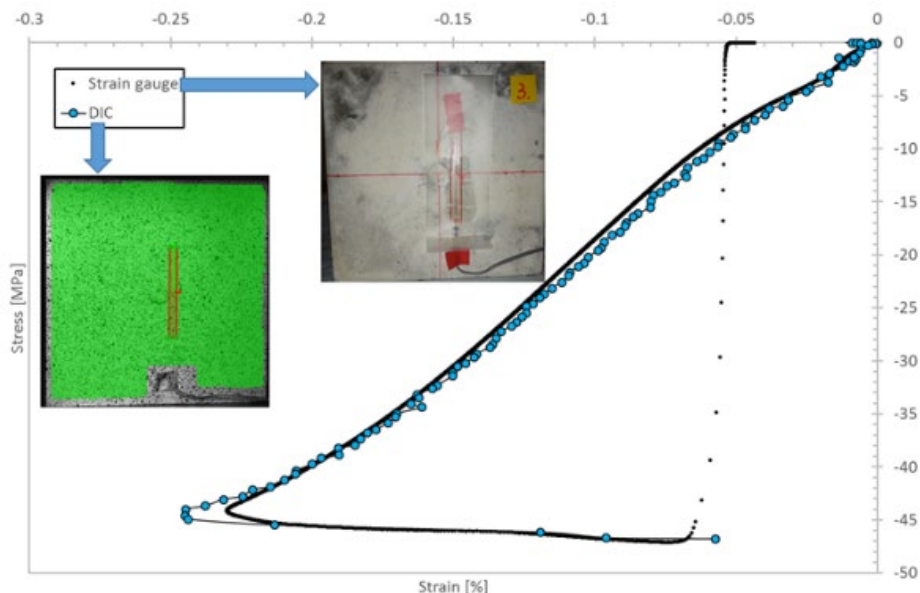


Figure 3. Comparison of vertical strain measurement results with a strain gauge and Digital Image Correlation.

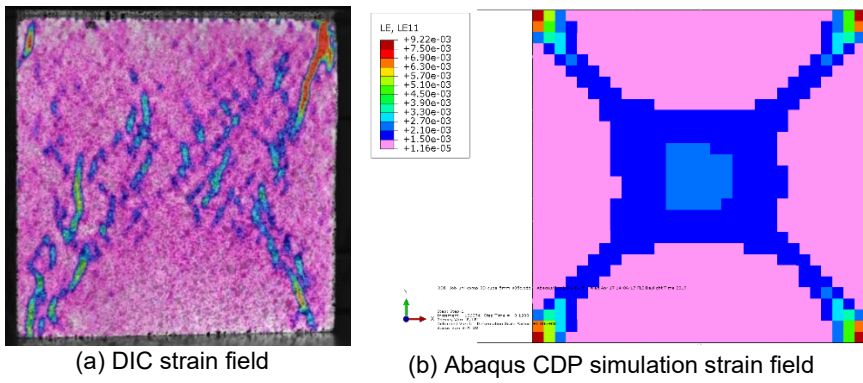


Figure 4. Comparison of strain fields DIC vs. simulation.

Understanding the effect of ageing and deterioration of reinforced concrete

Reinforced concrete structures used in NPPs are used for varying applications and environments. The long-term reliability of NPP safety-related concrete structures depends on the ability of these structures to withstand the time-dependent deterioration. Experience has shown that concrete is a durable material. However, faulty design, use of unsuitable materials, improper workmanship, exposure to aggressive environments, excessive structural loads, accident conditions and a combination of the above factors can compromise its performance. Many factors complicate the contribution of ageing effects to the residual life of the NPP safety-related concrete structures. Uncertainties arise due to differences in design codes and standards for components of different ages and lack of past measurements and records. During the exploitation phase, detection, inspection, surveillance, and maintenance methods or programs may be inadequate. In addition, there may be limitations in the applicability of time-dependent models for quantifying the contribution of ageing to concrete structures (Naus et al., 1996).

Concrete long-term reliability can be improved by limiting the exposure of the concrete structures to deteriorating effects, and by periodic inspection and maintenance procedures. The ageing research of concrete structures is to not only identify and mitigate the time-dependent deterioration mechanism on concrete, but also understand the implication for structural performance and characterise this performance in material models.

A degradation factor, or stressor, can be defined as an agent or stimulus resulting from construction or pre-operation and operation conditions that can result in the ageing process and failure of the structure. Different materials within the concrete structure are affected by different types of stressors (USNRC, 2013).

The implications of material ageing for structural performance assessment and especially for numerical modelling of reinforced concrete structures have been studied. The four main constituents of reinforced concrete (concrete, mild steel reinforcement, prestressing steel and steel liner) and their likely stressors, degradation mechanisms, potential failure modes, and in-service inspection methods have been reviewed (Ferreira & Fülöp, 2020).

The study provides a review of the current state of understanding of the effect of stressors on the material and mechanical properties that are currently used in concrete modelling. Focus has been on mechanical properties of concrete as a function of the “loading” conditions. The sources of the formulas are design codes, most prominently the fib Model Code (2010) and to a much lesser degree Eurocode 2 and the research literature. Generally, it is concluded that models exist for estimating the effect of aging and deterioration on a large number of mechanical properties (e.g. compressive strength, tensile strength, modulus of elasticity, etc.). Hence, the use of “as-new” properties for estimating performance of existing NPP structures should be critically revised. Aged concrete and its respective time-dependent properties should be considered in performance estimation for NPPs to accidental loads or DEC conditions.

Artificial ageing of reinforced concrete slabs for impact testing

Mechanical properties of concrete have a paramount influence on the behaviour of reinforced concrete structures under impact and impulsive loadings like aircraft crashes and blasts. These properties depend on the strain rate as well as phenomena related to ageing of concrete. Experimental tests are needed to characterize concrete as material in different stages of ageing as well as to study the behaviour of structures cast with this concrete under impact loading. The ultimate goal of this research is to define the effect of corrosion of bending reinforcement and minor degradation of surface concrete to the impact resistance of a reinforced concrete wall. To achieve the degradation of reinforcement and concrete, the slabs are artificially aged before impact testing. NDE is needed to assess the level of damage to the reinforcement inside the concrete slabs. The impact tests will be conducted in future.

Two slabs to be tested are 250 mm thick and reinforced with 10 mm reinforcement bars with spacing of 90 mm in both directions and on both surfaces. A projectile weighing approx. 47.5 kg will be shot at it with impact velocity of either around 100 m/s or around 135 m/s. The exact impact velocity will be fixed after the used batch of concrete has been tested for compressions strength. The goal is to reach a ballistic limit (i.e. the projectile will perforate the slab with minimal residual velocity). The reference test cases with undamaged slabs are the punching tests conducted in OECD IRIS_2012 benchmark and some punching tests in IMPACT projects.

The concrete slabs were exposed to accelerated ageing by use of impressed current. For that purpose, to establish an electrical field, a counter electrode mesh

out of stainless steel was placed on the top surface of the slabs. Since it was not embedded in the concrete slab, it needed to be placed in an electrolyte solution. A pool was prepared by fastening wooden beams on the concrete surface and sealing the joints, see Figure 5. Sodium chloride was dissolved in the water and the pool was covered with plastic sheets to prevent intensive evaporation.

Taking into account the top layer reinforcement steel surface area and assuming an estimated average current level for a duration of 11 months, the calculated total mass loss of reinforcing steel can be calculated and average uniform corrosion rates derived. The uniform corrosion rates are roughly in the range of 1–2mm of decrease of reinforcing bar diameter. Due to the nature of chloride-induced corrosion in concrete and the observation of high levels of gas production on the counter electrode surface during the impressed current feed the actual corrosion is most likely local type corrosion and the impressed current feed has not entirely been causing the dissolution of iron and production of corrosion products. Therefore the actual corrosion rate is difficult to predict based on the impressed current feed values. Locally there can be significant damage but in other locations it is possible that the reinforcing bars show zero or a negligible amount of corrosion.

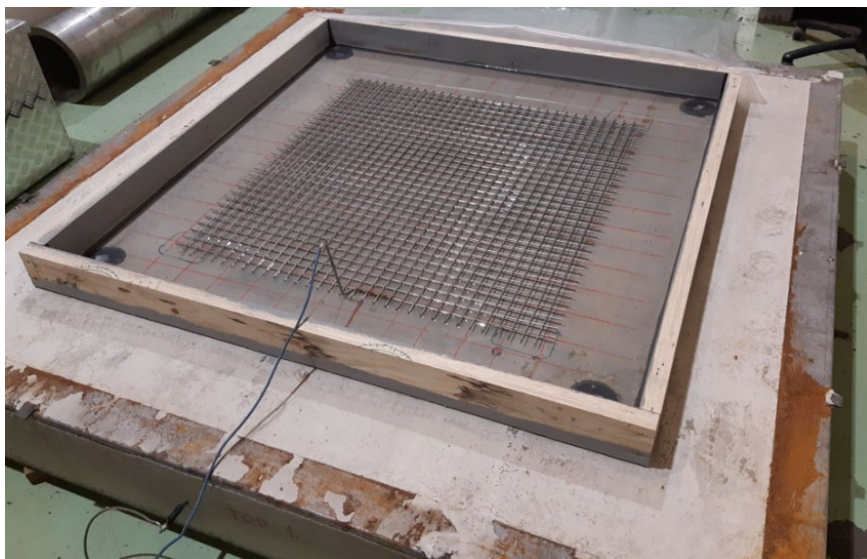


Figure 5. One of the slabs exposed to impressed current.

Before, during and after the end of the impressed current feed non-destructive electrochemical measurements were conducted by half-cell potential mapping and measurements of the electrical resistivity of the concrete. The results of these measurements show clearly that the conditions for active corrosion during the impressed current feed prevailed. They indicate as well that there are local differences of the extent of corrosion between both slabs, and on the investigated

surfaces of each slab. The magnitude or extend of damage cannot be assessed without local removal of the concrete cover and inspection of the condition of the reinforcing bars (Calonius, et al., 2023b)

Development of tensorial damage material model

Modeling of concrete structures under extreme loadings as explosion and impact is challenging. Both the material and geometric non-linearities have to be considered in the modelling. The ultimate failure of structures can be described as a continuous process of damage initiation, propagation and fragmentation.

In the simulation, it is extremely important that the failure pattern during the damage evolution is correctly described by the model. That is not the case in classical continuum models – the models target on the modelling of ultimate stress state and often neglect the associated failure patterns. Brittle kind of materials like concrete, natural rocks and natural ice tend to fail by axial splitting along the direction of uniaxial loading. As discussed by Schreyer (2007) the classical stress criteria do not have the flexibility to reflect the failure modes for various of stress states and “none predicts axial splitting”.

Formulation of the anisotropic tensorial damage model is done by specifying two potential functions, the specific Gibbs free energy and the dissipation potential. The isotropic potential functions are written in terms of invariants forming a functional, i.e. irreducible basis having two symmetric second-order tensor variables, namely the stress tensor and the damage tensor, which resembles the crack density tensor of Kachanov (1992). Therefore, the magnitude of the components of the damage tensor are not limited above, which makes numerical implementation somewhat simpler than using the standard definition of damage as a ratio of damaged to the undamaged area.

The specific Gibbs free energy is constructed to represent linear elastic solid in undamaged states. Furthermore, only linear terms of the damage tensor are retained, thus the “crack” interaction is not taken into account. Hardening and softening is modelled using a single internal variable. The dissipation potential is chosen in accordance to the famous Ottosen (1977) failure criterion, which captures the relevant features in concrete failure. The formulation is basically non-associated, however, the formulation follows closely the one for the standard dissipative solid. An additional convenient feature is that the material parameters of the model can be obtained in a closed form solution from standard material tests results: uniaxial compression/tension, equibiaxial compression and one extra point on the compressive meridian.

In Figure 6 the model predictions, stress-strain relations and damage evolutions, are shown in unconfined compression/tension and equibiaxial compression (Vilppu, et al., 2021 and 2022). Correspondence to the well-known experimental results by Kupfer et al. (1969) is good. It can also be seen from the damage-strain curves that the model is able to capture the correct failure mode. The model has been

implemented to Abaqus FE code. The calibration process of this model using cyclic compression tests and ultrasound NDE is described below.

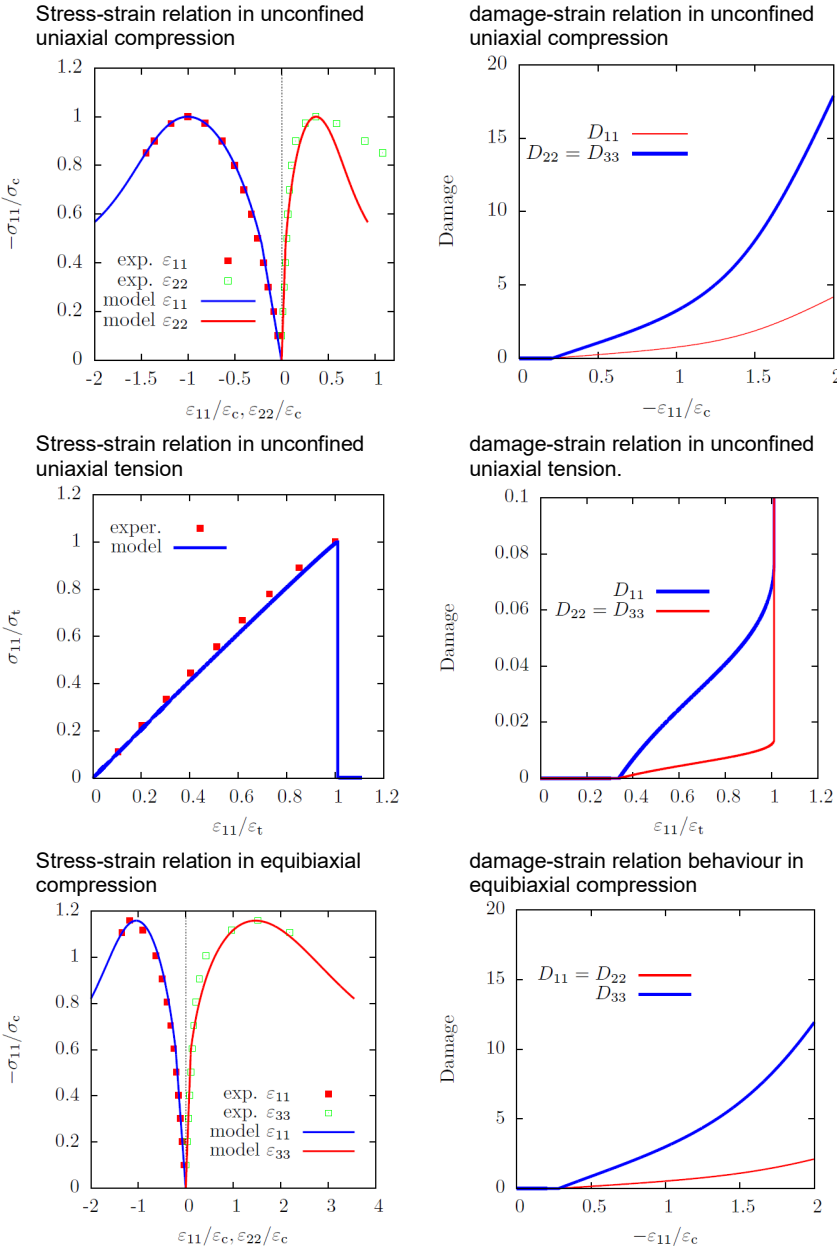


Figure 6. Stress-strain relations and damage evolutions in different directions predicted by the model under different types of loading schemes.

Evaluation of anisotropic material parameters in damaged concrete using ultrasound velocity data

In this research, a novel method of evaluating material stiffness parameters using ultrasound measurements on compressively damaged concrete cube specimens has been carried out. The method consists in measuring the soundwave velocity in principal and diagonal directions, both with longitudinal and shear waves, and computing the stiffness tensor components as a function of the measured soundwave velocities. The results show the method is capable of producing stiffness degradation profiles comparable to the ones obtained from traditional means of measurement from stress-strain data (Calonius, et al., 2022c and 2023a).

Concrete cube samples of 200mm were cast using C40/50 ready mixed concrete with evaluated air content of 2.1% and maximum aggregate size of 8mm. The loading surfaces of the cubes were smoothed and parallelized with a diamond grinding apparatus prior to testing. Three standard compression tests with average concrete strength of $f_{cm}=62.72\text{ MPa}$ were carried out to identify the reference loading capacity of the concrete batch. The engineering strain measured between the loading plates and corresponding to the peak load had an average value of $\varepsilon_{c1}=0.4383\%$. The experimental test setup consists of the following equipment:

- A hydraulic press suitable for uniaxial compression of concrete specimens and instrumented with a load cell for engineering stress measurement and two displacement sensors for engineering strain measurement between the loading plates in the loading direction.
- A digital image correlation (DIC) system, consisting of two cameras, computer hardware for data acquisition and software (LaVision StrainMaster) for data processing. The DIC data enables the computation of the strain tensor field at selected time frames from one of the free surfaces of the concrete cube.
- An ultrasonic measurement device (Proseq Pundit) with 54 kHz longitudinal wave transducers and 40 kHz shear wave transducers.

The pseudo-cyclic uniaxial compression tests were conducted on a total number of 18 concrete specimens with displacement control at a rate of 0.1 mm/min to obtain a controlled loading and unloading portion of the stress-strain curve. "Pseudo-cycle" is referred here to a loading pattern consisting of a single constant rate loading up to the target displacement value and a constant rate unloading down until the applied force is zero. Six target displacement values were chosen. For each target displacement three repetitions were carried out.

After the compressive tests, the concrete sample cubes are cut with a diamond saw along the edges to obtain a chamfered cube shape (see Figure 7). The ultrasound measurements are carried out by placing the emitter and receiver probes on opposite sides of the specimen along three principal directions and six diagonal directions. The first time arrival of the emitted signal is recorded by the ultrasound device as shown in Figure 7. For statistical significance, multiple time arrival and dimension readings are performed on each face of the chamfered cube. A stiffness degradation plot based on various measurements is shown in Figure 8.

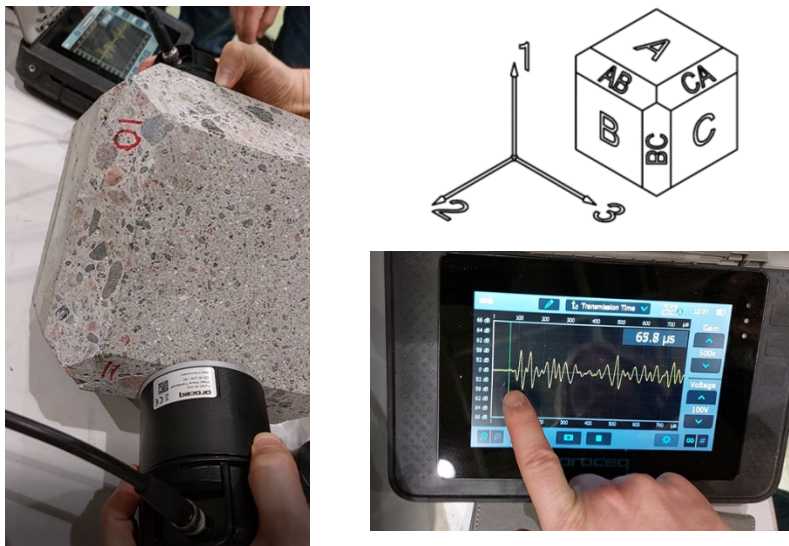


Figure 7. Views of a chamfered cube specimen and the first time arrival determination.

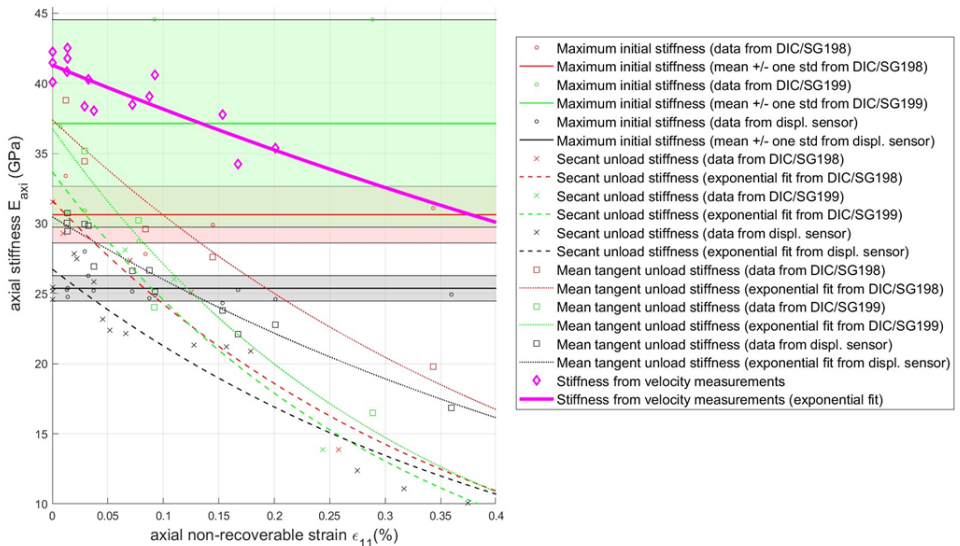


Figure 8. The plot shows: a) initial stiffness mean values from various data sources (solid horizontal lines), b) unload stiffness values as a function of non-recoverable strain from various data sources (dashed or dotted lines), and c) stiffness values from ultrasound velocity measurements (thick magenta line).

References

- Calonius, K. et al. 2019. Calibration of Abaqus CDP model parameters. Oulu, Proceedings of the 32nd Nordic Seminar on Computational Mechanics.
- Calonius, K., Fedoroff, A., Kolari, K., Vilppo, J., Jessen-Juhler, O. 2021. Development and calibration of user-extended Abaqus Concrete Damaged Plasticity material model, VTT Research Report VTT-R-00159-21.
- Calonius, K., Fedoroff, A., Forsström, A., Jessen-Juhler, O. 2022a. Comparison of ultrasonic, imaging and mechanical measurements for concrete stiffness determination in cyclic compression tests, VTT Research Report VTT-R-00926-21.
- Calonius, K., Fedoroff, A., Jessen-Juhler, O., Forsström A. 2022b. Calibration of tensorial damage concrete material model with cyclic compression tests and ultrasound measurements. SMiRT-26 conference, Berlin/Potsdam, Germany, July 10-15, 2022.
- Calonius, K., Fedoroff, A., Forsström, A., Hakala V., Piironen, J. 2022c. Determination of concrete stiffness tensor at different levels of damage, VTT Research Report VTT-R-00692-22.
- Calonius, K., Fedoroff, A., Forsström A. 2023a. Evaluation of anisotropic material parameters in damaged concrete using ultrasound velocity measurements. NDE NucCon 2023 - International Conference on Non-destructive Evaluation of Concrete in Nuclear Applications January 25-27, 2023, Espoo, Finland.
- Calonius, K., Fedoroff, A., Vepsä A., Ferreira M., Bohner E., Kinnunen, T., Trentin, A. 2023b. Artificial ageing of impact slabs, VTT Research Report VTT-R-01061-22.
- Fedoroff, A., Calonius, K. & Kuutti, J. 2019. Behavior of the abaqus CDP model in simple stress states. Rakenteiden Mekaniikka (Journal of Structural Mechanics), pp. 52(2), 87-113.
- Fedoroff, A. & Calonius, K. 2020. Using the abaqus CDP model in impact simulations. Rakenteiden mekaniikka (Journal of Structural Mechanics), pp. 53(3), 180-207.
- Ferreira, M. & Fülöp, L. 2020. Understanding the effect of ageing and deterioration of reinforced concrete on its durability and mechanical performance. SAFIR 2022 - CONFIT Project, VTT Research Report VTT-R-01115-20, 90p.
- Kachanov, M. 1992. Effective elastic properties of cracked solids: critical review of some basic concepts. Applied Mechanics Review 45, 304–335. doi: <https://doi.org/10.1115/1.3119761>

- Kupfer, H., Hilsdorf, H. & Rüsch, H. 1969. Behaviour of concrete under biaxial stresses. *Journal of the American Concrete Institute* 66, 656–666. doi: <https://doi.org/10.14359/7388>
- Lee, J. & Fenves, G. L. 1998. Plastic-damage model for cyclic loading of concrete structures. *J. Eng. Mech.*, pp. 892-900.
- Lubliner, J., Oliver, J., Oller, S. & Oñate, E. 1989. A plastic-damage model for concrete. *Int. J. Solids Structures*, pp. 299-326.
- Naus, D., Oland, C. B. & Ellingwood, B. 1996. Report on Aging of concrete containment structures in nuclear power plant. s.l.: U.S. Nuclear Regulatory Commission, 1996. p. 300. NUREG/CR-6424, BNL-NUREG-13148.
- Ottosen, N. 1977. A failure criterion for concrete. *Journal of the Engineering Mechanics, ASCE* 103, 527–535.
- Schreyer, H.L. 2007. Modelling surface orientation and stress at failure of concrete and geological materials. *International Journal for Numerical and Analytical Methods in Geomechanics* 31, 147–171. doi: <https://doi.org/10.1002/nag.557>, arXiv:nag.2347.
- USNRC (United States Nuclear Regulatory Commission). 2013. NUREG/CR-7153, Volume 4 – Expanded Materials Degradation Assessment (EMDA): Aging of Concrete and Civil Structures. p. 137. ORNL/TM-2013/532.
- Vilppo, J., Kouhia, R., Hartikainen, J., Kolari, K., Fedoroff, A., Calonius, K. 2021. Anisotropic damage model for concrete and other quasi-brittle materials. *International Journal of Solids and Structures* 225 (2021) 111048. <https://doi.org/10.1016/j.ijsolstr.2021.111048>
- Vilppo, J., Kouhia, R., Hartikainen, J., Kolari, K., Fedoroff, A., Calonius K. 2022. Continuum damage model for concrete. Proceedings for the 6th fib International Congress, 2022. 6th fib International Congress on Concrete Innovation for Sustainability, 2022 - Oslo, Norway. Duration: 12 Jun 2022 - 16 Jun 2022. ISBN: 978-2-940643-15-8. ISSN 2617-4820.

7.4 Safety criteria and improved ageing management research for polymer components exposed to thermal-radiative environments (SAMPO)

Konsta Sipilä¹, David Kiefer²

¹VTT Technical Research Centre of Finland Ltd
P.O. Box 1000, FI-02044 Espoo

²Rise Research Institutes of Sweden AB
P.O. Box 857, SE-501 15 Borås

Abstract

Polymer based components are applied in several parts of nuclear power plants, e.g. cables, sealants, paint coatings and lubricants to name a few. During their use they are subjected to ageing. In this project several polymer ageing related subjects are researched.

The lifetime of several components from nuclear power plants was estimated with traditional accelerated aging which may help to adjust exchange intervals and acceptance criteria for EPDM O-rings were established. In addition, isothermal micorcalorimetry was used to estimate the activation energy and several dielectric methods were tested for condition monitoring of polymer components.

Development of condition monitoring methods was performed with several methods. It was shown that thermogravimetric analysis (TGA) can be used to evaluate the filler content of the polymers which helps defining differences in material quality between material batches. Computational models that help to process non-destructively measured data and predict antioxidant consumption in materials were developed.

Introduction

Polymer based materials are used in several applications inside nuclear power plant (NPP) containments. Typical applications include cable jacketing and insulation, sealants, paint coatings and lubricants. These applications also tend to often have safety relevance, e.g. cabling of several safety related equipment. The most important stressors recognized for the ageing are temperature and ionizing radiation, but also the effect of moisture exists as well. In addition, the presence of oxygen has significant effect on the ageing process and the difference in ageing has been recognized between oxygen containing and inert atmospheres [Spång 1997]. The ageing itself is mainly due to chain scission process which decreases the chain length of a polymer and cross-linking which increases the network density. Other processes and additives also affect the ageing, e.g. antioxidant consumption. The interest in polymer ageing issues has increased nationally and internationally as the original planned lifetime of NPPs is about to be reached and extended lifetime is

desired. Feasibility studies have been conducted in Finland and Sweden to recognize the relevant polymer ageing issues [Penttilä et al. 2016, Granlund et al. 2015]. There are also IAEA documents that address the concerns related to cable ageing [IAEA 2012, IAEA 2000].

Quality control techniques for polymeric components

Quality control techniques for polymeric components, such as sealants, were developed to qualify poor material quality from good. Two methods, OIT and TGA measurements were applied for antioxidant and filler analyses, respectively. Instructions on how to perform the measurements were included in this framework [Sipilä & al. 2022].

OIT measurement seems to function with the commercial grade EPDM sealant material. However, with the model material the measured OITs seemed to be suspiciously low despite the initial differences could be extracted between the model materials with OIT measurement. It is suspected that the applied antioxidant system is not very well suited for the conventional OIT measurement or extensively long testing times are required. More detailed understanding regarding the antioxidant behaviour is required in order to explain the differences observed with the two EPDM qualities and to provide a more reliable on-site measurement procedure.

TGA seems to distinguish well the model EPDM materials from the commercial grade materials (see Figure 1). Three different temperature ranges were presented which could be used to distinguish quality differences between the materials. At high temperature range (around 600 °C) large differences in filler content can be observed. At temperature ranges around 400 °C, small differences in filler content can be seen when high-end materials are measured. Between 280 to 450°C the evaporation of mineral oils can be evaluated. No universal acceptance criterion could be suggested for TGA measurements due to the vast number of applications for these materials but when a good reference material is available for comparison, the suggested temperature areas in TGA curve can be used in verification of the polymer quality.

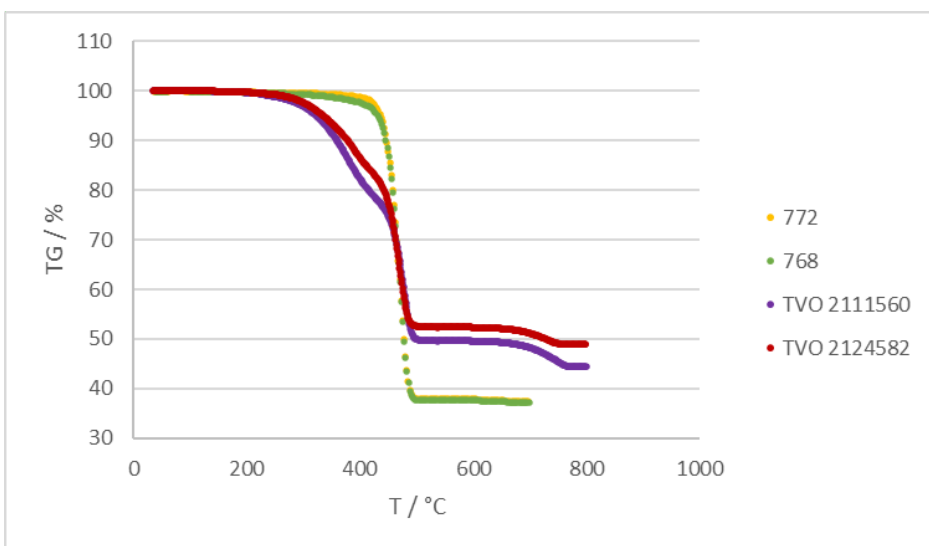


Figure 1. TGA results with the model EPDM materials and commercial EPDM material.

Predicting antioxidant behaviour in polymers

The development of numerical antioxidant consumption modelling beyond the state of the art have been initiated. The polymer degradation mechanism, oxygen diffusion, and antioxidant depletion were implemented in both 2D and 3D finite-element models to obtain realistic component-scale predictions on thermal degradation. As a novelty, antioxidant diffusion and evaporation models were added. [Vaari 2022]

The capabilities of the model were demonstrated by simulating aging of silane-crosslinked, 0.5 mm thick polyethylene up to 210 days (see Figure 2). It was shown that the model can reproduce experimentally observed levels of hydroperoxide and carbonyl species, and predict a decrease of the molecular weight of the material such that the cross-linked gel network is completely degraded, and that the mechanical properties of the material are severely compromised.

Several aspects of the model need further work. The kinetic parameters used in the model are compiled from several papers, and sometimes values for a given parameter differs from one source to another. The origin of the parameters should be better understood, which hopefully would give a better idea on their accuracy and applicability to various materials and aging conditions. The various experimental ageing treatments performed could be systematically employed for validation.

Further derived quantities can be developed. For example, the chain scission and cross-linking rates could be used as inputs for a numerical graph model in order to get more insight into the molecular-level structure of the material. It could be

envisioned that this way, the gradual changes in the mechanical properties such as elastic modulus, and elongation at break could be modelled in a physical rather than an empirical fashion. On the other hand, since concentration of oxygen-containing groups is known from the model, and their effect on the polarization is known, the dielectric properties can be included in the model.

The current work has not attempted to utilize the full power of Comsol to model complex geometries. Thus, extending the modelling to real components such as electrical cables with an internal structure and several material components could be done in the future. While a cable could be basically handled with a 2D model, it should be possible to develop also 3D models for more complex components. In addition, interaction of the component with environment could be included using the multi-physics capabilities of Comsol, adding for example a non-isotropic heat flux, mimicking a component near a hot spot.

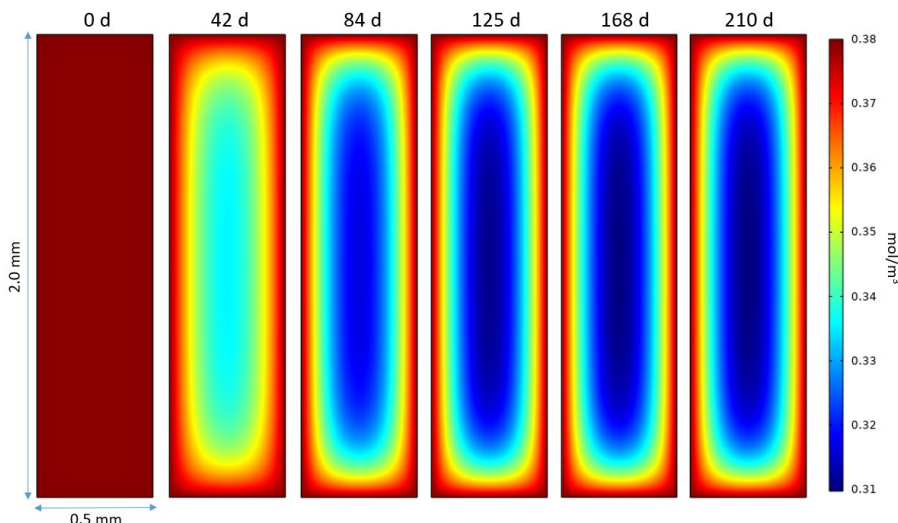


Figure 2. Distribution of oxygen concentration as a function of time for an aged XLPE material.

Improvements in interpretation of non-destructive testing data

United-atom molecular modelling was employed to build a polydisperse system for studying the dynamical cross-linking, crystallization, and evaluation of mechanical properties of cross-linked polyethylene. Effects of oxidative aging were simulated by causing chain scissions in the amorphous phase of the semicrystalline cross-linked structure. This resulted in enhanced mobility of chains, and thereby to chemicrystallization, i.e. increased crystallinity and crystal thickness. These structural changes also led to increase in elastic and bulk moduli. Based on these quantities, estimates for longitudinal sound speeds were calculated, which were

compared to experimental measurements (see Figure 3). Although the computational estimates were slightly lower than experimental values, they showed an increase in the sound speed by about 100 m/s due to aging. These results demonstrated the potential of the ultrasound technique as a non-destructive condition monitoring method.

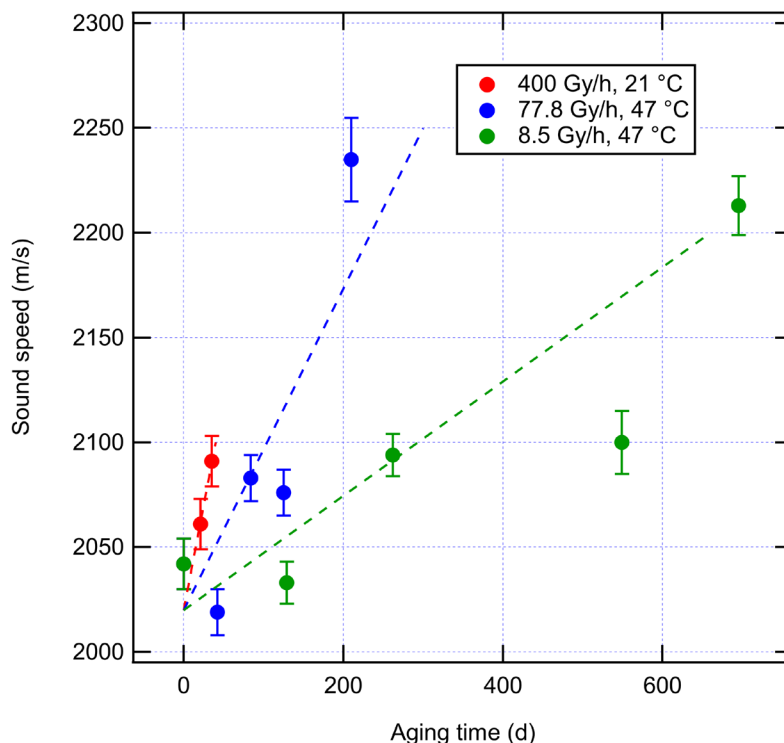


Figure 3. Calculated (dashed line) and experimentally measured (data points) ultrasound velocities for aged XLPE.

Development of ultrasonic measurement for cable condition monitoring

The sensitivity of ultrasonic method to detect ageing as well as the measurement procedure was developed further [Sipilä & al. 2023]. Additional artificial ageing data was produced to evaluate the sensitivity of the method to detect ageing. Producing moderately aged XLPE samples was shown to be challenging and thus the sensitivity analysis could not be performed properly. Based on the obtained results, it could be only concluded that ultrasonic method is not sensitive enough to distinguish slightly aged samples from unaged samples.

It was concluded that additional artificial ageing times is required to perform representative sensitivity analysis. Although advances have been made in developing the measurement approach, it would be still limited to locations where the cable insulator is well accessible. A potential application seems to be tests performed with surveillance samples as the ultrasonic method consumes only a small portion of the sample.

The main challenges related to developing ultrasonic technique further to perform measurements with real cable geometry were listed to be sensitivity of the method with moderately aged samples and accessibility to cable insulator.

Condition monitoring of joint sealants

Joint sealants are polymer-based sealing solutions that are applied in between structures, such as floor and wall elements, thus joining them together and forming a gas tight structure. Such sealants are widely applied in constructions, including nuclear power plants (NPPs). However, their ageing in nuclear power plant environment is less studied phenomenon.

The condition of joint sealant materials obtained from nuclear power plants and a reference new sealant material was determined [Sipilä & al. 2023]. The applied methods were tensile test DMTA and hardness measurement. Tensile test and DMTA samples were challenging to prepare from the delivered samples due to the quite severe ageing. When the results were compared, one of the aged samples showed higher elongation at break, elastic modulus and hardness values than the new reference sample. Hardness was concluded to be the most convenient material property to measure and representative as an ageing indicator for these types of materials (see Figure 11). Future work was suggested to develop hardness measurement further to be applied on-site conditions.

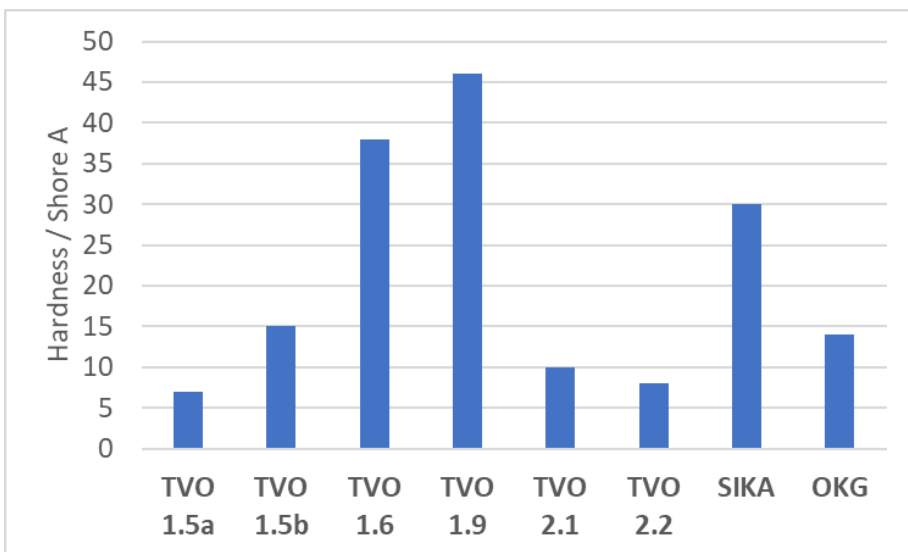


Figure 4. Hardness measurement results for unaged SIKA sealant and sealants obtained from nuclear power plants.

Improved estimation of lifetimes for polymer components in NPPs

Several workshops were held, where potential material candidates from the NPPs were collected and evaluated. Materials were then chosen based on suitability and availability. The workshops were complemented by update meetings and plans to extract more samples during revisions. Unfortunately, no material could be received from Oskarshamn due to staff shortage. Test plans were set up for each material containing traditional mechanical methods to estimate lifetime and compare with materials from outtakes.

EPDM O-rings from Ringhals after their service life were tested against new reference O-rings and their total expected lifetime was determined. The O-rings were found to be of very good quality with a slow aging profile, indicating that prolonged service times may be possible after further testing.

Neoprene membranes from water pumps at Ringhals with different dimensions were investigated. For one size (19.0 cm) reference membranes were available and the total expected lifetime was estimated. Comparison of the membranes after service life with the heat aged membranes indicated that it may be possible to extend the service time of membranes.

A joint seal sample from TVO was analysed without reference by measuring tensile properties and hardness. Due to the missing reference no estimation of total or remaining lifetime was possible.

CPE cables from Forsmark were analysed and compared to a similar reference cable. A total expected lifetime of 23 years was estimated for the reference cable which is shorter than the service time of the cables from Forsmark. This may be explained by different cable jacket material or differences in the aging mechanism at low and high temperatures.

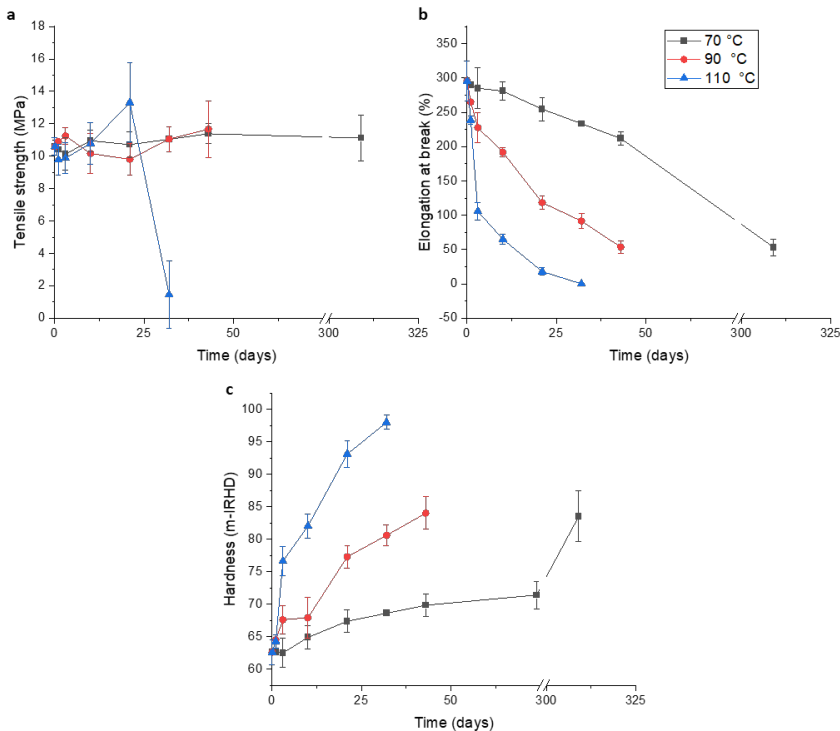


Figure 5. Tensile strength (a), elongation at break (b) and hardness (c) of heat-aged membranes from Ringhals NPP.

Setting up safety margins for O-rings

Three different EPDM grades for O-rings were tested using compression set and stress relaxation. As expected, the top-level grade 1 for nuclear applications performed best overall, followed by grade 2 for industrial applications. Instead, the commercial grade 3 performed significantly lower. Leak test performed showed that both grades 1 and 2 do not leak unless aged at high temperature (140°) for a long duration. Grade 2 is likely to represent the average of O-rings used in NPPs and despite a somewhat lower performance may be sufficient with suitable service intervals. Overall, it is shown that three different EPDM grades have significantly

different lifetimes and thus care should be taken when choosing EPDM components for safety critical infrastructure like NPPs.

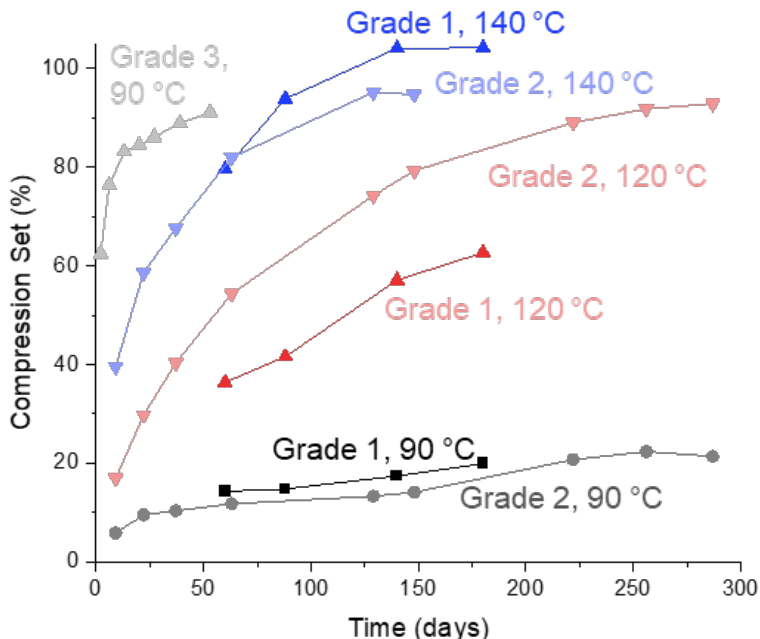


Figure 6. Comparison of compression set of EPDM grades 1 and 2 at 90 120 and 140 °C, as well as grade one at 90 °C. An activation energy of ~100 and ~103 kJ/mol was estimated by time-temperature superposition for grade 1 and 2, respectively.

Online condition monitoring techniques – Dielectric Properties

Measurement results achieved can be seen as indications that the permittivity might yet prove a useful indicator for aging monitoring of some polymeric materials. The reason for the seen reduction in permittivity is yet to be investigated. It should thus not be expected that all materials would behave the same. If the change in permittivity is due to the consumption of some component, the trend might also change at later stages of ageing of the material. If the changes can be tied to some specific reaction, the method could thus prove to be very useful for understanding approximately where in the ageing process a well-known material could be. A weakness of the method would be that the entire course of ageing would likely need to be recorded for the method to be of much use. The changes here recorded are also fairly small. It remains to see if the changes are still large enough to use a passive structure, like a simple resonance circuit or antenna-like element, as a probe.

Inspecting a single cable as it was done here appears to have provided very little information. We have come to realize that this might be due to poor experimental design. As the distance from the cable to ground is much larger than the thickness of the cable the effective permittivity will likely be dominated by the air between the cable and the ground plane. It would probably be a good idea for future measurements to place the cables directly on the ground plane or to create a coaxial structure with ground surrounding the insulating material.

When two cables were connected, we could however see some effect. This is probably because they are in much closer proximity and the effective permittivity between the cables is thus dominated by the CPE insulator instead of air. Even if only one cable was exchanged, from an unaged cable to an aged one, the effect could be observed in the reflection of both cables. We would suggest that this, together with the fact that it is more pronounced for the setup with shorted ends, shows that at least a part of the return current happens in the coupled conductor. If cables are mounted in a bundle, it could thus likely be useful to investigate them at least pairwise so that the effective permittivity of the cable will be dominated by the insulation material between the cables, and any distance to some other ground plane will be of less significance. In our measurements only one of the cables have been aged. If our argumentation is correct, the effective permittivity of the coupled cables should be dependent on the insulation material around both cables. If the other cable is aged as well, a larger effect on the effective permittivity should thus be expected.

The analysis could likely be improved by more in-depth circuit models to further understand the relation between the material changes and the effect on the measurements. This would likely also help in improving the measurement set-up. Unfortunately, there has not been time for this type of analysis as the samples arrived quite late in the project. The number of available samples have unfortunately not been large enough to properly evaluate the method with valid uncertainty estimates. This would have to be changed if the work is to be continued.

The method could likely be adapted to an online measurement set-up with the cables under test located in a hot/warm environment.

Parallel plate impedance measurements

Even though there have previously been expressed concern towards working at low frequencies due to the, sometimes, humid environment and the effect the wet atmosphere might have on the measurements, the results from these measurements show a clearly visible effect of the ageing. This renders them interesting for further investigation. One way forward would be to try to construct equivalent circuits with elements related to the different ageing mechanisms.

Normalized data with electrode area and sample thickness

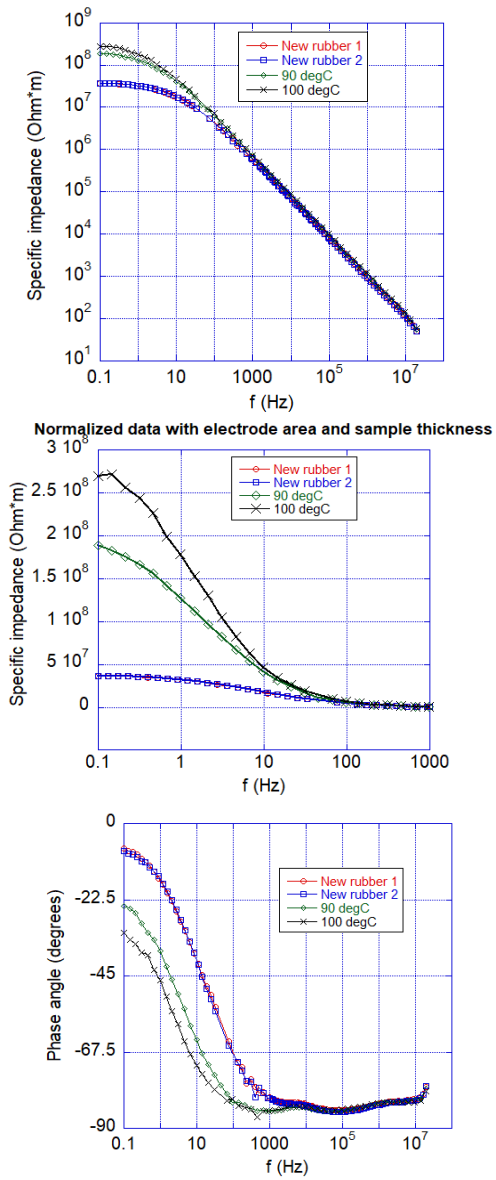


Figure 7. (top) Specific impedance (normalized with electrode area and sample thickness), (middle) zoomed in specific impedance at frequencies below 1 kHz and (bottom) phase angle (between excitation voltage and current), and versus excitation frequency. New rubber 1 and 2 are two fresh rubber samples and 90 degC and 100 degC are aged rubber samples aged in an oven for 2 weeks at 90 °C and 100 °C.

Sensitive analysing techniques

In work package 2 (WP2) of the SAMPO project, one of the objectives is to provide inputs for the ageing of polymeric components used in Nuclear power plants (NPPs). One of the suitable ways is to provide the techniques that can be used to measure thermal degradation in polymeric components non-destructively. One key issue in developing the non-destructive monitoring techniques is to verify how the results obtained using non-destructive testing relate to the polymer condition and its ageing in real life conditions. Task 2.2 under WP2 is focussed on the development of a technique, i.e. isothermal microcalorimetry (IMC), which can measure the thermal degradation non-destructively and closer to the temperature experienced by the material in NPPs.

Based on the MC tests and comparison with the ATA technique some conclusions can be drawn.

- MC can be used as a promising technique for the ageing tests closer to the service life of the polymeric material in NPP.
- Ageing tests can be conducted in real time and in significantly shorter duration for example 1 month activation energy can be obtained,
- Post analysis of the polymeric material at least using standard techniques for example SEM-EDX and FTIR may provide valuable information about the ageing mechanisms.

Table 1. Activation energy for different grades using MC and ATA.

Material	Activation energy KJ/mol	Temperature range	remarks
Grade 1, MC	81	80, 100 and 140 °C	
Grade 1, ATA	100	90, 120 and 140 °C	Using stress relaxation
Grade 2, MC	115±5	120 and 140 °C	
Grade 2, ATA	≈100 and ≈138	90, 120 and 140 °C	Using compression set and stress relaxation
Grade 3, MC	96±1	50, 60 and 70 °C	Temperature range is not same. Activation energy was obtained using stress relaxation
Grade 3, ATA stress relaxation	98	80, 90 and 100 °C	

Applications

The proposed applications from the project results and corresponding TRL levels are shown in Table 1.

Table 1. Summary on the proposed applications from the project results.

Application area	Proposed application	TRL level
Quality control of polymeric components	TGA measurement to identify variations in filler content	6
Lifetime prediction	Computational model for predicting antioxidant consumption	5
Condition monitoring	Hardness measurement for monitoring the condition of joint sealants	5
Condition monitoring	Complimentary ultrasound measurement for cable surveillance samples	5
Lifetime estimation	Arrhenius aging of critical component	9
Online condition monitoring	Dielectric methods to monitor condition of cables or other components	3
Lifetime estimation	Alternative method, i.e. microcalorimetry to estimate lifetime of critical components	4

Summary and conclusions

Polymers are applied widely in nuclear power plants and they are subjected to ageing. SAMPO-project focused on limited problems that had practical importance from the nuclear safety perspective. The main results included:

- Improvements in ageing management (lifetime assessment, quality control improvements, antioxidant study)
- Developments in condition monitoring (microcalorimetry, interpretation of NDT data, joint sealant study)

Acknowledgement

Finnish Nuclear Waste Management Fund VYR, VTT Technological Research Centre of Finland Ltd, Swedish Radiation Safety Authority SSM and Energiforsk AB are greatly acknowledged for funding this work.

References

- Grnlund, M. Almström, S. Jansson, A. Bondesson, Eriksson, J. 2015. Feasibility Study Acceptance Criteria For Poly-mers. Energiforsk report 2015:157.
- IAEA. 2012. Assessing and Managing Cable Ageing in Nuclear Power Plants. IAEA Nuclear Energy Series No. NP-T 3.6.
- IAEA. 2000. Assessment and management of ageing of major nuclear power plant components important to safety: In-containment instrumentation and control cables, IAEA-TECDOC-1188. Vienna, Austria: IAEA.

- Penttilä, S., Saario, T. and Sipilä, K. 2016. Polymeerien säteilykestävyyden arvioinnin ja tarkastettavuuden perusteiden selvitys. VTT-Customer report VTT-CR-04918-16.
- Sipilä, K., Björkqvist, I. & Joki, H. 2023. Defining joint sealant condition in nuclear power plants. VTT Research report VTT-R-00072-23. 15 p.
- Sipilä, K., Inc, Y. & Joki, H. 2023. Applicability of ultrasonic measurements in cable condition monitoring. VTT Research report VTT-R-00088-23. 11 p.
- Sipilä, K., Joki, H. & Björkqvist, I. 2022. Application of DSC and TGA in quality control of polymer-based components. VTT Research report VTT-R-01072-22. 14 p.
- Vaari, J. 2022. A finite-element model for antioxidant consumption. VTT Research report VTT-R-00972-22. 21 p.

7.5 Valorisation of probabilistic seismic hazard results in Finland (VALERI)

Päivi Mäntyniemi¹, Marianne Malm², Lauri Rinne², Ludovic Fülöp³

¹Institute of Seismology, University of Helsinki,

²AFRY Finland Oy

³VTT Technical Research Centre of Finland Ltd
P.O. Box 1000, FI-02044 Espoo

Abstract

Probabilistic seismic hazard analysis (PSHA) is the standard method to assess seismic hazard for nuclear power plants (NPPs). In Finland, the median confidence seismic hazard at annual frequency of exceedance (AFE) 10^{-5} is used for design-basis earthquake (DBE), with a minimum threshold of the horizontal peak-ground acceleration of 0.1g. Exceptional earthquakes for design extension conditions (DEC C) are proposed with median confidence at AFE $10^{-7}/\text{year}$ (STUK, 2019).

In this work, we explore the possibilities of DBE being anchored to other confidence level hazards, since the use of median is the minority position in Europe. We outline PSHA as a tool for hazard calculations, and how hazards are used in risk assessment and risk-informed decision-making. We particularly focus on the treatment of uncertainties and arguments about the mean and fixed-confidence hazards. The goal is to probe if regulatory transition away from median confidence hazard is (i) desirable, (ii) possible and (iii) identify the foreseeable difficulties. We discuss possible options for DBE and DEC C, for the consideration of the different stakeholders. Since the use of median hazard has a long tradition in Finland, an update would be no trivial undertaking.

Introduction

Probabilistic seismic hazard analysis (PSHA) is a methodology to estimate the likelihood that a threshold value of the earthquake ground-motion will be exceeded at the target site or region, in a specified time interval. The methodology was introduced several decades ago (Cornell 1968). PSHA is used in Finland, among many other countries, to provide site-specific input for probabilistic risk assessment (PRA) of nuclear power plants (NPPs). PSHA was primarily developed for the vibratory ground motions triggered by earthquakes, so-called primary earthquake effects. In Northern Europe, secondary earthquake effects, such as tsunamis and landslides or other types of ground failure, are infrequent, but not unprecedented (Mäntyniemi et al. 2021a).

A complete PSHA study integrates a wide range of disciplines (i.e., seismology, geology and tectonics, geodesy, statistics, probability theory, uncertainties, decision

theory, civil and geotechnical engineering). Many large-scale PSHA projects, particularly those conducted in the framework of the Senior Seismic Hazard Analysis Committee (SSHAC; Budnitz et al. 1997a, b) procedure also emphasize that cognitive psychology plays a role in making expert judgments. The primary output of PSHAs are hazard curves expressing the annual frequency of exceedance (AFE) of the selected ground-motion measures.

When a single threshold of seismic load is needed for instance in engineering work, two decisions must be made to obtain values for design: which AFE should be adopted, and from which hazard curve should the ground-motion value be read. The current regulatory status in Finland, given in the guide YVL B.7 (STUK, 2019), is that the median confidence seismic hazard at AFE 10^{-5} is used to substantiate the seismic design-basis earthquake (DBE) for NPPs with minimum horizontal PGA value as 0.1g.

Evidently, the DBE may be exceeded. Global examples of exceedance of the DBE ground motion include the Niigataken-Chūetsu-Oki earthquake (M6.6) in the Niigata Prefecture of Japan on 16 July 2007. The ground motion caused by the shallow earthquake at the site of the Kashiwazaki-Kariwa NPP (KKNPP) exceeded the plant's DBE ground motion by a significant amount, and all the seven reactors of the plant were shut down for an extended period (Johnson et al. 2017). The KKNPP units performed well in this situation, but a post-earthquake analysis concluded that similar performance cannot be assured for other NPPs given the same loading conditions. The KKNPP restart experience demonstrated the need for formulating specific and detailed criteria for addressing situations in which seismic events trigger ground shaking that exceeds the original design or evaluation basis. The International Atomic Energy Agency (IAEA) provided guidance to operating organizations (IAEA 2011). New definitions of the design basis were implemented in some cases.

The Tōhoku-Oki earthquake of 11 March 2011 was a megathrust event (M9.0) that generated very violent ground shaking, moved the Honshu Island 3.6 m to the east, shifted Earth's axis by 25 cm and accelerated its rotation by 1.8 microseconds (Norio et al. 2011). The 11 NPPs in Northeastern Japan stopped operating their reactors automatically, and the ground shaking did not significantly damage the safety-related structures, systems, and components of NPPs (Johnson et al. 2017), but the impact of the tsunami stopped the cooling system of three of the Fukushima Dai-ichi reactors, which, consequently, led to three core meltdowns. The earthquake-tsunami induced nuclear crisis drew attention to extreme events and large-scale disaster risks (e.g., Wong 2014). Upgrades were implemented to meet new definitions of the requirements for beyond DBE ground motion. The guide YVL B.7 (STUK, 2019) states that “*exceptional external events and conditions with an estimated frequency of occurrence less than 10^{-5} /year shall be considered design extension conditions (DEC C) events*”.

The aim of this work is to explore the seismic hazard and confidence levels that are relevant for NPPs in Finland, including comparisons and interdependences between DBE and DEC C. We draw specifically on the outcomes of the SENSEI

(SENsitivity study of SEIsmic hazard prediction in Finland) project, conducted 2019–2020 (Mäntyniemi et al. 2021b, Fülöp et al. 2022).

PSHA as tool to estimate seismic hazard

Probabilistic modelling of seismic hazard incorporates *aleatory variability* and *epistemic uncertainty*. Aleatory variability is inherent randomness to the phenomena or its representation with a certain model (i.e., apparent aleatory variability), while epistemic uncertainty is the lack of understanding of the models, the distributions of earthquake magnitude, location, etc. The specific terms were introduced into PSHA by Budnitz et al. (1997a, b), but were understood much earlier including the contested nature of the separation between the two types of uncertainties (Marzocchi and Jordan 2014).

Aleatory variabilities are directly included in the exceedance probability calculation, while epistemic uncertainties are handled by assembling a set of alternative PSHA models, each providing a hazard result. Epistemic uncertainty can, in concept, be reduced by collecting new observations and developing modelling. Improved datasets clearly advocate updating PSHA models. If the logic tree covered all the mutually exclusive and completely exhaustive (MECE) and appropriately weighted future earthquake scenarios, the result could be interpreted as the true hazard distribution (Bommer and Scherbaum 2008). In practice, logic trees also document and display in a transparent fashion the state of seismotectonic data and knowledge in the target region.

Seismic hazard in risk assessment and decision making

The obtained hazard results must be placed in the context of their practical application. In the nuclear framework, they serve as input for assessment, deterministic or probabilistic, of earthquake consequences. For instance, seismic probabilistic risk analysis (SPRA) is used to compute the risks posted by earthquakes, expressed as annual frequency of unacceptable performance of the NPP. This is obtained by integrating the seismic hazards with the plant fragility, over the relevant range of intensity measure levels. SPRA incorporates the entire range of uncertainties in seismic hazard, structural response, and capacity of the NPP components. The general procedure is shown in Figure 1, reproduced from Huang et al. (2011). Figure 1a represents a mean confidence fragility curve of core melt, while Figure 1b is the mean confidence hazard curve. The mean core melt probability for PGA in the range 0.45–0.55g is approximately 0.5, and the annual frequency of PGA between these two limits is about 0.0011. Their product is the annual frequency of core melt contributed by PGAs between 0.45–0.55g, and the contributions from all PGAs can be calculated by integrating over the entire range of PGAs (Huang et al., 2011).

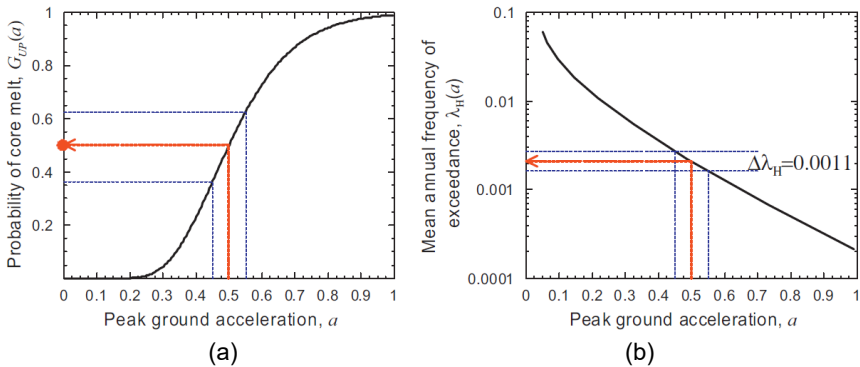


Figure 1. Generic mean core-melt fragility curve and mean hazard curve. The X-axis is commonly the peak-ground acceleration (PGA). Reproduced from Huang et al. (2011).

Mean and fixed-fractile hazards

McGuire (1993) emphasized that probabilistic hazard results should be reported by several fractiles and the mean hazard, to allow risk mitigation decision-makers to consider uncertainties in an appropriate manner. If a single result is needed, the mean should be selected, primarily because it is sensitive to all scenarios, including the extreme ones that drive the hazard at low AFEs. McGuire (1993) also argued that, in the decision-theoretic sense, the mean hazard allows target safety goals to be met over all sites.

An opposing opinion to using mean hazard was presented by Abrahamson and Bommer (2005). Their opinion note focused on low AFEs, and was argued from the point of view of critical infrastructure (i.e. NPPs and repository for high-level radioactive waste at Yucca Mountain). They remarked on the mean hazard curve increasing over high fractiles at low AFEs (this behavior is most noticeable in Figure 3), although they admitted that it is not alone a valid reason for adopting a different hazard curve. They based their argumentation on the interpretation of the branch weights, which in their view are confidence levels rather than probabilities, and on the instability of the mean hazard curve.

In their reply, McGuire et al. (2005) maintain that it is preferable to use the mean hazard, even from the risk calculation point of view. Their core argument relates to the widespread distinction used in PSHA between aleatory variability and epistemic uncertainty. McGuire et al. (2005) pointed out that mean hazard is stable against this distinction within the model, while median hazard is not. They list cases in which the distinction is not trivial to make, so expert judgment would influence the median hazard, but not the mean. They also point out that risk mitigation decisions are normally not influenced by the source of the uncertainty in hazard model. McGuire et al. (2005) also point out that implausible interpretations should be screened out from the PSHA model itself or weighted with low weights. This will preclude the

mean hazard to exceed larger fractiles. Choosing median may result in powerless decisions, since extreme scenarios would be completely disregarded.

Hazards in NPP regulations

Information about up-to-date PSHA practices in member countries of the Organization for Economic Co-operation and Development (OECD) was collected by a questionnaire sent to the representatives of countries participating in the OECD, Nuclear Energy Agency (OECD 2019; Okko et al. 2019). The questionnaire concerned details of the PSHA practice in the nuclear field, such as data collection, seismic source zones, logic trees, GMPE, ground condition, treatment of uncertainties, and the use of PSHA outputs. The respondent countries were situated in different tectonic environments and hazards are presented to AFEs in the range of 10^{-5} ... 10^{-9} , depending on the seismicity of the site. Very detailed PSHA output was given by Switzerland, where results for mean, median, and the 5th, 16th, 84th and 95th fractile hazard curves are normally reported. The common choice for single hazard definition is the mean hazard at AFE 10^{-4} or 10^{-5} (Table 1).

Table 1. AFE and confidence level used for the definition of SSE (i.e. similar to DBE in Finland) in nine European countries.

Country	PGA for SSE (m/s^2)	Fractile for SSE	AFE of SSE
Belgium	0.99–1.39	mean	10^{-4}
Finland	1	median	10^{-5}
France	0.5–1.5	-	-
Germany	North	84%	10^{-5}
	South	median	10^{-5}
Spain	-	-	10^{-4} – 10^{-5}
The Netherlands	0.6	-	10^{-4}
Sweden	1.1	-	10^{-5}
Switzerland	3–3.9	mean	10^{-4}
United Kingdom	1.4–2.5	mean	10^{-3} – 10^{-4}

Recent hazard results in Finland

The SENSEI project aimed at exploring the sensitivity of the PSHA models used in Finland (Mäntyniemi et al., 2021b, Fülöp et al. 2022). Figure 2 illustrates the mean and median hazard curves of the spectral frequencies of 1Hz, 5Hz, 25Hz, and PGA at the target sites. It shows how the mean hazard exceeds the median hazard in all cases. This is expected, because peak ground motion parameters, such as the PGA, are generally assumed to be skewed towards large values. The spectral

amplitude (SA) at 5Hz is approximately equal to the PGA. The 25Hz amplitude is above the PGA amplitude whereas the 1Hz spectral amplitude is below it.

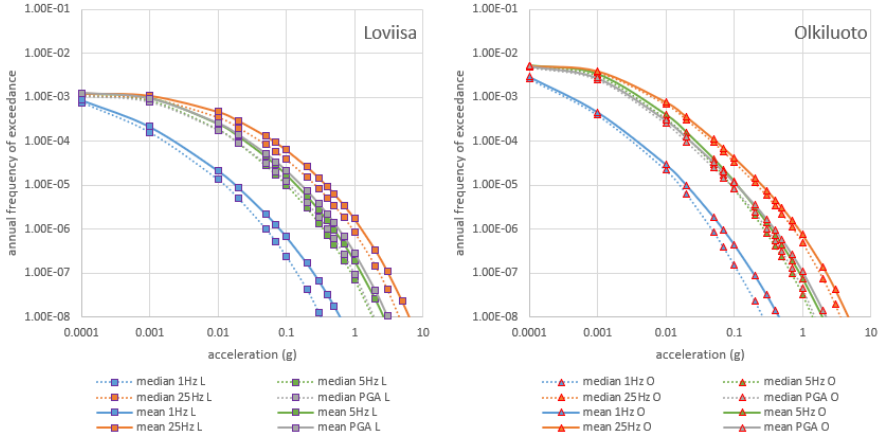


Figure 2. Median (dashed line) and mean (solid line) hazard curves for 1Hz (blue), 5Hz (green), 25Hz (orange), and PGA (gray) at Loviisa (L, purple square), Olkiluoto (O, red triangle).

A complete representation of the individual hazard curves for PGA is given in Figure 3. It shows that the mean estimate is very close to the median for higher AFEs. However, at lower AFEs the mean shifts towards the 84th percentile curves. The range of the hazard estimates is broadest at Loviisa for PGA, perhaps due to the use of two seismic source zonings for Loviisa and a single zoning for Olkiluoto. At very low PGA values, the hazard curves converge to the total activity level of the zones in the models. The uncertainties at very low PGA can be attributed to the effects of the zoning and Gutenberg-Richter parameters.

Properties of the distribution of AFEs extracted for PGA 0.0001g, 0.01g and 0.1g are given in Table 2. These can be interpreted as vertical cuts in Figure 2 at the given PGAs. The interesting quantities are the ratio of mean to median AFE. As expected, the mean AFE is higher, and the difference increases with larger PGAs. The coefficient of variation (COV) also increases with larger PGAs, and the observed trend that dispersion of the results is highest for Loviisa is quantified by the larger COV for this site. In addition, the Loviisa COV is larger for PGA 0.0001g, which is pointing at zonation as the source of the dispersion.

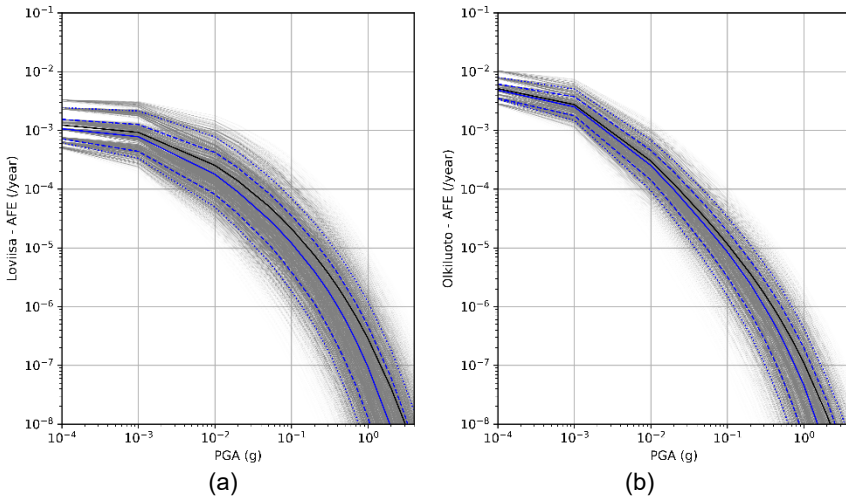


Figure 3. Range of hazard for the sites of (a) Loviisa and (b) Olkiluoto for PGA. The gray lines are the individual hazard curves, with intensity depending on the weight of the logic-tree branch producing them. Hence the more extreme (i.e. low and high) estimates are less visible. The black line is the mean, the continuous blue the median hazard. The dashed blue lines are 16th and 84th percentile, and the dotted blue lines the 5th and 95th percentile bounds.

Table 3 shows the ratio of the AFE 10⁻⁷ and AFE 10⁻⁵ amplitudes in terms of median and mean confidence. These numbers indicate how many times the hazard is larger at AFE 10⁻⁷ in comparison with AFE 10⁻⁵. The ratios are in the range of 4.8–14. They are highest for low frequencies at Loviisa and lowest for low frequencies at Hanhikivi.

Table 2. Properties of the AFE distribution at PGA 0.0001g, 0.01g and 0.1g for the three sites.

Site	PGA (g)	Median AFE	Mean AFE	STD	COV	Mean / Median AFE
Loviisa	0.0001	1.06E-03	1.23E-03	6.47E-04	0.53	1.16
	0.01	1.79E-04	2.54E-04	2.31E-04	0.91	1.42
	0.1	1.21E-05	2.13E-05	2.77E-05	1.30	1.76
Olkiluoto	0.0001	4.84E-03	5.14E-03	1.67E-03	0.32	1.06
	0.01	2.53E-04	3.01E-04	1.92E-04	0.64	1.19
	0.1	8.52E-06	1.16E-05	1.13E-05	0.97	1.37
Hanhikivi	0.0001	2.13E-02	2.13E-02	8.17E-03	0.38	1.00
	0.01	1.52E-03	1.64E-03	1.01E-03	0.62	1.08
	0.1	1.80E-05	2.95E-05	3.37E-05	1.14	1.64

Table 3. Ratio of intensity measure (IM) at AFE 10^{-7} and AFE 10^{-5} for the sites.

Site	Confidence level	IM $_{AFE\ 10^{-7}}$ / IM $_{AFE\ 10^{-5}}$			
		PGA	25Hz	5Hz	1Hz
Loviisa	Mean	8.8	8.1	8.8	13.9
	Median	8.7	8.6	8.8	11.7
Olkiluoto	Mean	9.5	8.8	8.2	9.5
	Median	8.4	8.3	7.6	7.6
Hahikivi	Mean	6.2	6.0	5.2	6.2
	Median	5.5	7.4	4.8	4.7

Finally, we present the mean AFEs that would give the same hazard as the currently used AFE 10^{-5} and 10^{-7} median values. Since, mean hazard always exceeds median, it is expectable that these *mean-equivalent* AFEs are larger than the current targets of 10^{-5} and 10^{-7} , for DBE and DEC C respectively. We calculated the AFE for hypothetical *mean-equivalent* and *84th percentile-equivalent* hazard definitions. It can be noted that for DBE mean equivalent, AFE would be above 10^{-5} in the range of $2 \cdot 10^{-5}$ in most cases. However, the values depend on the site and spectral frequency. For 84th percentile equivalent DBE, AFE would be even higher in the range of $AFE\ 3 \cdot 10^{-5}$. For the DEC C earthquake, the change would be to increase the AFE from 10^{-7} to the range of $2 \cdot 10^{-7}$ in most cases. The precise target thresholds are given in Mäntyniemi et al. (2022) for the sites.

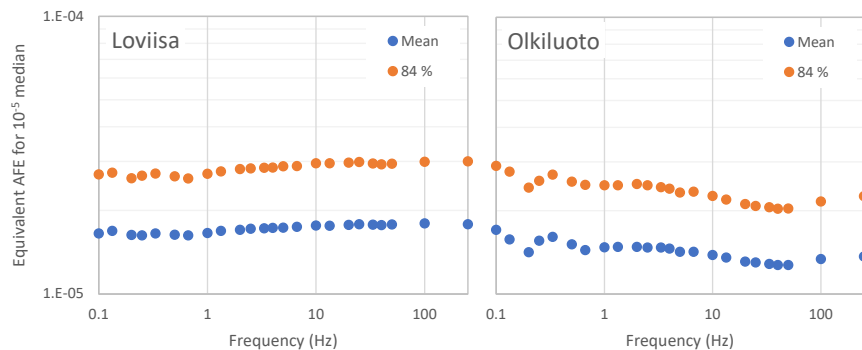


Figure 4. Target AFE for maintaining the current hazard level for DBE (i.e. 10^{-5} median), in case of a hypothetical change to mean or 84th percentile confidence.

Applications

The main application of this work is related to the definitions of seismic hazards at NPPs in Finland. One point to stress is the significant uncertainty of the hazard at all AFEs. This uncertainty is growing at lower AFEs and should be considered in PRA. Hence, we recommend that PSHA output should be reported for mean,

median, and the 5th, 16th, 84th and 95th fractile hazard. The second point to stress, relates to the definition of single hazard levels for DBE and DEC C, when they are made in the future update of the YVL guide. It appears that several arguments favor the use of mean hazard curves as basis for a single definition, when needed.

Summary and conclusions

There is currently no serious contender to PSHA in sight, despite some criticism (e.g., Mulargia et al. 2017). As a future direction, the quantification and reduction of the reducible uncertainties of seismic hazard is emphasized. Ideally, new extensive datasets allow the validation of individual hazard model inputs (e.g., Daxer et al. 2022), but the limited time spans of seismicity records remain an obstacle.

The present review shows that mean hazard is the target commonly utilized for engineering design. It is in line with probabilistic risk analysis and the choice for NPPs in many OECD member countries. That the mean represents a composite of all hazards is relevant to Finland as well, since low-probability earthquake scenarios cannot be disregarded.

For example, if a future earthquake scenario, let us say a magnitude M7.0 event occurring in Finland, is considered plausible but extremely rare, it would be associated with a low weight in the logic tree. Median hazard would erase the scenario entirely, while the mean hazard would still keep it, notwithstanding some debate among the experts about the exact value of the weight. At very low AFEs, the mean hazard increases over many fractiles, but this seems not to prevent its use. A good practice is to report a number of fractiles and the mean hazard, whether the focus is on hazard mapping for the general building code (Danciu et al. 2021) or for critical infrastructure such as NPPs (Abrahamson et al. 2004).

Mean is always larger than median, so the selection of the hazard curve to read for a ground-motion value affects the adoption of the corresponding AFE. For deterministic design, mean, median or another fractile can be used and are used in existing nuclear practice. The analyses based on the SENSI set of calculations show a variability of hazard levels at the different sites for different frequencies. We recommend that PSHA output should be reported for mean, median, and the 5th, 16th, 84th and 95th fractile hazard curves in the future to allow decision-making consider uncertainties in an appropriate manner.

Acknowledgement

We acknowledge the SAFIR2022 project VALERI for funding and the Radiation and Nuclear Safety Authority in Finland (STUK), Fortum Oy and TVO for their active participation in the steering of the VALERI project.

References

- Abrahamson, N.A., Bommer, J.J., 2005. Probability and uncertainty in seismic hazard analysis. *Earthq. Spectra* 21:603–607.
- Abrahamson, N.A., Coppersmith, K.J., Koller, M., Roth, P., Sprecher, C., Toro, G.R., Youngs, R., 2004. Probabilistic seismic hazard analysis for Swiss nuclear power plant sites (PEGASOS Project), Final Report, Vol. 1 (text). Retrieved from <https://www.swissnuclear.ch/upload/cms/user/PEGASOSProjectReportVolume1-new.pdf>
- Budnitz, R. J., Apostolakis, G., Boore, D. M., Cluff, L. S., Coppersmith, K. J., Cornell, C. A., Morris, P. A., 1997a. Recommendations for Probabilistic Seismic Hazard Analysis: Guidance on uncertainty and use of experts. NUREG/CR-6372 UCRL- ID – 122160, vol. 1.
- Budnitz, R. J., Apostolakis, G., Boore, D. M., Cluff, L. S., Coppersmith, K. J., Cornell, C. A., Morris, P. A., 1997b. Recommendations for Probabilistic Seismic Hazard Analysis: Guidance on uncertainty and use of experts. Appendices. NUREG/CR-6372 UCRL- ID – 122160, vol. 2.
- Cornell, C.A., 1968. Engineering seismic risk analysis. *Bulletin of the Seismological Society of America* 58, 1583–1606.
- Danciu, L., Nandan, S., Reyes, C., Basili, R., Weatherill, G., Beauval, C., Rovida, A., Vilanova, S., Sesetyan, K., Bard P.-Y., Cotton, F., Wiemer, S., Giardini, D., 2021. The 2020 update of the European Seismic Hazard Model: Model overview. EFEHR Technical Report 001, v1.0.0, doi:10.12686/a15
- Daxer, C., Huang, J.-J.S., Weginger, S., Hilbe, M., Strasser, M., Moernaut, J., 2022. Validation of seismic hazard curves using a calibrated 14 ka lacustrine record in the Eastern Alps, Austria. *Sci. Rep.* 12:19943. <https://doi.org/10.1038/s41598-022-24487-w>
- Fülöp, L., Mäntyniemi, P., Malm, M., Toro, G., Crespo, M.J., Schmitt, T., Burck, S., Välikangas, P., 2022. Probabilistic seismic hazard analysis in low-seismicity regions: An investigation of sensitivity with a focus on Finland. *Nat. Hazards*, <https://doi.org/10.1007/s11069-022-05666-4>
- Huang, Y.-N., Whittaker, A. S., Luco, N., 2011. A probabilistic seismic risk assessment procedure for nuclear power plants: (I) Methodology. *Nucl. Eng. Des.* 241:3996–4003. <https://doi.org/10.1016/j.nucengdes.2011.06.051>
- IAEA, 2011. Earthquake preparedness and response for nuclear power plants. International Atomic Energy Agency IAEA Safety Reports Series No. 66.
- Johnson, J. J., Gürpinar, A., Campbell, R. D., Kammerer, A., Rivera-Lugo, R., Stovall, S., 2017. Seismic design standards and calculational methods in the United States and Japan. United States Nuclear Regulatory Commission, Report NUREG/CR-7230.

- Marzocchi, W., Jordan, T. H., 2014. Testing for ontological errors in probabilistic forecasting models of natural systems. *Proceedings of the National Academy of Sciences* 111(33):11973–11978, <https://doi.org/10.1073/pnas.1410183111>.
- Mäntyniemi, P., Sørensen, M.B., Tatevossian, R.E., 2021a. Testing the Environmental Seismic Intensity scale on data derived from the earthquakes of 1626, 1759, 1819, and 1904 in Fennoscandia, northern Europe. *Geosciences* 11, 14. <https://doi.org/10.3390/geosciences11010014>
- Mäntyniemi, P., Malm, M., Burck, S., Okko, O., Välikangas, P., Fülöp, L., 2021b. Sensitivity of seismic hazard analysis in Finland: Overview of the SENSI project. *ATS Ydintekniikka* 50(2):19–23.
- Mäntyniemi, P., Malm, M., Rinne, L., Fülöp, L., 2022. Valorisation of probabilistic seismic hazard results in Finland (Research Report No. VTT-R-00978-22). VTT Technical Research Centre of Finland, Espoo.
- McGuire, R.K., 1993. Computations of seismic hazard. *Ann. Geofis.* 36:181–200. <https://doi.org/10.4401/ag-4263>.
- McGuire, R.K., Cornell, C.A., Toro, G.R., 2005. The case for using mean seismic hazard. *Earthq. Spectra* 21:879–886. <https://doi.org/10.1193/1.1985447>
- Mulargia, F., Stark, P.B., Geller, R.J., 2017. Why is probabilistic seismic hazard analysis (PSHA) still used? *Phys. Earth Planet. In.* 264:63–75. <https://doi.org/10.1016/j.pepi.2016.12.002>
- Norio, O., Ye, T., Kajitani, Y., Shi, P., Tatano, H., 2011. The 2011 Eastern Japan great earthquake disaster: overview and comments. *Int. J. Disaster Risk Sci.* 2:34–42. <https://doi.org/10.1007/s13753-011-0004-9>
- OECD, 2019. Comparison of probabilistic seismic hazard analysis of nuclear power plants in areas with different levels of seismic activity. Report NEA/CSNI/R(2019)1, Organization for Economic Co-operation and Development Nuclear Energy Agency (NEA), Paris.
- Okko, O., Fülöp, L., Sandberg, J., Välikangas, P., 2019. Comparison of probabilistic seismic hazard studies within the oecd countries, Proceedings of the Symposium on the Application of Geophysics to Engineering and Environmental Problems, SAGEEP 2019, Portland, United States.
- STUK, 2019. Guide YVL B.7 Provisions for internal and external hazards at a nuclear facility *and Explanatory memorandum*. Radiation and Nuclear Safety Authority. Retrieved from <https://www.stuklex.fi/en/YVLLB.7-memo.pdf>
- Wong, I. G., 2014. How big, how bad, how often: are extreme events accounted for in modern seismic hazard analyses? *Nat. Hazards* 72:1299–1309. <https://doi.org/10.1007/s11069-013-0598-x>

8 Severe Accidents

8.1 Analytical severe accident research (ANSA)

Korpinen Anna, Sevón Tuomo, Ojalehto Sara, Taivassalo Veikko, Ilvonen Mikko

VTT Technical Research Centre of Finland Ltd
P.O. Box 1000, FI-02044 Espoo

Abstract

The objective of the project was to develop national competence in the area of severe accidents and ensure that the analytical tools and methods in use are validated in their intended purposes and developed further if necessary.

Fukushima accident provides a unique opportunity to get more information on the progress of severe accidents. Adding water level measurement system to the models indicated a leak of superheated steam to the drywell. Stratification of the suppression pool has a major effect on the containment pressure. Sectoral nodalisation, with at least three layers, produced good results for annular geometry.

Hydrogen combustion constitutes a risk to the containment integrity. VTT has developed a model for the flame wrinkling factor that improves the modelling reliability. Pool scrubbing is an important mechanism in mitigating fission product release. Analytical results indicate need of model development especially for small particles, in jet regime and with gaseous iodine retention.

Understanding of dispersion and exposure phenomena is needed for all-encompassing nuclear safety. Sensitivity studies provided further information on how input data and modelling assumptions affect the results.

Fukushima analyses

The Fukushima accident provides a unique opportunity for obtaining more information about the progress of severe accidents and their prevention and mitigation. Analyzing the accidents was started already in 2012 and since then,

models of the three units are continuously developed further when new information is received.

To get further insights into the events at Fukushima, reactor water level measurement systems were added to the models. The measurement system is based on measuring the pressure difference between two water-filled pipelines that were connected to the reactor. Boiling of the water in the system may distort the measurements.

Most recently, the water level measurement system was added to the unit 1 model (Sevón, 2022). Figure 1 shows the calculated water level in the reactor compared to the measurement data. The actual water level dropped at 5 h because a lot of debris fell to the lower plenum.

The indicated water level, as calculated by the simulated measurement system, remained a bit above the bottom of active fuel until 6.5 h because this was the lower limit of the measurement range. At 6.5 h, a 1.7 cm^2 leak from the steam line to the drywell was assumed. This was sufficient to heat up the drywell and evaporate the water in the measurement system reference leg. As a result, the measurement data was relatively well reproduced.

The green line in Figure 1 shows the indicated water level without the assumed leak. So, a leak of superheated steam to the drywell is clearly necessary for reproducing the measurement data. This confirms earlier conclusions of the Japanese accident investigation committee (ICANPS, 2012) and analyses performed by TEPCO (2015).

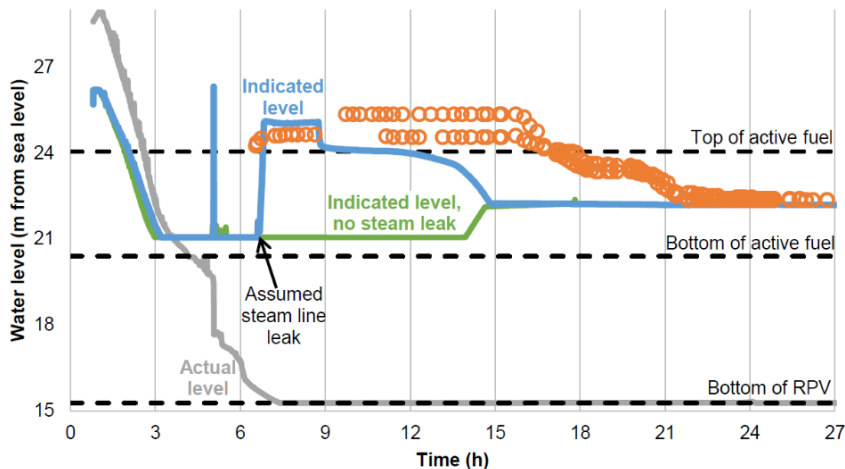


Figure 1. Unit 1 reactor water level.

The steam line leak at 6.5 h alone was not sufficient for reaching 0.6 MPa pressure in the drywell at 9 h. In addition, 0.3 cm^2 leaks were assumed to start at 1 h from both recirculation pump seals. Besides increasing the drywell pressure, these leaks decreased the water level in the reactor. This was necessary for the lower head

penetration failure and debris ejection from the reactor at 10.5 h. As a result, the measured pressure peak in the drywell at 12 h was reached in the simulation. With these assumptions, the drywell pressure (Figure 2) is well comparable with the available measurement data.

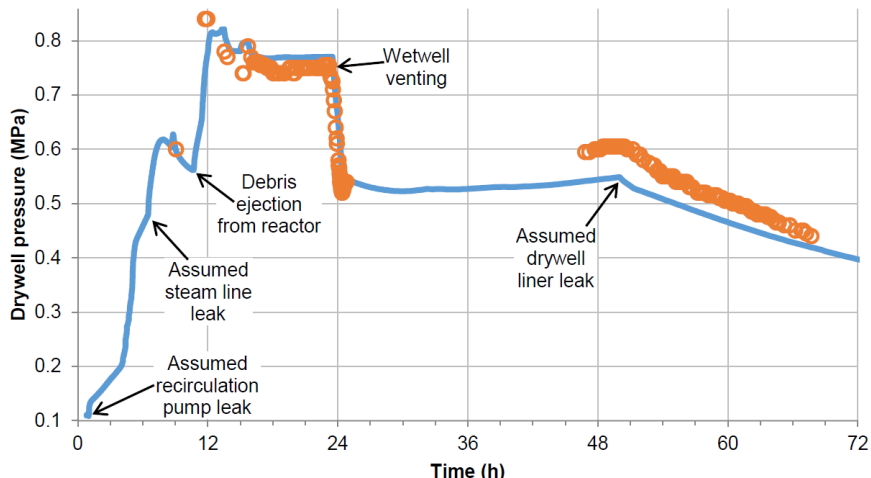


Figure 2. Unit 1 drywell pressure.

Suppression pool stratification

Calculations of the Fukushima accident have highlighted that stratification of the suppression pool has a major effect on the containment pressure. Traditionally, suppression pools are modelled as single volumes with lumped parameter codes, thus ignoring the thermal stratification completely. This approach could potentially result into significantly lower pool surface temperatures and gas space pressures.

The effect of nodalization on the thermal stratification of a suppression pool was first studied by modelling the PPOOLEX STR-11 experiment (Laine et al., 2010) using MELCOR (Ojalehto, 2021). Nodalizations ranging from one to twelve nodes were tested. The simulation results were compared against the measured pool bottom and top temperatures. Additionally, the effect of the nodalization on the pressure and the average temperature in the wet well gas space was studied.

The model accuracy was observed to differ between the stratification and mixing periods of the experiment. During the stratification period, the top temperatures corresponded the measured temperatures rather well regardless the number of nodes (Figure 3). As for the bottom temperature, the simulated values started to correspond the measured values after the bottom region was divided into two nodes (the cases with 8 nodes and up). Both bottom and top temperatures can be considered converging during the stratification period. In the gas space, the pressure and the average temperature seem to start converging once four or more nodes are used. This occurred both during the stratification and mixing periods.

During the mixing period, no convergence was observed in bottom or top temperatures, since increasing the number of nodes caused the top temperatures to increase (Figure 3) and the bottom temperatures to decrease. This also caused the simulated temperatures to diverge from the measured temperatures, so the nodalized modelling of the mixing period cannot be considered very accurate. However, it was also shown that the single node model gave results that are more accurate during the mixing period, and therefore it may be justified to use the single node model instead of the nodalized model during the mixing.

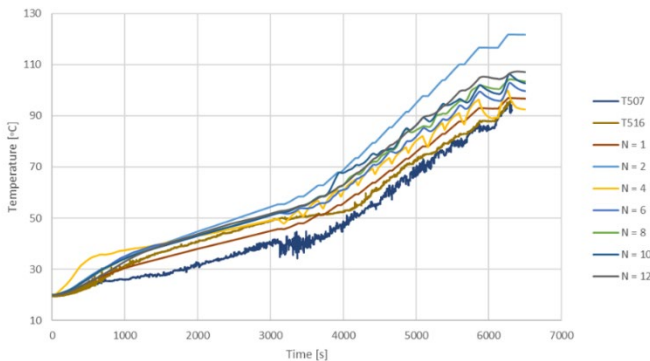


Figure 3. Suppression pool top temperature from STR-11 experiment compared to the simulation results with different nodalizations.

In order to investigate the effects of the nodalization on the thermal stratification of a suppression pool in a real scale and geometry, a stratification test conducted by TVO at Olkiluoto 1 reactor (Poikolainen, 2009) was simulated using MELCOR (Ojalehto, 2022b). Two different nodalization schemes were used with varying number of node layers. In the first case, the wet well was divided into four sectors, and in the second case, it was divided into three nested rings. In both nodalization schemes, the volume was further divided into two, three and four node layers. The nodalization schemes are illustrated in Figure 4.

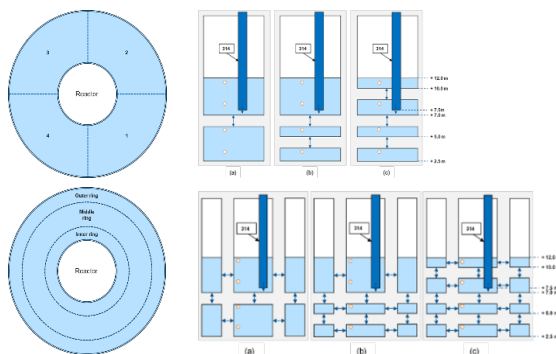


Figure 4. Different nodalization schemes for Olkiluoto 1 suppression pool.

With the sectoral nodalization, three and four layer configurations produced very similar results. In both cases, the temperatures were estimated with a sufficient accuracy, even though the simulated temperatures were a few degrees lower than in the test. In both cases, the stratification can be observed clearly. On the other hand, the two-layer configuration was not as successful in estimating the pool temperatures and stratification. While it produced better results in the bottom layer, it also severely underestimated the top layer temperature towards the end of the simulation. In Figure 5, the temperatures for sectoral nodalization with two and three layers are compared to the corresponding measurements.

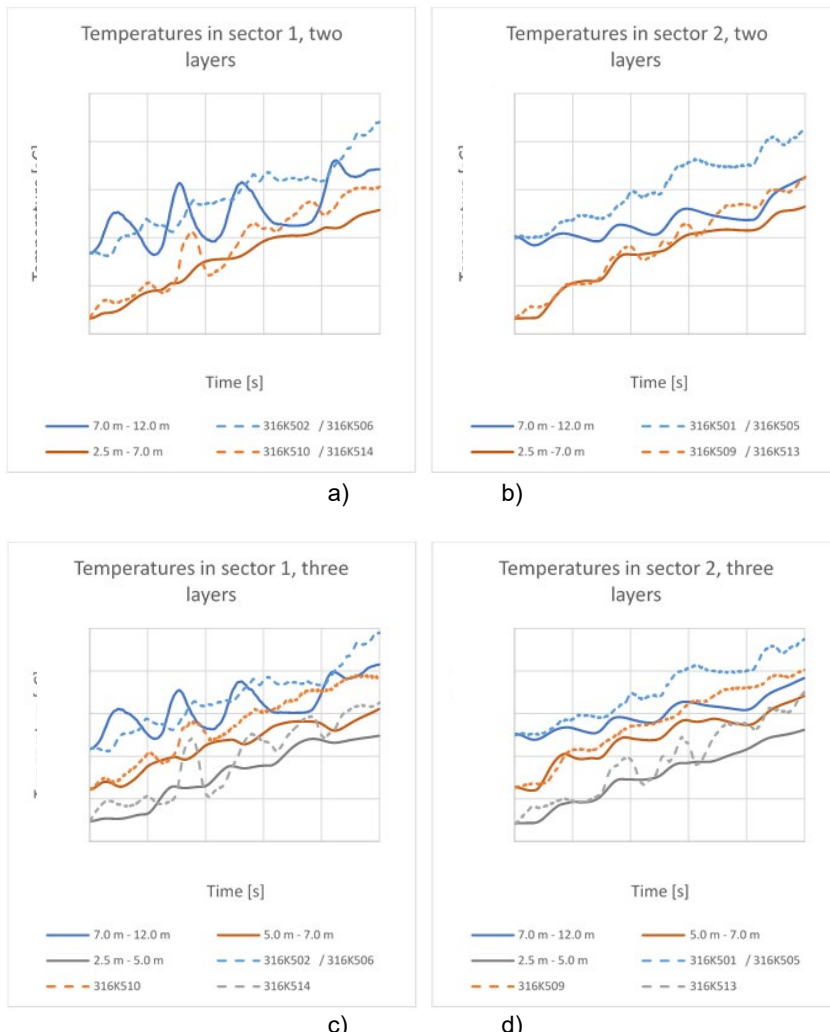


Figure 5. Comparison of simulated and measured temperatures for sectoral nodalization with two (a) and b)) and three layers (c) and d)) for two of the sectors.

Since the radial division of wet well did not match the sectoral division of the measurement points in the test, only layer average temperatures were compared in the case of radial nodalization. Figure 6 shows the average layer temperatures in a three-layer configuration. It was observed that, similar to the sectoral nodalization cases, three and four-layer configurations resulted into very similar results. Clear stratification was shown in the results, even though the layer temperatures were somewhat lower than in the test. The most notable difference compared to the sectoral nodalization was the significantly lower bottom temperatures. Overall, it seems that, even though the radial nodalization produced better results in the top region, it was not very successful in estimating the temperature of the bottom layer.

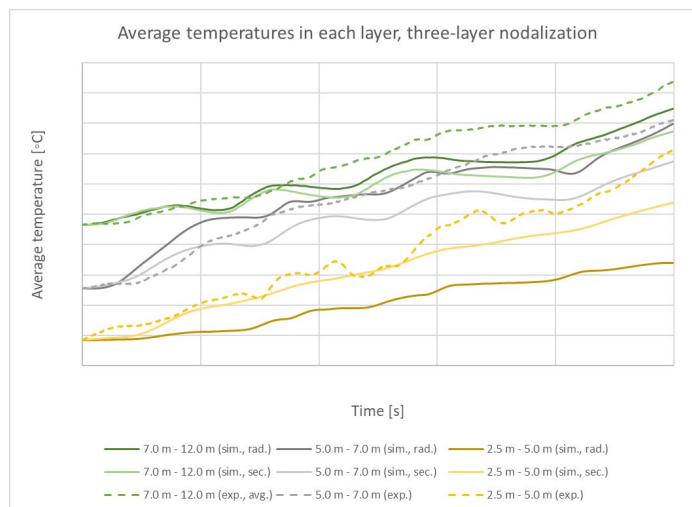


Figure 6. Average layer temperatures for the three-layer radial nodalization case compared with the corresponding average temperatures from the three-layer sectoral nodalization case and the test.

In all the nodalization cases, the difference in the temperatures between the simulation and test increased towards the end of the simulations, implying that not enough heat was transferred into the system. Despite the temperature differences in the results, the MELCOR model was able to estimate the stratification with a sufficient accuracy.

Hydrogen combustion

Containment is the last safety barrier preventing the release of fission products and therefore ensuring the integrity of the containment is extremely important. Hydrogen combustion constitutes a risk to the containment, but first hydrogen migration should be assessed to estimate the timing for the formation and composition of a flammable mixture.

The erosion of light gas layers caused by natural convection induced by temperature difference was studied modelling THAI TH-32 experiment (Freitag & Schmidt, 2020) with OpenFOAM CFD software (Ojalehto, 2022a). The calculations were carried out with two turbulence models: k-Omega SST and k-Omega SST-SAS. A mesh with 900 000 cells was used with both turbulence models, and a finer mesh of 1 200 000 cells was additionally used for the k-Omega SST-SAS model.

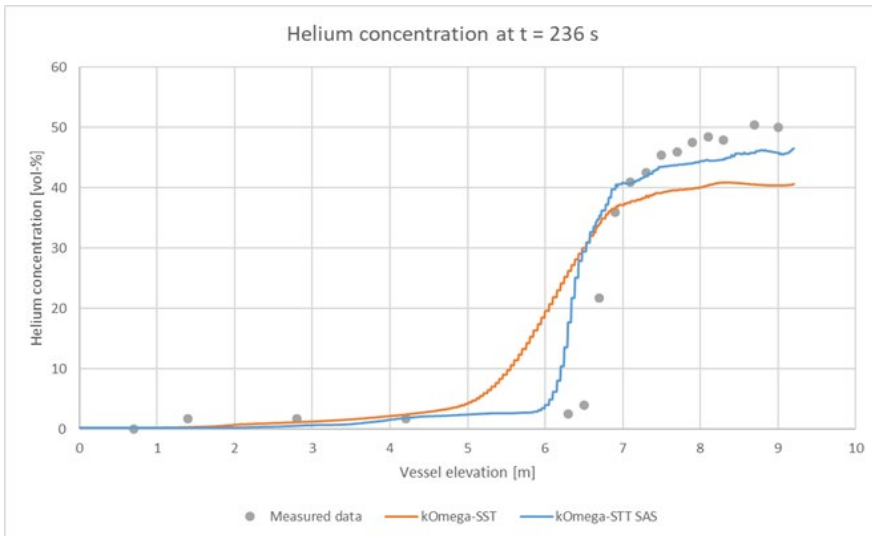


Figure 7. Measured helium concentration at the end of the injection phase compared to the simulation results.

With the SST-SAS model, helium injection was computed more accurately, whereas the SST model seemed to result into more diffusive results. Helium concentration along the vessel is plotted in Figure 7. This difference between the turbulence models is also demonstrated in the helium migration phase when the helium layer is eroded much sooner in the case of the SST model. The helium also spreads more uniformly around the vessel. With SST-SAS, the erosion is much slower.

According to the SST model, the erosion of the helium layer by natural convection would be quite efficient, whereas the SST-SAS simulation indicates that the erosion would be significantly slower and somewhat inefficient. Theoretically, the SST-SAS results are more justified.

During a combustion process, the flame front is known to accelerate in most cases. The flame acceleration is especially significant in lean hydrogen mixtures. In computational models, the increase in the flame speed is commonly incorporated in the wrinkling factor representing the area of reacting flame front. To model hydrogen combustion accurately, the development of the wrinkling factor during the whole combustion process has to be defined.

Determining the flame wrinkling factor is especially challenging for lean mixtures. Experimentally the wrinkling factor is typically obtained from Schlieren photographs, laser tomography or flame arrival. Now the feasibility of determining the development of the wrinkling factor from measured evolution of the pressure was studied (Taivassalo, 2023).

Thirteen combustion experiments with spherical flame configurations were analysed and the wrinkling factor was determined as a function of time. All the experiments, except one, were performed in a spherical combustion bomb. The diameter of the vessels ranged almost two orders of magnitude from the small scale (a few centimetres) up to the intermediate scale (3.66 m). The volume fraction of hydrogen varied from the stoichiometric value of 29.5% down to 10%. Most of the analysed tests were started at the ambient conditions. The initial pressure is about 1 bar except in the two cases of 0.5 and 2.5 bar. In three cases, the initial temperature is 100 °C and the other tests had started at the room temperature.

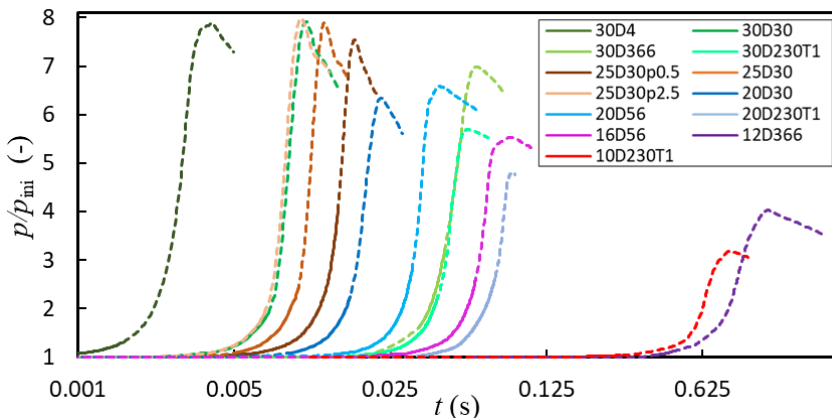


Figure 8. Relative pressure as a function of time in the analysed combustion experiments with spherical flame configurations. In the experiment ID, the first numbers indicate the hydrogen concentration (30-10 vol%). The numbers after letter D tell the diameter of the test vessel in centimeters. Letter p and the following value tell that the pressure in the experiment was something else than 1 bar and notation T1 indicate the experiments with the initial temperature of 100 °C.

During the constant volume experiments, the pressure rises significantly. Determination of the wrinkling factor was based on the time evolution of the pressure. The experimental pressure developments are plotted in Figure 8 relative to the initial pressures as a function of time. The combustion time ranges from milliseconds to about a second. Only parts of the pressure curves can be utilized in determining the wrinkling factor. Close to the chamber walls, the interaction of the flame front with the walls influences flame propagation and wrinkling. Therefore, the wrinkling factor was determined only until the time the flame was interpreted to have

interacted with the walls and the solid parts of the pressure curves in Figure 8 were used to determine the wrinkling factor.

The determined development of the flame wrinkling factor is plotted in Figure 9 as a function of the average radius of the burned volume for all of the analysed cases. The wrinkling factor increases with the distance from the ignition point and with the pressure. On the other hand, the wrinkling factor decreases with the hydrogen concentration and temperature. In some cases, the obtained wrinkling factor fluctuates significantly with radius and time. Furthermore, the end parts of most curves rise rapidly primarily because of the large pressure increase in the last stage in constant volume experiments. The pressure increase rate can also be magnified by other phenomena including the interaction of the flame front with the vessel wall. Compared to directly measured wrinkling factor, the obtained wrinkling characteristics are within the scatter of experimental data (Bauwens et al., 2012; Katsumi et al., 2017; Yaguchi et al., 2021).

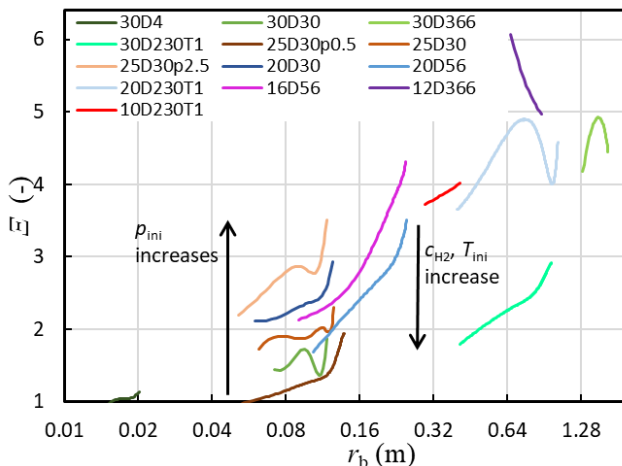


Figure 9. Wrinkling factor as a function of the average radius in some spherically propagating flames documented in literature.

The characteristics of the wrinkling factor in the analysed cases were used to develop an algebraic correlation for the flame wrinkling factor in hydrogen-air combustion. The primary parameters affecting flame wrinkling were concluded to be the distance from the ignition point, laminar burning velocity and the density difference between the unburned and burned gas mixtures. Figure 10 compares the values from the correlation with the ones determined from the pressure curves. In overall, the agreement is satisfactory and within the uncertainties of the determined values. The prediction of the correlation is also within experimental scatter in five constant-pressure cases for which the flame speed was determined experimentally. However, a more complex distance dependence instead of the applied linear one would likely improve the performance of the correlation.

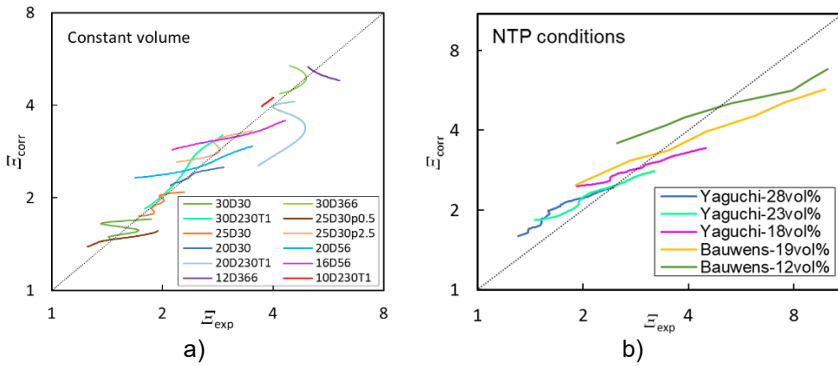


Figure 10. a) Comparison of the prediction of the correlation for the wrinkling factor with a) the determined wrinkling factor in some spherically propagating flames, and b) the experimental data in five spherical hydrogen-air combustion experiments performed in the ambient conditions (Bauwens et al., 2012; Yaguchi et al., 2021).

Pool scrubbing

Pool scrubbing is an important mechanism in mitigating fission product release from the containment. Experiments in the SAFIR2022 MANTRA project aim at completing the experimental matrix for the effect of pool depth, flow rate into the pool and pool chemistry both for particulate and gaseous iodine species. A few experiments performed with CsI aerosol were modelled with the most recent ASTEC version 2.2.0.1 (Kärkelä et al., 2023).

Comparison of the analytical and experimental Decontamination Factor (DF) values for E-1 series (Kärkelä et al., 2021) with particle diameter $0.004 \mu\text{m}$ – $4.7 \mu\text{m}$ is in Figure 11. When the carrier gas inlet flow rate is clearly in the jet regime ($\text{We} > 10^5$), the DF values produced by ASTEC are notably smaller than recorded in the experiments. The results are in a reasonably good agreement with smaller inlet flow rates. However, ASTEC overestimates the pool scrubbing efficiency especially with the most favourable pool scrubbing conditions, i.e. with the slowest inlet flow rates combined with deep pool.

The difference could originate from particle size distribution. It should also be noted, that the experimental DF values remain nearly the same despite the pool scrubbing conditions become more favourable. This behaviour is unexpected and was not detected in later experiments (Kärkelä, 2022).

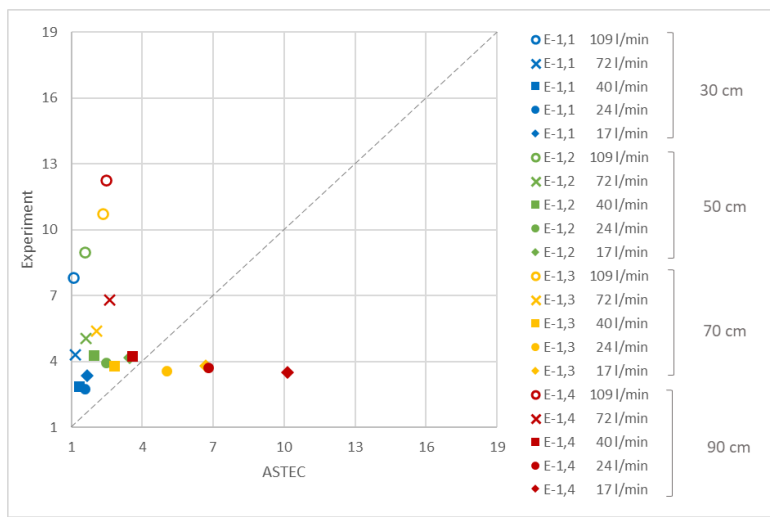


Figure 11. Comparison of the analytical and experimental DF values for E-1 series. Five different N₂ inlet flow rates and four different pool depths were examined.¹⁰⁹ 1/l/min and 72 l/min N₂ inlet flow rates are in jet regime.

Comparison of analytical and experimental DF values for B-1 series (Kärkelä, 2022) with particle diameter $0.01 \mu\text{m}$ – $0.76 \mu\text{m}$ is in Figure 12. Now ASTEC clearly underestimates the efficiency of pool scrubbing also in the globular regime.

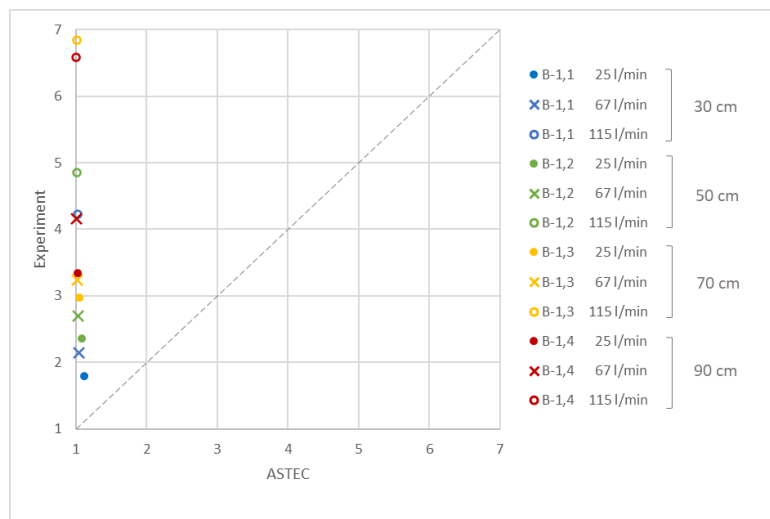


Figure 12. Comparison of the analytical and experimental DF values for B-1 series. Three different N₂ inlet flow rates and four different pool depths were examined. 115 l/min and 67 l/min N₂ inlet flow rates are on jet regime.

CRIEPI has performed pool scrubbing experiments with gaseous iodine (Kanai, 2020/2021). Their experimental facility represents Filtered Containment Venting System. Experimental set performed with 0.5 wt% NaOH solution was modelled with ASTEC.

The DFs recorded in the experiment varied between 100 and 45 000. ASTEC resulted DF values close to 1. All DF values are illustrated in Figure 13. It should be noticed that the y-axis for the experimental values and x-axis for the ASTEC results are in a fully different scale. So, the Figure 13 should not be used for comparing the experimental and analytical values, but to track the effect of different variables, such as inlet flow rate and pool depth.

In the experiment, the influence of inlet gas flow rate into pool scrubbing efficiency was not observed whereas ASTEC clearly predicts smaller DF values for higher inlet flows. Experimental results showed increasing DF values with increasing pool depth until 1.5 m. This can be observed also in the ASTEC results. With pool depths above 1.5 m, the experimental DF becomes nearly constant with inlet iodine concentrations of 170-550 ppm. High inlet iodine concentrations around 900 ppm showed clearly larger DF values in the experiment. This is not visible in the analytical results.

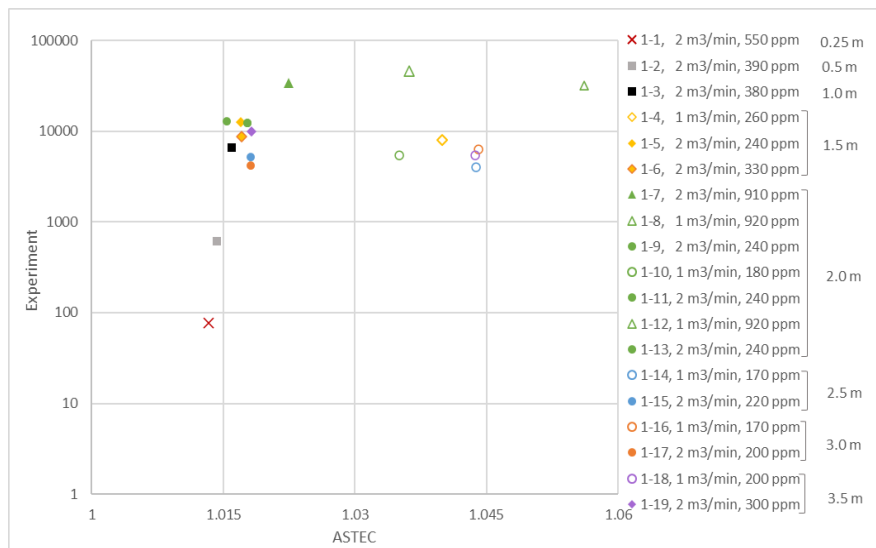


Figure 13. DF values for eight different pool depths with two different air inlet flow rates. Ppm values indicate the inlet iodine concentration.

Analytical results indicate need of model development for small particles, jet regime and gaseous iodine. In all these cases, DF values produced by ASTEC are notably smaller than recorded in the experiments.

Environmental consequences

Severe accidents have shown that understanding of dispersion and exposure phenomena are needed for all-encompassing nuclear safety. Assessing the transport of radioactive release to evaluate the environmental consequences is especially important for defining the necessary protective actions. The physical phenomena are complicated, and they can be modelled by codes featuring various levels of sophistication.

Atmospheric dispersion simulations studying the Fukushima accident were performed using the VTT-made VALMA code (Ilvonen, 2022) dedicated for estimating the consequences of radioactive releases. VALMA is based on the Lagrangian principles of dispersion modelling and calculates phenomena along the trajectories of the pollutant particles in the atmosphere.

Two source distribution assumptions were used: JAEA by Terada et al. 2020 and MELCOR-based, calculated by VTT in the frame of ANSA project. The former has time span of about 3 weeks, whereas the latter has releases essentially during the first five days. However, during the first five days, most of the spread was over the ocean.

The meteorological data was obtained from FMI and it is based on the weather prediction model of the ECMWF. It consists of trajectories calculated by the FMI SILAM dispersion model, made up of trajectory points which carry many kinds of associated information, like precipitation and stability etc.

The main comparison data for VALMA predictions were the detailed deposition density maps of Saito et al. (2015). When comparing the measurements and VALMA results (Figure 14) we see that the measured deposition field has a sharper shape (more pronouncedly high deposition values near the source), whereas the VALMA predictions seem to have a more smooth or convex surface. The reasons for this are very difficult to find out, but one factor might be that particle sizes were bigger than assumed in VALMA and as a result their gravitational settling occurred closer to the source.

It is generally difficult to characterize the differences, which can be due to transport time, trajectory paths, cloud spread and deposited amounts, but also simply due to assumed source term temporal behaviour. Preliminarily it can be said that VALMA deposition predictions are in the correct order of magnitude, but all geographical details of the deposition patterns cannot be satisfactorily reproduced.

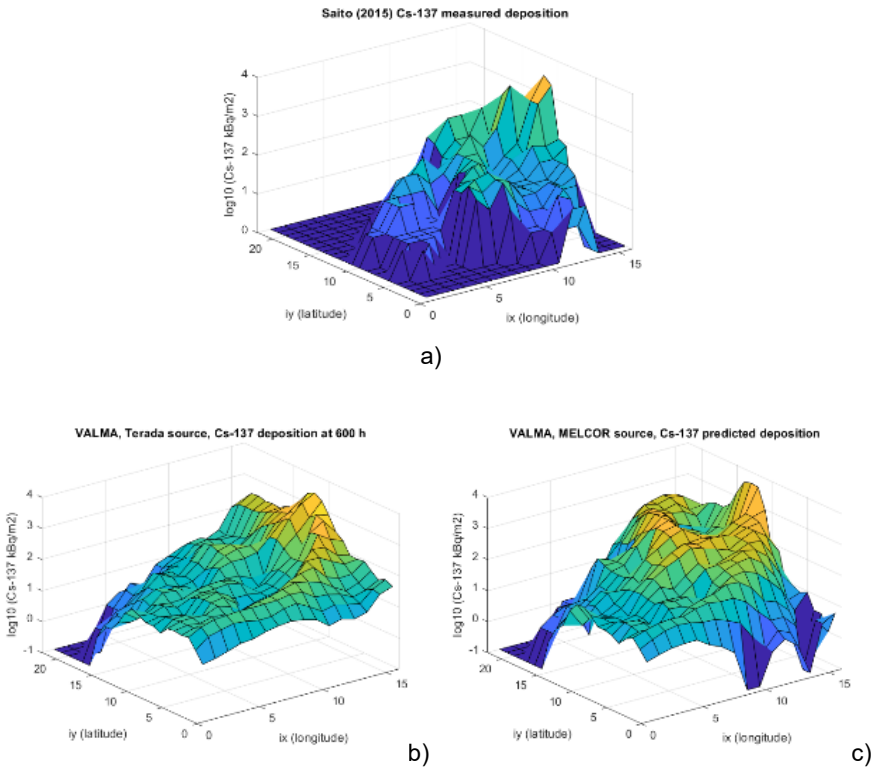


Figure 14. a) Cs-137 deposition measurements of Saito et al. (2015) in the Fukushima area in June 2011, b) VALMA Cs-137 deposition prediction in the Fukushima area at 20:00 UTC on 5 April 2011, calculated from the JAEA source term, and c) VALMA Cs-137 deposition prediction in the Fukushima area at 15:46 UTC on 19 March 2011, calculated from the VTT MELCOR source term.

In the next phase, a sensitivity study was performed to have further information on how input data and modelling assumptions affect the results of atmospheric dispersion and dose assessment (Ilvonen, 2023). By sensitivity studies, we get some useful rule-of-thumb type information on what we should expect, if the initial data on the release source term is going to change (when better information becomes available) in one direction or other. This kind of calculations could be done also during the actual emergency itself, but experiences from emergency drills have shown that time is then very scarce, and it is sometimes much better to have beforehand-generated knowledge of some important basic relationships.

The VTT-developed code ARANO was used to investigate the sensitivity of dose results with respect to changing parameters of weather and source term. Atmospheric dispersion in ARANO is traditional Gaussian in the lateral direction,

but a more advanced K_z model based on turbulent exchange coefficients is used in the crucially important vertical direction.

The chosen weather parameters for the sensitivity study were stability class, wind speed and rain. Source term parameters were effective release height, delay after reactor SCRAM and duration of the release. In addition, dose pathways, integration times and distances from source were studied. Released activities were always set as 1% of the LDR-50 reactor core radioactive inventory.

For the investigated weather parameters, wind speed variation produced more difference in doses than stability or occurrence of rain for all nuclide groups and all distance points. For the source term parameters, biggest differences in doses were caused by either effective release height or the delay between reactor SCRAM and start of the atmospheric release depending on nuclide group. Distance from source has by far the biggest effect on doses, bigger than exposure pathway or integration times in this study. However, when looking at only the first 5 km from source, we see that the differences between exposure pathways are much bigger than those caused by distance. Usually cloudshine is the least important. Figure 15 illustrates the variability of dose results for iodine nuclide group, for distances up to 100 km and Figure 16 for distances up to 5 km.

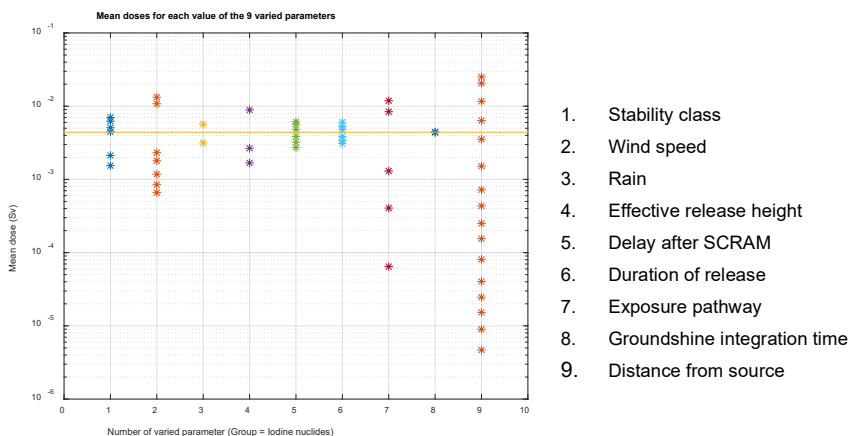


Figure 15. Variability of dose results resulting from changing parameter values, for the iodine nuclide group, for distances up to 100 km. The horizontal orange line shows the overall 'grand total mean value' of all doses.

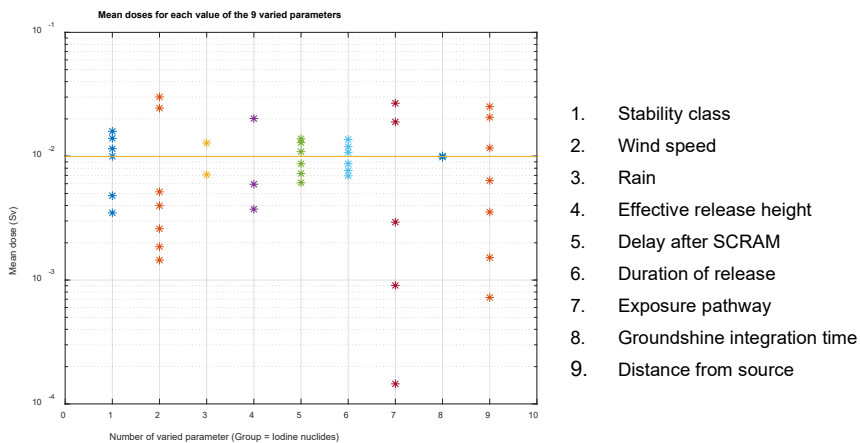


Figure 16. Variability of dose results resulting from changing parameter values, for the iodine nuclide group, for distances up to 5 km. The horizontal orange line shows the overall 'grand total mean value' of all doses.

References

- Bauwens, C. R., Chao, J. & Dorofeev, S. B. 2012. Effect of hydrogen concentration on vented explosion overpressures from lean hydrogen-air deflagrations. Int. J. Hydrogen Energy. Volume 37, Issue 22. pp. 17599–17605.
- Freitag, M., Schmidt, E. 2020. Tests on experimental uncertainties of light gas stratifications and their dissolution by natural convection. Test TH-32 Report No. 1501594–SR–TH-32. 24 p.
- ICANPS. 2012. Final report. Investigation Committee on the Accident at the Fukushima Nuclear Power Stations of Tokyo Electric Power Company. <http://www.cas.go.jp/jp/seisaku/icanps/eng/final-report.html>
- Ilvonen, M. 2022. IAEA CRP J15002: Exercises & Fukushima deposition simulations with VALMA, VTT Research Report VTT-R- 00155-22. 79 p.
- Ilvonen, M. 2023. Parameter sensitivity analysis with the ARANO dose code. VTT Research Report VTT-R- 00074-23. 53 p.
- Kanai, T. 2020/2021. Overview of CRIEPI Test I2 Decontamination. NUGENIA TA2 IPRESCA meeting presentation in 2020/2021.
- Katsumi, T., Aida, T., Aida, K. & Kadowaki, S. 2017. Outward propagation velocity and acceleration characteristics in hydrogen-air deflagration. Int. J. Hydrogen Energy, Volume 42. pp. 7360–7365.
- Kärkelä, T., Korpinen, A. & Gouëllo, M. 2021. Pool Scrubbing of CsI Aerosol. VTT Research Report VTT-R-00175-21. 22 p.

- Kärkelä, T. 2022. Pool Scrubbing of CsI Aerosol and Gaseous I₂. VTT Research Report VTT-R-00164-22. 28 p.
- Kärkelä, T., Korpinen, A. & Pasi, A.E. 2023. Pool Scrubbing of CsI, Te and I₂. VTT Research Report, VTT-R-00087-23. 32 p.
- Laine, J. Puustinen, M., Räsänen, A. & Tanskanen, V. 2010. PPOOLEX experiments on stratification and mixing in the wet well pool. NKS-240. ISBN 978-87-7893-312-6. 25 p. + app. 9 p.
- Ojalehto, S. 2021. Analysis of nodalization effects on thermal stratification of a suppression pool, VTT Research Report VTT-R- 01065-21. 15 p.
- Ojalehto, S. 2022a. CFD modelling of light gas migration in THAI TH-32 experiment, VTT Research Report VTT-R-00188-22. 22 p.
- Ojalehto, S. 2022b. Study of nodalization effects on thermal stratification of Olkiluoto 1 suppression pool. VTT Research Report VTT-R-00772-22. 26 p.
- Poikolainen, J. 2009. Report on the Test of Thermal Stratification in the Condensation Pool. 131562. Teollisuuden Voima Oyj.
- Saito, K., Tanihata, I., Fujiwara, M., Saito, T., Shimoura, S., Otsuka, T., Onda, Y., Hoshi, M., Ikeuchi, Y., Takahashi, F., Kinouchi, N., Saegusa, J., Seki, A., Takemiya, H. & Shibata, T. 2015. Detailed deposition density maps constructed by large-scale soil sampling for gamma-ray emitting radioactive nuclides from the Fukushima Dai-ichi Nuclear Power Plant accident. Journal of Environmental Radioactivity, Volume 139. pp. 308-319.
- Sevón, T. 2022. Analyzing reactor water level measurements in the Fukushima Daiichi 1 accident. Article draft. Submitted for review.
- Taivassalo, V. 2023. Development of the flame wrinkling factor in quiescent hydrogen-air mixtures. Article draft.
- TEPCO. 2015. Estimation of accident progression based on the data measured for Unit-1 and the analyses available to date. https://www.tepcō.co.jp/en/press/corp-com/release/betu15_e/images/150520e0113.pdf
- Terada, H., Nagai, H., Tsuduki, K., Furuno, A., Kadouki, M., & Kakefuda, T. 2020. Refinement of source term and atmospheric dispersion simulations of radionuclides during the Fukushima Daiichi Nuclear Power Station accident. Journal of Environmental Radioactivity, Volume 213.
- Yaguchi, J., Kim, W., Mogi, T. & Dobashi, R. 2021. Flame acceleration and blast wave of H₂-O₂-N₂-Ar mixtures in unconfined areas. Int. J. Hydrogen Energy. Volume 46 pp. 12329-12337.

8.2 Mitigation and analysis of fission products transport (MANTRA)

Teemu Kärkelä¹, Mélany Gouëllo¹, Ilona Lindholm¹, Anna-Elina Pasi¹, Unto Tapper¹, Tuomo Sevon¹, Anna Korpinen¹

¹VTT Technical Research Centre of Finland Ltd
P.O. Box 1000, FI-02044 Espoo

Abstract

The aim in the MANTRA project during 2019-2022 was to investigate the transport and chemistry of gaseous and particulate fission products in severe accident conditions. The main focus was on the behaviour of iodine, caesium and tellurium, which are highly radiotoxic and the mitigation of their possible source term is of utmost importance. It was observed that the fission product deposits on the reactor coolant system (RCS) surfaces act as an important source of gaseous iodine, which can enhance the iodine source term. The tellurium transport was related to the oxidizing or reducing conditions in the RCS. The containment spray system was efficient in removing the airborne tellurium species. The pool scrubbing of fission product aerosols was notable and the decontamination factor increased significantly in the jet regime (high flow rates). Fission product deposits on containment building surfaces may react with the surfaces and form volatile species. Further actions to consider the long-term severe accident management issues were also taken. The follow-up of OECD/NEA STEM-2, BIP-3 and ESTER projects was carried out.

Introduction

In Fukushima Daiichi nuclear plant cooling of the reactor cores at units 1, 2 and 3 was lost due station black out. Since the cooling could not be restored in time, fuel damage took place in all three reactors and fission products were partly released from the core. As expected in a such severe accident, a high contribution to the source term to the environment was from iodine isotopes. In case of the Chernobyl accident, a high release of fission products to the environment took place and fission products (FPs) were spread e.g. across the continent of Europe.

Traditionally, it has been assumed that in a severe accident most iodine would be released from the fuel. Release to the containment would take place mostly as aerosol particles with gaseous fraction of about 5%. Concerning studies on iodine chemistry in the primary circuit, it is typically assumed that caesium iodide is the main iodine compound formed in the reactor coolant system. This assumption leads to a low release of gaseous iodine into the containment, because the current severe accident (SA) integral codes do not take into consideration the effect of FP deposits chemical reactions on the primary circuit surfaces. Also, the previous studies have mainly focused on the reactions taking place in the gas phase [Gouëllo et al., 2013;

Grégoire et al., 2012]. However, the importance of surface reactions as a source of volatile iodine is even increased at the late phase of accident when the thermalhydraulic conditions of the circuit are changing, as it has also been verified in the SAFIR2018 CATFIS and SAFIR2022 MANTRA projects [Gouëllou et al., 2018; Miyahara et al., 2020].

After being released from the reactor core the FPs, including tellurium, are transported to the containment through the reactor coolant system. In the RCS, the FPs released from the core are subjected to the surrounding prevailing conditions (e.g., oxidizing, reducing) and significantly lower temperatures than in the core. The change of conditions enables the FPs to condense and form aerosols of different composition and size. Once the FPs have reached the containment, they are exposed to various removal processes. One of the important safety features is the containment spray system (CSS), which removes especially particulate fission product species from the containment atmosphere and flushes them down to the sump. Although tellurium source term has been relatively well studied in terms of its release behavior from the core, the reactions and behavior of tellurium species following the core release still remain unclear.

Pool scrubbing is an important phenomenon in mitigating the source-term to the environment by retention of fission products passing through water pools of containment building. The majority of the experimental studies related to pool scrubbing have been conducted in 1980s and 1990s in order to establish suitable models for predicting the pool decontamination efficiency under reactor-typical conditions. Results from past research on pool scrubbing showed that both experimental data on fission products retention in water pools as well as related model predictions were affected by large uncertainty bands, which make application to reactor cases questionable. Particularly, the retention of fission products in pools at high temperatures and high gas flow rates through the pool are not well-understood.

Fission products in the containment building atmosphere may eventually deposit on the surrounding surfaces. When these deposits are exposed to elevated temperatures, they pose a potential threat of releasing gaseous species back into the containment atmosphere. This phenomenon could be an important source of volatile radionuclides, especially for delayed releases.

Long-term severe accident management address physical and chemical processes in a severely damaged nuclear power plant after the period of 72 hours or after the plant has reached the safe stable state. The maintenance of safe stable state requires continuous decay heat removal, sub-criticality and prevention of uncontrolled leakages of radioactive material from the containment. The lessons learnt e.g. from the Fukushima accident need to be exploited.

Both OECD/NEA STEM-2 (Source Term Evaluation and Mitigation Issues) and OECD/NEA BIP-3 (Behaviour of Iodine) projects were followed-up and the projects ended in 2019. As a continuation, the follow-up of a new, four-year OECD/NEA ESTER (Experiments on Source Term for Delayed Releases) project started in 2020.

Primary circuit chemistry of iodine and caesium

After fission products have been released from the overheated and molten fuel, they are transported through the reactor coolant system and fission products will reach areas at lower temperature. As a consequence, vapour condensation and particle nucleation processes takes place in the gas flow. If vapour condensation takes place close to the surfaces of primary circuit, a layer of condensate can be formed on it. Particles in the gas flow may also deposit on the circuit surfaces together with control rod and structural materials. The set-up of the EXSI-PC experimental facility used for the studies on iodine and caesium chemistry in the primary circuit conditions is presented in Figure 1. Inactive materials have been used to simulate fission products. The precursor materials were CsI, CsOH, I₂ and H₃BO₃.

For the first set of experiments, I₂ vapour was generated by the sublimation of molecular iodine pellets. The gaseous I₂ passed above an evaporation crucible filled with CsOH aqueous solution and placed inside the furnace.

During the second set of experiments, CsI particles were generated by nebulization of a concentrated caesium iodide aqueous solution and then passed through a Thermal Gradient Tube (TGT). The gaseous H₃BO₃ was generated by vaporisation from a crucible placed inside the furnace.

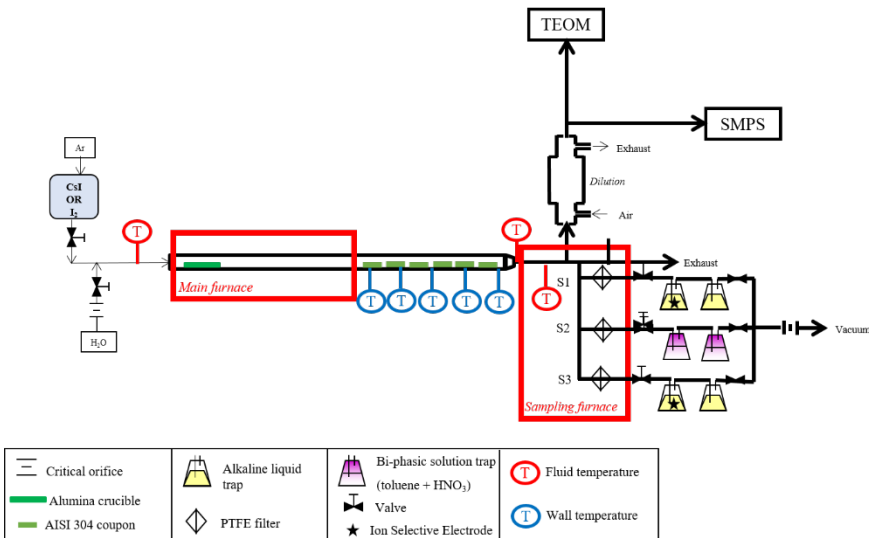


Figure 1. Schematics of the EXSI-PC experimental facility.

The evaporation crucible containing the precursor material was placed in a tube inside the reaction furnace. The furnace tube used in the experiments was made of stainless steel (AISI 304), which was pre-oxidized before the experiment. The furnace was heated to 700 °C. The carrier gas was then fed into the heated furnace, where the source materials reacted with each other, with gas and with the surface

of the crucible. Reaction products were then transported with the gas flow through four sampling lines:

1. The first line was dedicated for aerosol on-line measurement. Upstream from the online aerosol measurement devices, the flow was diluted in order to decrease the concentration of the produced particles low enough for the instrumentation as well to decrease the temperature of the flow below 313 K. The particle number size distributions were measured with a TSI Scanning Mobility Particle Sizer (SMPS), with series 3080 platform, series 3081 Differential Mobility Analyser (DMA) and series 3775 Condensation Particle Counter (CPC). The aerosol mass concentration was monitored by Tapered Element Oscillating Microbalance Series 1400a (TEOM).
2. The second line was used to sample particles and gaseous species. The line was equipped with a polytetrafluoroethylene (PTFE) membrane filter (hydrophobic, poral grade 5.0 µm, 47 mm, Mitex®) and two liquid traps assembled in series. They were filled with a solution of 0.1 M sodium hydroxide (NaOH) in water (150 ml). During the test, the first liquid trap was equipped with the Ion Selective Electrode (ISE) in order to monitor on-line the concentration of iodine. After the test, the solutions and the leachants from filters (50 ml) were analysed by Inductively Coupled Plasma Mass Spectrometry (ICP-MS). The analyses were performed with a Thermo Fisher Scientific HR-ICP-MS Element2 apparatus. This line was used for the first 20-minute sampling (S1).
3. The third line was used with a similar configuration as the second line, except the nature of the liquid traps. The liquid traps were filled with an immiscible solution composed of aqueous phase (nitric acid, pH=3; 50 ml) and an organic phase (toluene; 100 ml) in order to selectively separate hydrogen iodide (HI) from molecular iodine (I₂). Due to its non-polarity, molecular iodine is expected to be trapped in the organic phase while hydrogen iodide would stay in the aqueous phase. This line was used for the second 20-minute sampling (S2). The quantification of molecular iodine in toluene was carried out by UV-visible spectroscopy using a Perkin Elmer spectrophotometer model Lambda 900.
4. The last line had the same configuration as the second line. This line was used for the third 20-minute sampling (S3).

Table 1 describes the test matrix and conditions.

Table 1. Experiments conducted on primary circuit chemistry of iodine and caesium.

Exp.	Precursor	Carrier gas composition	Other
MANTRA-1	I ₂	Ar/H ₂ O (86.7/13.3 vol-%)	Reference experiment for I ₂ behaviour
MANTRA-2	CsOH	Ar/H ₂ O (86.7/13.3 vol-%)	Reference experiment for CsOH behaviour
MANTRA-3	I ₂	Ar/H ₂ O (86.7/13.3 vol-%)	
	CsOH		
MANTRA-3bis	I ₂	Ar/H ₂ O (86.7/13.3 vol-%)	
	CsOH		

Exp.	Precursor	Carrier gas composition	Other
MANTRA-4	I ₂	Ar/H ₂ O (86.7/13.3 vol-%)	
	CsOH		
MANTRA-5	CsI particles	Ar/H ₂ O (86.7/13.3 vol-%)	Deposition phase (i.e. "phase 1")
MANTRA-6	H ₃ BO ₃ gas	Ar/H ₂ (95/5 vol-%)	Blank behaviour
MANTRA-7	CsI particles	Ar/H ₂ O (86.7/13.3 vol-%)	Deposition phase (i.e. "phase 1")
MANTRA-7_Re	Deposited CsI	Ar/H ₂ (95/5 vol-%)	Reaction/vaporisation phase (i.e. "phase 2")
MANTRA-8	CsI particles	Ar/H ₂ O (86.7/13.3 vol-%)	Deposition phase (i.e. "phase 1")
MANTRA-8_Re	Deposited CsI + H ₃ BO ₃ gas	Ar/H ₂ (95/5 vol-%)	Reaction/vaporisation phase (i.e. "phase 2")

The first set of experiments with I₂ and CsOH confirmed the formation of CsI particles [Gouëllo, 2019]. From the second set of experiments, it was highlighted that the deposited CsI particles were subjected to revaporation process in Ar/H₂ atmosphere; gaseous iodine was released from the deposits. When H₃BO₃(g) was present in the carrier gas (Ar/H₂), the percentage of gaseous iodine released was higher, see Figure 2. The interpretation of the SMPS and TEOM results [Gouëllo, 2021] also suggested that the presence of H₃BO₃(g) would then have an influence on the transport of the deposited/condensed CsI as it showed different behaviour than during revaporation/resuspension under Ar/H₂.

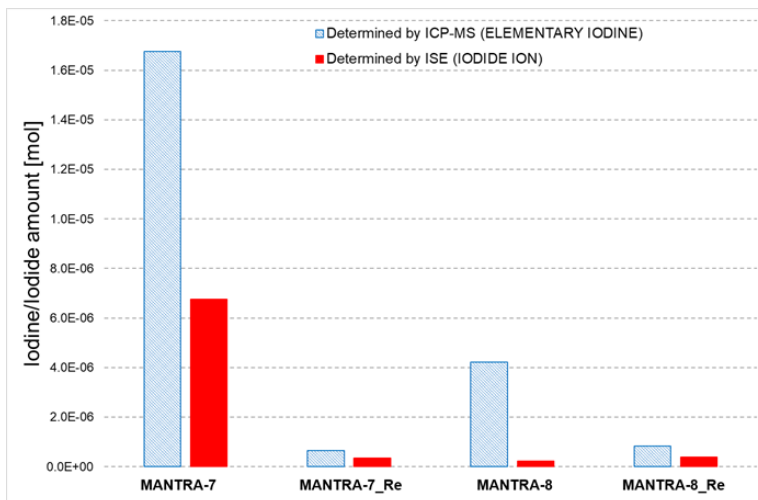


Figure 2. Amount of gaseous iodine transported during the second set of experiments [Gouëllo, 2021].

In parallel to the experimental work, analytical work was initiated in 2019. It consisted in validating the models implemented in the SOPHAEROS module (version v2.1.1.6) of the Accident Source Term Evaluation Code (ASTEC) [Cousin et al., 2008] on the basis of a comparison with the obtained experimental results. As a first step, comparison was made with the experimental data of several experiments performed previously under Ar/H₂O atmosphere [Gouëllo, 2021]. The analytical work has highlighted good agreement on the behaviour of compounds between SOPHAEROS models and the experimental results obtained for pure compounds (I₂, CsI). However, it has shown discrepancies when another compound was considered in the chemical system. Especially looking at the release of gaseous iodine, the amount of gaseous iodine was systematically underestimated, see Figure 3. This stresses the need to take into account condensed-phase reactions in the SOPHAEROS code in future.

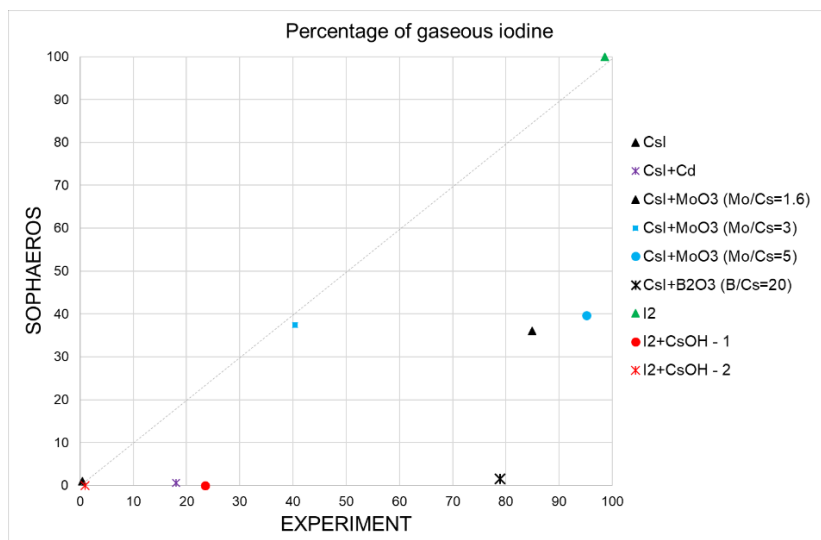


Figure 3. Comparison of the ASTEC/SOPHAEROS V2.1.1.6 results to the experimental values for the percentage of gaseous iodine [Gouëllo, 2021].

Tellurium transport in the RCS and mitigation by the containment spray system

The radiotoxic tellurium has two main features, which emphasize its safety importance: 1) tellurium is highly volatile and 2) the decay products consist of iodine. As the behaviour of tellurium after being released from fuel is not fully understood, a study to improve the knowledge was initiated. These experiments covering the transport of tellurium in the RCS and the mitigation of airborne tellurium species using a containment spray system were conducted using the experimental facilities

of VTT in collaboration between VTT, Chalmers University of Technology and Oslo University as part of NKS-R activity.

The transport of tellurium in primary circuit conditions was investigated [Espegren et al., 2020]. Metallic tellurium precursor was exposed to oxidizing and reducing conditions at ca. 1200 °C. The release and transport of gaseous and aerosol species was examined. As an example, a micrograph of the formed tellurium containing aerosol is shown in Figure 4.

The metallic tellurium precursor was released and transported with a rather constant rate in a dry or humid nitrogen atmosphere. In case of an air atmosphere, the transport of tellurium was notably higher at first. However, the metallic tellurium seemed to be oxidised by the oxygen in the course experiments. It led to a reduction of tellurium release. The fraction of tellurium transported through the model primary circuit (in comparison to the release) was the highest in the air atmosphere, see Figure 5.

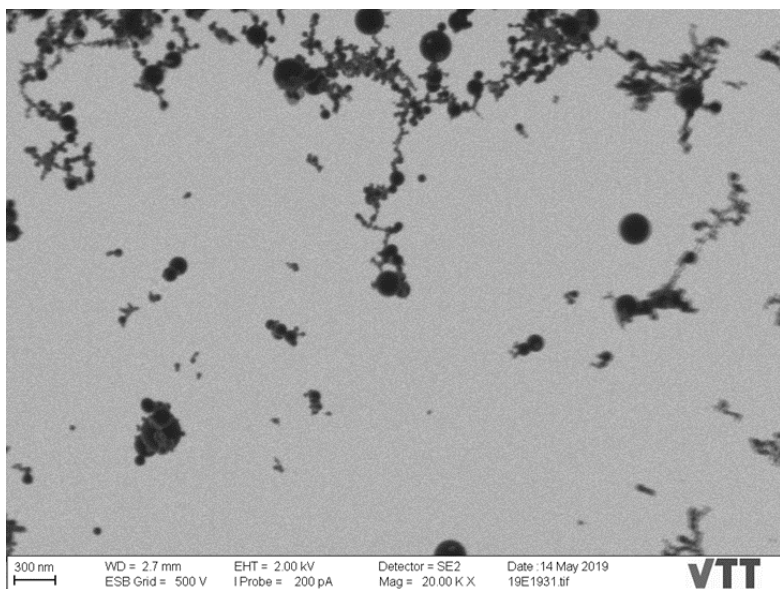


Figure 4. Micrograph of tellurium containing aerosol – precursor Te vaporized in a dry air atmosphere at ca. 1200 °C. A significant fraction of the analyzed particles were long agglomerate chains composed of primary particles with a diameter of less than 100 nm.

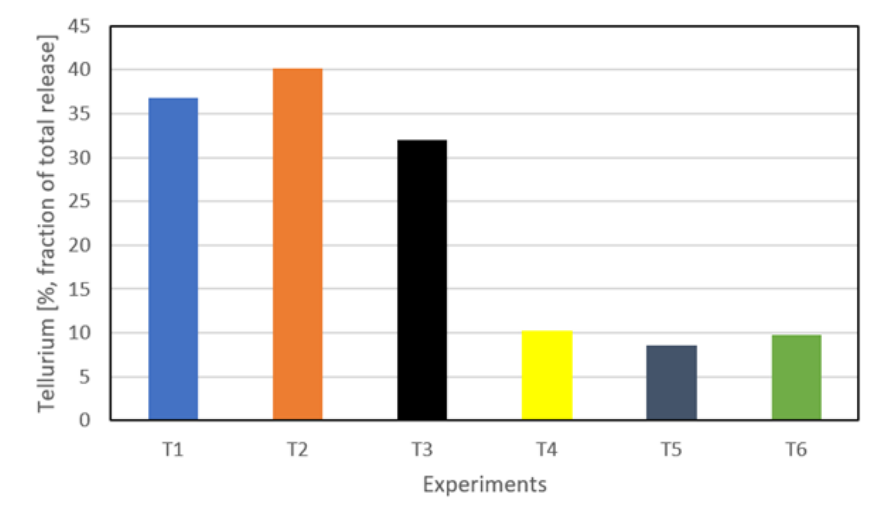


Figure 5. Fraction of tellurium transported through the model primary circuit (in comparison to the release) was higher in the air atmosphere (Experiments T1 to T3) than in the nitrogen atmosphere (Experiments T4 to T6). The temperature of the circuit decreased from ca. 1200 °C to 30 °C in the experiments.

The retention of tellurium aerosols (Te , TeO_2) by a containment spray system model was also examined [Kärkelä et al., 2020]. Tellurium dioxide and metallic tellurium precursors were exposed to oxidizing and reducing conditions. The chemistry of spray droplets was varied from water to alkaline borate solutions. The removal efficiency was derived.

The water droplets were efficient in trapping the airborne particles. Further increase in the trapping efficiency was observed when the chemistry of droplets was varied, see Figure 6. The removal efficiency was high for TeO_2 and Te in an air atmosphere, but the removal efficiency for metallic tellurium decreased in a nitrogen atmosphere.

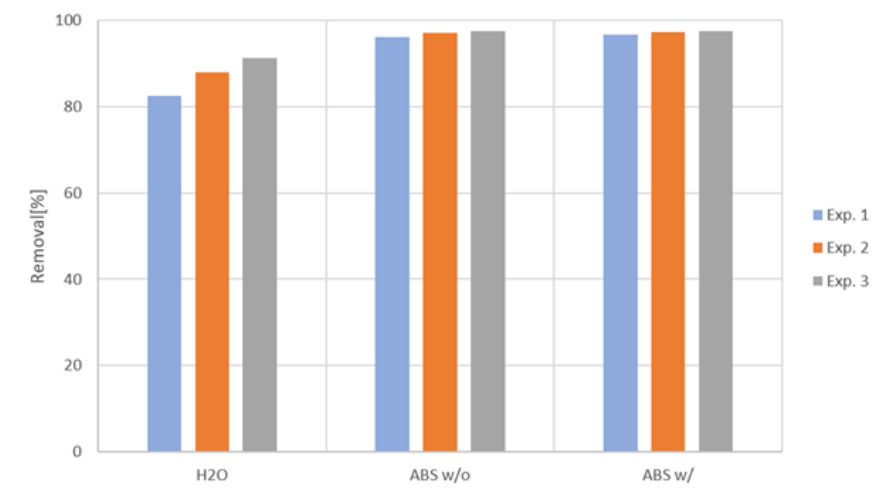


Figure 6. Removal efficiency of a containment spray system model for tellurium dioxide particles in an air atmosphere. The water droplets were efficient in trapping the airborne particles. Further increase in the trapping efficiency was observed when the chemistry of droplets was varied using alkaline borate solutions.

Pool scrubbing of CsI aerosol

The water pools of containment building may act as important sinks for the fission products by trapping the radiotoxic species from the gas flow directed into the pool. However, most of the existing information on this phenomenon is based on the data of experiments performed at low temperatures and low flow rates into the pool. Therefore, the current models for this phenomenon in the severe accident analysis codes are also lacking of data and thus, the models are not able to simulate the pool scrubbing in detail.

As part of MANTRA, several series of experiments have been performed using CsI, I₂ and CH₃I as precursors [Kärkelä et al., 2020; Kärkelä et al., 2021; Kärkelä et al., 2023]. The pool temperature has ranged from low pool temperatures up to 70 °C. The gas flow rate into the pool has been varied from the low (globular regime) to high (jet regime) flow rates. The pool depth has ranged from 10 cm to 70 cm. The performed experiments have been simulated using the ASTEC code in the SAFIR2022 ANSA project.

For the CsI aerosol experiments in 2019-2020, the obtained decontamination factor was in a range from 2 to 4 in the globular regime and it increased up to ca. 12 in the jet regime (at the studied conditions), see Figure 7.

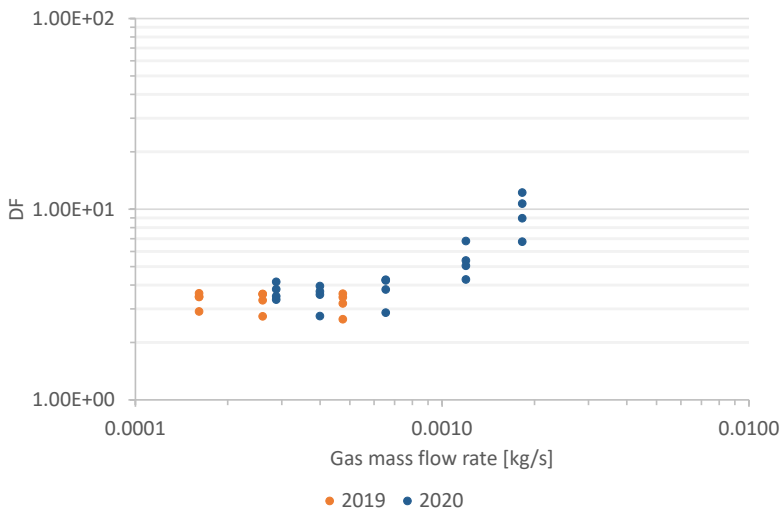


Figure 7. Decontamination factor results for CsI aerosol (VTT studies in 2019 and 2020). The decontamination factor (DF) results are given as a function of gas mass flow rate into the pool (jet regime > 0.001 kg/s).

In 2021–2022, the effect CsI particle diameter on the decontamination factor was examined. The decontamination factor for supermicron particles was notably higher in comparison to submicron particles, especially in the jet regime flow range, see Figure 8.

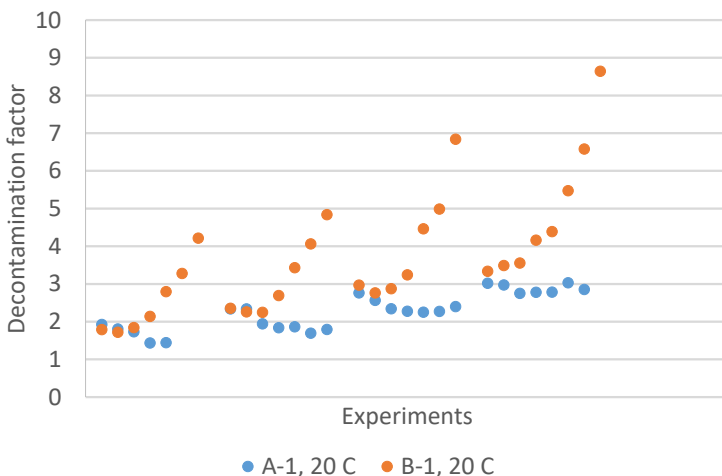


Figure 8. Decontamination factor results for CsI aerosol (VTT studies in 2021 and 2022), A-1 submicron particles and B-1 supermicron particles. The decontamination factor (DF) results are given as a function of gas flow rate into the pool and increasing pool depth.

Related to the NUGENIA TA2.4 area IPRESCA project dedicated to (gaseous and aerosol FP) pool scrubbing research, MANTRA is coordinating a task on gaseous iodine retention in the pool. The project includes over 30 international organizations around the world. A summary of IPRESCA activities and results on both gaseous and aerosol fission products pool scrubbing and pool hydrodynamics research topics was prepared [Gupta et al., 2023].

Fission product chemistry on containment surfaces

A literature review about the composition and main qualifications of the surface materials of nuclear power plant containments was carried out. The study addressed cable materials, paint coatings, catalyst plates of hydrogen recombiners, thermal insulation material, and additives for water pool pH control. Additionally, concrete material was of interest due to release of non-radioactive species during core melt – concrete interaction [Lindholm, 2022].

Cs, I and Te chemistry on the containment surface materials (304L, 316L, Pt, Zn) was investigated experimentally [Kärkelä, 2023]. The reactions were studied in a temperature range from 20 to 900 °C. The results indicated the existence of solid CsI and Te and a formation of Cs_xTe and TeO_x on the surface samples in a dry air atmosphere. I₂ was also observed as a solid residue on the samples. It indicated the release of gaseous iodine from the deposits at elevated temperatures.

Long-term severe accident management

In the long-term severe accident management study during 2019, the key outcomes and recommendations of OECD/NEA, IAEA, US DOE and EU SARNET working groups or projects was reviewed and a limited scope overview of recent Fukushima-related journal articles from the past three years for the background information was summarized. To recognize useful and sustainable research topics close discussions with all Finnish utilities and STUK were carried out. The long-term accident management research topics that are interesting for the Finnish NPPs were identified and listed. The behaviour of caesium was emphasized.

In 2020, the goal was to investigate (based on the published literature during 2010's) what is the chemical form and morphology of caesium contamination after a severe accident [Lindholm, 2020]. The post-accident investigations at and around the Fukushima plant site provide a broad scope of information. Where applicable, the observations and outcomes obtained from Fukushima were compared with the Chernobyl accident data. In addition to characterization of contamination, the study addressed the latest developments in the clean-up methods of caesium contamination. The study also supports thinking of aspects related to long-term severe accident management.

The follow-up of OECD/NEA STEM-2, BIP-3, ESTER projects

The follow-up of both four-year OECD/NEA STEM-2 and three-year BIP-3 projects [OECD, 2017] continued until 2019. The OECD/NEA STEM-2 project composed of two experimental main topics: ruthenium transport in primary circuit conditions and behaviour of particulate iodine on containment surfaces. The OECD/NEA BIP-3 project focused especially on the adsorption and desorption phenomena of gaseous inorganic and organic iodine on the painted containment surfaces. The four-year OECD/NEA ESTER project follow-up started in 2020 [OECD, 2021]. The objective is on the delayed releases due to chemical remobilisation from high temperature (reactor coolant system) fission product deposits. Another objective in the ESTER project is to study the iodine reactivity (I_2 and IO_x) with organic compounds, which may be present in the containment atmosphere. The aim is to assess the source of organic iodine formation, other than iodine-paint interaction.

Another important part of the ESTER project is to compare the performance of various severe accident analysis codes and the user effect. The ESTER analytical working group organised a sensitivity study to analyse iodine revolatilization and the effect of the delayed release to the potential source term. The sensitivity study included three cases. The first was the base case with no delayed release. The second was the slow-release case with 0.133 kg of released I_2 during seven days and the third was the fast-release case with a total of 1.33 kg of released I_2 . The containment geometry was similar to a French PWR. This study was participated using ASTEC/SOPHAEROS code [Korpinen, 2023].

References

- Cousin, F., Dieschbourg, K., Jacq, F., 2008. New Capabilities of Simulating Fission Product Transport in Circuits With ASTEC/SOPHAEROS v. 1.3. Nucl. Eng. Des. 238, 2430–2438.
<https://doi.org/https://doi.org/10.1016/j.nucengdes.2008.03.018>
- Espegren, F., Kärkelä, T., Pasi, A.-E., Tapper, U., Kučera, J., Lerum, H.V., Omtvedt, J.P., Ekberg, C., 2020. Tellurium transport in the RCS under conditions relevant for severe nuclear accidents, Progress in Nuclear Energy, Vol. 139, 103815.
- Gouëllo, M., Mutelle, H., Cousin, F., Sobanska, S., Blanquet, E., 2013. Analysis of the iodine gas phase produced by interaction of CsI and MoO_3 vapours in flowing steam, Nuclear Engineering and Design 263, 462-472.
- Gouëllo, M., Hokkinen, J., Kärkelä, T., Auvinen, A., 2018. A Scoping Study of Chemical Behaviour of Caesium Iodide in Presence of Boron in Condensed Phase (650 °C and 400 °C) under Primary Circuit Conditions. Nucl. Technol. 203, 66–84.
<https://doi.org/https://doi.org/10.1080/00295450.2018.1429111>
- Gouëllo, M., 2019. Experiments and ASTEC Analyses on Iodine and Caesium Chemistry Report VTT-R-01244-19. Espoo, Finland.

- Gouëllo, M., 2021. Progress report of the Experiments and ASTEC Analysis on Iodine and Caesium Chemistry Report VTT-R-00042-21. Espoo, Finland.
- Grégoire, A.-C., Mutelle, H., 2012. Experimental study of the [Mo, Cs, I, O, H] and [B, Cs, I, O, H] systems in the primary circuit of a PWR in conditions representative of a severe accident, In the proceedings of NENE2012 conference, Ljubljana, Slovenia.
- Gupta, S., Herranz, L.E., Lebel, L.S., Sonnenkalb, M., Pellegrini, M., Marchetto, C., Maruyama, Y., Dehbi, A., Suckow, D., Kärkelä, T., 2023. Integration of pool scrubbing research to enhance source-term calculations (IPRESCA) project – Overview and first results, Nuclear Engineering and Design, 404, 112189.
- Korpinen, A., 2023. Sensitivity study for I₂ revolatilization in OECD/NEA ESTER project, VTT-R-00104-23. 17 p.
- Kärkelä, T., Pasi, A.-E., Espegren, F., Sevón, T., Tapper, U., Ekberg, C., 2020. Tellurium retention by containment spray system, Annals of Nuclear Energy, Vol. 164, 108622.
- Kärkelä, T., Korpinen, A. & Gouëllo, M., 2020. Pool Scrubbing of Gaseous and Particulate Iodine. Espoo: VTT. VTT Research Report VTT-R-00201-20. 34 p.
- Kärkelä, T., Korpinen, A. & Gouëllo, M., 2021. Pool Scrubbing of CsI Aerosol. Espoo: VTT. VTT Research Report VTT-R-00175-21. 22 p.
- Kärkelä, T., Korpinen, A., Pasi, A.-E., 2023. Pool scrubbing of CsI, Te and I₂, VTT-R-00087-23. 32 p.
- Kärkelä, T., Cs, I and Te chemistry on containment surfaces, 2023. VTT-R-00001-23. 20 p.
- Lindholm, I., 2020. Literature survey on radiocesium source term in severe accidents - chemistry, morphology and clean-up, VTT-R-01248-20. 53 p.
- Lindholm, I., 2022. Cables, paints, catalyst plates, and other surface materials in nuclear containment, VTT-CR-00684-22. 23 p.
- Miyahara, N., Miwa, S., Gouëllo, M., Imoto, J., Horiguchi, N., Sato, I., Osaka, M., 2020. Experimental Study on Transport Behavior of Cesium Iodide in the Reactor Coolant System under LWR Severe Accident Conditions [WWW Document]. J. Nucl. Sci. Technol. [https://doi.org/https://doi.org/10.1080/00223131.2020.1782281](https://doi.org/10.1080/00223131.2020.1782281)
- OECD, 2017: https://www.oecd-nea.org/jcms/pl_32256/nea-joint-projects
- OECD, 2021: https://www.oecd-nea.org/jcms/pl_46387/new-joint-project-experiments-on-source-term-for-delayed-releases-ester

9 Research Infrastructure

9.1 Barsebäck reactor pressure vessel material used for true evaluation of embrittlement (BRUTE)

Sebastian Lindqvist, Noora Hytönen, Jari Lydman, Laura Sirkia, Jussi Loporanta, Jarmo Saarinen, Mika Jokipii, Johanna Lukin, Siddharth Suman, Alex Norrgård, Pentti Arffman

VTT Technical Research Centre of Finland Ltd
P.O. Box 1000, FI-02044 Espoo

Abstract

The objective of BRUTE is twofold; 1) to perform mechanical and microstructural investigations of Barsebäck 2 (B2) BWR reactor pressure vessel (RPV) welds and surveillance weld, enabling validation of embrittlement predictions based on the RPV surveillance programme 2) to pioneer the new infrastructure in the Centre for Nuclear Safety, CNS, VTT. The B2 plant was operated for 27 years.

During the project, the new CNS infrastructure key-processes were accredited, round robin investigations were performed, the personal got experience with standardized testing of irradiated materials, specimen preparation inside hot-cells and the whole material flow, best practice guidance was established, and tools to ease specimen handling were prepared.

The results confirm that the surveillance results describe the mechanical behavior of the reactor pressure vessel. There are no significant changes in mechanical properties after 27 years of operation. The axial beltline weld has higher toughness and lower strength than the other investigated welds which is possibly caused by variations in thermal histories.

Introduction

Ensuring safe operation and the durability of the reactor pressure vessel (RPV) is one of the most important tasks for nuclear power plants (NPP's). The RPV is not

regarded as a replaceable component, which thus means that condition of the RPV must be known to ensure for safe nuclear power production. The most pronounced ageing mechanism of the RPV and especially of the weld in the beltline region is radiation-induced embrittlement, which cause an increase in the ductile to brittle transition temperature (DBTT). The DBTT must have a safety margin in respect to the lowest possible temperature in the RPV in connection, e.g., to an emergency cooling scenario, as brittle fracture of the RPV would create loss of one of the defence levels and intense pressure release. The embrittlement is monitored through a surveillance program, in which mechanical test specimens are placed in the reactor at a position with normally a higher dose rate, i.e., with a lead factor, than the pressure vessel. A prognosis of the RPV behaviour is made based on the mechanical test results obtained from these specimens, and this is used in the safety assessment to ensure safe NPP operation.

A unique opportunity to determine the mechanical and microstructural characteristics of material removed from a decommissioned RPV (Barsebäck 2, Sweden), and compare them with material from the surveillance program opened with the BREDA (Barsebäck REsearch&Development Arena) project. This opportunity to make a comparison between material from a real component and material used for lifetime assessment will give unique results on how well these two correlate, which is the basis for the lifetime assessment. Verification of this correlation is extremely important for the overall safety assessment of NPPs. By testing material from different depths of the RPV wall, with different dose, data will be produced to answer e.g. the question on how the mechanical properties correlate throughout the RPV wall, and what the effect of dose attenuation (reduction) is. The dose of the pressure vessel is typical for BWR's, which is much lower than that for PWR's, but also surveillance material with a dose in the PWR-typical region is included in the material selection.



Figure 1. Barsebäck 2 reactor pressure vessel.

Besides irradiation embrittlement, thermal ageing of low alloy steels and their welds has been a matter of debate. It has been shown to be a parameter of importance for Russian VVER-1000 RPV materials with a high Ni/Mn-content, but mostly been evaluated to be of minor importance compared to radiation embrittlement in most other materials. However, recent results from plant components in Sweden has shown, that thermal embrittlement can be significant during NPP operation, at least at pressurised temperatures, which are higher than the RPV temperature. The B2 trepans from the RPV head area opens the possibility to explore the effect of thermal ageing.

The mechanical and microstructural characterisation work needed to answer these questions is performed in the SAFIR2022 BRUTE project, which is collaborating with the Swedish BREDA project, giving a very large in-kind contribution to the BRUTE project. The BREDA project in Sweden has planned, executed and funded the cutting of the trepans, and is a prerequisite for the BRUTE project.

The BRUTE project will pioneer the use of the new infrastructure in the VTT CNS, which was constructed and licensed for operation during the 2013–2018 period. In addition to being a project with high scientific goals, the BRUTE project has also been a project enabling development of the handling processes and tools for executing this type of research. Supporting the infrastructure in this way is important for the execution of future nuclear safety research activities, for knowledge build-up in a new environment and for production of high-quality data. That this opportunity

is unique and important to grasp has also been emphasised in the letter of support on research of B2 materials, written by MEAE in March 2018.

The weld metal in the B2 RPV is relevant for the Finnish NPP's, as it is the same, high Ni/Mn-material as used in Ol1 and Ol2 BWR's. The objective of the BRUTE project is also to increase the amount of mechanical data, which is used to further develop prediction models, on the correlation between different mechanical test types, on the thermal ageing of RPV weld metal, on prediction models for DBTT shift due to irradiation and on the correlation between microstructural features and mechanical behaviour.

In addition to the high scientific and safety aspects of the BRUTE project, the project also creates a superb opportunity for knowledge transfer from experienced persons to the young generation, a topic which is very timely, and for taking the new infrastructure of the CNS into active use. The tight co-operation between Finland and Sweden through the two projects BRUTE and BREDA, facilitates co-operation between licensees, authorities, researchers as well as doctoral students in these two Nordic countries. The work is performed in tight co-operation between Nordic NPP utilities (BWR and PWR), safety authorities, research organisations and stakeholders (Energiforsk, NKS), and a Nordic knowledge cluster on RPV embrittlement issues is formed, and new experts are brought up. This is important also because Finland and Sweden may soon be the only countries with operating BWRs in Europe, as most countries are closing their BWRs.

Eight trepans with a diameter of 200 mm and full RPV wall thickness (~130–160 mm) was cut from the B2 RPV, from both the beltline welds, subjected to thermal load and neutron irradiation during 27 year of operation at 288 °C, as well as from the vessel head, subjected only to thermal load. Materials from surveillance programmes and from accelerated irradiation to mimic about 200 years of operation are also available as well as data from earlier test campaigns. This makes the material selection unique. Pioneering the new CNS hot cell infrastructure will fully commission the new infrastructure, prove the functionality of the equipment in normal project work, confirm the quality of the results in routine testing situations and give a valuable reference for future assignments.

Trepan transportations

Four trepans from the reactor pressure vessel head (RPVH) were delivered to VTT CNS in March 2019 and four from the beltline area in February 2020. The main investigations focused on trepan 3, 8 and 6. The RPVH trepan 3 is from weld W28, which is made from high Ni/Mn weld metal. The same filler material is used for the beltline welds and additionally for all other RPVs manufactured by Uddcomb, i.e., the welds in most Nordic NPPs. The chemical composition, determined in the BRUTE2019 is seen in Table 1.

Table 1. Average chemical composition of the submerged arc weld (SAW) of the B2 RPVH.

	C	Si	Mn	S	P	Cr	Ni	Mo	Cu	Al	W	V	Ti	Co	B	Fe
SAW	0.057	0.15	1.43	0.007	0.008	0.03	1.48	0.41	0.06	0.024	<0.01	0.006	0.003	0.020	0.0003	bal.

This section summarizes information about the trepans (see Figure 3) removed from the Barsebäck 2 reactor pressure vessel beltline area and head. Related to beltline weld trepans, two of the trepans were cut from the circumferential weld W16, and two from the axial weld W14. They have a diameter of about 197 mm and a thickness of about 121–124 mm. The weight is about 27–28 kg. The stainless-steel cladding (approx. 10 mm) on the inner surface of the RPV has been removed at Ringhals before delivery of the trepans to VTT, same was done for the RPVH trepans. Table 2 summarizes the properties of the Trepan 3, 6 and 8 investigated in more detail. (Ehrnstén & Lydman, 2019, 2020)

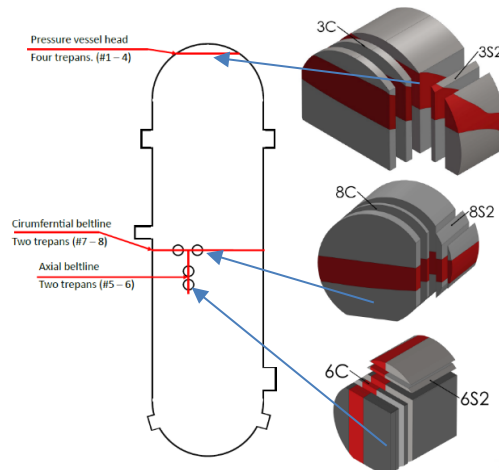


Figure 2. Trepan extraction locations from Barsebäck 2 RPV. Red regions illustrate the weld seam in the trepan.

Table 2. Trepan specifications

Weld	Trepan	Trepan thickness	Weld ID	Weight before cladding removal	Weight after cladding removal	Trepan original thickness	Removed thickness
Axial	T6	122	W14	30,7	27,5	136	14
Circumferential	T8	121	W16	31	27,5	136	15
RPVH	T3	73	W28	21			

The beltline trepans have experienced different doses during operation due to their different location in the RPV. The total reported activity of the trepans is between 24.5 and 40.8 MBq, and the surface dose rates at 10 cm distance from the inner surface, measured at VTT, is 7 - 320 μ Sv/h, see Table 3. The X-weld in the trepans is perpendicular to the inner and outer surfaces of the trepans. The width of the weld is between 37 and 44 mm on the inner surfaces and between 30 and 37 mm on the outer surfaces of the trepans.

At arrival the dimensions of the weld were measured and were used for preparation of cutting plans. The trepans were removed one by one from their aluminium boxes, and put on a table behind a local shield. Lifting was performed using a magnetic lifter, which had been shielded with plastic to restrict contamination of the contact surface. The dose rate of each trepan was measured from the inner and outer surfaces at the location of the weld using a Canberra Colibri VLD survey meter. The meter was attached to a bar such that the distance from the end to the measuring surface of the meter was 10 cm. The samples were remotely handled. The markings on the trepans were recorded, and those markings, which had been made using a pen, were copied to the surface in question using a vibration pen. The trepans were documented using photography. The welds were clearly visible on the surfaces with a bare eye, and thus etching was not needed, as was done with the trepans from the RPVH area. The dimensions of the trepans and the weld on the inner and outer surfaces were measured using a calliper and a ruler. The ruler was used for the larger distances, e.g. the main dimensions of the trepans and the calliper for smaller measures, e.g. the width of the weld, and the distance of the weld fusion line to the edge of the trepan. The trepans were given the numbers 5-8, instead of 1-4, as marked on the trepans, as the numbers 1-4 has been used to identify the trepans from the RPVH. (Ehrnstén & Lydman, 2019, 2020)



Figure 3. Trepan sample cut from the RPV.

The measurements showed a clear difference between the two trepans from the axial trepans, with the dose rate at 10 cm distance being 1.3 and 1.5 times higher on the inner and outer surfaces in trepan 6 compared to trepan #5, respectively. When comparing the trepans from the two different welds, the measurement show that the dose rate at 10 cm distance on the outer surfaces of the trepans is about 3-5 times higher in the trepans from the axial weld compared to those from the circumferential weld. The corresponding numbers for the dose rate ratios on the inner surface at 10 cm distance is 22-46.

The dose rate on the inner surface of the two trepans from the circumferential weld is lower than on the outer surface, which at first glance is surprising, but is most probably a result of neutron reflection from the containment, shielding effects from the internals or differences in the chemical composition. The observed differences puts even more emphasis on the hardness profiles for all trepans, as this technique is one tool verify the reasons for the observed differences. Fluence calculations and measurements are also very important to enable a correlation between mechanical properties and dose.

Table 3. Summary of activities and dose rates.

Trepan No VTT	Ringhals measurements			CNS measurements			
	Activity MBq	Dose rate at surface, mSv/h	Dose rate at 1m mSv/h	Dose rate Inner surface at 10cm, μSv/h	Dose rate Outer surface at 10cm, μSv/h	Calculated dose rate at 1 m μSv/h Inner /Outer	Calculated dose rate at 1 mm μSv/h Inner /Outer
5 (axial W14)	32.5	1.40	0.030	215	62	0.21 / 0.06	21.5 / 0.6
6 (axial W14)	40.8	2.20	0.045	320	82	0.32 / 0.08	32 / 0.8
7 (circ. W16)	24.5	0.12	0.015	7	17	0.01 / 0.02	0.7 / 1.7
8 (circ. W16)	29.5	0.14	0.030	10	21	0.01 / 0.02	1 / 2.1

Cutting and specimen preparation

Beltline weld trepan 6, the axial weld, identified also as W14, is located closest to the maximum dose region. The fluence at the outer surface before removal of cladding is 7.9×10^{17} n/cm² ($E > 1$ MeV). The total trepan length is 136 mm. After removal of cladding, the length is 122 mm. Cladding thickness is estimated to be 10 mm, so some weld is also removed. For Trepan 8, the circumferential weld, identified also as W16, the fluence is 2.9×10^{16} n/cm² ($E > 1$ MeV) at the outer surface. Trepan 8 is of the same size as trepan 6.

The trepans were cut into slices and from the slice close to the $\frac{1}{4}$ thickness location, mechanical test specimens were extracted, tensile, impact and fracture toughness specimens, see Figure 4. Table 4 specifies the mechanical test carried out during the project.

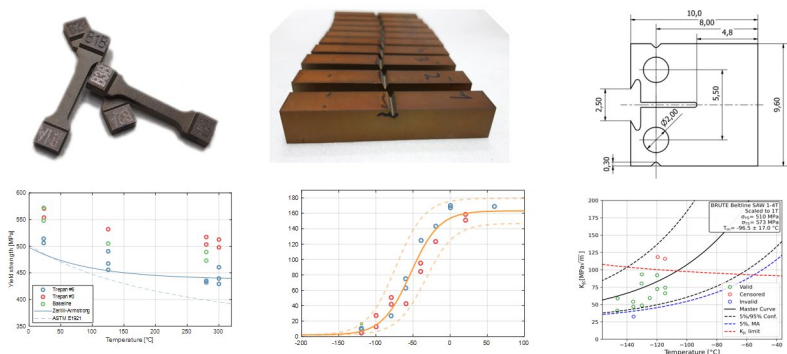


Figure 4. Mechanical testing with three methods.

Table 4. Mechanical test matrix carried out during the project.

Specimens	Material	Depth	Orientation	Number of specimens
CVN	RPV head weld trepan #2	1/4 Thickness	T-S	7
C(T)	RPV head weld trepan #3	1/4 Thickness	T-S	15–20
CVN	RPV head weld trepan #3	1/4 Thickness	T-S	15–20
Tensile	RPV head weld trepan #3	1/4 Thickness	T	15–20
Metallography sample	RPV head weld trepan #3	Through thickness		1
C(T)	Beltline weld trepan #6	1/4 Thickness	T-S	15–20
CVN	Beltline weld trepan #6	1/4 Thickness	T-S	15–20
Tensile	Beltline weld trepan #6	1/4 Thickness	T	15–20
Metallography sample	Beltline weld trepan #6	Through thickness		1
C(T)	Beltline weld trepan #8	1/4 Thickness	T-S	15–20
CVN	Beltline weld trepan #8	1/4 Thickness	T-S	15–20
Tensile	Beltline weld trepan #8	1/4 Thickness	T	15–20

Specimens	Material	Depth	Orientation	Number of specimens
Metallography sample	Beltline weld trepan #8	Through thickness		1
C(T)	Surveillance chain G		T-S	15
C(T)	Surveillance chain C		T-S	15

Before the cutting was started, the cutting procedures used in the BRUTE project were evaluated using a mock-up made from steel with similar dimensions as the trepans. The accuracy and quality of EDM cutting was verified and the results fulfil the set requirements for slice cutting and specimen cutting. The accuracy and quality of the milling machine for preparation of loading holes in 4mm thick C(T) specimens was evaluated using the same mock-up material. Satisfactory results can be achieved with a combination of boring using the milling machine and EDM-finishing. Cutting drawings were prepared and used for cutting of specimens for metallographic investigations, impact testing, tensile testing and fracture toughness testing. Cutting was successful, further proving that the selected methods results in high-quality specimens. (Ehrnstén, Tähtinen, et al., 2020)



Figure 5. Picture of cutting the trepan into slices using an EDM saw.

As stated earlier, the four beltline trepans are from two different welds, i.e., two are from the axial weld W14 (trepans 5 and 6), and two from the circumferential weld W16 (trepans 7 and 8). They have a diameter of about 197 mm and a thickness of about 121–124 mm. The weight is about 27–28 kg. The stainless steel cladding on the inner surface of the RPV has been removed at Ringhals before delivery of the

trepans to VTT. Investigations was decided to start on the trepan with the highest activity, i.e., trepan 6 from the axial weld W14. The preparation of cutting plans, and the performed cutting in 2020 is reported in this report, to be updated when further cutting is performed. (Ehrnstedt, Arffman, & Loporanta, 2020; Pentti Arffman & Loporanta, 2022)

Cutting of trepan 6 from the B2 RPV beltline area in 2020 consisted of major cuts to make the trepan smaller, and continued with cutting slices for preparation of mechanical tests specimens for tensile and impact toughness specimens Figure 6 and Figure 7). Cutting of specimens for microstructural characterization of the weld metal was also performed. Specimens were further cut from one of the two base materials for fluence measurements. In total 54 specimens were cut from trepan 6 in 2020. (Ehrnstedt, Arffman, & Loporanta, 2020; Pentti Arffman & Loporanta, 2022)

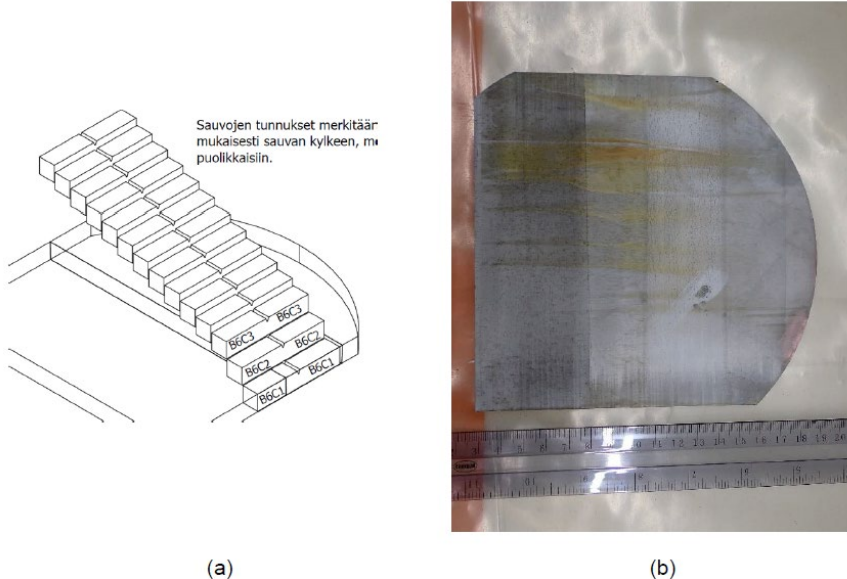


Figure 6. Sliced cut in order to retrieve specimens from different depths, starting with 1/4T depth. To minimize the contamination of the EDM water circulation system, which was simultaneously under further development by a subcontractor, only one slice was cut, i.e., slice 6C. The remain can be cut later into slices 6A and 6B as well as slices 6D-K.

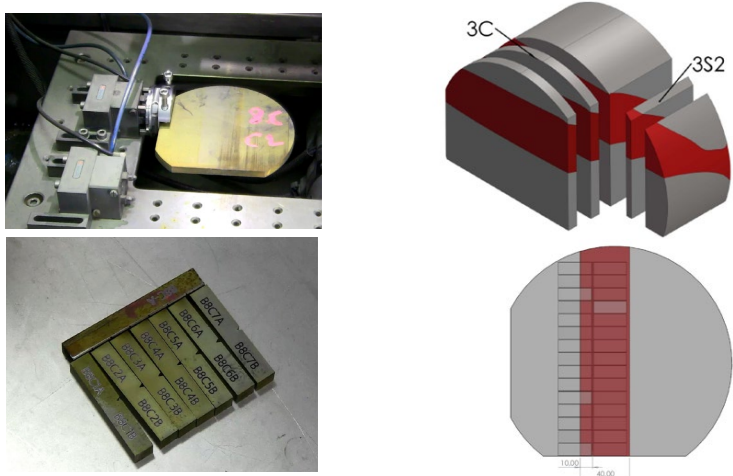


Figure 7. Cutting drawings and final execution.

Mechanical characterisation

In 2019, the following equipment at VTT CNS were validated in the comparison tests using the equipment in the new facilities and in research hall (RH): 1) impact test hammer RKP450, 2) tensile test machine Z250SW, 3) hardness tester DuraScan80, 4) fracture toughness test machine. Additionally the following auxiliary equipment were used in the validation: 1) pre-fatigue equipment Piezomatic, 2) environmental chamber, 3) dimension measurement unit OGP SmartScope Flash 200, 4) laser extensometer LaserXtens HP, 5) displacement gauges. (Ehrnstén, Arffman, & Tähtinen, 2020)

Based on the results achieved, the performance of the impact hammer RKP450, the tensile machine Z250SW and the hardness tester DuraScan80 is equal to that of similar equipment with known, good, performance and the results are comparable. Concerning impact energy, HV1, and HV10 results, comparison could also be done to a national comparison campaign, and in both methods, the results were within the $\pm 2\sigma$ range of variation or within the acceptable error limits.

The comparison testing for the tensile tests was done between the CNS and RH, and the results showed that the load and strength values were in good agreement while a clear difference was observed in the values for elongation. The second tensile test series, after maintenance and modifications of the laser measurement set-up, showed high quality tensile curves and valid results.

Based on the comparison test results, VTT applied and achieved accreditation. It should be noted that the results of the comparative tests were examined in the accreditation process and thus checked by an independent third party. The accreditation is given for a procedure, while validation of every possible test specimen type is not included in the accreditation, but need verification in-house.

Original fracture toughness test validation was performed with SE(B) specimens, while BRUTE utilizes miniature C(T) specimens. While the primary test machine is the same, the pre-fatiguing is performed with a different machine. Furthermore, the specimen fixtures and holding arrangements are different. The validation of the machining of miniature C(T) specimens has been done. (Ehrnstén, Tähtinen, et al., 2020)

The validation of the procedures for miniature C(T) testing were reported in (Arffman & Saarinen, 2020b). Encompassed in the validation are pre-test measurements, fatigue pre-cracking, proper testing, fracture surface imaging as well as data analysis. The validation is performed with two different materials, NESC-1 project material and CRIEPI material from an earlier round-robin.

The tests and analyses demonstrate that CNS testing facilities are capable of high quality Master Curve testing. After some challenges were handled, the load-displacement curves have been consistent and the resulting Master Curves correspond with reference data. Furthermore, supplementary measurements such as dimensions, crack length measurements and fracture surfaces can be made with good accuracy.

The other investigations on mechanical properties carried out on the Barsebäck welds follow the methodology laid out and validated in 2019 as described above. In 2019, Trepan 2 and 3 were extracted from the Barsebäck 2 RPVH weld W28. From these, 23 Charpy V-notch specimens were fabricated from one-quarter depth ($\frac{1}{4}T$). One test was deemed invalid due to a recoil bounce towards the anvil. The impact energy transition curve of valid results indicates a reference temperature $T_{41J} = -75$ °C. In comparison to the B2 baseline data, the reference temperature is 2 °C lower. This difference is less than half of the estimated uncertainty of 5 °C. Therefore, the transition temperature can be considered unchanged and no thermal embrittlement has occurred.

The report describes the tensile testing of weld material in trepan 3. The trepan is extracted from Barsebäck 2 RPV head, weld W28. Eight flat miniature tensile specimens were fabricated from the remaining weld material in trepan 3 slice B after Charpy impact specimens had been cut. Slice B was cut from one-quarter depth ($\frac{1}{4}T$). (Arffman et al., 2020)

Tensile tests were performed with Zwick Z250 universal testing machine in accordance to tensile testing standard ISO 6892. Laser extensometer Zwick LaserXtens was utilized for elongation measurement. A temperature chamber is installed in the test frame. Specimens were tested in temperatures between room temperature and +300 °C. After the test the fracture surfaces were measured an optical microscope. Analysis of all test data was done in MATLAB.

Seven valid tests were performed in total. One test was invalid due to program malfunction. The results provide estimates of the mechanical properties for Master Curve testing. Comparing to the B2 baseline data, there is no notable development in the material at room temperature.

Specimens fabricated with EDM met the dimension requirements and the dimensions were measured accurately with optical measurement system. Each specimen was conditioned to the desired temperature in a disciplined manner and

testing was commenced after a period of settling. The post-test measurements provided high quality images of the fracture surfaces. Furthermore, all these methods can be utilised while testing irradiated materials.

In 2020, fracture mechanical tests were conducted on the weld metal of Barsebäck 2 reactor pressure vessel head. The miniature C(T) specimens were fabricated from previously tested impact specimens. The impact specimens were previously cut from BRUTE trepan 3, from $\frac{1}{4}$ T depth. Fracture toughness testing in broad sense encompasses the pre-test measurements, fatigue pre-cracking, testing and fracture surface imaging as well as data analysis. The stress intensity factors at the onset of cleavage fracture K_{Ic} varied widely, and the test series did not pass homogeneity screening. Both bimodal and multimodal analyses boasted high confidences of correct identification of inhomogeneity. The test series and the consequently the material was qualitatively considered bimodally inhomogeneous. The multimodal master curve represented the test series best, however, and had a mean reference temperature of $-102,9 \pm 38,0$ °C. (Arffman & Saarinen, 2020a)

In 2021, the following testing was done, impact toughness (T_{41J}), fracture toughness (T_0) and tensile testing ($R_{p0.2}$). The testing was done for trepan 6 at $\frac{1}{4}$ thickness, the axial beltline weld. The T_0 for RPV beltline weld, trepan 6, at $\frac{1}{4}$ thickness is -101 ± 6.7 °C, T_{41J} is -95 °C, T_{28J} is -106 °C, and average yield strength is 510 MPa at room temperature. Based on inhomogeneity screening of the fracture toughness data, the material tends to behave in an inhomogeneous manner like the RPVH weld. Compared to the reactor RPVH, the impact toughness of the beltline weld is higher but fracture toughness appears to be marginally lower, but the difference is statistically less significant. The differences in strength correlate with the hardness, Figure 14. (Arffman, 2022)

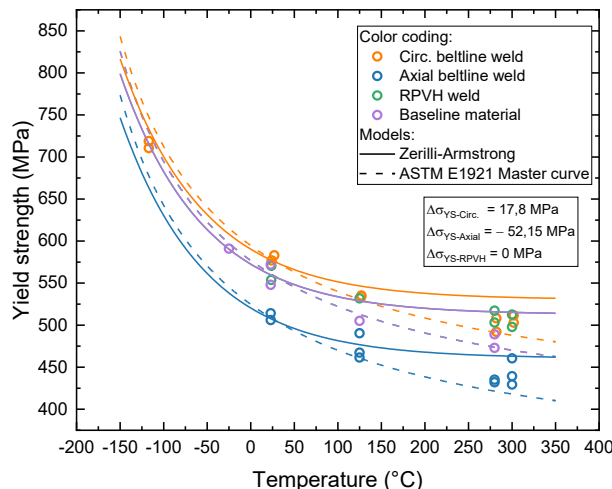


Figure 8. Tensile test results of beltline weld materials. Reactor pressure vessel head (RPVH) results and reference results from the surveillance program (baseline) are also included for comparison.

In 2022, the focus was on testing of the circumferential belt line weld (trepan 8) and the surveillance specimens. The surveillance specimens are non-tested Charpy-V specimens from the surveillance programme. Three specimens are from surveillance chain C (Fluence is $0.1 \cdot 10^{19} \text{ n/cm}^2$) and three from chain G (Fluence is $5.9 \cdot 10^{19} \text{ n/cm}^2$). The fluence of G-chain is at the level of a PWR. For the circumferential weld, T8, tensile testing, impact testing and fracture toughness testing was performed. The material was extracted at $\frac{1}{4}$ thickness location. From the surveillance material, fracture toughness specimens were manufactured. Tensile test results are illustrated in Figure 8, and compared to the other welds. The strength of the circumferential beltline weld material is comparable to reactor pressure vessel head (RPVH) and the baseline non-irradiated reference material.

The impact tests illustrated in Figure 9 indicate for the circumferential beltline weld material that the impact toughness is comparable to the RPVH and the baseline data. Supplementary impact tests were performed with specimens reconstituted from tested specimen halves. The reconstitution technique had not previously been utilised at VTT's CNS, giving the tests an additional value by development of techniques at CNS. The impact toughness of the axial beltline weld is higher.

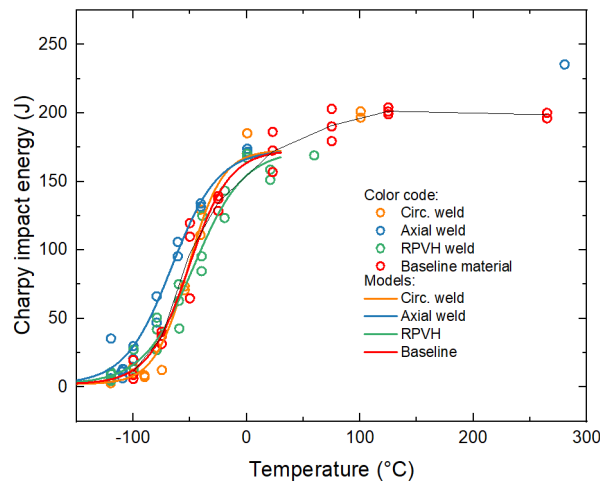


Figure 9. Impact test results and fitted ductile-to-brittle transition curves of the beltline and reactor pressure vessel head (RPVH) materials. Reference results from the surveillance program (baseline) are also included.

Contrary to the RPVH tests, the crack opening displacement (COD) of the specimens was measured from the load-line. The handling of the load-line clip gage with manipulators is more secure and effective than a front-face clip gage. The fatigue pre-cracking of the specimens from the load-line was unreliable, however. The pre-crack lengths were inconsistent, and COD measurement during fatiguing

was reverted to the front-face. This led to delays in testing, since new manipulator applicators had to be designed.

The successful fracture toughness tests, illustrated in Figure 10, demonstrate the inhomogeneity of the weld materials resulting from the regular as-welded and reheated multilayer structure. For the circumferential beltline weld, the multimodal $T_m = -78^\circ\text{C}$, $T_M = -100^\circ\text{C}$ for surveillance chain C, and $T_M = +90^\circ\text{C}$ for chain G. Figure 11 shows the fracture toughness of the axial beltline weld and RPVH at $\frac{1}{4}$ thickness.

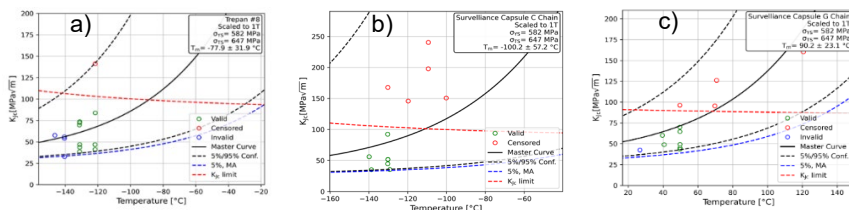


Figure 10. Regular multimodal master curves (a) of the beltline weld material from trepan no. 8., circumferential, (b) Capsule C chain, (c) Capsule G-chain.

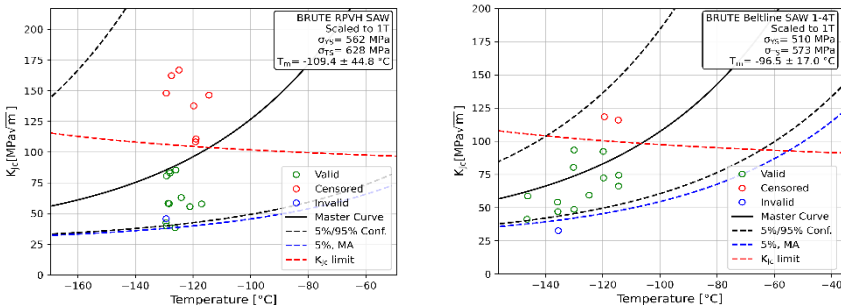


Figure 11. Multimodal master curves on left) RPVH, and right) trepan 6, axial beltline weld.

The following conclusions were formulated based on the mechanical results:

1. The embrittlement trend curve based on impact toughness results from the surveillance program describes sufficiently the embrittlement behavior of the RPV welds subjected to a high temperature close to 270°C , irradiation and pressure during operation.
2. The RPVH weld impact toughness results are similar to the reference condition, indicating that the temperature of 288°C does not cause significant thermal embrittlement during the 23 epy.
3. Compared to the surveillance/reference, RPVH and circumferential beltline welds, the axial beltline weld is softer and has a higher impact toughness. The yield strength of the reference material, RPV head and circumferential

weld is close to 565 MPa at room temperature, and T_{41J} is close to -73 °C. For the axial beltline weld yield strength is 510 MPa at room temperature and T_{41J} is -95 °C. The chemistry of the axial and circumferential weld is similar. The general welding parameters are the same for the welds, but the small differences in mechanical properties possibly originate from variations in the PWHT temperature and time. A PWHT temperature difference of 30 °C can cause a change in hardness equal to the difference in hardness between the axial and circumferential beltline weld.

4. The ASTM E900, FFI and VVER embrittlement trend curve predictions for welds give a decent estimation of the embrittlement behavior of the investigated high-Ni/Mn (Ni > 1.5%, Mn = 1.5%) weld in the low fluence region (< 0.5·10¹⁹ n/cm², E > 1 MeV). Thus, the possible synergistic effect of Ni and Mn appears to be less significant at lower fluences. ASTM E900-21 prediction describes better the investigated weld compared to the VVER and FFI prediction developed for PWRs. (Lindqvist et al., 2024)

Microstructural characterisation

The microstructural characterisation includes investigations of metallographic microstructure, hardness assessment and fracture surface analysis. The metallographic microstructure was analysed for all trepans 3, 6, and 8 through wall thickness at weld, fusion boundaries and base material. The method for characterisation and hardness measurements in CNS was significantly developed within the project. A full weld through wall thickness is shown in Figure 12. Macrohardness HV10 was measured from inner wall side to outer wall side at weld and base material and HV1 across fusion boundaries on both sides of the weld to assess differences in local toughness properties through the weld and the wall thickness. Microhardness HV0.3 was measured on cross-section specimens for the weld metal and different regions of the multipass weld (Que et al., 2022).

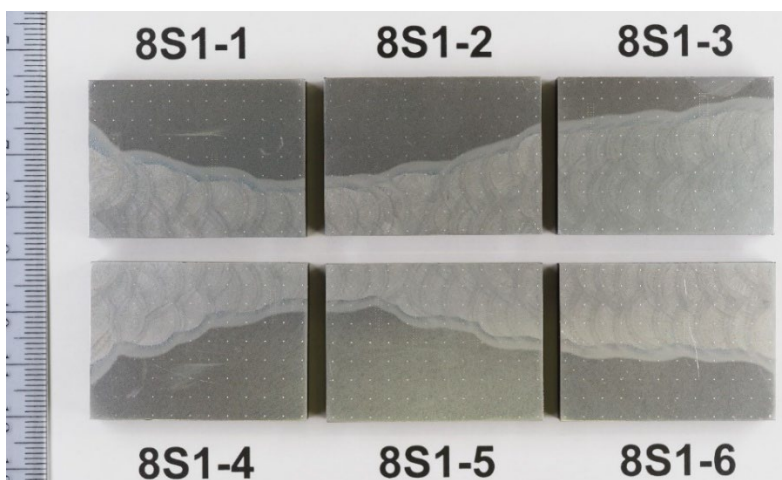


Figure 12. The multipass weld through wall thickness in trepan 8.

The multipass weld consists of as-welded and reheated regions. The weld microstructure of all the investigated trepans represents that typical of high quality welds with a desirable microstructure consisting mainly of acicular ferrite. Acicular ferrite is tougher and more desirable phase than the other competing microstructures such as grain boundary ferrite or Widmanstätten side plates. About 70%–80% acicular ferrite is desirable, and this weld fulfils this criteria well. The as-welded region consists mainly of acicular ferrite and grain boundary ferrite shown in Figure 13. The reheated microstructure consists mainly of polygonal ferrite.

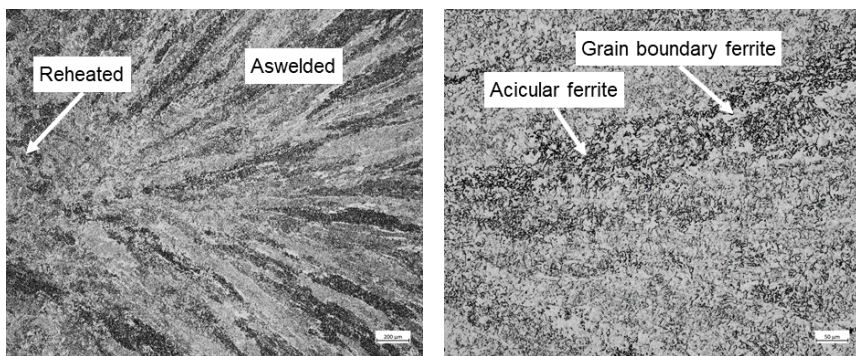


Figure 13. Metallographic microstructure on a typical weld bead and aswelded microstructure consisting mainly of acicular ferrite.

The average hardness on the RPVH weld is ~210 HV10. The hardness of the circumferential beltline trepan 8 is on similar level to RPVH trepan 3 with an average of 218 HV10 being almost ~30 HV10 higher than the average hardness of the beltline axial weld of trepan 6 at average of ~190 HV10. The HV10 results are shown in Figure 14 from inner wall side to outer wall side. The difference in hardness level is in conflict with the radiation dose these materials have been subjected to, as the trepan 6 has the highest measured dose, but since the trepan 6 weld was subjected possibly to a longer PWHT time or temperature it has caused decrease in hardness level. The trend is similar in all welds, where the hardness slightly increases at the region where the weld root has been removed and the welding direction changes.

The HV1 hardness was measured across the fusion boundary to identify local changes in microstructure and toughness in the interface. The HV1 hardness levels are in correlation with the HV10 showing lowest hardness for the trepan 6 and similar for trepan 3 and 8. Main difference is seen in the peak at the heat affected zone (HAZ), as the trepan 8 shows significantly higher hardness peak adjacent to the fusion boundary at 337 HV1 compared to the two other HAZ's remaining well below 300 HV1. Hardness at this high level may indicate local martensite grains in the coarse-grained HAZ.

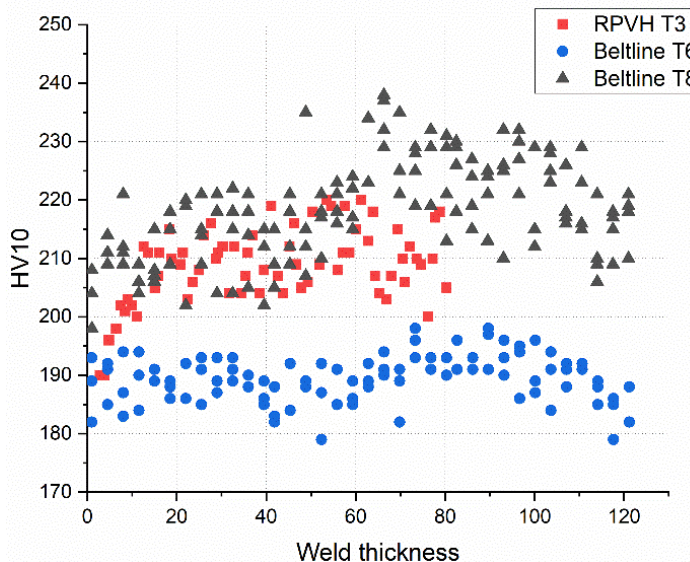


Figure 14. HV10 hardness of the three welds through wall thickness from inner wall side to the outer wall side.

Table 5. HV1 hardness measured across the fusion boundary. The average results are given for the welds and base material and hardness peak-value in HAZ adjacent to the fusion boundary.

HV1	Avg Weld	Avg BM	Peak HAZ
RPVH T3	227	198	276
Beltline T6	199	184	255
Beltline T8	234	191	337

In fracture surface analysis, the primary initiators of the brittle fracture specimens are investigated systematically using scanning electron microscope (SEM) with energy dispersive X-ray spectroscopy (EDS). All fracture toughness specimens and CVN specimens tested in the brittle region of the DBTT curve, below T_{41J} , were examined and imaged as in Figure 15. Summary of all trepans initiators are in Table 6.

In the RPVH material, trepan 3, brittle fracture primarily initiated from an inclusion with larger size ($0.5\text{--}2.5\ \mu\text{m}$) in all CVN specimens (Hytönen et al., 2021). The cleavage fracture initiated either within the brittle multiphase oxide inclusions or from the debonded interfaces between the uncracked inclusion and weld metal matrix. The inclusions have chemical composition of FeMnAlSi(S)O . All the investigated miniature C(T) specimens initiated from a particle, the size of which is $0.3\text{--}1.8\ \mu\text{m}$. The size of the initiating particles is larger than the average inclusion size, which is about $0.3\ \mu\text{m}$ according to the performed inclusion analysis.

In the axial beltline weld, trepan 6, the primary initiation site with a brittle roundish inclusion was found in six CVN specimens and two miniature-C(T) specimens. The inclusion is comparative to those found in the RPVH CVN and miniature-C(T) specimens initiation sites, having chemical composition of FeMnAlSi(S)O. The size of these inclusions is similar (~1–2 µm). Irregular-shaped inclusions with a different chemical composition, FeMnMo(C), were observed in three CVN and at least ten miniature-C(T) specimens primary initiation sites. The irregular-shaped inclusions were broken as the inclusion was seen on both mating fracture surfaces. The fracture of the inclusion is within one plane and appears smooth on the surface. The inclusions were also debonded from the surrounding matrix on one side and local intergranular cracking was observed adjacent to the inclusion. Due to the irregular shape, the true size of the inclusion was not possible to determine, however, the visible part was on a range of ~1–1.5 µm.

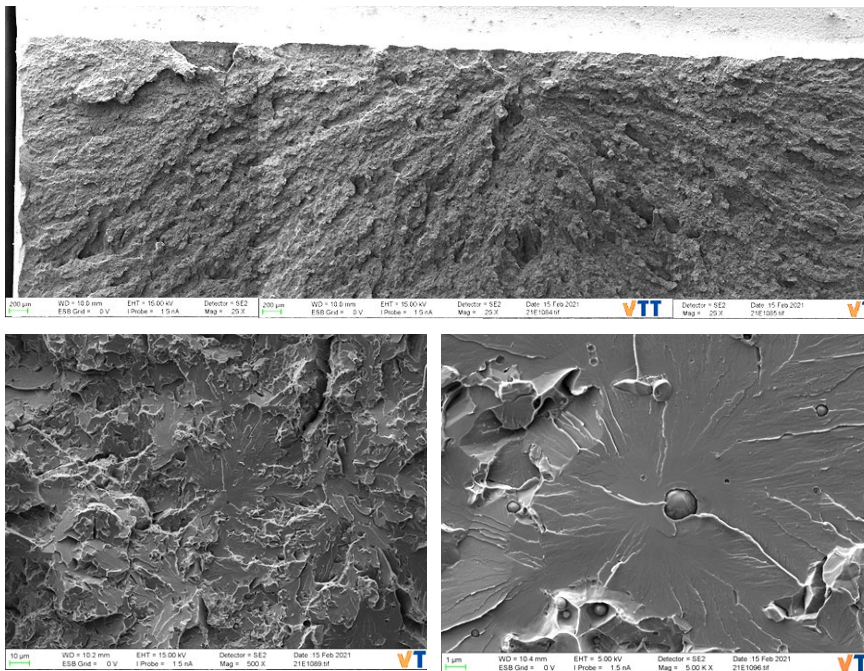


Figure 15. Fracture surface of a brittle CVN specimen and primary initiation site with a multiphase oxide inclusion as an initiator.

The primary initiation site with a brittle roundish inclusion was found in all CVN specimens and miniature C(T) specimens of trepan 8. The inclusion is comparative to those found in the RPVH CVN and miniature C(T) specimens initiation sites, having chemical composition of FeMnAlSi-O. The size of these inclusions is similar

(~0.7–2.5 µm). The oxide-inclusion are typically considered as brittle and are either found broken or debonded from the surrounding matrix.

Correlations in microstructural features and brittle fracture properties were obtained for specimens tested below T_{41J}. A trend between the particle size with the impact energy and initiation location with the impact energy were obtained. Lower impact energy is associated with a larger initiator particle size and the primary initiation site closer to the V-notch. This correlation is in line with fracture mechanics as the initiating particle is typically the largest in the mapped area. The correlation trend was obtained for fracture toughness specimens as well, where the lower fracture toughness values were obtained in specimens with large initiating particle size (Hytönen et al., 2021).

Table 6. Summary of the primary initiators in all investigated brittle fracture specimens in trepans 3, 6, and 8.

Weld metal	Test type	Number of specimens	Initiator	Size (µm)	Initiator shape and integrity
RPVH T3	CVN	9	FeAlSiMnO	0.5–2.5	Roundish debonded or broken
RPVH T3	MCT	20	FeAlSiMnO	0.3–1.8	Roundish debonded or broken
Beltline T6	CVN	9 (4 reconstitution)	FeAlSiMnO (7/9) FeMnMo (2/9)	1.0–2.3 ~1–2	Roundish debonded or broken Irregular-shaped broken and debonded
Beltline T6	MCT	15	FeAlSiMnO (3/15) FeMnMo (11/15) 1 uncertain	0.2–1.0 ~0.5–2	Roundish debonded or broken Irregular-shaped broken +IG
Beltline T8	CVN	8 (2 reconstitution)	FeAlSiMnO	0.7–2.5	Roundish debonded or broken
Beltline T8	MCT	15	FeAlSiMnO	0.6–2.2	Roundish debonded or broken, mild deformation

Chemical composition of the trepan 3, 6 and 8 welds were measured through wall thickness using optical emission spectroscopy (OES) methods. The trepan 3 weld was measured using spark OES and trepan 6 and 8 in CNS using glow-discharge (GD) OES. The BRUTE project material was first irradiated material tested using the CNS GD-OES. Table 7 shows the average composition for trepan 3 and 6 and whole weld for trepan 8. The results show variation in the composition from inner wall side to outer wall side and between the welding directions. Main differences based on relative variation were noticed in contents of C, Cr, Ni, Cu, and Al.

Table 7. Chemical composition of the three investigated welds analysed using OES methods.

	C	Si	Mn	S	P	Cr	Ni	Mo	Cu	Al	Co	Fe
T3	0.057	0.15	1.43	0.007	0.008	0.03	1.48	0.41	0.06	0.024	0.020	bal.
T6	0.074	0.17	1.44	0.007	0.010	0.03	1.63	0.44	0.09	0.026	0.018	Bal.
	C	Si	Mn	S	P	Cr	Ni	Mo	Cu	Al	Co	Fe
T8_1	0.085	0.173	1.46	0.006	0.008	0.054	1.48	0.450	0.083	0.065	0.018	96.1
T8_2	0.096	0.186	1.49	0.006	0.008	0.054	1.47	0.452	0.105	0.089	0.018	96.0
T8_3	0.094	0.177	1.45	0.006	0.008	0.055	1.47	0.452	0.081	0.087	0.019	96.1
T8_4	0.093	0.165	1.48	0.006	0.008	0.048	1.52	0.445	0.085	0.118	0.017	96.0
T8_5	0.056	0.150	1.43	0.005	0.009	0.033	1.64	0.438	0.076	0.038	0.018	96.1
T8_6	0.072	0.170	1.42	0.006	0.008	0.027	1.68	0.438	0.093	0.117	0.018	95.9
Mean	0.083	0.170	1.45	0.006	0.008	0.045	1.54	0.446	0.087	0.086	0.018	96.0
STDEV	0.016	0.012	0.026	0.000	0.000	0.012	0.095	0.007	0.010	0.031	0.001	0.067
%-DEV	19.28	7.06	1.79	0.000	0.000	26.67	6.17	1.57	11.49	36.05	5.56	0.07

The microstructural investigations found a correlation between the metallographic microstructure of the weld and brittle fracture initiation. The weld metal consists of heterogeneous multipass weld bead structure with majority of acicular ferrite. During weld solidification, nucleation of acicular ferrite initiates from non-metallic inclusions, hence the inclusions are a requirement in the weld. However, all brittle fracture primary initiation sites in this investigation included inclusions, where the fracture initiation could be located. Most of the primary initiators are those of non-metallic oxide type inclusions but relatively large in size (~1–2 µm), larger than the average non-metallic inclusion (~0.3 µm) in this weld metal. The orientation of the weld bead, i.e., orientation of aswelded microstructure, to the fracture crack propagation plane was found to correlate with the amount of interdendritic fracture due to the dendritic microstructure of aswelded regions and with relative long regions of grain boundary ferrite. Additionally, according to the cross-sectional studies, the fracture initiation in the aswelded region shows mildly higher toughness properties compared to the initiation in the reheated region. However, this is not fully confirmed since the positioning of the crack has been done independently from the weld bead structure.

Additional to scientific results, through the project systematic fracture surface analysis methodology was developed in CNS and safe practices obtained for metallographic characterisation in hotcells.

Stakeholder activities and international co-operation

The consortium for BRUTE forms a strong Nordic group of end-users, authorities and research organisations in Finland and Sweden. The importance of such a group becomes even more important, when the decommissioning plans in Europe continues, making Finland and Sweden the only European countries with operating BWRs.

SSM (Strålsäkerhetsmyndigheten) has a position in the BREDA advisory board, and SSM finances doctoral students at KTH in Stockholm (Kungliga Tekniska Högskolan) under the supervision of Professor Pål Efsing. Magnus Boåsens thesis is published, with the dissertation date being September 18th, 2020. The work on

modelling thermal ageing mechanical behaviour is continued by Daniela Klein. A doctoral thesis work on Barsebäck materials is in its final phase at Chalmers University by Kristina Lindberg, under the supervision of Matthias Thuvander, was finalised in 2018, and she has continues to work on the issue as a post-doc. Additional funding has been obtained also from NKS (Nordisk Kärnsäkerhet). This funding is divided between VTT, KTH and Chalmers, further adding to strengthening the Nordic co-operation in this area, as depicted in Figure 16.



Figure 16. The BRUTE consortium.

Fluence measurements

In BRUTE, the nuclide activities present were determined from beltline trepan 6 and 8. The aim of the gamma spectrometry system used in VTT is to determine the activity of a given sample by measuring the energy and the intensity of specific gamma rays emitted by the sample upon the decay of a given (unstable) radioisotope. The energy of gamma radiation is a footprint of every radioactive isotope, and thus it is possible to identify numerous gamma emitters in an unknown sample. (Dorval, 2021)

A total of 21 samples, Figure 17, from the RPV base material of the Barsebäck 2 nuclear reactor were prepared with electronic discharge machining (EDM) in 2020. These samples were specifically prepared for gamma-spectrometry purposes. The main requirements imposed by the technique relate to consistent geometry and

avoiding the presence of corrosion. The samples, with approximate dimensions of 1 mm x 10 mm x 10 mm, were individually pickled after fabrication.



Figure 17. Activity measurement samples cut from Trepan 6, still attached together in a comb-shaped blank.

Before fluence measurements, each sample was weighed three times. As the specimens were stored with silica gel and in individual paper bags, there was negligible amounts of surface corrosion. Therefore, there is certainty about the measured masses corresponding to the RPV base material only.

Measurements were carried out using a p-type, HPGe semiconductor detector with 18% relative efficiency. In all 21 BRUTE samples studied in this work, ^{60}Co was the only gamma-emitting nuclide present. The considerable time elapsed between the final shutdown of the reactor and the measurements meant in practice that most gamma-emitting activation products had already decayed, with the exception of ^{60}Co . Since there is a certified ^{60}Co calibration source in VTT's CNS, it was possible to carry out the measurements using the relative activity measurement method. By doing so, substantially lower uncertainties were reached.



Figure 18. Activity sample holder in measurement position.

In order to obtain accurate results, the ratio of transmissions has to be carefully assessed. In this work, two different approaches were adopted, and both yielded consistent results. Thanks to the excellent dimensional consistency in fabrication, the same transmission ratio correction factor could be utilised for all samples. All specimens were measured at a close, 2-cm sample-detector distance, Figure 18. Gamma spectra were acquired in 8016 channels.

For trepan 6, the specific activities of ^{60}Co are displayed in Figure 19. The activities evidence a smooth decaying profile from the inner to the outer surfaces of the RPV, as expected. In spite of the overall decaying trend, a statistically significant increase in specific activities takes place at thickness values beyond approximately 97 mm. This increase is associated with the leakage of fast (i.e., high-energy) neutrons from the core beyond the outer surface of the RPV. At some point, these fast neutrons undergo collisions with the concrete in the biological shield. Since concrete contains hydrogen, some neutrons undergo moderation and scatter back towards the outer surface of the RPV. When this happens, neutron activation in the form of radiative capture takes place with ^{59}Co nuclei present in the base material. For trepan 8, this scatter back was observed to have a significant effect.

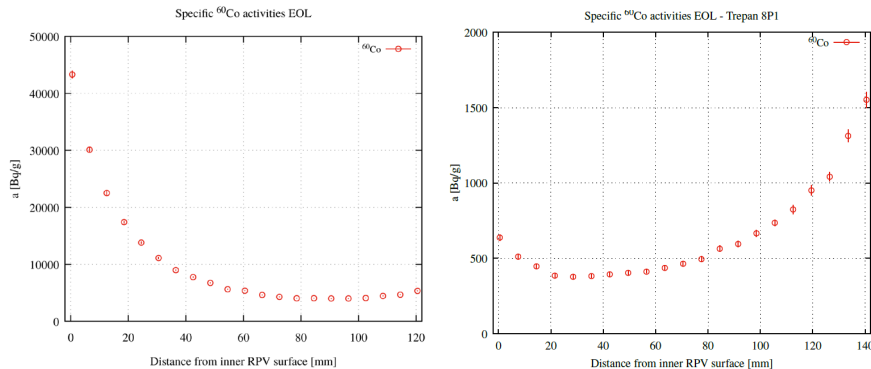


Figure 19. ^{60}Co activity profile. Left) Trepan 6, Right) Trepan 8. As the fluence is relatively low at the circumferential beltline weld (Trepan 8), the back scatter from the containment building has a bigger effect on the activity.

The real values of the activities were planned to be compared to the computational estimates and subsequently utilised in the calculation of corrected fast neutron fluences at different positions. Unfortunately, the collaboration plan was not realized.

Conclusions

The objective of BRUTE is twofold; 1) to perform mechanical and microstructural investigations of Barsebäck 2 BWR reactor pressure vessel (RPV) welds and surveillance weld, enabling validation of embrittlement predictions based on the

RPV surveillance programme 2) to pioneer the new infrastructure in the Centre for Nuclear Safety, CNS, VTT. The B2 plant was operated for 27 years.

During the project, the new CNS infrastructure key-processes were accredited, round robin investigations were performed, the personal got experience with standardized testing of irradiated materials, specimen preparation inside hot-cells and the whole material flow, best practice guidance was established, and tools to ease specimen handling were prepared.

The results confirm that the surveillance results describe the mechanical behavior of the reactor pressure vessel. There are no significant changes in mechanical properties after 27 years of operation. The axial beltline weld has higher toughness and lower strength than the other investigated welds which is possibly caused by variations in thermal histories.

Acknowledgement

BRUTE is a project in the SAFIR2022 program. It is funded by VYR (Nuclear Waste Management Fund), VTT Technical Research Centre of Finland and NKS (Nordisk Kärnsäkerhet). Furthermore, the objectives of BRUTE are set out in the Nordic BREDA (Barsebäck Research & Development Arena) project. The contributions of BREDA are substantial, as it has also planned and executed the cutting of the trepans used in BRUTE from the pressure vessel, among others. Also, the scientific support and background information provided by the Swedish stakeholders from Energiforsk, Ringhals, Forsmark and OKG have been significant in the success of the project. The funding, materials and technical support are all greatly appreciated.

References

- Arffman, P. (2022). Mechanical testing in BRUTE in 2021. VTT-R-00234-22.
- Arffman, P., & Saarinen, J. (2020a). Fracture mechanical properties of Barsebäck 2 RPVH weld metal. VTT-R-01455-20.
- Arffman, P., & Saarinen, J. (2020b). Validation of fracture mechanical testing at CNS using miniature compact tension specimens. VTT-R-01174-20.
- Arffman, P., Saarinen, J., & Lukin, J. (2020). Tensile test results from B2 RPV head SAW weld metal. VTT-R-00073-20.
- Dorval, E. (2021). Nuclide activity measurements of trepan #6 from the Barsebäck 2 reactor by gamma-spectrometry. VTT-R-00073-21.
- Ehrnstén, U., Arffman, P., & Leporanta, J. (2020). Cutting plans for B2 RPV beltline trepan #6 - cutting in 2020. VTT-R-01526-20.
- Ehrnstén, U., Arffman, P., & Tähtinen, S. (2020). Updated report on validation of mechanical test methods used in the BRUTE project. VTT-R-00087-20.
- Ehrnstén, U., & Lydman, J. (2019). Reception of BRUTE reactor head trepans. VTT-R-00430-19.

- Ehrnstén, U., & Lydman, J. (2020). Reception of BRUTE trepans from the Barsebäck 2 reactor beltline area. RESEARCH REPORT VTT-R-00379-20.
- Ehrnstén, U., Tähtinen, S., Arffman, P., Loporanta, J., & Lydman, J. (2020). Validation of cutting procedures and cutting plans for first BRUTE RPVH trepans. RESEARCH REPORT VTT-R-00051-20.
- Hytönen, N., Que, Z. qing, Arffman, P., Lydman, J., Nevasmaa, P., Ehrnstén, U., & Efsing, P. (2021). Effect of weld microstructure on brittle fracture initiation in the thermally-aged boiling water reactor pressure vessel head weld metal. *International Journal of Minerals, Metallurgy and Materials*, 28(5), 867–876. <https://doi.org/10.1007/s12613-020-2226-6>
- Lindqvist, S., Norrgård, A., Arffman, P., Hytönen, N., Lydman, J., Efsing, P., Suman, S., & Nevasmaa, P. (2024). Mechanical behavior of Barsebäck 2 reactor pressure vessel welds after 28 years of operation. *Journal of Nuclear Materials*.
- Pentti Arffman, & Loporanta, J. (2022). Specimen fabrication and cutting in BRUTE 2021. VTT-R-00235-22.
- Que, Z., Lindroos, M., Lydman, J., Hytönen, N., Lindqvist, S., Efsing, P., Nevasmaa, P., & Arffman, P. (2022). Brittle fracture initiation in decommissioned boiling water reactor pressure vessel head weld. *Journal of Nuclear Materials*, 569, 153925. <https://doi.org/10.1016/j.jnucmat.2022.153925>

9.2 Infrastructure development at LUT safety research laboratory (IDEAL)

Joonas Telkkä¹, Elina Hujala¹, Eetu Kotro¹, Lauri Pyy¹, Antti Räsänen¹

¹LUT University
P.O. Box 20, FI-53851 Lappeenranta, Finland

Abstract

The general objective of the IDEAL project (2019–2022) was to develop the experimental thermal hydraulic infrastructure at LUT University nuclear safety research laboratory. The project comprised maintenance of the thermal hydraulic test facilities, development and upgrade of the instrumentation and data acquisition capabilities, as well as the implementation of the new modular test facility, MOTEL, which models a SMR. The motivation for the project is in providing state-of-the-art experimental thermal hydraulic capabilities, which benefit the whole Finnish nuclear community. The maintained and upgraded facilities are used in other important projects. Enhancement of the measurement capabilities enables production of high-quality data for better understanding of the thermal hydraulic phenomena and for the development and validation of computational tools. Procurement and implementation of novel measurement techniques promote growth of expertise and offer topics for master's and bachelor's theses. Maintenance of the facilities and expertise enables rapid solution of problems that arise in the Finnish nuclear power plants. Upgrade of the process control, computational and data storage systems enables better handling and archiving of the large amounts of experimental data.

Introduction

In the SAFIR2014 research programme, the research project ELAINE was launched for the enhancement of measurement instrumentation available for the thermal hydraulic experiments in LUT University. Significant milestones in the project were the acquisitions of a particle image velocimetry (PIV) measurement system, wire-mesh sensor (WMS) electronics and a system of three modern high-speed cameras (HSC). In addition to acquisitions of experimental hardware, a new data storage system for the experimental data (EDS) was developed and taken into active use. In addition, one important task in the project was the maintenance of the (PWR) PACTEL test facility in order to secure its operability and availability for the experiments.

In the SAFIR2018 programme, the INFRAL project was launched in 2015, and it aimed for the further development of the techniques related to the advanced measurement techniques and their applications. The goal was to build good in-house expertise in the use of the acquired techniques to facilitate the needs of computational modellers in the future experiments in the best way technically

possible. Further, the goal of the INFRAL project was to secure the operability of the PACTEL test facilities and to launch a study on the new major test facility to prepare for the post-PACTEL era.

The IDEAL project was launched in 2019 to continue the LUT thermal hydraulic infrastructure development work done within ELAINE and INFRAL. The IDEAL project is divided into five different work packages. The first work package (Development of instrumentation) includes activities that are related to the procurement and use of advanced measurement techniques in the LUT laboratory. These techniques include so far PIV, WMS, high-speed cameras, optic fibers for longitudinal temperature distribution measuring, and ultrasonic flow meters. The second work package (Maintenance of test facilities) aims on the maintenance of test facilities such as (PWR) PACTEL, MOTEL and PASI, and it comprises also the yearly pressure vessel inspections, calibrations and other maintenance actions in the laboratory. Planning and creating a component stock, as well as planning and execution of the laboratory power upgrade from 1 MW to approximately 2.5 MW are part of the work package, too.

The third work package (Process control and computational systems) was a new addition to the infrastructure development project compared with the previous ELAINE and INFRAL projects. The work package includes renewing of the laboratory's field and process instrumentation, upgrade of the computation servers and enlargement of the available experimental data storage space. The work also includes archiving of the old test data from previous decades.

The fourth work package (Development of the MOTEL test facility) continued the work initiated in INFRAL to develop the LUT laboratory's new large-scale test facility, MOTEL (MOdular TEst Loop). The work package comprises the assembling and erecting of the first version of the facility, MOTEL-SMR, as well as the implementation of MOTEL including the shakedown and characterizing experiments of the facility. MOTEL has been successfully taken into operation during the IDEAL project. The fifth work package (Project management) includes the tasks related to the project management and participation in the reference group meetings and seminars. International co-operation is included in this work package. International co-operation is realized by participating in the SILENCE (SIgnificant Light and heavy water reactor thermal-hydraulic Experiments Network for the Consistent Exploitation of the data) network, which is a global network for the operators of thermal hydraulic test facilities.

IDEAL is essentially an infrastructure development project. Thus, a large share of the project funding during the programme has been allocated to materials and supplies, especially concerning the laboratory maintenance in WP2, the server procurements in WP3 and the building of MOTEL in WP4. Nevertheless, as reported in the following chapters, a significant amount of scientific research has been done within the project.

Development of instrumentation

The WP1 of IDEAL concerns the development of advanced measurement techniques, such as particle image velocimetry, wire-mesh sensors, high-speed cameras and the related pattern recognition technology, optic fibers for longitudinal temperature distribution measurement and ultrasonic flow meters.

Particle image velocimetry

In 2019, the main focus for PIV was in literary work as there were no measurements involved within the SAFIR-related projects. The theoretical background survey and feasibility study for high-speed PIV (HS-PIV) was started, partly as a summer trainee work. An inventory of all PIV and high-speed camera and other imaging equipment was conducted in 2019.

The high-speed PIV study was finalized in 2020. The study is summarized in the following paragraphs.

Earlier, it was considered that choosing between high spatial resolution or high temporal resolution was a compromise that has to be made when executing PIV measurements. However, with the recent developments in high-speed imaging, high-speed Particle Image Velocimetry can also offer high spatiality. The HS-PIV technique allows the measurement of turbulent quantities in transient flows. High speed measurements both in time and space also allow the measurements of acceleration fields. The HS-PIV technique is simply conducted as a normal PIV measurement but using higher repetition laser unit (or continuous wave laser) and high-speed cameras (HS-cameras) for image acquisition. The HS-PIV technique can offer a kilohertz temporal resolution with a multiple megapixel spatial resolution depending on the hardware used. Naturally, high spatial resolution HS-cameras are still very expensive, so there are still compromises in the final composition of a HS-PIV system, depending on the budget. In addition, the amount of RAM drives the HS-camera price up, but it gives a possibility to make either longer measurements or more measurements without the need for uploading the captured images to the system computer. For the laser units, the repetition rate and the pulse energy are the defining factors of the price. The faster the laser with higher laser pulse energy, the more expensive it will be if using pulsed.

Previously, the LUT laboratory has used PIV in many occasions in different thermal hydraulic studies, e.g. in direct contact condensation (DCC) experiments with blowdown or sparger pipes in the PPOOLEX facility, as well as for particle size measurements of nozzles with a Shadowgraphy extension of the PIV system. In addition, several non-SAFIR related studies have been conducted over the years. The current PIV system was acquired in late 2011 and it is a so-called slow-speed PIV system with the measurement frequency of 7 Hz, later 15 Hz after the upgrade of the existing system with the LaVision sCMOS cameras in 2017.

The existing system has a high spatial resolution capable of measuring thousands of velocity vectors within a measurement area in the range of tens of centimeters per side (the size is naturally dependent on the wanted spatial

resolution). So far, it has been found out that the temporal resolution of the current system is not always ideal, as the timescales of turbulent and other thermal hydraulic phenomena are very short. For example, the rapid condensation of a steam slug in the SEF-POOL facility occurs in a millisecond timeframe. In addition, measuring transient conditions or keeping constant ambient conditions for long time frames in large test facilities, like PPOOLEX, is challenging. Thus, one advantage of a HS-PIV system would be the possibility to gather time-averaged data samples faster. In other words, the existing slow-speed PIV system can be mainly used in time-averaging of vector velocity fields in constant ambient conditions. The flow measurement infrastructure of LUT Nuclear Engineering is capped due to this limitation. With a HS-PIV system, it would be possible to extend the flow measurements to wider array of thermal hydraulic studies where the optical requirements for the PIV measurement are met.

The minimum requirement for updating the existing PIV system to a high-speed use is a new laser unit with a higher repetition rate. In addition, the Programmable Timing Unit (PTUX) needs to be upgraded for the high-speed use. PTUX synchronizes camera(s) with laser pulses. The currently used measurement and analysis software DaVis 10 is suitable for the HS-PIV use without upgrades. LUT Nuclear Engineering has acquired Phantom Miro M310 high-speed cameras previously for the pattern recognition purposes and they could be used as a part of the system. A hardware registration for the Phantom Miro M310 is needed for DaVis 10. Phantom Miro M310 is equipped with a 1280x800 pixel sensor with a maximum image acquisition rate of 3200 fps resulting in a throughput of 3.2 Gpx/s (gigapixels per second). The camera is equipped with 12 GB RAM. This enables a 1.6 kHz measurement frequency in a PIV use for roughly 3.75 seconds in total. Or, total of 6000 image pairs with a chosen frequency as the sensor is roughly the size of one megapixel.

The preliminary plan for HS PIV system has been ongoing with the help of LaVision, the prior supplier of the existing PIV system, on behalf of the laser unit and auxiliary system updates. For a possible upgrade of HS cameras, talks with Citius Imaging Ltd Oy have been ongoing. Both companies have also supplied preliminary quotations in order to have the sense of the overall budget needed for a HS PIV system. As stated above, using the existing Miro M310 HS cameras is possible, but high-speed cameras with a better spatial resolution, RAM and throughput can offer a better result. In addition, the future needs of pattern recognition analysis will take part in deciding the need for the upgrading of the HS cameras.

It was decided in the autumn of 2020 that the purchase of a high-speed PIV system will take place later since there are more important procurements to be made in the project. Thus, the possible procurement shifts to the future.

During 2021, the PIV system was utilized in Joona Saira's Bachelor's Thesis. PIV was one measurement system used in the validation of ultrasonic flow measurements in a mock-up channel that represents the MOTEL facility's downcomer channel. Due to the different approach of measurement systems used in the validation, full in-detail comparison was not possible. The mock-up channel

needed to be fit to the PIV measurements in retrospect and was not able to fulfill the demands for full comparison by limiting the measurement area in the z direction towards the PIV system's cameras. But the results gave confidence that ultrasonic measuring is a valid way to measure the MOTEL downcomer flow velocity.

In addition, two researchers from LUT attended LaVision's Online PIV Seminar in October 2021. The seminar offered good practical and theoretical aspects on the very complex measurement technique of PIV. One advantage was also to broaden the PIV knowledge in LUT. The seminar also fulfilled the need to have redundant PIV operational skills in case of staff changes in the future.

High-speed cameras and pattern recognition

Within the LUT infrastructure development projects, high-speed cameras have been used to support data analyses of various condensation experiments. A pattern recognition algorithm has been created and developed with the high-speed camera measurement results. In 2019, the cameras were applied to sparger experiments in the SEF-POOL test facility (experiments of the SAFIR SPASET project). The pattern recognition algorithm was improved in 2019 using the HSC data from the 2018 SEF-POOL experiments. A conference paper based on this analysis was written and presented in the NURETH-18 (the 18th International Topical Meeting on Nuclear Reactor Thermal Hydraulics) conference in Portland, USA in August 2019 (Hujala et al., 2019).

In 2019, a dissertation named "Quantification of large steam bubble oscillations and chugging using image analysis" was finalized and presented by Elina Hujala with due permission for public examination and criticism on the first of November 2019 at LUT University.

In the dissertation, a pattern recognition-based image analysis algorithm for vertical vent pipes was designed and developed. The direct contact condensation experiment (DCC-05) of the LUT University's PPOOLEX test facility was used as a reference test. The algorithm consists of three parts: pre-processing, where all image processing takes place, pattern recognition, where the edges of the bubbles are detected, and post-processing, where all images are analyzed, and data collected. The algorithm evaluates basic properties of large steam bubbles, such as volume, surface area, surface velocity and acceleration, and different frequencies.

Frequency analysis was also conducted in the DCC-05 case. The analysis showed two main frequencies: 53 Hz and 126 Hz. The algorithm was also applied to computational fluid dynamics (CFD) simulations, where the algorithm was used to determine critical wavelengths of condensation driven Rayleigh-Taylor instability in succession to establish the most suitable grid density for the simulations. A frequency analysis was also performed for the CFD simulation cases and compared to the results of the algorithm. This is illustrated in Figure 1.

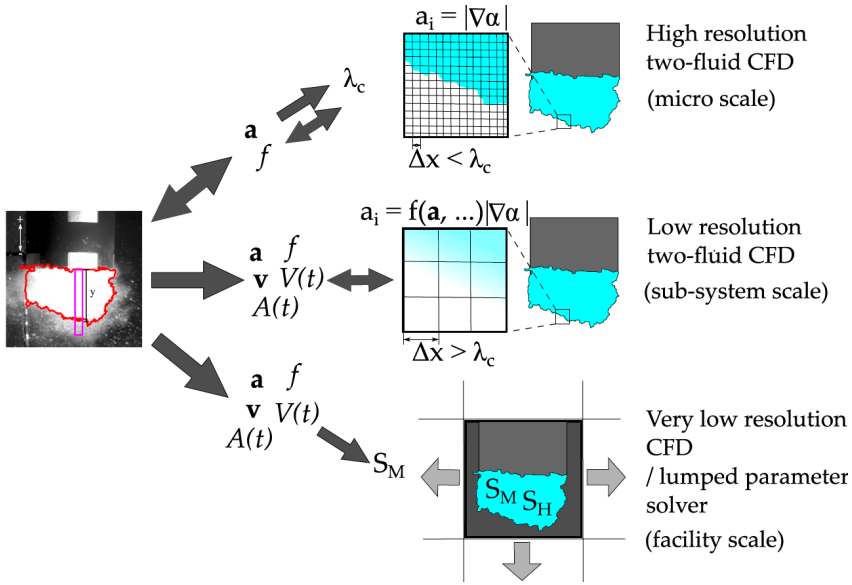


Figure 1. Validation data from image analysis for different scale numerical DCC models.

The algorithm was extended to cover cases where multiple bubbles travel at the same time in the frame being analyzed. The extended algorithm tracks multiple bubble properties in the same image. The evaluation of surface velocities and acceleration were also improved.

The algorithm works well in evaluating volume, surface area, velocities and accelerations of large steam bubbles. The research verified that even from moderate quality video material, it is possible to acquire high quality quantitative data, if the frame rate of the video had been high enough and the most obtrusive objects could be filtered out from it. The algorithm can help to understand phenomena that underlay the design of BWR safety systems.

In 2020, a plan for the further high-speed camera testing with stand-alone HSC measurements focusing only on the cameras to be conducted in 2021 was made. In 2020, an extempore test was carried out to prepare for the 2021 studies. In this test, pressurized air was injected into the water of the SEF-POOL test facility. Short test shots were recorded using a single camera. Either the flow rate of the pressurized air or the temperature of the pool water was not measured. With the pressurized air, clearly defined bubbles were produced. Because of the small flow rate, the air does not mix the water, and the background of the images stays clear and calm. The clear bubbles with an even background gives a good starting point for the error estimation and image analysis. The conducted test showed that the SEF-POOL test facility is an appropriate base when testing the features of the HSC system. Thus, there is no need for a separate test facility for this purpose. Also, an

improved backlight proved to be better than the lighting used in the SEF-INF experiments.

In 2021, the stand-alone HSC testing was done in SEF-POOL as horizontal steam and air blowdown testing, named SEF-INF3. The aim of the study was to test different camera settings and their effects to the image analysis algorithm development process. Also, a conference paper named “Modelling of Horizontal Steam Injection in a Water Pool” was written and accepted for the 19th International Topical Meeting on Nuclear Reactor Thermal Hydraulics (NURETH-19) in Brussels in March 2022 (Patel et al., 2022).

The general idea of the testing was to capture high-speed camera images of nearly similar field-of-views and change different camera parameters to see what the practical effects on the pattern-recognition results are. This was done by placing two HS cameras next to each other equidistant to SEF-POOL. In addition, changing parameters gives indication on what is the ideal imaging frequency for the pattern-recognition algorithm. The slower the frequency can be, the longer the measurement can be captured and with larger pixel count as the throughput is constant for HS cameras (for Phantom Miro-M310 the throughput is 3.2 gigapixel/s).

All the experiments were shot with the aperture 1.4 to ensure the maximum amount of light exposure. The experiment parameters were chosen as follows:

- Experiments 1-9: changing fps keeping the left camera with constant camera parameters and changing the right camera parameters
- Experiment 10: the effect of the video length for pattern-recognition
- Experiment 11: the same as above but in addition lowering the exposure time
- Experiment 12: the same as above but with even lower exposure
- Experiment 13: rerun of experiment #1
- Experiment 14-15: testing of low frequency and low exposure
- Experiment 16-18: testing of higher frequency and low exposure

The calibration was done with a single image by using the in-house built checker calibration board with a checker size of 10 mm x 10 mm. The used lenses were 24 mm in focal length without any filters. The number of images were kept at maximum depending on the used sensor size. The sensor for the right camera was cropped into size of 1280 x 400 pxl (~0.512 Mpixl) and the sensor for the left camera into size of 1216 x 800 pxl (~0.973 Mpixl). For the backlight, the normal LED rig of SEF-pool was used.

In the previous experiments in which the pattern recognition and image analysis algorithms were applied, an uneven backlight lighting of the test facility was a large problem. A part of each bubble was overexposed while the rest of the bubble was too dark and recognition of the border of the bubbles was sometimes impossible. A new LED rig assembled to SEF-POOL gives more even lighting, and the borders of the bubbles are easily detected, making the pattern recognition easier and the whole procedure more reliable. Unfortunately, the LED rig creates very visible flickering to the videos, which might disturb possible frequency analysis. The possibility to connect the LED rig for pure DC power supply should be considered.

The aperture of 1.4 was chosen for all cases in the SEF-INF3 experiment. Small aperture makes the depth of field limited, but allows to focus the area of the bubbles, making the background blurry. Thus, if the bubbles' path changes off the axis, they will become blurry as well. This, however, is less disturbing in pattern recognition point of view, than too sharp background objects such as swarms of small bubbles on the pool water.

In the experiments from 1 to 9, the frame rate of the left camera was kept constant 3200 fps, while the frame rate of the right camera was modified between 200 fps to 6400 fps. The reference value was 3200 fps. The selected frame rate affects other properties of the camera, especially the amount of the data, that is the length of the recorded video. The larger the frame rate, the shorter the video. If the frame rate is too low, rapid condensation of the steam bubbles may stay unrecognized, which affects for example to the frequency analysis of the condensing bubbles. Too low frame rate skips some bubbles, which makes the condensation frequency lower than with an appropriate frame rate. When comparing different frame rates, 800 fps shows almost all the same bubbles as 3200 fps shows, but some changes of the bubble sizes will be lost. If the calculation time is limited or there is a need for a longer data set, 800 fps would be appropriate, but if there isn't these kinds of limitations, a larger frame rate is recommended. When 1600 fps frame rate was compared to 3200 fps, all bubbles are visible and only a quick change in the bubble size at the beginning is lost. Only fast formation of the bubble can be missed, which might affect the volume evaluations. 1600 fps is a safe choice of frame rate for almost any experiment. This frame rate is appropriate for frequency analysis and also for volume evaluation. The volume evaluation method assumes bubbles to be spherical, which makes its own error to the measurements.

Exposure in photography or filming represents the amount of light that is let to reach the camera sensor. In other words, it is the overall brightness or darkness of the image. In experiments such as SEF-INF3, brightness of the image brings out the surface of the bubbles, which is an important feature in some cases. However, in simplified pattern recognition analysis where only a border of the bubble is the region of the interest, a certain amount of darkness is desirable.

In the SEF-INF3 experiment, different exposures values between 25 μ s to 4999.564 μ s were tested. Figure 2 presents the right camera images in two different frame rates 200 fps and 3200 fps in four different exposures (the experiments 13–18). As can be seen in the figure, the larger exposure rate brings out the surface of the bubble (top right image) when the bubble is detached from the orifice plate, but otherwise all images look quite similar regardless of the exposure value. Before these experiments 13–18, already 12 experiments were made. The pool was full of swarms of small bubbles. This affects much the brightness/darkness level of the images; thus, the change of the exposure value does not make difference. In this case the exposure rate does not change the quality of the images, but in general the exposure rate depends on the system and it is good to test different values at time to time, especially if the experimental set-up has changed.

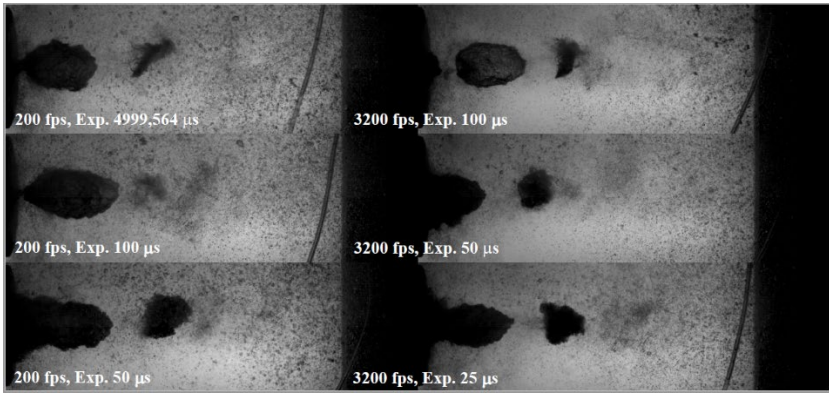


Figure 2. Effect of different exposure values.

In the SEF-INF3 experiment, two different image resolutions were tested: 1216x800 pxl (left camera) and 1280x400 pxl (right camera). Algorithms should always be as efficient as possible, meaning that the calculation time should be appropriate. Images are always cropped as small as possible in the pattern recognition process to save calculation time. If the resolution is too small, the borders of the bubbles contain clear steps and bubbles will lose their round shape. If the resolution is correct, the borders of the bubbles change smoothly.

The pixel/mm ratio is crucial for the detection of the bubbles. The field-of-view (FOV), with a fixed local lens is decided by the distance to the measurement plane. In these cases, there will always be quite a lot of extra area in the images. But if we compare cases where bubble covers 10% of the image area to the cases where bubbles cover more than 80% of the image area, then the large resolution gives more precise recognition for the border area. In SEF-INF3, the resolution of the right camera is more suitable for pattern recognition purposes because it needs less cropping, but otherwise, in this case, the resolution does not matter so much – both resolutions are suitable for the experiment.

Length of the data needed for appropriate results depends on the frame rate and the type of post-processing, in other words, what is calculated. If the frame rate is thousands of frames per second, even less than a second video can be enough. For low frame rates, such as 200 fps, a 5 s video can be too short. 1000 images start to be a suitable number of images, but it is always better if the number of images is larger than that. It is still good to remember that larger number of images means longer calculation time, thus in experiments like SEF-INF3 where there are 36 different cases, the shorter videos are appropriate. For frequency analysis, at least 1 s video with a large enough frame rate is needed. Frequency analysis was not included in this experiment, thus both lengths 2914 and 5536 images were suitable. For frequency analysis purposes 2914 images in the frame rate of 3200 fps would have been inappropriate.

Instead of steam injection, pressurized air injection was also tested in the SEF-INF3 experiment. Similar cases were recorded as were made with steam, using a

single camera. Due to the fixed focal length lens and the air injection system, bubbles remained small. As the shape of the bubble is not spherical, the volume calculations were not tested. Air injection was made from the bottom of the pool to get a better visibility. An example image of the testing is presented in Figure 3. What can be seen is that the new backlight rig offers very even background intensity, and bubbles would be easy to measure if there weren't the swarms of small bubbles as there are with steam injection. This shows that there will always be some limitations, which cannot be changed by the users. With air injection the exposure value also affects more than with steam due to the lack of disturbance. Even though the volume of the bubbles was not calculated due to the random shape of the bubbles, these experiments are suitable when testing the effect of the backlight flickering. At least there are no disturbing extra objects, which would affect the frequency analysis



Figure 3. Test in SEF-POOL with pressurized air.

Wire-mesh sensors

The studies with the axial wire-mesh sensor develop at LUT, named AXE, have been conducted during the previous project in the HIPE test facility. In 2019, a conference paper based on the results of the AXE void fraction measurements in swirling two-phase flow was published and presented in the SWINTH-2019 (the Specialist Workshop on Advanced Instrumentation and Measurement Techniques for Experiments related to Nuclear Reactor Thermal Hydraulics and Severe Accidents) workshop in Livorno, Italy in October 2019 (Telkkä et al., 2019).

The results presented in the paper from the axial sensor measurements with both 30° and 60° swirl generators together with the comparative measurements with the traditional radial WMS (TRAD) reveal that the axial sensor is not able to produce reliable enough void fraction data. The axial sensor produces void fraction values, which are significantly lower than those measured with the TRAD sensor. Also, the shapes of the void fraction profiles differ from the traditional sensor data. The axial sensor produces much more asymmetric void fraction distributions compared to the radial sensor. This results from the intrusive character of the AXE sensor, especially its leading edge, which significantly disturbs the swirling flow.

The previous studies of the performance of the axial sensor with non-swirling flow showed that the AXE sensor was able to produce reliable void-fraction data. In non-swirling flow, the void fraction distributions were qualitatively very similar for both

the axial and radial sensors (Ylönen & Hyvärinen, 2015, Telkkä et al., 2018). It was concluded in the earlier studies that the axial sensor can be applied to the measurement of non-swirling two-phase flows, for the sensor did not cause an irrecoverable redistribution of the flow in the performed tests (Ylönen & Hyvärinen, 2015, Telkkä et al., 2018). The studies presented in the SWINTH-2019 paper clearly indicated that when the two-phase flow is transformed into a swirling flow, the intrusive structure of the sensor becomes significant, and the sensor is not able to produce reliable void fraction data anymore.

Possible procurement and application of a high pressure/temperature capable WMS has been considered. So far, there has not been a need for this kind of technique at LUT.

Optic fibers

The optic fiber technique was tentatively tested in 2019 in the passive heat removal test facility, PASI, in the natural circulation experiment NC-03, which was conducted within the SAFIR2022 PAHE project. The fiber was placed in the water pool of PASI in order to see the temperature profile in the tank. In the testing, the measurement system worked but didn't provide reliable temperature data. The temperature values measured with the fiber were larger than those measured with reference thermocouples (TC). The difference increased as a function of temperature: the higher the temperatures were, the bigger the difference to the TC measurements was. Significant differences were observed.

The reason for the difference between the measurements was considered to be the bends of the thin steel capillary pipes (outer diameter 3 mm), inside of which the fiber was placed. Temperature measurement with the optic fiber is based on thermal expansion of the fiber. The bends affect the expansion of the fiber. Hence, the accuracy of the measurements suffers, since the fiber does not expand purely according to the thermal expansion.

In 2020, the fibers were further tested as a Bachelor's Thesis work (Kinnunen, 2020). The measurement set-up was simpler water pool measurement with both a straight fiber and fibers bent to U-curves. In the work, the effect of the capillary pipe curves of different radii was studied. In addition, the aim was to study the effect of vibration to the measurement accuracy since there was indication from the previous measurements that vibration may affect the results. The vibration was executed by means of shaking the measurement set-up before the measurement. Also, the effect of temperature was studied: all measurements were conducted with cold water ($\sim 10\text{--}20^\circ\text{C}$) and hot water ($\sim 50^\circ\text{C}$). The spatial resolution used in the measurements was 0.65 mm, which is the highest possible with the current system. The measurements were conducted inside the water pool of the HIPE (Horizontal and Inclined Pipe Experiments) test facility.

Two series of measurements were conducted in the work. The first series was done with three fibers: one straight fiber, one fiber with one U-curve with a 97 mm diameter, and one fiber with two U-curves with 97 mm diameters. The second series was done with one fiber with six U-curves with tighter, 43 mm diameters. Each used

fiber was a five-meter-long fiber, and the ends of the fibers were used in the measurements. Thermocouples were used to gain reference temperature data in both measurement series. An example of the measurement results is shown in Figure 4. In the figure, the gray dots are average values of the optic fiber temperature data with the spatial resolution of 0.65 mm. The red dots are the reference thermocouple measurement values. The black dots are the average optic fiber temperature values in the locations of the thermocouples.

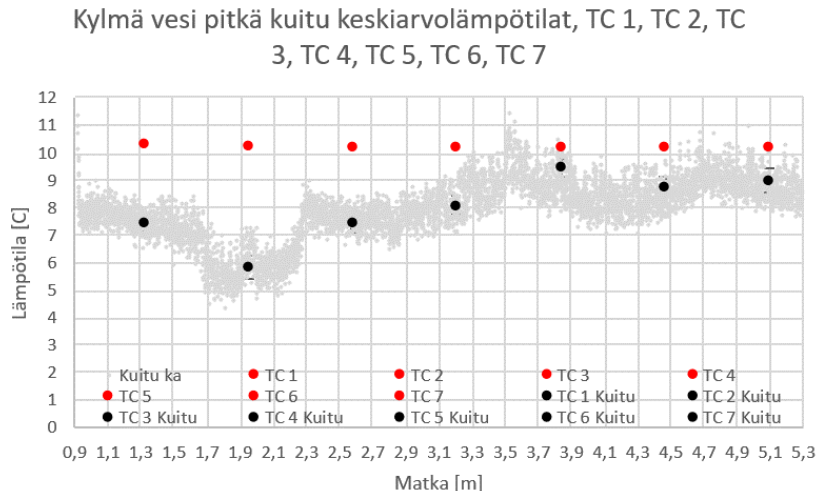


Figure 4. Example of temperature measurement results of optic fiber with six bends in cold water in the HIPE water pool. (Kinnunen, 2020)

The example figure above shows really large differences between the fiber and thermocouple measurements. It also shows that the deviation of the fiber measurement is approximately 2 °C in this case. Further, we can see that the effect of the bends on the measurement result is difficult to interpret from the results.

The gained results showed in general that the fibers produce data, which differs relatively much from the reference thermocouple measurements. Based on the results of the thesis work, there seemed not to be a clear indication on which factors affect the results most (bends, temperature, length of the fiber...). It was concluded that the testing of the fibers must be further continued at least with measurements with different spatial resolutions. In the thesis work, the measurements were conducted only with the maximum resolution, which probably causes larger deviation of the temperature data.

In 2022, testing of the fibers continued. The system was upgraded with new strain-compensated (SC) fibers, which should mitigate the inaccuracy of the results caused by the strain, albeit with lower maximum spatial resolution compared with the traditional fibers. The testing was conducted in the PASI experiments within the EU-funded PASTELS project. The fibers were installed in the PASI facility's water pool with thermocouples that supplied the validation data for the temperature

readings for individual points. One motivation was also to see how the fibers work with higher temperatures nearing 100 °C. Altogether, optic fibers were used in six PASI experiments in 2022, named PAS-01–PAS-05 and PAS-10. Figure 5 shows the schematic installation of the fibers and the elevations of the reference thermocouple measurements in the PASI water pool. Fibers were used in two different configurations: with a straight fiber (red color in Figure 5) and a fiber with one U-bend (yellow color in Figure 5). Testin was done both with old and new fibers.

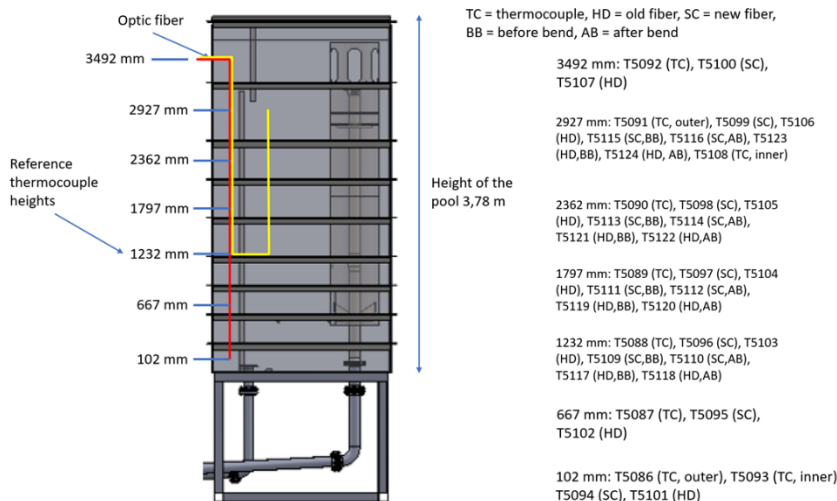


Figure 5. Schematic presentation of the fiber installation and thermocouple elevations in the PASI facility's water pool.

Figure 6 and Figure 7 present examples of the results of the fiber testing. The figures show that on some locations, the strain-compensated fiber measures quite accurately the same data as the reference thermocouple, whereas on some locations there are relatively big deviations between the measurements. Based on the results it seems to be arbitrary where the inaccuracies exist. Thus, at the moment it is recommended to always use reference measurements when applying the fibers. In general, temperature profiles and fluctuations are captured well with both old and new SC fibers. For very small fluctuations, the noise of SC fiber data may be so strong that the fiber is not capable to detect the possible temperature fluctuations. In general, LUT sees big potential of the optic fiber technique as the fibers offer possibility to measure 1D distribution of temperatures with high spatial resolution. The studies related to the fibers will continue in the future.

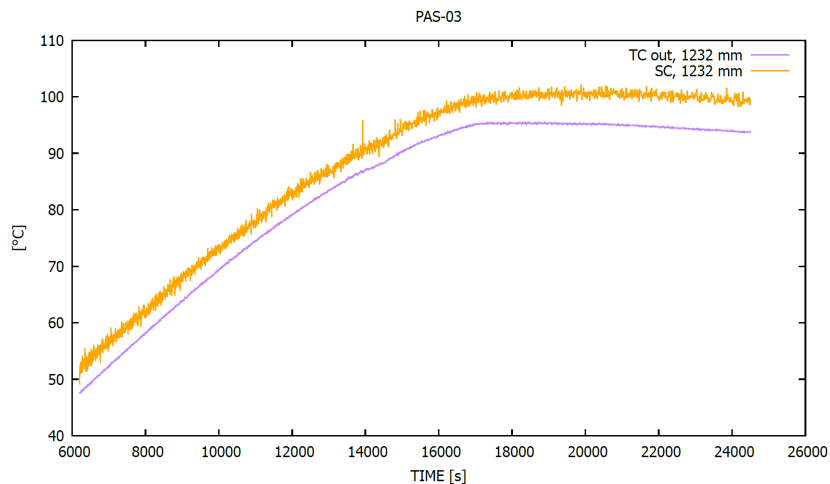


Figure 6. Data of straight SC fiber and reference thermocouple from elevation 1232 mm during the PAS-03 test, temporal resolution 1/1.4 Hz.

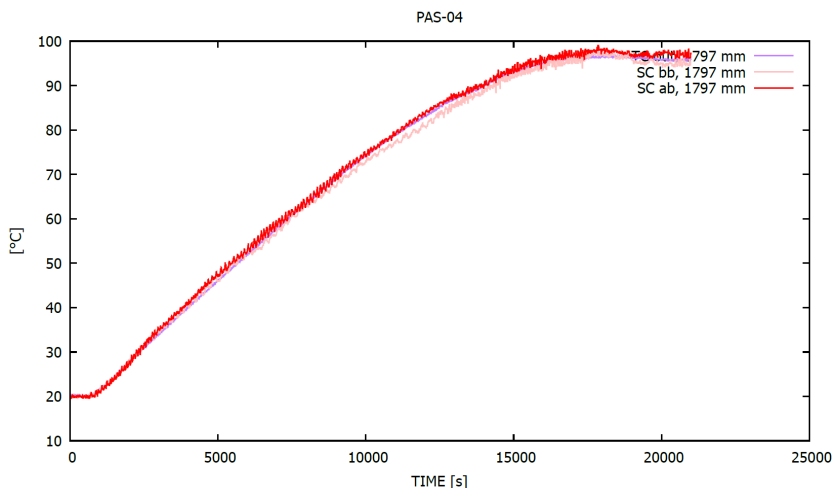


Figure 7. Data of bent SC fiber from before and after the bend, and reference thermocouple data from elevation 1797 mm during the PAS-04 test, temporal resolution 1/1.4 Hz.

Ultrasonic flow meters

Ultrasonic flow meters were initially tested in a PASI natural circulation experiment NC-03 in 2019. In these measurements, one flow meter was attached on the outer surface of each of the 15 PASI heat exchange tubes in the tube parts outside the

PASI containment vessel. The results of the testing in 2019 were not convincing. Figure 8 shows the results of these measurements. The figure presents the PASI loop (downcomer) flow rate and the combined flow rates of the 15 ultrasonic flow meters during the whole duration of the NC-03 experiment. The period from the beginning to approximately 10 000 s was single-phase natural circulation with a steady loop flow rate. From ~10 000 s begins the phase of two-phase flow natural circulation, during which the loop flow strongly oscillates

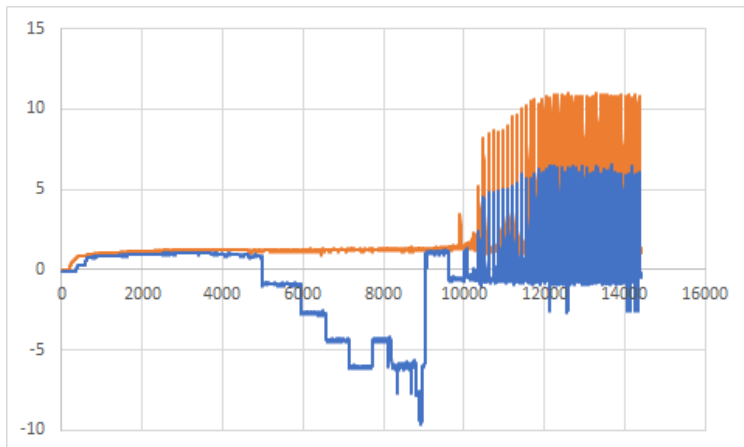


Figure 8. PASI downcomer flow rate (orange curve) [kg/s] and the combined flow rates of the 15 ultrasonic flow meters (blue curve) [kg/s] as a function of time during the PASI NC-03 experiment.

The results show that the ultrasonic flow meters provided relatively reliable flow rate data during the first approximately 5000 seconds of the NC-03 experiment. The sum of the measured flow rates of the ultrasonic flow meters almost equals to the PASI downcomer flowrate measured with a magnetic flow meter. After that, there are significant differences in the results between the measurement techniques. The reason for this is presumably the fact that the flow rates after 5000 s were between the laminar and turbulent flow areas. The ultrasonic flow measuring technique assumes the measured flow to be either laminar or turbulent, and the flow areas between those provide imprecise flow rate data.

The testing of the ultrasonic flow meters was continued in 2020 in a separate test set-up to prepare for the use in the annular downcomer of the MOTEL test facility. A mock-up of the annular downcomer space, a rectangular flow channel with a 3.5 cm x 51.5 cm cross-sectional area, was attached to the HIPE test facility water tank. The water was circulated from the water tank to the flow channel and back. The testing set-up is presented in Figure 9. The flow meter was attached on the surface of the flow channel.



Figure 9. Ultrasonic flow meter testing set-up attached to the HIPE test facility.

The testing was conducted in atmospheric pressure and temperature. The challenge in this measurement configuration is that the ultrasonic flow meter assumes circular flow channel (the diameter of the channel is put in the meter before measuring). Therefore, a correction factor has to be used in order to correct the measurement data to correspond the situation in the annular downcomer space. The effect of the curvature of the MOTEL downcomer was considered negligible. Measurements were conducted on various lateral locations of the flow channel.

The reference flow velocity data was measured from the HIPE test facility flow channel as volumetric flow. This was converted into velocity, assuming that the flow is evenly distributed inside the mock-up flow channel. This was one uncertainty in this study since there was no information on how the flow was distributed in the channel.

Based on the results of this testing, it was difficult to draw clear conclusions on how accurately the ultrasonic flow meters measure the flow velocity. At some velocity levels the correction factor corrected the measured velocity to correspond the reference velocity. Nevertheless, at some velocity levels the effect of the correction factor was opposite – the corrected values differed even more from the reference velocity than the data before the correction. The results seemed to differ according to the lateral location of the channel, too. In addition, as mentioned above, the reference velocity was very much assumed/approximated, thus any clear conclusions were hard to draw. These initial results were promising, though, because the magnitude of the measurement results seemed to be correct.

The testing of the flow meters continued in 2021 as a Bachelor's Thesis work (Saira, 2021). The original purpose of the study was to measure reference velocity data from the mockup channel with the PIV system in order to verify the

measurement result of the ultrasonic flow meter in a rectangular flow channel for the use in MOTEL annular downcomer. The original thesis was evolved along the process as the measurements and the validation methods developed, and thus the research question slightly changed during the study.

For the measurements, The front wall and part of the side of the mock-up channel were made transparent for the PIV measurements by replacing steel with transparent polycarbonate sheet. The cross section of the channel was rectangular with a 497 mm width and 35 mm depth mimicking the dimensions of the MOTEL annular downcomer. The PIV measurement were conducted as a planar-PIV setup with one camera, a double-pulsed Nd:YAG laser and PMMA-RhB polymer particles. The third flow measurement in the study was the magnetic flow meter in the inlet pipe of the mock-up channel. This measured the volume flow coming from the HIPE water tank into the mock-up channel. From the volume flow data, an approximated average flow velocity of the mock-up channel was calculated using the dimensions of the rectangular channel and assuming that the flow would be distributed evenly inside the channel and assuming a constant channel cross-sectional area.

In the results of the work, the results of the PIV data, the ultrasonic measurement results from the measurements through the steel wall, and the velocity data derived from the magnetic flow meter measurements were compared against each other. The results showed that the ultrasonic flow meter is able to provide reliable enough velocity data from this kind of flow channel application. Overall, based on the study it was concluded that the ultrasonic flow meter can be applied to MOTEL downcomer and it is able to provide velocity data with an adequate accuracy. Saira (2021) provides more detailed description of the conducted study and the results.

Maintenance of test facilities

The WP2 of IDEAL includes continuous maintenance work in the laboratory, as well as the yearly maintenance actions, which are carried out in the laboratory in order to ensure availability of the test facilities for thermal hydraulic experiments that are conducted within other research projects.

Annual outages have been carried out every summer, including calibrations of all the important measurements. Periodical pressure vessel inspections have been done according to the pressure equipment legislation.

In 2019, the PASI facility steam supply system was renewed. In the PASI experiments conducted earlier, steam supply to the containment vessel was executed by means of an external steam supply system. In the natural circulation experiment NC-03 of the SAFIR2022 PAHE project, the used external system was able to use only a part of its nominal power for the steam production, and it was not able to produce completely dry steam. Hence, it was decided that in the future PASI experiments, this kind of steam supply system will not be used, but the steam for the experiments will be produced with the PACTEL facility. During the summer 2019, a steam line was built from PACTEL, which is located in the old LUT

laboratory building, to PASI, which is located in the new laboratory building. Hence, there is no need for a rental, moveable steam supply system anymore.

In 2020, The main safety valve of the PACTEL facility was changed to new one. This was required in the previous pressure vessel inspection. During this operation, the condition of the accompanying rupture disc was inspected and found to be intact. This inspection was also done for the rupture disc of the pressurizer.

Part of the compressed air system was renewed, and new shutoff valves were installed in order to minimize the use of compressed air during non-activity periods of the PACTEL facility. Also, some of the valve actuators and pilot valves were either fixed or swapped for new components. These modifications were made to significantly reduce the amount of compressed air wasted.

In WP2, also 3D laser scanning of the PASI test facility was conducted in 2020. The purpose of this was that with the results of the scanning the accurate pipeline diameters for the test facility in the SolidWorks model would be gained. The heat exchanger and the riser and downcomer lines of PASI were scanned, and the results are not fully convincing. It seems that when scanning bright surfaces with lots of "interference sources" (thermo couple wires etc.), the result is not perfect. The gained data should be processed more in order to use it to support the design and scaling of test facilities.

The work package 2 included also creating of a component stock in the laboratory. The idea behind the component stock is to ensure the functionality of the existing test facilities and thus reduce the off-production and repairs time in case of component breaks, to ensure the laboratory's ability to construct new testing systems that require components with long delivery times without any delays and to have a variety of sensors for different applications with different working principles. The components include e.g. valves and gauges for high pressures and temperatures.

The upgrade of power transformers has been prepared for several years in order to increase the electrical power available for the thermal hydraulic experiments. Currently the maximum power available is 1 MW, and the aim is to increase the power into approximately 2.5 MW. The upgrade process has been delayed from the original schedule due to the complexity of the process. The options for the upgrade have been studied in the many organizations involved. In addition to the three affected laboratories of LUT School of Energy Systems, also Suomen Yliopistokiinteistöt as the owner of the buildings, Lappeenrannan Energia as the power provider, as well as electrical system design consultants have been part of the process. In 2019, new initiation concerning the power upgrade was made for the 2019 LUT University's internal investment program. The options to execute the upgrade were either to add a new power transformer or replace the old transformer by a new bigger one. The process proceeded a bit in 2020. The LUT investment program granted 150 k€ for the task. The preliminary estimation of the costs (used in the LUT investment application) was 200 k€. 50 k€ was budgeted in IDEAL for 2021 to complement the LUT investment funding.

A tendering process was executed in the spring 2021, but as a result only one offer was received, which was way too expensive to be realized with the budget.

The biggest cost is the new transformer station that must be built. The issue was re-studied with the LUT lab team, a consultant, and a representative from LUT Facility Services. It was decided that the project will be executed in small steps.

The required local electric switchboard was tendered and ordered in the end of 2021. The remaining budget of IDEAL 2021 was reserved for this, and the 2021 project was allowed to be continued to June 2022. The switchboard was delivered to LUT in April 2022. The costs were covered from the remaining IDEAL 2021 budget and partly from the LUT Investment Project. The execution of the other parts of the power upgrade project will be done within SAFER2028, if a suitable way is found, or with some other funding. The power upgrade would still require the building of a new transformer station and the cabling from the transformer to the laboratory. The transformer station, particularly, would be a very large investment in the current world situation. Thus, this complex project remains unfinished.

The tests performed with the PACTEL facility have been hampered by a loss of inventory from the primary side during the tests. Even though this has not been detrimental to the work performed, this has been a constant source of questions from the end users of the test data. In the spring 2021, a series of tests were designed and executed in order to find out where and how much the facility really leaks. It turned out that actually the leakage paths in the facility are numerous, from mechanical faults such as leaking gaskets or pipe connectors, to complex problems such as insufficient clamping forces in valves that start leaking only at higher pressure levels. Some of these leakages could be observed by the laboratory staff as steam trails or puddles of water on the floor and are easily rectified. Nevertheless, most of the problems are hidden within the complex pipework inside the facility. The locations of the leakages are the upper plenum bleed valve, lower plenum inventory reduction line, the HPIS system, two horizontal steam generators, and some other sources. The valve seals in the upper plenum bleed valve, lower plenum drain valve and HPIS were renewed, and hence the leakage through these orifices was reduced to practically zero. Unfortunately, the leaks in one of the steam generators proved much harder to fix. Couple of the leaking pipes were welded, but some of the leaks in horizontal SG2 were in inaccessible places so it was blanked off from the PACTEL primary loop and was put in a long-time storage.

Construction of a steam line from the MOTEL test facility to PASI in the new laboratory was planned and mostly executed in 2022. This will offer a steam source in the new laboratory for the PASI experiments and other possible purposes in the future. The capacity of the pipeline is designed for the MOTEL primary pressure/temperature values: 40 bar/250 °C. At the moment, the swap-tank limits the steam capacity to 10 bar/180 °C. The construction work was done in late 2022 and will be finalized in early 2023. The welding work of the supports was done by the resources of LUT Voima. Also external work force was required. The steam line will help the conduction of the EU PASTELS PASI experiments, which will continue in 2022 and 2023. Further PASI experiments are planned also for the SAFER2028 programme for 2024-2025. Sketch of the pipeline is presented in Figure 10.

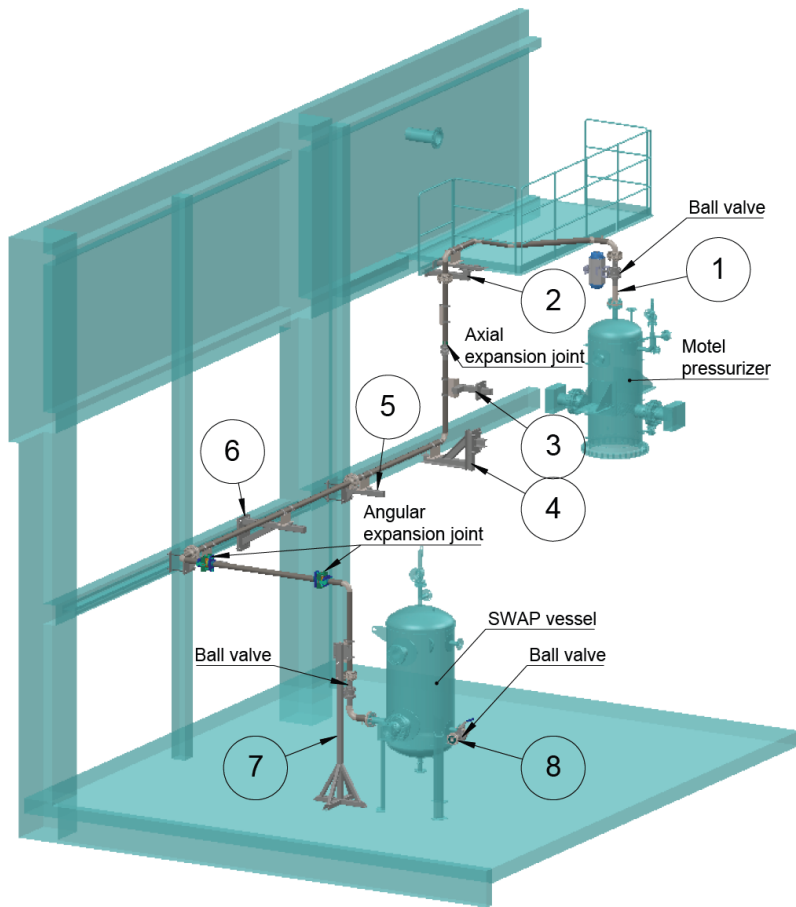


Figure 10. Sketch of the steam line from MOTEL to PASI (swap vessel).

Process control and computational systems

The third work package includes renewal of the laboratory's field and process instrumentation, upgrade of the high-performance computing (HPC) infrastructure and enlargement of the available storage space for the measurement and calculation data.

The field instrumentation of the PWR PACTEL facility was renewed during SAFIR2022. In 2019, the necessary components were purchased: a safety valve to the PWR PACTEL primary side, a Coriolis flow meter to the accumulator line, a Vortex flow meter to the downcomer line, three pressure transducers and twelve differential pressure transducers. Installations were done during the three last years of the project.

The amount of data from the experiments in the LUT laboratory has been expanding due to advanced and high-speed measurement capabilities. Similarly, the use of modern computational tools, such as CFD, to support and supplement experiments produces large data sets. The current EDS storage system is not suitable for large data files. Thus, enlargement of the data storage space was planned and executed within the IDEAL project. The storage of data will be done tripartite in the future: the first stage is the data space of the measurement computers and HPC servers; the second stage for large amounts of data will be a new centralized data space located in conjunction of the HPC servers; the third stage is the EDS system for the traditional test data plus a new FairData cloud service for advanced data to be stored for longer time. This system is illustrated in Figure 11.

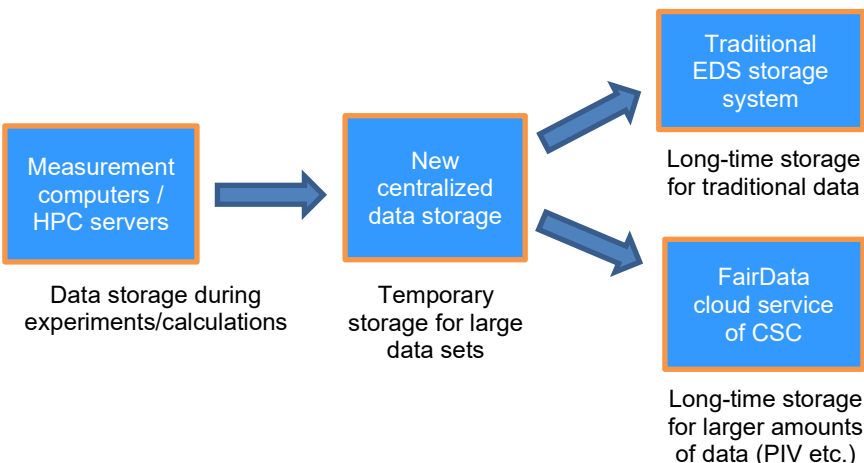


Figure 11. Data storage system of the LUT laboratory.

In addition, upgrade of the HPC infrastructure was realized jointly within IDEAL and the internal investment project of LUT. This includes increasing the capacities of the cooling and power supply systems and replacing outdated computing hardware with newer. IDEAL contributed to the planning of the overall work and to a part of the computing hardware investment. Planning of the server room modifications including cooling and power supply systems and the corresponding tendering process for these contracts was completed in 2020. The construction works and acquisition of cooling and UPS equipment realized with LUT internal budget were completed by the end of 2020. New computing hardware and the new data storage servers were purchased in 2020. The installation work of the new servers was done later during the project. Filing of the old test data was also included in the task of data storage space enlargement. There was lots of data from the previous decades that were archived. Within the task, the EDS database of LUT was upgraded in 2021

to use the newest supported platform (.NET Core 5) and to better support external storages.

Development of the MOTEI test facility

The WP4 deals with the development of the new modular integral test facility, MOTEI (MODular TEst Loop). The first version of the MOTEI test facility is a model of a small modular reactor (SMR), and the design resembles to that of NuScale's SMR. Figure 12 presents a general view of MOTEI. The first configuration of MOTEI is comprised of three interchangeable modules: the core module, the steam generator and the pressurizer.

Regarding the design of MOTEI, the design of the heater element (core module) was emphasized, in particular. Traditionally, in integral test facilities the heater element is long and thin in order to have the height scaling 1:1 compared to the reference power plant in question. With MOTEI, the intention was to break this rule. The core section of MOTEI was made wider and shorter than usually in order to study both axial and radial flow phenomena inside the core. The SMR design enabled to design the core this way.

The fuel rod bundle geometry in MOTEI does not accurately model any existing plant type, although MOTEI is loosely based on NuScale's SMR design. The MOTEI core is a general representation of a fuel rod bundle. The core is comprised of 132 electrically heated heating rods and 16 instrumentation rods. The heated length of a single heating rod is 1830 mm. The diameter of a single rod is 19.05 mm, and the maximum heating power of one rod is 7.5 kW. Hence, the maximum heating power of the facility is 990 kW. The axial power distribution of the core is cosine-shaped, likewise in real NPP cores. The radial power distribution of the core is adjustable with 12 power segments. The arrangement of the heating rods is in a rectangular grid, which is more practical concerning instrumentation and investigation of flow phenomena inside the core. The core module of the test facility can be swapped to a different setup, if needed. Thus, it can be replaced in the future with a core representing a specific reactor core design.

An essential and unique feature of NuScale's SMR design is the helical coil steam generator, whose behavior is one of the key interests regarding the experimental activities with MOTEI. A special characteristic of this type of steam generator is that boiling happens inside the steam generator tubes, whereas the primary water flows outside the tubes. The MOTEI steam generator is comprised of 16 steam generator tubes. Half of the tubes circulate clockwise and the other half counterclockwise.

The pressurizer is located at the top part of the test facility. The pressurizer has two heating elements (30 kW heating power each) to adjust the pressure inside the test facility. There is a relief valve at the top of the pressurizer.

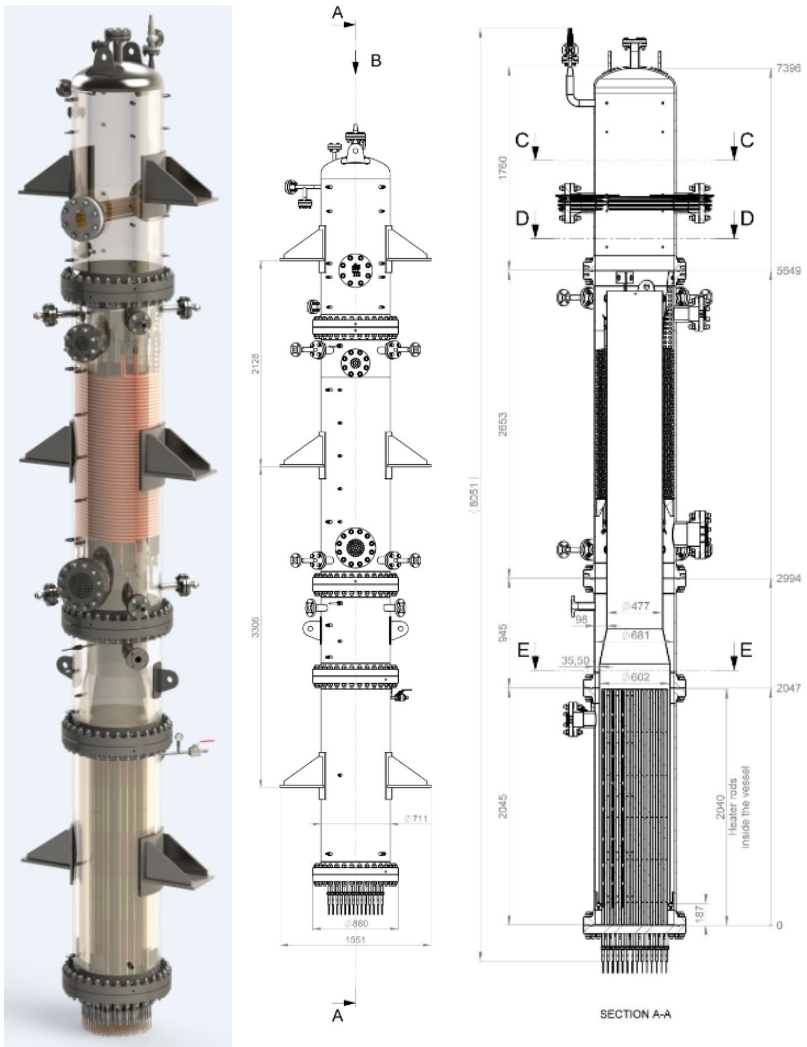


Figure 12. General view and the dimensions of the MOTEL test facility. The three changeable modules can be detected: core module, steam generator and pressurizer.

The first version of MOTEL represents a SMR; hence, the whole primary circuit is located inside a single pressure vessel. The system operates by natural circulation, and thus no pumps are needed to circulate the primary water. As the water heats up in the core section, it rises in the riser located in the center of the vessel. Once the heated water reaches the top of the riser, it flows down inside the annular downcomer space through the steam generator tubes where the heat is transferred to the secondary side. After the SG the cooled water continues in the annular

downcomer located in the outer edge of the vessel. The cooler water has a higher density, and it is driven by gravity to the bottom of the vessel, where the water heats up again in the core section. The secondary side water is pumped into the steam generator tubes where the boiling happens. The secondary water enters the SG tubes through four inlet collectors. Four SG tubes are connected to each collector. The generated steam is directed out of the test facility via four outlet collectors, respectively. Feedwater is highly purified, and its conductivity is measured online to prevent the build-up of limescale.

The total height of the MOTEL test facility is 7.7 m, and the diameter of the vessel is approximately 700 mm. The riser inner diameter is 477 mm, and the width of the annular downcomer is 100 mm. The design pressure of the facility is 40 bar, and the design temperature is 250 °C. Table 1 summarizes the main characteristics of the facility.

Table 1. Main characteristics of the MOTEL test facility.

Characteristics	MOTEL
Total height [m]	7.7
Main diameter [mm]	~700
Maximum primary pressure [bar]	40
Maximum secondary pressure [bar]	40
Maximum temperature [°C]	250
Number of helical steam generator tubes	16
Maximum heating power [kW]	990
Number of heating rods	132
Heated length of the heating rods [mm]	1830
Diameter of the heating rods [mm]	19.05
Number of instrumentation rods	16
Number of dummy rods	145
Main material of the components	Stainless steel
Insulation material / thickness [mm]	Mineral wool / 120

In 2019, the MOTEL framework and the facility itself were erected in the laboratory. All the components were assembled, and instrumentation was installed. The final insulation and pipeline/valve works were done in 2020.

The shakedown tests of MOTEL were conducted in December 2020. The purpose of these tests was to ensure that all the facility systems including the process control and data acquisition systems work as expected. In the shakedown test, the power feed systems and the steam generator operation were tested. In addition, the functioning of the measurement systems was checked.

After the shakedown test, the official commissioning test of MOTEL was conducted. This test can be considered as a second part of the shakedown tests. In the commissioning test, the operation of the pressure-related safety equipment

as mandated by the Finnish law was tested. The safety automation against over-pressurization of the facility as well as the core overheating protection system were tested. Kotro et al. (2020) present more detailed description and the results of the MOTEL shakedown tests.

The characterizing experiments of MOTEL were conducted in 2021. These included the pressure loss experiments, the heat loss experiment, and an experiment characterizing the natural circulation – i.e. the general behavior – of the facility.

The pressure loss experiment was conducted in four stages. In each experiment, the facility was heated with a fixed power level. Power levels were 250 kW, 500 kW, 750 kW and 1000 kW. The starting temperature in the facility was approximately 30–40 °C and the heating was terminated when the facility reached 70–80 °C. Higher temperatures were tried but boiling in the core started affecting the measurement readings and therefore this approach was scrapped. The water inventory in the facility was kept at almost full. This increased the thermal capacity of the system and allowed longer measurement periods and more data points for each stage. The pressure losses calculated from the test data are presented in Figure 13. The differential pressure measurements used in the testing are presented in Figure 14. Results show relatively small pressure losses for the facility. Clearly the highest pressure loss was measured over the steam generator.

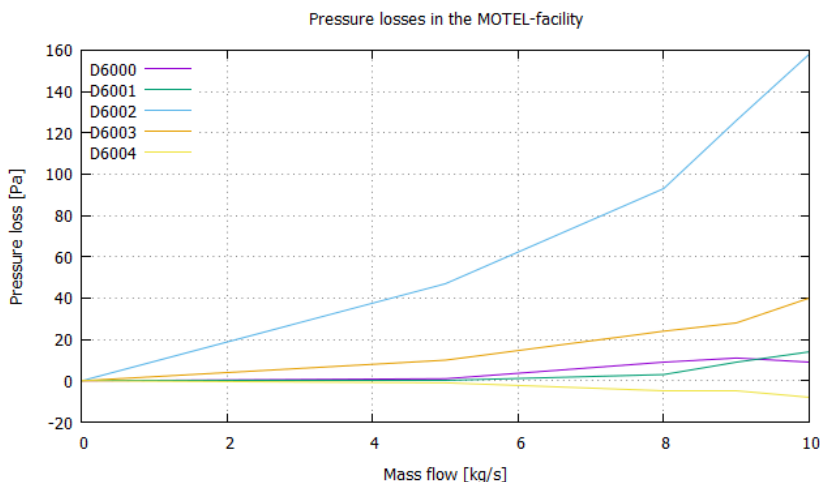


Figure 13. Pressure losses in the MOTEL facility.

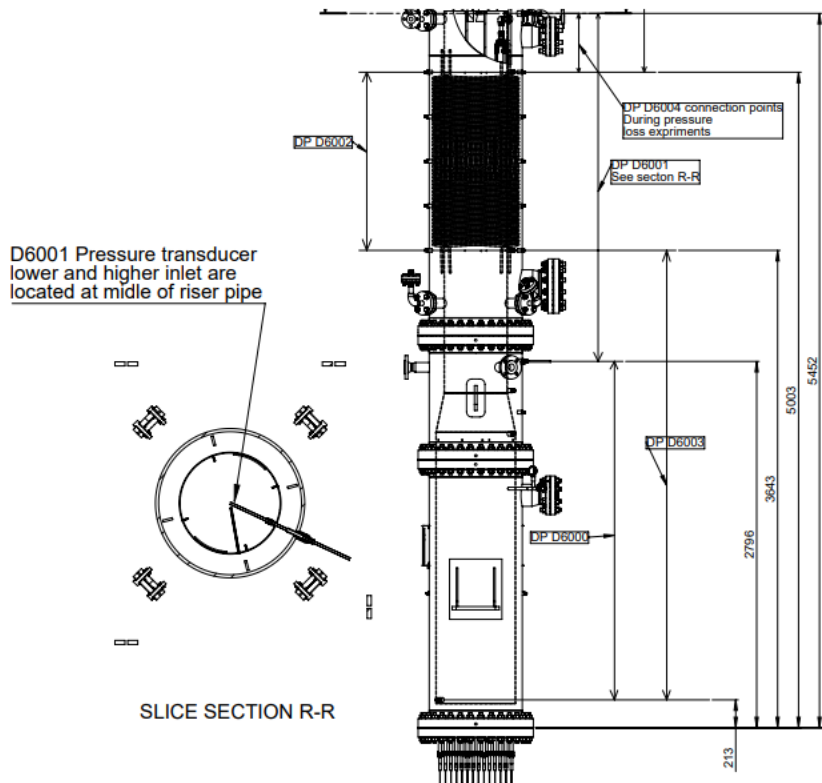


Figure 14. Differential pressure measurements used in the pressure loss experiment.

The heat losses in the MOTEL facility were measured in the spring of 2021. The total duration of the heat loss experiment was roughly one week. The heating phase lasted a few hours, and the rest of the time was spent cooling down the facility. Temperature range was roughly from 20 °C to 240 °C. The cooling phase was cut short as the temperature after a full week's worth of cooling was still around 60 °C. The primary side averaged temperature is presented in Figure 15.

Heat losses can be calculated with multiple different methods. Since the MOTEL facility is quite simple in its construction, the calculation method was chosen to be the Newton's cooling law-based method. Figure 16 presents the calculated MOTEL heat loss as a function of temperature. The figure also presents the lower and upper error limits of the heat loss calculation. The determined heat losses were relatively small, being a few kilowatts depending on the temperature.

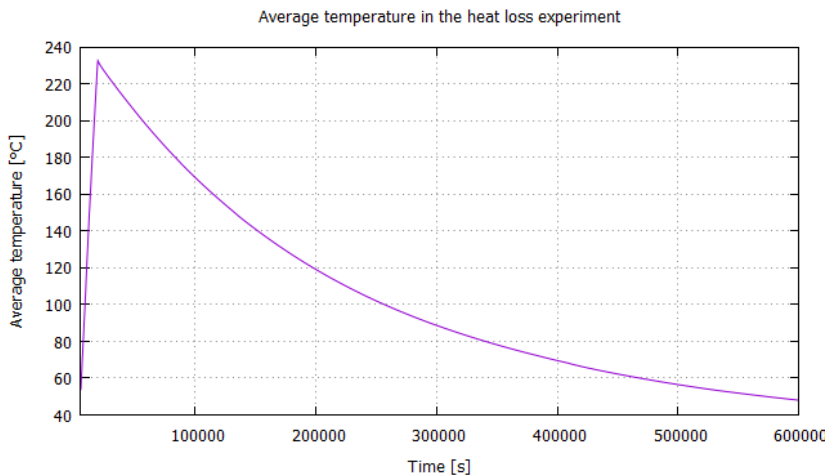


Figure 15. MOTEI primary side average temperature during the heat loss experiment.

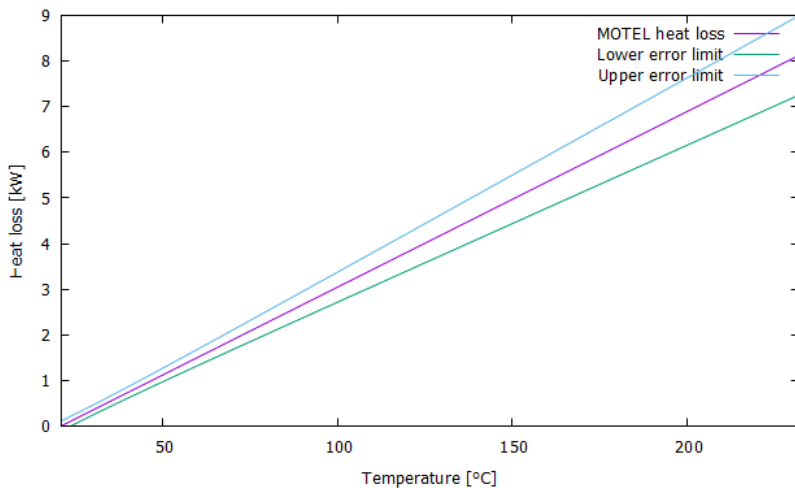


Figure 16. MOTEI heat loss as a function of temperature.

The natural circulation experiment was done in the spring of 2021. The purpose of the experiment was to get data on normal operating pressures and temperatures and to test the behavior of the system with stepwise changes to the core power and secondary pressure. The experiment consisted of four steady-state steps at 250 kW, 500 kW, 750 kW and 1000 kW power levels and three transients between these levels. In addition, there was a power transient from 1000 kW to 250 kW, secondary

pressure transient from 20 bar to 10 bar and finally a reduction of steam generator capacity. These steps are shown in Figure 17.

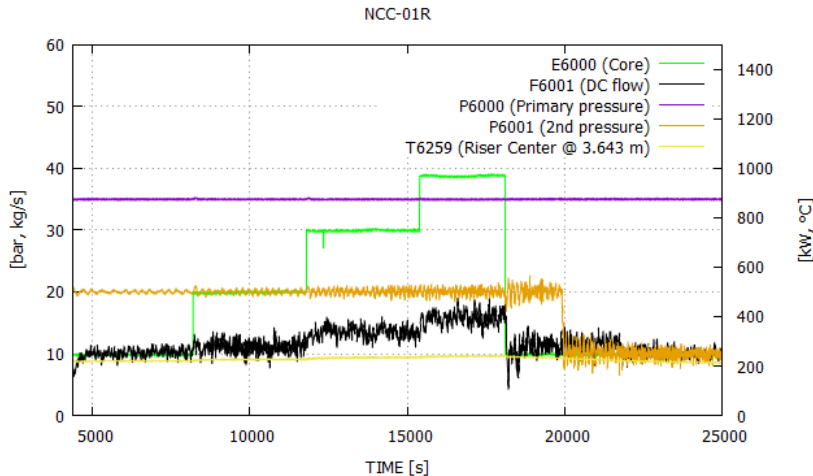


Figure 17. General behavior of MOTEL during the natural circulation experiment.

Figure 18 presents an example result from the experiment, including a secondary side temperature data inside one steam generator tube during the 1-MW steady-state step. The figure shows a strong oscillating behavior of the secondary side temperature. There was fluctuation of the primary flow and the secondary pressure, too, as seen in Figure 17.

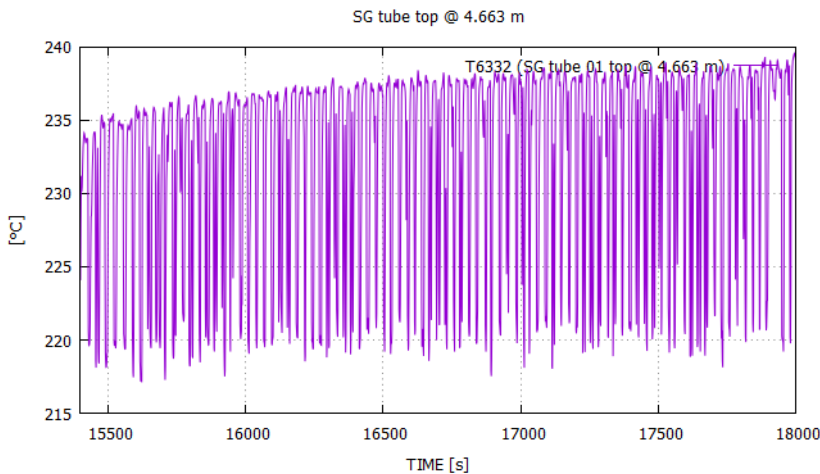


Figure 18. Single secondary side temperature during the 1-MW step.

Telkkä & Räsänen (2021) present more detailed description of the conduction and the results of the MOTEL characterizing experiments.

After MOTEL was taken into operation in the IDEAL project, it has been utilized within the EU-funded McSAFER project to produce validation data for system, CFD and subchannel codes.

Project management

The work package 5 includes the tasks related to the project management and participation to the reference group meetings and seminars. Also, international co-operation activities are a part of the work package.

International co-operation is essentially fulfilled by taking part in SILENCE, an international network for owners of thermal hydraulic test facilities all around the world. Networking and maintaining good communication with other test facility operators is very important and may produce valuable co-operations and participations to the international research projects. In June 2019, three researchers from LUT attended the SILENCE network meeting, which was held at LUT University, Lappeenranta. In 2020, the meeting was originally scheduled for March, but due to the worldwide Covid-19 situation, it was postponed and arranged as a remote meeting in June. In 2021, there were two meetings, both of them arranged as remote meetings. In 2022, there were also two meetings; one remotely and one meeting in Aix-en-Provence, France.

The SILENCE meetings in 2021 revealed that there is an international interest in experimental studies related to critical flow, especially measuring of two-phase critical flow. LUT has participated in the discussions, and in 2022 LUT launched the CRITFLO project with a literature survey on the issue. The international interest within SILENCE may lead to some kind of collaboration on critical flow studies. Anyway, LUT will continue the critical flow studies in the C-FLOW project within the SAFER2028 programme.

Acknowledgements

The Finnish Research Program on Nuclear Power Plant Safety 2019–2022 (SAFIR2022) has provided the funding for the IDEAL project.

The design and construction of the MOTEL test facility were funded partly with the Finnish Academy of Sciences.

References

- Hujala, E., Tanskanen, V., Patel, G. & Hyvärinen, J. 2019. Image analysis of bubbling mode condensation oscillations in horizontal saprger. Proceedings of the 18th International Topical Meeting on Nuclear Reactor Thermal Hydraulics (NURETH-18), Portland, U.S., August 18-23, 2019. 12 p.

- Hujala, E. 2019. Quantification of large steam bubble oscillations and chugging using image analysis. Doctoral dissertation, LUT University, 2019.
- Kinnunen, S. 2020. 1D temperature distribution measuring in the HIPE test facility water tank with fiber optic cable. Bachelor's Thesis, LUT University, 2020.
- Kotro, E., Pyy, L., Räsänen, A. & Telkkä, J. 2020. Shakedown tests of MOTEL. Research Report IDEAL 2/2020, LUT University, Nuclear Engineering, 2020. 27 p.
- Patel, G., Hujala, E., Puustinen, M. & Hyvärinen, J. 2022. Modelling of Horizontal Steam Injection in a Water Pool. Proceedings of the 19th International Topical Meeting on Nuclear Reactor Thermal Hydraulics (NURETH-19), Brussels, Belgium, March 6-11, 2022. 15
- Saira, J. 2021. Ultraääänivirtausmittauksen validointi PIV-mittauksella MOTEL-koelaitteiston alasmenotilan koemallissa. Bachelor's Thesis, LUT University, 2021.
- Telkkä, J. & Räsänen, A. 2021. MOTEL characterizing experiments. Research Report IDEAL 2/2021, LUT University, Nuclear Engineering, 2021. 38 p.
- Telkkä, J., Jämsén, S. & Hyvärinen, J. 2019. Defining void fraction with axial wire-mesh sensor in a swirling two-phase flow. Proceedings of the Specialist Workshop on Advanced Instrumentation and Measurement Techniques for Experiments related to Nuclear Reactor Thermal Hydraulics and Severe Accidents (SWINTH-2019), Livorno, Italy, October 22-25, 2019. 16 p.
- Telkkä, J., Ylönen, A., Hyvärinen, J. & Varju, T. 2018. Estimation of velocity fields from the axial wire-mesh sensor data. Nuclear Engineering and Design 336 (2018), 34-44. 11 p.
- Ylönen, A. & Hyvärinen, J. 2015. Study of Two-Phase Pipe Flow using the Axial Wire-Mesh Sensor. Proceedings of the 16th International Topical Meeting on Nuclear Reactor Thermal Hydraulics (NURETH-16), Chicago, U.S., August 30-September 4, 2015. 10 p.

9.3 Participation in the Jules Horowitz Reactor Project (JHR2022)

Ville Tulkki¹, Jussi Peltonen¹, Pekka Moilanen¹, Seppo Hillberg¹, Caitlin Huotilainen¹, Petri Kinnunen¹

VTT Technical Research Centre of Finland Ltd
P.O. Box 1000, FI-02044 Espoo

Abstract

JHR2022 project is responsible for the Finnish collaboration in the Jules Horowitz Reactor international working groups as well as other associated OECD/NEA's international irradiation experiment frameworks, Halden Programme Group and FIDES. The working groups are planning the future operation of Jules Horowitz Reactor and fostering scientific collaboration between the consortium parties, the main part of the Halden Program Group activities during this period has been to safeguard the 60 years worth of experimental data to end users, and the FIDES framework has been initiated.

JHR2022 also has enabled the further development of Melodie II biaxial creep device as well as two secondments to CEA Cadarache which have created long term research collaborations.

Introduction

Over the past forty years, materials testing reactors (MTR) in Europe have provided essential and invaluable support to the nuclear power plant community and nuclear industry. They have played an important role in the development and qualification of both materials and nuclear fuel used in today's nuclear power plants (NPP), along with ensuring the continued safety in current and future reactor concept designs. As the existing fleet of MTRs continues to age, they will face an increasing probability of shut down due to outdated safety standards and experimental capabilities that are no longer able to respond to today's increasing demands and requirements. The only MTR under construction in Europe is the Jules Horowitz Reactor (JHR) at CEA in Cadarache, France. The JHR has been labeled as a European Strategic Forum Research Infrastructure (ESFRI) since 2008 and will become an important part of European nuclear research infrastructures (NRI) in the coming years. Finland is participating in the construction of the JHR with at 2% in-kind contribution, which includes the delivery of several experimental devices to serve the needs of the JHR and the nuclear community.

The JHR2022 project is comprised of four work packages (WP). WP1 focusses on participation in the JHR Working Groups (WG) and international collaboration activities. WP2 focuses on materials investigations, including MeLoDIE II developments and MeLoDIE II's role in the OECD/NEA Framework Programme for

In-pile Fuel and Materials Irradiation Experiments (FIDES), along with the JHR Archive Material Programme (JAM). WP3 focuses on nuclear fuel and, more specifically, the reporting from the secondee exchange at CEA-Cadarache. WP4 includes all project management activities.

International activities

In the JHR2022 project, participation in the materials (MWG), fuel (FWG) and technology (TWG) working groups of the JHR consortium took place. The annual technical meetings were participated, as well as individual working group meetings. During the covid pandemic restrictions the meetings were held as telemeetings. The working groups discussed research needs, were given updates on the reactor construction projects, and prepared research project proposals for projects that would build up the community competences prior to the startup of the reactor.

The OECD/NEA Framework for In-pile Fuel and Materials Irradiation Experiments (FIDES) preparation was participated in. The framework started in May 2021. Several experimental projects for the new framework, termed Joint Experimental Programmes (JEEPs), have been initiated. The initiated JEEPs include the P2M project (tests in BR2 reactor in Belgium and PIE investigations at CEA), and the INCA project (in-pile creep studies of advanced technology fuel (ATF) claddings at the LVR-15 reactor in Czech Republic). Finland is participating in the INCA project. In 2021, the (i) FIDES Technical Advisory Board meeting and the (ii) INCA Project Workshop were organized virtually and attended by project members.

Participation in the Halden Reactor Programme Group meetings was part of the project. These meetings were held twice a year. For 2022, V. Tulkki / VTT acted as the chair of Halden Programme Group.

In addition, two secondee exchange to CEA-Cadarache took place. First was from October 2019 – March 2020 with the focus on JHR irradiation test device inspection methods, specifically initiating how and where the inspections take place. The irradiation test devices are inserted in the vicinity of the reactor core and contain material or fuel samples. According to French regulation, JHR irradiation test devices must undergo a periodic non-destructive inspection every 40 months. Select inspection methods were evaluated and the focus of this secondee exchange was on ultrasonic (volumetric) and eddy current (surface C-scan) inspection methods. The second exchange to CEA-Cadarache took place from September – December 2021 with the focus on JHR reactor's modelling activities. Peltonen developed a Serpent model of JHR reactor core and reflector area, compared the simulation results to CEA's TRITON-4 results and investigated the neutron flux of OCCITANE irradiation capsule. The work was reported in scientific publications in 2022. The work continued with further examinations of irradiation conditions of JHR.

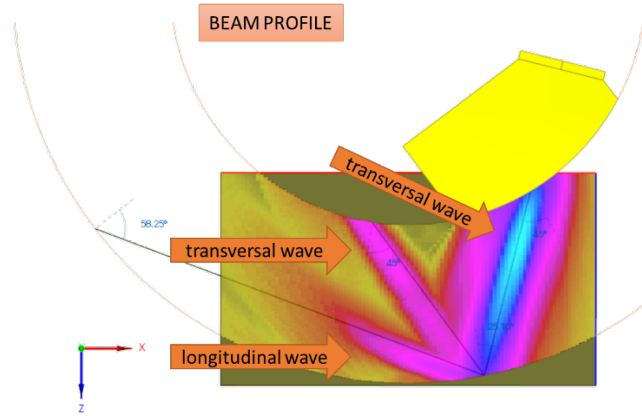


Figure 1. Example of the simulation of ultrasonic inspection simulations from the first secondment to CEA.

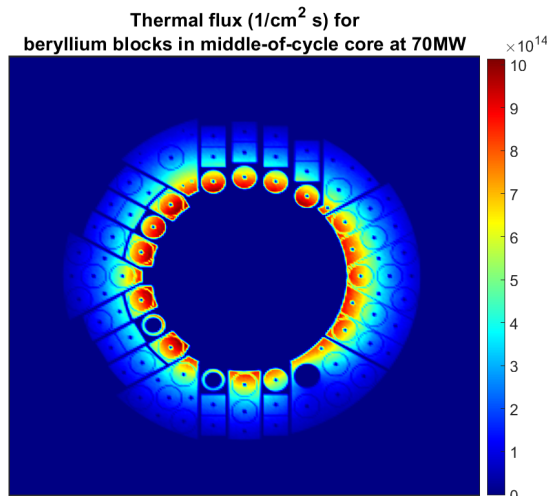


Figure 2. Example of the simulation investigation from the second secondment to CEA.

MeLoDIE II development

The MeLoDIE mechanical loading device destined for use at the JHR for in-pile fuel cladding irradiation creep testing is being developed within this project. VTT according to necessary modifications for exploitation in the LVR-15 reactor in Rez, Czech Republic. The eventual deployment of the device in LVR-15 would be part of

the OECD/NEA FIDES framework in the INCA proposal that will be coordinated by Centrum výzkumu Řež (CVR). Eventually, based upon both the experience gained and improvements, a third version will be adapted for experiments in JHR.

MeLoDIE I is an instrumented in-reactor creep experiment for fuel cladding tube specimen under controlled bi-axial loading to be carried out in the Osiris research reactor. The original MeLoDIE device was designed and delivered to CEA in 2012 for use in the OSIRIS Reactor at CEA Saclay in France. The MeLoDIE loading device is part of the sample holder installed in the CHOUCa capsule and the targeted test temperature will be 350 °C. The internal pressure of the zirconium tubular sample will be 160 bar.

The design of the MeLoDIE II device is based on the lessons learned from the use of the MeLoDIE I device. The main emphasis in the design is on changing the structure of the load frame so that it can be made simpler, lighter and stronger. Also, the redesign of the diameter measuring device is an important part of the design of the MeLoDIE II device. The structure of the loading frame must allow the use of different type of the DG (diameter gauge) methods. The device has been redesigned in JHR2022 project, and materials for the safety reports for use in LVR-15 reactor have been prepared in the project.

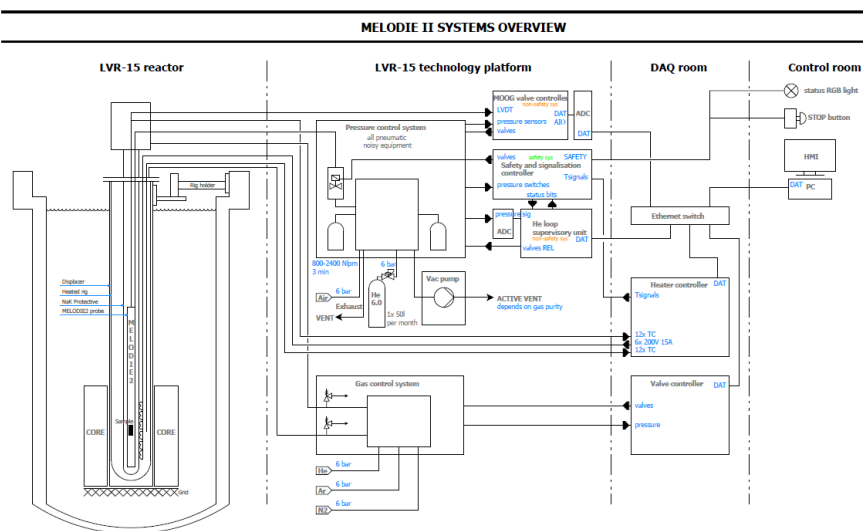
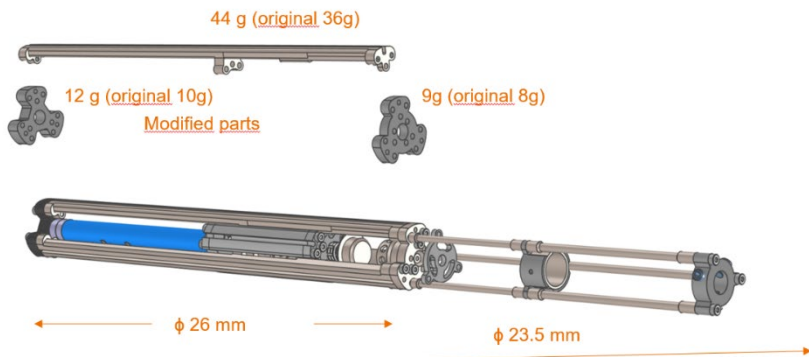


Figure 3. Overview of the systems associated with Melodie II.



VTT – beyond the obvious

Figure 4. New rig for Melodie II.

9.4 Radiological laboratory facility costs of the Centre for Nuclear Safety (RADCNS)

Wade Karlsen¹

¹VTT Technical Research Centre of Finland Ltd.
P.O. Box 1000, FI-02044 Espoo

Abstract

The infrastructure renewal of the radiological research infrastructure hosted by VTT is embodied in the new VTT Centre for Nuclear Safety. Funded in large part by SAFIR and KYT, in the ten years since the decision was made to renew the research infrastructure for radioactive materials at VTT, the new facility has been designed, built, equipped and successfully taken into use in support of nuclear safety research in Finland. While the facility can be considered fully underway, the investment aid provided through RADCNS is slated to continue through 2025. As a research laboratory, the facility continues to evolve going forward as well, thanks to continuous additional investments in equipment and facility improvements being made by VTT.

Introduction

In May 2012, the Finnish Ministry of Employment and the Economy (so-named at that time) published a report of the Committee for Nuclear Energy Competence in Finland (MEAE, 2012). The report not only addressed personnel resources, but also included research infrastructure competencies. It specifically endorsed the construction of a whole new radiological facility, with the additional goal of gathering most of the VTT Nuclear Safety research personnel scattered around the Otaniemi campus, into a single, compact facility called the VTT Centre for Nuclear Safety (CNS). Some rounds of vigorous discussions with the national stakeholders ultimately led to an agreement prompting VTT to go forward with such a new facility. Central to the agreement was a means to provide investment aid through the the Finnish State Nuclear Waste Management Fund (VYR).

The VTT CNS and its hot cell facility is a national infrastructure hosted by VTT, and is considered an important element in fulfilling the national requirements for independent competencies for domestic nuclear power generation. As such, from 2016 onward, VYR has supported the renewal of the radiological laboratory research infrastructure via three instruments: 1) the research and infrastructure instrument, generally comprised mainly of personnel, travel and associated research execution expenses; 2) a special allocation for supporting the VTT Ltd. Centre for Nuclear Safety radiological laboratory facility cost (RADCNS), and 3) a special allocation for supporting the VTT Ltd. Centre for Nuclear Safety radiological laboratory equipment investment expenses as investment aid (RADINFRA). All

three instruments have been jointly supported by the SAFIR (nuclear power plant safety) and KYT (nuclear waste management) research programmes.

The largest equipment investment was the hot cells enabling safe handling and orderly storage of activated and contaminated materials, shown in Figure 1. The other equipment investments have primarily focused on devices for materials testing and examination activities related to assessing the structural integrity of the materials from which safety-critical components are fabricated, and analyzing deficiencies and failures of such materials that may emerge during regular inspection campaigns. The latter in particular require rapid-response availability of appropriate equipment and resources, to minimize plant shut-down time. In consideration of the co-funding by the KYT program, and reflecting the broader applicability of the VTT CNS laboratories in the nuclear sector, several devices have also been procured for bentonite studies, analytical radiochemistry, and aerosol (sever accidents) research. Such devices were described in the Final Report of the SAFIR 2018 program (Karlsen, 2019), as well as in the Interim Report of the SAFIR 2022 program (Karlsen, 2021).



Figure 1. The hot cells of the VTT Centre for Nuclear Safety were installed in 2017 during the SAFIR2018 program.

Additional project activities have included the design, fabrication and installation of self-built research facilities, and materials and waste-handling and storage facilities, as well as the full laboratory infrastructure commissioning and ramp-up of operations for both reactor safety and nuclear waste management research. The SAFIR2022 LABWAST project in particular already looked to the future and eventual decommissioning of the facilities, with a particular focus on efforts to better utilize existing research materials, and to develop effective means of handling the radioactive waste generated over the long term during the operation of the facilities.

The latter goal is in line with the expectation set forth in the “Final Report of the National Co-operation Group on Nuclear Waste Management” (MAEA, 2019).

Utilization of investment aid

As introduced above, the RADINFRA investment aid instrument was provided for supporting the procurement of laboratory devices and equipment. In addition to the hot cell facilities themselves, investment aid enabled a number of pieces of equipment to be procured as a part of the infrastructure renewal. Many of these were procured simultaneous to building and equipping the new laboratory, being either moved into the readied laboratories from a temporary location, or directly installed into the new laboratory, or into the completed hot cells.

The last remaining large investment made in this manner, was the procurement of a custom-designed, Type-A certified, radioactive materials transport cask and its associated transportation and handling gear (Figure 2). This was ordered at the end of 2019, and following some unexpected delays, was ultimately delivered in the middle of 2021. Besides the cask and its lifting gear, the delivery included two IP-2 certified ISO-containers, primarily to house and transport the cask and its auxiliaries, but also suitable for IP-2 transports more generally.

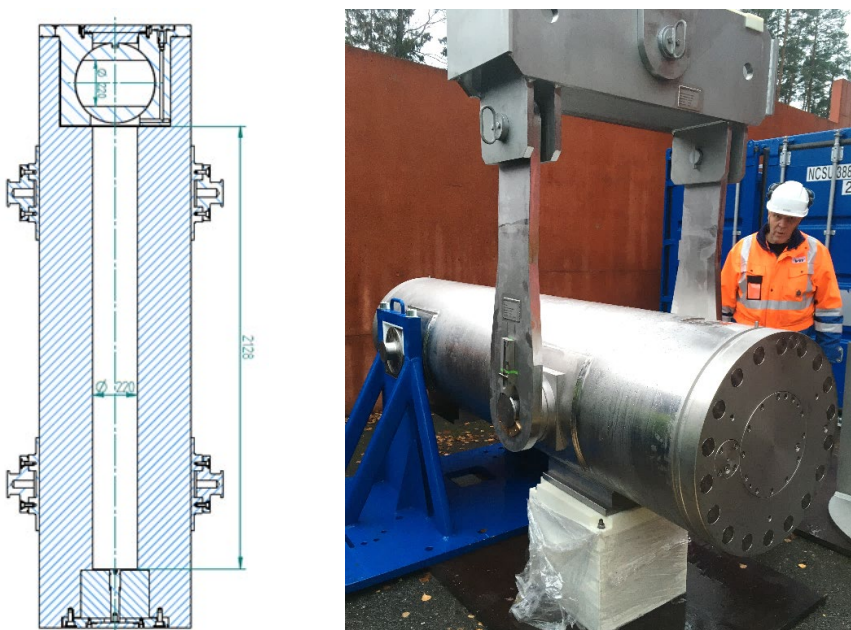


Figure 2. The DNT21 radioactive materials transport cask was the last procurement of the RADINFRA investment aid project. The Type A cask is dimensioned to accommodate all of the expected domestic RPV surveillance capsules.

The internal cavity of the cask was sized to accommodate all of the known surveillance specimen packages at the time, coming from all four types of plants foreseen to be employed in Finland, so is over 2 meters long and 22 cm in diameter. The technical features of the cask are described in more detail in the Proceedings of the Nuclear Science and Technology Symposium – SYP2022 (Karlsen, 2022). With an internationally recognized certification, the cask will also be employable in shipments from other countries as well, opening a whole range of new opportunities.

Another important investment made with investment aid, was a water filtration circuit for handling the radioactive debris produced by the EDM. As was described in the SAFIR Interim Report (Karlsen, 2019), VTT had conducted a series of piloting trials involving centrifuging, automatically reversible permanent filtration, and magnetic separation, which ultimately led to the decision to abandon the involvement of such additional devices in favor of simply utilizing disposable filter cartridges that are merely significantly smaller than the large OEM filter cartridges. The device was procured as a custom design from Platom Oy, and was delivered and installed in Q2/2021. As illustrated in Figure 3, it is comprised of a bank of three debris filters and one resin filter, featuring self-closing filter containers and means for dewatering the filters with compressed air. The system enables integral operation with the EDM and safe filter handling for changing the filters out. VTT is now designing and fabricating the needed shielding and remote-handling devices for handling the debris-laden filters and activated resins. The most appropriate packaging for final disposal will be determined in collaboration with the ultimate recipient of VTT's operational waste.



Figure 3. EDM auxiliary water loop for debris separation is comprised of a bank of three debris filters and one resin filter, featuring self-closing filter containers and means for dewatering the filters with compressed air.

Continued investments by VTT

Having fully utilized the investment aid allocation for equipment procurements, VTT is demonstrating its own commitment to ensuring that the radiological laboratory stays abreast of the latest technology, by making a variety of further investments since then. As shown in Table 1, the portfolio of device procurements beyond those made with investment aid has benefited all of the main activities in the laboratory, from the hot cells for irradiated structural materials testing, to the radiochemistry laboratories, and including the specialty laboratories for iodine filter testing, bentonite clay studies and aerosol experiments.

Table 1. Updates to CNS laboratory equipment portfolio by VTT in recent years

Device	Capabilities and primary purpose
Focused Ion Beam addition to SEM	Precision in situ sectioning of specimens in the analytical scanning electron microscopy, to explore surface crack propagation, oxide layers, etc. Also for extraction of specimens for analytical transmission electron microscopy.
Instrumented pendulum impact tester calibrator	Calibration of impact testing device to maintain accredited testing capabilities for e.g. surveillance specimens, since use of instrument with radioactive materials prevents use of external calibration services.
Gas analyzer	Quantifying from trace amounts up to high contents of hydrogen, oxygen and nitrogen in metals via quadrupole mass spec. (for isotopic differentiation) and thermal conductivity detection.
Gamma spectrometer	Determining the gamma-emitting nuclide constituents of a sample, essential for reactor dosimetry, and useful in a variety of radiochemistry experiments and in rad-waste characterization.
Aerosol generator	Generator and accompanying photomultiplier are used in the iodine laboratory set-up employed for testing the filters of the exhaust stacks of NPP containments.
Aerosol monitors	For continuous and simultaneous online measurement of aerosol mass concentration at inlet and outlet of processes, as a part of overall aerosol laboratory activities such as severe accident emissions modelling.
Radiochemistry specimen pyrolyzer	For evaporating and oxidizing difficult solid specimens in order to measure radionuclide concentrations such as tritium from substances such as the concrete of decommissioned radiological or nuclear facilities.
Mobile Raman spectroscope	For investigating molecular chemical composition in real-time, such as in uranium-oxide dissolution experiments for second phase identification. Fiber-optic cable detector also enables testing in oxygen free environments.
Gradient Ion Chromatography System	Used on its own for anion analysis, or connected to the HR-ICP-MS (in the CNS clean-room facility), for full ionic speciation analyses. Ion speciation analyses can separate and quantify different molecular versions of a compound.
Heating pack for triaxial loading cell	For the existing triaxial loading cell, this addition enables thermomechanical testing of clays, such as bentonite as backfill for spent nuclear fuel storage canisters in a deep underground repository.

Device	Capabilities and primary purpose
Syringe pump and environmental chamber	For compaction of powders with controlled moisture contents, to produce clay specimens such as bentonite for subsequent thermomechanical testing.

Constant capabilities development

Following the 2019 LABWAST project, further development of personnel skills, competencies and capabilities in hot laboratory operations was funded by VYR mainly through the BRUTE project, and other SAFIR and KYT projects utilizing the CNS facilities. Table 2 shows the KYT and SAFIR projects in the 2022 program that utilized the capabilities provided in the laboratories.

Many people are working in the projects utilizing the CNS infrastructure. Currently there are over 40 research scientists, engineers and technicians with personal film dosimeters for the CNS, showing that they work in the laboratories for more extensive periods. Meanwhile, almost 70 different VTT staff members are listed in the e-dosimeter register, indicating they enter the laboratory for one purpose or another.

Table 2. Projects funded by KYT and SAFIR in the 2019-2022 period that utilize the research and testing infrastructure in the CNS

Short name	Topic	Relevant Infrastructure
BRUTE	Barsebäck RPV material used for true evaluation of embrittlement	Hot cells, specimen fabrication, mechanical testing, electron microscopy
LABWAST	Handling of radiological facility operational waste	Supporting processes for all areas of research and testing of radioactive materials
JHR	Participation in Jules Horowitz Reactor project	Preparations for PIE of JHR irradiations
ELIAS, FENIX	Aging and environmentally assisted cracking of NPP component materials	Specimen fabrication, autoclave testing, electron microscopy
MANTRA	Fission product transport analysis and capture in severe accidents	Aerosol laboratory, analytical radiochemistry
ANSA	Analytical severe accident research	Aerosol laboratory, analytical radiochemistry
PORA	Nuclear fuel microstructure and radium solubility	Fissile materials handling, analytical radiochemistry
INFLAME	Interdisciplinary Research on Fuels and Materials	Fissile materials handling, furnace treatment, electron microscopy
SUCCESS	Sulfide-induced stress corrosion cracking in copper	Autoclave laboratory
BROCTIO	Bentonite-rock interaction	Bentonite testing facilities

Short name	Topic	Relevant Infrastructure
DEMONI	Decommissioning and final disposal studies on steel and concrete materials	Microscopy and analytical radiochemistry

In addition to SAFIR and KYT projects, during the 2019-2022 program years, VTT has funded 190 person months of skills development, to improve the equipment and devices in the laboratory and utilize them more safely and effectively. Examples of some of those capabilities include the following:

- Precision opening of surveillance capsules with different geometries by remotely-operated in-cell CNC milling machine.
- Remote manufacturing of small C(T) test specimens by utilising both the in-cell CNC milling machine and EDM
- Utilization of the in-cell model Z250 electro-mechanical tensile testing device to accurately test mini-CT specimens over a range of temperatures, including development of several devices to facilitate remote manipulation of such small specimens.
- In-cell measurement of fracture toughness specimen deformation by optical means.
- Refinement of laser extensometer employment in comparison to clip-type extensometers for measuring strain during mechanical testing.
- Calibration of thermocouples employed in mechanical testing.
- Calibration of instrumented impact testing probe.
- Employment of multi-axial robotic arm for careful installation of small test specimens into mechanical testing frame.
- Employment of machine vision technology for more rapid and accurate fracture quantification.
- Deployment and utilization of remotely-operated laser-engraving device for durable labelling of radioactive specimens fabricated in the hot cell.
- Employment of laser engraving equipment for precise extraction of small specimens from dosimeter materials for reactor dosimetry by gamma spectroscopy.
- Proficiency in remotely-operated mechanical grinding and polishing equipment for metallography of active specimens.
- Preparation of very small specimens of active materials for transmission electron microscopy (TEM), involving in-cell grinding and punching and out-of-cell finish grinding and electropolishing.
- Development, deployment and demonstration of special set-up for novel high-temperature fuel sintering studies.
- Utilization and proficiency of newly-procured alpha spectrometer.
- Utilization and proficiency of newly-procured ion chromatograph in radiochemistry applications.
- Analysis of NORM (naturally occurring radioactive materials) nuclides by combining radioanalytical methods and equipment such as radiochemical separation methods, gamma, beta and alpha spectrometry, and HR ICP-MS.
- Measurement of the gas pressure of voids and in-situ deformation measurement of bentonite specimens.

- Thermomechanical testing of bentonite at higher temperature with a newly-procured triaxial cell for the universal mechanical testing.
- Proficiency in utilization of newly-procured glow-discharge optical emission spectroscope for precision chemical analysis of solids, also as a function of depth from surface.
- Development and deployment of dedicated setup for generation and collection of radioactive iodine for testing exhaust filters of nuclear power plant containment.
- Utilization of ion-selective electrode technology in experiments simulating the aerosol behavior of severe accidents involving the primary circuit and/or containment pool.
- Adaptation of the aerosol testing set up and development of the methods for testing severe accident scenarios involving iodine.
- Measurement of iodide (I^-) by Reagent-Free Ion Chromatography, for comparing to results with already-qualified Ion Selective Electrode method.
- Deployment and utilization of hot cell mounted gamma spectrometer for recording the spectra of material transports received into the hot cell facilities.
- Management of nuclear materials inventories in accordance with safeguards legislation and periodic inspection regimes.
- Handling of large radioactive transport cask in conjunction with all of its auxiliaries for road transport, lifting and turning.
- Development of technological solutions for separating the cutting debris from the electric-discharge machine (EDM) waste stream.
- Development and deployment of EDM waste handling solution for captured cutting debris and ion exchange resins.
- Operational radioactive waste sorting and minimization methods.
- Material-specific nuclide vector assessment of realized and postulated future operational radioactive waste.

A decade on

Ten years after first deciding to pursue the building of a totally new laboratory, activities in the new facilities are fully underway. From a technical aspect, the equipment and devices are fully operational. An important milestone illustrating this was when the first proper surveillance test series was taken into the new facility. The shipment was received from the plant, unloaded directly into the shielded facility, and the surveillance specimens, dosimetry coupons, and thermal monitors were recovered by machining open their container in a fully remote fashion. The in-cell CNC device custom manufactured by Finnish company Metecno, shown in Figure 4, was instrumental in that operation. Thanks to the modern hot cells, the total worker dose accrued for those activities was zero!

Currently there are over fifty different projects on-going that utilize some aspect of the infrastructure in the CNS, comprising contract services and publicly-funded research, involving both domestic and international clients and financers. About a dozen projects funded by Euratom and NKS demonstrate how the infrastructure is also being leveraged to facilitate international collaboration, which is an efficient way

to also build the knowledge and know-how for the benefit of domestic radiation safety.



Figure 4. The in-cell CNC milling machine was instrumental for the precision cutting required to open the first surveillance capsule for testing in the new hot cell.

While continuing to increase the overall number of active users of the facility, efforts still continue to make the facilities and their capabilities more widely known to the global nuclear community as a whole. The completed facility has been visited by thousands of people, from organizations around the globe, receiving positive feedback from the likes of IAEA Director General Rafael Grossi and U.S. NRC Commissioner Annie Caputo, as well as fellow research scientists, experts and clients in the topics of study in the CNS.

One last hurdle

Since growth is expected primarily from international activities, the rational handling of the waste associated with normal research and testing activities in the radiological facility is the final issue being tackled for the CNS operations. As described in the Final Report of the National Cooperation Group on Nuclear Waste Management, the activities in the facilities can produce radioactive wastes for which no individual customer can be readily identified, to whom the wastes could be returned. Additionally, returning wastes abroad is relatively expensive and labour-intensive, and not possible or practical in all cases. Other countries are also mainly reluctant to accept such returned wastes. For that reason, VTT is preparing a tender for execution in 2023, with the aim to secure a domestic waste repository. When a service provider is selected and the appropriate agreements made, it is foreseen that the waste handling of the facility's operational waste can be substantially streamlined and standardized to a single waste acceptance criterion.

Looking to the future

With more-or-less normal operations now underway in the CNS, the overall reach of activities is being broadened to further grow the order books. This is illustrated by several substantial new investments that are currently underway.

Firstly, to meet the requirements of an important international client, while expanding the capacity for fracture toughness testing, VTT has procured an Instron servo-hydraulic testing machine and associated environmental chamber. The device is the first new device procured for installation in an in-cell position, which will actually expand the capacity of the hot cell further, for greater throughput. Simultaneously, additional tools for the device were ordered to enable low-cycle fatigue testing of irradiated materials, to meet requirements brought by entering the fusion materials testing arena.

Fusion materials research and testing are also in mind with VTT's plans to procure a Time-of-flight Secondary Ions Mass Spectrometer. The substantial scientific potential of this device is evident in that VTT was awarded a FIRI investment grant for its procurement. Although the device has broad applications in other nuclear materials research, and across many other sectors at VTT as well, it will be installed in the CNS laboratory so that tritium-containing Be-materials can be tested for fusion reactor first wall tile applications.

Another strategy to increase the utilization of the CNS facilities, is by consolidation and collaboration with VTT's other research and testing activities. Closely related to the irradiated nuclear materials research, the water chemistry and autoclave testing activities for non-irradiated nuclear and conventional materials are moving to space made available in the CNS laboratory.

More creatively, synergy is also being leveraged by joint procurement of a new inductionally-coupled plasma mass spectrometer to replace the current one located in the CNS dedicated clean-room facility. The new device will also be used to support silicon-wafer quality assurance activities of VTT's Micronova laboratory, which have formerly had to send test materials to the U.S. for analysis.

Topics also continue to evolve, and while reactor materials testing and characterization continues to be an important activity, applications involving SMR technology and additively manufactured materials are growing in interest. Likewise, while bentonite and other final repository-related research still continues, topics more related to fuel itself, and to nuclear facility decommissioning are getting increased attention in the project portfolio.

Summary and conclusions

Since the first design drafts of the CNS radiological laboratory were put on paper a little over a decade ago, the site has been prepared, the buildings constructed, the hot cells installed and laboratories equipped and taken into use. The materials testing and microscopy facilities are in use for reactor pressure surveillance testing and NPP component failure analyses, the radiochemistry laboratories have served

a variety of topics beyond just answering important questions related to the spent fuel final repository safety case, and important data has been produced related to nuclear fuel and severe accident scenarios. The number of experts utilizing the facility have increased along with the number and variety of projects being executed in the facility for both the KYT and SAFIR programs as well as international collaboration in EURATOM. And VTT continues to invest in new devices to stay at the forefront, while investing in developing its own personnel. As such, fuller utilization of the new facility is now limited more by the availability of personnel resources, than by a lack of adequate tools. And so, considering that just over a decade ago the CNS site was still a quiet, wooded corner of the Otaniemi campus, it is exciting to consider where things could be in another decade from now!

Acknowledgment

VTT wishes to acknowledge the important support of the Finnish Nuclear Waste Management Fund, VYR for making the infrastructure renewal financially possible.

References

- Aurela, J., Melkas, E., Avolahti, J. "Report of the Committee for Nuclear Energy Competence in Finland," Chair Riku Huttunen, Secretaries Jorma Aurela, Eriika Melkas until 3/2011 and Jaana Avolahti from 3/2011. Published by Ministry of Employment and the Economy, May 2012, ISSN 1797-3562, ISBN 978-952-227-600-1, pp. 299.
- Karlsen, W. "7.4 Radiological laboratory commissioning (RADLAB)" in SAFIR2018 – The Finnish Research Programme on Nuclear Power Plant Safety 2015-2018, eds. Jari Hämäläinen & Vesa Suolanen, March 2019, ISBN 978-951-38-8682-0, p.471-492.
- Karlsen, W. "9.4 Pre-emptive reduction of radiological laboratory legacy waste (LABWAST)" in SAFIR2022 – The Finnish Research Programme on Nuclear Power Plant Safety 2019-2022, eds. Jari Hämäläinen & Vesa Suolanen, March 2021, ISBN 978-951-38-8743-8, p. 457-472.
- Linda Kumpula, Outi Slant, "Final Report of the National Cooperation Group on Nuclear Waste Management", published by the Ministry of Economic Affairs and Employment TEM, reports 2019:45, <http://urn.fi/URN:ISBN:978-952-327-441-9>
- Karlsen, W., "Procurement of a New A-type Transport Cask for Radioactive Structural Materials", Suomalaisen Ydintekniikan Päivät 2022 – SYP2022. ats-fns.fi/images/files/2022/syp2022/papers/wade_karlsen_paper.pdf, 2022.
- Karlsen, W. "The VTT Centre for Nuclear Safety, up-grading Finnish nuclear safety research", ATS Ydintekniikka 2/2022, Vol. 51, p. 44-47.

Title	SAFIR2022 – The Finnish Research Programme on Nuclear Power Plant Safety 2019–2022 Final Report
Author(s)	Jari Hämäläinen & Vesa Suolanen (eds.)
Abstract	<p>The Finnish Research Programme on Nuclear Power Plant Safety 2019–2022, SAFIR2022, continues a series of Finnish national research programmes in nuclear energy that started in 1989. The programmes were initially carried out separately in the fields of operational aspects of safety (YKÄ 1990–1994, RETU 1995–1998) and structural safety (RATU 1990–1994, RATU2 1995–1998, OHA 1995–1998), and then in combined programmes (FINNUS 1999–2002, SAFIR2003–2006, SAFIR2010 2007–2010, SAFIR2014 2011–2014, SAFIR2018 2015–2018). Simultaneously research has been carried out in the national nuclear waste management programmes (KYT2022 runs in parallel with SAFIR2022).</p> <p>SAFIR2022 consists of four main research areas: (1) Overall safety and systemic approach to safety; (2) Reactor safety; (3) Structural safety and materials; and (4) Research infrastructure. Research has been carried out in 36 projects that are guided by eight reference groups. The research results of the projects are published in scientific journals, conference papers and research reports.</p> <p>The programme management structure consists of the Management Board, four steering groups managing the research areas, eight reference groups, and programme administration. SAFIR2022 Management Board has representatives of the Radiation and Nuclear Safety Authority (STUK), the Ministry of Economic Affairs and Employment (MEAE), Fennovoima Oy, Fortum, Teollisuuden Voima Oyj (TVO), Technical Research Centre of Finland Ltd (VTT), Lappeenranta-Lahti University of Technology (LUT), Aalto University (Aalto), Tampere University (TAU) and the Swedish Radiation Safety Authority (SSM).</p> <p>Research in the programme has been carried out by VTT, LUT, Aalto, Finnish Meteorological Institute (FMI), Finnish Institute of Occupational Health (FIOH), TAU and RISE Research Institutes of Sweden. A few subcontractors have also contributed to the work in the projects.</p> <p>This report has been prepared by the programme management in cooperation with the project leaders and project staff.</p> <p>More information on SAFIR2022 can be found on the programme website http://safir2022.vtt.fi/. Finnish national research on nuclear power plant safety continues in SAFER2028 programme for the years 2023–2028, see https://safer2028.fi/.</p>
ISBN, ISSN, URN	ISBN 978-951-38-8776-6 ISSN-L 2242-1211 ISSN 2242-122X (Online) DOI: 10.32040/2242-122X.2023.T414
Date	March 2023
Language	English
Pages	618 p.
Name of the project	The Finnish Nuclear Power Plant Safety Research Programme 2019–2022, SAFIR2022
Commissioned by	MEAE
Keywords	nuclear safety, safety management, nuclear power plants, human factors, safety culture, automation systems, control room, nuclear fuels, reactor physics, core transient analysis, thermal hydraulics, modelling, severe accidents, structural safety, construction safety, risk assessment, research infrastructure
Publisher	VTT Technical Research Centre of Finland Ltd P.O. Box 1000, FI-02044 VTT, Finland, Tel. 020 722 111, https://www.vttresearch.com

SAFIR2022 – The Finnish Research Programme on Nuclear Power Plant Safety 2019-2022

Final Report

ISBN 978-951-38-8776-6
ISSN-L 2242-1211
ISSN 2242-122X (Online)
DOI: 10.32040/2242-122X.2023.T414



beyond the obvious